ICPPP21 International Conference on Photoacoustic and Photothermal Phenomena

June 19 - 24, 2022
Bled, Slovenia

BOOK OF ABSTRACTS

https://indico.ung.si/event/5/

ORGANIZERS:

- UNIVERSITY OF NOVA GORICA
- UNIVERSITY OF LJUBLJANA
- JOŽEF STEFAN INSTITUTE

University *of Ljubljana*

Jožef Stefan Institute

Abtracts of the ICPPP21 Conference 2022

ICPPP21
19 – 24 June 2022, Bled, Slovenia

Organizing and Programme Committee

Chair:
Mladen Franko (University of Nova Gorica, Slovenia)

Vice-Chairs:
Dorota Korte (University of Nova Gorica, Slovenia)
Boris Majaron (Jožef Stefan Institute; University of Ljubljana, Slovenia)
Rok Petkovšek (University of Ljubljana, Slovenia)

Members:
Hanna Budasheva (University of Nova Gorica, Slovenia)
Humberto Cabrera (The Abdus Salam International Centre for Theoretical Physics, Italy)
Aljaž Čujec (University of Nova Gorica, Slovenia)
Petra Makorič (University of Nova Gorica, Slovenia)
Claudia D'ercole (University of Nova Gorica, Slovenia)
Petra Makorič (University of Nova Gorica, Slovenia)
Griša Močnik (University of Nova Gorica, Slovenia)
Nives Štefančič (University of Nova Gorica, Slovenia)
Iain R. White (University of Nova Gorica, Slovenia)
Nadja Lovec Santaniello (University of Nova Gorica, Slovenia)
Neža Golmajer Zima (Jožef Stefan Institute, Slovenia)
Martina Bergant Marušič (University of Nova Gorica, Slovenia)
Maria Chiara Magnano (University of Nova Gorica, Slovenia)
Martina Bergant Marušič (University of Nova Gorica, Slovenia)
Swapna Nair Sindhu (University of Nova Gorica, Slovenia)

International Scientific Committee:
Juan José Alvarado-Gil (Mexico)
Nelson Astrath (Brazil)
Bertrand Audoin (France)
Mauro L. Baesso (Brazil)
Jerzy Bodzenta (Poland)
Peter Burgholzer (Austria)
Mihai Chirtoc (France)
Nicu D. Dadarlat (Romania)
Gerald Diebold (USA)
Stanislav Emelianov (USA)
Mladen Franko (Slovenia)
Christ Glorieux (Belgium)
Xinxin Guo (Canada)
Vitaliy Gusev (France)
Daniel Lanzillotti Kimura (France)
Bincheng Li (China)

International Steering and Advisory Board:
Walter Arnold (Germany)
Stephen E. Bialkowski (USA)
Gabriel Bilmes (Argentina)
Paolo G. Bison (Italy)
Silvia Braslavsky (Germany)
Edson Corrêa da Silva (Brazil)
Danièle Fournier (France)
Yuri Gurevich (Mexico)
Frans J.M. Harren (Holland)
Peter Hess (Germany)
Alexander A. Kolomenskii (USA)
Jean-Claude Krapez (France)
Junyan Liu (China)
John F. McClelland (USA)
Humphrey Maris (USA)
Fulvio Mercuri (Italy)

ICPPP21 SILVER SPONSOR

ICPPP21 SILVER SPONSOR

ICPPP21 SILVER SPONSOR

ICPPP21 SILVER SPONSOR

ICPPP21 SILVER SPONSOR

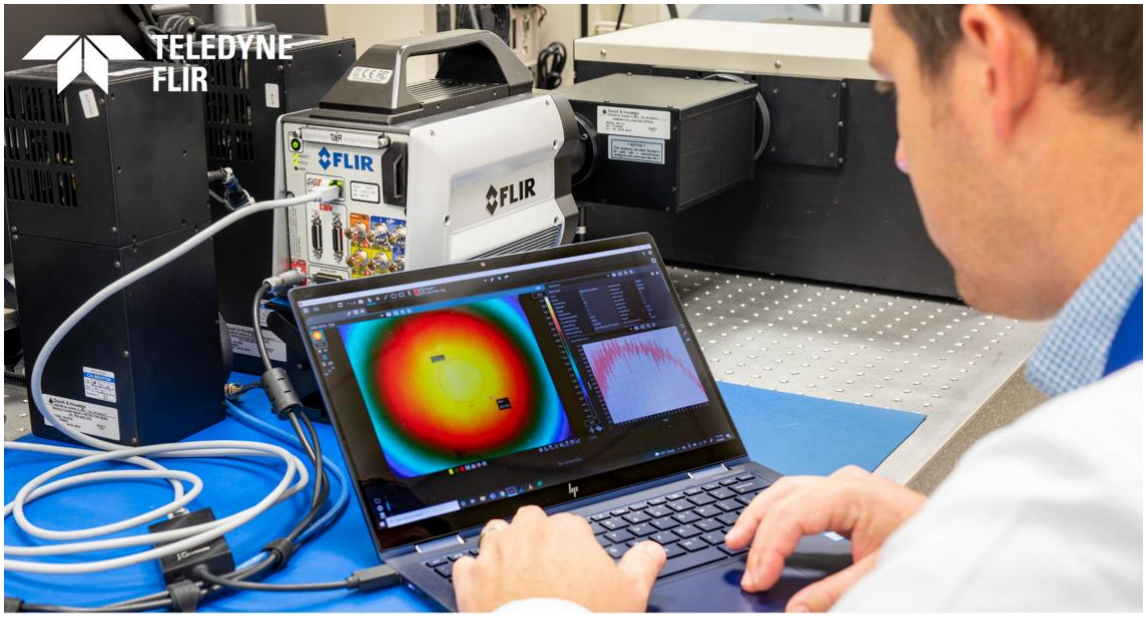

ICPPP21 BRONZE SPONSOR

MEDIS

ICPPP21 BRONZE SPONSOR

ICPPP21 BRONZE SPONSOR

ICPPP21 Exhibitors and Donators:

KEFO d.o.o. | Brnčičeva 29, p.p. 4905, Ljubljana, Slovenia

Chemass d.o.o., Baznikova ulica 2, SI-1000 Ljubljana

InnoLas Laser GmbH, InnoLas Photonics GmbH, Justus-von-Liebig-Ring 8, 82152 Krailling, Germany

Omega d.o.o., Dolinskova 8, 1000 Ljubljana, Slovenia

ORAL PRESENTATIONS

CONTENTS – Oral Presentations

IPPA Awards

Photoacoustic and photothermal: progress to date towards fostering multidisciplinarity
Baesso ML ..... - 8 -

Photothermal lens and photothermal mirror techniques: effects and applications
Lukasievicz GVB ..... - 9 -

Validated and potential mechanisms for photothermal actuators, modulators and transducers
Glorieux C ..... - 10 -

Optical tracking of ultrafast surface vibrations
Wright OB ..... - 11 -

01 Thermophysical Properties

Photothermal and photoacoustic exploration of relaxation in supercooled liquids
Liu L *et al.* **(PLENARY SESSION with Christ Glorieux)** ..... - 13 -

Thermal properties and critical behaviour in rare-earth based magnetocaloric materials
Oleaga A *et al.* **(KEYNOTE by Alberto Oleaga)** ..... - 15 -

Thermal characterization of composites and layered systems: Challenges and opportunities
Alvarado-Gil JJ **(KEYNOTE by Juan Jose Alvarado Gil)** ..... - 18 -

Decoupling bulk and surface radiation forces in a dielectric liquid
Astrath NGC *et al.* **(KEYNOTE by Nelson Astrath)** ..... - 19 -

Advantages and disadvantages of photothermal measurement methods estimating thermal transport properties (such as thermal conductivity, diffusivity and boundary resistance) of multilayered samples
Mikaeeli A *et al.* (presented by Ameneh Mikaeeli) ..... - 22 -

Photothermal study of structural relaxation in supercooled glycerol by fast fluorescence thermometry
Wei Q *et al.* (presented by Qi Wei) ..... - 24 -

Photopyroelectric investigation of the *trans-cis* isomerization effect on phase transitions of a liquid crystalline azobenzene
Paoloni S *et al.* (presented by Stefano Paoloni) ..... - 27 -

Photothermal characterization of obsidian
Martínez-Garcia MM *et al.* (presented by Fernando Cervantes-Alvares) ..... - 29 -

Pulsed thermography in the assessment of in-plane thermal diffusivity: aperiodic, periodic and random patterns
Bison P *et al.* (presented by Paolo Bison) ..... - 30 -

Structural, thermal, and electrical transport correlations in p-type Si as a function of carrier concentration: the effect of intrinsic and extrinsic defects
Martinez-Hernandez HD *et al.* (presented by Harol D. Martinez-Hernandez) ..... - 33 -

Characterization of TiO_2 thin films deposited on silicon membranes using neural networks
Djordjević KLj *et al.* (presented by Mioljub Nešič) ..... - 35 -

02 Materials Research and Characterization

Mid-infrared photothermal microscopy
Cheng J-X **(PLENARY SESSION with Ji-Zin Cheng))** ..... - 38 -

Photoacoustic and photothermal methods towards the characterization of solar energy conversion technologies: progress to date
Baesso ML *et al.* **(KEYNOTE by Mauro L. Baesso)** ..... - 40 -

Thermographic imaging for applications in cultural heritage
Mercuri F *et al.* **(KEYNOTE by Fulvio Mercuri)** ..... - 42 -

Front detection laser-spot active infrared thermography for thermal characterisation of insulating solids
Bedoya A *et al.* **(KEYNOTE by Ernesto Marin-Moares)** ..... - 46 -

Refractive index changes in solid state laser materials
Catunda T *et al.* **(KEYNOTE by Tomaz Catunda)** ..... - 48 -

Topological insulator nanoparticles – material with prospect for photo-thermal applications
Belec B *et al.* (presented by Blaž Belec) ..... - 51 -

3D imaging of water ice under high-pressure non-hydrostatic load by time-domain Brillouin scattering
Sathyan S *et al.* (presented by Saumel Raetz) ..... - 53 -
Real-time monitoring of light-induced curing of organosilicate glass low-k films by time-domain Brillouin scattering
Sathyan S *et al.* (presented by Samuel Raetz) ..... - 55 -
High-frequency heterodyne lock-in carrierography (HeLIC) and thermography (HeLIT) imaging of optoelectronic materials
Melnikov A *et al.* (presented by Alexander Melnikov) ..... - 57 -
Characterization of photocarrier properties and their associated trap-state transport parameters of CdZnTe using heterodyne lock-in carrierography imaging and deep level photothermal spectroscopy
Mandelis A *et al.* (presented by Andreas Mandelis) ..... - 60 -
Thermal and optical properties of mixed CdTe and ZnTe based crystals
Singh D *et al.* (presented by Diksha Singh) ..... - 63 -
Photothermal spectroscopy of $Cd_{1-x}Be_xTe$ mixed crystals
Zakrzewski J *et al.* (presented by Jacek Kakrzewski) ..... - 64 -
Simultaneous thermal and optical characterization of semiconductor materials exhibiting high optical absorption by photopyroelectric spectroscopy
Strzałkowski K *et al.* (presented by Karol Strzałkowski) ..... - 66 -
Correctness of assessment of thermophysical properties of solvents by dual-beam thermal-lens spectrometry
Khabibullin VR *et al.* (presented by Vladislav R. Khabibullin) ..... - 67 -
Combining micro- and macroscopic approaches in a model of a thermal lens experiment in disperse media
Vyrko EA *et al.* (presented by Evgeny Vyrko) ..... - 70 -
Heat transport in polycrystalline oxide thin films
Kaźmierczak-Bałata A *et al.* (presented by Kaźmierczak-Bałata) ..... - 73 -
Characterization of smart and biocompatible materials based on chitosan:cellulose composites containing sporopollenin exine capsules
Budasheva H *et al.* (presented by Hanna Budasheva) ..... - 75 -
Thermoelastic and optical properties of PLLA estimated by photoacoustic measurements
Nešić MV *et al.* (presented by Mioljub Nešić) ..... - 77 -

03 Laser Ultrasonics

Driving coherent phonons and magnons by light
Scherbakov AV **(KEYNOTE by Alexev V. Scherbakov)** ..... - 80 -
Imaging acoustic waves in 2D confined by hook or by crook
Wright OB **(KEYNOTE by Oliver Wright)** ..... - 83 -
Optical generation and detection of GHz longitudinal and transverse acoustic waves in transparent medium with metallic grating structure
Matsuda O *et al.* **(KEYNOTE by Osamu Matsuda)** ..... - 84 -
In-situ laser-ultrasonic characterization of plates through zero-group-velocity and thickness resonance
Watzl G *et al.* (presented by Georg Watzl) ..... - 86 -
Zero-Group-Velocity Lamb mode's behaviour in the vicinity of a thickness step
Kiefer DA *et al.* (presented by Sylvain Mezil) ..... - 88 -
Zero-group velocity resonance spectroscopy for bulk acoustic wave resonator characterization
Yan G *et al.* (presented by Guqi Yan) ..... - 90 -
Laser-ultrasonic characterization of plates based on discrete points in their Rayleigh-Lamb dispersion spectra
Grünsteidl C *et al.* (presented by Clemens Grünsteidl) ..... - 92 -
Giant photoelasticity of the superlattice polaritons for laser ultrasonics
Kobecki M *et al.* (presented by Michal Kobecki) ..... - 94 -
Defect detection in additively manufactured parts by laser ultrasonic tomography
Reitinger B *et al.* (presented by Bernhard Reitinger) ..... - 97 -
Measurement of the acoustic loss at GHz frequencies using laser-excited plate resonances
Ryzy M *et al.* (presented by Martin Ryzy) ..... - 99 -
Reaching the shock limit via synchronous laser ultrasonics
Deschamps J *et al.* (presented by Jude Deschamps) ..... - 101 -

Broadband high-frequency laser ultrasound generation and applications towards biological membranes
Serpa C *et al.* (presented by Carlos Serpa) ..... - 103 -
Optical and ultrasound imaging of shear wave generated by laser induced cavitation bubbles
Ghasemian SI *et al.* (presented by Izak Ghasemian) ..... - 105 -
Ultrasonic emitter based on photoacoustic polymer graphene nanocomposites
Vella D *et al.* (presented by Danielle Vella) ..... - 106 -
Laser-induced shock wave expanded nanobubbles in spherical geometry
Horvat D *et al.* (presented by Darja Horvat) ..... - 108 -
Microscale shockwave characterization following dual threshold laser-induced breakdown
Mur J *et al.* (presented by Jaka Mur) ..... - 110 -
Ultrafast measurement of laser induced shockwaves
Petelin J *et al.* (presented by Žiga Lokar) ..... - 112 -

05/09 Infrared Thermography & Non-destructive Evaluation

Modalities of photothermal coherence tomography for enhanced three-dimensional imaging contrast, resolution and quantitative depth profilometry
Mandelis A **(SPECIAL PLENARY SESSION with Andreas Mandelis)** ..... - 115 -
Imaging thermal properties by super resolution far-infrared thermography
Bouzin M **(KEYNOTE by Margaux Bouzin)** ..... - 118 -
Non-destructive evaluation of materials in motion using laser-spot thermography
Mendioroz A **(KEYNOTE by Arantza Mendioroz)** ..... - 120 -
Detectability of noisy signals for photothermal and photoacoustic reconstruction
Burgholzer P **(KEYNOTE by Peter Burgholzer)** ..... - 123 -
Photothermal radiometry data analysis with machine learning
Xiao P **(KEYNOTE by Perry Xiao)** ..... - 126 -
Automatic inspection of surface breaking cracks using laser scanning thermography
Pech-May NW *et al.* (presented by Nelson W. Pech-May) ..... - 127 -
New options for finding defects on and below the surface using structured laser thermography
Ziegler M *et al.* (presented by Mathias Zielger) ..... - 128 -
Towards hyperspectral in-situ temperature measurement in metal additive manufacturing
Altenburg SJ *et al.* (presented by Simon J. Altenburg) ..... - 129 -
Photoacoustic reconstruction formulas exploiting known location of 2D initial pressure
Dreier F *et al.* (presented by Florian Dreier) ..... - 131 -
Spatio-temporal imaging of the thermally hardened surface layer in steel parts
Haderer W *et al.* (presented by Wolfgang Haderer) ..... - 133 -
Restriction on the laser wavelengths for imaging of metal/epoxy interfaces by time-domain Brillouin scattering
Sathyan S *et al.* (presented by Sandeep Sathyan) ..... - 135 -
Application of all-optical and non-destructive laser ultrasonic in imaging of CFRP subsurface defects
Song P *et al.* (presented by Peng Song) ..... - 137 -
Lock-in thermography of compressed metal powder metallurgy in pre-sintered state as flaw preventive non-destructive evaluation modality
Sebastian K *et al.* (presented by Alexander Melnikov) ..... - 139 -
Three-dimensional reconstruction of subsurface absorbing structures in human skin from photothermal radiometric records
Cvetko T *et al.* (presented by Boris Majaron) ..... - 141 -

06 Ultrafast Phenomena & Spectroscopy

Novel nanophononic structures and devices
Esmann M *et al.* **(PLENARY SESSION with Daniel Lanzillotti Kimura)** ..... - 144 -
Time-domain Brillouin scattering in paraxial sound and light beams: Contra-intuitive features
Gusev VE **(KEYNOTE by Samuel Raetz)** ..... - 146 -
Ultrafast photoacoustic assessment of mechanical properties in InAs nanowires
Gandolfi M *et al.* (presented by Francesco Banfi) ..... - 148 -

Detection of coherent acoustic phonons in thin gold films by surface plasmon resonance
Noll F *et al.* (presented by Felix Noll) ..... - 149 -
Temperature dependent elastic properties and glass transition of nanometric PMMA films by picosecond ultrasonics
Brick D *et al.* (presented by Mike Hettich) ..... - 151 -
Development of models for the study of heat transport in ultra-thin layers by transient grating spectroscopy
Aguilar-Jimenez JA *et al.* (presented by Jose A. Aguilar-Jimenez) ..... - 153 -

07 Biomedical imaging and applications

Three-dimensional quantitative optoacoustic tomography
Oraevsky AA **(PLENARY SESSION with Alexander Oraevsky)** ..... - 156 -
A photoacoustic-ultrasound transmission breast tomography system: system overview and first imaging results
Dantuma M *et al.* **(PLENARY SESSION with Srirang Manohar)** ..... - 160 -
Structured illumination photoacoustic imaging using Hadamard encoding
Paltauf G *et al.* **(KEYNOTE by Guenter Paltauf)** ..... - 162 -
Triple modality transmission-reflection optoacoustic ultrasound (TROPUS) computed tomography of small animals
Lafci B *et al.* **(KEYNOTE by Daniel Razansky)** ..... - 165 -
Molecular-specific imaging of tissue with photo-thermal optical coherence tomography
Salimi SH *et al.* **(KEYNOTE by Nima Tabatabaei)** ..... - 168 -
Camera based photoacoustic imaging: sensitivity and resolution improvement
Nuster R *et al.* (presented by Robert Nuster) ..... - 173 -
Nanodroplets loaded with tetrapyrrolic dyes for photoacoustic tomography
Mendes MIP *et al.* (presented by M. Ineš P- Mendes) ..... - 176 -
Photoacoustic delivery of photosensitizers for photodynamic therapy
Pereira DA *et al.* (presented by Diogo A. Pereira) ..... - 178 -
Multispectral pulse truncated-correlation photothermal coherence tomography with applications to dental imaging
Shokouhi EB *et al.* (presented by Elnaz B. Shokouhi) ..... - 181 -
Probing cell mechanics with photoacoustic and photothermal methods
Liu L *et al.* (presented by Liwang Liu) ..... - 183 -
Subsurface temperature monitoring during hyperthermic laser treatment
Košir J *et al.* (presented by Jure Košir) ..... - 185 -
Hemodynamics in self-healing human bruises assessed by combined optical spectroscopy and pulsed photothermal radiometry
Marin A *et al.* (presented by Boris Majaron) ..... - 187 -
Breast cancer and biomineralization: New insights by means of infrared nanospectroscopy
Petay M *et al.* (presented by Margaux Petay) ..... - 189 -

08 Novel Methodologies, Instrumentation, and Applications

Quartz tuning fork based photoacoustic spectroscopy and sensing
Spagnolo V **(PLENARY SESSION with Vincenzo Spagnolo)** ..... - 192 -
Mid-IR laser based photothermal sensing of gases, liquids and imaging
Lendl B *et al.* **(PLENARY SESSION with Bernhard Lendl)** ..... - 195 -
Probing micron-sized objects with photoacoustic sensing: Theory and applications
Kolios MC *et al.* **(KEYNOTE by Michael Kolios)** ..... - 198 -
Nanoscale structural dynamics by extreme ultraviolet transient gratings
Bencivenga F *et al.* **(KEYNOTE by Filippo Bencivenga)** ..... - 201 -
Scanning Thermal Microscopy – current applications and perspectives
Bodzenta J *et al.* **(KEYNOTE by Jerzy Bodzenta)** ..... - 202 -
Pulse gas-microphone photoacoustic signal measured by minimum volume cell set-up including thermal relaxations: Theoretical consideration
Galović SP *et al.* (presented by Mioljub Nešić) ..... - 205 -
Development of a differential photoacoustic system for the determination of the effective permeability coefficient
Martinez-Munoz PE *et al.* (presented by Porfirio E. Martinez-Munos) ..... - 207 -

Open photoacoustic cell for concentration measurements at high flow rates
Fekete J *et al.* (presented by Zoltan Bozoki) ..... - 210 -
Verification of the basic equation of gas phase photoacoustics
Végh P *et al.* (presented by Panna Vegh) ..... - 212 -
Determination of cell constant via combined photoacoustic and direct absorption measurement
Fekete J *et al.* (presented by Janos M. Fekete) ..... - 214 -
Clinical validation of handheld thermo-photonic device for rapid detection and quantification of anti-SARS-CoV-2 antibodies
Thapa D *et al.* (presented by Nima Tabatabaei) ..... - 216 -
Optical photothermal infrared spectroscopy
Prater CB *et al.* (presented by Craig Prater) ..... - 218 -
Photon-phonon interaction in submicron particles systems – new method of Q-switching
Bi D *et al.* (presented by Anna D. Kudryavstseva) ..... - 221 -

10 Low-Dimensional Systems, Nanoscale Phenomena and Nanostructures

Surface phonon-polaritons conduction and radiation
Volz S **(PLENARY SESSION with Sebastian Volz)** ..... - 224 -
Photothermal characterization at a nanoscopic scale
Li Voti R **(KEYNOTE by Roberto Li Voti)** ..... - 226 -
Optomechanical strong coupling in lattices of light fluids and sound
Chafatinos DL *et al.* **(KEYNOTE by Aleks Fainstein)** ..... - 229 -
Thermal-wave diode
Ordonez-Miranda J *et al.* **(KEYNOTE by Jose Ordonez Miranda)** ..... - 230 -
Ultrafast excitation of water-immersed Carbon Nanotubes: thermophone vs mechanophone effect
Diego M *et al.* (presented by Michele Diogo) ..... - 232 -
Laser-induced coherent GHz surface acoustic waves in cleaved superlattices
Li C *et al.* (presented by Changxiu Li) ..... - 234 -
Photoacoustic monitoring of the process of alignment in liquid dispersions of magnetized carbon nanotubes
Franco-Bacca AP *et al.* (presented by Fernando Cervantes-Alvarez) ..... - 236 -
Unwrapping the soot assisted intra-pigment energy transfer in leaves through the thermal lens technique: Time series analysis in nanobiophotonics
Swapna MS *et al.* (presented by Swapna Mohanachandran) ..... - 238 -
Elastic properties effect of nanoparticles- functionalized alpaca fibers by the photoacoustic method
Quispe-Siccha RM *et al.* (presented by Rosa M. Quispe-Siccha) ..... - 240 -
Design, fabrication and characterization of Bragg reflectors based on porous silicon monitored by photoacoustics
Rodriguez-Garcia ME *et al.* (presented by Mario E. Rodriguez-Garcia) ..... - 243 -
Multiple Stokes and anti-Stokes components generation by biharmonic pumping via stimulated low-frequency Raman scattering
Tareeva MV *et al.* (presented by Maria V. Tareeva) ..... - 245 -

11 Environmental, Agricultural, and Food Applications

FTIR photoacoustic spectroscopy of soils: comparison of FTIR modalities for soil fractions of various agrogenesis
Volkov DS *et al.* **(KEYNOTE by Mikhail Prokurnin)** ..... - 247 -
AFM-IR study of carbonaceous chondrites and Ryugu samples returned by the Hayabusa 2 space mission
Mathurin J *et al.* (presented by Jeremie Mathurin) ..... - 249 -
Soot selective size distribution measurement. A demonstrative study
Hodovány S *et al.* (presented by Szabolcs Hodovany) ..... - 252 -
Air pollutants detection with QEPAS sensors
Giglio M *et al.* (presented by Marilena Giglio) ..... - 254 -
Optimization of PTD system for characterization of transparent and semi transparent samples
Budasheva H *et al.* (presented by Hanna Budasheva) ..... - 256 -

12 Analytical Chemistry and Photochemistry

Time-resolved detection of photoinduced heating and volume changes during protein reactions

Terazima M **(PLENARY SESSION with Masahide Terazima)** ..... - 260 -

Photothermal spectroscopy for nanoscale chemical imaging

Ramer G *et al.* **(KEYNOTE by Georg Ramer)** ..... - 263 -

Calibrating filter photometers with direct measurements of aerosol absorption using a dual-wavelength photo-thermal interferometer

Drinovec L *et al.* (presented by Griša Močnik) ..... - 265 -

Selective measurement of ammonia isotopes by using photoacoustic spectroscopy

Awuor E *et al.* (presented by Emily Awuor Ouma) ..... - 268 -

H_2S detection in complex gas matrices

Sampaolo A *et al.* (presented by Angelo Sampaolo) ..... - 270 -

POSTER CONTRIBUTIONS ..... - 274 -

IPPA Awards

Photoacoustic and photothermal: progress to date towards fostering multidisciplinarity

Baesso ML[(1)*]

(1) Photothermal Phenomena Laboratory, State University of Maringá, Maringá, PR, Brazil

*Corresponding author's email: mlbaesso@uem.br

IPPA Senior Scientist Award 2022

Photoacoustic and photothermal spectroscopies have experienced remarkable progress in the last six decades in both, their fundamental understanding as well as application in an increasingly large number of research areas. In this talk of the special section of the Senior Scientist IPPA 2022 award, a comprehensive overview on these aspects of thermal lens, thermal mirror, photomechanical mirror, and photoacoustic methods will be presented. It is of particular interest their application in physics, material science as well as the exploitation of such techniques towards clinical diagnosis. In relation to the latter, their utilization is particularly warranted on account of their non-destructive and non-invasive characteristics, in addition to the ability to use them in depth profiling and tissue physicochemical evaluation. Thus, those aspects will be accordingly highlighted.

Photothermal lens and photothermal mirror techniques: effects and applications

Lukasievicz GVB[(1)*]

(1) Departamento de Física, Universidade Tecnológica Federal do Paraná, Medianeira, PR 85884- 000, Brazil

*Corresponding author's email: gustavov@utfpr.edu.br

IPPA Young Scientist Award 2022

The photothermal lens (PTL) and photothermal mirror (PTM) techniques detect a broad range of phenomena arising from the interaction of tightly focused laser beams and matter at different time scales. In these techniques, a continuous or pulsed laser beam may induce a thermal perturbation and momentum transfer from the light to the sample. The effect is probed by monitoring the probe beam phase shift caused by the bulging of the heated area, the photoelastic effects, and the spatial distribution of the refractive index within the sample and in the fluid surrounding it. The transient signal is monitored at the far-field detector by analyzing the wavefront distortion of the probe beam. The mode-mismatched dual-beam PTL and PTM have been widely applied in the characterization of solid and liquid samples due to their remote, sensitive, and non-destructive characteristics. Thermal diffusivity, thermo-optical and mechanical properties can be quantitatively determined for solids and liquids materials. The applications involve material characterization of optical glasses, polymers, metals, alloys, semiconductors, and liquids. Here we show applications of Photothermal Lens and Photothermal Mirror methods under continuous or pulsed Gaussian laser excitations and the advances in its theoretical description over the past few years. The advances comprise investigating the effects of radiation forces in liquids and solids, generation and detection of pressure transients in liquids and thermoelastic waves in metals using photothermal techniques with pulsed excitation, and analytical description of sample–fluid heat coupling effect in photothermal techniques.

Validated and potential mechanisms for photothermal actuators, modulators and transducers

Glorieux C[(1)*]

(1) Laboratory of Soft Matter and Biophysics, Department of Physics and Astronomy, KU Leuven, Celestijnenlaan 200D, B-3001 Heverlee, Belgium

*Corresponding author's email: Christ.Glorieux@fys.kuleuven.be

James Smith Award

In most of the scientific literature, photothermal effects have been exploited to characterize the optical or thermal properties of materials, or to induce photoacoustic effects, which are in turn used to characterize mechanical material properties. The present contribution highlights a selection of photothermal effects that have been or could potentially be exploited for remote actuation, modulation or transduction in an interdisciplinary context. Estimates are given for the magnitude of the effects, and an assessment is made of the feasibility for exploitation.

Optical tracking of ultrafast surface vibrations

Wright OB[(1)*]

(1) Hokkaido University, Sapporo 060-8628, Japan

*Corresponding author's email: olly@eng.hokudai.ac.jp

James Smith Award

Tracking phonons at surfaces is crucial to understanding the internal structure of solids. This talk describes how to do this by spatiotemporal mapping of surface motion at frequencies from 100 MHz up to above 100 GHz, giving a new eye for subsurface features down to the atomic scale as well as revealing artistic phonon fields in crystals, cavities and waveguides.

References

[1] O.B. Wright, K. Kawashima, Coherent phonon generation from ultrafast surface vibrations, Phys. Rev. Lett. 69 (1992) 1668.

[2] Y. Sugawara et al., Watching ripples on crystals, Phys. Rev. Lett. 88 (2002) 185504.

[3] D.M. Profunser et. al., Imaging ripples on phononic crystals reveals acoustic band structure and Bloch harmonics, Phys. Rev. Lett. 97 (2006) 055502.

[4] T. Tachizaki et al., Acoustic whispering-gallery modes generated and dynamically imaged with ultrashort optical pulses, Phys. Rev. B 81 (2010) 165434-1-5.

[5] P.H. Otsuka et al., Broadband evolution of phononic-crystal-waveguide eigenstates in real- and k-spaces, Sci. Rep. 3 (2013) 3351.

[6] P.H. Otsuka et al., Time-domain imaging of gigahertz surface waves on an acoustic metamaterial, New J. Phys. 20 (2018) 013026.

[7] Q. Xie et al., Imaging GHz zero-group-velocity Lamb waves, Nat. Comm. 10 (2019) 2228.

01
Thermophysical Properties

PLENARY SESSION

Photothermal and photoacoustic exploration of relaxation in supercooled liquids

Liu L[(1)], Zhang P[(1)], Gandolfi M[(2)], Banfi F[(3)], Deschaume O[(1)], Bartic C[(1)], Glorieux C[(1)*]

(1) Laboratory for Soft Matter and Biophysics, Department of Physics and Astronomy, KU Leuven, Celestijnenlaan 200D, B301 Heverlee, Belgium

(2) Dipartimento di Matematica e Fisica, Università Cattolica del Sacro Cuore, Via Musei 41, 25121 Brescia, Italy

(3) FemtoNanoOptics group, Université de Lyon, CNRS, Université Claude Bernard Lyon 1, Institut Lumière Matière, F-69622 Villeurbanne, France

*Corresponding author's email: Christ.Glorieux@kuleuven.be

Background – Supercooled liquids exhibit the interesting property that a part of their dynamic response slows down over a large number of decades by cooling them down over some tens of degrees, with response times in the picosecond range at room temperature or higher till hours and even centuries at cryogenic temperatures, when a glass is formed. In view of applications, attention is typically given to their mechanical (translational and shear) and dielectric (rotational) response, which reflect the positional flexibility of atoms or molecules. Given the need for probing the response in a wide range of timescales, the large bandwidth provided by photoacoustic and photothermal (PAPT) techniques makes these very suitable for investigating glassy dynamics. In addition, the employed optical excitation mechanism gives experimental access not only to the mechanical response but also to the dynamics of the light to heat, heat to temperature change and heat to volume change or thermal expansion response, where the latter two can be characterized by a time/frequency dependent heat capacity and thermal expansion coefficient respectively.

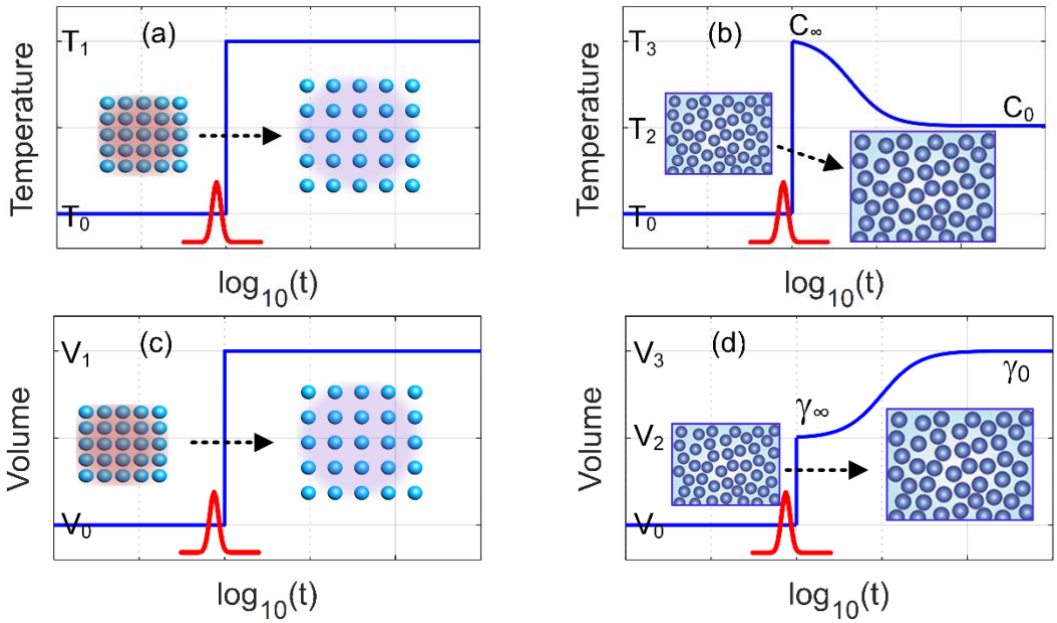

Fig. 1. Temperature variation (top) and volume variation (bottom) after transient photothermal heating to non-relaxing (left) and relaxing (right) system in adiabatic/isobaric conditions.

Methods – During the past years, the use of different PAPT approaches to extract information on the relaxation of the thermomechanical response has been explored, ranging from the photopyroelectric technique [1-2] to impulsive stimulated scattering [3-8], thermal lens detection [9] to fluorescence thermometry [10-11].

Results – In this contribution, a review is given of the methodology of the PAPT approaches that have been used in the past years and of the most recent advances. A new approach to model the combined phenomenology of photothermally induced temperature and volume changes in relaxing materials is presented. The contribution of the resulting findings to advances in the scientific field of soft matter physics is highlighted and perspectives are given for possible further steps to take.

References

[1] E.H. Bentefour, C. Glorieux, M. Chirtoc, J. Thoen, Broadband photopyroelectric thermal spectroscopy of a supercooled liquid near the glass transition, J. App. Phys. 93, 12 (2003) 9610-9614.

[2] E.H. Bentefour, C. Glorieux, M. Chirtoc, J. Thoen, Thermal relaxation of glycerol and propylene glycol studied by photothermal spectroscopy, J. Chem. Phys. 120, 8 (2004) 3726-3731.

[3] Y.X. Yan, E.B. Gamble, K. A. Nelson, Impulsive stimulated scattering: General importance in femtosecond laser pulse interactions with matter, and spectroscopic applications, J. Chem. Phys. 83, 11 (1985) 5391-5399.

[4] Y.X. Yan, K.A. Nelson, Impulsive stimulated light scattering. I. General theory, J. Chem. Phys. 87, 11 (1987) 6240-6256.

[5] Y.X. Yan, K.A. Nelson, Impulsive stimulated light scattering. II. Comparison to frequency-domain light-scattering spectroscopy, J. Chem. Phys. 87, 11 (1987) 6257-6265.

[6] C. Glorieux, K.A. Nelson, G. Hinze, M. D. Fayer, Thermal, structural, and orientational relaxation of supercooled salol studied by polarization-dependent impulsive stimulated scattering, J. Chem. Phys.116, 8 (2002) 3384-3395.

[7] D.H. Torchinsky, J.A. Johnson, K. A. Nelson, A direct test of the correlation between elastic parameters and fragility of ten glass formers and their relationship to elastic models of the glass transition, J. Chem. Phys. 130, 6 (2009).

[8] C. Klieber, T. Pezeril, S. Andrieu, K. Nelson, Optical generation and detection of gigahertz-frequency longitudinal and shear acoustic waves in liquids: Theory and experiment, J. App. Phys. 112 (2012).

[9] P.F. Zhang, M. Gandolfi, F. Banfi, C. Glorieux, L.W. Liu, Revisiting impulsive stimulated thermal scattering in supercooled liquids: Relaxation of specific heat and thermal expansion, J. Chem. Phys. 155, 7 (2021).

[10] L.W. Liu, S. Creten, Y. Firdaus, J. Cuautle, M. Kouyate, M. Van der Auweraer, C. Glorieux, Fluorescence spectra shape based dynamic thermometry, App. Phys. Lett. 104, 3 (2014).

[11] L.W. Liu, K. Zhong, T. Munro, S. Alvarado, R. Cote, S. Creten, E. Fron, H. Ban, M. Van der Auweraer, N.B. Roozen, O. Matsuda, C. Glorieux, Wideband fluorescence-based thermometry by neural network recognition: Photothermal application with 10 ns time resolution, J. App. Phys. 118, 18 (2015).

KEYNOTE SPEAKER

Thermal properties and critical behaviour in rare-earth based magnetocaloric materials

Oleaga A[(1)*], Herrero A[(1)], Aseguinolaza IR[(1)], Apiñaniz E[(1)], García-Adeva AJ[(1)]

(1) Departamento de Física Aplicada, Escuela de Ingeniería de Bilbao, Universidad del País Vasco UPV/EHU, Bilbao, Spain

*Corresponding author's email: alberto.oleaga@ehu.es

The need to introduce environmentally friendly technology in the energy field has led to huge advances in the research and development of a new refrigeration technology based on the magnetocaloric effect, with the aim of replacing the classical gas compression-expansion cycles [1, 2]. Hence, a thorough search for magnetocaloric materials which present suitable properties for technological applications in different temperature ranges is currently under way. Different types of materials are being studied, among them a huge variety of intermetallics. We have been focusing our attention in the last years on rare-earth based intermetallic families which can compete in this field in a wide temperature span, from the gas liquefaction ranges to room temperature. There is a need to properly characterize the magnetic and magnetocaloric properties of these materials as well as their thermal ones. As the magnetocaloric materials will work in a cycle in a refrigeration system, the heat exchange between the magnetocaloric material and the fluid in the refrigerator must be efficient and quick, allowing high working frequencies, highlighting the relevant role of the thermal diffusivity, as it is a non-steady heat transfer situation. Besides, the study of the thermal behaviour at the phase transition will complement the magnetic one in order to understand the underlying physics, through the study of the critical behaviour of the second order magnetic transition.

This work will present a selection of results for the following families: R_6(Fe,Mn)X_2 (R=Tb, Gd, Ho, Dy; X=Sb, Bi, Te), R_3CoNi (R=Tb, Dy, Ho), Tb_3Co, Tb_3Ni, covering a wide range of temperatures, magnetic transitions and properties.

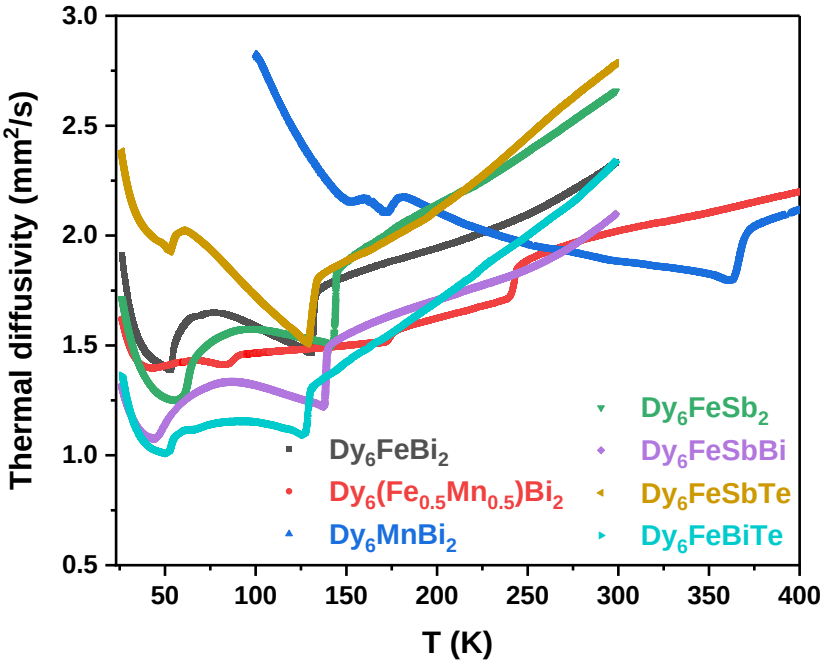

Fig. 1. Thermal diffusivity curves for Dy_6(Fe,Mn)X_2

Concerning the thermal properties, an ac photopyroelectric calorimeter in the back detection configuration has been used to measure thermal diffusivity (D) and specific heat (c_p), due to its high resolution and sensitivity. Fig. 1 shows an example of D for the $Dy_6(Fe,Mn)X_2$ family, where the paramagnetic to ferromagnetic (PM-FM) second order phase transitions are signalled as dips in the higher temperature part of each curve, while at lower temperature there are different spin reorientation transitions. These curves will be discussed in parallel to magnetization curves as a function of temperature [3]. Fig. 2 shows the succession of a second order PM-FM and a weakly first order FM-AFM transition in the case of Tb_3Co [4].

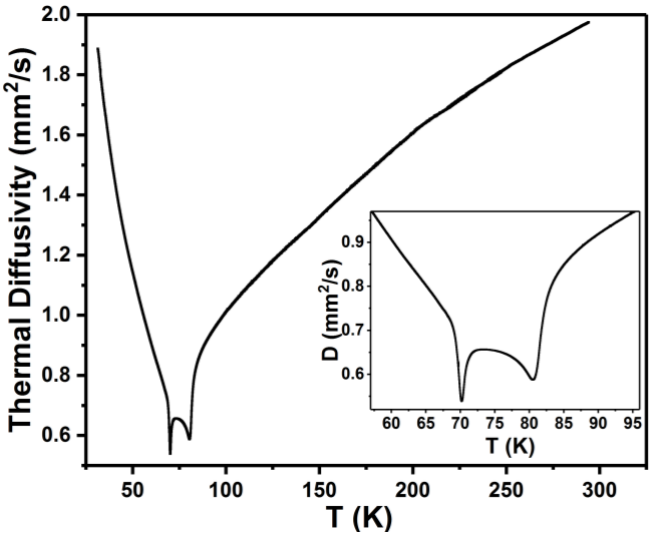

Fig. 2. Thermal diffusivity curve for Tb_3Co. The inset highlights the most relevant part.

The critical behaviour of the second order phase transitions has been analysed by thermal, magnetic and magnetocaloric techniques. According to the renormalization group theory, the critical behaviour of these transitions in the near vicinity of the critical temperature is characterized by a set of critical exponents (α, β, γ, δ, related to specific heat, spontaneous magnetization, inverse of the initial susceptibility and magnetization at the critical temperature, respectively) corresponding to different universality classes.

The magnetic interaction range, as well as the ordering of the spins, have therefore been studied using the different scaling equations, such as the following one for c_p:

$$c_p = B + Ct + A^{\pm}|t|^{-\alpha}(1 + E^{\pm}|t|^{0.5}) \qquad \text{Eqn. 1}$$

where t is the reduced temperature and $A^{\pm}$, B, C, $E^{\pm}$ are fitting parameters.

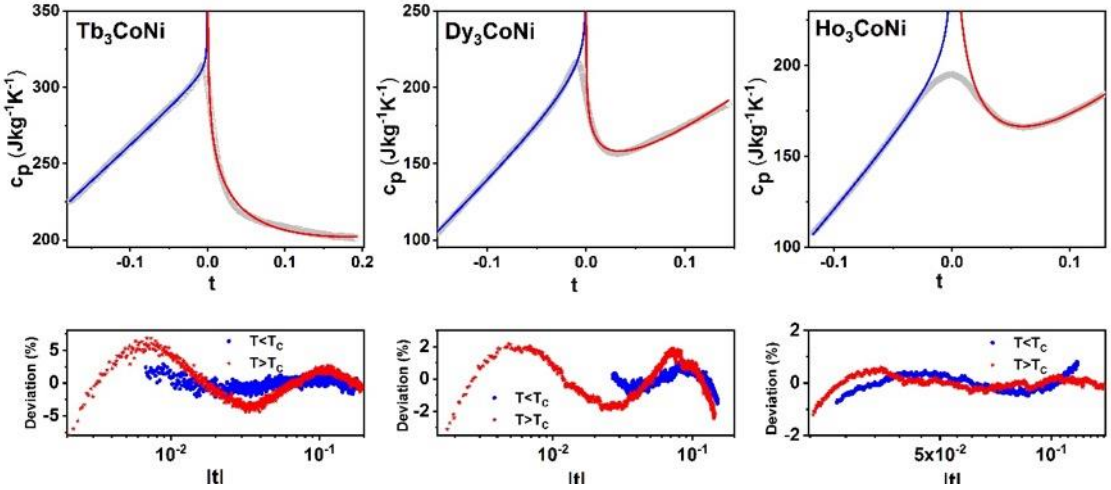

Fig. 3. Top line: Experimental (grey open circles) and fitted curves (continuous lines) of the specific heat as a function of the reduced temperature for the three compounds in the near vicinity of T_C. Bottom line: deviation plots for the fittings, blue circles correspond to $T < T_C$, red stars for $T > T_C$.

We will show that, among these families, we have found phase transitions belonging to the Mean Field class (long range order magnetic ordering), 3D Heisenberg (short range order, isotropic distribution of spins), Chiral classes (short range order with complex magnetic ordering), even unconventional critical behaviours with critical exponents whose values do not fit in any theorized universality class. Fig. 3 shows an example of the specific heat fittings for R_3CoNi [5].

We will show that the thermal diffusivity values of these families are among the highest in the magnetocaloric field, being competitive with High Entropy Alloys such as several Heusler alloys, which make them interesting even if the magnetocaloric variables (magnetic entropy change, refrigerant capacities) are not among the highest ones.

References

[1] V. Franco, J.S. Blázquez, J.J. Ipus, J.Y. Law, L.M. Moreno-Ramírez, A. Conde, Magnetocaloric effect: From materials research to refrigeration devices, Prog. Mat. Sci. 93 (2018) 112-232. https://doi.org/10.1016/j.pmatsci.2017.10.005.

[2] T. Gotschall, K.P. Skokov, M. Fries, A. Taubel, I. Radulov, F. Scheibel, D. Benke, S. Riegg, O. Gutfleisch, Making a cool choice: The materials library of magnetic refrigeration, Adv. Energy Mater. 9 (2019) 1901322. https://doi.org/10.1002/aenm.201901322.

[3] A. Herrero, A.Oleaga, I. R. Aseguinolaza, A.J. Garcia-Adeva, E. Apiñaniz, A.V. Garshev, V.O. Yapaskurt, A.V. Morozkin, Tailoring the magnetocaloric, magnetic and thermal properties of Dy6(Fe,Mn)X2 intermetallics (X=Sb, Te, Bi), Journal of Alloys & Compounds 890 (2021) 161849.
https://doi.org/10.1016/j.jallcom.2021.161849.

[4] A. Herrero, A.Oleaga, P. Manfrinetti, A. Provino, A. Salazar, Comprehensive study of the magnetic phase transitions in Tb3Co combining thermal, magnetic and neutron diffraction measurements, Intermetallics 111, (2019) 106519. https://doi.org/10.1016/j.intermet.2019.106519.

[5] A. Herrero, A. Oleaga, A. Provino, I. R. Aseguinolaza, A. Salazar, D. Peddis, P. Manfrinetti, Crystallographic, magnetic and magnetocaloric properties in novel intermetallic materials R3CoNi (R = Tb, Dy, Ho, Er, Tm, Lu), Journal of Alloys & Compounds 865 (2021) 158948. https://doi.org/10.1016/j.jallcom.2021.158948.

KEYNOTE SPEAKER

Thermal characterization of composites and layered systems: Challenges and opportunities

Alvarado-Gil JJ[(1)*]

(1) Applied Physics Department, CINVESTAV-Unidad Mérida, Carretera Antigua a Progreso km. 6, Cordemex, 97310 Mérida, Yucatán, México

*Corresponding author's email: juan.alvarado@cinvestav.mx

One of the most challenging areas in material science involves the management and control of heat transfer, being the basis of numerous ongoing and emerging technological applications. Composites and layered materials constitute the core of a broad variety of high-performance systems, which are in the vanguard to face the high and increasing demand of new and more efficient devices, machines, and instruments. Photothermal techniques are well-established methodologies, with the capability to address the study of this kind of systems and having the flexibility to perform reliable analyses at a broad range of scales [1]. We present results on the study of heat transfer of a variety of composites and layered systems, aimed at showing the capacity of the photothermal techniques in supporting the study of complex systems and processes. Our studies involve polymers, phase changing materials, as well as composites formed by filler in matrices, as well as multilayered systems. Strategies for increasing, in a controlled form, the thermal conductivity in composites are presented. In the case of matrices with fillers, the factors defining the development of high thermal conductivity composites, the role of the form, distribution, geometry and connectivity of the phases, and the key role of the thermal interfacial resistance is discussed. In particular, the possibility of observing thermal percolation in this kind of systems is addressed [2]. The development of novel configurations and methodologies, aimed at surmounting the inherent restrictions, associated with the study of heat transfer in these systems, is discussed. Additionally, the limitations established by the thermal diffusion length in the study of heat transfer as well as methodologies to face these constraints are described [3].

References

[1] S.E. Bialkowski, N.G.C. Astrath, M.A. Proskurnin, Photothermal Spectroscopy Methods, 2nd Edition, Wiley (2019).

[2] F. Kargar, Z. Barani, R. Salgado, B. Debnath, J.S. Lewis, E. Aytan, R.K. Lake, A.A. Balandin, Thermal Percolation Threshold and Thermal Properties of Composites with High Loading of Graphene and Boron Nitride Fillers, ACS Appl. Mater. Interfaces 10 (2018) 37555. https://doi.org/10.1021/acsami.8b16616.

[3] P. Martínez-Torres, J.J. Alvarado-Gil, Photoacoustic monitoring of thermal wave interference effects during the formation of polymeric thin films from solutions, Appl. Phys. A, 105 (2011) 975–986. https://doi.org/10.1007/s00339-011-6524-8.

KEYNOTE SPEAKER

Decoupling bulk and surface radiation forces in a dielectric liquid

Astrath NGC[(1)*], Flizikowski GAS[(1)], Anghinoni B[(1)], Malacarne LC[(1)], Baesso ML[(1)], Požar T[(2)], Brevik I[(3)], Razansky D[(4)], Bialkowski SE[(5)]

(1) Department of Physics, Universidade Estadual de Maringá, Maringá, Brazil
(2) Faculty of Mechanical Engineering, University of Ljubljana, Ljubljana, Slovenia
(3) Department of Energy and Process Engineering, Norwegian University of Science and Technology, Trondheim, Norway
(4) Institute for Biomedical Engineering and Institute of Pharmacology and Toxicology, Faculty of Medicine, University of Zurich, Switzerland; Institute for Biomedical Engineering, Department of Information Technology and Electrical Engineering, ETH Zurich, Switzerland
(5) Department of Chemistry and Biochemistry, Utah State University, Utah, USA

*Corresponding author's email: ngcastrath@uem.br

The effect of radiation forces within a dielectric material and at its interface has been a long-standing debate for over a century. Yet there has been so far only limited experimental verification in complete accordance with the concurrent electrodynamic theories. Here, we use tightly focused pulsed laser beam to detect bulk and boundary optical forces in a dielectric fluid. From the optical convoluted signal, we decouple thermal and nonlinear optical effects from the radiation forces using a theoretical interpretation based on the Microscopic Ampère force density. It is shown, for the first time, that the time-dependent pressure distribution within the fluid chiefly originates from the electrostriction effects. Our results shed light on the contribution of optical forces to the surface displacements observed at the dielectric air-water interfaces, thus shedding light on the long-standing controversy surrounding the basic definition of electromagnetic momentum density in matter [1-4].

The effects of radiation pressure exerted on a dielectric surface parallel to the propagation of the incident electromagnetic radiation can be interpreted as the transfer of momentum from the photons at the surface. Radiation pressure effects were predicted by Maxwell in 1871 and experimentally observed by Lebedew in 1900. In 1905, Poynting presented a detailed geometrical calculation of the force by radiation pressure of light incident from free space on a transparent and non-dispersive dielectric medium, which predicted an outward force normal to the surface of the dielectric, opposite to the direction of propagation of the incident electromagnetic field. Conflicting theories for the energy-momentum tensor were proposed by Minkowski in 1908 and Abraham in 1909 to explain this effect. These have subsequently been extensively debated in the literature over the past century. The most-used electrodynamic theories are the Abraham, Minkowski, Einstein-Laub, Chu, and Amperian formulations [3]. These theories can be used in conjunction with the elastodynamic theory to simulate the shape, amplitude, and speed of momentum-driven elastic waves using the elastic properties of the medium and the properties of the incident light. The absolute surface displacement measurements and the simulated displacements, based on first principles, would provide a highly rigorous method to correlate the elastic waves in an illuminated object to the electromagnetic momentum delivered by the incident light.

The measurements of the surface deformation at the air-liquid interface are performed using the photomechanical mirror technique [2,3]. In this method, the probe laser is reflected off the water surface

and the cylindrically symmetric surface deformation generated by the laser excitation causes focusing or defocusing of the central portion of the probe laser beam. A convex deformation is similar to a convex mirror in turn causing the intensity of the probe laser to decrease in the far field while a concave deformation focuses the probe and thereby increases the power that passes through the pinhole placed in front of the detector (Fig. 1a). In the continuous irradiation experiment, the calculated surface distortion is always convex and the corresponding signal shows a decrease in the probe power past the pinhole at all times. As illustrated in Fig. 1b, during pulsed irradiation, the surface first produces a convex column. The column subsequently collapses after irradiation causing a concave surface perturbation. This behavior corresponds to the probe laser power initially decreasing then increasing past the pinhole. The numerical calculations are in excellent agreement with our experimental results, in a test that is significantly more discerning than the earlier experiments by Ashkin and Dziedzic [5]. This demonstrates that this light-matter system is well modeled by our present understanding of radiation forces that lead to the momentum transfer. The Helmholtz force density is used to describe the imparted pressure on the surface of the liquid.

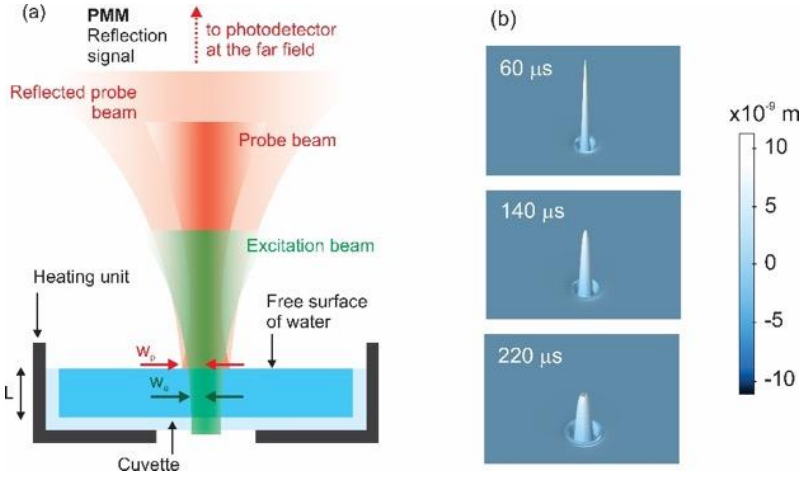

Fig. 1. (a) Schematic diagram of the apparatuses for the time-resolved photomechanical mirror used for pulsed excitation. The probe beam senses the entire region affected by the excitation laser. The complex reflection pattern of the probe beam just out of the sample propagates to the detector plane. The intensity variation measured at the center of the probe beam in the far field consists of complex contributions originating from all the surface waves created on the water. **(b)** The numerical simulation of the time evolution of the water surface deformation under pulsed excitation. A sharp peak appears a few microseconds after irradiation and is subsequently dispersed on the surface. The probe beam senses the entire region affected by the excitation laser. The complex reflection pattern of the probe beam just out of the sample propagates to the detector plane. The intensity variation measured at the center of the probe beam in the far field consists of complex contributions originating from all the surface waves created on the water.

To experimentally detect the dynamics of the pressure-induced acoustic waves by optical forces within water, we exploit a high sensitive detection of wavefront distortions by a time-dependent photo-induced lensing (PL) technique (Fig. 2). Nanosecond laser pulses irradiate the sample, changing the local pressure due to the radiation forces in addition to a small heat deposition. Nonlinear optical Kerr effect is also observed during the pulse duration. A low-irradiance laser beam traverses the sample thus probing the induced effects. Intensity of the probe beam is monitored in the far field by a fast photodetector.

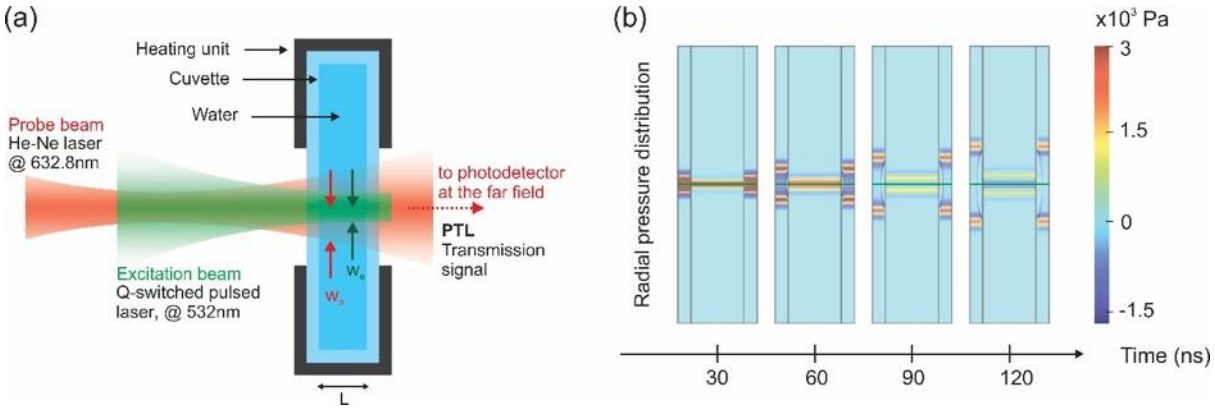

Fig. 2. (a) Photo-induced lensing method - schematic of the time-dependent photo-induced lensing measurement set-up. Green and red routes represent pump and probe laser beams, respectively. (b) Radial pressure distribution built up in the sample over time.

The wavefront distortion sensed by the probe beam originates from the non-uniform excitation interaction with the sample leading to an increase in the internal energy, the latter being dispersed in two different modes of hydrodynamic relaxation. The increased internal energy results in a temperature change in the sample or the coupling material placed next to the sample. This temperature change results in a change in sample density. If the photothermally induced temperature alteration occurs faster than the time required for the fluid to expand (or contract, in some cases), then the rapid temperature change will result in a pressure change. The pressure perturbation then relaxes by emitting an acoustic wave. Once the pressure has relaxed to its equilibrium level, a density change proportional to the temperature will remain. The time-dependent intensity signal detected in the experiments shows only the center of the probe beam spot at the detector plane in the far-field region. The calculation of the PL signal requires the determination of the temperature and pressure fields considering all the effects of the radiation forces in the liquid and in the cuvette walls.

This work presents experimental methods to quantitatively measure the momentum coupling between the electromagnetic field and matter [1-4]. These methods can be applied to characterize materials, to further advance optical manipulation technology of deformable matter, and to provide the means to empirically validate differing electrodynamic formalisms, commonly known as the Abraham–Minkowski controversy. Even though substantial efforts have so far been devoted to addressing the question of the basic definition of electromagnetic momentum density in matter, this fundamental problem in classical and quantum mechanical theory of electrodynamics has not been unequivocally resolved. Our work represents a bold step in this direction, facilitating resolution of the century old Abraham-Minkowski controversy.

References

[1] N.G.C. Astrath, G.A.S. Flizikowski, B. Anghinoni, L.C. Malacarne, M.L. Baesso, T. Požar, I. Brevik, D. Razansky, S.E. Bialkowski, submitted to Nature Physics (2022).

[2] N.G.C. Astrath, L.C. Malacarne, M.L. Baesso, G.V.B. Lukasievicz, S.E. Bialkowski, Nature Communications 5 (2014) 4363. doi:10.1038/ncomms5363.

[3] O.A. Capeloto, V.S. Zanuto, L.C. Malacarne, M.L. Baesso, G.V.B. Lukasievicz, S.E. Bialkowski, N.G.C. Astrath, Scientific Reports 6 (2016) 20515. doi.org/10.1038/srep20515.

[4] T. Požar, J. Laloš, A. Babnik, R. Petkovšek, M. Bethune-Waddell, K.J. Chau, G.V.B. Lukasievicz, N.G.C. Astrath, Nature Communications 9 (2018) 3340. doi:10.1038/s41467-018-05706-3.

[5] A. Ashkin, J.M. Dziedzic, Physical Review Letters 30 (1973) 139. doi.org/10.1103/PhysRevLett.30.139.

Advantages and disadvantages of photothermal measurement methods estimating thermal transport properties (such as thermal conductivity, diffusivity and boundary resistance) of multilayered samples

Mikaeeli A[(1,2)*], Chatterjee A[(1,2)] , Korte D[(3)], Cabrera H[(4)], Derkowska-Zielińska B[(1)], Pawlak M[(1)]

(1) Institute of Physics, Faculty of Physics, Astronomy and Informatics, Nicolaus Copernicus University in Torun, Grudziadzka 5, 87-100 Torun, Poland
(2) Chair of Applied Solid-State Physics, Experimental Physics VI, Ruhr-University Bochum, Universitaetsstrasse 150, D-44780 Bochum, Germany
(3) University of Nova Gorica, Vipavska 13, SI-5000 Nova Gorica, Slovenia
(4) Optics Lab, STI Unit, The Abdus Salam International Centre for Theoretical Physics, Strada Costiera 11, 34151 Trieste, Italy

*Corresponding author's email: 503392@doktorant.umk.pl

Since thermal conductivity plays a significant role in applications focused on accurately measuring the amount of energy dissipation, investigating this parameter will pave the way for fundamental research related to thin film characterization. Thermal conductivity can be measured using frequency domain (FD) methods. Compared to time domain (TD) methods, FD methods can also measure thermal diffusivity. In this paper we compare four FD thermal methods for measuring thermal transport properties as shown in figure 1.

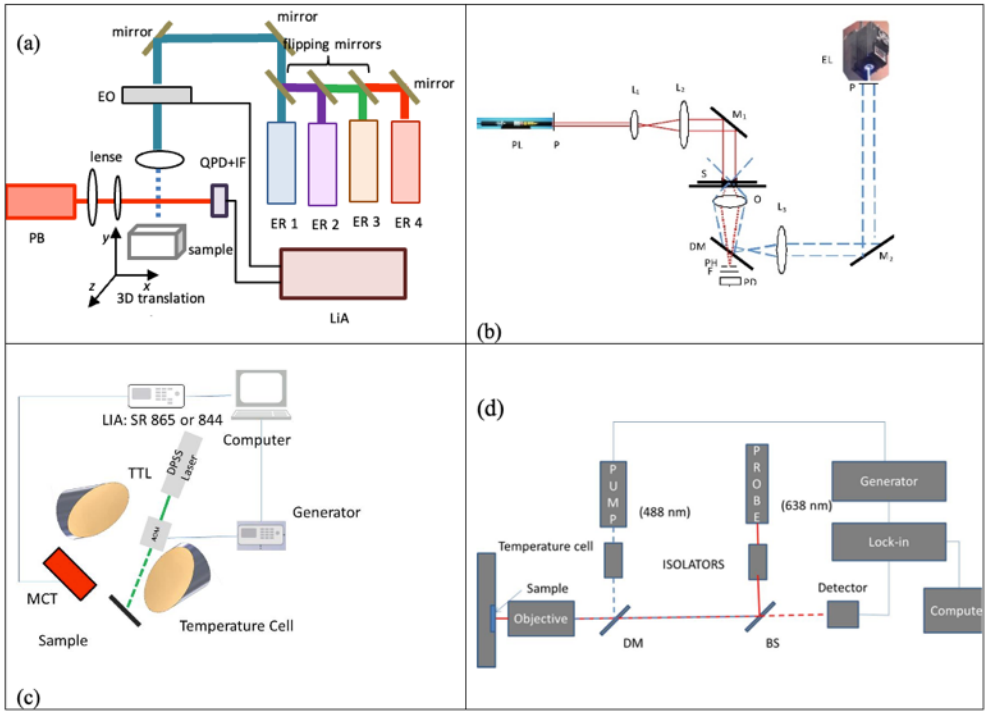

Figs. 1a) to d) present the most used important methods for measuring the thermal transport properties [1-4]. Table 1 summarizes the degree of difficulty of studying thermal transport properties of thin layers superlattices and few layers graphene using frequency-domain photothermal radiometry (PTR) [1,2], frequency-domain thermoreflectance [2], beam deflection spectrometry (BDS) [3], and photothermal lens microscopy (PTM) [4].

Table 1. Summary of frequency-domain thermal wave methods.

Feature	PTR	TR	PTM	BDS
Measurement of cross-plane thermal transport properties	Applicable	Difficult but Applicable	Difficult	Applicable
Measurement of in-plane thermal transport properties	Difficult but Applicable	Applicable	Applicable	Possible
Complexity of optical system	Relatively easy	Relatively difficult	Relatively easy	Relatively easy
Temperature-measurements at low temperatures	Difficult, due to physical limitations	Applicable	Difficult	Difficult
Temperature measurements at high temperatures	Applicable	Applicable	Difficult	Difficult
Photoluminescence measurements	Applicable	Not Applicable	Not Applicable	Not Applicable

References

[1] M. Pawlak, N. Jukam, T. Kruck, D. Dziczek, A. Ludwig, A.D. Wieck, Measurement of thermal transport properties of selected superlattice and thin films using frequency-domain photothermal infrared radiometry, Measurement 166 (2020), 108226.

[2] M. Pawlak, T. Kruck, N. Spitzer, D. Dziczek, A. Ludwig, A. Wieck, Experimental validation of formula for calculation thermal diffusivity in superlattices performed using a combination of two frequency-domain methods: photothermal infrared radiometry and thermoreflectance, Appl. Sci.-Basel 11 (2021), 6125-6140.

[3] D. Korte, M. Franko. Application of complex geometrical optics to determination of thermal, transport, and optical parameters of thin films by the photothermal beam deflection technique. Journal of the Optical Society of America. A, Optics, image science, and vision. 32 (2015) 61-74.

[4] H. Cabrera, D. Mendoza, J. L. Benítez, C. Bautista Flores, S. Alvarado, E. Marín, Thermal diffusivity of few-layers graphene measured by an all-optical method, J. Phys. D: Appl. Phys. 48 (2015) 465501.

Photothermal study of structural relaxation in supercooled glycerol by fast fluorescence thermometry

Wei Q(1), Zhang P(1), Liu L(1), Deschaume O(1), Bartic C(1), Glorieux C(1)*

(1) Laboratory for Soft Matter and Biophysics, KU Leuven, BE-3001 Heverlee, Belgium

*Corresponding author's email: email: Christ.Glorieux@kuleuven.be

Background – Structural relaxation refers to a part of the response to a stimulus (e.g. mechanical) of glassforming liquids being slow, due to the involvement of time-consuming cooperative changes of the atomic or molecular network, with a characteristic relaxation time that strongly increases with decreasing temperature [1]. In case the stimulus is (photo)thermal, the response to the optically supplied thermal energy can be observed both as a volume change (thermal expansion) and a temperature change. The temperature change gives information on how the supplied thermal energy is distributed over different vibrational degrees of freedom. Given sufficient time, in a relaxing material, part of the thermal energy is channeled from vibrational energy to configurational energy. Many methods have been proposed to observe this "thermal relaxation", which is typically quantified by invoking an effective frequency- dependent heat capacity C(ω): the 3-ω technique [2], photopyroelectric spectroscopy (PPE) [3,4], and AC-chip nano-calorimetry [5]. The volume response to supplied heat can be expressed by a frequency- dependent thermal expansion coefficient $\gamma(\omega)$, which can e.g., be characterized using capacitive scanning dilatometry [6]. The above methods have limited bandwidth. In the following, we report on an all-optical photothermal approach to characterize the frequency dependence of the heat capacity of glycerol. The detection of fast temperature changes is achieved by fluorescence-based thermometry [7].

Methods – Fluorescence-based thermometry is based on the temperature dependence of the fluorescence spectrum (in this work: Rhodamine B (RhB)). The concept is depicted in Figure 1(a). Optically excited electrons go back to the ground state, releasing their stored energy by emitting a photon, i.e., fluorescence light. The energy and thus wavelength of the emitted photons is determined by the previous interactions of the electron with vibrational motions in the surroundings. The temperature dependence of these interactions makes the fluorescence spectrum temperature-dependent. The fluorescence lifetime of RhB is of the order of nanoseconds, making it feasible to use the evolution of the spectrum as a fast, optical quantifier of temperature. Figure 1(b) shows the temperature-dependent fluorescence of RhB in glycerol. The peak wavelength, full-width-at-half-maximum (FWHM), and the integrated intensity of the fluorescence are all sensitive to the temperature variations, and these relations can be calibrated and parametrized by model functions or trained neural networks (NN) [7].

In order to characterize thermal relaxation in glycerol (purity>99%), the sample was doped with RhB with a low concentration, 2×10^{-6} mol/L, making it fluorescent. Copper chloride (CuCl2) was added (0.1 mol/L) to enhance the absorption of the sample to the pump laser (1064 nm, 50 mJ/pulse, 8 ns pulse duration, Quantaray®). As shown in Figure 1(c), the fluorescence emission of RhB was excited by a CW-532 nm probe laser (06-DPL, Cobolt®) and was continuously collected by a fiber-coupled

spectrometer. During the experiments, the starting temperature of the sample (before the photothermal excitation laser pulse) was measured by a platinum thermometer near the region of interest.

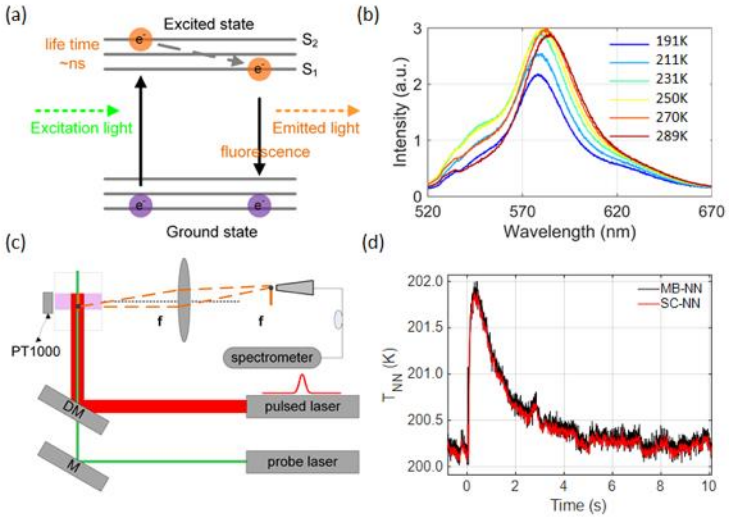

Fig. 1. (a) Fundamentals of laser-induced fluorescence: Jablonski energy diagram of the excited molecule; **(b)** Fluorescence emission spectra of RhB at different temperatures; **(c)** Experimental setup for fluorescence-based thermometry implemented in a pulsed photothermal measurement; **(d)** Reconstructed photothermally induced temperature evolution by two different spectral shape based neural networks ("multi-band" and "spectral-shape") after stimulating the sample with a single laser pulse.

Results – Figure 1(b) shows the temperature dependence of the fluorescent intensity spectrum. Both the intensity and shape (redshift) change with temperature. By making use of calibration curves or a trained neural network, these spectra were used to extract the temperature from the fluorescence spectrum both during static and dynamic heating) experiments. Figure 1(d) shows an example of an experimental trace of the measured temperature response when the sample was subjected to transient photothermal heating from the ns laser pulse. The extraction of the temperature from the normalized (to the maximum value) fluorescence spectrum was done by two different neural network configurations that used 4 bands of the spectrum (multi-band - MB) and the detailed spectrum (shape-based - SC), respectively. The main challenge of this approach is to combine a high signal-to-noise ratio (SNR) on the collected fluorescence signals with a high acquisition speed. Without averaging, the noise limit of the implemented experimental setup was around 20 $mK/Hz^{1/2}$.

References

[1] U. Bengtzelius, W. Gotze, A. Sjolander, Dynamics of supercooled liquids and the glass transition, J. Phys. C: Solid State Phys. 17 (1984) 5915.

[2] N.O. Birge, P.K. Dixon, N. Menon, Specific heat spectroscopy: Origins, status and applications of the 3ω method, Thermochim. Acta 304 (1997) 51.

[3] E.H. Bentefour, C. Glorieux, M. Chirtoc, J. Thoen, Thermal relaxation ofglycerol and propylene glycol studied by photothermal spectroscopy, J. Chem. Phys. 120 (2004) 3726.

[4] E.H. Bentefour, C. Glorieux, M. Chirtoc, J. Thoen, Broadband photopyroelectric thermal spectroscopy of a supercooled liquid near the glass transition, J. Appl. Phys. 93 (2003) 9610.

[5] Y.Z. Chua, G. Schulz, E. Shoifet, H. Huth, R. Zorn, J.W.P. Scmelzer, C. Schick, Glass transition cooperativity from broad band heat capacity spectroscopy, Colloid Polym. Sci. 292 (2014) 1893.

[6] C. Bauer, R. Böhmer, S. Moreno-Flores, R. Richert, H. Sillescu, D. Neher, Capacitive scanning dilatometry and frequency-dependent thermal expansion of polymer films, Phys. Rev. E 61 (2000) 1755.

[7] L. Liu, K. Zhong, T. Munro, S. Alvarado, R. Côte, S. Creten, E. Fron, H. Ban, M. Auweraer, N.B. Roozen, O. Matsuda, C. Glorieux, Wideband fluorescence-based thermometry by neural network recognition: Photothermal application with 10 ns time resolution, J. App. Phys., 118 (2015) 184906.

Photopyroelectric investigation of the *trans-cis* isomerization effect on phase transitions of a liquid crystalline azobenzene

Paoloni S[(1)*], Orazi N[(1)], Mercuri F[(1)], Zammit U[(1)]

(1) Department of Industrial Engineering, University of Rome Tor Vergata, Rome, Italy

*Corresponding author's email: stefano.paoloni@uniroma2.it

Over the recent period, photothropic liquid crystals (LC) have attracted considerable attention because of the possibility to very their properties by optical means. Such compounds may consist of photoactive molecules which possess self-ordering capabilities such as to give rise to LC mesophases. One example is constituted by p,p'-diheptylazobenzene (7AB) molecules that in their ground *trans* state do not significantly affect the LC ordering because of their elongated shape. Upon UV irradiation, the molecules convert into their bent *cis* form, thus destabilizing the LC phases to an extent that, under some circumstances, can possibly lead to an isothermal LC phase transition from a more to a less ordered phase. The reverse conversion into the *trans* ground state can occur either by visible light irradiation or through thermal relaxation in the dark. Despite the large number of investigations carried out in 7AB-LC mixtures, only few studies concerning the effect of UV irradiation on the phase transitions of pure 7AB have been reported in the literature [1,2].

Calorimetry has been proven a very effective technique for the analysis of phase transition in a wide range of different materials. However, as regards the investigation of photochromic LC, most of the calorimetric techniques suffer from severe limitations mainly because of the difficulty to introduce the optical beam in order to stimulate the phase transitions. Unlike such techniques, photopyroelectric calorimetry (PPE) has been demonstrated to be a very effective tool. In fact, thanks to the optical transparency of the pyroelectric transducer the UV beam to stimulate the *trans* to *cis* form isomerization can be directed onto the sample during the calorimetric measurements. Moreover, a linearly polarized white light beam can also be directed onto the sample to carry out reflection polarization microscopy observations of the sample texture simultaneously with the thermal properties measurements, being such a possibility of crucial importance for the interpretation of the experimental results.

In this study, PPE has been employed for the study of the transition between the nematic (N) and the isotropic (I) phase in pure 7AB upon varying degrees of UV sample irradiation so as to induce different concentrations of *cis* isomers. Beside the measurement of the temperature dependence of the thermal parameters for stationary values of the *cis* concentration, the dynamics of the *trans-cis* isomerization has been investigated by analysing the time-dependence of both the specific heat *c* and the thermal conductivity *k* following the onset of the UV irradiation and its subsequent switching off. As it can be seen in Fig. 1, right after the beginning of the UV irradiation, both *c* and *k* show a step decrease because of the progressive conversion of the N phase into the I one due to the disorder introduced by the *cis* isomers as confirmed by Fig. 2a where the bright and dark areas correspond to N and I domains, respectively. Upon further UV irradiation, the N-I transition is induced through the entire sample, even beyond the illuminated area (see Fig 2b). Finally, once the UV irradiation is turned off, the *cis* isomers covert into the ground *trans* ones over their relaxation period and, consequently, the transition from the

I phase to the N one takes place (see Fig.2c and 2d) as evidenced by the corresponding time–dependence of the thermal parameters.

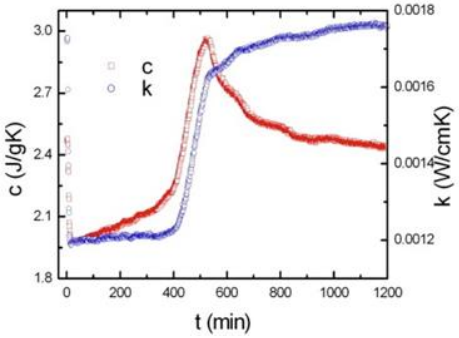

Fig. 1. Time-dependence of the specific heat (□) and the thermal conductivity (○) following the onset and the subsequent turning off of the UV radiation at t=3 min and t=16 min, respectively.

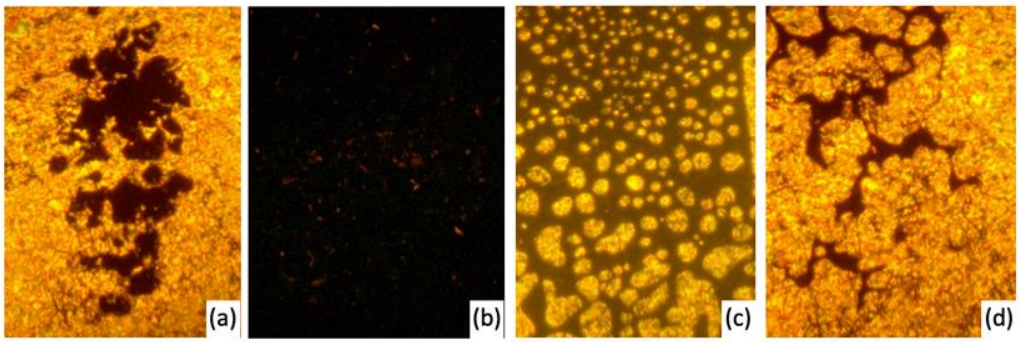

Fig. 2. Sample textures observed during the cis-trans isomerization shown in Fig. 1 at t=4 min (a), t=30 min (b), t=480 min (c), and t=520 min (d)

Acknowledgements – Prof. J. Thoen and Prof. C. Glorieux from Katholieke Universiteit, Leuven, Belgium are gratefully acknowledged for providing us with the 7AB specimen.

References

[1] W.H. de Jeu, Molecular structure and the occurrence of smectic A and smectic C phases, Journal de Physique 38 (1977) 1265-1273. https://doi.org/10.1051/jphys:0197700380100126500.

[2] S. Paoloni, U. Zammit, N. Orazi, F. Mercuri, L. Mattiello, D. Rocco, C. Glorieux, J. Thoen, High resolution study of the n = 7–9 p,p'-n-alkylazobenzenes phase transitions by photopyroelectric and adiabatic scanning calorimetries, Thermochim. Acta 706 (2021) 179077. https://doi.org/ 10.1016/j.tca.2021.179077.

Photothermal characterization of obsidian

Martínez-Garcia MM(1), Macias JD(1), Franco-Bacca AP(1), Cervantes-Alvarez F(1), May-Crespo F(2), Martínez-Torres PG(3), Alvarado-Gil JJ(1)*

(1) Department of Applied Physics, Cinvestav-Unidad Mérida, Carretera Antigua a Progreso, Km. 6, CP. 97310 Mérida, Yucatán, México
(2) CONACYT Research Fellow-El Colegio de Michoacán A.C. Cerro de Nahuatzen No. 85, Fracc.Jardines del Cerro Grande, La Piedad de Cavadas, Michoacán, 59370, México
(3) Institute of Physics and Mathematics, Universidad Michoacana de San Nicolás de Hidalgo, Edificio C-3, Ciudad Universitaria, CP. 58040 Morelia, Michoacán, México

*Corresponding author's email: juan.alvarado@cinvestav.mx

Obsidian is a volcanic glass formed when volcanic rhyolitic material is expelled, and formed when the igneous material with a low gas concentration and water content cools fast enough to avoid the crystalline phase, producing an isotropic glass [1,2]. This material is one of the most used through human history, due to the fact that it can form sharp edges, which are ideal for the fabrication of tools and other artifacts [2]. The study of the properties is a fundamental question in archeology and anthropology. Additionally, obsidian analysis is also relevant in the fabrication of synthetic glass, but the main importance is the hydrated form of it, where can be used in a variety of modern applications, such as insulation, remediation of oil spills and as filter, among others. To evaluate the composition and properties of obsidian glass, several techniques have been developed and applied [3,4]. In this work, the thermal properties of obsidian glass from center of Mexico are measured using photothermal techniques. Our studies are complemented by X-Ray diffraction, FTIR and Raman spectroscopy. Our results show that the thermal properties depend strongly on the origin of the material and are the basis for applications of the obsidian as a utilitarian and reinforcing material as well as for the modelling of the formation and evolution of this kind of volcanic glasses.

References

[1] S. Elias, D. Alderton, Encyclopedia of Geology. Academic Press (2020). https://doi.org/10.1016/B978-0-12-409548-9.12527-8

[2] P.J. Sheppard, Obsidian Hydration Dating. (2008) 1695-1698. https://doi.org/10.1016/B978-012373962-9.00220-X

[3] C.M Stevenson, A.K. Rogers, Calibrations for the determination of water species in bulk and hydrated obsidian by infrared photoacoustic spectroscopy. J. Archaeol. Sci. Rep. 6 (2016) 109-114. https://doi.org/10.1016/j.jasrep.2016.01.033

[4] N. Yüksel, The review of some commonly used methods and techniques to measure the thermal conductivity of insulation materials. In Insulation materials in context of sustainability. IntechOpen (2016).

Pulsed thermography in the assessment of in-plane thermal diffusivity: aperiodic, periodic and random patterns

Bison P[(1)*], Ferrarini G[(1)], Glorieux C[(2)]

(1) ITC-CNR, Padova, Italy
(2) Laboratory for Soft Matter and Biophysics, Department of Physics and Astronomy, KU Leuven, Belgium

*Corresponding author's email: paolo.bison@itc.cnr.it

Background – Parker's method [1] is widely used in commercial and laboratory setups to measure the thermal diffusivity of solids. It adopts a photothermal *transmission* scheme in which one side of a slab, of the material of which the thermal diffusivity is to be assessed, is heated by a light pulse and the temperature of the other side, typically detected by IR radiometry or IR thermography, is recorded and analysed in time. When the thickness of the specimen is so large to prevent a reliable measurement (poor S/N ratio), or, when the transmission mode is not feasible, a *reflection* scheme must be adopted. In case of a thermally thin plate, both the *in-plane* and *in-depth* thermal diffusivity can be measured. For thick samples (ideally semi-infinite), only the in-plane diffusivity can be measured. In case the in-plane thermal diffusivity is the quantity of interest, then use can be made of contactless photothermal excitation, by illuminating the sample surface by a time dependent (e.g. pulsed or step-like) inhomogeneous light pattern. The measured surface temperature field is then initially isomorphic with the (sharp) illumination pattern $I(x,y)$ [W m^{-2}], and gradually evolves to a smooth pattern, where the smoothing distance is of the order of the thermal diffusion length $\mu = \sqrt{\alpha \cdot t}$ with a [m^2 s^{-1}] the thermal diffusivity and t [s] the time. Several patterns have been proposed in literature, ranging from a gaussian spot [2], to a gaussian line, a periodic grating source [3,4] and a random pattern [5].

This article reports on the use of different impulsive light patterns, projected on different specimens, and of a 2D spatial Fourier transform approach that was used to extract the thermal diffusivity from the spatiotemporal evolution of the temperature, as measured by an IR camera. Limitations of the technique, related to the finite spatial resolution and spatial windowing are discussed.

Methods – When the surface of an opaque semi-infinite body is impulsively (delta function) heated by a generic spatial function, then, assuming absence of heat exchange with the environment, the spatial Fourier transform of the surface temperature field is described by:

$$\Theta\left(k_x, k_y, z=0, t\right) = \frac{g\left(k_x, k_y\right)}{e\sqrt{\pi\, t}}\; e^{-\left(k_x^2+k_y^2\right)\alpha t}$$

with k_x and k_y the wavenumbers [m^{-1}] of the x and y directions, respectively; z [m] the in-depth coordinate, t the time, g the spatial Fourier Transform of the function describing the heat released on the surface as a result of the excitation pattern $I(x,y)$, and e [J m^{-2} K^{-1}s$^{-1/2}$] the thermal effusivity. The experimental lay-out that was used to approximately realize the above geometry is depicted in Fig. 1. A slab of clay brick of 2.8 cm x 2.5 cm x 1 cm with nominal thermal diffusivity $\alpha \cong 5.0\times10^{-7}$ [m^2 s^{-1}] (top-left) was mounted on the sample holder (top-center). A pulsed Nd:YAG laser beam (Fig. 1 bottom-left) (1064 nm, max energy 30 J, pulse duration 50-2000 μs) with a top-hat beam profile with 0.5 inch

diameter, was patterned by passing through a metallic flame diffuser (Fig. 1 top-right), and was photothermally exciting the sample. A FLIR SC3000 IR camera (LW), was collecting a sequence of images @150 Hz from shortly before the impulsive excitation till about 2s after. One pixel of the image covered an area of 108x108 μm^2. An example of the IR image, acquired immediately after the laser pulse is shown (bottom-right).

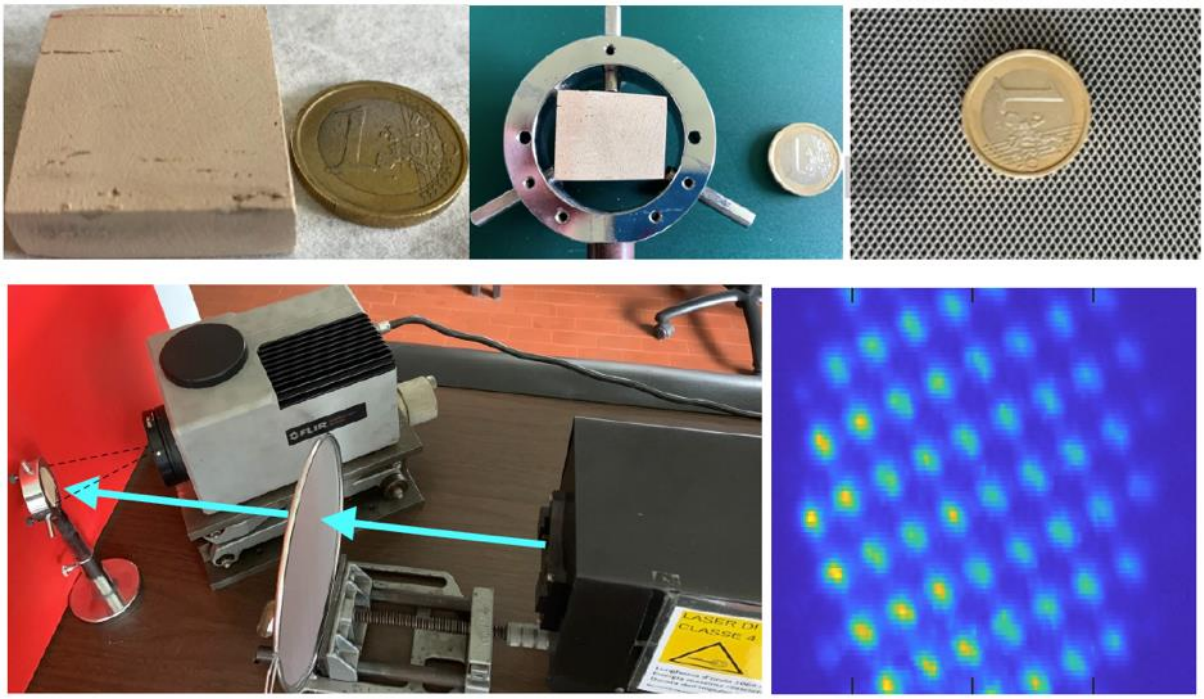

Fig. 1. Top: the clay brick sample (left), sample holder (center), pattern generator-flame diffuser (right). Bottom: experimental lay-out (left) including sample holder, IR camera, laser, flame diffuser; IR image just after the laser pulse (right).

Results – A spatial fast Fourier transform (FFT) was applied to each IR image, thus acquiring the temporal evolution of $\Theta(k_x,k_y)$. The thermal diffusivity was then determined by performing linear regression on $\ln(\Theta(k_x,k_y)t^{1/2})$ for different wavenumber combinations, yielding slope values s [s^{-1}] and diffusivity values $\alpha = -s/k^2$, with $k=(k_x^2+k_y^2)^{1/2}$ the wavenumber magnitude. Slope values that correspond with pronounced and therefore most reliable spatial Fourier components were selected and are shown in Fig. 2. Linear regression of $s(k^2)$, with intercept forced to zero (cfr model expectations), yielded $\alpha = (5.1\pm0.3)\ 10^{-7}$ m^2·s^{-1}, consistent with the nominal value. Not forcing the intercept yielded $\alpha = (4.4\pm0.4)\ 10^{-7}$ m^2·s^{-1}.

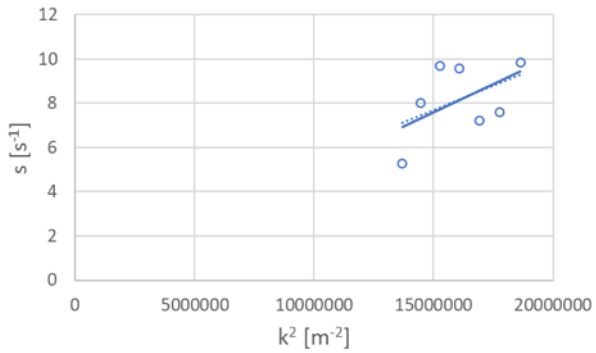

Fig. 2. Dependence of the slopes that were obtained by linear regression of $\ln(\Theta(k_x,k_y)t^{1/2})$ vs time on the square of the wavenumber magnitude. The trendlines are linear regression fits with (dotted line) and without (full line) intercept forced to zero.

Acknowledgements – This work has been supported by the Consiglio Nazionale delle Ricerche, Short Term Mobility Program – 2021 (STM 2021) n. 57862.

References

[1] W.J. Parker, R.J. Jenkins, C.P. Butler, G.L. Abbott, Flash Method of Determining Thermal Diffusivity, Heat Capacity, and Thermal Conductivity, J. App. Phys. 32, 1679-1684. https://doi.org/10.1063/1.1728417.

[2] F. Cernuschi, A. Russo, L. Lorenzoni, A. Figari, In-plane thermal diffusivity evaluation by infrared thermography, Review of Scientific Instruments 72 (2001) 3988-3995 https://doi.org/10.1063/1.1400151.

[3] G. Kalogiannakis, D. Van Hemelrijck, S. Longuemart, J. Ravi, A. Okasha, C. Glorieux, Thermal characterization of anisotropic media in photothermal point, line, and grating configuration, Journal of Applied Physics 100, 063521 (2006). https://doi.org/10.1063/1.2335381.

[4] J.C. Krapez. Diffusivity measurement by using a grid-like mask. Journée SFT Thermographie infrarouge 03 1999.

[5] J.-C. Batsale, J.-L. Battaglia, O. Fudym, Autoregressive algorithms and spatially random flash excitation for 2D non-destructive evaluation with infrared cameras, Quantitative InfraRed Thermography Journal, 1:1 (2004) 5-20. DOI: 10.3166/qirt.1.5-20.

Structural, thermal, and electrical transport correlations in p-type Si as a function of carrier concentration: the effect of intrinsic and extrinsic defects

Martinez-Hernandez HD[(1)*], Martinez-Munoz PE[(1)], Ramirez-Gutierrez CF[(2)], Martinez-Ascencio EU[(3)], Millan-Malo B[(4)], Rodriguez-Garcia ME[(4)]

(1) Posgrado en Ciencia e Ingeniería de Materiales, Centro de Física Aplicada y Tecnología Avanzada Universidad Nacional Autónoma de México, Campus Juriquilla, Querétaro, Qro., 76230, México
(2) Universidad Politécnica de Querétaro, El Marqués, Qro., México
(3) Departamento de Nanotecnología, Centro de Física Aplicada y Tecnología Avanzada, Universidad Nacional Autónoma de México, Campus Juriquilla, Querétaro, Qro., 76230, México

*Corresponding author's email: hdmartinezh@uqvirtual.edu.co

Studying the thermophysical properties of semiconductor materials used in the electronics industry is essential to improve electronic device design and integrated circuits, where performance depends heavily on electro-thermal interactions. These materials can transfer heat through lattice vibrations and energy transport by free electrons [1].

Intrinsic (carrier distribution, carrier lifetime, diffusion coefficient, recombination velocity) and extrinsic (defect densities, pressure for growing, annealing) parameters are involved in silicon (Si) wafers machining. Electronic-phonon interactions and carrier concentration variations from 10^{17} to 10^{21} cm^{-3} have been considered in the thermal conductivity modelling. Due to the increase in the carrier density, there is an increase in the electronic thermal conductivity; therefore, the phononic thermal conductivity decreases by up to 45 % [2].

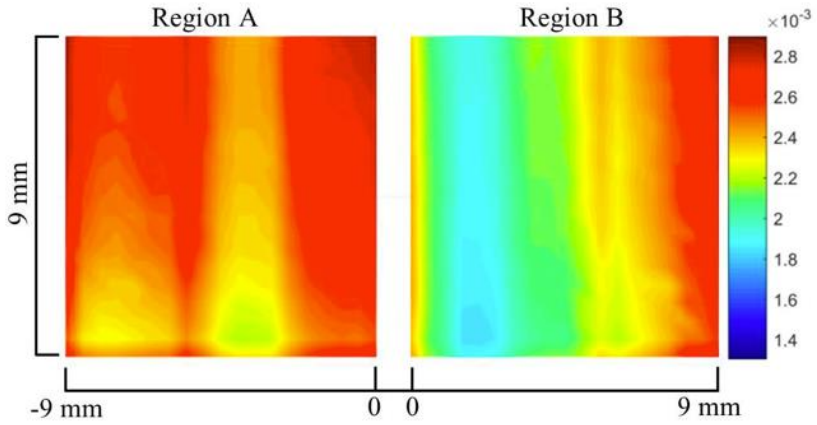

Fig. 1. Photocarrier images for two regions located at the centre of a Si wafer with a resistivity of 0.1 Ω·cm.

In monocrystalline semiconductor material, its structural properties govern thermal and electrical ones. Here, it was investigated the effect of defects induced by intrinsic and extrinsic parameters on the structural, thermal, and electrical properties during manufacturing processes and samples preparation in *p*-type Si wafers with different carrier concentrations. Photocarrier images showed that Boron carrier

distribution exhibits local variation across a wafer as is indicated in Fig. 1. Fig. 2 shows a thermal diffusivity mapping for a wafer without cuttings where local variations in this property are evidenced. The Hall effect measurements in cut and polished samples delivered structural damages effecting the carrier lifetime changes. The crystalline quality obtained by studying the FWHM of the X-Ray patterns elucidated the effect of intrinsic carrier contribution on the structural properties. Thermal diffusivity and heat capacity of the cut samples exhibit a decrease as carrier concentration increases and are negative affected by the crystal damage. Thermal and electrical properties are governed by structure state determined by intrinsic and extrinsic parameters.

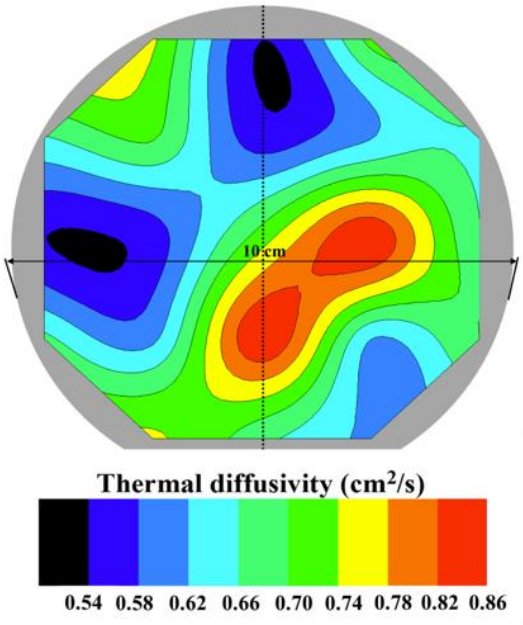

Fig. 2. Thermal diffusivity contour map taken from a p-type Si wafer with a resistivity of 0.1 Ω·cm.

References

[1] M.E. Rodriguez, A. Mandelis, G. Pan, L. Nicolaides, J.A. García, Y. Riopel, Computational aspects of laser radiometric multiparameter fit for carrier transport property measurements in Si wafers, J. Electrochem. Soc. 147 (2000) 687-98. https://doi.org/10.1149/1.1393254.

[2] B. Liao, B. Qiu, J. Zhou, S. Huberman, K. Esfarjani, G. Chen. Significant reduction of lattice thermal conductivity by the electron-phonon interaction in silicon with high carrier concentrations: A first-principles study. Phys. Rev. Lett. 114 (2015) 115901. https://doi.org/10.1103/PhysRevLett.114.115901.

Characterization of TiO_2 thin films deposited on silicon membranes using neural networks

Djordjević KLj[(1)*], Markushev DK[(2)], Popovic MN[(2)], Nesic MV[(1)], Galović SP[(1)], Lukić DV[(2)], Markushev DD[(2)]

(1) University of Belgrade, „VINČA" Institute of Nuclear Sciences - National Institute of the Republic of Serbia, University of Belgrade, PO box 522, 11000 Belgrade, Serbia
(2) University of Belgrade, Institute of Physics Belgrade, National Institute of the Republic of Serbia, Pregrevica 118, 11080 Belgrade (Zemun), Serbia

*Corresponding author's email: katarina.djordjevic@vin.bg.ac.rs

Background – This paper presents a theoretical analysis of the possibility of thermal characterization of a thin TiO_2 film deposited on a 30 μm thick Si membrane as a wafer in the frequency domain of photoacoustics from 20 Hz to 20 kHz. For this purpose, photoacoustic signals generated by such a sample were used (Figure 1) in which the membrane parameters were known and constant, while the film parameters were changed in the ranges of thickness $l_f = (475-525)\,\mathrm{nm}$, thermal expansion coefficient $\alpha_f = (1.045-1.155)\cdot 10^{-5}\,\mathrm{K}^{-1}$, and thermal diffusivity $D_f = (3.515-3.885)\cdot 10^{-6}\,\mathrm{m^2 s^{-1}}$. It can be seen from the Figure 1 that changes in the signal amplitude for the given changes in the film parameters cannot be noticed, while in the phase such changes are clearly noticeable. Within the classical approach of photoacoustic signal processing, non-distinguishing of amplitudes requires the introduction of an additional process of their normalization. In this paper, we will show that well-trained neural networks have no problem distinguishing signal amplitudes and that networks recognize precisely the parameters of thin films on such signals, knowing that the thickness of the films can be two orders of magnitude thinner than their wafers.

Results – The neural networks used in this paper were trained with the basis of photoacoustic signals from Figure 1. The supervised learning algorithm was used by connecting the data of the frequency amplitude-phase characteristics of the input layer signals with the values of the given parameters of the output layer change. The network architecture is very simple and consists of one input (144 neurons), one hidden (10 neurons), and an output layer (3 neurons). The number of input layer neurons corresponds to 144 points that define the photoacoustic signal (72 amplitudes + 72 phases). The three neurons of the output layer are connected to the thin-film parameters: l_f, α_f and D_f. In the case of the thin film thickness, the obtained network performances are 4.3106 x 10^{-6} for 4 epochs, in the case of coefficient of thermal expansion 3.567 x 10^{-5} for 7 epochs, and in the case of thermal diffusivity 0.0044842 for 4 epochs. The prediction of neural networks on test signals with errors of less than 1% shows that the networks are sensitive to small changes in TiO_2 parameters.

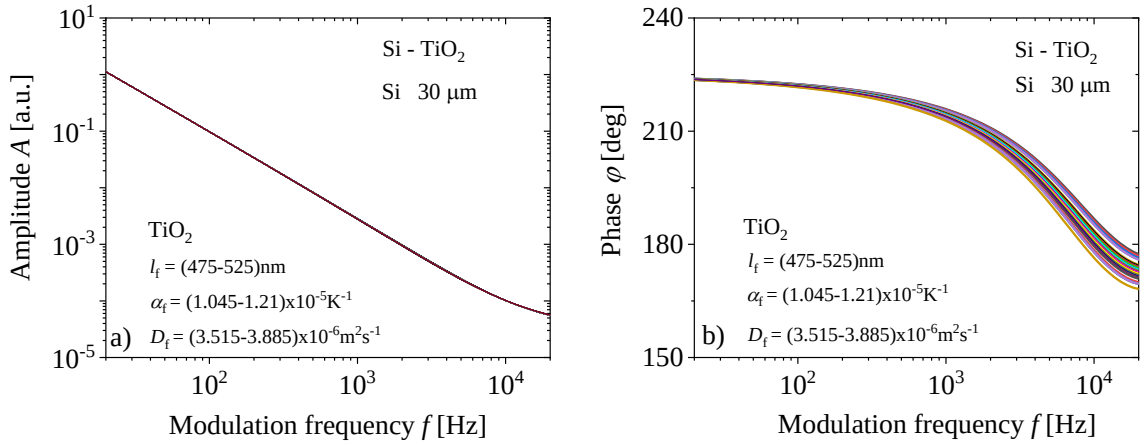

Fig. 1. Photoacoustic signals: a) amplitudes and b) phases of the two-layer model of the TiO2 layer on the Silicon sample obtained by changing the parameters of thickness l_f, expansion α_f and diffusivity D_f of the TiO_2 layer.

Conclusions – Our analysis shows that neural networks have a significant sensitivity to changes in the characteristics of thin layers of TiO_2 deposited on silicon membranes. This fact points to the possibility that neural networks, in combination with photoacoustics, can be a powerful tool in characterizing thin single-layer or multilayer coatings, important for the production of MEMS and NEMS sensors, as well as for the electronics and automotive industries in general.

References

[1] D.M. Todorović, M.D. Rabasović, and D.D. Markushev, Photoacoustic elastic bending in thin film—Substrate system, J. Appl. Phys. 114 (2013) 213510. doi: 10.1063/1.4839835.

[2] N. Jovančić, D. K. Markushev, D.D. Markushev, S.M. Aleksić, D.S. Pantić, D. Korte, M. Franko, Thermal and Elastic Characterization of Nanostructured Fe2O3 Polymorphs and TiO2-Coated Fe2O3 Using Open Photoacoustic Cell, Int. J. Thermophys. 41 (2020) 90. https://doi.org/10.1007/s10765-020-02669-w.

[3] K. Lj. Djordjevic, D.D. Markushev, Ž.M. Ćojbašić, et al. Photoacoustic Measurements of the Thermal and Elastic Properties of n-Type Silicon Using Neural Networks. Silicon (2019) doi:10.1007/s12633-019-00213-6.

[4] K. Lj. Djordjevic, D.D. Markushev, Ž.M. Ćojbašić, S.P. Galović, Inverse problem solving in semiconductor photoacoustics by neural networks, Inv. Prob. Scie. En. 29 (2020) 248 - 262. https://doi.org/10.1080/17415977.2020.1787405.

[5] S.M. Aleksić, D.K. Markushev, D.D. Markushev, D.S. Pantić, D.V. Lukić, M.N. Popović, S.P. Galović, Photoacoustic Analysis of Illuminated Si-TiO_2 Sample Bending Along the Heat-Flow Axes. Silicon (2022). https://doi.org/10.1007/s12633-022-01723-6.

02
Materials Research and Characterization

Mid-infrared photothermal microscopy

Cheng J-X(1)*

(1) Boston University Photonics Center, Boston, USA

*Corresponding author's email: jxcheng@bu.edu

Mid-infrared (IR) spectroscopic imaging using inherent vibrational contrast has been broadly used as a powerful analytical tool for sample identification and characterization. However, the low spatial resolution and large water absorption associated with the long IR wavelengths hinder its applications to study subcellular features in living systems. Recently developed mid-infrared photothermal (MIP) microscopy overcomes these limitations by probing the IR absorption–induced photothermal effect using a visible light [1-6]. MIP microscopy yields sub-micrometer spatial resolution with high spectral fidelity and reduced water background. In this presentation, we overview different mid-infrared photothermal contrast mechanisms and discuss instrumentations for scanning and widefield MIP microscope configurations. We highlight a broad range of applications from life science to materials. We further provide future perspective and potential avenues.

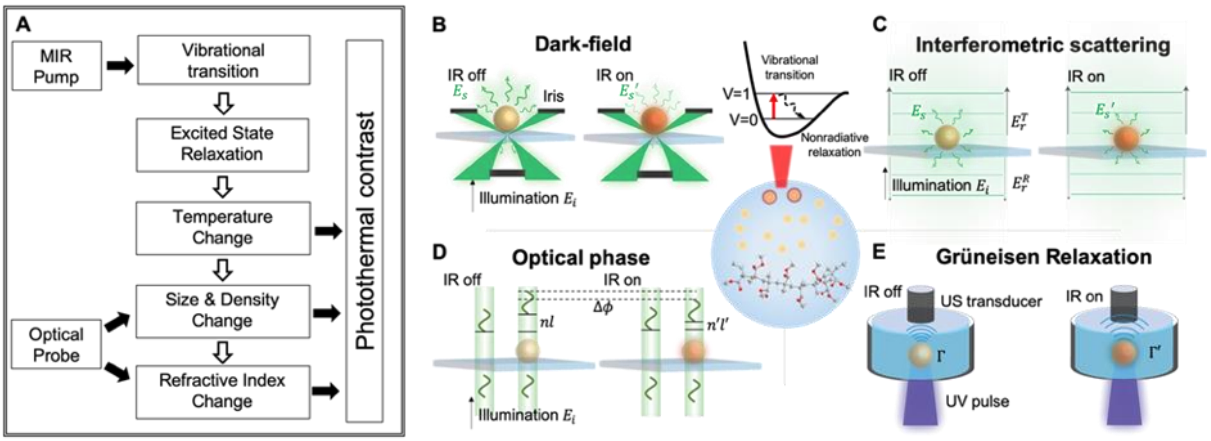

Fig. 1. principle and contract mechanism of mid-infrared photothermal microscopy, adapted from Science Advances, 2021, 7: eabg1559.

References

[1] J. Yin, L. Lu, Y. Zhang, H. Ni, Y.Tan, M. Zhang, Y. Bai, J.-X. Cheng, Nanosecond-resolution photothermal dynamic imaging via MHZ digitization and match filtering, Nature Comm. 12 (2021) 7097.

[2] Y. Zhang, H. Zong, C. Zong, Y. Tan, M. Zhang, Y. Zhan, J.-X. Cheng, Fluorescence-detected mid-infrared photothermal microscopy, Journal of Am. Chem. Soc. 43 (2021) 11490-9.

[3] Y. Bai, J. Yin, J.-X. Cheng, Bond-Selective Imaging by Optically Sensing the Mid-Infrared Photothermal Effect, Science Advances, review, 7: eabg1559 (2021).

[4] D. Zhang, L. Lan, Y.Bai, H. Majeed, M.E. Kandel, G. Popescu, J.-Xi. Cheng, Bond-selective transient phase microscopy via sensing the infrared photothermal effect, Light Sci & Appl. 8 (2019) 116.

[5] Y. Bai, D.g Zhang, Y. Huang, L. Lan, K. Maize, A. Shakouri, Ji-Xin Cheng, Ultrafast Chemical Imaging by Widefield Photothermal Sensing of Infrared Absorption, Science Advances, 5: eaav7127 (2019).

[6] D. Zhang, C. Li, C. Zhang, M.N. Slipchenko, G. Eakins, J.-X. Cheng, Depth-resolved mid-infrared photothermal imaging of living cells and organism with sub-micron spatial resolution, Science Advances, 2:e1600521 (2016).

KEYNOTE SPEAKER

Photoacoustic and photothermal methods towards the characterization of solar energy conversion technologies: progress to date

Baesso ML[(1)*], Bento AC[(1)], Astrath NGC[(1)], Lima SM[(2)], Andrade LHC[(2)], Nunes LAO[(3)], Catunda T[(3)], Calvo-Castro J[(4)], Cella N[(5)]

(1) Department of Physics, State University of Maringá, Maringá, Brazil
(2) CERNA, Universidade Estadual de Mato Grosso do Sul, Dourados, Brazil
(3) Instituto de Física de São Carlos, Universidade de São Paulo, São Carlos, SP, Brazil
(4) School of Life and Medical Sciences, University of Hertfordshire, Hatfield, UK
(5) Instituto Politécnico, State University of Rio de Janeiro, Nova Friburgo, Brazil

*Corresponding author's email: mlbaesso@uem.br

Despite the advancements in the field of solar energy production, there remains an acknowledged challenge associated to efficiency losses due to arguably low spectral overlap between that of the active material and the solar spectrum (Figure 1(a) for a crystalline single junction silicon solar cells (c-Si) [1-3]). As a consequence, a significant part of the incident sunlight energy is converted into heat, accounting for losses over 80% of the incident solar energy [1]. In response to this, significant efforts have been devoted to the realisation of novel materials with improved solar cell efficiency as well as reduced production costs. The achieved technological advances already resulted in new emerging technologies, such as the so-called 'Third generation solar cells" based on tandem, perovskite, dye-sensitized, organic, as well as spectral converters [1-3]. In fostering the development of superior active materials in such optoelectronic devices, the reliable determination of the photovoltaic efficiency is paramount, with photoacoustic and photothermal methods representing highly desirable techniques to do so. Both are based on the detection of heat induced in a sample after light excitation. These techniques can be applied to evaluate the photovoltaic efficiencies of the devices as well as the thermophysical parameters of related materials used in their construction. Motivated by this, herein we report on the utilisation of state-of-the-art photoacoustic and photothermal methods for the characterization of solar cell devices and their built-in materials. In addition, we comment on our views to shed light and pave the way for the development of superior technologies.

In this context, we deem as particularly relevant the use of photoacoustic spectroscopy for the determination of band gaps, evaluation of the photovoltaic effect as well as thin film thickness measurements. In short, we report on the use of thermal lens and thermal mirror methods to measure the fraction of the energy converted into heat in optical materials referred to as spectral converters. Such architectures are characterized by a pair of rare earth ions having the highly-desirable capability to undergo down-conversion processes, whereby high energy photons are converted into low energy ones in the infrared, at the c-Si band gap. As an example, Figure 1(b) illustrates pairs of ions (Eu^{2+} and Nd^{3+}) that could induce down-conversion processes, e.g. these ions can efficiently absorb UV and visible light with Yb^{3+} acting as the acceptor ion due to its emission around 980 nm matching to that of (c-Si) absorption (bandgap ~1.1 eV). In such processes, Eu^{2+} and Nd^{3+} are called activators and Yb^{3+} the sensitizer ions, respectively. Importantly, when coupled to single junction silicon solar cells, these spectral converters can enhance their PV efficiency.

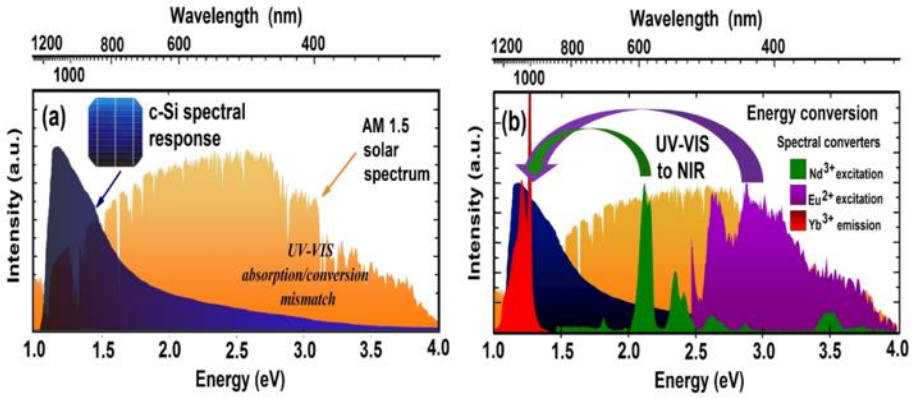

Fig. 1. (a) Solar spectrum (AM1.5G) in the UV-Vis-NIR regions and the spectral response of the c-Si solar cell. **(b)** Optical absorption coefficients of Eu^{2+} and Nd^{3+} activators and the Yb^{3+} sensitizer emission around 980 nm, close to the c-Si band gap [3].

In this work, we will be presenting a number of studies exemplifying the critical role that thermal lens and thermal mirror techniques can play in the quantitative characterization of these aforementioned processes. As a result, we strongly believe this work to be of significant interest to those engaged in the development of superior solar energy conversion technologies as well as the utilisation of photoacoustic and thermal methods as characterization alternatives.

[1] S. Almosni et al., Material challenges for solar cells in the twenty-first century: directions in emerging technologies, Sci. Technol. Adv. Mater. (19) (2018) 336-369. Doi:10.1080/14686996.2018.1433439.

[2] E.L. Savi et al., Thin-film of Nd^{3+}–Yb^{3+} co-doped low silica calcium aluminosilicate glass grown by a laser deposition technique, J. Appl. Phys. 131 (2022) 055304-1-8. doi.org/10.1063/5.0067794.

[3] A.C. Bento et al., Photoacoustics and photothermics and the photovoltaic efficiency of solar cells: A tutorial, *submitted to J. Appl. Phys.*

KEYNOTE SPEAKER

Thermographic imaging for applications in cultural heritage

Mercuri F[(1)*], Orazi O[(1)], Zammit U[(1)], Ceccarelli S[(1)], Caruso G[(2)], Paoloni S[(1)]

(1) Department of Industrial Engineering, University of Rome Tor Vergata, Rome, Italy
(2) Institute of Heritage Science- National Research Council of Italy (ISPC-CNR), Montelibretti (Rome), Italy

*Corresponding author's email: mercuri@uniroma2.it

Introduction – In the investigation of cultural heritage items, most of the valuable information often lies below the surface and, therefore, it is not accessible by means of ordinary visual inspection. On the other hand, such information is of the highest importance for scholars and conservators and highly fascinating to the general public. Due to this reason, over the recent years, non-destructive techniques for the analysis of artworks have been developed and, among others, infrared thermography is nowadays established as one of the most effective tool [1-5].

Although most of the thermographic studies have initially been carried out on mainly a qualitative way by the mere analysis of the recorded images, more recently a number of artefacts have been also quantitatively characterized by means of infrared thermography. Such characterizations require different thermographic approaches, both in terms of experimental configuration and of signal modelling, depending on both the optical and thermal properties of the artefact constituent materials.

In this work, after briefly reviewing the main aspects underlying the employ of the active thermography to the study of the cultural heritage, we report on some relevant results obtained by the application of the above mentioned thermographic approaches to the study of different kind artefacts characterized by semi-transparent external layers like paintings [6], illuminations and book-bindings [5].

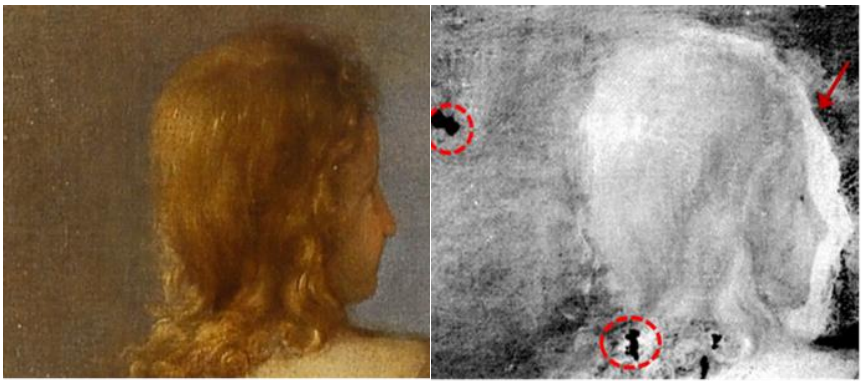

Fig. 1. Photo (left) and thermogram (right) of a painting revealing some *pentimenti* (arrow) and restorations (circles) beneath the surface [6].

In the case of book-bindings, we performed a quantitative analysis of those effects affecting the image quality of the features lying beneath paper and parchment layers, shown by means of the pulsed thermography. This can be particularly useful in the study of the historical book-bindings often made

by using waste library materials of earlier periods consisting of written or printed scraps which are now buried beneath the cover or the counterguard and no longer visible.

Experimental and samples – The investigations have been carried out by means of the Pulsed Thermography (PT). The samples were heated by flash lamps delivering 3ms long pulses. The stimulated Mid Wave Infrared (MWIR) radiation emitted from the sample have been recorded by a MWIR camera in the 3.6–5.1μm wavelength range. Thermograms have been recorded over an acquisition time of up to 2 s after the pulsed heating with frame rates in the range between 150 and 500 Hz.

In order to explore the PT capability to detect and characterize graphic elements hidden beneath paper and parchment, some laboratory test samples consisting in ink layers laying beneath paper leaves of different thickness, have been prepared. They have been exploited to study the contrast of the buried ink features shown by the thermogram, as a function of time and depth. The quantitative analysis of the contrast *C*, assumed as the difference between the PT signal values taken on the inked and non-inked areas of the sample, respectively, was performed by adopting a simple theoretical 3D heat diffusion model implemented by a Finite Element Method (FEM) which accounts for the thermographic signal evolution.

Results and discussion – In the following, some results of a study carried out on the readability of hidden text are reported [7]. In this kind of investigation, the lateral diffusion of heat, which blurs the edges of buried writing, plays a crucial role, and the need to adopt a 3D analysis for the interpretation of PT thermograms is therefore essential. In particular, it is shown how the adopted 3D model proved effective in determining the PT signal profile across the edge of buried ink elements, and how it depends on the physical-geometric characteristics of the ink-paper structure. Finally, the soundness of the theoretical results was evaluated by comparing them with the experimental ones obtained by measuring the test sample described above.

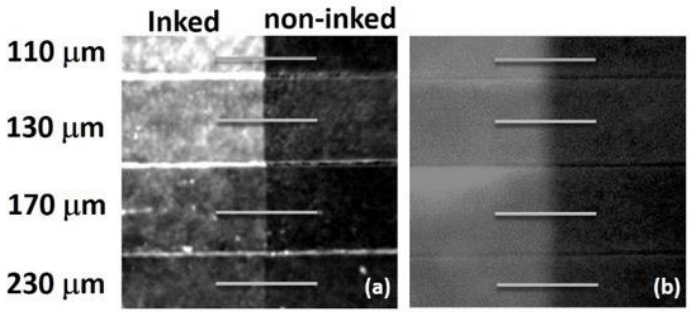

Fig. 2. Thermograms of the edge of the inked areas buried at different depths, recorded at (a) t=0.06s and (b) t=0.93s delays.

Fig. 2 shows two thermograms of the test sample, taken from the front side of the paper sheets of different thickness lying on top of the buried inked feature edge. They have been recorded at delay times of t=0.06s and t=0.93s from the heating light pulse. In the thermogram taken at later time the edge of the inked region appears broadened because of the lateral heat diffusion having occurred for a longer time and therefore being of a greater extent. In order to quantify such edge smearing effect, the following distortion parameter

$$\Delta(t) = x_{max}(t) - x_{min}(t) \qquad \text{Eqn. 1}$$

has been introduced. It accounts for the distance between the maximum and minimum contrast that occurs in the thermogram across the ink edge and defines how differently from an ideal step like profile ($\Delta = 0$) the signal contrast appears.

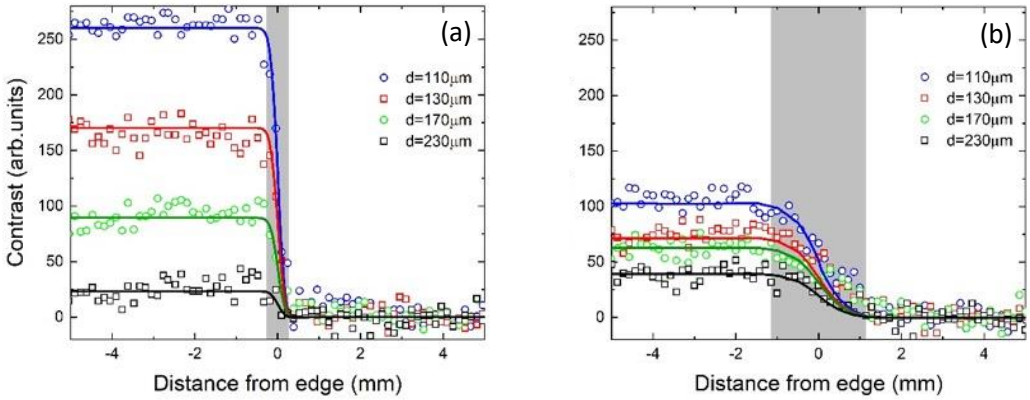

Fig. 3. Experimental (symbols) and theoretical (lines) contrast profiles across the inked edge areas recorded at two different delays: t=0.06s **(a)** and t=0.93s (**b)**. The corresponding distortion indexes are Δ=0.56 mm (a) and Δ=2.30 mm (b), respectively.

In Fig. 3 shows the contrast curves obtained with the experimental data extracted from the thermograms of Fig. 2 along the highlighted lines crossing the edge of inked areas, lying at different depths. The curves obtained by the theoretical model for the corresponding depths have been also reported. The experimental data clearly show that the contrast decreases, as expected, with increasing ink layer depth, while the range where the distortion is relevant (highlighted in the figures) becomes broader for increasing delay times because of the increasing lateral heat diffusion. Moreover, at equal delay times, the distortion index Δ of the different contrast profiles, turns out to be the same for all the ink depth values. Finally, it is worth mentioning that the theoretical curves, if properly rescaled, superimposes very well the corresponding experimental data, witnessing the effectiveness of the adopted model.

References

[1] D. Gravilov, R.Gr. Maev, D.P. Almond, A review of imaging methods in analysis of works of art: Thermographic imaging method in art analysis, Can. J. Phys. 92 (2014) 341-364. http://dx.doi.org/10.1139/cjp-2013-0128.

[2] F. Mercuri, U. Zammit, N. Orazi, S. Paoloni, M. Marinelli, F. Scudieri, Active infrared thermography applied to the investigation of art and historic artefacts, J. Therm. Anal. Calorim. 104 (2011) 475-485. http://dx.doi.org/10.1007/s10973-011-1450-8.

[3] C. Ibarra-Castanedo, F. Khodayar, M. Klein, S. Sfarra, X. Maldague, H. Helal, M. Tayoubi, B. Marini, J.C. Barré, Infrared vision for artwork and cultural heritage NDE studies: principles and case studies, Insight 59 (2017) 243. https://doi.org/10.1784/insi.2017.59.5.243.

[4] K. Blessley, C. Young, J. Nunn, J. Coddington, S. Shepard, The Feasibility of Flash Thermography for the Examination and Conservation of Works of Art, Stud. Conserv. 55 (2010) 107. https://doi.org/10.1179/sic.2010.55.2.107.

[5] S. Paoloni, F. Mercuri, N. Orazi, G. Caruso, U. Zammit, Photothermal approach for cultural heritage research, J. Appl. Phys. 128 (2020) 023432. https://doi.org/10.1063/5.0023432.

[6] S. Ceccarelli, N. Orazi, F. Mercuri, S. Paoloni, U. Zammit, F. Petrucci, Thermographic and reflectographic imaging investigations on Baroque paintings preserved at the Chigi Palace in Ariccia, ACTA IMEKO 10 (2021) 187-192.

[7] G. Caruso, F. Mercuri, U. Zammit, S. Paoloni, S. Ceccarelli, N. Orazi, 3D heat flow effects in the imaging of subsurface graphical features in semi-transparent media by pulsed thermography, Measurement 185 (2021) 110111. https://doi.org/10.1016/j.measurement.2021.110111.

KEYNOTE SPEAKER

Front detection laser-spot active infrared thermography for thermal characterisation of insulating solids

Bedoya A[(1)], Rodríguez F[(2)], Jaime J[(2)], García-Segundo C[(2)], Marín E[(2)*]

(1) Instituto de Ciencias Aplicadas y Tecnología, Universidad Nacional Autónoma de México, Circuito Exterior S/N, Ciudad Universitaria, AP 70-186, CP 04510, Ciudad de México, Mexico

(2) Instituto Politécnico Nacional, Centro de Investigación en Ciencia Aplicada y Tecnología Avanzada, Unidad Legaria, Legaria 694, Colonia Irrigación, Delegación Miguel Hidalgo, Ciudad de México 11500, Mexico

*Corresponding author's email: emarinm@ipn.mx

Infrared thermography is a useful tool for thermal characterization of materials in a non-destructive way. The parameter usually determined by this technique is the thermal diffusivity. Recently, the usefulness of laser-spot active lock-in infrared thermography technique to also recover the thermal conductivity of bad thermal conductors, taking advantage of the heat losses by conduction from the sample to the surrounding air [1]. The experimental results presented in the mentioned paper were taken using a rear detection configuration. In this work, we show the usefulness of the front detection configuration for the same purpose. The experimental set-up is shown schematically in Fig. 1.

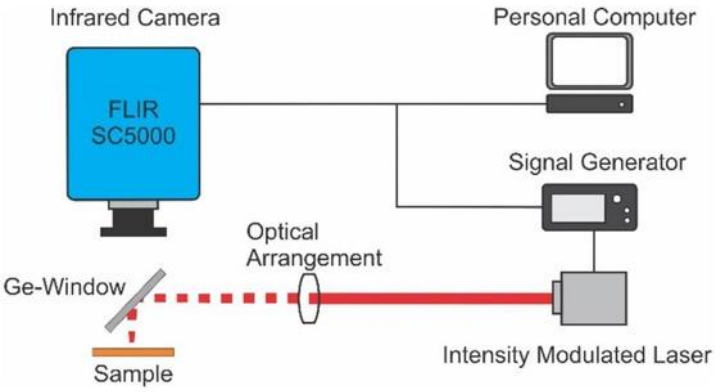

Fig. 1. Schema of the experimental setup. The laser intensity was periodically modulated at a given frequency using a signal-generator. The laser spot size and a mean power at the sample's position were 300 μm (radius) and 10 mW, respectively. A Ge-window was used as a mirror to steer the laser beam to the sample, allowing the heat radiated by the sample to be pictured by the IR camera (Spatial Resolution of 89.5 μm at 100 images/s. Working distance: 17 cm).

A surface thermogram is recorded at the modulation frequency using a thermographic video camera equipped with a Lock-in amplifier unit, from which amplitude and phase profiles are obtained as a function of the radial distance from the heating spot point. Then, the values of the two mentioned thermal properties are accurately determined by a simultaneous multiparametric fit of the amplitude and phase profiles to the analytical expression describing the temperature field. We show the appearance of maxima and minima in the amplitude profiles at distances from the heating point that are closely related to the thermal wavelength, a behavior that reminds us of interference conditions like those that have been used in a common way to explain other photothermal phenomena [2]. Several samples were studied. Fig. 2 shows a typical result obtained for Polymethyl methacrylate (PMMA). The possibility

of using the method for recovering the components of the in-plane thermal properties' tensor in anisotropic samples is discussed too.

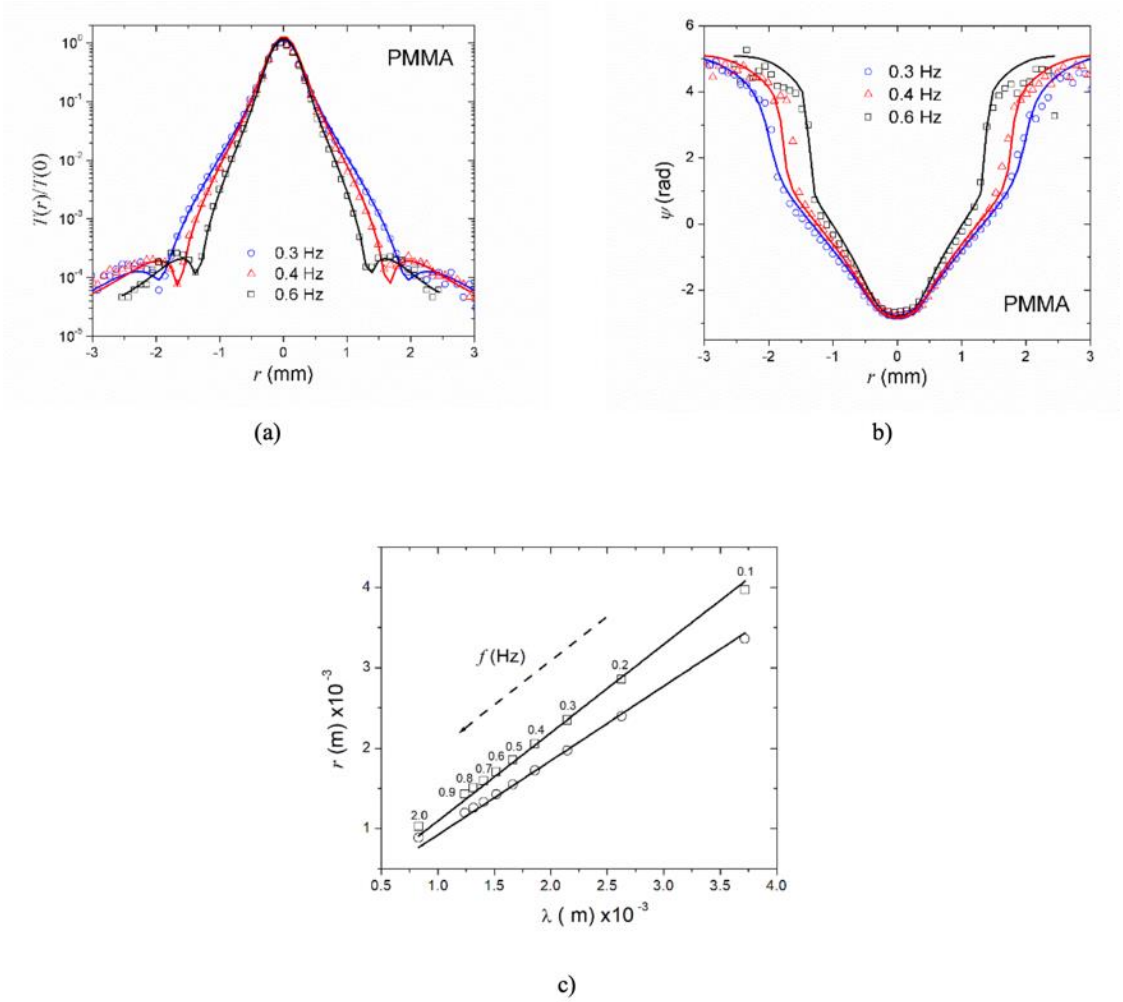

Fig. 1. Normalized amplitude **(a)** and phase **(b)** as a function of the radial distance from the heating point at three modulation frequencies for a PMMA sample. The symbols are the experimental data points, and the solid curves are the results of the best least squares fits using the expression given by the theoretical model described in Ref. [1]. The obtained values of thermal conductivity and diffusivity were (1.06 ± 0.02) × 10^{-7} m^2 s^{-1} and (0.20 ± 0.01) W m^{-1} K^{-1}, respectively, in good agreement with literature reported ones. **c)** The positions of the maxima (squares) and minima (circles) of the amplitude versus r curves as a function of the thermal wavelength in the sample for PMMA. The solid curves are the best least squares linear fits with slopes 1.09 ± 0.01 and 1.85 ± 0.02.

References

[1] A. Cifuentes, A. Mendioroz, A. Salazar, Simultaneous measurements of the thermal diffusivity and conductivity of thermal insulators using lock-in infrared thermography, Int. J. Thermal Sci. 121 (2017) 305-312. http://dx.doi.org/10.1016/j.ijthermalsci.2017.07.023.

[2] J.A.P. Lima, E. Marın, M.G. da Silva, M.S. Sthel, S.L. Cardoso, D.F. Takeuti, C. Gatts, H. Vargas, On the use of the thermal wave resonator cavity sensor for monitoring hydrocarbon vapors, Rev. Sc. Instrum. 71 (2000) 2928-2932. https://doi.org/10.1063/1.1150712.

KEYNOTE SPEAKER

Refractive index changes in solid state laser materials

Catunda T[(1)*], Moncorgé[(2)] R, dos Santos JFM[(1)], Zanuto VS[(3)]

(1) Instituto de Fisica de Sao Carlos, Universidade de Sao Paulo, USP C.P. 369, CEP 13560-970 Sao Carlos, SP, Brazil

(2) Centre de Recherche sur les Ions, les Materiaux et la photonique (CIMAP), UMR 6252 CEA-CNRS-ENSICAEN, Universite de Caen, France

(3) Departamento de Física, Universidade Estadual de Maringá, Av. Colombo 5790, 87020-900, Maringá, PR, Brazil

*Corresponding author's email: tomaz@ifsc.usp.br

A few years after the invention of the ruby laser it became clear that laser-induced refractive index changes (RIC) have a major impact in laser behavior. In fact, all the main laser features (monochromaticity, directionality, coherence and brightness) are affected by RIC [1,2]. The propagation of intense optical beams through dielectric media induces RIC which cause self-focusing, beam breakup and damage in high power pulsed laser systems. For a laser beam of intensity, I, the fast host nonlinearity (crystal or glass) is important in high power short pulsed lasers, causing RIC with $\Delta n = \gamma I$ and $\gamma \sim 10^{-16}$ cm^{2}W^{-1}. Besides this effect, very important slow (~ 10^{-4}sec) thermal and electronic RIC appears due to the pumping of the upper laser level which, for Solid-State Lasers (**SSL**) is usually the metastable state of a doping ion . For instance, in ruby and glass lasers it was soon realized that optical distortions caused by heat deposition could virtually preclude diffraction-limited laser operation. Moreover, athermal RIC associated with the excited state population of dopand ions (Cr^{3+}, Ti^{3+}, Nd^{3+}, Yb^{3+}, Tb^{3+}, etc.) usually have magnitude comparable to the thermal ones. This electronic contribution to the RIC arises from the fact the polarizability of the ion in its excited state (α_{pex}) is different from its value in the ground state (α_{pg}), so this RIC is proportional to $\Delta\alpha_p = (\alpha_{pex} - \alpha_{pg})$. The importance of $\Delta\alpha_p$ also appeared to explain frequency drifts as well as transverse or lensing effects observed in many SSL lasers. In fact, this lens like behavior determined the names Population Lens (PL) and Thermal Lens (**TL**) related to electronic (athermal) and thermal effects, respectively.

The refractive index change associated with the PL effect of an ion doped material is given by:

$$\Delta n_{PL} = \frac{2\pi}{n} N_{ex} f_L^2 \Delta\alpha_p \qquad \text{Eqn. 1}$$

where $f_L = (n_o^2 + 2)/3$ is the Lorenz local field correction factor, N_{ex} is the excited state population. We assumed that the system has only one excited metastable state, so the total ion concentration is given by $N_t \sim N_{ex} + N_g$, N_g being the ground state population. Let´s consider the case of ruby (Al_2O_3:Cr^{3+}) where $\Delta\alpha_p = 1.8\ 10^{-25}$ cm^{-3} with typical Cr^{3+} concentration $N_t \sim 1.6\ 10^{19}$ cm^{-3}. According to eq.(1) the maximum RIC can be estimated considering $N_{ex} \sim N_t$ so $\Delta n_{max} \sim 3\ 10^{-5}$. Analogously for a typical Nd:YAG crystal $N_t \sim 1.4\ 10^{20}$ cm^{-3}, $\Delta\alpha_p = 5\ 10^{-25}$ cm^{-3} and $\Delta n_{max} \sim 9\ 10^{-5}$. Although these Δn_{max} are not large, they are comparable to RIC due to TL effect or Δn of Fiber Braag Gratings, consequently they have important consequences in laser behavior.

For rare earth (RE) and transition metals doped materials, $\Delta\alpha_p$ is mainly accounted by transitions in the UV. Although far from resonance for visible light, these UV transitions have high oscillator strength,

typically 4 orders of magnitude greater than the forbidden transitions in the visible. In the case of rare earth doped materials, it is generally accepted that the 4f → 5d dipole allowed UV transitions in the should give the main contribution to the ion polarizability since their oscillator strength are typically 3 - 4 orders of magnitude higher than the 4f → 4f. Moreover, it has been observed in Cr^{3+}, Nd^{3+}, Yb^{3+} and Tb^{3+} doped materials that $\Delta\alpha_p$ varies strongly with the host character (~1 order of magnitude): fluorides < phosphates < silicates < oxides. In the case of RE ions, this observation is in qualitative agreement with higher energy position of the 5d levels of fluorides compared to other hosts. Fig.1.(a) show some data of Cr^{3+} doped oxide crystals where $\Delta\alpha_p$ decreases monotonically with the parameter ΔE, the energy difference between $^4T_2$ and ^2E levels of Cr^{3+} [3]. Not shown in Fig.1(a) is the case of the fluoride crystal $\Delta\alpha_p$ = 0.31 10^{-25} cm^3. Fig.1.(b) shows $\Delta\alpha_p$ of Nd doped crystals using the value of Nd:YAG as a reference ($\Delta\alpha_{pYAG}$). This procedure was adopted in to minimize experimental discrepancies between several experimental $\Delta\alpha_p$ data , determined by different groups and using different techniques. It appears that $\Delta\alpha_p$ decreases with band gap of the crystal host and this behavior is also related to the energy position of the 5d levels. Although we do not have the energy position of Nd^{3+} 5d level for all hosts, in general materials with high E_g values (like fluorides) present high energy 5d levels.

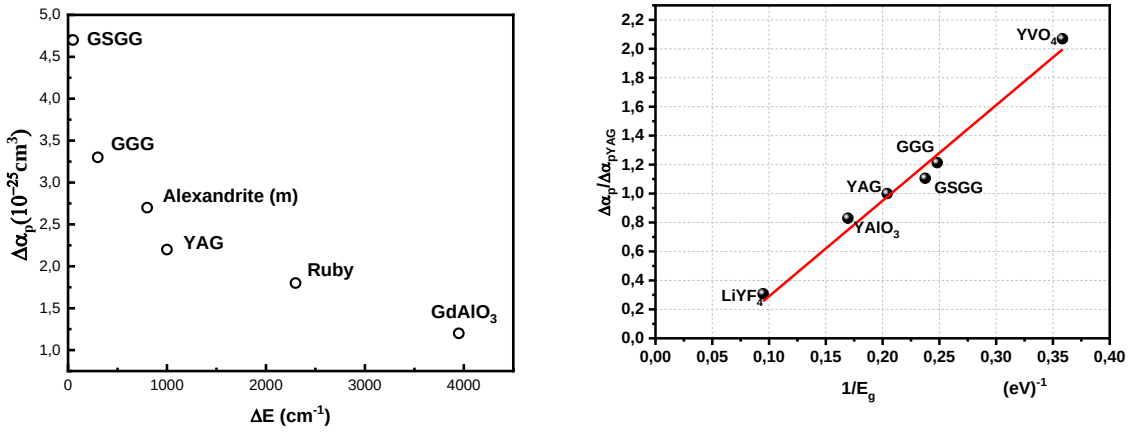

Fig. 1. The strong dependence of $\Delta\alpha_p$ of ion doped materials with the host character. (a) shows the dependence of $\Delta\alpha_p$ of Cr^{3+} doped crystals with the spectroscopic parameter ΔE, which is related to crystal field parameter Dq/B. (b) the dependence of $\Delta\alpha_p$ on Nd^{3+} doped crystal normalized by the value of Nd:YAG, showing that $\Delta\alpha_p$ increases with the inverse of the crystal bandgap (E_g).

The magnitude of the TL effect is related to the phase shift parameter θ_{PL}, which for solids is given by [1]:

$$\theta_{TL} = -\frac{P_{abs}}{\lambda K}\eta_h \frac{ds}{dT}. \qquad \text{Eqn. 2}$$

in which P_{abs} is the absorbed laser power, K is thermal conductivity, (ds/dT) is the temperature coefficient of the optical path length change [$\Delta s = \Delta(nL)/nL$]. The fraction of absorbed energy converted into heat is given by $\eta_h = 1 - \Phi_f.\lambda_{exc}/\langle\lambda_{em}\rangle$, where Φ_f is the fluorescence quantum efficiency, λ_{exc} is the excitation wavelength, and $\langle\lambda_{em}\rangle$ is the average emission wavelength. For instance, for Nd^{3+} doped materials ($\langle\lambda_{em}\rangle$ ~1060nm) and excitation at λ_{exc} ~808nm, η_h~ *24%* for Φ_f ~1. One very important feature of Yb^{3+} doped materials is the low quantum defect with η_h~ *9%* (λ_{exc} ~ 941nm, $\langle\lambda_{em}\rangle$ ~1030nm and Φ_f ~1).

The TL response time is related to heat diffusion time, $t_c = w^2/4D$, where w is the waist of the pump beam and D is the heat diffusion (related to thermal conductivity by $K = \rho C_p D$, ρ is the density and C_p the specific heat).

The TL technique have been applied to the determination of important thermo-optical parameters like K and ds/dT, as well as the determination of small absorption coefficients of transparent solids. Moreover, the determination of the parameter η_h can be used in the determination of Φ_f as well as the study of energy transfer process. Other expressions for η_h can derived in order to consider other effects like laser action, amplified stimulated emission, energy transfer, upconversion, etc.

Most materials present simultaneously PL and TL so it is important to discriminate electronic and thermal effects. The magnitude of PL and TL phase-shifts can be compared considering the parameter θ_{PL}/θ_{TL}, where $\theta_{PL} = (2\pi/\lambda)\Delta n_{PL}L$. In the case of pulsed excitation, when heat diffusion can be neglected, the parameter $(\theta_{PL}/\theta_{TL})_{pul}$ is proportional to $\eta_h\rho C_p\Delta\alpha_p(ds/dT)^{-1}$. For cw excitation, $(\theta_{PL}/\theta_{TL})_{cw} = (\tau/t_c)\,(\theta_{PL}/\theta_{TL})_{pul}$, where τ is the PL response time (given by the ion excited metastable state lifetime).

In this talk we review the subject of RIC changes in ion doped SSL materials. The experimental techniques are based on the TL and PL effects, using the time-resolved Z-scan and mode-mismatched TL techniques. The measurements were performed with a single laser or pump-probe mode, using single frequency or tuneable lasers in order to study line shapes. Moreover, techniques to discriminate TL and PL effects will be discussed since in most cases they appear simultaneously. A comparison of the magnitude of thermal and electronic contributions to RIC in most relevant SSL lasers and amplifiers. Finally, perspectives and challenges will be discussed.

References

[1] C. Jacinto, D.N. Messias, A.A. Andrade, S.M. Lima, M.L. Baesso, T. Catunda, Thermal lens and Z-scan measurements: Thermal and optical properties of laser glasses - A review, J. Non. Cryst. Solids. 352 (2006). https://doi.org/10.1016/j.jnoncrysol.2006.04.025.

[2] R. Soulard, A. Zinoviev, J.L. Doualan, E. Ivakin, O. Antipov, R. Moncorgé, Detailed characterization of pump-induced refractive index changes observed in Nd:YVO_4, Nd:$GdVO_4$ and Nd:KGW, Opt. Express. 18 (2010) 1553. https://doi.org/10.1364/OE.18.001553.

[3] C.R. Kesavulu, R. Moncorg, M. Fromager, K. Ait-Ameur, T. Catunda, Electronic refractive index changes and measurement of saturation intensity in Cr^{3+} doped YAG crystal, Opt. Materials 78 (2018) 107-112. https://doi.org/10.1016/j.optmat.2018.02.013.

Topological insulator nanoparticles – material with prospect for photo-thermal applications

Belec B[(1)*], Kostevšek N[(2)], Pelle GD[(2)], Gardonio S[(1)], Fanetti M[(1)], Valant M[(1)]

(1) Materials Research Laboratory, University of Nova Gorica, Ajdovščina, Slovenia
(2) Department for Nanostructured materials, Jožef Stefan Institute, Ljubljana, Slovenia

*Corresponding author's email: blaz.belec@ung.si

Bismuth selenide (Bi_2Se_3) is one of the most investigated topological insulators (TI). Due to its topological surfaces states (TSS), it displays unique electronic and optical properties [1, 2]**.** Unlike conventional surface states, TSS are robust and unaffected by almost any type of non-magnetic impurities due to the combined effect of the time-reversal symmetry and spin-orbit coupling. However, TSS are stable up to a critical concentration of dopants [3, 4], and as we propose in our study, they can also be disturbed by an organic layer coated on the surface of TI nanoparticles. Namely, the adsorbent-free Bi_2Se_3 nanoparticles display localized surface plasmon resonance (LSPR) due to electronic bulks states and their peculiar TSS, while the coated counterparts do not [5].

The existence of LSPR is also a reason that the TI nanoparticles display a photo-thermal effect [6, 7]. A number of publications on the photo-thermal effect of the TI nanoparticles is scarce. Additionally, all the research was conducted on the nanoparticles, synthesized in presence of organic solvents and/or surfactants, or they were deliberately coated with organic molecules [6, 8-10]. Since the organic molecules affect the TSS, the true photo-thermal effect (the real ΔT induced by illumination) of the TI nanoparticles has not been measured yet.

We recently developed a hydrothermal method for synthesis of the adsorbent-free Bi_2Se_3 nanoparticles [5]. According to a UV-vis spectroscopy, the particles display peak, which corresponds to the LSPR. The photo-thermal experiment reveals that they heat when illuminated with a laser of 808 nm [11]. Since they are free of any adsorbents, we have measured their true photo-thermal effect.

The electronic surface properties of TI and consequently their photo thermal effect can be tuned or even enhanced by shifting the position of the Fermi level. This can be achieved by doping the nanoparticles, but only up to the certain concentration. Till now, there is no research on doping the Bi_2Se_3 nanoparticles, and how this effect their optical and photo-thermal properties [3, 4].

With our developed hydrothermal method, we have successfully synthesized In- and Cr-doped Bi_2Se_3 nanoparticles ($Bi_{2-x}M_xSe_3$, M = In^{3+}, Cr^{3+}). With the UV-vis spectroscopy we have confirmed the presence of the LSPR peaks in all prepared samples showing the TSS are still present. The photo-thermal experiment (808 nm, 3 W/cm^2, 5 min) revealed that the In- and Cr-doped Bi_2Se_3 particles heat under the irradiation. The heating effect was similar or even higher than in the reported studies [6, 8-10]. Such doped TI nanoparticles have a potential to be further used, for instance in bio-medical applications. The TI nanoparticles can be coated with a thin film of porous amorphous silica, which gave us the base for numerous possibilities to attach different targeting molecules. As we recently demonstrated, a thin silica layer does not interfere with TSS and such coated particles still heat under the irradiation. Moreover, ΔT of silica-coated Bi_2Se_3 was higher compared to uncoated one [11].

References

[1] M.Z. Hasan, C.L. Kane, Colloquium: Topological insulators. Rev. Mod. Phys. 82 (2010) 3045-3067.

[2] W. Tian, W. Yu, J. Shi, Y. Wang, The Property, Preparation and Application of Topological Insulators: A Review. Materials 10 (2017).

[3] J. Sánchez-Barriga, I. Aguilera, L. V. Yashina, D.Y. Tsukanova, F. Freyse, A.N. Chaika, C. Callaert, A.M. Abakumov, J. Hadermann, A. Varykhalov, E.D.L. Rienks, G. Bihlmayer, S. Blügel, O. Rader, Anomalous behavior of the electronic structure of (Bi1−xInx)2Se3 Across the Quantum Phase Transition From Topological to Trivial Insulator. Phys. Rev. B. 98 (2018).

[4] J. Moon, N. Koirala, M. Salehi, W. Zhang, W. Wu, S. Oh, Solution to the Hole-Doping Problem and Tunable Quantum Hall Effect in Bi2Se3 Thin Films. Nano Lett. 18 (2018) 820-826.

[5] B Belec, K. Ferfolja, T. Goršak, N. Kostevšek, S. Gardonio, M. Fanetti, M. Valant, Inherent Surface Properties of Adsorbent-Free Ultrathin Bi2Se3 Topological Insulator Platelets. Sci. Rep. 9 (2019)119057-190579.

[6] J. Guozhi, W. Peng, Z. Yanbang, C. Kai, Localized surface plasmon enhanced photothermal conversion in Bi2Se3 topological insulator nanoflowers. Sci. Rep. 6 (2016) 25884.

[7] Y. Zhao, A. Dunn, J. Lin, D. Shi, D. Photothermal Effect of Nanomaterials for Efficient Energy Applications. Micro and Nano Tech (2015) 415-434. 10.1016/b978-0-12-814497-8.00013-8.

[8] Z. Li, Y. Hu, K.A. Howard, T. Jiang, X. Fan, Z. Miao, Y. Sun, F. Besenbacher, M. Yu, Multifunctional Bismuth Selenide Nanocomposites for Antitumor Thermo-Chemotherapy and Imaging. ACS Nano 10 (2016) 984-997.

[9] Z. Li, J. Liu, Y. Hu, K.A. Howard, Z. Li, X. Fan, M. Chang, Y. Sun, F. Besenbacher, C. Chen, M. Yu, Multimodal Imaging-Guided Antitumor Photothermal Therapy and Drug Delivery Using Bismuth Selenide Spherical Sponge. ACS Nano 10 (2016) 9646-9658.

[10] J. Li, F. Jiang, B. Yang, X.R. Song, Y. Liu, H.H. Yang, D.R. Cao, W.R. Shi, G.N. Chen, Topological Insulator Bismuth Selenide as a Theranostic Platform for Simultaneous Cancer Imaging and Therapy. Sci. Rep. 3 (2013) 1998.

[11] B. Belec, N. Kostevšek, S. Nemec, S. Kralj, S. Gardonio, M. Fanetti, M. Valant, Silica coated Bi2Se3 topological insulator nanoplatelets: the way of making them colloidally stable but preserving their optical properties. In 27th Annual Meeting of the Slovenian Chemical Sociedy Portorož (2021) pp 56.

3D imaging of water ice under high-pressure non-hydrostatic load by time-domain Brillouin scattering

Sandeep S[(1)], Thréard T[(1)], De Lima Savi E[(1)], Chigarev N[(1)], Bulou A[(2)], Tournat V[(2)], Zerr A[(3)], Gusev VE[(1)*], Raetz S[(1)*]

(1) Laboratoire d'Acoustique de l'Université du Mans (LAUM), UMR 6613,
Institut d'Acoustique – Graduate School (IA-GS), CNRS, Le Mans Université, Le Mans, France
(2) Institut des Molécules et Matériaux du Mans, UMR 6283 CNRS, Le Mans Université,
Le Mans, France
(3) Laboratoire de Sciences des Procédés et des Matériaux (LSPM-CNRS UPR-3407),
Université Sorbonne Paris Nord (USPN), Villetaneuse, France

*Corresponding authors' email: vitali.goussev@univ-lemans.fr, samuel.raetz@univ-lemans.fr

Background – Time-domain Brillouin scattering (TDBS) technique is an opto-acousto-optic pump-probe technique [1] that uses ultrashort laser pulses to generate coherent acoustic pulses (CAPs) of picoseconds duration in a solid sample and follow their propagation in order to image inhomogeneities of acoustic, optical and/or photo-elastic parameters of materials transparent to the probe light wavelength [2]. This technique presents an axial resolution deeply sub-optical (to nm-scale), controlled by the CAPs width, and a lateral one down to the optical diffraction limit, controlled by lateral focusing of used laser beams. Detection of propagating CAPs is possible because they scatter time-delayed probe laser pulses heterodyned by the probe-pulse reflections from stationary sample surfaces, giving rise to an oscillating component in a transient reflectivity signal: the so-called Brillouin oscillation (BO).

The instantaneous frequency of the BOs is proportional to the product of local optical refractive index (n) and sound velocity along the beam path (v). Hence, in polycrystalline transparent samples made of anisotropic materials where n and v change from grain to grain, the Brillouin frequency changes with the probe delay give access to the depth arrangement of grains. Two-dimensional lateral scanning of the sample hence allows the TDBS technique to provide 3D-imaging of sample texture. In anisotropic grains, up to three bulk acoustical modes, one longitudinal and two shear, might be monitored. The time-frequency analyzes of frequency contents of the TDBS signals provide then access to shapes, relative coordinates of all grains (if resolved), as well as crystallographic orientation of the identified grains with respect to a common coordinate system [3].

The non-contact feature of the TDBS technique further permits to examine samples located in devices used to reproduce extreme conditions such as diamond anvil cells (DACs) for ultrahigh pressure. We report here on the 3D imaging of water ice under high-pressure non-hydrostatic load by TDBS. The 3D characterization of individual grains of two coexisting high-pressure water ice phases is reported, as well as imaging of a monocrystal fracture induced by non-hydrostatic compression allowing to follow the polycristallization process occurring upon load increase in a DAC.

Methods – The TDBS experimental set-up (Fig. 1(a)) was based on asynchronous optical sampling, where accumulating time delay between green pump (515 nm, 198 fs duration) and green probe (535 nm, 130 fs duration) laser pulses is due to difference in the repetition rates of these lasers, allowing fast

data acquisition. It was hence possible to obtain 3D images of the Brillouin frequency distribution (of any detected acoustical modes) in a 100×100×10 μm^3 volume with a lateral resolution of 2.5 μm limited by the overlap of pump and probe laser beams. The data collection rate depended on the chosen pump and probe laser powers and the number of averages needed to reach acceptable signal-to-noise ratio.

As depicted in Fig. 1(b), the generation of CAPs propagating in the transparent water ice compressed in the DAC occurred thanks to an absorbing metal layer serving as an optoacoustic transducer (OAT). Pressure inside the DAC was measured using fluorescence spectra of (embedded) ruby grains which R1-line position is calibrated vs. pressure. The optical path for pressure monitoring was included in the set-up (Fig. 1(a)) to allow measurement without removing the DAC from the sample stage, hence facilitating the comparison of 3D images at different pressures and visualizing evolution of crystallite shapes with compression.

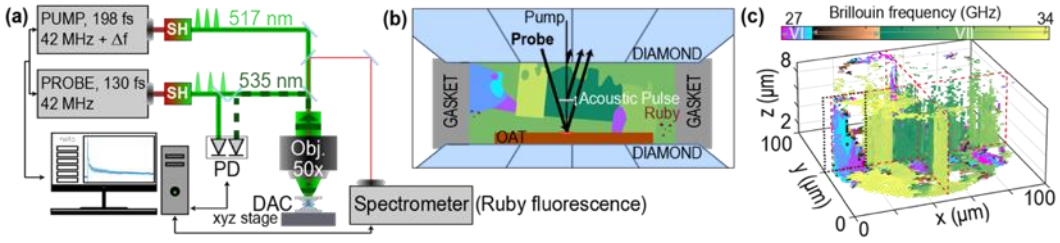

Fig. 1. (a) Experimental set-up and (b) TDBS experiment scheme, where the pump absorbed in OAT launched a CAP in the polycrystalline water ice where it scatters the probe. (c) 3D visualization of polycrystalline water ice microstructure.

Results summary and conclusive remarks – The used TDBS set-up provided a comprehensive, reliable high-resolution *in-situ* 3D visualization of microstructure of a transparent polycrystalline sample of water ice compressed in a DAC to 2.15 GPa where two phases, ice VI and ice VII, coexist (Fig. 1(c)). We observed, for the first time at high pressures in a DAC, TDBS signals containing contribution of quasi-shear CAPs, fruitfully used for grains characterization. Grain boundaries were also localized by identifying specific TDBS signals, caused by CAPs simultaneously propagating in two adjacent grains. Last but not least, the monocrystal fracture induced by non-hydrostatic loading was followed in 3D, further extending the horizons of investigation of solids and their evolution at (changing) extreme conditions.

Acknowledgments – This research is supported by the Agence Nationale de la Recherche (project ANR-18-CE42-I2T2M).

References

[1] C. Thomsen, H.T. Graham, H.J. Maris, J. Tauc, Picosecond interferometric technique for study of phonons in the Brillouin frequency range. Opt. Commun. 60 (1986) 55. https://doi.org/10.1016/0030-4018(86)90116-1.

[2] V.E. Gusev, P. Ruello, Advances in applications of time-domain Brillouin scattering for nanoscale imaging. Appl. Phys. Rev. 5 (2018) 031101. https://doi.org/10.1063/1.5017241.

[3] S. Sandeep, T. Thréard, E. de Lima Savi, N. Chigarev, A. Bulou, V. Tournat, A. Zerr, V.E. Gusev, S. Raetz, 3D characterization of individual grains of coexisting high-pressure H2O ice phases by time-domain Brillouin scattering. J. Appl. Phys. (2021) 130 053104. https://doi.org/10.1063/5.0056814.

[4] A. Bandari, 3D-imaging of polycrystal texture, boundaries using time-domain Brillouin scattering, AIP Scilight (2021). https://doi.org/10.1063/10.0005895.

Real-time monitoring of light-induced curing of organosilicate glass low-k films by time-domain Brillouin scattering

Sandeep S[(1)], Vishnevskiy AS[(2)], Raetz S[(1)*], Naumov S[(3)], Seregin DS[(2)], Vorotilov KA [(2)], Gusev VE [(1)*], Baklanov MR[(2)*]

(1) Laboratoire d'Acoustique de l'Université du Mans (LAUM), UMR 6613, Institut d'Acoustique – Graduate School (IA-GS), CNRS, Le Mans Université, Le Mans, France
(2) MIREA—Russian Technological University, Moscow 119454, Russia
(3) The Leibniz Institute of Surface Engineering (IOM), Leipzig 04318, Germany

*Corresponding authors' email: samuel.raetz@univ-lemans.fr, vitali.goussev@univ-lemans.fr, baklanovmr@gmail.com

Background – Organosilicate glass (OSG) films, developed as low dielectric constant (low-k) insulators for interconnects in advanced ULSI (Ultra Large-Scale Integration) devices, are used to insulate metal conductors and, together with low resistivity metal wires, improve the integrated circuits performance by reducing the signal propagation delay (resistive-capacitive delay) and cross talk noise [1]. Reduction of dielectric constant of OSG films is done by introducing porosities, which are usually obtained by using sacrificial porogens (organic polymers) co-deposited with the silica-like matrix material [1]. The porogens are removed after deposition by thermal annealing, potentially assisted by UV light or electron beam [2]. The control of the curing is of utmost importance for low-k properties and films integration in on-chip interconnects, as porogens curing controls low-k and mechanical properties of the films.

Previously, we showed that the time-domain Brillouin scattering (TDBS) technique is very efficient for nanoscale imaging of porous low-k films [3, 4]. TDBS is a pump-probe technique where the absorption of a fs pump laser pulse launches a coherent acoustic pulse (CAP) that propagates and scatters a time-delayed fs probe laser pulse in a transparent-to-the-probe-wavelength material. The scattered-by-the-CAP light is heterodyned by a reflection of the probe on a stationary surface, giving rise to an oscillating signal. The so-called Brillouin oscillations (BOs) provides information on film properties in the current position of the CAP inside the film, e.g., their frequency is proportional to the product of local optical refractive index (n) and sound velocity (v). In low-k films, TDBS allowed to extract the depth profiles of optical refractive index and longitudinal elastic modulus in partially cured low-k films with remaining porogen residue. Here, we used the TDBS technique for its unique ability to remove porogen residues by the UV probe light action and monitor, at the same (real) time, the changes in Brillouin frequency due to light-induced optical and mechanical property changes associated with the curing.

Methods – Porous organosilicate-based low-k 700 nm-thick films were deposited by a spin-on-glass technique on a Si substrate covered with a 600 nm-thick Al layer. The low-k films were thermally cured at 400°C in air and nitrogen (N) for one or two hours to reach the critical region where films have maximum porosity and lowest dielectric function after the complete porogen removal. This region is crucial for low-k properties because of the matrix re-arrangement leading to the highest quality of low-k films.

The TDBS experimental set-up (Fig. 1(a)) was based on asynchronous optical sampling, where accumulating time delay between green pump and UV probe femtosecond laser pulses is due to difference in the repetition rate of both lasers, allowing fast data acquisition time (5 s/measurement here). The latter allowed real-time monitoring of Brillouin frequency (BF) changes while each sample was exposed to different green pump and UV probe powers.

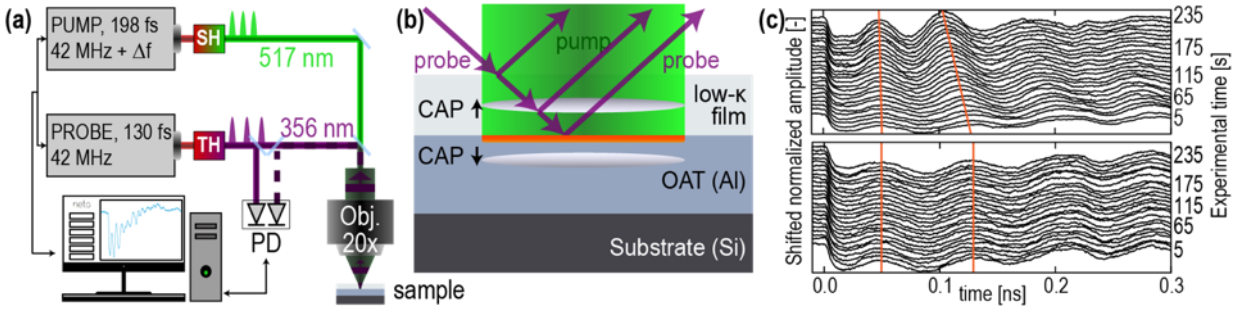

Fig. 1. Schemes of (a) the fast experimental set-up and (b) the TDBS experiment, where the pump absorbed in Al launched CAPs in Al and low-k films where they scatter the probe. (c) BOs period examples vs. the experiment duration in two films annealed for: (top) one hour in N and (bottom) one hour in air.

Results summary and conclusive remarks – As depicted in Fig. 1(c), the BOs period (interval between the two lines) is diminishing with the experiment duration in the film annealed for one hour in N (top), while it is not in that annealed for one hour in air (bottom). The BF increase is a signature of a continuous increase with the experiment duration of the product *nv*. The TDBS technique allowed to detect extremely small differences existing in the films cured in the critical region where porogen is completely removed but the matrix shrinkage is still not significant. The results also demonstrated local modification of low-k films based on 2-photon absorption, which can be important for atomic layer deposition processes, where the in-situ monitoring ability of TDBS to follow in real time the modification process can be important.

Acknowledgments – This research is supported by the Agence Nationale de la Recherche (project ANR-18-CE42-I2T2M), the Russian Foundation for Basic Research (grant number 18-29-27022) and the Ministry of Science and Higher Education of Russian Federation (project number 0706-2020-0022).

References

[1] K. Maex, M.R. Baklanov, D. Shamiryan, F. Lacopi, S.H. Brongersma, Z.S. Yanovitskaya, Low dielectric constant materials for microelectronics. J. Appl. Phys. 93 (2003) 8793–8891. https://doi.org/10.1063/1.1567460.

[2] M.R. Baklanov, V. Jousseaume, T.V. Rakhimova, D.V. Lopaev, Yu.A. Mankelevich, V.V. Afanas'ev, J.L. Shohet, S.V. King, E.T. Ryan, Impact of VUV photons on SiO2 and organosilicate low-k dielectrics: General behavior, practical applications, and atomic models. Appl. Phys. Rev. 6 (2019) 011301. https://doi.org/10.1063/1.5054304.

[3] C. Mechri, P. Ruello, J.M. Breteau, M.R. Baklanov, P. Verdonck, V. Gusev, Depth-profiling of elastic inhomogeneities in transparent nanoporous low-k materials by picosecond ultrasonic interferometry. Appl. Phys. Lett. 95 (2009) 091907. https://doi.org/10.1063/1.3220063.

[4] A.M. Lomonosov, A. Ayouch, P. Ruello, G. Vaudel, M.R. Baklanov, P. Verdonck, L. Zhao, V.E. Gusev, Nanoscale noncontact subsurface investigations of mechanical and optical properties of nanoporous low-k material thin film. ACS Nano 6 (2012) 1410. https://doi.org/10.1021/nn204210u.

High-frequency heterodyne lock-in carrierography (HeLIC) and thermography (HeLIT) imaging of optoelectronic materials

Melnikov A[1,2], Mandelis A[1,2]*, Subramani S[1], Sivagurunathan K[1,2], Pawlak M[3]

(1) Center for Advanced Diffusion-Wave and Photoacoustic Technologies (CADIPT), Department of Mechanical and Industrial Engineering, University of Toronto, Toronto, Ontario M5S 3G8, Canada
(2) Institute for Advanced Non-Destructive and Non-Invasive Diagnostic Technologies (IANDIT), University of Toronto, Ontario M5S 3G8, Canada Department of Mechanical & Industrial Engineering, University of Toronto, Toronto, Canada
(3) Institute of Physics, Nicolaus Copernicus University, Torun, Poland

*Corresponding author's email: mandelis@mie.utoronto.ca

Background – Camera-based photothermal imaging has been widely used for qualitative and quantitative thermographic characterization of wide spectra of materials. However, the relatively low frame rate of mid-infrared (MIR) cameras strongly restricts the benefits of high frequency imaging. The new photocarrier diffusion-wave modality of heterodyne lock-in carrierography (HeLIC) allows for the elimination of this limitation for high-frequency dynamic imaging of (opto)electronic kinetic phenomena using a near-infrared (NIR) InGaAs camera [1, 2]. The ability to use frequency imaging scans over wide ranges raises the possibility of evaluating the lateral and spatial distributions of various kinds of defect in semiconductor materials with high spatio-temporal resolution. The possibility of heterodyne photothermal radiometry (HePTR) with a single detector was also recently demonstrated [3].

Methodology – The method presented here used two excitation beams with frequencies *f1* and *f1* + 5 Hz. Lock-in demodulation was performed at a beat frequency of 5 Hz. The low beat frequency allowed the use of a low-frame-rate MIR camera to produce images of fast (high-frequency) dynamic thermoelectronic processes. The appearance of signals and images at the beat frequency is due to the nonlinear character of the photothermal response across the illuminated area. Also the NIR InGaAs camera was used in experiment for comparison HeLIC and HeLIT imaging results.

Results – HeLIT imaging was investigated in the frequency range 100 Hz-10 kHz. An example of HeLIT amplitude image of CdZnTe at 10 kHz is presented in Fig. 1a and the corresponding dependence on frequency of one pixel in Fig. 1b. The HeLIC frequency dependence shows a clearly pronounced notch ("dip") at a resonance frequency where the trapping rate into a trap state of a carrier-density-wave matches the trap thermal emission rate superposed on the non-linear electron- hole recombination interactions. The absence of the notch phenomena from the PTR and LIT data may be due to the fact that these modalities are only sensitive to non-radiative kinetics with the thermal field obliterating the phase sensitivity of carrier motion that gives rise to the dip in LIC when opposing trap filling / emptying rates become equal.

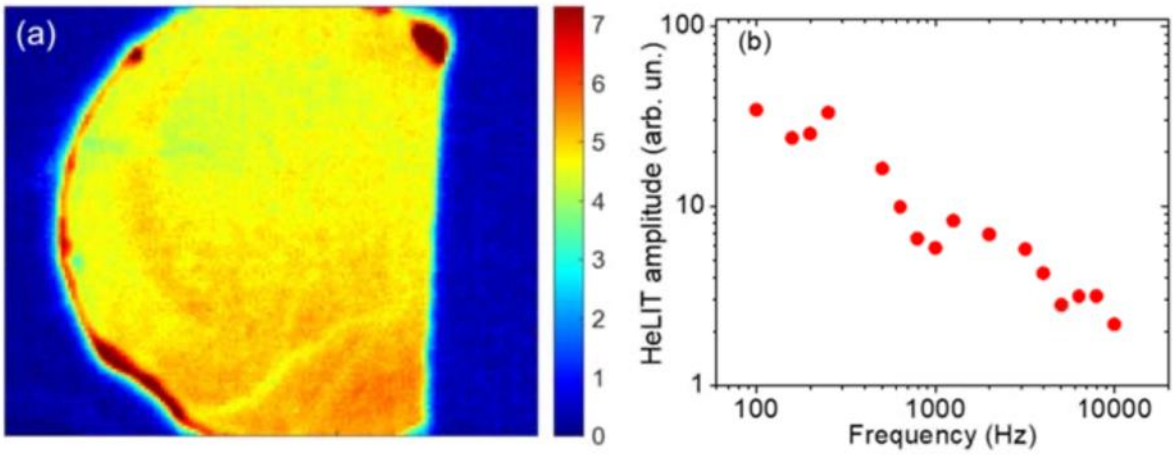

Fig. 1. (a) MIR camera HeLIT amplitude image of CdZnTe at 10 kHz; and **(b)** amplitude dependence on frequency of one pixel near the center of the sample. Measurements were carried at 100K.

The same sample was measured using HeLIC. The corresponding HeLIC dependencies are shown in Fig. 2.

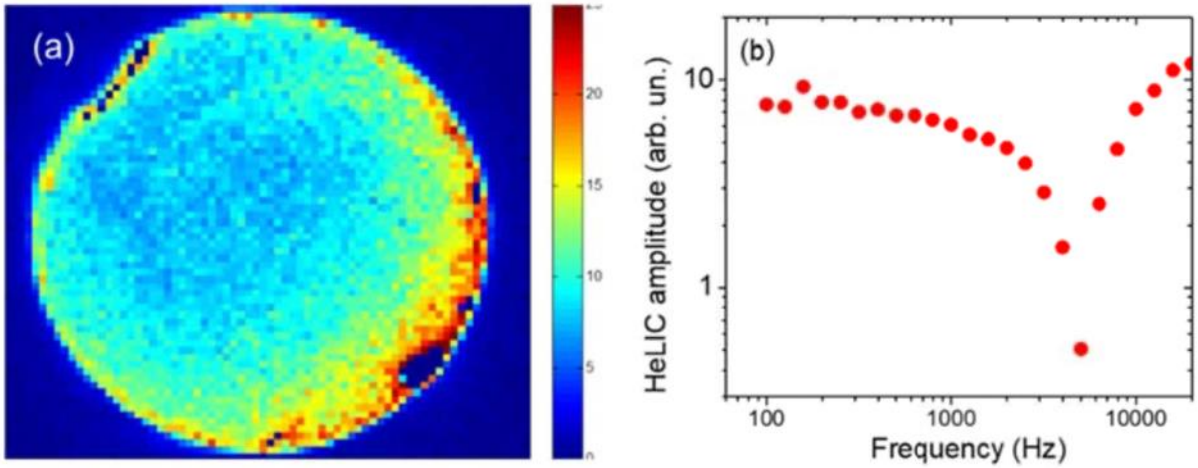

Fig. 2. (a) NIR camera HeLIC amplitude image of CdZnTe at 10 kHz; and **(b)** amplitude dependence on frequency of one pixel near the center of the sample. Measurements were carried at 100K.

Conclusions – Dynamic non-radiative (LIT) and radiative (LIC) images of CdZnTe wafers with intraband-gap trap densities were compared for their sensitivity to defect states and photocarrier kinetic effects. Although HeLIT is less sensitive to defect state kinetics, this imaging method allows the exploration of dynamic photothermal imaging of non-radiative photocarrier kinetics at modulation frequencies much higher than accessed by conventional mid-infrared camera frame rates. As a result, spatial distributions of defect topologies shown in Fig. 2(a) are matched with higher resolution details of the same kinetic processes in Fig. 1(a).

References

[1] Q. Sun, A. Melnikov, A. Mandelis, Camera-based high frequency heterodyne lock-in carrierographic (frequency domain photoluminescence) imaging of crystalline silicon wafers, Phys. Status Solidi A 163 (20016) 405-411. https://doi.org/10.1002/pssa.201532033.

[2] A. Melnikov, A. Mandelis, A. Soral, C Zavala-Lugo, M Pawlak, Quantative imaging of defect distributions in CdZnTe wafers using combined deep-level photothermal spectroscopy, photocarrier radiometry, and lock-in carrierography, ACS Appl. Electron. Mater. 3 (2021) 2551-2563. https://doi.org/10.1021/1acsaelm.1c00100.

[3] M. Chirtoc, A. Fleming, N. Horny, N Ban, Nonlinear heterodyne photothermal radiometry for emissivity- free pyrometry, J. Appl. Phys. 128 (2020) 153101. https://doi.org/10.1063/5.0020406.

Characterization of photocarrier properties and their associated trap-state transport parameters of CdZnTe using heterodyne lock-in carrierography imaging and deep level photothermal spectroscopy

Mandelis A[(1)*], Melnikov A[(1)], Soral A[(1)], Zavala-Lugo C[(2)], Pawlak M[(3)]

(1) Center for Advanced Diffusion-Wave and Photoacoustic Technologies (CADIPT), Department of Mechanical and Industrial Engineering, University of Toronto, Toronto, Ontario M5S 3G8, Canada.
(2) Technical University of Queretaro, Queretaro, Mexico
(3) Institute of Physics, Nicolaus Copernicus University, Torun, Poland

*Corresponding author's email: mandelis@mie.utoronto.ca

Backgound. –The wide use of CdZnTe in detector and solar cell fabrication makes imperative the non-destructive characterization of its transport and defect properties. Homodyne and heterodyne photocarrier radiometry (Ho- and HePCR) as well as deep level photo-thermal spectroscopy (DLPTS) demonstrate high capability for evaluating recombination times, kinetic parameters of traps such as capture and emission coefficients, trap densities, emission/capture relaxation times, and defect level energetics [1-3]. Recently the He-PCR method was extended to camera based heterodyne lock-in carrierography (He-LIC) imaging for constructing images of lateral distribution of optoelectronic parameter in CdZnTe using an InGaAs NIR camera [4].

Methodology. -The method presented here used two spread and homogenized 808-nm laser beams with modulation frequencies $f1$ and $f1 + \Delta f$. The beams were sine-waveform modulated using a two- channel function generator in the range 0.1 -100 kHz. Lock-in demodulation was performed at a beat frequency of Δf =10 Hz. The DLPTS measurement was carried using a cryogenic chamber and an InGaAs single detector in the frequency range 25 – 700 kHz. The evaluation of transport and defect parameters was performed on the basis of a two trap/defect state theoretical model developed using nonlinear rate equations for *p*-type carrier kinetics [1] and various excitation intensities.

Results. –The DPLTS investigation clearly showed the presence of two bandgap traps in our CdZnTe wafer (Fig. 1a). The activation energies were found to be 0.148 and 0.175 eV through fitting to Arrhenius plot of e/T^2 vs. 1/kT. The HeLIC images show inhomogeneous distribution of defects over the wafer (Figs. 2a,b). The kinetics of trap carriers produced a pronounced notch ('dip') phenomenon in the HePCR/HeLIC amplitude frequency response (Fig. 2c) and a phase jump (Fig. 2d). The spatial distribution images of parameters such as recombination lifetime, capture coefficients, emission rates, and concentrations of both traps (Figs. 2e,f) were evaluated from a theoretical dynamic nonlinear rate-equation model with two bandgap traps. HeLIC imaging was used to discuss dynamic photocarrier interactions with CdZnTe traps. Relaxation time images were derived from the kinetic optoelectronic quantities and can be used for optoelectronic characterization of entire CdZnTe wafers.

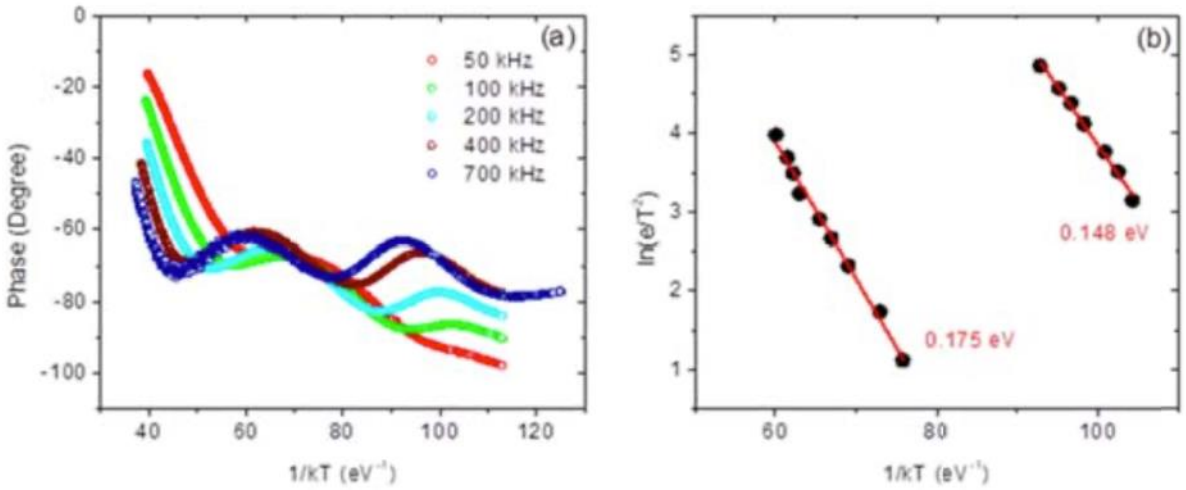

Fig. 1. (a) Homodyne PCR phase of CdZnTe vs. 1/kT at various frequencies; and (b) Arrhenius plots with extracted activation energies. Thermal emission rate at each peak was estimated using $e_n(T_{peak})f = 2.86\pi f$.

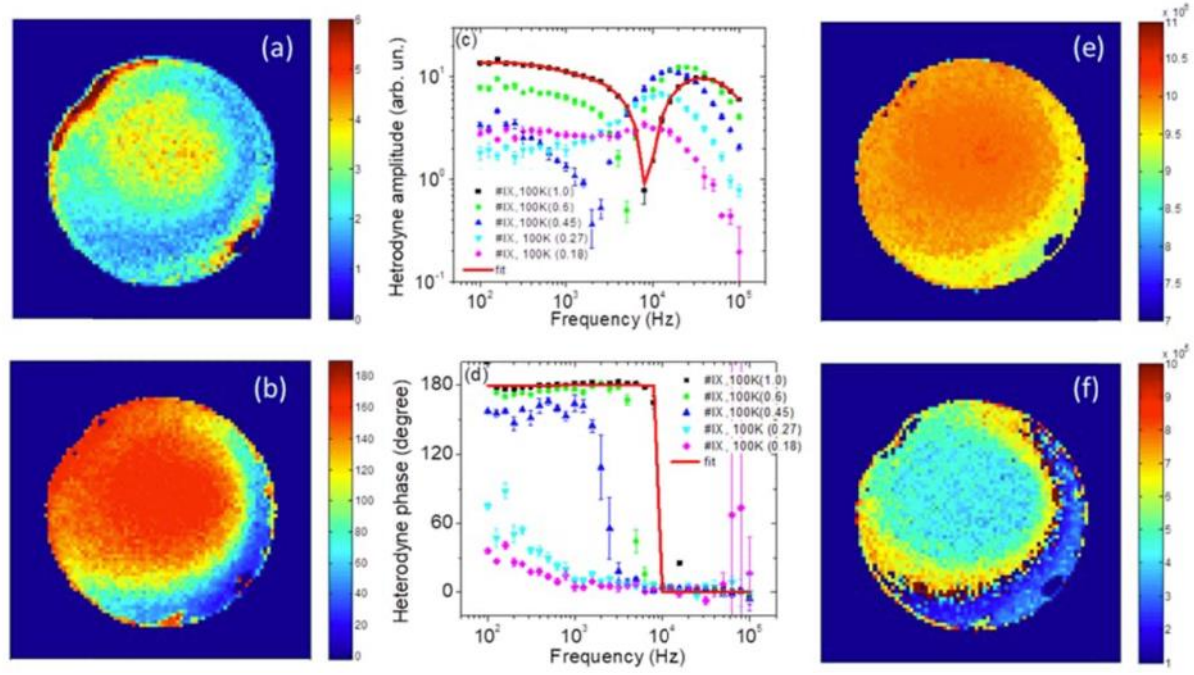

Fig. 1. HeLIC amplitude **(a)** and phase **(b)** image of CdZnTe at 0.25 kHz and intensity $0.45 \cdot I_{max}$, I_{max}=1.9W/cm^2; and amplitude **(c)** and phase **(d)** near-center pixel dependence on frequency at several intensities. Measurements were carried out at 100K. Derived trap #1 **(e)** and trap #2 **(f)** density images at intensity $0.45 \cdot I_{max}$.

Conclusions. –Dynamic radiative HeLIC imaging of CdZnTe wafers coupled with deep level photo-thermal spectroscopy can be effectively used for kinetic and defect characterization toward quality control of photovoltaic devices and detectors fabricated on this type of substrate.

References

[1] Y. Song, A. Mandelis, A. Melnikov, Q. Sun, An optoelectronic notch (‘dip’) phenomenon in the heterodyne photocarrier radiometry frequency response of Si wafers: a route to quantitative trap-state dynamic processes in semiconductors, Semicond. Sci. Technol. 36 (2020) 115024. https://doi.org/10.1088/1361-6641/abb8fc.

[2] A. Mandelis, J. Xia, Deep level photothermal spectroscopy: Physical principles and applications to semi-insulating GaAs band-gap multiple trap states, J. Appl. Phys. 103 (2008) 153101. https://doi.org/10.1063/5.0020406.

[3] J. Xia, A. Mandelis, Broadening effects and ergodicity in deep level photothermal spectroscopy of defect state kinetics in semi-insulating GaAs: A combined temperature-, pulse rate-, and time domain study of defect state kinetics, J. Appl. Phys. 105 (2009) 103712. https://doi.org/10.1063/1.3131673.

[4] A. Melnikov, A. Mandelis, A. Soral, C Zavala-Lugo, M Pawlak, Quantative imaging of defect distributions in CdZnTe wafers using combined deep-level photothermal spectroscopy, photocarrier radiometry, and lock-in carrierography, ACS Appl. Electron. Mater. 3 (2021) 2551-2563. https://doi.org/10.1021/1acsaelm.1c00100.

Thermal and optical properties of mixed CdTe and ZnTe based crystals

Singh D[(1)*], Strzałkowski K[(1)], Abouais A[(1,2)], Belghiti AA[(2)]

(1) Institute of Physics, Faculty of Physics, Astronomy and Informatics, Nicolaus Copernicus University in Toruń, ul. Grudziądzka 5, 87-100 Toruń, Poland

(2) Laboratory of Engineering Sciences for Energy, National School of Applied Sciences of El Jadida, BP 1166, EL Jadida, Morocco

*Corresponding author's email: 503386@doktorant.umk.pl

CdTe-based mixed compounds in bulk crystal form have a fairly long history. They are used in various applications as x-ray and gamma-ray detectors, in electro-optic and photorefractive devices, and as substrates for epitaxy in the case of infrared sensors. The variation in composition allows tuning of their fundamental parameters like energy band-gap and lattice constant, which is very important from the application point of view.

Investigated in this work, CdTe-based crystals were grown with the help of the vertical Bridgeman technique [1]. Zinc, Beryllium, and Magnesium atoms were incorporated into the matrix of CdTe. We examined their physical properties such as accurate composition, nature of the atom substitution, segregation coefficients, structural (XRD), thermal, optical (energy gap, energy structure), and defects (with photoluminescence spectroscopy) properties. The composition's energy gap as a function was determined from photoluminescence spectroscopy. The segregation coefficient of Zn in a CdTe matrix has been evaluated as being close to unity [2].

The thermal diffusivity and effusivity of the investigated crystals were derived from the experimental data and allowed the thermal conductivity to be calculated. To achieve this goal, a photopyroelectric technique in both, back (BPPE) and front (FPPE) configuration will be applied for thermal inspection of the samples. The critical property of materials used for detecting application is their quality. Since the efficiency and sensitivity of the potential detector strongly depend on the quality of the used crystal, it is essential to define its lattice disorder. It was shown how lattice disorder effects in CdTe-based mixed crystals affect their physical properties.

References

[1] K. Strzałkowski, F. Firszt, A. Marasek, Thermal Diffusivity, Effusivity, and Conductivity of CdMnTe Mixed Crystals, Int J Thermophys 35 (2014) 2140–2149.

[2] K. Strzałkowski, The composition effect on the thermal and optical properties across CdZnTe crystals, J. Phys. D: Appl. Phys. 49 (2016) 435106.

Photothermal spectroscopy of $Cd_{1-x}Be_xTe$ mixed crystals

Zakrzewski J(1)*, Marasek A(1), Abouais A(1,2)

(1) Institute of Physics, Nicolaus Copernicus University, ul.Grudziadzka 5/7, 87-100 Torun, Poland
(2) Laboratory of Engineering Sciences for Energy, National School of Applied Sciences of El Jadida, BP 1166, EL Jadida, Morocco

*Corresponding author's email: jzakrzew@umk.pl

Cadmium telluride-based materials are still promising as materials for x-ray and γ-ray detectors [1,2]. An important problem is to find the best substituting atoms with optimal composition in the matrix of CdTe crystal. The potential candidate to incorporate CdTe is Be atom. The mixing of the compounds during the growth procedure gives the possibility to change electronic and thermal properties, lattice parameters, and bandgap energies.

The paper shows the application of piezoelectric photothermal spectroscopy to determine the energy gap values for different beryllium content and the influence of the surface preparation on the character of the amplitude and phase piezoelectric photothermal spectra.

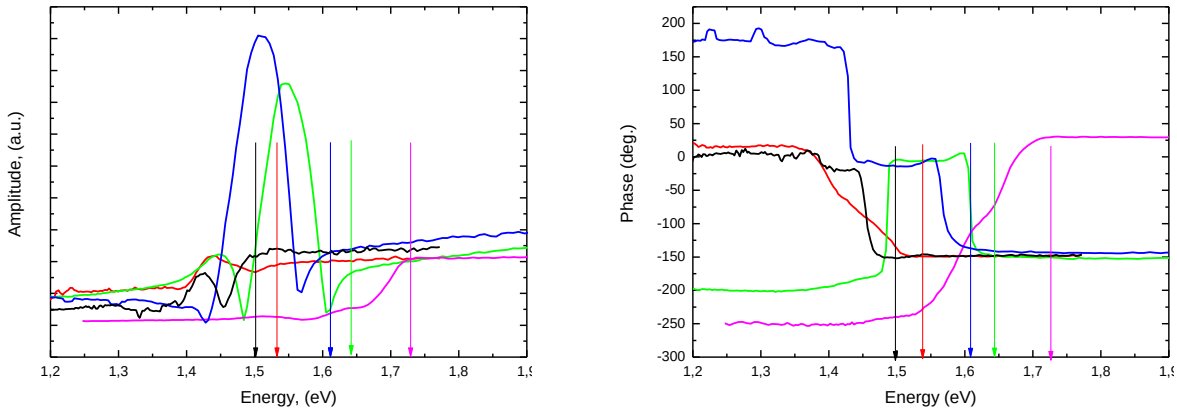

Fig. 1. Amplitude **(a)** and phase **(b)** spectra of $Cd_{1-x}Be_xTe$ for different beryllium content in rear configuration mode, black line – x=0, red – x=0.01, blue- x=0.03, green – x=0.05, magenta – x=0.1. The colour arrows indicate the values of energy gaps.

The rear and front configurations were used in the investigations. They are associated with the geometry of the sample and a detector position. At the rear configuration, the sample is irradiated from one side, and the detector is located on the other (non-illuminated); at the front one, a detector is located at the illuminated surface. As the theory shows, each of these configurations could give a different character of the amplitude and phase spectra [3].

The investigated crystals were grown by the high-pressure Bridgman method under argon overpressure. The crystals were cut into 1-1.2 mm thick plates and mechanically grounded, polished, and chemically etched.

The proper method of surface treatment of the material is essential for the device quality, and the piezoelectric photothermal method gives the possibility to choose and evaluate the appropriate one [4].

For semiconductors, there are three main sources of photothermal signal: thermal, plasma waves (associated with diffusion and recombination of carriers). In the investigation of transport in semiconductors, one can also take into account the immediate thermalization of carriers and nonradiative surface recombination. Their influence on the character of amplitude and phase piezoelectric spectra is shown and discussed.

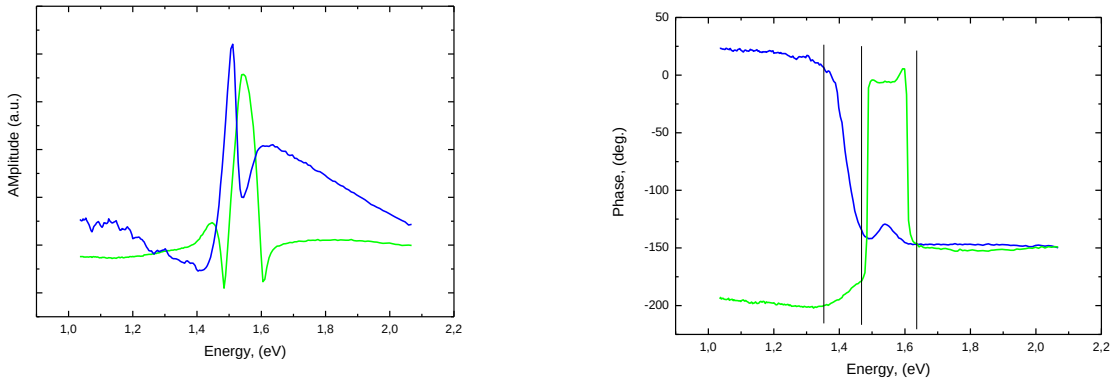

a) b)

Fig. 2. Amplitude **(a)** and phase **(b)** spectra for the ground (green lines) and etched (blue lines) $Cd_{0.95}Be_{0.05}Te$ sample.

References

[1] T.E. Schlesinger, J.E. Toney, H. Yoon, E.Y. Lee, B. A. Brunett, L. Franks, R. B. James, Mater. Sci. Eng. R 32, 103 (2001) 103.

[2] H. Choi, Growth and Fabrication Method of CdTe and Its Performance As a Radiation Detector, J. Korean Phys. Soc. 66, (2015) 27.

[3] J. Zakrzewski, M. Maliński b, A. Bachiri c, K. Strzałkowski, Materials Science & Engineering B 271 (2021) 115305.

[4] J. Zakrzewski, M. Maliński, K. Strzałkowski, Int. J. Thermophys. 33 (2012) 1228–1238.

Simultaneous thermal and optical characterization of semiconductor materials exhibiting high optical absorption by photopyroelectric spectroscopy

Strzałkowski K(1)*, Dadarlat D(2)

(1) Institute of Physics, Faculty of Physics, Astronomy and Informatics, Nicolaus Copernicus University in Toruń, ul. Grudziądzka 5, 87-100 Toruń, Poland

(2) National R&D Institute for Isotopic and Molecular Technologies, Donat Str. 67-103, POB-700, 400293 Cluj-Napoca, Romania

*Corresponding author's email: skaroll@fizyka.umk.pl

The development of new techniques for non-destructive testing of the materials is still critical in view of scientific activity and potential application in the industry. Among other issues, the determination of the thermal and optical properties of materials is in the spotlight. The photopyroelectric (PPE) method belongs to modulated techniques where the excitation light intensity varies periodically in time, and the signal is processed with a lock-in phase-sensitivity technique. The PPE method is now a well-established measurement technique for the thermal characterization of condensed matter samples. Mandelis and Zver [1] and Chirtoc and Mihailescu [2] made the first systematic theoretical approach for the PPE technique over thirty years ago.

This work presents the results of the investigations on the thermal and optical properties of materials exhibiting high optical absorption. As test samples, some II-VI binary semiconductors were grown by using the Bridgman-Stockbarger method. The photopyroelectric (PPE) method, in two configurations (calorimetric and spectroscopic), was applied for both thermal and optical characterization of the specimens. The thermal diffusivity was obtained in the back detection configuration (BPPE) with an intensity-modulated laser as an excitation source.

The same detection configuration, but with a tunable light source, provided information about the energy gap, the absorption coefficient, and the investigated sample's thermal diffusivity. The results obtained with these two methods were also compared with the data collected by conventional transmission and luminescence spectroscopies (absorption coefficient, energy gap). The main conclusion is the photopyroelectric spectroscopy (PPES) can provide in one measurement good quality information about the thermal and optical properties of the specimen.

References

[1] A. Mandelis, M.M. Zver, Theory of photopyroelectric spectroscopy of solids, J. Appl. Phys. 57 (9) (1985) 4421–4430.

[2] M. Chirtoc, G. Mihilescu, Theory of the photopyroelectric method for investigation of optical and thermal materials properties, Phys. Rev. B 40 (14) (1989) 9606–9617.

Correctness of assessment of thermophysical properties of solvents by dual-beam thermal-lens spectrometry

Khabibullin VR(1)*, Volkov DS(1), Proskurnin MA(1)

(1) Department of Analytical Chemistry, Chemistry Department, Lomonosov Moscow State University, Moscow, Russia

* Corresponding author's email: vladhab1995@gmail.com

The paper presents a dual-beam thermal-lens spectrometer with a mode-mismatch configuration. The most significant factors influencing the correctness of the measurement of thermophysical parameters are considered. Reference solvents (water, ethanol, acetonitrile, toluene, and chloroform) were studied, and thermophysical parameters (thermal diffusivity and heat capacity) were calculated. The experimental and theoretical values show a good concordance, indicating the correct operation.

Thermal lens spectrometry (TLS) is essential in photothermal spectroscopy due to its high sensitivity, rapidity, and simplicity of approach. From the viewpoint of chemical analysis, thermophysical parameters of complex samples are often more informative than optical ones. Studying the kinetics of processes, controlling chemical reactions, complex formation, and dimerization are solved with higher accuracy due to the registration of changes in sample thermal diffusivity (D) and specific heat (C_p). Currently, the primary attention is focused on the dual-beam version of the TLS with mode mismatch configurations, for which in 1992, Shen et al. [1] published a theoretical model describing the behavior of a thermal lens in a sample with high accuracy. On the other hand, the development of the instrumentation of the method (especially in the dual-beam version) cannot be called fast and straightforward. Therefore, all attention is paid to the accuracy of measurements, but not their correctness. This study presents the results of designing and implementing a setup for dual-beam TLS, studying reference solvents (water, ethanol, chloroform, acetonitrile, toluene), and finding D.

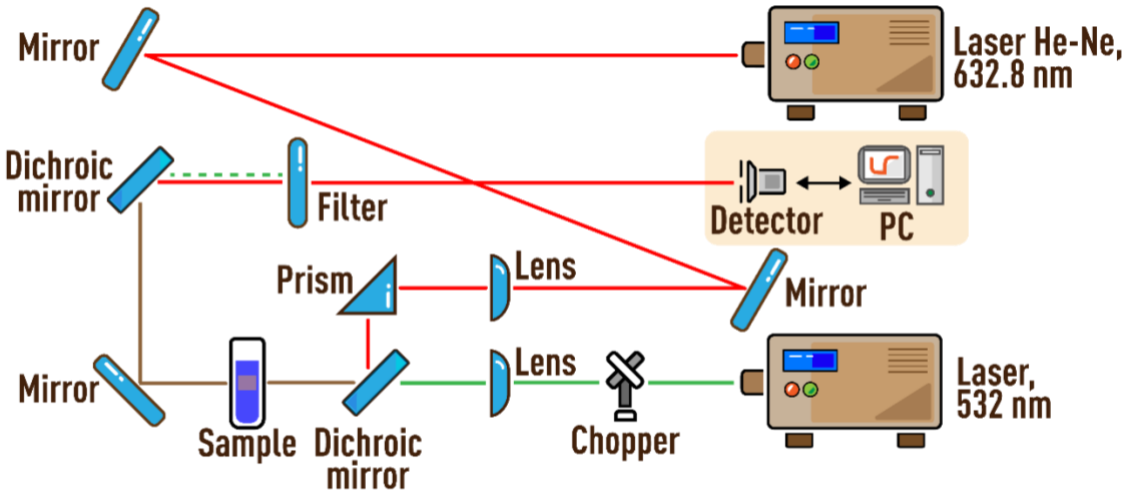

Fig. 1. Scheme of a two-beam thermal lens spectrometer

Figure 1 shows the scheme of the setup. A high-power solid-state laser (λ = 532 nm, *P* = 200.0 mV) was used as an excitation beam, and a He–Ne laser (λ=632.8 nm, *P* = 7.1 mV) was used as a probe. The waist size of the excitation beam is 42 ± 1 μm, while the probe-beam radius in the cell center is 60 ± 1 μm. Thus, the degree of mode-mismatch (m) is equal to 2. The chopper frequency was 0.01 Hz. The calculation of the characteristic time (t_c) and thermal diffusivity (*D*) was carried out according to the equation $t_c = \omega_{0e}^2/4D$.

The effects of fluctuations in the divergence of laser beams, incorrect measurement of the size of the beams in the sample, the frequency of the shutter operation, etc., on thermophysical parameters were studied. E.g., it was found that fluctuations in the divergence of the excitation laser beam of 5% lead to an error in determining *D* of 10% (Fig. 2).

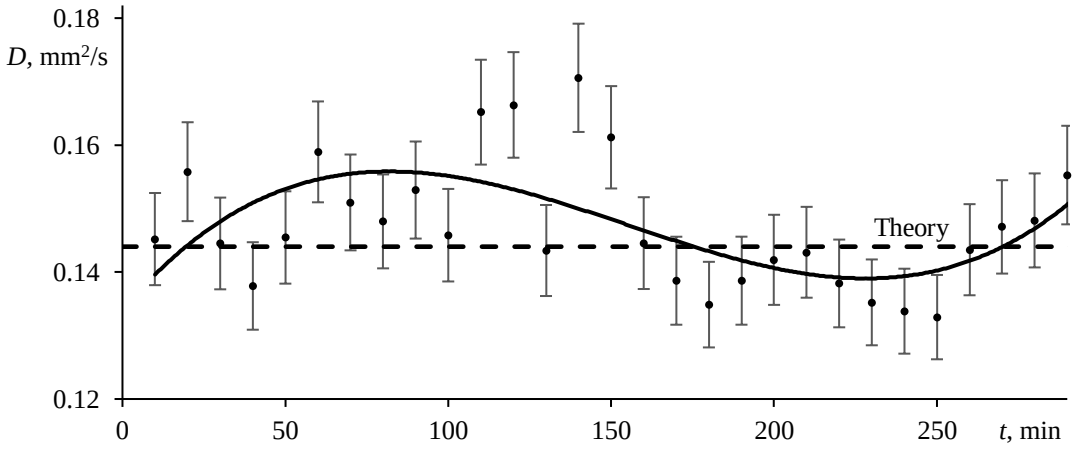

Fig. 2. Behavior of the thermal diffusivity of water with the course of measurements

As a result, considering all the factors, we got the correct results for thermal diffusivity on the instrument. Furthermore, the comparison of theoretical and experimental thermal diffusivity values showed a close-ratio, indicating the correct operation (Table 1).

Table 1. Thermal diffusivity of feference solvents, (mm²/s)

Solvent	Theory	Experiment
Water	0.144	0.149 ± 0.009
Ethanol	0.089	0.087 ± 0.004
Chloroform	0.083	0.086 ± 0.005
Toluene	0.091	0.090 ± 0.004
Acetonitrile	0.111	0.115 ± 0.008

Thus, a TLS setup in a dual-beam version was made. Many factors that affect the accuracy of measurements were considered. The results show the concordance of experimental and theoretical thermal conductivity values, which indicates the possibility of using the setup in further research work.

The study was funded by the Russian Foundation for Basic Research, project number 21-33-70143. This research was performed according to the Development program of the Interdisciplinary Scientific and Educational School of Lomonosov Moscow State University, “The future of the planet and global environmental change”.

The reported study was funded by RFBR, project number 21-33-70143.

References

[1] J. Shen, R.D. Lowe., R.D. Snook, A model for cw laser induced mode-mismatched dual-beam thermal lens spectrometry, Chemical Physics. 165 (1992) 385-396. https://doi.org/10.1016/0301-0104(92)87053-C.

Combining micro- and macroscopic approaches in a model of a thermal lens experiment in disperse media

Vyrko EA[(1)*], Khabibullin VR[(1)], Volkov DS[(1)], Proskurnin MA[(1)]

(1) Department of Analytical Chemistry, Chemistry Department, Lomonosov Moscow State University, Moscow, Russia

*Corresponding author's email: evgvyr@disroot.org

An exact mathematical solution for the problem of heat dissipation by a single immobile sphere was combined with ideas of the aberrant approach to thermal-lens signal computation into a simplified computational model of a thermal lens experiment in a solution of noble metal nanoparticles. The model predictions for solutions of 5, 20, and 40 nm gold and silver nanoparticles were compared with the behavior of the homogeneous system with equivalent optical properties to estimate the individual impact of such heterogeneous factors as particle size and concentration on the divergence of the model from the homogeneous system was estimated.

Natural and technological finely dispersed heterogeneous systems are essential chemical and biochemical objects and materials. Identifying and determining the components of such systems in several forms and the composition of different phases *in vivo* or *in situ* are required. Often, solving these tasks requires highly sensitive and non-destructive methods simultaneously. Today, there is no straightforward solution to this problem; various approaches are being developed. Photothermal spectroscopy (PTS) provides simultaneous non-destructive chemical-analysis opportunities in a wide spectral range and non-destructive testing (size and thermophysical parameters estimation) of dispersed systems and nanosystems, which most other methods cannot implement.

However, the multisignal nature of PTS is also a disadvantage since it requires understanding the signal-generation mechanisms for practically significant objects. Despite a relatively large number of models considering individual aspects of liquid heterogeneous systems, there is still no general model that describes all the photothermal features in such systems. This problem complicates the use of PTS in the qualitative and quantitative assessment of dispersed systems.

The aim of this study is the development of a photothermal response model for finely dispersed systems with thermal lens spectrometry (TLS) as the universal method of PTS and determination of analytical parameters for components of such systems in macro- and microscopic versions on several models and natural systems (nanoparticles of noble metals, carbon nanomaterials, and natural nanoparticles).

On the one hand, we started from the models based on the so-called efficient heat capacity, but they have limitations. In particular, it is assumed that the kinetics of the photothermal effect remains unchanged, which is not always valid for natural objects. On the other hand, photothermal confocal microscopy and femtosecond photoabsorption spectroscopy have models of heat propagation from a single particle. Such models can be used in TLS but need to be generalized to a system of many particles. Thus, we developed static models of a photothermal signal for TLS based on thermodynamic models of heat propagation, electromagnetic interaction of nanosized particles (homogeneous and of the core-

shell type) with laser radiation, and the aberration model of the thermal lens effect. Static models are the basis for the next stage, dynamic models, considering the influence of local dynamic concentration fluctuations of dispersed particles on developing a photothermal signal.

An exact mathematical solution for the problem of heat dissipation by a single immobile sphere was combined with ideas of the aberrant approach to thermal-lens signal computation into a simplified computational model of a thermal lens experiment in a solution of noble metal nanoparticles. A model of thermal-lens experiment in a solution of noble metal nanoparticle built upon the problem of heat dissipation by an immobile sphere of a perfect conductor in an infinite medium was implemented as a software unit. The spatial frame of nanoparticles in a disperse solution was regarded as a rigid rectangular lattice. This simplified model considers the specificities of heat exchange at the particle-liquid interface and the discrete nature of heat generation in a disperse system.

The model predictions for solutions of 5, 20, and 40 nm gold and silver nanoparticles for a wide range of conditions (particle size and concentrations, excitation power, thermophysical parameters; see Fig. 1, as an example of transient calculations) were compared with the behavior of the homogeneous system with same optical properties. The latter was used to estimate the individual impact of such heterogeneous factors as particle size and concentration on the divergence of the model from the homogeneous system. The details of the used approach and applicability limits of both the classical theory of the thermal lens effect and variants of the heterogeneous model will be discussed in the presentation.

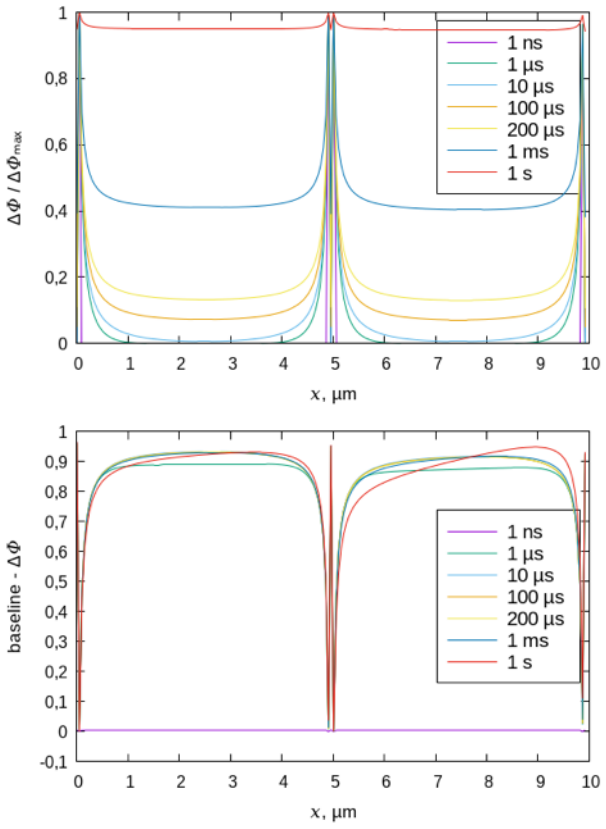

Fig. 1. Initial segment of the temperature curve in a monodisperse 40 nm gold nanoparticle solution. Dashed line demarcates the phase shift curve for a homogeneous solution with the equivalent optical and thermophysical properties; absorption cross-section, 3.38172×10^{-15} m²; nanoparticle volume concentration, 8.2×10^{14} particles/m³ (0.53 mg/L), excitation power, 1 mW; absorbance, 0.012.

Further tests showed that these two typical heterogeneous features, taken alone, cannot describe the complexity of the transient thermal-lens experiment in a real heterogeneous system. Instead, it suggests the existence of other factors playing a significant role in the time domain of the standard thermal lens technique. A plausible candidate is the thermally induced particles drift.

Acknowledgments – The study was funded by the Russian Foundation for Basic Research, project number 21-33-70143 mol_a_mos. This research was performed according to the Development program of the Interdisciplinary Scientific and Educational School of Lomonosov Moscow State University, “The future of the planet and global environmental change”.

Heat transport in polycrystalline oxide thin films

Kaźmierczak-Bałata A[(1)*], Bodzenta J[(1)], Trefon-Radziejewska D[(1)], Juszczyk-Synowiec J[(1)], Guziewicz M[(2)], Venkatachalapathy V[(3)], Mayandi J[(4)]

(1) Silesian University of Technology, Konarskiego 22B, 44-100 Gliwice, Poland
(2) Institute of Electron Technology, Al. Lotników 32/46, 02-668 Warszawa, Poland
(3) Department of Physics, University of Oslo, P. O. Box 1048 Blindern, NO-0316 Oslo, Norway
(4) Department of Materials Science, School of Chemistry, Madurai Kamaraj University, Madurai 625 021, India

*Corresponding author's e-mail: akazmierczak@polsl.pl

Progressive miniaturization and increasing integration and higher operating frequency of electronic devices cause problems with efficient heat dissipation from devices. This is why the thermal properties of thin films became very important for their specific applications, e.g. in TFTs and LDs. Knowledge about film thermal conductivity can allow to engineer heat extraction and then to improve reliability and efficiency of electronic structures.

This work presents the study of morphology and thermal properties of various oxide thin films, among them zinc oxides (ZnO) and indium tin oxides (ITO). The ZnO thin films were fabricated by the atomic layer deposition (ALD) method on Si substrates. The ITO samples were commercially available thin films deposited on glass (Hoya, Japan). The thickness of films used in the present work varied from 100 nm to 170 nm. Atomic force microscopy topographic images showed that the surface morphology is typical for polycrystalline thin layers with roughness equal to few nm. The X-ray diffraction measurements revealed polycrystalline structure with preferred orientation (100) for ZnO films and preferred orientation (222) for ITO films. Determination of the thermal conductivity of oxide thin films was realized by the use of scanning thermal microscopy (SThM). This nondestructive method allowed for quantitative measurements of thermal properties with high spatial resolution. Determination of the thermal conductivity was based on calibration curve build on SThM signal measured for reference sample of well-known thermal conductivity. These apparent thermal conductivities of the thin layer – substrate system were corrected in correlation to the spreading resistance analysis. The corrected values of the thermal conductivity of oxide thin films are gathered in the Table 1. Correlations between structure and morphology and thermal properties of the thin films and allowed to study the influence of deposition parameters like substrate temperature on thermal properties of the layers.

Table 1. Thermal conductivity of oxide thin films.

ITO Samples	κ / [$Wm^{-1}K^{-1}$]
REF	0.97
3A	3.6
9A	1.7
11A	1.6

ZnO Samples	**κ** / [$Wm^{-1}K^{-1}$]
330c	1.12
900c	2.81

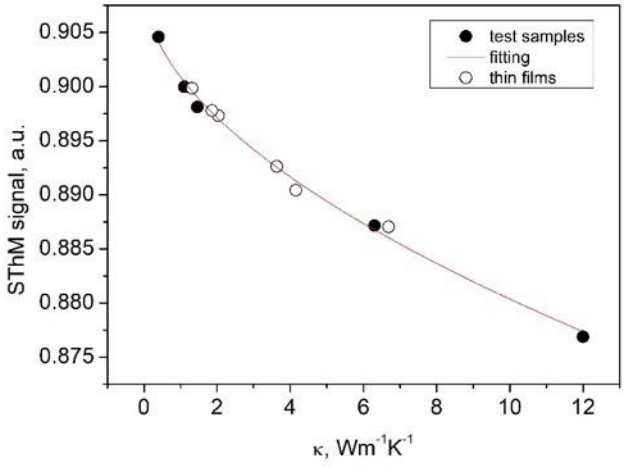

Fig. 1. SThM signal vs sample thermal conductivity measured for test samples and oxide thin films.

References

[1] U. Ozgur, Ya. I. Alivov, C. Liu, A. Teke, M. A. Reshchikov, S. Doğan, V. Avrutin, S.-J. Cho,H. Morkoc,. J. Appl. Phys. 98 (2005) 041301-103.

[2] S.J. Pearton, D.P. Norton, M.P. Ivill, A.F. Hebard, J.M. Zavada, W.M. Chen, I.A. Buyanova, IEEE Trans. Electron Devices 54 (2007) 1040 - 1048.

[3] T. Ashida, A. Miyamura, N. Oka, Y. Sato, T. Yagi, N. Taketoshi, T. Baba, Y. Shigesato, J. Appl. Phys. 105 (2009) 073709 - 4.

[4] E. Fortunato, A. Gonçalves, A. Pimentel, P. Barquinha, G. Gonçalves, L. Pereira, I. Ferreira, R. Martins, Appl. Phys. A Mater. Sci. Process. 96 (2009) 197–205.

Characterization of smart and biocompatible materials based on chitosan:cellulose composites containing sporopollenin exine capsules

Budasheva H(1), Cazon Diaz P(1), Korte D(1), Franko M(1)*, Tran CD(2)

(1) Laboratory for Environmental and Life Sciences, University of Nova Gorica, Vipavska 13, Nova Gorica, SI-5000, Slovenia

(2) Department of Chemistry, Marquette University, P.O. Box 1881, Milwaukee, WI 53201, USA

*corresponding author's email: Mladen.Franko@ung.si

Healing of chronic ulcerous infected wounds is nowadays one of the biggest public health challenges that affect a significant number of people. The proper wound dressing should not only provide the antimicrobial activity but should also have some other characteristics. Among them proper porosity is of high importance since it enables controlling the moisture around wound and provide oxygen/water vapour exchange between wounded tissue and environment. Furthermore, surface of dressing should have proper roughness to enhance epidermal migration and synthesis of connective tissue [1]. Of high importance are also the dressing thermal properties that maintain appropriate tissue temperature ensuring the proper blood flow, as well as expresses the extent of metabolic heat transfer from the tissues under the dressing, outward through the dressing structure. Excessive heating of skin under a dressing leads to perspiration that correlates with a state of tissue inflammation. Thus, both the structural and thermal properties of wound dressing materials belong to the fundamental physical properties of high clinical relevance in both prevention and treatment of acute and chronic wounds. All of these factors strongly affect the healing process. Thus, should be carefully designed when developing a new type of functionalized dressing for wound healing. Because of that, big efforts are made to invent smart materials that can react to the environmental conditions present at the site of a wound (presence of moisture, oxygen, temperature etc.) and adapt their properties to ensure optimal functionalization as sophisticated wound dressings. Since such materials tend to be used in medicine, they are required to be biodegradable and biocompatible, thus, must be generated from renewable biomass feedstock. It has been already shown that such biocomposite materials can be obtained from natural and sustainable biopolymers as cellulose (CEL) from plants, chitosan (CS) from animals and keratin (KER) from wool, hair or chicken feathers [2]. Furthermore, they have many required properties provided by their components as superior mechanical strength delivered by CEL or anti-inflammatory/antimicrobial activity provided by the presence of both CS and CEL [10-13]. Unfortunaltely, their porosity appears to be rather low (below 0.1 % according to our preliminary measurements), which represents one of the key obstacles to final application of such materials. The solution of this problem requires application of novel approaches to determination of porosity of such materials since existing techniques based on pichnometry or SEM analysis, do not provide sufficient accuracy [3]. For this reason, a photothermal beam deflection spectrometry (BDS) [4] was further developed, validated and applied for characterization of CS:CEL based biocomposite materials with different concentration of natural sporopollenin microcapsules (SEC) and different content of CS and CEL synthesised by the latest green

chemistry approaches [2]. It was found that these materials exhibit rather low porosity (below 0.1 %), that can be increased to 0.44 % with increase in CEL content or by addition of sporopollenin exine capsules. The increase in CEL content from 25 % to 75 % results in 50 % increase in total porosity (from 0.4 to 0.6 %) and by nearly 100 % in case of opened one (from 0.05 % to 0.09 %), whereas the addition of SEC at the level of 50% shows up to 4 times increase in both types of porosity, depending on the CS:CEL content.

Futhermore, addition of sporopollenin exine capsules increase significantly the surface roughness of the biocomposites what can mask the low porosities values and make the material useful for desired application. The biocomposites without SEC have rather flat surface with the amplitude of the roughness at the level of single nm and its periodicity at the level of single μm. After deposition of SEC the surface roughness significantly increases to the value of around 0.4 μm and 50 μm for 10 % of SEC loading in case of the roughness amplitude and periodicity, respectively. Increasing the amount of SEC up to 30 % increases the amplitude of surface roughness 10 times, whereas its periodicity nearly twice. Further increase in the amount of SEC deposited on the biocomposite surface causes nearly 50 % further increase in the surface roughness.

It was also found the presented biocomposites material have low values of thermal properties- The obtained values were at the level of 10s mW m-1 K-1 and fraction of mm2 s-1 in case of thermal conductivity and diffusivity, respectively and are decreased by about 25% with increase of CEL content from 25 % to 75 % (0 % SEC concentration). Addition of SEC also reduces the values of thermal diffusivities and conductivities up to 30 % for the SEC concentration at the level of 50 %.

The physical properties of wound dressing play a key role in the healing process. They create a specific microenvironment that provide protection from contamination, enhance the activity of enzymatic and cellular systems required for effective re-epithelialization, as well as control the fluids exchange with external world to control the moisture around the wound.

The results obtained by BDS measurements are in good agreement with those obtained by SEM, AFM and optical microscopy and indicate that the presented biocomposites are interesting materials with their possible applications in medicine.

References

[1] P.G. Bowler, B. I. Duerden, D.G. Armstrong, Wound microbiology and associated approaches to wound management, Clin. Microbiol. Rev. 14 (2001) 244–269.

[2] C.D. Tran, F. Prosenc, M. Franko, G. Benzi, Synthesis, structure and antimicrobial property of green composites from cellulose, wool, hair and chicken feather, Carbohyd. Polym. 151 (2016) 1269–1276.

[3] L. Cui, J. Gong, X. Fan, P. Wang, Q. Wang, Y. Qiu, Transglutaminase-modified wool keratin film and its potential, Eng. Life Sci., 13 (2013) 149–155.

[4] D. Korte, M. Franko, Application of complex geometrical optics to determination of thermal, transport, and optical parameters of thin films by the photothermal beam deflection technique, J. Opt. Soc. Am. A, 32 (2015) 61–74.

Thermoelastic and optical properties of PLLA estimated by photoacoustic measurements

Nešić MV(1)*, Miletic VV(2), Milicevic DS(1), DjordjevicKLj(1), Jordovic-Pavlovic MI(3), Markushev DK(4), Popovic MN(4)

(1) "VINCA" Institute of Nuclear Sciences - National Institute of the Republic of Serbia, University of Belgrade, PO box 522, Belgrade 11351, Serbia
(2) Faculty of Philosophy, University of East Sarajevo, Pale 71420, Bosnia and Herzegovina
(3) Faculty of information technology, Metropolitan University, Belgrade, Serbia
(4) Institute of Physics, University of Belgrade, Pregrevica 118, Belgrade 11080, Serbia

*Corresponding author's email: mioljub.nesic@vin.bg.ac.rs

Polylactides, like all polymers, are materials with low coefficient of optical absorption. Transmission photoacoustic measurements on such materials require that a transparent sample be coated with a thin layer of good optical absorption, such as ink, dye or metal foil, in order to ensure optical opacity and to protect the microphone. The photoacoustic response of the Poly-(L-lactide) (PLLA), on which a thin layer of ink dye was previously applied, is measured in a minimum volume cell transmission configuration for two different positions of the two-layer sample: 1) the absorption layer is directly illuminated and 2) the transparent polymeric layer is directly illuminated. Thermal diffusivity, linear expansion coefficient and optical absorption coefficient of PLLA are determined by applying the boundary model of photoacoustic response for a two-layer sample in the case of optically thick and thermally thin absorption layer and self-consistent procedure for the inverse solution of the photoacoustic problem is derived. The obtained properties are in the range of literary expectations.

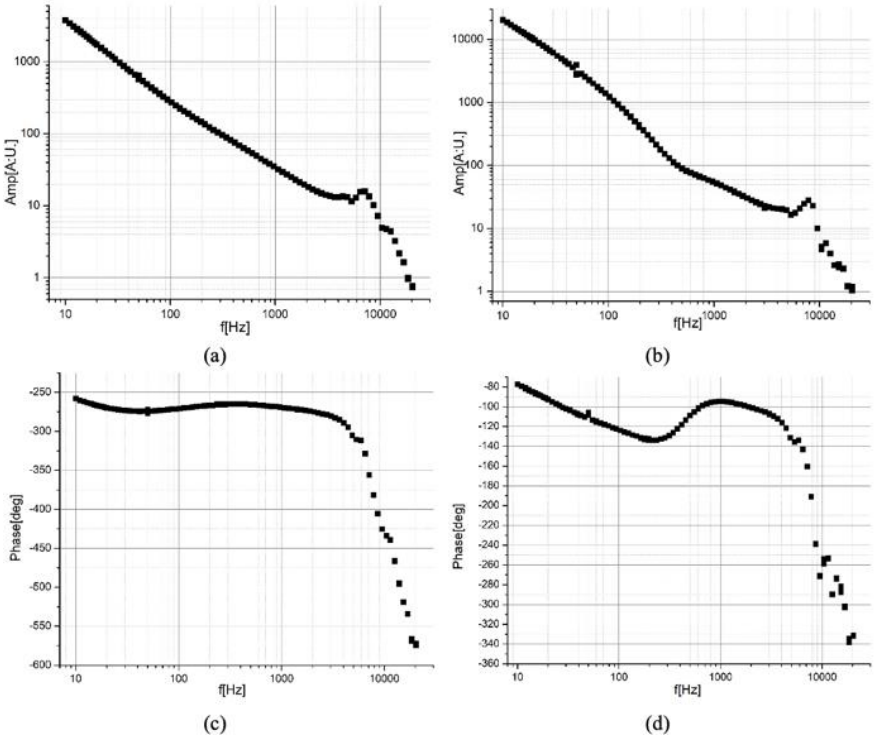

Fig. 1. Experimentally obtained photoacoustic response of 516 μm thick PLLA sample, coated with black acrylic dye 44 μm thick. Amplitude and phase characteristics when front-side illuminated **(a,c),** and when back-side illuminated **(b,d).**

References

[1] Popovic, M.N., Nesic, M. V, Zivanov, M., Markushev, D.D., Galovic, S.P.: Photoacoustic response of a transmission photoacoustic configuration for two-layer samples with thermal memory. Opt. Quantum Electron. 50, 1–10 (2018). https://doi.org/10.1007/s11082-018-1586-x.

[2] Ordóñez-Miranda, J., Alvarado-Gil, J.J.: Frequency-modulated hyperbolic heat transport and effective thermal properties in layered systems. Int. J. Therm. Sci. 49, 209–217 (2010). https://doi.org/https://doi.org/10.1016/j.ijthermalsci.2009.07.005.

[3] Popovic, M.N., Nesic, M. V., Markushev, D.D., Jordovic-Pavlovic, M.I., Galovic, S.P.: Optically induced temperature variations in a two-layer volume absorber including thermal memory effects. J. Appl. Phys. (2021). https://doi.org/10.1063/5.0015898.

[4] Nesic M. V., Popovic M. N., Galovic S. P., Djordjevic K. Lj.,Jordovic-Pavlovic M. I., Miletic V. V., Markushev, D.D.,Estimation of linear expansion coefficient and thermal diffusivity by photoacoustic numerical self-consistent procedure, J. Appl. Phys. – accepted for publication.

[5] Milicevic, D., Suljovrujic, E.: The resistance of poly-(l-lactide) to gamma radiation: effect of initial preparation and crystallinity. Polym. Bull. 77 (2020). https://doi.org/10.1007/s00289-019-02880-2.

03
Laser Ultrasonics

KEYNOTE SPEAKER

Driving coherent phonons and magnons by light

Scherbakov AV(1)*

(1) Experimentelle Physik 2, Technische Universität Dortmund, Dortmund, Germany

*Corresponding author's email: alexey.shcherbakov@tu-dortmund.de

Phonons and magnons are two fundamental collective excitations in solids, i.e. the quanta of the vibrational motion of the atoms in a crystal lattice and the precessional motion of spins in magnetically-ordered materials, respectively. In the frequency range between 10 and 100 GHz, they have close wavelengths of ~100 nm. When phonons and magnons' wave vectors and frequencies coincide, they form a hybridized state due to magneto-elastic coupling [1]. It gives us additional degrees of freedom in manipulating excitations of both types by light and opens new perspectives for nanoscale communications and data processing [2,3].

The present talk gives an overview of the recent experiments with metallic ferromagnetic nanostructures, in which coherent phonons and magnons of GHz frequencies are excited and detected by ultrashort light pulses [4,5]. While in a metallic ferromagnet, fast dephasing of phonons and magnons typically prevents their strong coupling and long-range propagation, we show how to overcome these limitations. We demonstrate the strong magnon-phonon coupling and the phonon-driven transport of coherent magnons on long distances.

A schematic of the studied structures and the experimental scheme are shown in Figs. 1a and 1b. A layer of Galfenol (a ferromagnetic metallic alloy of Fe and Ga with enhanced magneto-elastic interaction) is deposited on the top of a GaAs/AlAs superlattice grown on the GaAs substrate. Parallel grooves of width w = 30÷100 nm and depth h = 5÷25 nm milled by a focused Ga-ions beam (Raith VELION) form a lateral nanograting with the period d = 100÷200 nm. The optical excitation of the nanograting by the pump pulses (1050 nm, 150 fs, diameter 3 μm, up to 8 mJ cm^{-2}) generates wave packets of the spatially periodic phonon and magnon modes. The excitation is based on instant laser-induced heating, which results in thermal extension of the crystal lattice and modulation of the magnetic anisotropy, respectively [4]. The coherent lattice response is measured by detecting modulation of the reflected linearly polarized probe pulse (780 nm, 150 fs, 0.5 μm diameter, 2 mJ cm^{-2}) due to the photoelastic effect. Rotation of the probe polarization plane due to the magneto-optical Kerr effect serves to detect the spin system's coherent response. The varied time delay between the pump and probe pulses realized in the scheme of asynchronous optical sampling (ASOPS) provides sub-ps time resolution. The transient signals are measured at the spatial overlap of the pump and probe beams and at a distance of up to 100 microns between them.

Figs. 1(c) – 1(e) illustrate the principles of the developed concept. The optically excited wave packet consists of symmetric and antisymmetric surface Rayleigh (R1) and Sezawa (R2) modes and a bunch of the modes localized in the superlattice (W-modes) [5]. The spatial profiles of the selected phonon modes are shown in Fig 1(c). The magnon modes with complex spatial profiles and field-dependent frequencies form the dense discrete magnon spectrum. The external magnetic field, B,

applied in the layer plane tunes the magnon frequencies and, thus, their interaction with specific phonon modes. The coupling strength of selected phonon and magnon modes is determined by their spatial overlap. The adjusted magnon-phonon interaction as well as the mode's spectral widths (damping rates), velocities, and spatial localization, determine the spatial-time evolution of the hybridized excitations. An example is the transient Kerr rotation signals measured at several distances from the pump spot, and their fast Fourier transforms shown in Fig. 1(f) and 1(e), respectively. While the surface R-modes demonstrate rapid decay due to scattering at the corrugated surface, the wave packet of W-modes propagates at a distance up to 100 microns. It drives magnons coherently to the distance not available for pure spin waves.

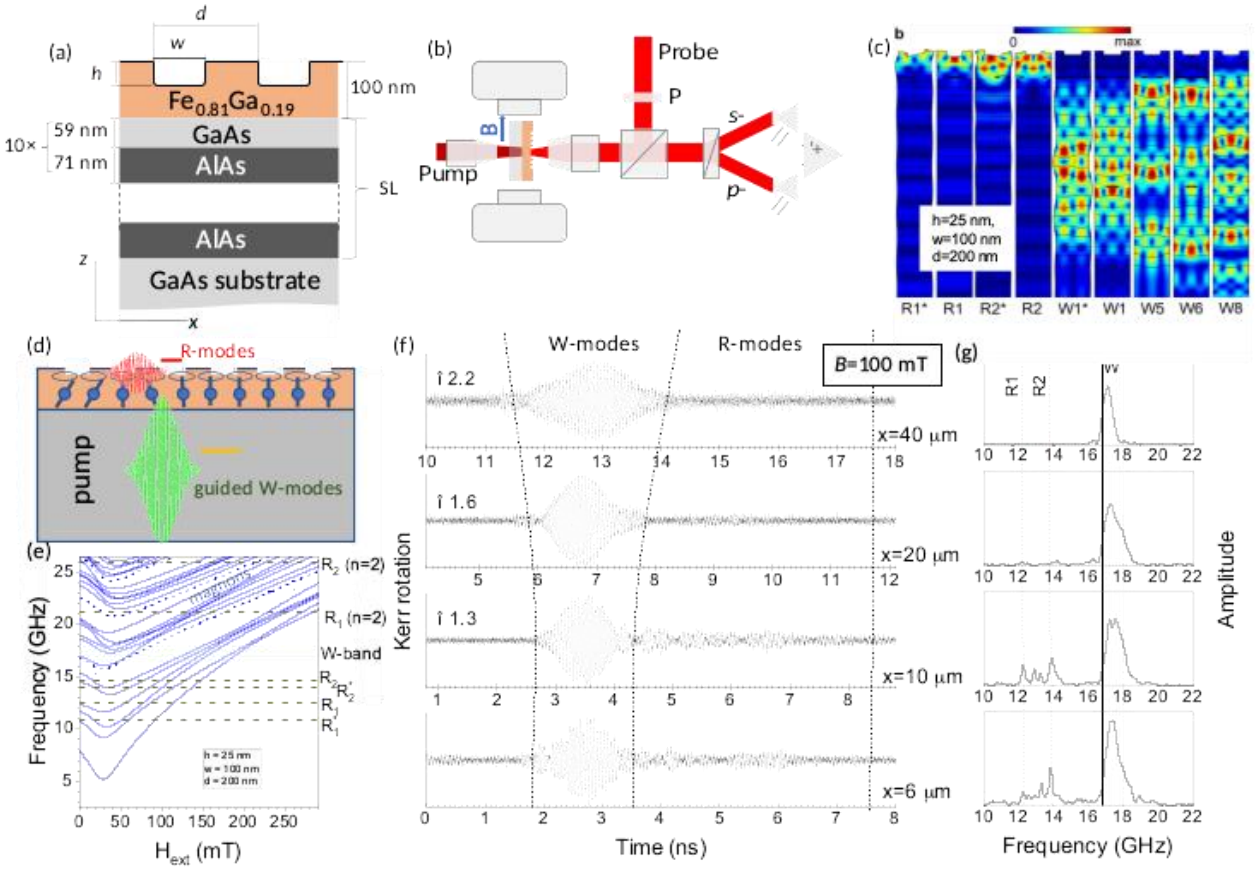

Fig. 1 (a) Schematic of the studied hybrid structures with a ferromagnetic nanograting on the top of a semiconductor superlattice. **(b)** Experimental geometry with the pump and probe beams focused to the spots of 3 and 0.5 mm diameter, respectively, from the opposite sides of the studied structure. The modulation of the probe pulse intensity and polarization is measured in a differential scheme by means of a balanced photoreceiver. **(c)** Spatial distributions of the strain of the several selected phonon modes excited in the studied hybrid structure with h=25 nm, w=100 nm and d=200 nm [5]. **(d)** The experimental idea: a coherent phonon wave packet of the surface (R) and guided (W) phonon modes propagating along the surface drives magnons in the top ferromagnetic layer. **(e)** Calculated magnetic field dependences of the magnon frequencies (blue lines). The red dashed lines and the green dashed rectangular show the field-independent frequencies of the surface phonon modes (R-modes) and the guided modes (W-modes), respectively. **(f and g)** Transient Kerr rotation signals (f) and their fast Fourier transforms (g) measured in the structure with parameters given above at the varied distance x between the pump and probe spots. Time t = 0 ns corresponds to the moment when the pump pulse hits the structure. The spectra shown in (g) are not normalized.

Despite on complexity of the studied system, it is possible to achieve its specific response to the ultrafast optical excitation. We can realize selective coupling of certain magnon and phonon modes with required parameters adjusted by a structural design. Among the range of observed effects, the most interesting ones are the following:

- *Strong coupling of the low order magnon and phonon modes with unprecedently high cooperativity C = 8* [4]. The strong coupling is achieved by the spatial overlap of the selected phonon and magnon modes in combination with their long lifetimes. We show that the symmetries of the localized magnon and phonon states play a crucial role in the magnon-phonon hybridization and its manifestation in the optically excited transient signals.

- *Strongly volatile spatial-time evolution of the guided magnon-phonon wave packet due to the interference of the propagating coupled modes*. The spatial-time volatility results in modification of the transient signal induced by a propagating wave packet detectable with ~100 nm spatial resolution, which is much smaller than the laser spots size.

The talk will present the experimental manifestations of these effects as well as theoretical modelling. We will also discuss potential applications, such as non-conventional computing on the nanoscale.

Acknowledgments – The present study is the result of cooperation between TU Dortmund (Felix Godejohann, Dmytro Yaremkevich, Alexey Scherbakov and Manfred Bayer), the University of Nottingham (Andrey Akimov, Andrew Rushforth, Richard Campion), Lashkaryov Institute (Serhii Kukhtaruk, Tetiana Linnik), Le Mans Université (Vitaliy Gusev), Ioffe Institute (Nikolay Khokhlov, Alexander Poddubny) and Raith GmbH (Achim Nadzeika). The work was supported by the Deutsche Forschungsgemeinschaft (Grant No. TRR160) and the Volkswagen Foundation (grant no. 97758).

References

[1] C. Kittel, Interaction of spin waves and ultrasonic waves in ferromagnetic crystals, Phys. Rev. 110 (1958) 836. https://doi.org/10.1103/PhysRev.110.836.

[2] Y. Li, W. Zhang, V. Tyberkevych, W.-K.Kwok, A. Hoffmann, V. Novosad, Hybrid magnonics: Physics, circuits, and applications for coherent information processing, J. Appl. Phys. 128 (2020) 130902. https://doi.org/10.1063/5.0020277.

[3] D.D. Awschalom et al., Quantum Engineering With Hybrid Magnonic Systems and Materials. IEEE Trans. Quantum Eng. 2 (2021) 5500836, https://doi.org/10.1109/TQE.2021.3057799.

[4] F. Godejohann, A.V. Scherbakov, S.M. Kukhtaruk, A.N. Poddubny, D.D. Yaremkevich, M. Wang, A. Nadzeyka, D. R. Yakovlev, A.W. Rushforth, A.V. Akimov, M. Bayer, Magnon polaron formed by selectively coupled coherent magnon and phonon modes of a surface patterned ferromagnet, Phys. Rev. B 102 (2020)144438. https://doi.org/10.1103/PhysRevB.102.144438.

[5] D.D. Yaremkevich, A.V. Scherbakov, S.M. Kukhtaruk, T.L. Linnik, N.E. Khokhlov, F. Godejohann, O.A. Dyatlova, A. Nadzeyka, D.P. Pattnaik, Mu Wang, S. Roy, R.P. Campion, A.W. Rushforth, V.E. Gusev, A.V. Akimov, M. Bayer, Protected long-distance guiding of hypersound underneath a nano-corrugated surface, ACS Nano, 15 (2021) 4802. https://doi.org/10.1021/acsnano.0c09475.

KEYNOTE SPEAKER

Imaging acoustic waves in 2D confined by hook or by crook

Wright OB[(1)*]

Hokkaido University, Sapporo 060-8628, Japan

*Corresponding author's email: olly@eng.hokudai.ac.jp

This talk describes experiments and simulations on two different ways to confine surface acoustic waves in two-dimensions on microscopic scales: by the use of a surface phononic crystal cavity [1] or by the use of zero-group-velocity waves in a thin plate [2]. In the former case, a quasi-hexagonal cavity in a honeycomb-lattice surface phononic crystal formed in crystalline silicon is imaged by means of an ultrafast technique, and the acoustic energy confinement is quantified. In the latter case, Lamb waves are similarly imaged in a micron-scale thickness silicon-nitride plate coated with a titanium film. We discuss the dispersion relations and spatial localization in detail in these two cases. Applications include sensing and the testing of bonded nanostructures.

References

[1] P.H. Otsuka, R. Chinbe, M. Tomoda, O. Matsuda, Y. Tanaka, D.M. Profunser, S. Kim, H. Jeon, I.A. Veres, A.A. Maznev, O.B. Wright (2022) *unpublished*.

[2] Q. Xie, S. Mezil, P.H. Otsuka, M. Tomoda, J. Laurent, O. Matsuda, Z. Shen, O.B. Wright, Imaging gigahertz zero-group-velocity Lamb waves, Nat. Comm. 10 (2019) 2228.

KEYNOTE SPEAKER

Optical generation and detection of GHz longitudinal and transverse acoustic waves in transparent medium with metallic grating structure

Matsuda O[(1)*], Tsutsui K[(1)], VaudelG [(2)], Pezeril T[(2)] , Fujita K[(1)], Gusev V[(3)]

(1) Division of Applied Physics, Faculty of Engineering, Hokkaido University, Sapporo, Japan
(2) Institut des Molecules et Materiaux du Mans, UMR 6283 CNRS, Le Mans Universite, Le Mans, France
(3) Laboratoire d'Acoustique de l'Université du Mans, UMR 6613 CNRS, Le Mans Université, Le Mans, France

*Corresponding author's email: omatsuda@eng.hokudai.ac.jp

Background – Understanding propagation of GHz-THz acoustic waves in materials is important for both fundamental physics and applications. For this it is efficient to use a method called picosecond laser ultrasonics in which ultrashort light pulses (named pump light pulses) with femtosecond-picosecond temporal width are focused to the sample to generate the acoustic waves up to THz frequency region and the propagating acoustic waves are detected with delayed light pulses (named probe light pulses) by the transient optical reflectivity change caused by the photoelastic effect[1]. In this sort of measurement, when the pump light is absorbed at the surface of a uniform and isotropic semi-infinite sample, only the longitudinal acoustic waves are generated because of the symmetry of the system and the measurement configuration. It has, however, been suggested that the optical generation of transverse acoustic waves is possible by laser-induced gratings[2].

Methods – To confirm the transverse acoustic wave generation and detection, we studied a metallic grating structure with picosecond laser ultrasonics. The aluminum grating structure of the period 390 nm and the thickness 40 nm is fabricated on a surface of fused silica substrate of thickness 1 mm using the electron beam lithography and the lift-off technique. A mode-locked Ti:sapphire laser is used as a light source. The fundamental light pulses of the central wavelength 800 nm and the temporal width 100 fs are used for the pump, whereas the frequency doubled light pulses of the wavelength 400 nm are delayed and used for the probe. The pump light pulses absorbed at the metallic grating generate the acoustic waves propagating not only along the direction perpendicular to the surface but also along the directions of their diffraction by the periodic grating structure. The probe light is obliquely incident from the back surface (without grating) and the first order diffracted light is fed to the photodetector to record the transient optical reflectivity change as a function of delay time between the pump and probe light pulse arrival to the sample. The probe light scattered by the propagating acoustic waves and that reflected/diffracted by the grating interfere and thus the light intensity at the photodetector shows the so-called Brillouin oscillations having rich frequency spectra in GHz region owing to the variety of combinations of possible acoustic and optical diffraction directions by the metallic grating [3,4].

Results – Figure 1 shows the Fourier spectra of the transient reflectivity change measured at several probe light incident angles. The + and × symbols indicate the expected Brillouin oscillation frequencies calculated from the assumed (in fact, optimized, see below) longitudinal and transverse sound

velocities, respectively, with the refractive index in a fused silica for the given probe light incident angles (not mentioned here). The calculated peaks for the longitudinal waves agree well with the experimental results in all curves, whereas those for the transverse waves are only partially observed in curves b) and c). All these agree well with the theoretically predicted selection rules, as it will be explained in detail in the presentation. By comparing the calculated and experimental peak positions, the sound velocities and refractive index can be refined. The calculated frequencies in Fig. 1 are obtained with the most optimized values which also agree well with the literature values.

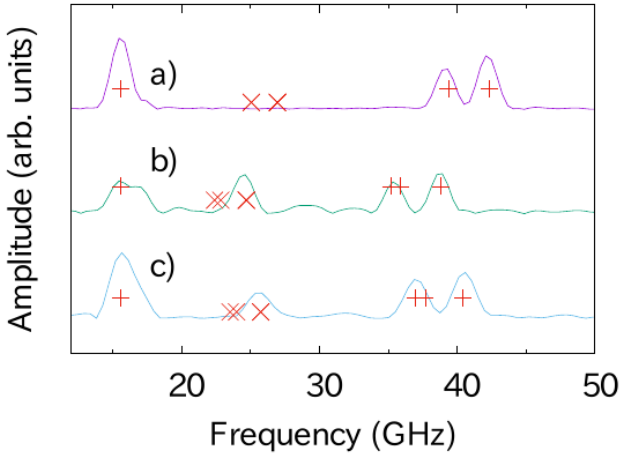

Fig. 1. Fourier spectra of Brillouin oscillation for the fused silica sample with metallic grating at several probe incident angles. The + and × symbols indicate the calculated peak positions for longitudinal and transverse acoustic waves, respectively.

Conclusions – We have demonstrated the optical monitoring of both longitudinal and transverse acoustic waves in a transparent medium using metallic grating structure. Especially we clarified the necessary condition for the generation and detection of transverse acoustic waves in this configuration. The obtained knowledge opens up a way to exploit the transverse acoustic waves as well as the longitudinal acoustic waves in various applications such as sensors.

References

[1] C. Thomsen, H. T. Grahn, H. J. Maris, J. Tauc, Surface generation and detection of phonons by picosecond light pulses, Phys. Rev. B 34 (1986) 4129-4138. https://doi.org/10.1103/PhysRevB.34.4129.

[2] V. Gusev, On generation of picosecond inhomogeneous shear strain fronts by laser-induced gratings, Appl. Phys. Lett. 94 (2009) 164105-1-3. https://doi.org/10.1063/1.3125243.

[3] O. Matsuda, T. Pezeril, I. Chaban, K. Fujita, V. Gusev, Time-domain Brillouin scattering assisted by diffraction gratings, Phys. Rev. B 97 (2018) 064301-1-11. https://doi.org/10.1103/PhysRevB.97.064301.

[4] O. Matsuda, K. Tsutsui, G. Vaudel, T. Pezeril, K. Fujita, V. Gusev, Optical generation and detection of gigahertz shear acoustic waves in solids assisted by a metallic diffraction grating, Phys. Rev. B 101 (2020) 224307-1-9. https://doi.org/10.1103/PhysRevB.101.224307.

In-situ laser-ultrasonic characterization of plates through zero-group-velocity and thickness resonances

Watzl G(1)*, Mitter T(2), Grünsteidl C(1)

(1) Research Center for Non-Destructive Testing GmbH, Linz, Austria
(2) voestalpine AG, Linz, Austria

*Corresponding author's email: georg.watzl@recendt.at

Background – Heat treatment is a commonly used method in metal manufacturing to adjust the mechanical properties of the product. The sample undergoes various microstructural changes (e.g., phase composition, texture, grain size) during the temperature curve, whose understanding is crucial for controlling and improving the production process.

Current standard methods for sample monitoring during thermal processing are either ex-situ or require special sample preparation and therefore cannot be used on the production line. The potential of laser-ultrasound (LUS) techniques for material characterization by measuring longitudinal pulses and thickness resonances on hot and moving metal sheet samples has been demonstrated previously [1,2]. However, these methods are sensitive to thickness variations, which are common in an industrial setting, limiting their achievable accuracy. Clorennec, et al. have shown, that the Poisson's ratio of plates can be found through the measurement of two resonance frequencies of different type, which does not require knowledge on the thickness [3].

Methods – We use an adaption of the method of Clorennec, et al. to determine Poisson's ratio (ν) of plates, while the sample undergoes heat treatment. The sample is positioned in a heating chamber above an induction coil, and its surface displacement (u_z) following a short laser-pulse is measured with a vibrometer, where excitation and detection is on the same spot (see Fig.1).

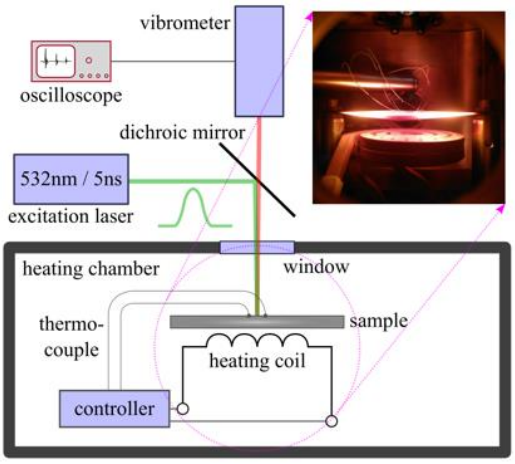

Fig. 1. Experimental setup.

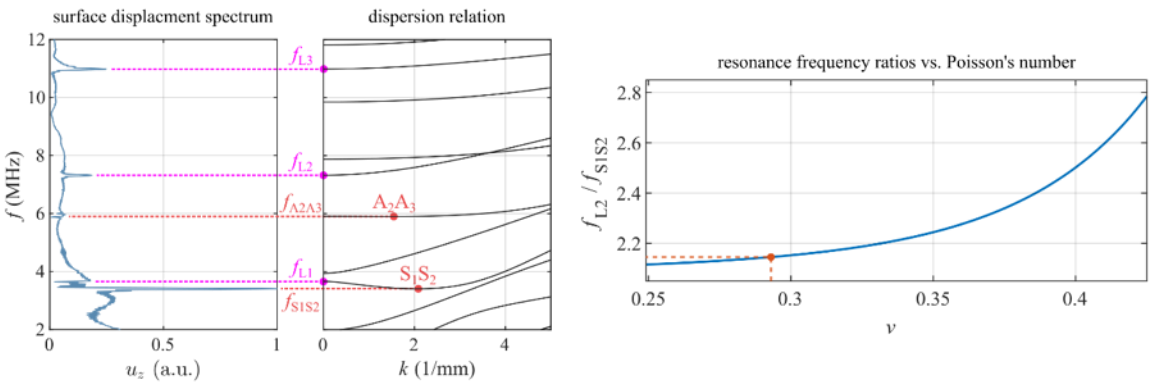

Fig. 2. Operating principle for determining Poisson's ratio of isotropic plates through local LUS measurements.

We determine a thickness resonance (L) frequency and the S_1S_2 zero-group-velocity (ZGV) mode, whose ratios yield the Poisson's number, if isotropy is assumed [4] (see Fig. 2). With additional knowledge on the thickness, the longitudinal and transversal sound velocities (c_L, c_T) can also be found. Due to the occurrence of additional resonances not used in the determination of ν, the validity of the results can be checked by comparing resonance frequencies calculated from the measured quantities with the recorded spectra.

Results – We demonstrate the measurement of Poisson's ratio during thermal processes on different metal samples and temperature curves. The measured quantities (ν, c_L, c_T) are compared to results from dilatometry and thermodynamic simulations and their correlation to microstructural changes are analysed.

Conclusions – Contact-free determination of the Poisson's ratio of plates during thermal processing can be achieved through the measurement of plate resonances with laser-ultrasound, without requiring exact knowledge on the sample's thickness. The method is robust, and the gained information can reveal material transitions in steel plates. Especially above the Curie temperature, ν is more sensitive to changes in phase composition than c_L.

References

[1] A. Moreau, et al., On-line measurement of texture, thickness and plastic strain ratio using laser-ultrasound resonance spectroscopy, Ultrasonics 40 (2002) 1047–1056. https://doi.org/10.1016/S0041-624X(02)00255-X.

[2] S. E. Kruger, E. B. Damm, Monitoring austenite decomposition by ultrasonic velocity, Mater. Sci. Eng. A 425 (2006) 238–243. https://doi.org/10.1016/j.msea.2006.03.056.

[3] D. Clorennec, C. Prada, D. Royer, Local and noncontact measurements of bulk acoustic wave velocities in thin isotropic plates and shells using zero group velocity lamb modes, J. Appl. Phys. 101 (2007) 1–6. https://doi.org/10.1063/1.2434824.

[4] C. Prada, D. Clorennec, D. Royer, Local vibration of an elastic plate and zero-group velocity lamb modes, J. Acoust. Soc. Am. 124 (2008) 203–212. https://doi.org/10.1121/1.2918543.

Zero-Group-Velocity Lamb mode's behaviour in the vicinity of a thickness step

Kiefer DA[(1)], Diboune H[(1)], Mezil S[(1)*], Prada C[(1)*]

(1) Institut Langevin ESPCI, UMR 7587, 1 rue Jussieu, Paris, France

*Corresponding author's email: sylvain.mezil@espci.fr

Lamb modes are commonly used for nondestructive testing of thin structures that can be seen as waveguides. These modes are strongly dispersive. When two mode branches from a same symmetry (i.e., symmetric or anti-symmetric) have close cut-off frequencies, a repulsion between these two modes is observed. This results in a local minimum in the dispersion curve that corresponds to a nonpropagating Lamb mode having a zero group velocity (or ZGV) whereas its phase velocity remains finite. Because of their zero group velocity, the energy is trapped under the excitation source, offering a sharp resonance. Quality factors up to 10^4 have been measured in a 0.5 mm thick Duralumin plate [1]. This enables local measurements with high sensitivity. Laser-based ultrasonic techniques, as they are contactless, offer a very adequate tool to observe these resonances [2]. In the last decade, ZGV resonances have been observed in many different structures (e.g., plates, tubes, and ribbons). This allowed to locally determine, with a high sensitivity, various parameters such as the Poisson ratio, the sample thickness, or the adhesion between two plates [3-4].

Because of its group velocity being null, usual ZGV Lamb mode measurements are performed with pump and probe beams aligned to one location of the sample with the beams being either in the same side of the sample (reflection measurement) or on each side of it (transmission measurement). To map the spatial evolution of a sample parameter—for example its thickness—one must perform a one- or two-dimensional scan point-by-point. This requires the sample's surface to be optically reflective at the laser probe wavelength and to be orientated normally to the probe beam to ensure the detection of the acoustic signal. In order to lift this strong limitation, we investigate the possibility to detect the ZGV frequency associated with different excitation points while the detection is fixed at one location. In particular, we investigate the possibility to retrieve the ZGV frequency in the presence of a thickness step, where the nonpropagative ZGV Lamb mode can convert to propagative ones. Such mechanism would enable measurements to be performed in the far field.

The samples are millimeter thick Duralumin plates containing either a small thickness step (a few percent thickness variation), a large one (around 10%), or a thickness gradient for comparisons. Experiments are achieved all-optically. A Q-switched Nd:YAG laser (λ=1064 nm) delivers 10 ns pulses of ~10 mJ energy that generates the acoustic waves. The normal surface displacement is detected on the opposite side of the plate with an interferometer (λ=532 nm). 1D and 2D scans are performed by shifting only the pump beam and with the probe beam fixed either on the thick or the thin section of the sample. An example of a triangle exhibiting a ~8% thickness variation and the experimental setup is depicted in Fig. 1(a). The 2D spatial thickness, observed from the measurement of the ZGV resonant frequency associated with the excitation point, is presented in Fig. 1(b).

The mode conversion phenomena in the aforementioned configurations are further analyzed using numerical studies. This allows to assess the necessary conditions under which the ZGV resonance

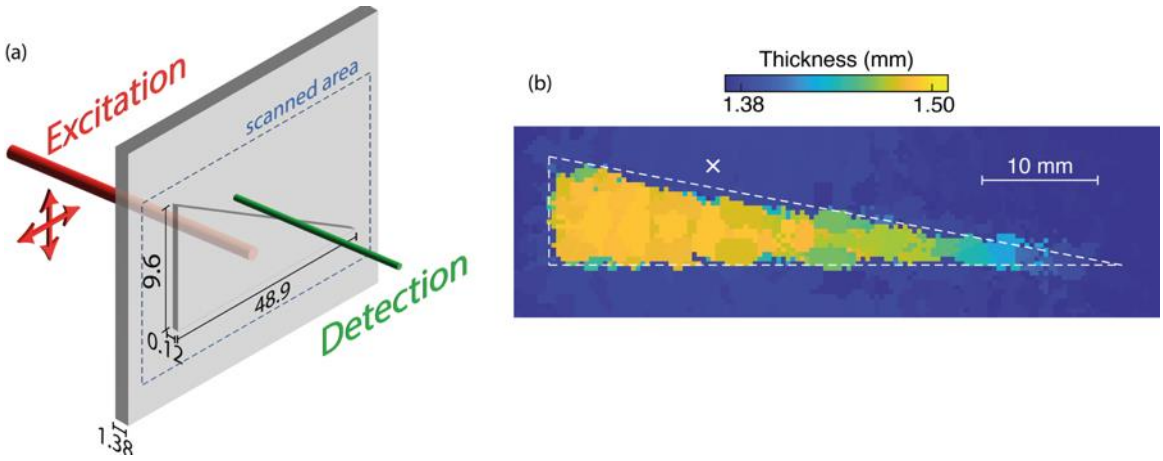

Figure 1: (a) Schematic representation of the Duralumin plate and the experimental setup. Dimensions in millimeters. **(b)** Thickness locally measured at the excitation position for a fixed probe beam located in the thinner part (white cross). The triangle limit is depicted in dashed-line.

frequency of different excitation points can be accessed from a unique detection point. Harmonic Finite Element simulations with absorbing layers are exploited for this end. Moreover, the computation of modal conversion coefficients provides quantitative information about the formation of propagative waves at the thickness step. The numerical and experimental results are in good agreement and the implications for the ZGV measurement technique are discussed.

We hope that these new results will pave the way to exploiting ZGV Lamb mode techniques in materials having a surface not favorable for interferometric laser detection, thus significantly extending this laser ultrasonic technique applicability.

References

[1] D. Clorennec, C. Prada, D. Royer, T.W. Murray, Laser impulse generation and interferometer detection of zero group velocity Lamb mode resonance, Appl. Phys. Lett., 89, 024101 (2006). https://doi.org/10.1063/1.2220010.

[2] Q. Xie, S. Mezil, P. H. Otsuka, M. Tomoda, J. Laurent, O. Matsuda, Z. Shen, O. B. Wright, Imaging gigahertz zero-group-velocity Lamb waves, Nat. Commun. 10 (2019) 2228, https://doi.org/10.1038/s41467-019-10085-4.

[3] D. Clorennec, C. Prada, D. Royer, Local and noncontact measurements of bulk acoustic wave velocities in thin isotropic plates and shells using zero group velocity Lamb modes, J. Appl. Phys., 101 (2007) 034908, https://doi.org/10.1063/1.2434824.

[4] S. Mezil, J. Laurent, D. Royer; C. Prada, Non contact probing of interfacial stiffnesses between two plates by zero-group velocity Lamb modes, Appl. Phys. Lett., 105 (2014) 021605, https://doi.org/10.1063/1.4890110.

Zero-group velocity resonance spectroscopy for bulk acoustic wave resonator characterization

Yan G(1), Ryzy M(1)*, Veres I(2), Berer T(2), Kreuzer S(2)

(1) Research Center for Non-Destructive Testing GmbH, Linz, Austria
(2) Qorvo, Inc., Apopka, FL 32703 USA

*Corresponding author's email: martin.ryzy@recendt.at

Background – Bulk Acoustic Wave (BAW) filters are broadly used in modern mobile telecommunication systems and are designed to feature a strong thickness (bulk) resonance. Besides this resonance, a Zero-group velocity (ZGV) resonance can be observed in the investigated resonator structures, commonly known in thin plates and layered systems [1-3]. In this work, we utilize the ZGV modes in thin-film BAW resonators to conduct spatially resolved measurements of ZGV resonances in the GHz frequency range [4-5]. To demonstrate their spatial confinement, the area of a resonator with a checker-board pattern of varying thicknesses of the topmost layer was scanned, and the ZGV center frequency was used to provide spatial images of the thickness pattern.

Methods – A schematic view of the resonators cross section is shown in Fig. 1(a). It was structured by lithographic means to introduce an artificial thickness variation (1/4/8 nm), as shown by pink areas in Fig.1 (b). Two patterns were produced, a step-pattern [Fig. 1(b), top] and a checker-board pattern with 33x33μm^2 squares with alternating stack heights [see Fig. 1(b), bottom].

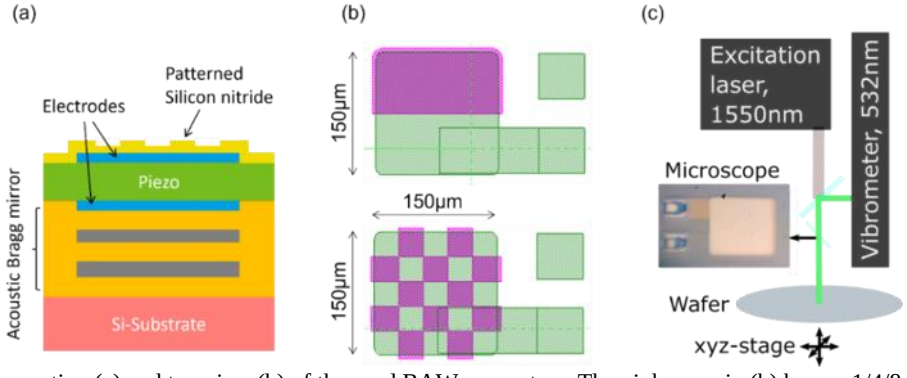

Fig. 2. Cross section (a) and top view (b) of the used BAW-resonators. The pink areas in (b) have a 1/4/8 nm thinner topmost Silicon nitride layer. Two different geometries were fabricated: A single step (top image in b) and a checkerboard pattern (bottom image in b) with 33x33μm^2 large squares. Figure (c) shows a sketch of the used frequency domain LU setup.

For excitation and detection of ZGV-modes we use a frequency domain laser ultrasound (LUS) system [see Fig. 1(c)], which has been described in Ref. [4]. It uses an electro-optically modulated diode laser with a wavelength of 1.55μm that is amplified to about 200mW by an erbium doped fiber amplifier and focused onto the sample with a microscope objective. The surface normal displacement is detected with a path-stabilized Michelson Interferometer that is connected to a vector network analyzer for phase sensitive detection. A white light microscope provides a magnified top-view of the samples which facilitates aiming at specific structures and aligning the laser spot positions.

Results – We performed a spatial scan in a narrow frequency range around the first ZGV-resonance on quadratic regions on the resonator surfaces. To extract the ZGV-center frequency, 2nd -order polynomials were fit to the raw data. Fig. 2 shows the ZGV-center frequencies extracted from a spatial scan (lateral resolution 1μm) of a 65x65μm^2 large region in three 'checkered'-resonators. The imprinted pattern is clearly visible. The thickness variations of 3 checkered resonators are 1, 4 and 8 nm, respectively, and the corresponding frequency shifts agree to expected thickness changes (inversely proportional to thickness variations) to be 0.4, 1.5 and 3 MHz. The spatial resolution of the used method is currently under study, to that effect, a stepped resonator [see Fig. 1(b), top] is utilized, with consideration of edge effects to ZGV resonance [6].

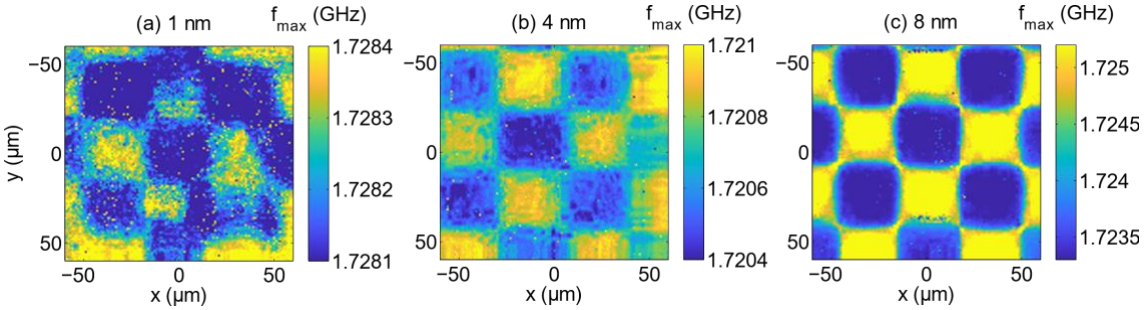

Fig. 2. 2D imaging of checkerboard BAW-resonators utilizing the extracted ZGV resonance center frequencies for cases of thickness variations equal to (a) 1 nm, (b) 4 nm and (c) 8 nm.

Conclusions – We demonstrated a method for imaging nm-scaled thickness variations in BAW resonators, based on the precise measurement of the center-frequency of zero-group velocity plate resonances at GHz frequencies. The imaging capabilities were shown by reproducing a checkered pattern, imprinted in the topmost layer of a BAW-resonator. The method may serve as an inspection tool for BAW-resonators and other layered systems used in the semiconductor industry and complement existing non-local methods.

References

[1] C. Prada, O. Balogun, T.W. Murray, Laser-based ultrasonic generation and detection of zero-group velocity Lamb waves in thin plates, Appl. Phys. Lett., 87 (2005) 194109. 10.1063/1.2128063.

[2] S. Mezil, F. Bruno, S. Raetz, J. Laurent, D. Royer, C. Prada, Investigation of interfacial stiffnesses of a tri-layer using Zero-Group Velocity Lamb modes, J. Acoust. Soc. Am., 138 (2015) 3202-3209. 10.1121/1.4934958.

[3] C. Caliendo, E. Giovine, M. Hamidullah, Design and Fabrication of Zero-Group-Velocity Lamb Wave Resonator onto Silicon Nitride/Aluminum Nitride Suspended Membrane, AIP Conf. Proc., 1990 (2018) 020013. https://doi.org/10.1063/1.5047767.

[4] C. Grunsteidl, I. Veres, T. Berer, S. Kreuzer, R. Rothemund, M. Hettich, E. Scherleitner, M. Ryzy, Measurement of the attenuation of elastic waves at GHz frequencies using resonant thickness modes, Appl. Phys. Lett., 117 (2020) 164102. 10.1063/5.0026367.

[5] Q. Xie, S. Mezil, P.H. Otsuka, M. Tomoda, J. Laurent, O. Matsuda, Z. Shen, O. B. Wright, Imaging gigahertz zero-group-velocity Lamb waves, Nat.Commun., 10 (2019) 2228. 10.1038/s41467-019-10085-4.

[6] A. Veres, C. Grunsteidl, D.M. Stobbe, and T. W. Murray, Broad-angle negative reflection and focusing of elastic waves from a plate edge, Phys. Rev. B, 93 (2016) 174304. 10.1103/PhysRevB.93.174304.

Laser-ultrasonic characterization of plates based on discrete points in their Rayleigh-Lamb dispersion spectra

Grünsteidl C(1)*, Watzl G(1)

(1) Research Center for Non Destructive Testing GmbH, Linz, Austria

*Corresponding author's email: clemens.gruensteidl@recendt.at

Background – Plates and similar geometries involving two parallel surfaces like pipes, are common products and techniques for non-destructive quality inspection at different production stages are beneficial. Their characterization in terms of thickness and elastic properties is possible, based on guided ultrasonic waves, sustained in such structures. For plates these are called Rayleigh-Lamb waves, and their dispersion curves depend on longitudinal and transverse sound velocities (c_L, c_T), and the thickness (h). Dispersion curves can be measured and mathematically inverted to determine the plates' properties. This is feasible using laser-ultrasound (LUS), however non-local and time-consuming scanning procedures are necessary to obtain the dispersion curves in high detail.

Method – We are working on a LUS method to determine c_L, c_T and h of a plate, which keeps the collected information on the dispersion curves, and the complexity of the measurement at a required minimum. We propose this can be achieved by measuring two zero-group velocity resonance [1] frequencies f_{ZGV1}, f_{ZGV2} in a combination with the fundamental mode (which at high frequencies is in approximation a surface wave) frequency f_{SAW} at a specific wavenumber k_{SAW} (see Figure 3).

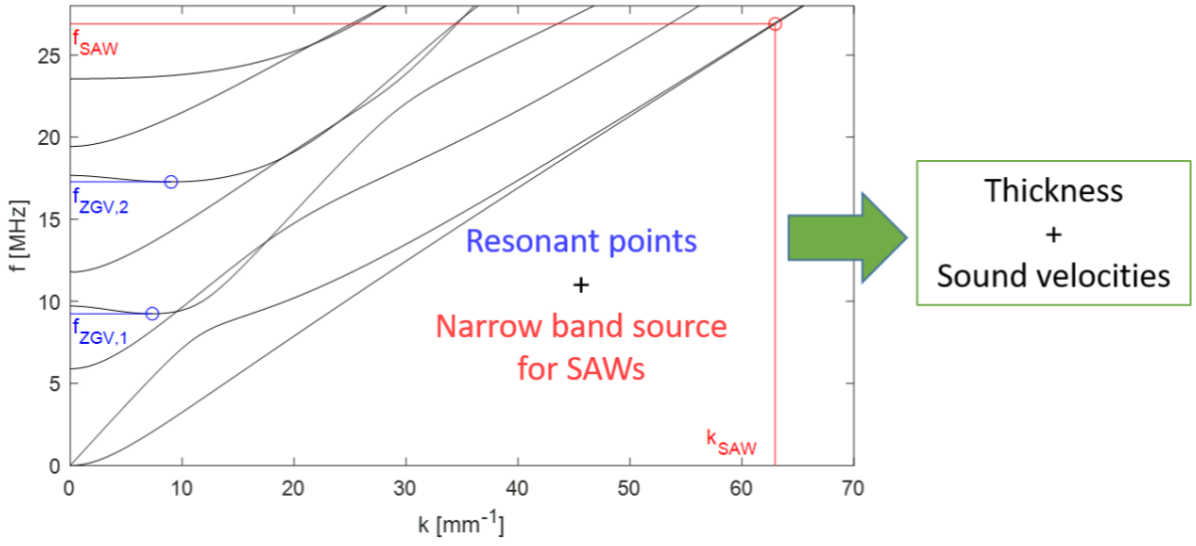

Figure 3: Dispersion curves of a plate and reduced information acquired

The latter is done in the transient grating method and related approaches by using a periodic line pattern for excitation [2,3]. The periodicity forces the k vector and the corresponding frequency of the surface wave is recorded. In a first step we use the sum of a responses from a single line at different distances

to the detection point to synthesize the response of a periodic source. Due to linearity, the result is equivalent and optimum source parameters can be confirmed in experiments.

Results – We show that for plates with thicknesses in the mm-range, a finite sized periodic pattern can be used, which yields f_{SAW} at k_{SAW} set by the periodicity. If additionally, the total size of the pattern is below the half wavelengths of the ZGV resonances in the investigated plate, coupling into these resonances is achieved with the same source. When chosen appropriately, the ZGV resonances show in the lower frequency-region (e.g. f_{ZGV1}, $f_{ZGV2} < 10$ MHz) of the response spectrum while the SAW peak occurs in the higher region (e.g. $f_{SAW} > 30$ MHz) and the can be separated. The frequencies peaks are enhanced by signal processing. From the experimental quantities, we deduce c_L, c_T and h. The influence of uncertainties in the measured quantities on the results is investigated by Gaussian error propagation.

Conclusions – The simultaneous measurement of a forced SAW resonance and intrinsic ZGV resonances can be achieved using a periodic excitation pattern. The balance of periodicity and total size of the pattern is crucial, and technical and physical limitations restrict the range of plate thicknesses and materials which can be investigated. From the single recorded response spectrum c_L, c_T and h are found. The periodic source, which in the first stage of the work is realized as a synthesis from single line responses, will replaced by a phase mask. This provides the possibility to advance from 1D periodic lines towards 2D concentric rings, with the benefit of larger displacements due to focusing of the launched waves in the centre. The aim is a single-shot, spatially resolved measurement of c_L, c_T and h.

References

[1] X. Prada, D. Clorennec, D. Royer, Local Vibration of an Elastic Plate and Zero-Group Velocity Lamb Modes, J. Acoust. Soc. Am., 124:1 (2008), 203–212.

[2] A.A Maznev, K.A. Nelson, J.A Rogers, Optical Heterodyne Detection of Laser-Induced Gratings, Opt. Lett. 23:16 (1998) pp. 1319.

[3] S.D. Sharples, M. Clark, M.G. Somekh, Spatially Resolved Acoustic Spectroscopy for Fast Noncontact Imaging of Material Microstructure.," Opt. Express, 14:22 (2006) 10435–10440.

Giant photoelasticity of the superlattice polaritons for laser ultrasonics

Kobecki M[(1)*], Scherbakov AV[(1,2)], Kukhtaruk SM[(1,3)], Yaremkevich DD[(1)], Henksmeier T[(4)], Trapp A[(4)], Reuter D[(4)], Gusev VE[(5)], Akimov AV[(6)], Bayer M[(1,2)]

(1) Experimentelle Physik 2, Technische Universitaet Dortmund, Dortmund, Germany
(2) Ioffe Institute, St. Petersburg, Russia
(3) Department of Theoretical Physics, V.E. Lashkaryov Institute of Semiconductor Physics, Kyiv, Ukraine
(4) Department Physik, Universitaet Paderborn, Paderborn, Germany
(5) Laboratoire d'Acoustique de l'Uiversit´e du Mans (LAUM), Institut d'Acoustique - Graduate School (IA-GS), CNRS, Le Mans Universit´e, Le Mans, France
(6) School of Physics and Astronomy, University of Nottingham, Nottingham NG7 2RD, UK

*Corresponding author's email: michal.kobecki@tu-dortmund.de

High-frequency coherent phonons in the GHz range have a potential for application in quantum technologies due to their nanometer wavelengths being comparable with the size of quantum nano-devices. Such phonons can be excited and detected optically with the all-optical laser ultrasonics. Single quanta of localized phonons are possible to excite and detect by suspended structures and non-suspended optomechanical resonators. While propagating phonons are prospective logistic elements of quantum networks, their detection sensitivity remains so far insufficient. Therefore, increasing strength of photon-photon coupling became of interest to the community [1,2]. In this work, we show that it is possible to reach quantum sensitivity of the detection with a standard pump-probe set-up by exploiting giant photoelasticity of exciton-polariton resonance in a short period GaAs/AlAs superlattice (SL) [3].

The examined SL structure contains 30 periods of GaAs and AlAs layers with 12 and 14.2nm thicknesses deposited on the GaAs substrate. The initial measurements of reflectivity spectrum R_0 (solid line in Fig.1a) show clear polariton resonance positioned at $\hbar\omega_0$ = 1.55eV where the dielectric permittivity function is steepest. For excitation and detection of the coherent phonon wave packet, we used a standard pump-probe experimental set-up with a mechanical delay line and a lock-in amplifier. A coherent acoustic phonon wave packet is generated by absorption of 200fs pump laser pulse by a metal transducer at the back of the sample. Strain pulse propagates into GaAs substrate and reaches the GaAs/AlAs SL at the front, where it gets detected (Fig.1b). In order to resolve the effect of SL polariton on the transient reflectivity signal $\Delta R(t)$, we have used probe laser pulse with a narrow spectrum of 1.4meV (dashed line in Fig.1a)- comparable with the width of the resonance. By sweeping the central wavelength of the probe in the vicinity of the resonance we obtained signals for several detuning values of probe photon energy. Transient reflectivity signals are presented in Fig.1c; they possess clear oscillatory behaviour called Time Domain Brillouin Scattering (TDBS). The amplitude of the TDBS signal depends strongly on the photon energy of the probe and it is presented in Fig.1d. For a qualitative description of obtained results, we have created a theoretical model which fits experimental data (blue line in Fig.1d). The most important experimental result is the observation of enhanced sensitivity of the TDBS signal at the polariton resonance, for probe photon energy $\hbar\omega = \hbar\omega_0$. For pump fluence $J \sim 0.1 mJ/cm^2$, we obtain the TDBS signal with amplitude $\frac{\Delta R}{R} \sim 10^{-2}$, which is three orders of magnitude larger than for a similar phonon wave packet detected in a material without presence of polariton resonance [4].

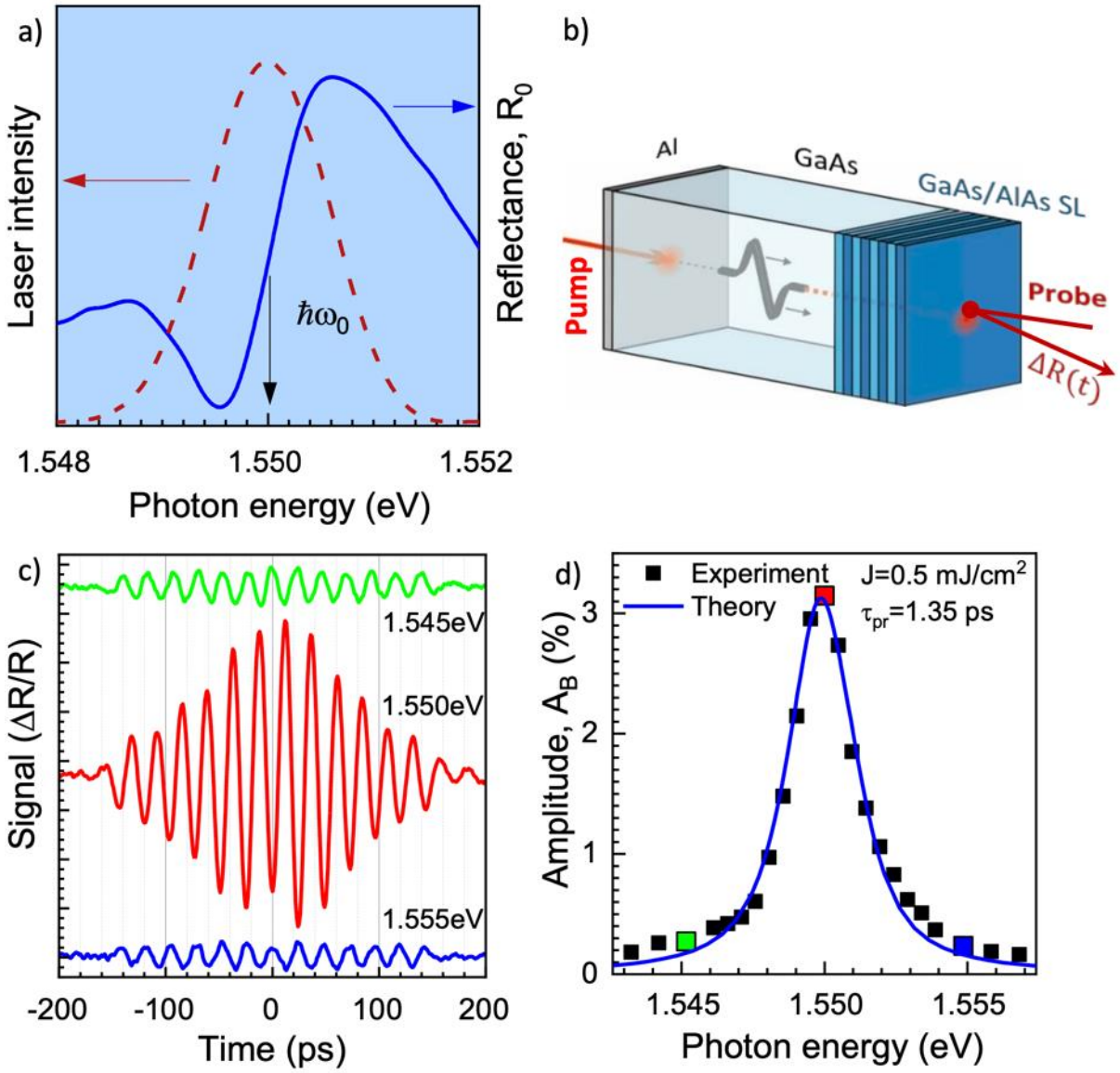

Fig. 1. a) Reflectivity spectrum in the vicinity of the polariton resonance (blue solid curve). The red dashed curve shows the spectrum of the probe beam. **b)** Schematics of excitation and detection of propagating coherent phonon wavepacket. **c)** TDBS signals measured in the vicinity of polariton resonance. **d)** TDBS amplitude dependence on probe beam energy.

Our experiments reveal giant photoelasticity of polaritons and extremely high sensitivity to propagating coherent phonons. The strong dispersion of the dielectric permittivity in the vicinity of the polariton resonance results in a strong ultrafast response of the optical properties to dynamical strain which accompanies the coherent phonons. This discovery opens new possibilities of ultrasensitive measurements of extremely low-density phonon fluxes. The presented technique can find its applications in the detection of phonons on the quantum level as well as phonon imaging exploited in laser ultrasonics.

References

[1] B. Jusserand, A.N. Poddubny, A.V. Poshakinskiy, A. Fainstein, A. Lemaitre, Phys. Rev. Lett. 115 (2015) 267402. 10.1103/PhysRevLett.115.267402.

[2] A.N. Poddubny A.V. Poshakinkiy, B. Jusserand, A. Lemaitre, Phys. Rev. B. 89 (2014) 235313. 10.1103/PhysRevB.89.235313

[3] M. Kobecki, A.V. Scherbakov, S. M. Kukhtaruk, D.D. Yaremkevich, T. Henksmeier, A. Trapp, D. Reuter, V.E. Gusev, A.V. Akimov, M. Bayer, arXiv:2106.07019v2 [cond-mat.mes-hall]

[4] A.V. Scherbakov, M. Bombeck, J.V. Jager, A.S. Salasyuk, T.L. Linnik, V.E. Gusev, D.R. Yakovlev, A.V. Akimov, M. Bayer, Opt. Express 21 (2013) 16473. https://doi.org/10.1364/OE.21.016473.

Defect detection in additively manufactured parts by laser ultrasonic tomography

Reitinger B[(1)*], Watzl G[(1)] , Meirer K[(1)], Hatzenbichler M[(2)], Senck S[(3)], Scherleitner E[(1)], Hettich M[(1)]

(1) Research Center For Non-Destructive Testing GmbH (RECENDT), Altenberger Straße 69, Linz, Austria
(2) FOTEC Forschungs- und Technologietransfer GmbH, Viktor Kaplan-Str. 2, 2700 Wiener Neustadt, Austria
(3) Research Group Computed Tomography, University of Applied Sciences Upper Austria, Stelzhamer-Str. 23, 4600 Wels, Austria

*Corresponding author's email: mike.hettich@recendt.at

Background – As a potential breakthrough technology, the additive manufacturing of metallic parts has raised tremendous interest. It is thus not surprising that methods are highly sought after, that can provide information on the quality of the manufactured parts in a non-destructive and non-contact way. Laser-based ultrasonics is a potential candidate to provide insight into fabricated parts either in-line or as quality check after fabrication [1]. Detection of defects is a) mandatory prerequisite for industrial application and b) optimization of the additive production process. This motivated us to explore this challenge in Ti-6Al-4V parts with intentionally created defects. These are further characterized with µCT as reference method as shown in Fig. 1a).

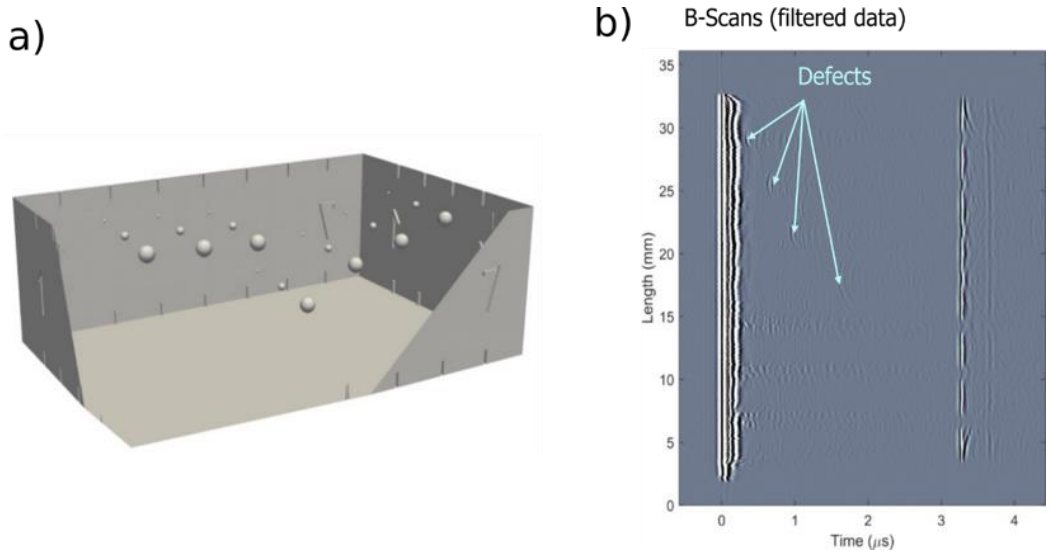

Fig. 1. a) Sketch sample geometry **b)** Exemplary time domain signals along a spatial line scan (B-scan)

Methods – We employ laser- based ultrasound to the optical excitation and subsequent detection of acoustic pulses in the additively manufactured part shown in Fig. 1a). Since the surface is rough a two-wave mixing interferometer is used for the detection due to its robustness against optically scattering surfaces. Several defect sizes (0.1-1mm) in varying depths (0.1-5mm) were intentionally printed in the structure. Characterization with µCT however revealed that only the bigger defects were actually printed as powder filled spheres. A spatial scanning scheme is employed along the sample surface where the time resolved pulse-echos are recorded for each position.

Results – The time-position data (B-scan) shown in Fig. 1b) then reveals the typical signatures of defect backscattering for the deeper defects. Surface near defects exhibit a different spatio-temporal behavior in our data. We find an excellent agreement of µCT and laser-based ultrasonic results for deeper defects but the analysis of surface near signals showed some peculiarities that we will discuss. Furthermore, we find that actual ultrasonic tomography, i.e. applying a spatial 2D scan is very sensitive to unwanted defects that are just barely visible in µCT images under close inspection. Studying the observed features in more detail with supporting simulations are currently under way.

Conclusions – The preliminary findings show a high sensitivity to small defects barely recognizable in µCT images which makes this straightforward approach already a very promising tool for 3D imaging of subsurface defects of additively manufactured parts. All printed defects are recognizable in the ultrasonic scans but a better understanding of the surface near signals is a prerequisite for actual application and further improvements.

References

[1] Honarvar, F., Varvani-Farahani, A. A review of ultrasonic testing applications in additive manufacturing: Defect evaluation, material characterization, and process control. Ultrasonics 108 (2020) 106227. https://doi.org/10.1016/j.ultras.2020.106227.

Measurement of the acoustic loss at GHz frequencies using laser-excited plate resonances

Ryzy M(1)*, Grünsteidl C(1), Istvan V(2), Thomas B(2)

(1) Research Center for Non-Destructive Testing GmbH, Linz, Austria (2) Qorvo, Inc., Apopka, FL 32703 USA

*Corresponding author's email: martin.ryzy@recendt.at

Background – State of the art wireless telecommunication is based on the transmission of electromagnetic (EM) waves at GHz-frequencies. For filtering broadband EM signals in telecommunication devices, electro-acoustic resonators (like BAWs or SAWs) are used. Filter manufacturers desire a precise knowledge of the acoustic loss (attenuation) of their constituent materials at the operating frequencies. This benefits device optimization and the design of filters for new generation telecommunication standards (like 6G).

Laser ultrasonic (LUS) techniques have a small spatial footprint and thus provide a unique way for exciting and detecting acoustic waves at high frequencies. Particularly, plate-resonance can be effectively accessed with LUS and they are well suited for elastic material characterization [1]. As their resonance frequency inversely scales with the plate thickness, samples can be tailored to target specific acoustic frequencies. In recent years, the boundaries of associated LUS techniques were continuously extended, so that nowadays measurements at GHz frequency can be readily performed [2]–[4].

Methods – A frequency-domain laser ultrasound setup is used for the measurement of plate-resonances in free-standing metallic plates (Fig. 1 (a)). To obtain a series of resonance frequencies in the low GHz frequency regime, we produce micron-scaled samples by lithographic means. The decay-rate of two different resonance types, thickness stretch resonances and zero-group-velocity (ZGV) resonances, is obtained from recorded acoustic spectra (Fig. 1 (b) and (c)). For thickness stretch resonances, this directly yields the longitudinal acoustic loss. For ZGV resonances, two resonances at the same frequency are required to disentangle longitudinal and transverse wave attenuation. Therefore, two separate plates with different thicknesses are used, that provide that the first ZGV resonance in sample one and the second ZGV resonance in sample two appear at the same frequency. A mathematical model has been developed, that connects the ZGV decay rate with the fundamental attenuation coefficients α_L and α_T, for longitudinal and transvers waves.

Results – The longitudinal quality factor $Q = f/2\alpha_L$ of aluminium is obtained in a frequency range between 1.5GHz and 3GHz from a series of measurements (see for example Fig. 1 (b)) in six aluminium plates with thicknesses ranging from 1.1 to 2.15µm. The quality factor follows a frequency power-law with an exponent around -1.5 (see Fig. 1 (d)). Comparison with the theoretical thermoelastic damping limit suggests the presence of additional loss mechanisms like (grain-boundary) scattering or different intrinsic losses [4]. Measurements of the decay rate of the first ZGV resonance in a 1.1µm thick tungsten plate, and of the second ZGV resonance in a 1.8µm thick tungsten plate (Fig. 1 (c)) yield ZGV decay rates of $12.97\ 10^6 s^{-1}$ and $19.86\ 10^6 s^{-1}$ at a frequency of around 2.16GHz. Applying a derived linear model, longitudinal and transvers attenuation coefficients of $\alpha_L = 18.2\text{dBmm}^{-1}$ and $\alpha_T = 29.2\text{dBmm}^{-1}$ are obtained.

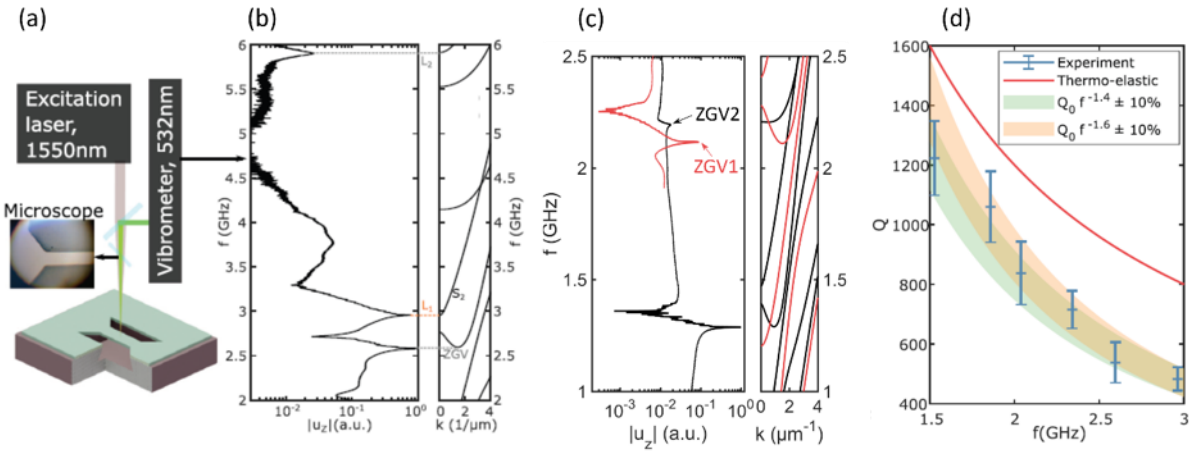

Fig 1 (a) Schematic of the used frequency domain laser ultrasound setup. (b) Measured acoustic spectrum and calculated dispersion curves of a 1.8µm thick aluminium plate. (c) Measured acoustic spectra and calculated dispersion curves of a 1.8µm (black) and a 1.1µm (red) thick tungsten plate. (d) Frequency dependence of the longitudinal quality factor of aluminium, obtained from a series of six aluminium plates with different thicknesses. The theoretical thermoelastic limit is shown as red solid line. Figures (a), (b) and (d) are extracted from reference [4].

Conclusions – Methods for the determination of the acoustic loss, based on the measurement of different types of acoustic plate resonances by laser-ultrasonic means are presented. Longitudinal loss at a certain frequency can be directly obtained from a single thickness stretch resonance. The simultaneous determination of longitudinal and transverse losses can be achieved by the measurement of two independent resonances at the same frequency, and the application of a mathematical model that connects ZGV decay rates with the fundamental attenuation coefficients. The methods were applied to determine the acoustic losses of aluminium and tungsten at low GHz frequencies.

References

[1] D. Clorennec, C. Prada, D. Royer, Local and noncontact measurements of bulk acoustic wave velocities in thin isotropic plates and shells using zero group velocity Lamb modes, Journal of Applied Physics, 101: 3 (2007), pp. 034908. doi: 10.1063/1.2434824.

[2] T. Berer et al., Determination of longitudinal and transversal attenuation coefficients in the frequency domain using zero group velocity Lamb waves, in 2019 IEEE International Ultrasonics Symposium (IUS), Glasgow, United Kingdom, Oct. 2019, pp. 1974–1976. doi: 10.1109/ULTSYM.2019.8925923.

[3] Q. Xie et al., Imaging gigahertz zero-group-velocity Lamb waves, Nat Commun, 10: 1 (2019) pp. 2228. doi: 10.1038/s41467-019-10085-4.

[4] C. Grünsteidl et al., Measurement of the attenuation of elastic waves at GHz frequencies using resonant thickness modes, Appl. Phys. Lett., 117:16 (2020) pp. 164102. doi: 10.1063/5.0026367.

Reaching the shock limit via synchronous laser ultrasonics

Deschamps J[(1)*], Kai Y[(1)], Lem J[(1)], Chaban I[(1)], Lomonosov A[(2)], Anane A[(3)], Kooi SE[(4)], Nelson KA[(1)], Pezeril T[(1,5)]

(1) Department of Chemistry, Massachusetts Institute of Technology, Cambridge, MA 02139, USA
(2) Prokhorov General Physics Institute of the Russian Academy of Sciences, 117942 Moscow, Russian Federation
(3) Unité Mixte de Physique CNRS/Thales, UMR CNRS 137, 91767 Palaiseau, France
(4) Institute for Soldier Nanotechnologies, Massachusetts Institute of Technology, Cambridge, MA 02139, USA
(5) Institut de Physique de Rennes, UMR CNRS 6251, Université Rennes 1, 35042 Rennes, France

*Corresponding author's email: jdesch@mit.edu

In recent years, controlling emergent phenomena in correlated materials through collective lattice vibrations has attracted more and more attention. Strain engineering methods favoring superconductivity [1], ferroelectricity, or adequate for tuning excitonic, magnetic, metal-insulator transitions [2] are among the latest examples. Large elastic static strains of several percents can be applied to bulk or nano samples up to the onset of plasticity or fracture. However, the excitation of ultrashort vibrations carrying out large strains to percent levels—the threshold at which many physico-chemical properties of materials would be significantly perturbed—still remains a challenge. Conventional laser-shock experiments, based on single-shot laser absorption in a transducer layer, can generate the strains required, although at the price of irreversible sample damage and noisy data.

Using ultrafast optics to build up propagative strain waves from the linear to the nonlinear regime, we introduce a non-destructive method of laser-shock wave generation and detection. The methodology is based on the synchronous spatiotemporal laser excitation of numerous distinct photoacoustic sources for additive superposition of multiple strain waves, as shown in Fig. 1. An input beam is split into a pulse train by using a FACED device [3]. The output is then focused on a sample as an array of lines, each arriving a set amount of time after the preceding. Each line in turn generates a thermoelastic response from the material, launching acoustic waves in both directions. The array of lines is spaced such that the waves propagating along one direction constructively superpose. The surface displacement of the propagating wave can be monitored using phase-mask interferometry [4] or time-resolved reflectivity.

The current approach can efficiently excite substantial strain waves in the range of a few percents, up to the mechanical failure, at a kHz repetition rate for optimal detection sensitivity, and offers new possibilities for the extensive study of subtle strain-induced effects in correlated materials where lattice degrees of freedom play a crucial role.

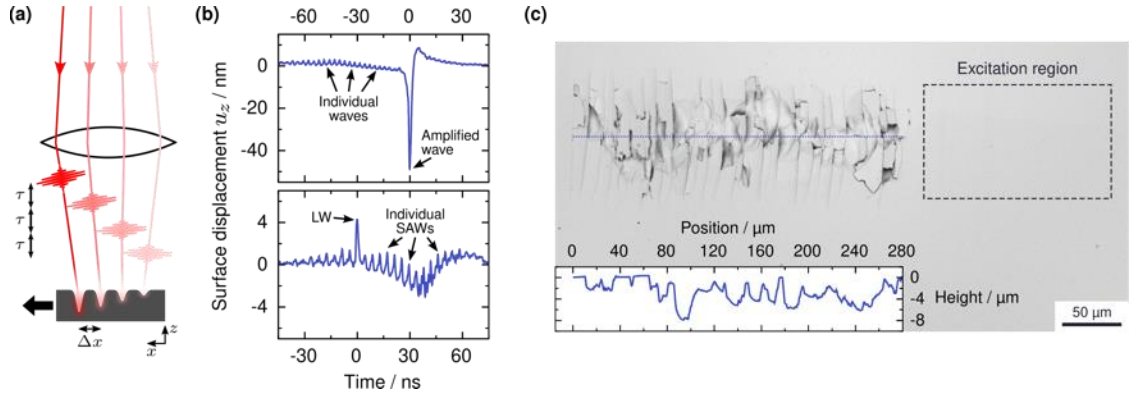

Fig. 1. (a) A pulse train with a temporal separation τ is focused on the sample surface; each laser pulse is laterally displaced by an amount Δx to match the propagation of the generated wave. **(b)** Displacement of a Nb:STO sample surface measured as a function of time upon thermoelastic excitation, for two different phase-matching conditions (surface acoustic wave and longitudinal wave). **(c)** SEM image of the surface of a Nb:STO sample showing SAW-induced damage hundreds of microns away from the excitation region. Inset: depth profile along the dotted line, extracted from confocal microscopy.

References

[1] A. Cavalleri, Photo-induced superconductivity, Contemp. Phys. 59 (2017) 31. https://doi.org/10.1080/00107514.2017.1406623.

[2] M. Rini, R. Tobey, N. Dean, J. Itatani, Y. Tomioka, Y. Tokura, R.W. Schoenlein, and A. Cavalleri, Control of the electronic phase of a manganite by mode-selective vibrational excitation, Nature 449 (2007) 72. https://doi.org/10.1038/nature06119.

[3] J.-L. Wu, Y.-Q. Xu, J.-J. Xu, X.-M. Wei, A.C.S. Chan, A.H.L. Tang, A.K.S. Lau, B. M. F. Chung, H. C. Shum, E.Y. Lam, K.K.Y. Wong, and K.K. Tsia, Ultrafast laser-scanning time-stretch imaging at visible wavelengths, Light Sci. Appl. 6 (2016) e16196. https://doi.org/10.1038/lsa.2016.196.

[4] C. Glorieux, J.D. Beers, E.H. Bentefour, K. Van de Rostyne, and K.A. Nelson, Phase mask based interferometer: Operation principle, performance, and application to thermoelastic phenomena, Rev. Sci. Instrum. 75 (2004) 2906. https://doi.org/10.1063/1.1781386.

Broadband high-frequency laser ultrasound generation and applications towards biological membranes

Serpa C[(1,2)*], Pereira DA[(1)], Pinto T[(1)], Silva AD[(1)], Moreno MJ[(1)], Arnaut LG[(1)]

(1) CQC-IMS, Department of Chemistry, University of Coimbra, 3004-535 Coimbra, Portugal
(2) LaserLeap Technologies, Rua Coronel Júlio Veiga Simão, CTCV Edifício B S/N, 3025-307 Coimbra, Portugal

*Corresponding author's email: serpasoa@ci.uc.pt

Background – Photoacoustic light-to-pressure conversion offers the ability to generate ultrasound pulses with high peak pressures, high central frequencies and large bandwidths, using laser pulses with fluences below 100 mJ/cm2. Generation of those intense ultrasound pulses is achieved by the pulsed irradiation of high absorption coefficient thin films. Dyes with fast and high quantum yield of non-radiative decay imbedded in polystyrene, nanostructured carbon particles or nanostructured TiO2 with adsorbed dye permeated with high thermal expansion polydimethylsiloxane, are among the materials being used.[1-3] Laser ultrasound pulses have shown remarkable application versatility, namely towards transient breaching of biological membranes, e.g. transient permeabilization of the outer layers of cell membranes or skin.[1] The non-destructive laser ultrasound pulses interaction with biological membranes is exemplified by the unloading of Green Fluorescence Protein from giant unilamellar vesicles,[4] and by enabling the transfection of plasmid DNA towards COS-7 monkey fibroblast cell line.[5] The ability to transiently and without pain permeabilize the skin is exemplified by the efficient permeabilization of the stratum corneum induced by photoacoustic waves of targets of therapeutic and aesthetic relevance: a 1.1 kDa bacteriochlorin, minoxidil, a precursor of vitamin C and hyaluronic acid.

Methods – Ultrasound pulses were generated by the photoacoustic effect. Pulsed Nd:YAD lasers coupled to an optical parameter oscillator when needed were used: EKSPLA OPO Model PG-122 pumped by a EKSPLA NL301G laser with pulse width 6 ns; a Quantel Big Sky Ultra 50 with pulse width 8 ns; and a EKSPLA PL2143A laser with pulse width 30 ps. Carbon nanotubes permeated with polydimethylsiloxane films were produced with thicknesses between 30 μm and 200 μm. Large superficial area and a thickness <5 μm TiO2 thin films with a Mn porphyrin dye adsorbed were produced by screen-printing. Mn porphyrin was imbedded in polystyrene making ≤80 μm films by casting. Photoacoustic waves were detected by a high frequency contact transducer with maximum sensitivity at 225 MHz (Panametrics/Olympus, model V2113) and by a needle hydrophone (Precision Acoustics, model NH0200).

Results – The characteristics of laser ultrasound pulses generated by fast and efficient conversion of energy from a laser pulse into a pressure transient were measured. CNT functionalized with siloxane groups produce thin films that generate exceptionally wide bandwidths (170 MHz at −6 dB) and peak pressures >1 MPa when excited by pulsed ps lasers.[3] Vertically-aligned CNT grown to distinct thicknesses and infused with PDMS were tested using 8 ns and 30 ps laser pulses. High pressure transient with a peak of 14 MPa and a bandwidth of 180 MHz at -10 dB using a 1064 nm 100 mJ/cm2 laser pulse for excitation was achieved.[4] Efficient release of FITC-dextran and GFP from a giant unilamellar vesicles (GUVs) core was observed, without damaging the phospholipid bilayer. Laser

ultrasound promotion of the permeabilization of GUVs was imaged using real-time interferometric imaging. At a repetition rate of 10 Hz, ultrasound pulses enable to release 25% of the FITC-dextran content of GUVs in 15 min.[4] High stress gradients, produced when picosecond laser pulses with a fluence of 100 mJ/cm ^{2} absorbed by piezophotonic materials formed by a dye incorporated in a thin polystyrene polymer film, enable transfection of a plasmid DNA encoding Green Fluorescent Protein (gWizGFP, 3.74 MDa) in COS-7 monkey fibroblast cells with an efficiency of 5% at 20 °C, in 10 minutes, and without any significant cytotoxicity observed.[5] By exposing skin to photoacoustic waves for two minutes using a laser pulse frequency of 20 Hz, the increase of transepidermal water loss of healthy human skin by a factor of 2.5 was observed, and the skin relaxes to normal two minutes later.[1] Such ultrasound pulses also increased significantly the initial fluxes of a 1.1 kDa bacteriochlorin and a 28 kDa protein through the stratum corneum of minipigs. Such an effect was also observed with other therapeutically relevant molecules as minoxidil or vitamin C precursors in ex vivo skin experiments. The intraepidermal delivery observed in minipigs does not lead to observable adverse effects.

Conclusions – The broad bandwidths and high central frequencies of the photoacoustic waves generated with nanostructured materials constitute a valuable stimulus for the promotion of cell transfection, through skin permeation and controlled drug delivery. Laser ultrasound pulses appear to be a very generic method to promote the temporary destabilization of the outer layers of the skin and promote the effective passage of molecules and macromolecules of therapeutic and aesthetic interest. Tailor made laser ultrasound may potentially enable non-invasive targeted release of GUVs and cell transfection over large volumes of tissues in a few minutes.

Acknowledgments – This work was supported by the Portuguese Science Foundation FCT through grant UIDB/00313/2020 for the Coimbra Chemistry Centre and through research project number PTDC/QUI-OUT/0303/2021.

References

[1] G.F.F. Sa, C. Serpa, L. G. Arnaut, Stratum Corneum Permeabilization with Photoacoustic Waves Generated by Piezophotonic Materials, J. Control. Release, 167 (2013) 290. http://dx.doi.org/10.1016/j.jconrel.2013.02.005.

[2] S. Noimark, R.J. Colchester, R.K. Poduval, E. Maneas, E.J. Alles, T. Zhao, E.Z. Zhang, M. Ashworth, E. Tsolaki, A.H. Chester, N. Latif, S. Bertazzo, A.L. David, S. Ourselin, P.C. Beard, I. P. Parkin, I. Papakonstantinou, A.E. Desjardins, Polydimethylsiloxane composites for optical ultrasound generation and multimodality imaging. Adv. Funct. Mater., 28 (2018) 1704919. https://doi.org/10.1002/adfm.201704919.

[3] A.D. Silva, C.A. Henriques, D. Malva, M.J.F Calvete, M.M. Pereira C. Serpa, L.G. Arnaut, Photoacoustic Generation of Intense and Broadband Ultrasound Pulses with Functionalized Carbon Nanotubes, Nanoscale, 12 (2020) 20831-20839. https://doi.org/10.1039/D0NR04986G.

[4] D.A. Pereira, A.D. Silva, P.A.T. Martins, A.P. Piedade, D. Martynowych, D. Veysset, M.J. Moreno, C. Serpa, K.A. Nelson, L.G. Arnaut, Imaging of photoacoustic-mediated permeabilization of giant unilamellar vesicles (GUVs), Sci. Rep., 11 (2021) 2775. https://doi.org/10.1038/s41598-021-82140-4.

[5] A.D. Silva, C. Serpa, L.G. Arnaut, Photoacoustic transfection of DNA encoding GFP, 9 (2019) 2553. https://doi.org/10.1038/s41598-018-37759-1.

Optical and ultrasound imaging of shear wave generated by laser induced cavitation bubbles

Ghasemian SI[(1)*], Reuter F[(1)], Ohl CD[(1,2)]

(1) Institute of Physics, Otto-von-Guericke Universität, Universitätsplatz 2, 39016 Magdeburg, Germany

(2) Research Campus STIMULATE, University of Magdeburg, Otto-Hahn-Straße 2, 39106 Magdeburg, Germany

*Corresponding author's email: saber.izak@ovgu.de

While active shear wave elastography for creating tissue elasticity map has mushroomed over the years, there are only a few kind of sources for shear generation utilised in medical applications. Here we show that the oscillations of non-spherical bubbles can generate shear wave in a tissue mimicking material. These bubbles may form in thermal ablation or from non-linear absorption of pulsed laser beams. Here we report on shear waves generation from laser induced cavitation bubbles. Using a thin layer of graphite powder allows measuring optically with high-speed imaging and acoustically with plane wave imaging the shear wave propagation. A comparison between both methods demonstrates excellent agreement. The long term aim of the research is to utilise naturally occurring bubble oscillation during thermal tissue ablation for a shear wave based thermal dose quantification.

Ultrasonic emitter based on photoacoustic polymer graphene nanocomposites

Vella D[(1)]*, Marzel A[(2)], Drnovšek A[(3)], Shvalya V[(4)], Jezeršek M[(1)]

(1) Faculty of Mechanical Engineering, Laboratory for Laser Techniques, University of Ljubljana, Aškerčeva 6, 1000 Ljubljana, Slovenia
(2) Jožef Stefan Institute, Department of Complex Matter, Jamova 39, 1000 Ljubljana, Slovenia
(3) Jožef Stefan Institute, Department of Thin Films and Surfaces, Jamova 39, 1000 Ljubljana, Slovenia
(4) Jožef Stefan Institute, Department of gaseous electronic, Jamova 39, 1000 Ljubljana, Slovenia

*Corresponding author's email: daniele.vella@fs.uni-lj.si

Focused high amplitudes and high frequency ultrasounds pulses are difficult to achieve with a traditional piezo-electric based technologies. A photoacoustic approach, employing pulsed optical excitation of photoacoustic materials or nano-absorber sandwiched with a polymer, results in ultrasound pulses with high amplitudes as well as high frequency [1,2]. This minimizes the electrical components and cabling usually used in a traditional piezoelectric approach and creates new opportunity for the integration of miniaturized optoacoustic devices. In a photoacoustic lens the ultrasound can be generated by light-induced material ablation [3] or thermoelastic effect. Moreover, if a focusing geometry is adapted, due to the acoustic gain, the achievable transient pressure can exceed 40 MPa and the negative pressure can easily lead formation of cavitation bubbles.

Here, we present a single-laser-pulse-induced ultrasound wave through thermoelastic effects. The photoacoustic nanocomposite was made of few layers graphene nanoflakes (FLG) and Polydimethylsiloxane (PDMS) polymer matrix. The excitation photon energy (1.1 eV) is absorbed by the FLG and is immediately transfer (within tens of ps), through acoustic phonon, to the polymer matrix that expands and successively contracts, giving rise to a high frequency ultrasound (Fig. 1). Despite the others method that used nano-absorbers sandwiched between two polymer layers [2], the challenge here was to embed the nanoflakes (absorber) into the PDMS (expander) and create a thin film with sufficient optical density. For the purpose, a controlled protocol was developed to obtain well dispersed FLG in the polymer matrix at different weight percentages, form 0.7 wt% to 1.1 wt%, and with different values of optical density (up to 94% light absorbed and less than 3% of scattered light) and thickness (from 4 to 22 µm). The measured ultrasound frequency was >15 MHz, with a maximum amplitude of 10 MPa in a planar geometry. The signal amplitude linearly depends on the laser fluence, and it shows an onset of saturation at higher fluence, up to 350 mJ/cm2, probably associated to the dependency of Grüneisen parameter on temperature. The maximum optoacoustic efficient conversion estimated was 1.2×10^{-3}, comparable to others carbon-based nanomaterial directly grow on a substrate. The FLG composite (freestanding) was easily embedded in an optical lens to produce high amplitude focused ultrasound and cavitation microbubbles in free field with lifetime of few tens of µs. These results bear the scope for compact, high-efficient, and inexpensive photoacoustic components for biomedical application or sonochemistry.

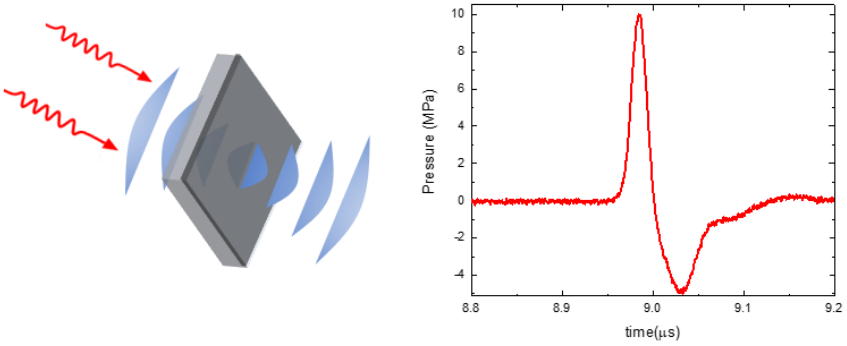

Fig. 1. Schematic illustration of the optical excitation (1064 nm) of the photoacoustic FLG composites (left panel). Ultrasound wave recorded with a hydrophone needle (right panel).

References

[1] T. Lee and L. J. Guo, Adv. Opt. Mater. 5 (2017) 1–9. https://doi.org/10.1002/adom.201600421.

[2] T. Lee, H. Won Baac, Q. Li, L. J. Guo, Adv. Opt. Mater. 6 (2018) 1–30. https://doi.org/10.1002/adom.201800491.

[3] B. T. Muc, D. Vella, N. Lukač, M. Kos, and M. Jezeršek, Results Phys. 20 (2021) 103721. https://doi.org/10.1016/j.rinp.2020.103721.

Laser-induced shock wave expanded nanobubbles in spherical geometry

Horvat D[(1)*], Agrež V[(1)], Požar T[(1)], Starman B[(1)], Halilovič M[(1)], Petkovšek R[(1)]

(1) Faculty of Mechanical Engineering, University of Ljubljana, Ljubljana, Slovenia

*Corresponding author's email: darja.horvat@fs.uni-lj.si

Background – Lasers are used routinely in many kinds of medical procedures, surgical and other, as well as for diagnostic purposes. Because of the versatility of laser methods their use is still growing. In any procedure, the optical energy absorbed in the tissue is converted to other forms - heat, chemical and mechanical energy. Following laser-induced breakdown in liquids or tissue the mechanical energy is often manifested in the rapid formation of a bubble and creation of shock waves which propagate into surrounding tissue. The evolution of the propagating wave depends on the geometry and can in special cases lead to effects that up to the present time were not researched or even understood enough and can in even be potentially harmful. Such a case could occur in eye surgery where the geometry is spherical, since the curved boundaries of the eye can focus also the generated shock waves, not just light.

In the study we investigate the propagation of laser induced shock waves in spherical geometry and the subsequent phenomenon of secondary cavitation.

Methods – Experiments were performed in distilled water in geometry exactly imitating the geometry of a human eye which is approximately a spherical object. Single shot laser pulses were tightly focused in various points inside the "eye" and the resulting phenomena, mainly the growing bubble and the propagating shock wave were recorded using schlieren technique, at several key points in time. In addition, a detailed simulation of the shock wave propagation using finite elements method (FEM), similar to the one described in [1] and [2] was performed to find the shape of the transient positive and negative pressure field of the shock wave.

Results – The experimental setup is based on a highly adaptable laser-diode-based illumination system which generates arbitrary trains of pulses having variable pulse duration and adjustable energies per pulse. The illumination system can be synchronized with an external trigger, in this case a camera. The system is designed to capture multiple snapshots of the same region at several times during a single frame. An example of a triple exposure showing the propagating shock wave at three instances (before it reaches the acoustical focal point, at the focal point and after it passes it) is shown in Fig. 1 (top row), together with the corresponding computed three pressure fields and the resulting simulated shadowgraph (second row). A single exposure shadowgraph of the same event, 5 μs later, is shown in the top row (right), with already visible secondary cavitation bubbles.

The experimental results allowed us to identify regions of secondary cavitation, that is the volume in which small bubbles occur after the passage of the negative pressure transient of the shock wave which was reflected at the curved boundary of the "eye" and thus focused.

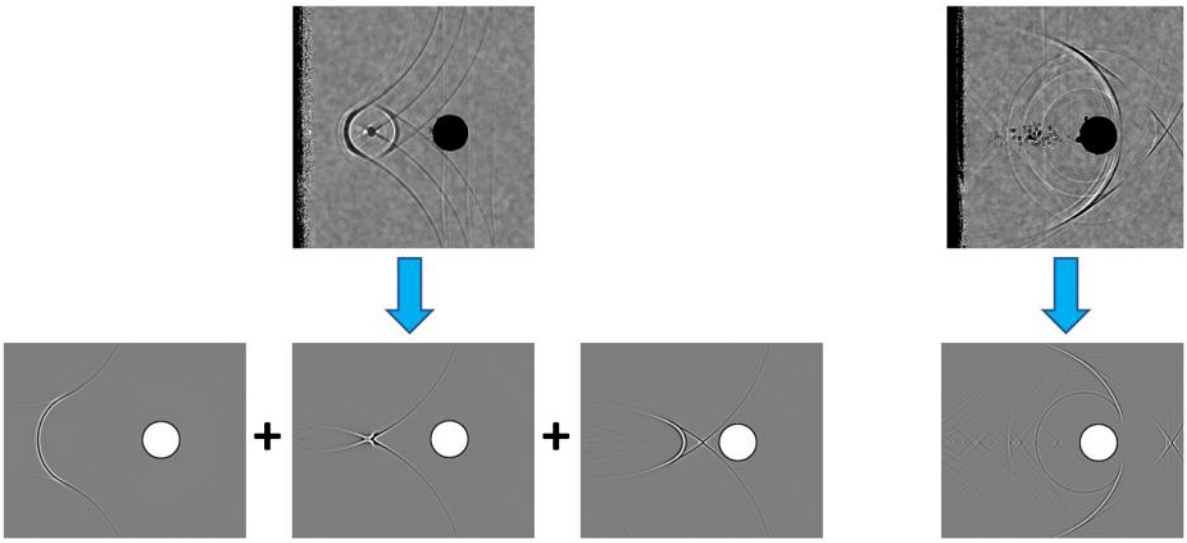

Fig. 1. Top row: A triple exposure schlieren shadowgraph of the reflected and focused shock wave approximately 10 µs after the laser induced breakdown with 0,75 µs between exposures (left) and a single exposure shadowgraph of the same event 5 µs later, at 15 µs after the breakdown. The secondary cavitation bubbles are already visible. The black circle is the bubble at the breakdown. Bottom row: numerical shadowgraph (simulation results) of the same event at approximately the same times. Here the bubble is white.

The comparison with the computation shows very good agreement and in general gives the expected results. In addition, the analysis reveals new features regarding the onset of secondary cavitation. The results namely suggest that the nanobubbles which are the prerequisite for the secondary cavitation are much more abundant in the volume which has recently been illuminated, supporting the findings of recent study by Roselló et al. [3]).

Conclusions – The secondary cavitation is initiated at the nanobubbles sites and is caused by the transient negative pressure of the propagating shock wave. The results of the study suggest that one possible mechanism for the introduction of nanobubbles into the liquid bulk is illumination. The knowledge of this effect allows one to avoid the possible unwanted consequences, while on the other hand, it can be a means to spatially and temporally control the generation of secondary bubbles in dedicated applications (drug delivery, bulk water cleaning).

References

[1] T. Požar, D. Horvat, B. Starman, M. Halilovič, R. Petkovšek, Pressure wave propagation effects in the eye after photoablation, J. Appl. Phys. 125(20) (2019) 204701. https://doi.org/10.1063/1.5094223.

[2] D. Horvat, T. Požar, B. Starman, M. Halilovič, R. Petkovšek, Pressure wave focusing effects following laser medical procedures in human eyes, Appl. Phys. A-Mat. Sci&Proc. 126(6) (2020) 414. https://doi.org/10.1007/s00339-020-03539-w.

[3] J.M. Rosselló, C.-D. Ohl, On-demand bulk nanobubble generation through pulsed laser illumination, Phys. Rev. Lett. 127(4) (2021) 044502-(1–6). https://doi.org/10.1103/PhysRevLett.127.044502.

Microscale shockwave characterization following dual threshold laser-induced breakdown

Mur J(1), Agrež V(1), Petelin J(1), Petkovšek R(1)*

(1) Faculty of Mechanical Engineering, University of Ljubljana, Aškerčeva cesta 6, SI-1000 Ljubljana, Slovenia

*rok.petkovsek@fs.uni-lj.si

Laser induced cavitation through a breakdown in liquid is extensively investigated for its important role in different technological and medical processes. The latter example is laser induced breakdown (LIB) assisted laser nano-surgery of cells and tissues for which an investigation was made on the formation of cavitation bubbles caused by the interplay of multiphoton and cascade ionization of water by the femtosecond laser [1]. It was shown that femtosecond laser pulses can produce a highly localized LIB, but according to [2], similar effect with an even lower energy conversion to mechanical effects can be achieved by using few tens of picosecond long excitation laser pulses.

In this work we have performed microscale shockwave characterization following LIB caused by the MOPA based fiber laser (pulse duration 60 ps at 515 nm wavelength) and monitored the cavitation bubble size and plasma. The detection of shockwaves and cavitation bubbles was realized by a laser diode short pulsed illumination system [3], while the pressure gradients and shockwave duration were measure by both a high performance custom-made optical hydrophone and a piezo-resistive sensor (results partially presented in Figure 1).

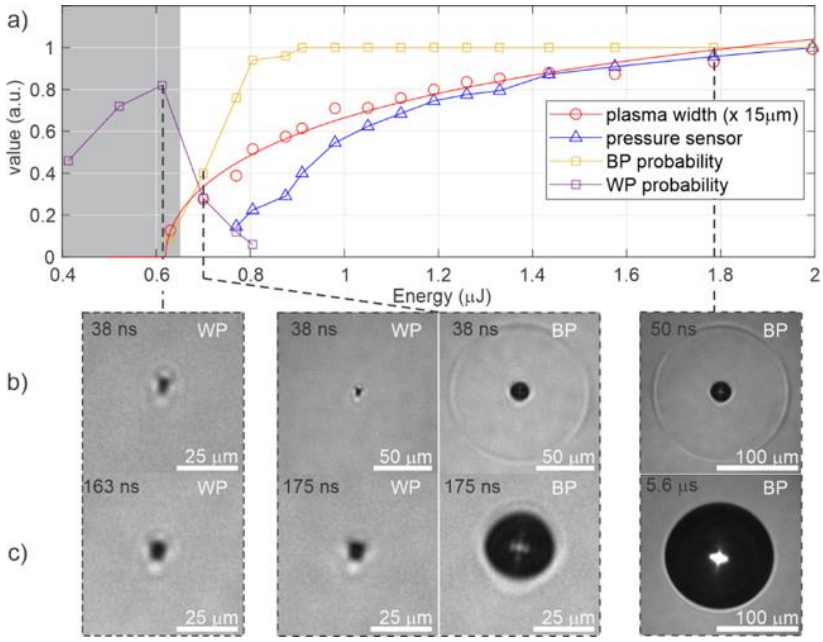

Fig. 1. Cavitation bubble generation in dependence to excitation laser energy. Plot a) shows measured plasma width, pressure sensor measurements and event probabilities for the bright plasma (BP) and weak plasma (WP) events. The row of images noted with b) show bubble with and without optically resolved shockwave formation right after the LIB while the c) row show images of the bubble nearing its maximum radius. At 0.7 µJ both event types can be detected. The black time values are the time stamps of the illumination pulse after LIB.

At excitation pulse duration of 60 ps, a weak overlap in time between the free electron population and the laser pulse can be expected [4], limiting the cascade ionization and heating up of the focal volume. Two types of events were observed when varying the excitation energy, either a few microns diameter cavitation bubble formation was observed above a certain minimal energy density threshold (WP event), or an approximately ten times larger bubble above a second energy density threshold (BP event). Fifty events at the same energy were captured at the 1s interval between laser shots, with the experiments repeated for each type of event at varied energies. The two event groups had a difference in the transferred laser energy to mechanical effects on the order of a few hundred times at minimal change in laser energy, placing the energy either above or below the second threshold. A sharp drop in the shockwave pressure was measured between the high energy and low energy bubbles. This can have a beneficial result in the reduced mechanical stress on the water-based media, such as tissues.

To confirm the cavitation events leading to low energy bubble formation, fifty shots were imaged at varied delay of the illumination system capturing the bubble growth dynamics and extracting both the maximum bubble radius and bubble lifetimes. From this a probability graph for the corresponding event type is shown in Figure 2.

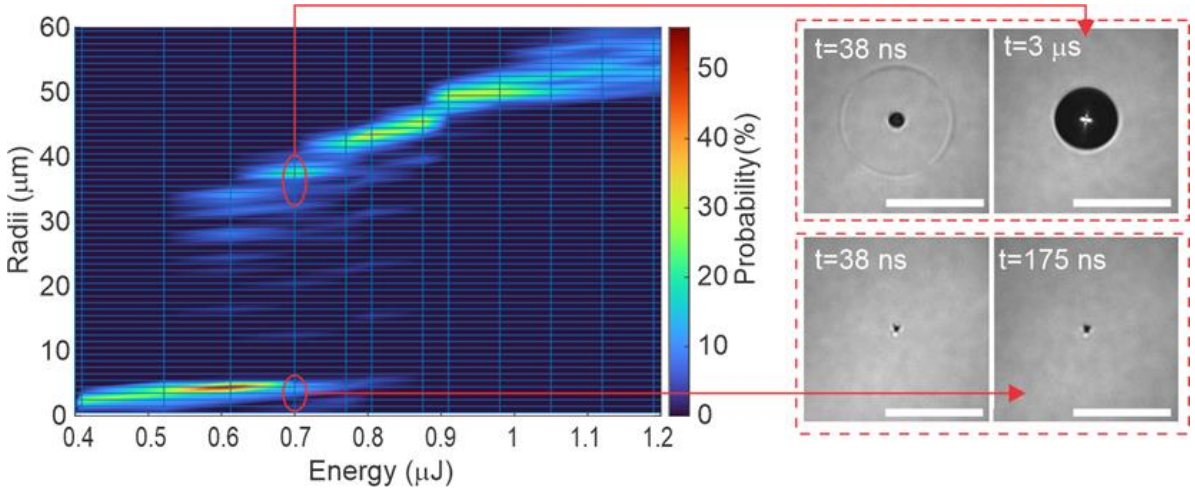

Fig. 2. *Probability graph of produced cavitation bubble maximum radius vs excitation laser energy. Two groups of events were identified with notable difference in deposited excitation laser energy seen in cavitation bubble size difference and lifetime. The white scale bar equals 100 μm.*

References

[1] A. Vogel, J. Noack, G. Hüttman, G. Paltauf, Mechanisms of femtosecond laser nanosurgery of cells and tissue, Appl. Phys. B 81 (2005) 1015–1047. https://doi.org/10.1007/s00340-005-2036-6.

[2] J. Noack, D.X. Hammer, G.D. Noojin, B.A. Rockwell, A. Vogel, Influence of pulse duration on mechanical effects after laser-induced breakdown in water, J. App. Phys. 83 (1998) 7488–7495. https://doi.org/10.1063/1.367512.

[3] V. Agrež, T. Požar, R. Petkovšek, High-speed photography of shock waves with an adaptive illumination, Opt. Lett. 45 (2020) 1547–1550. https://doi.org/10.1364/OL.388444.

[4] C.B. Schaffer, N.Nishimura, E.N. Glezer, A.M.-T. Kim, E. Mazur, Dynamics of femtosecond laser-induced breakdown in water from femtoseconds to microsecond', Opt. Express 10 (2002) 196. https://doi.org/10.1364/OE.10.000196.

Ultrafast measurement of laser induced shockwaves

Petelin J(1), Lokar Ž(1)*, Horvat D(1), Petkovšek R(1)

(1) Faculty of Mechanical Engineering, University of Ljubljana, Ljubljana, Slovenia.

*corresponding author's email: ziga.lokar@fs.uni-lj.si

Background – During laser induced breakdown, shock waves are generated. The rise time of shock waves in solids and glycerol was studied before, however, their time resolution was insufficient for measurements in water [1].

Our single mode fiber optic hydrophone is uniquely suitable for such fast measurements. The measurements were performed in distilled water (~0.7 cst, R > 1 MΩ) as well as in oil (5 and 50 cst, Sigma Aldrich). In addition, shockwave rise time dependence on the distance from the centre of the laser induced breakdown for extremely small distances was measured.

Methods – Single pulses of a 60 ps, 1030 nm laser, having energies from 1.5 µJ to 7.5 µJ were used to initiate breakdown in experiments. The breakdown threshold (50% probability of breakdown) is 1.1 µJ.

A custom made fiber optic probe hydrophone (FOPH) was used to measure the shock wave pressure. Single mode fiber with 5 µm core and 125 µm cladding was used. The very small dimension of the sensing area (5 µm) results in a very fast and spatially almost point-like detection as described in [2]. The shockwave pressure changes the refractive index of water or oil, which in turn changes the optical reflectance at the fiber tip – the measured quantity. For both water and oil the reflectance decreases with pressure.

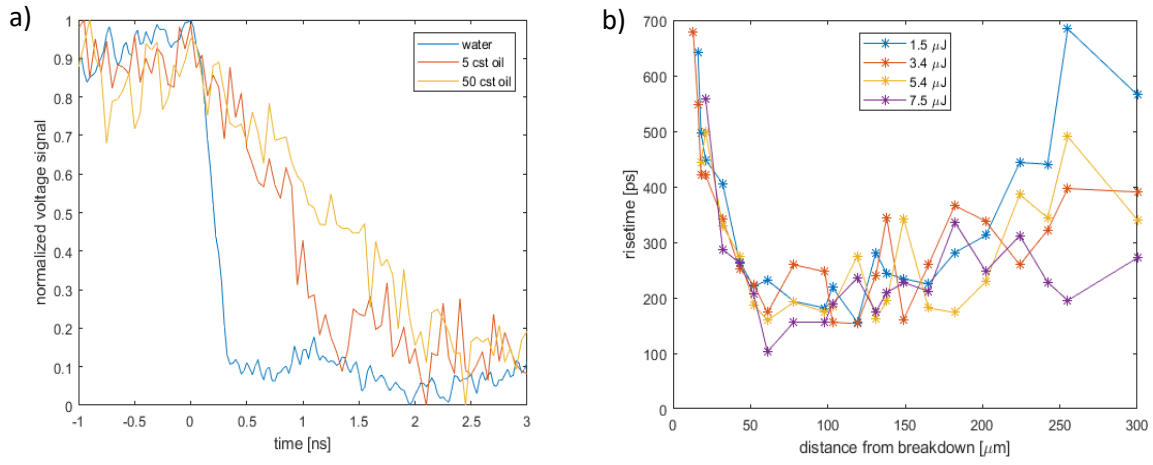

Figure 4: a) Shock wave traces in water and oil. The arrival of the wave is at t=0. The 20-80% shockwave pressure rise times in water, 5 cst and 50 cst oil are measured to be 180 ps, 500 ps and 1100 ps, respectively; and approximately twice as much for 0-100% pressure change. **b)** Shock wave rise time measured in water at very small distances form the source for various laser pulse energies. Shortest rise times of approximately 150 ps are observed for distances from 60-100 µm.

Results – The laser induced breakdown at 3.4 µJ pulse energy produces a shock wave, which is measured at a distance of approximately 80 µm from the breakdown for all three liquids (Fig. 1 a). The shock wave in water is measured to have a rise time of 180 ps between 20% and 80% of the pressure

(equivalently – change between 80% and 20% of the voltage). This short rise time is significantly sharper compared to rise times in 5 cst and 50 cst oils (500 ps and 1100 ps, respectively). This observation is in agreement with theoretical predictions [3] and with previous studies in glycerol and solids that also showed smaller rise time for lower viscosity materials. Shock wave rise time trends are significantly slower than linear, with a factor of 6 change in rise time corresponding to the factor of 70 change in viscosity.

In addition, we analyse the rise time variation with the breakdown distance and breakdown energy in water. There are two observable trends – the rapid rise time decrease with distance in the first 50 µm from the breakdown, and the gradual rise time increase with increasing distance beyond approximately 150 µm. We believe that the main reason for the first trend is the fact that at such small distances, the shock wave is not yet fully developed [4] and the fact that at such small distances the contributions from different parts of the laser induced plasma arrive at the sensor at measurably different times. At distances of approximately 100 µm, the shock wave is already developed – all the partial contributions coalesce together to a single shock wave. Finally, at large distances, both the attenuation of shock waves due to propagation, as well as the decreasing pressure with distance, influence the resulting rise time. The comparison of these two reasons is difficult due to noise, however, it seems that the high frequency attenuation contributes to the rise time increase slightly more than the pressure decrease due to spherical spreading of the wave.

Conclusions – We have measured and analysed the rise times of the laser induced shock wave of lower viscosity fluids. The results suggest a similar trend as reported for solids and highly viscous glycerol. The extremely fast and small area measurements of the rise time very close to the source will provide the necessary data for the study and understanding of the shock wave formation and propagation in fluids.

References

[1] G.I. Kanel, A.S. Savinykh, G.V. Garkushin, A.V. Pavlenko, S.V. Razorenov, Shock Wave Rise Time and the Viscosity of Liquids and Solids, in Mechanics for Materials and Technologies, vol. 46, H. Altenbach, R. V. Goldstein, and E. Murashkin, Eds. Cham: Springer International Publishing (2017) pp. 257–263. doi: 10.1007/978-3-319-56050-2_13.

[2] J. Petelin, Z. Lokar, D. Horvat, R. Petkovsek, Localized Measurement of a Sub-Nanosecond Shockwave Pressure Rise Time, IEEE Trans. Ultrason., Ferroelect., Freq. Contr., 69:1 (2022) 369–376. doi: 10.1109/TUFFC.2021.3115629.

[3] I.B. Zel′dovich, I.P. Raĭzer, Physics of shock waves and high-temperature hydrodynamic phenomena. Mineola, N.Y: Dover Publications (2002).

[4] M. Vassholz et al., “Pump-probe X-ray holographic imaging of laser-induced cavitation bubbles with femtosecond FEL pulses,” Nat Commun, vol. 12:1 (2021) pp. 3468 doi: 10.1038/s41467-021-23664-1.

05/09
Infrared Thermography & Non-destructive Evaluation

SPECIAL PLENARY SESSION

Modalities of photothermal coherence tomography for enhanced three-dimensional imaging contrast, resolution and quantitative depth profilometry

Mandelis A[(1,2)*], Tavakolian P[(1,2)], Sivagurunathan K[(1,2)], A. Risheh[(1,2)]

(1) Center for Advanced Diffusion-Wave and Photoacoustic Technologies (CADIPT), Department of Mechanical and Industrial Engineering, University of Toronto, Toronto, Ontario M5S 3G8, Canada
(2) Institute for Advanced Non-Destructive and Non-Invasive Diagnostic Technologies (IANDIT), University of Toronto, Ontario M5S 3G8, Canada

*Corresponding author's email: mandelis@mie.utoronto.ca

Introduction – Photothermal coherence tomography (PCT) enables thermal waves to exhibit *energy localization* akin to non-diffusive waves like ultrasound, despite their diffusive nature. It uses laser-pulse-induced thermal excitation and performs pulse compression and matched filtering, two encoded waveform processes inspired by radar science. In the enhanced truncated correlation (eTC-PCT) modality of PCT, time-windowed thermal diffusion transient signals are cross-correlated with the delay-shifted reference signal and used to reconstruct slice-by-slice depth distribution of optical and thermal sources in opaque and multi-absorber solids.

I. Spatially filtered PCT for enhanced spatial resolution imaging – A unique spatial gradient-window adaptive thermophysical filter was introduced [1] in a scanned mode along the *(x,y)* coordinates of camera images from various sub-surface depths, revealing absorber true spatial extent from diffusive photothermal images and restoring pre-diffusion lateral image resolution beyond the Rayleigh criterion limit in diffusion-wave imaging science. An example is shown in Fig. 1.

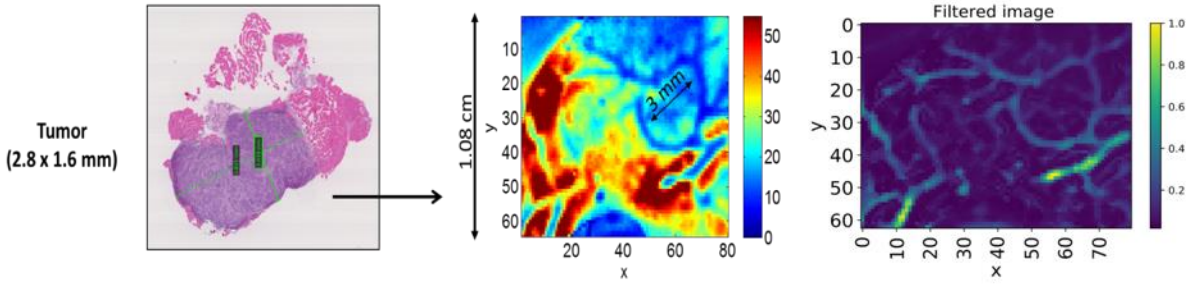

Fig. 1: (a) Immunohistochemistry stain of tumor cells surrounded by normal muscle cells in a mouse thigh. **(b)** eTC-PCT phase image shows the tumor with size of 2.8 mm and the vascular network around the tumor in dark blue. **(c)** Filtered image of combined eTC-PCT amplitude and phase reveals the presence of smaller vessels.

II. Image segmentation using K-means clustering for enhanced feature boundary imaging – K-means is an iterative algorithm that aims to partition a dataset into K pre-defined distinct non-overlapping subgroups (clusters) where each data point (datum) belongs to only one group. In PCT non-destructive imaging, K is initialized by selecting 3 distinct areas: 1) The area of the defect or the inhomogeneity; 2) the area with higher thermal-wave accumulation due to encompassing a defect or an

inhomogeneity; and 3) a remote (reference) area away from the defect. The next step after preparing a *Segmented Image (SI)* is to detect edges and delineate the boundary/ies of the defect or inhomogeneity. Furthermore, the Canny edge detection algorithm is one of the most strictly well-defined methods that provides good and reliable detection of subsurface region-of-interest (ROI) edges [2]. Fig. 2 shows the effects of applying these algorithms to PCT imaging, resulting in sharp boundary delineation of defect boundaries.

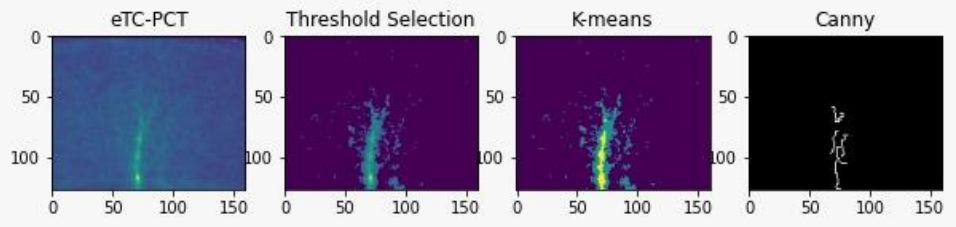

Fig. 2: eTC-PCT images of a surface-terminating crack in a steel sample. The raw eTC-PCT images of the crack are presented before processing and after threshold selection (step 1), K-means clustering (step 2); and the final canny edge detection (step 3). The result is a crack image reconstruction with sharply delineated boundaries.

III. Multispectral Pulsed PCT for enhanced contrast and quantitative depth profilometry imaging – To obtain molecular specificity in biological samples we introduced multispectral (MS) PCT that employs a Nd:YAG pulsed laser which pumps an optical parametric oscillator (OPO) for wavelength tunability, Fig. 3 [3]. As a first application, the quantitative detection of early stage caries in photothermal images of teeth using MS eTC-PCT is reported.

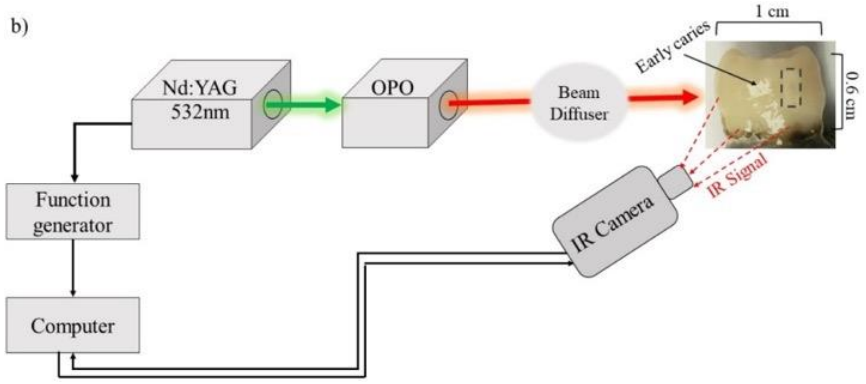

Fig. 3. Experimental configuration of multispectral eTC-PCT system and photograph of a tooth sample with early caries.

An extracted healthy tooth was used in this study, as can be seen in Fig. 3. To closely mimic the natural formation of dental caries, a treatment protocol using highly cariogenic bacteria was used to produce a carious lesion. The bacterial-induced caries was limited to a rectangular section on the smooth surface of the tooth for a total exposure time of 8 days to induce early caries. As a result, the overall appearance of the extracted tooth in visible light remained unchanged. These data were either directly used for 3D reconstruction through ImageJ software [4] or imported into MATLAB 2021a for data analysis (e.g. normalization and SNR calculation) of the images obtained from the TC-PCT amplitude and phase channels.

Fig. 4 shows the MS eTC-PCT amplitude reconstructions of the investigated tooth at 0.5 Hz single repetition frequency and at OPO wavelengths 532 nm, 675 nm, 700 nm, 750 nm, 808 nm, 850 nm, and 900 nm. The location and extent of the lesion in the tooth is seen in the top cross-sectional views, with

the 0.5-Hz repetition frequency at 675-700 nm offering the optimal visualization of the subsurface extent of the caries. Aside from the bacterial-induced caries, one can see another carious region highlighted by the red arrow that is only captured by the 532-nm wavelength. We concluded that this carious region is positioned very close to the surface that only one highly scattered wavelength, i.e. 532 nm, is able to capture this feature. Micro-computed tomography (μCT) analysis of the deep lesion showed it is indeed a deeper lesion compared to other defects on the tooth with an approximate depth of 400 μm, in agreement with the depth profile reconstructed from the 675 nm and 700 nm images.

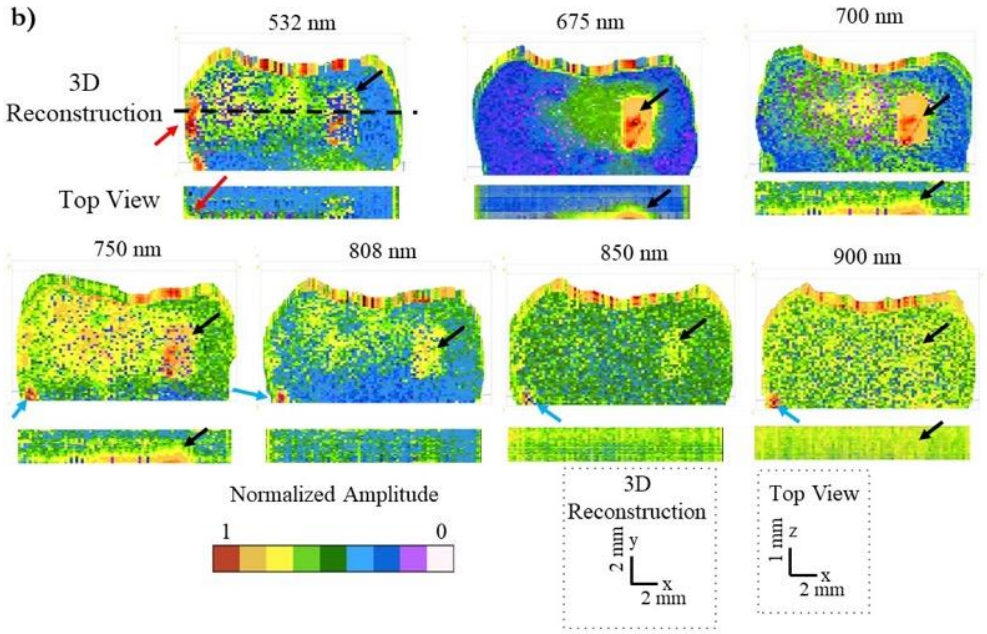

Fig. 4. 3D eTC-PCT amplitude reconstruction of a carious lesion in a tooth sample taken at 0.5 Hz and pulsed Nd:YAG laser OPO wavelengths 532 nm, 675 nm, 700 nm, 750 nm, 808 nm, 850 nm, and 900 nm. Below each 3D reconstruction, the top view of the cross-section of the reconstructed 3D model is shown, cut along the dashed black line, as marked in the 532-nm 3D reconstruction. The extent of the lesion inside the tooth is seen in the top view of the cross-section. Note that the x- and z-axis scales are different in the 3D reconstruction and the top view for better visualization. The bacterial-induced caries is shown by a black arrow in each reconstruction. Red and blue arrows identify a shallow and a deep natural lesion on the tooth, respectively.

Conclusions – This talk reports on the implementation of three PCT imaging modalities and explores their impact in spatial resolution, feature/defect boundary delineation, contrast and quantitative depth profilometry in photothermal/theorphotonic applications ranging from soft and hard tissue imaging to non-destructive testing of manufactured materials with defects.

References

[1] P. Tavakolian, K. Sivagurunathan, A. Mandelis, Enhanced truncated-correlation photothermal coherence tomography with application to deep subsurface defect imaging and 3-dimensional reconstructions, J. Appl. Phys., 122:2 (2017) 023103.

[2] A. Risheh, P. Tavakolian, A. Melinkov, A. Mandelis, Infrared computer vision in non-destructive imaging: Sharp delineation of subsurface defect boundaries in enhanced truncated correlation photothermal coherence tomography images using K-means clustering, NDT&E Int. 125 (2022) 102568.

[3] E. Baradaran Shokouhi, R. Welch, K. Sivagurunathan, A. Mandelis, Multispectral truncated-correlation photothermal coherence tomography imaging modality for detection of early stage dental caries, Biomed. Opt. Express, 13:5 (2022) 2772-2781.

[4] "ImageJ," https://imagej.nih.gov/ij/

KEYNOTE SPEAKER

Imaging thermal properties by super resolution far-infrared thermography

Bouzin M(1)*, Marini M(1), D'Alfonso L(1), Sironi L(1), Granucci F(2), Mingozzi F(2), Gorini G(1), Di Martino D(1), Chirico G(1), Collini M(1)

(1) Physics Department, Università degli Studi di Milano-Bicocca, Milan, Italy
(2) Biotechnology and Biosciences Department, Università degli Studi di Milano-Bicocca, Milan

*Corresponding author's email: margaux.bouzin@unimib.it

Non-contact thermal imaging quantifies temperature by detecting the sample surface radiance in the mid- to far- infrared spectral band via Stefan-Boltzmann's law and the grey-body approximation. It offers the main advantage of non-invasive absolute temperature measurements over wide (>cm^2-sized) sample areas. However, the spatial resolution of thermographic sequences is intrinsically limited by the combined effect of light diffraction at the thermal-camera collecting lens (i.e., Abbe's law) and of heat diffusion across the sample: the spatial resolution of low-cost commercially available microbolometer cameras is typically limited to the mm- range, thereby hampering the routine exploitation of conventional far-infrared thermography for microscale imaging applications. Furthermore, temperature maps are not easily converted into quantitative images of any sample thermal property (e.g., the thermal conductivity), which would be beneficial instead for a variety of applications ranging from the characterization of cultural heritage artifacts to the development of heat transfer models for biological soft materials for disease diagnosis and hyperthermia-based therapeutics.

We tackle here both these limitations by combining the implementation of a super-resolution far-infrared image acquisition scheme [1] with quantitative data analysis protocols aimed at the space-resolved extraction of the sample thermal properties [2,3].

Our strategy takes advantage of the photo-thermal effect primed by the sample absorption of modulated and raster-scanned visible laser light. A sequence of sparse temperature variations is laser-primed on the sample and, by the automated non-linear surface fit of the images acquired by a thermal camera, the location of light-absorbing and heat-releasing species is retrieved with an uncertainty that is only assigned by the signal-to-noise ratio of the detected temperature increments and by the tunable excitation laser spot size. By the centroid coordinates of all the localized temperature peaks, a super-resolution image of the sample can be reconstructed at sub-diffraction ~10-50 μm resolution on a typical far-infrared camera with ~300-μm diffraction-limited resolution and ~400-μm pixel size on the sample plane [1].

The amplitude and temporal kinetics of laser-primed temperature variations are exploited instead to extract information on the sample thermal properties. To this aim, we rely on the analytical/numerical solution of the three-dimensional heat equation in the presence of focused laser-light illumination, and by properly modelling camera-based temperature detection via Stefan-Boltzmann's law, we provide the theoretical framework to model experimentally detected temperature increments as a function of both instrumental parameters and the sample thermal properties. We outline therefore the data analysis protocols to recover, on both thermally thin and thermally thick solid-state samples, either the concentration of laser-excited photo-thermal probes or the sample thermal conductivity over the broad 0.1-100 W/mK range.

We finally provide experimental validation of our results and report two exemplary applications demonstrating the feasibility of the proposed approach. On the one hand, we focus on cultural heritage conservation, and we characterize the deterioration state of eighteenth-century tin organ pipe fragments by spatially mapping the product of the sample thickness and thermal conductivity. Such a parameter, which is related here to sample oxidation, is pointed out as a relevant indicator for the non-destructive characterization of the sample conservation state [2]. On the other hand, we demonstrate quantitative far-infrared super-resolution thermography on biological tissues, and provide the space-resolved quantification of the molar concentration of melanin pigments in excised murine melanoma biopsies at 40-µm spatial resolution [3]. By coupling temperature maps with the extraction of thermal properties at high spatial resolution, our results significantly expand the capability of state-of-the-art infrared imaging technology in capturing the structural heterogeneity of the imaged tissue in a label free configuration, and suggest potential impact in complementing standard histopathological analyses of pigmented skin lesions ex-vivo.

References

[1] M. Bouzin et al., Photo-activated raster-scanning thermal imaging at sub-diffraction resolution, Nat. Commun. 10 (2019) 1–9. https://doi.org/10.1038/s41467-019-13447-0.

[2] M. Marini et al., A novel method for spatially-resolved thermal conductivity measurement by super-resolution photo-activated infrared imaging, Mater. Today Phys. 18 (2021) 100375. https://doi.org/10.1016/j.mtphys.2021.100375.

[2] M. Bouzin et al., Melanin concentration maps by label-free super-resolution photo-thermal imaging on melanoma biopsies, Biomed. Opt. Expr. 13:3 (2022). https://doi.org/10.1364/BOE.445945.

KEYNOTE SPEAKER

Non-destructive evaluation of materials in motion using laser-spot thermography

Mendioroz A[(1)*], Rodriguez-Aseguinolaza J[(1)], Salazar A[(1)]

(1) Departamento de Física Aplicada, Escuela de Ingeniería de Bilbao, Universidad del País Vasco UPV/EHU, Plaza Ingeniero Torres Quevedo 1, 48013 Bilbao, Spain

*Corresponding author's email: arantza.mendioroz@ehu.eus

We present recent advances in monitoring materials in motion using laser-spot infrared thermography aimed at the non-destructive evaluation of industrial parts in production chains. First, we focus on anisotropic materials moving in an arbitrary direction with respect to the principal directions in the sample surface. We present analytical expressions for the surface temperature showing that any radial profile features a linear behaviour with the distance to the laser spot. The principal thermal directions and diffusivities in the sample surface are determined by fitting the slopes of the linear profiles as a function of their orientation. This finding has straightforward applications in monitoring thermal anisotropies in moving parts. Second, the technique is applied to the characterization of planar cracks in materials that move at constant speed. We show that the surface temperature of a material containing an ideal infinite vertical crack can be written semi-analytically and the effective crack width can be determined by fitting the theoretical expression to experimental data. For other crack configurations, numerical methods are necessary to calculate the surface temperature. We present a numerical approach to calculate the temperature field when the sample and the laser are in relative motion, together with some applications.

I – Principal thermal directions and diffusivities of moving samples

Laser-spot infrared thermography (IRT) is a well-known technique to measure the in-plane thermal diffusivity of solids at rest. Recently, it has been applied to determine the thermal diffusivity of materials moving at constant speed [1] with some limitations, such as the use of scarce information of the thermogram, which limits the accuracy of the results, and the necessity of having anisotropic samples moving in one of the principal directions. Here we present a general approach to characterize the thermal diffusivity of isotropic and anisotropic materials that makes use of the whole thermogram and allows determining the orientation of the in-plane principal directions and the principal diffusivities of anisotropic samples moving in an arbitrary direction.

Let us consider an anisotropic sample whose principal directions x and y, with diffusivities D_x and D_y, respectively, are parallel to the sample surface. The sample moves at constant speed v along a direction that makes an angle α with principal direction x. A tightly focused continuous wave (CW) laser spot is illuminating the sample at the origin of coordinates. The geometry is depicted in Fig.1a. After reaching the steady state, the temperature at the surface in polar coordinates writes:

$$T(r,\varphi) = \frac{A}{r} e^{m_{\varphi,\alpha} r} \qquad \text{Eqn. 1}$$

where A is a constant. Eqn. 1 shows that the natural logarithm of any radial temperature profile multiplied by the distance to the laser spot r is a straight line. The slope $m_{\varphi,\alpha}$, which is a function of the

in-plane principal diffusivities D_x and D_y, and the (unknown) angles that the principal x direction makes with the particular profile φ and with the direction of motion α, writes:

$$m_{\varphi,\alpha} = -\frac{v}{2}\left[\frac{\cos\varphi\cos\alpha}{D_x} + \frac{\sin\varphi\sin\alpha}{D_y} + \sqrt{\left(\frac{\sin^2\alpha}{D_y} + \frac{\cos^2\alpha}{D_x}\right)\left(\frac{\sin^2\varphi}{D_y} + \frac{\cos^2\varphi}{D_x}\right)}\right], \quad \varphi = \beta + \alpha \qquad \text{Eqn.2}$$

The fitting of these slopes as a function of the angle β between each profile and the direction of motion (which is the angle that can be controlled) allows obtaining the principal diffusivities D_x and D_y and the orientation of the principal x-axis, α.

In Fig. 1b we show a thermogram taken on a carbon fiber reinforced composite (CFRC) sample moving at v = 5.55 mm/s, with unidirectional fibers making an angle of 60º with the direction of motion. The spatial resolution of the thermal image is 30 μm. Unlike the case of static samples, the orientation of the principal axes is not obvious from the thermogram. Several experimental ln ($T \cdot r$) profiles are depicted in Fig. 1c for different values of β. In Fig 1d we show the slopes of the linear fits of the data in Fig. 1c as a function of β, together with the fitting to Eqn. 2.

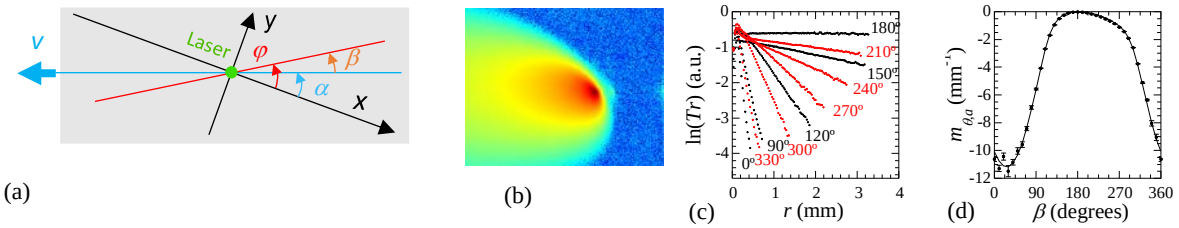

Fig. 1. (a) Geometry of the problem. **(b)** Experimental thermogram on a unidirectional CFRC sample moving at v = 5.55 mm/s along a direction that makes an angle of 60º with the fibers. **(c)** Experimental radial ln ($T \cdot r$) profiles of the thermogram in Fig. 1b for several angles β. **(d)** Values of the slopes of the profiles in Fig.1c (symbols) and fitting to Eqn. 2 (solid line).

The diffusivities in the directions parallel and perpendicular to the fibers are retrieved with an accuracy of about 10%. The estimated angle values are remarkably precise, featuring an accuracy of about 1º. This reliability in the evaluation of angles opens the possibility of using laser-spot thermography for monitoring thermal anisotropies in moving parts such as the non-destructive assessment of fiber orientation in the production of CFRC.

II – Crack characterization in isotropic materials in motion

Laser spot thermography can also be applied to characterize cracks in samples in motion. In these experiments, a crack of width w behaves as a thermal barrier whose thermal resistance per unit area is $R_{th}=w/K_{air}$, (K, thermal conductivity). In the ideal case of "infinitely deep" vertical cracks, the surface temperature of the moving cracked sample illuminated with a CW laser spot can be modelled semi-analytically. A fast characterization of the effective width of the crack can be carried out by fitting the model to experimental temperature data at different positions of the sample [2]. However, out of these ideal conditions, the surface temperature of the cracked material has to be calculated numerically.

In this work we present recent advances based on finite elements methods (FEM) that allow calculating numerically the temperature of an isotropic sample illuminated by a CW laser spot when relative velocity is $\vec{v}$. The problem consists in solving the heat diffusion equation:

$$\frac{\partial T(\vec{r},t)}{\partial t} = D\nabla^2 T(\vec{r},t) \qquad \text{Eqn.3}$$

with boundary condition:

$$K\nabla T(\vec{r},t)\cdot\vec{n} = \frac{2P_0}{\pi a^2} e^{\frac{-2(\vec{r}-\vec{v}t)^2}{a^2}} \Big|_I - \gamma(T(\vec{r},t)-T_{amb})\Big|_{n-I} \qquad \text{Eqn. 4}$$

where $\vec{n}$ is the unit vector normal to the surface, $|_I$ and $|_{n-I}$ stand for the illuminated and non-illuminated surfaces, P_0 and a are the laser power and radius, γ is the coefficient of heat losses and T_{amb} is room temperature. A planar crack is introduced in the numerical domain as a thermal resistance R_{th}, described by boundary conditions of heat flux continuity and temperature jump over the crack:

$$\left[\left[K\nabla T(\vec{r},t)\right]\right]\Big|_{crack} = 0 \qquad \Delta T(\vec{r},t)\Big|_{crack} = R_{th} K\nabla T(\vec{r},t)\Big|_{crack} \qquad \text{Eqn. 5}$$

In order to calculate the temperature field with accuracy but keeping a reasonable computational cost, a dynamic FEM spatial discretization refinement has been applied. Fig. 2 shows a simulation for a stainless steel sample ($D = 3.8 \cdot 10^{-6}$ m^2/s, $K = 15$ Wm^{-1}K^{-1}) moving at 5 cm/s, containing a planar vertical crack 20 μm wide that penetrates 1 mm into the material. We present the validation of the numerical method in different cases.

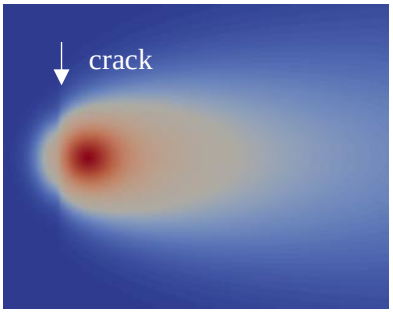

Fig. 2. FEM simulation of a stainless steel cracked sample moving at 5 cm/s. Crack width 20 μm and depth 1 mm.

These methods open the possibility of modelling a wide variety of practical situations and promise a high potential of laser-spot IRT for the quantitative assessment of materials condition in production chains and for the development of flying-spot thermography.

Acknowledgments – This work has been supported by Ministerio de Ciencia e Innovación (Grant PID2019-104347RB-I00 funded by MCIN/AEI/10.13039/501100011033) and by Universidad del País Vasco UPV/EHU (GIU19/058).

References

[1] A. Bedoya, J. González, J. Rodríguez-Aseguinolaza, A. Mendioroz, A Sommier, J.C. Batsale, C. Pradere, A. Salazar, Measurement of in-plane thermal diffusivity of solids moving at constant speed using laser spot infrared thermography, Measurement. 134 (2019) 519–526. https://doi.org/10.1016/j.measurement.2018.11.013.

[2] J. González, A. Mendioroz, A. Sommier, J.C. Batsale, C. Pradere, A. Salazar, Fast sizing of the width of infinite vertical cracks using constant velocity, NDT&E Int. 103 (2019) 166-172. https://doi.org/10.1016/j.ndteint.2019.03.003.

KEYNOTE SPEAKER

Detectability of noisy signals for photothermal and photoacoustic reconstruction

Burgholzer P(1)*, Mayr G(2), Thummerer G(2), Haltmeier M(3)

(1) RECENDT, Research Center for Non-Destructive Testing, Linz, Austria
(2) Josef Ressel Centre for Thermal NDE of Composites, University of Applied Sciences Upper Austria, Wels, Austria
(3) Department of Mathematics, University of Innsbruck, Innsbruck, Austria

*Corresponding author's email: peter.burgholzer@recendt.at

Background – in this work, we combine the different scientific fields of information theory, thermodynamics, regularization theory and non-destructive imaging, especially for photoacoustic and photothermal imaging [1]. The goal is to get a better understanding of how information gaining for subsurface imaging works and how the spatial resolution limit can be overcome by using additional information. Here, the resolution limit in photoacoustic and photothermal imaging is derived from the irreversibility of attenuation of the pressure wave and of heat diffusion during propagation of the signals from the imaged subsurface structures to the sample surface, respectively. The acoustic or temperature signals are converted into so-called virtual waves, which are their reversible counterparts and which can be used for image reconstruction by well-known ultrasound reconstruction methods. The conversion into virtual waves is an ill-posed inverse problem which needs regularization. The reason for that is the information loss during signal propagation to the sample surface, which turns out to be equal to the entropy production. As the entropy production from acoustic attenuation is usually small compared to the entropy production from heat diffusion, the spatial resolution in acoustic imaging is higher than in thermal imaging. Therefore, it is especially challenging to overcome this resolution limit for thermographic imaging. Incorporating additional information such as sparsity and non-negativity in iterative regularization methods gives a significant resolution enhancement, which is experimentally demonstrated by one-dimensional imaging of thin layers with varying depth or by three-dimensional imaging, either from a single detection plane or from three perpendicular detection planes on the surface of a sample cube (Fig. 1).

The virtual wave concept – the formal relationship between temperature field $T(\mathbf{r}, t)$ and virtual wave field $T_{\text{virt}}(\mathbf{r}, t')$, for the same position vector $\mathbf{r}$ but different time scales t and t', is given by a Fredholm integral of the first kind:

$$T(\mathbf{r}, t) = \int_{-\infty}^{\infty} K(t, t')\, T_{\text{virt}}(\mathbf{r}, t')\, \mathrm{d}t' \quad \text{with} \quad K(t, t') = \frac{c}{\sqrt{\pi \alpha t}} e^{-\frac{c^2 (t')^2}{4 \alpha t}} \quad \text{for} \quad t > 0. \qquad \text{Eqn. 1}$$

The thermal diffusivity α and the virtual speed of sound c are the characteristic parameters for heat and virtual wave propagation. While $T(\mathbf{r}, t)$ obeys the heat equation, $T_{\text{virt}}(\mathbf{r}, t')$ fulfils the photoacoustic wave equation. The above equation is valid for a Dirac-Delta-like heating in time domain, for other temporal heating functions the solution is the convolution in time with this function. The kernel $K(t, t')$ works as transition function and contains the characteristic parameters α and c. It is important to note that $K(t, t')$ is independent of the position vector $\mathbf{r}$.

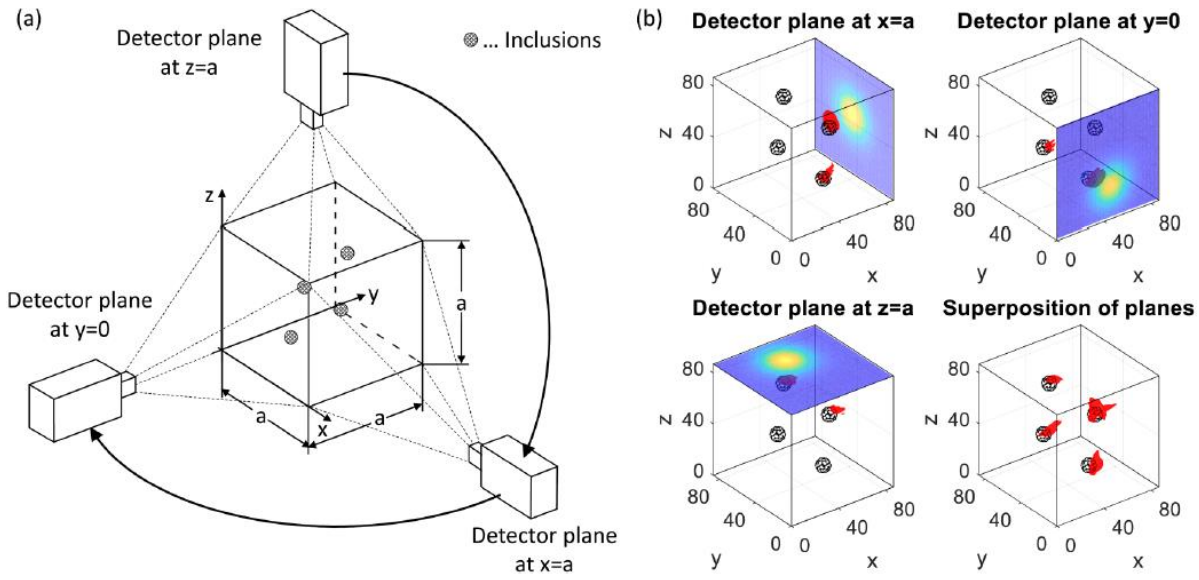

Fig. 1. (a) Experimental setup and detection planes of the thermographic measurements and **(b)** the isosurface illustration of the reconstructed internal heat sources obtained with reconstruction using sparsity and positivity for three different detector planes and a superposition of the single detector plane reconstructions [1]. The steel spheres had depths of 4.3 mm, 7.5 mm and 10.7 mm from the detection planes.

That means, when considering surface temperature data, that is acquired by an IR-camera, we have a pixel-wise transformation. Since thermography data is discrete in time and space, we have to discretize the above relationship between $T(\mathbf{r},t)$ and $T_{\mathrm{virt}}(\mathbf{r},t')$:

$$\mathbf{T} = \mathbf{K}\mathbf{T}_{\mathrm{virt}} \qquad \text{Eqn. 2}$$

The matrix **K** has rapidly decaying singular values, hence calculating $\mathbf{T}_{\mathrm{virt}}$ based on **T** is a severely ill-posed inverse problem. Due to this, we need regularization. In principle, we can employ direct or iterative regularization methods. By using the truncated singular value decomposition (T-SVD) or Tikhonov regularization the pseudo-inverse or Moore-Penrose $\mathbf{K}^{\dagger}$is approximated.

In Figure 2, the process steps of the virtual wave concept based on simulated data are depicted. Here we consider an experiment, where a laser pulse heats a 2D sample to be imaged. Because of the transparency of the bulk material in the wavelength of the laser only the inclusions are heated. Consequently, they act as internal heat sources and we have a certain initial temperature distribution $T_0(\mathbf{r})$. The heat diffuses to the surface, where the spatial and temporal surface temperature signal $T(\mathbf{r},t)$ is recorded. Then, as mentioned before, we have to solve a severely ill-posed inverse problem. In this case, for the computation of the virtual wave field $T_{\mathrm{virt}}(\mathbf{r},t)$, we have employed ADMM, which is an efficient iterative algorithm for constrained optimization. We have incorporated positivity and sparsity as prior information. Sparsity is respected because we assume that we only have a few point scatterers in the sample under test and hence a sparse virtual wave field. As one can see the computed virtual wave field $T_{\mathrm{virt}}(\mathbf{r},t)$ meets the ideal virtual wave field $T_{\mathrm{virt}}^{\mathrm{ideal}}(\mathbf{r},t)$ well but the blurring due to information loss cannot be fully eliminated. As a last step, we can apply well developed ultrasonic methods in order to reconstruct the initial temperature distribution $T_0^{\mathrm{rec}}(\mathbf{r})$. Despite the rather strong blurring of $T_{\mathrm{virt}}(\mathbf{r},t)$for deeper lying structures, even deeper structures can be well reconstructed by ultrasonic reconstruction techniques because they “average” signals from all directions and therefore the noise is reduced very effectively in $T_0^{\mathrm{rec}}(\mathbf{r})$.

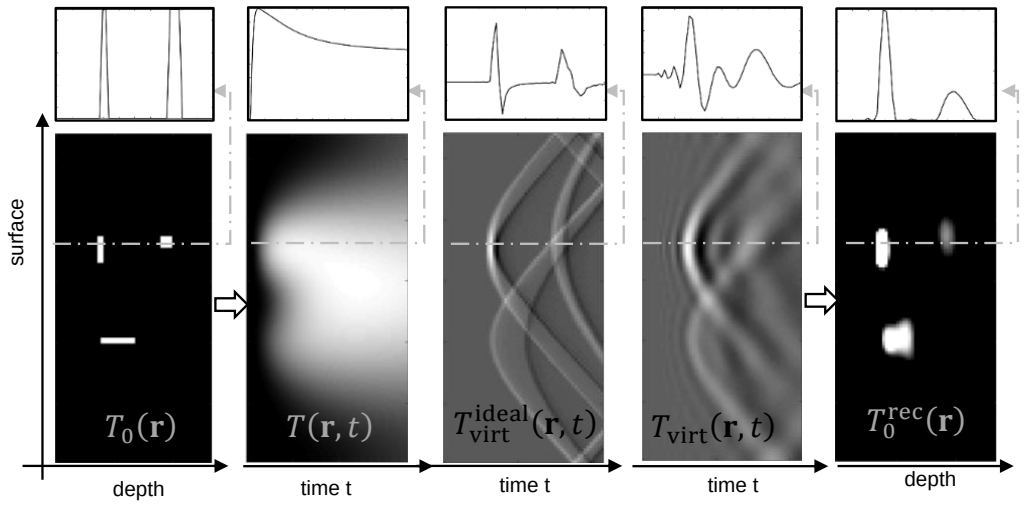

Fig. 2. Process steps of the virtual wave concept: First, the internal sources are heated, by e.g. optical excitation, yielding a certain initial temperature distribution $T_0(\mathbf{r})$. Simultaneously, the surface temperature signal $T(\mathbf{r},t)$ is measured using an IR-camera. Then the temperature signal is transformed into an acoustic virtual wave signal $T_{\mathrm{virt}}(\mathbf{r},t)$. When comparing $T_{\mathrm{virt}}(\mathbf{r},t)$ with the ideal virtual wave field $T_{\mathrm{virt}}^{\mathrm{ideal}}(\mathbf{r},t)$, we see that the former is blurred because of entropy production during heat diffusion. As a final step, we can employ ultrasonic methods to reconstruct the initial temperature distribution $T_0^{\mathrm{rec}}(\mathbf{r})$.

[1] P. Burgholzer, G. Mayr, G. Thummerer, M. Haltmeier, Linking information theory and thermodynamics to spatial resolution in photothermal and photoacoustic imaging, J. Appl. Phys. 128 (2020) 171102 https://doi.org/10.1063/5.0023986.

KEYNOTE SPEAKER

Photothermal radiometry data analysis with machine learning

Xiao P[(1)*]

(1) School of Engineering, London South Bank University, London, UK

*Corresponding author's email: xiaop@lsbu.ac.uk

Photothermal radiometry is an infrared remote sensing technique that has been used for skin and skin appendages research, in the areas of skin hydration, hydration gradient, skin hydration depth profiling, skin thickness measurements, skin pigmentation measurements, effect of topically applied substances, transdermal drug delivery, moisture content of bio-materials, membrane permeation, and nail and hair measurements. Compared with other technologies, photothermal radiometry has the advantages of non-contact, non-destructive, quick to make a measurement (a few seconds), and being spectroscopic in nature. It is also colour blind, and can work on any arbitrary sample surfaces. It has a unique depth profiling capability on a sample surface (typically the top 20 μm), which makes it particularly suitable for skin measurements. Photothermal radiometry is information rich, however to analyze the signal and get the information is often difficult. In this paper, we present our latest study on the photothermal radiometry data analysis with Machine Learning. We have investigated different algorithms such as Random Forest Regression, Gradient Boosting Regression, Support Vector Machine (SVM) Regression, Partial Least Squares Regression, as well as Deep Learning Neural Networks Regression. We will first introduce the theoretical background, then illustrate its applications with experimental results.

Automatic inspection of surface breaking cracks using laser scanning thermography

Pech-May NW[(1)*], Hirsch P[(1)], Ziegler M[(1)]

(1) Bundesanstalt für Materialforschung und -prüfung (BAM), 12200 Berlin, Germany

*Corresponding author's email: nelson-wilbur.pech-may@bam.de; https://www.bam.de/thermography

In this work, we report on a method for automatic inspection of components using laser scanning thermography, in which the relative motion is performed by a robot to fully inspect complex test objects such as turbine blades. We demonstrate our evaluation algorithms with the aim of automatically detecting surface defects on calibrated specimens. We show the influence of the excitation laser, which can be varied in terms of spot geometry, wavelength, and scan scheme. Additionally, we show some advantages, versatility, and current challenges of using a programmed robot for non-destructive evaluation in thermography.

Overview – Schlichting *et al.* [1] proposed an efficient algorithm, based on the Sobel-derivatives along horizontal and vertical directions, to detect surface breaking cracks by analysis of thermographic films obtained from flying spot tests. Recently, we have developed a similar algorithm, based on the Canny approach, for automatic surface defect detection.[2] The detection algorithms are combined with automatic thermographic testing using a previously simulated scanning path in a 3D environment. This allows to visualize and optimize the scanning parameters before actual measurement. Additionally, it improves reproducibility of the tests, because the defined scanning path can be made independent of the positioning of the specimen on the robot arm. However, some limitations in the accuracy of the positioning of the robot arm will be discussed. On the other hand, different configurations of the thermographic setup can be combined with such a robot arm: A blue laser is a better alternative compared to a NIR laser for testing some metals, like Cu. The scanning parameters, such as scanning speed, input power, spot dimension, camera frame rate might be optimized for the crack sizes one is looking for. The aim will be to have a 3D representation of the detected surface defects on the CAD model of the tested specimen.

References

[1] J. Schlichting, M. Ziegler, A. Dey, C. Maierhofer, M. Kreutzbruck. Efficient data evaluation for thermographic crack detection. Quant. Infrared Thermogr. J. 8 (2011) 119-23. https://doi.org/10.3166/qirt.8.119-123.

[2] N.W. Pech-May, M. Ziegler, Surface breaking crack detection algorithm for flying spot and line thermography based on the Canny approach. SPIE Future Sensing Technologies 2021: Proc. SPIE (2021). https://doi.org/10.1117/12.2603913.

New options for finding defects on and below the surface using structured laser thermography

Ziegler M(1)*, Ahmadi S(1), Lecompagnon J(1), Hirsch PD(1), Pech-May NW(1), Thiel E(1)

(1) Bundesanstalt für Materialforschung und -prüfung (BAM), 12200 Berlin, Germany

*Corresponding author's email: mathias.ziegler@bam.de

In infrared thermography, the transient temperature distribution is used, for example, to non-destructively detect defects caused by the externally applied heat flow interacting with the internal geometry of the sample or with inhomogeneities enclosed within it. An equivalent way of describing this interacting heat flow is the propagation of thermal waves inside the sample. Although thermography is suitable for a wide range of inhomogeneities and materials, the fundamental limitation is the diffuse nature of thermal waves and the need to measure their effect radiometrically at the sample surface only. The crucial difference between diffuse thermal waves and propagating waves, as they occur e.g., in ultrasound, is the rapid degradation of spatial resolution with increasing defect depth. This degradation usually limits the applicability of thermography for finding small defects on or below the surface.

A promising approach to improve the spatial resolution and thus the detection sensitivity and reconstruction quality of the thermographic technique lies in the shaping of these diffuse thermal wave fields using structured laser thermography. Some examples are:

- Narrow crack-like defects below the surface can be detected with high sensitivity by superimposing several interfering thermal wave fields,
- Closely adjacent defects can be separated by multiple measurements with varying heating structures,
- Defects at different depths can be distinguished by an optimized temporal shaping of the thermal excitation function,
- Narrow cracks on the surface can be found by robotic scanning with focused laser spots.

We present the latest results of this technology obtained with high-power laser systems and modern numerical methods.

References

[1] https://www.bam.de/thermography

Towards hyperspectral in-situ temperature measurement in metal additive manufacturing

Altenburg SJ[(1)*], Becker T[(1)], Breese PP[(1)], Maierhofer C[(1)]

(1) Bundesanstalt für Materialforschung und -prüfung (BAM), 12200 Berlin, Germany

*Corresponding author's email: Simon.Altenburg@bam.de

The industrial use of additive manufacturing for the production of metallic parts with high geometrical complexity and lot sizes close to one is rapidly increasing as a result of mass individualisation and applied safety relevant constructions. However, due to the high complexity of the production process, it is not yet fully understood and controlled, especially for changing (lot size one) part geometries.

Due to the thermal nature of the Laser-powder bed fusion (L-PBF) process – where parts are built up layer-wise by melting metal powder via laser - the properties of the produced part are strongly governed by its thermal history. Thus, a promising route for process monitoring is the use of thermography. However, the reconstruction of temperature information from thermographic data relies on the knowledge of the surface emissivity at each position on the part. Since the emissivity is strongly changing during the process due to phase changes, great temperature gradients, possible oxidation, and other potential influencing factors, the extraction of real temperature data from thermographic images is challenging. While the temperature development in and around the melt pool, where melting and solidification occur is most important for the development of the part properties. Also, the emissivity changes are most severe in this area, rendering the temperature deduction most challenging.

A possible route to overcome the entanglement of temperature and emissivity in the thermal radiation is the use of hyperspectral imaging in combination with temperature emissivity separation (TES) algorithms. As a first step towards the combined temperature and emissivity determination in the L-PBF process, here, we use a hyperspectral line camera system operating in the short-wave infrared region (0.9 µm to 1.7 µm) to measure the spectral radiance emitted. In this setup, the melt pool of the L-PBF process migrates through the camera's 1D field of view, so that the radiation intensities are recorded simultaneously for multiple different wavelength ranges in a spatially resolved manner. At sufficiently high acquisition frame rate, an effective melt pool image can be reconstructed. Using the grey body approximation (emissivity is independent of the wavelength), a first, simple TES is performed, and the resulting emissivity and temperature values are compared to literature values. Subsequent work will include reference measurements of the spectral emissivity in different states allowing its analytical parametrisation as well as the adaption and optimisation of the TES algorithms. An illustration of the proposed method is shown in Fig.1.

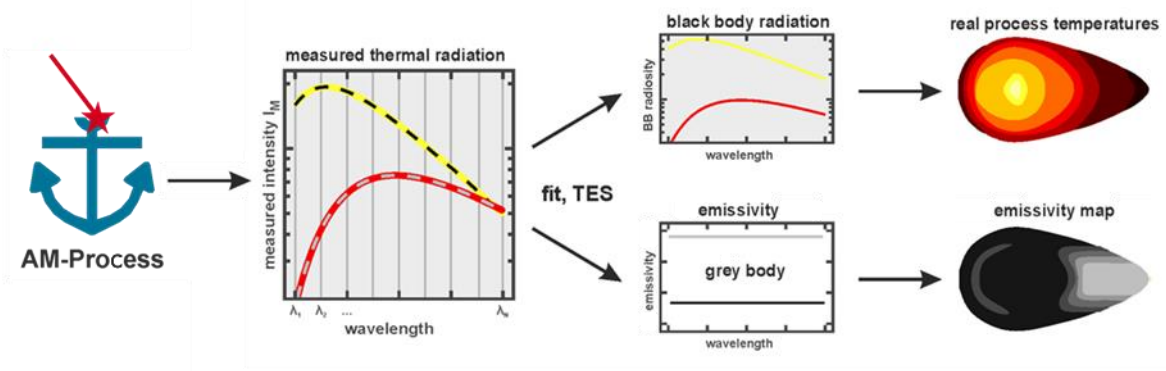

Fig. 1. Schematic illustration of the proposed method. The yellow and black (dashed) lines correspond to a region in the centre of the melt pool with high temperature and low emissivity (liquid metal), the red and grey (dashed) lines correspond to a region behind the melt pool (on the very right- hand side), where the material is solidified and possibly oxidised, at a lower temperature and with a higher emissivity.

The investigated method will allow to gain a deeper understanding of the L-PBF process, e.g., by quantitative validation of simulation results. Additionally, the results will provide a data basis for the development of less complex and cheaper sensor technologies for L-PBF in-process monitoring (or for related process), e.g., by using machine learning.

References

[1] https://www.bam.de/thermography

Photoacoustic reconstruction formulas exploiting known location of 2D initial pressure

Dreier F[(1)*], Obmann D[(1)], Haltmeier M[(1)], Felbermayer K[(2)], Hinterleitner F[(2)], Burgholzer P[(2)]

(1) Department of Mathematics, University of Innsbruck, Innsbruck, Austria,
(2) Research Center for Non Destructive Testing (RECENDT), Linz, Austria

*Corresponding author's email: Florian.Dreier@uibk.ac.at

Background – The image reconstruction problem in photoacoustic tomography (PAT) is inherently three-dimensional because of the propagation of waves in 3D space. However, with an advanced measurement technique based on integrating line detectors an analogous reconstruction problem also occurs in two dimensions [1]. The 2D wave equation is different from the 3D wave equation, because the pressure in 2D does not become zero after some finite time. This phenomenon is also reflected in known inversion formulas which use all pressure signals up to infinite time. This leads to several practical disadvantages due to noise, reflection artifacts and damping. Therefore, in practice, the inversion formulas are cut off at a certain time, leading to errors in the reconstruction. In 3D, this is not the case, because in contrast it is necessary to integrate only over a finite time interval, which is derived from the known location of the object (Huygens' principle). In this work, we also establish similar formulas in 2D using pressure data only from a finite time interval.

Methods – In the following, we consider a domain $\Omega \subset \mathbb{R}^2$ in the plane with a smooth boundary $\partial\Omega$. Moreover, we suppose that the initial pressure $f\colon \mathbb{R}^2 \to \mathbb{R}$ of the two-dimensional wave equation

$$\begin{aligned} \partial_t^2 p(x,t) - c^{-2}\Delta p(x,t) &= 0, \\ p(x,0) &= f(x), \\ \partial_t p(x,0) &= 0 \end{aligned}$$

is located in some smaller domain $\Omega' \subset \Omega$, where $(x,t) \in \mathbb{R}^2 \times (0,\infty)$, ∂_t is the time derivative, Δ denotes the Laplacian with respect to the space variable and c describes the speed of sound in a medium. As mentioned before, we are interested to recover the initial pressure f from photoacoustic pressure signals that are measured only within a certain finite time interval $[T_1(y), T_2(y)]$ for each detector located at $y \in \partial\Omega$. As we will see in the results, theoretical exact reconstruction of f is possible by explicit inversion formulas if the data of the pressure wave is collected between the times points

$$0 \le T_1(y) \le c^{-1}\inf\{\|y-z\| \mid z \in \Omega'\},\ T_2(y) \ge c^{-1}\sup\{\|y-z\| \mid z \in \Omega'\}. \qquad \text{Eqn. 1}$$

Fig. 1. and 2. visualize the upper bound of $T_1(y)$ and the lower bound of $T_2(y)$ in Eqn. 1 with a simple initial pressure and the corresponding pressure signals. It should be noted that even if an optimal domain Ω' is not known, one can at least take $\Omega' = \Omega$, since the initial pressure is contained in Ω. Such a situation has previously been studied in [2]. Opposed to [2], previous formulas, as for example derived in [3,4], require pressure signals on the whole time interval $(0,\infty)$.

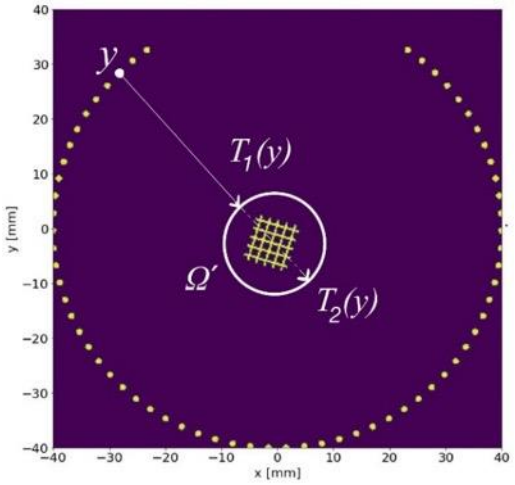

Fig. 1. A simple initial pressure located in the domain Ω'. The yellow dots describe the location of the detector points on the boundary of Ω.

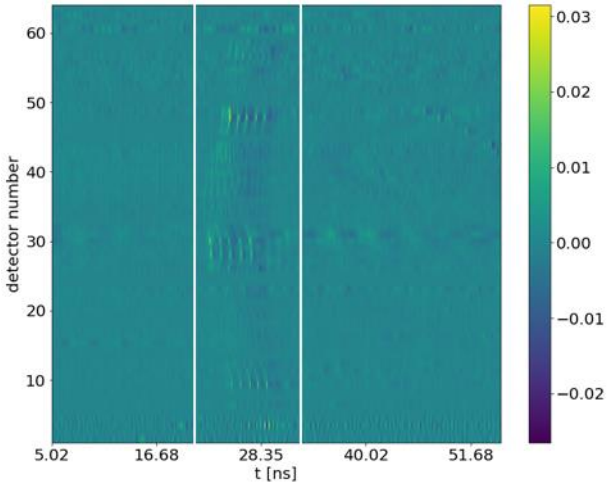

Fig. 2. Corresponding measured acoustic signal. The area between the two white stripes describes the data between the constant time points $T_1(y)$ and $T_2(y)$.

Results – The following main theoretical result of this work gives an inversion formula for 2D PAT using measured pressure signals on finite time intervals only. It is an extension of the results in [2], where $T_1(y)$ equals zero and $T_2(y)$ is set to the diameter of domain Ω for all $y \in \partial\Omega$.

Theorem. Let $\Omega \subset \mathbb{R}^2$ be bounded by an ellipse $\partial\Omega = Q\{x \in \mathbb{R}^2 \mid (\mathrm{x}_1/a)^2 + (\mathrm{x}_2/\mathrm{b})^2 \leq 1\}$, where $a, b > 0$, Q is an orthogonal matrix, $\Omega' \subset \Omega$ and $T_1(y)$ and $T_2(y)$ are such that Eqn. 1 for all $y \in \partial\Omega$ is satisfied. Furthermore, suppose that initial pressure $f: \mathbb{R}^2 \to \mathbb{R}$ vanishes outside of Ω'. Then, the following reconstruction formula for all $x \in \Omega$ holds:

$$f(x) = \frac{1}{\pi}\nabla_x \cdot \int_{\partial\Omega} \nu(y) \int_{T_1(y)}^{T_2(y)} k_{T_2(y)}(\|x-y\|, t)\, p(y,t)\, dt\, d\sigma(y).$$

Here, ∇_x denotes the gradient with respect to x and $\nu(y)$ the outward unit normal vector of $\partial\Omega$ at y. For the definition of the function $k_{T_2(y)}: (0, T_2(y)) \times \big(0, T_2(y)\big) \to \mathbb{R}$ we refer to [2] where the same kernel function has been used.

Conclusion – In this work, we derived a new inversion formula on finite time intervals in 2D for recovering the initial data in PAT that make use of additional available information of the location of the acoustic pressure source. In the final talk, we will also present reconstruction results from simulated as well as experimental data, demonstrate benefits of the new formula and compare the results with previous formulas requiring data for all times.

References

[1] P. Burgholzer et al. Temporal back-projection algorithms for photoacoustic tomography with integrating line detectors. Inverse Problems 23:6 (2007) S65.

[2] F. Dreier, M. Haltmeier, Photoacoustic inversion formulas using mixed data on finite time intervals. arXiv preprint arXiv:2111.02262 (2021) (submitted).

[3] M. Haltmeier, Universal inversion formulas for recovering a function from spherical means. SIAM Journal on Mathematical Analysis 46:1 (2014) 214-232.

[4] F. Dreier, M. Haltmeier, Recovering the initial data of the wave equation from Neumann traces. SIAM Journal on Mathematical Analysis 53:2 (2021) 2427-2451.

Spatio-temporal imaging of the thermally hardened surface layer in steel parts

Haderer W(1)*, Scherleitner E(1) , Gseller J(2), Heise B(1), Mitter T(1,3), Reitinger B(1), Hettich M(1)

(1) Research Center For Non-Destructive Testing GmbH (RECENDT), Altenberger Straße 69, Linz, Austria
(2) Maschinenfabrik ALFING Kessler GmbH, 73433 Aalen/Germany
(3) voestalpine Stahl GmbH, voestalpine Straße 3, 4020 Linz, Austria

*Corresponding author's email: wolfgang.haderer@recendt.at

Background – Surface hardening is a widely applied method to improve surface properties of steel parts like train wheels and rails or automotive parts like crank shafts, gears or bearings. Different methods of surface hardening exist. Here we focus on thermally hardened and quenched parts which exhibit a change in the surface near microstructure. The extend of this layer into the depth of the part is the hardening penetration depth (HPD). Two parameters are crucial for industrial applications: the absolute hardness and the HPD of the surface layer. Standardized approaches to characterize these quantities include indentation tests on sample cross sections and optical imaging techniques. Since destructive methods require an extensive effort in the production process, non-destructive methods which can be incorporated into in-line production are highly sought after. This has stimulated research in different directions based on Barkhausen noise, Eddy current testing and ultrasound based methods, each with their own respective advantages and disadvantages. Here, we will discuss an improved methodology based on laser ultrasound and supervised machine learning to provide a calibration-free determination of the HPD in non-destructive and contact free manner.

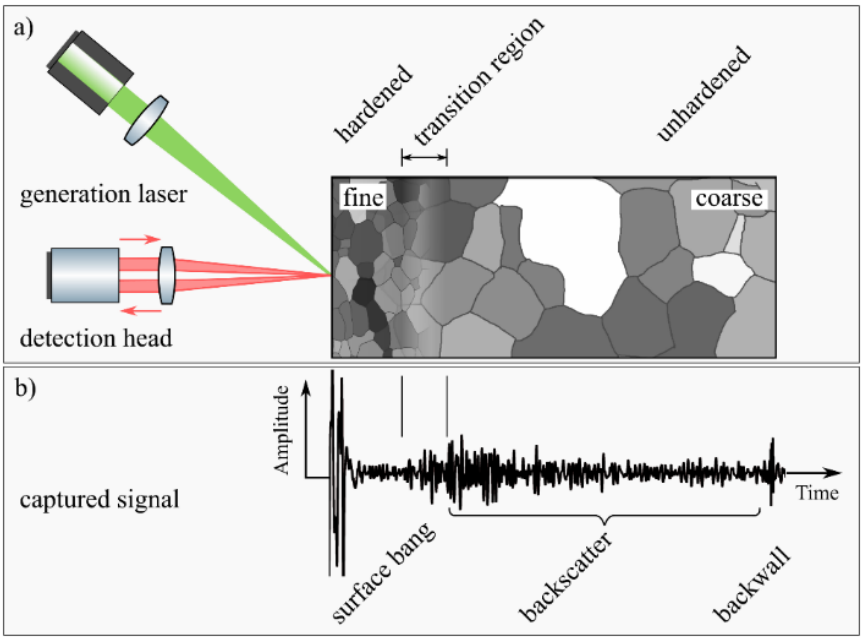

Fig. 1. a) Sketch of measurement geometry and sample microstructure **b)** Exemplary time domain signal

Methods – The working principle of the laser ultrasound approach is depicted in Fig. 1. Ultrasound pulses are excited at the surface of steel parts by a pulsed laser source. These propagate into the sample and are preferentially backscattered at the interface between hardened layer and core due to the difference in grain size. The backscattered waves are subsequently detected at the sample surface by a second laser and a two-wave mixing interferometer that is capable of measuring on rough surfaces. The backscattered acoustic waves carry the information of the extend of the hardened layer similar to pulse-echo schemes.

Results – We demonstrate the method on three industrial grade samples with different microstructural peculiarities accounting for typical difficulties arising in the industrial production process. Due to the inherent fast data acquisition in our laser ultrasonics setup we are able to perform lateral scans along the sample and use the additional spatial information to apply a supervised machine learning approach (1) that provides us with the sub-surface lateral and axial contour of the hardened layer. In general the method performs excellent if no additional scatterers, e.g. segregations are present in the hardened layer. In particular, we require no additional calibration step for the data evaluation which is in stark contrast to the usual time-domain evaluation methods and a major improvement regarding industrial needs. Currently the method is limited to layer thicknesses exceeding the time extent of the initial blind zone, termed surface bang in our data. This contribution stems from optical and acoustic noise caused by the excitation pulse.

Conclusions – A spatio-temporal measurement method based on laser ultrasound is applied to industrial samples with hardened surface layers. The subsurface spatial profile of the hardness penetration depth can be determined by a supervised machine learning approach without additional calibration step. Our current findings also show the need for more sophisticated measurement schemes in the presence of additional scatterers in the hardened layer and a more fundamental understanding of the spatio-temporal scattering in heterogeneous microstructures for quantitative evaluation would be beneficial for further improvements of this technique. Furthermore, the method needs to extended to thinner layers that are currently masked by the initial opto-acoustic noise of the laser excitation mechanism.

References

[1] S. Berg, D. Kutra, T. Kroeger, C.N. Straehle, B.X. Kausler, C. Haubold, M. Schiegg, J. Ales, T. Beier, M. Rudy, K. Eren, J.I. Cervantes, B. Xu, F. Beuttenmueller, A. Wolny, C. Zhang, U. Koethe, F.A. Hamprecht, A. Kreshuk, Ilastik: Interactive Machine Learning for (Bio)Image Analysis, Nat. Methods. 16 (2019) 1226–1232. https://doi.org/10.1038/s41592-019-0582-9.

Restriction on the laser wavelengths for imaging of metal/epoxy interfaces by time-domain Brillouin scattering

Sathyan S[(1)*], Raetz S[(1)], Nicol E[(2)], Edely M[(2)], Pajusco N[(1)], Chigarev N[(1)], Cuvillier N[(3)], Delozanne J[(3)], Ducousso M[(3)], Tournat V[(1)], Gusev VE[(1)*]

(1) Laboratoire d'Acoustique de l'Université du Mans (LAUM), UMR 6613,
Institut d'Acoustique – Graduate School (IA-GS), CNRS, Le Mans Université, Le Mans 72085, France
(2) Institut des Molécules et Matériaux du Mans (IMMM), UMR 6283, CNRS, Le Mans Université,
Le Mans, France
(3) SAFRAN TECH, Magny les Hameaux, France

*Corresponding authors' email: sandeep.sathyan@univ-lemans.fr, vitali.goussev@univ-lemans.fr

Background – The time-domain Brillouin scattering (TDBS) is a rapidly developing all-optical experimental technique that uses ultrafast laser pulses to generate and monitor the propagation of coherent acoustic pulses (CAPs) in transparent media. In TDBS, the absorption of pump laser pulses in a metallic layer attached to a transparent sample launches CAPs into the media. The time-delayed probe pulse monitors the CAPs propagation. The imaging and depth profiling capabilities of TDBS have already been demonstrated for various systems, including 3D imaging of biological cells and polycrystalline materials [1].

Here we use TDBS to examine an academically-prepared and an industrial epoxy resin interface with metals such as Al and Ti. Epoxies are the type of reactive polymers used as adhesive or paints in a wide range of industrial applications such as automotive and aerospace. In these applications, the mechanical properties in the vicinity of the metal/epoxy interface play a crucial role in the bond strength and stability of adhesion. The metal/epoxy interface is generally studied using techniques like atomic force microscopy (AFM) and frequency-domain Brillouin scattering (FDBS) microscopy. In AFM, the studies on depth inhomogeneities at nanoscale are destructive/invasive as they require cutting of the sample normally to the surface/interface, whereas FDBS has an axial resolution limited by the probe optical wavelength and has never been applied closer than 10 µm from the metal/epoxy interface [2]. The axial resolution of TDBS imaging is limited by the length of the CAP and can be potentially better than sub-µm scale, i.e., comparable with that of AFM, while it can access the material inhomogeneity below single digit µm distances from the surfaces/interfaces [1,3]. When limited by signal processing the depth resolution of TDBS can be controlled by the acoustic wavelength $\lambda_{ac} = \frac{\lambda_{probe}}{2n}$, where n is the refractive index of the medium and λ_{probe} is the probe laser wavelength. So, by diminishing λ_{probe}, the spatial resolution of TDBS imaging could be enhanced. Yet, our experiments demonstrate that near-UV and visible wavelengths modify the physical properties of the epoxy resin. To our knowledge, the usual FDBS technique used to study the metal epoxy/interface is conducted with visible laser because of its availability in the commercial spectrometers. Our homemade TDBS experimental setup, using near-IR pump and probe lasers, thus enables us to study the metal/epoxy interface non-destructively.

Methods – We implemented TDBS with a fast data acquisition technique based on asynchronous optical sampling (ASOPS). For the generation and detection of the CAPs, we applied femtosecond laser

pulses at pump/probe wavelengths 345/356, 517/535, and 1035/1068 nm. For preparing epoxy academically, we used the combination of diglycidyl ether of bisphenol-A (DGEBA) and diethylenetriamine (DETA). The industrial epoxy used by SAFRAN TECH was the AF 191 structural adhesive film reference of 3M™ Scotch-Weld™. In the DGEBA/DETA case, thin metal film depositions provided opportunity for the CAPs generation in metal and their detection in epoxy from opposite sides (Fig 1a), which helps to reduce pump-related heating of epoxy and where sapphire substrate additionally acts as a heat sink. For AF 191 epoxies prepared on 30 µm-thick aluminium sheets, the pump and probe beams are incident at the metal/epoxy interface from the same side (fig. 1b).

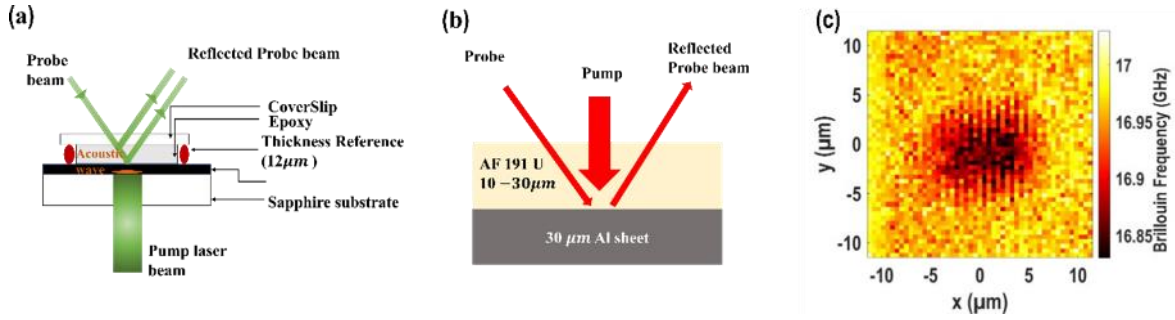

Fig. 1. TDBS experimental configurations in: (a) opposite side, (b) same side. (c) 2D map of residual depth-averaged Brillouin frequency obtained with visible pump and probe wavelength around the position where curing was studied.

Results/Discussion – We observed modification of physical properties of epoxy with the near-UV and visible wavelengths, whereas the experiments with near-IR wavelengths demonstrate the non-destructive probing of the metal/epoxy interface. Fig. 1(c) shows the laser-induced lateral variation of Brillouin frequency around the position where curing is studied with the visible laser. In TDBS experiments, signals are observed up to ~1.5 ns duration, implying GHz CAPs propagation to a depth of ~5 µm from the interface. Analyzing these oscillations as a function of time delay between the pump and probe laser pulses at various lateral locations at the interface produces three-dimensional images of epoxy, which are accumulated during the curing process.

Acknowledgments – This research is supported by the Agence Nationale de la Recherche (project ANR-18-CE42-I2T2M).

References

[1] V.E. Gusev, P. Ruello, Advances in applications of time-domain Brillouin scattering for nanoscale imaging. Appl. Phys. Rev. 5 (2018) 031101. https://doi.org/10.1063/1.5017241.

[2] J.K. Krüger, W. Possart, R. Bactavachalou, U. Müller, T. Britz, R. Sanctuary, P. Alnot, Gradient of the mechanical modulus in glass-epoxy-metal joints as measured by Brillouin microscopy. J. Adhes. 80 (2004) 585–599. http://dx.doi.org/10.1080/00218460490476973.

[3] A.M. Lomonosov, A. Ayouch, P. Ruello, G. Vaudel, M.R. Baklanov, P. Verdonck, L. Zhao, V.E. Gusev, Nanoscale noncontact subsurface investigations of mechanical and optical properties of nanoporous low-k material thin film. ACS Nano 6 (2012) 1410–1415. https://doi.org/10.1021/nn204210u.

Application of all-optical and non-destructive laser ultrasonic in imaging of CFRP subsurface defects

Song P[(1,2)], Zhao JH[(3,4)], Liu JY[(3,4)*], Sun XG[(1,2)], Yue HH[(3,4)]

(1) School of Instrumentation Science and Engineering, Harbin Institute of Technology, Harbin P. R. China
(2) HIT Wuhu Robot Technology Research Institute, Wuhu, P.R. China.
(3) School of Mechatronics Engineering, Harbin Institute of Technology, Harbin, P. R. China
(4) State Key Laboratory of Robotics and System, Harbin Institute of Technology, Harbin, P. R. China

*Corresponding author's email: ljywlj@hit.edu.cn

Subsurface defects such as delamination and disbond, could severely affect the performances of composite materials and need to be evaluated in time. In this work, a variety of artificial subsurface defects in carbon fiber reinforced polymer (CFRP) composites was characterized using an all-optical and nondestructive laser ultrasonic (LU) technique with an optical microphone. Rigrsure thresholding selection role was selected and convinced to effectively denoise the LU signals using the wavelet transform denoising method. Four kinds of featured C-scan images of the artificial defects were proposed to determine the size of artificial flaw regions and compared each other. A model for determination of the depth of flat-bottom holes in CFRP composites was proposed and simultaneously confirmed with experiments. This investigation has carried out successful applications of the all-optical and nondestructive LU technique for quantitative imaging of subsurface defects in CFRP composites with advantages of non-contact, and quantitive determination of the size and depth of flat bottom holes.

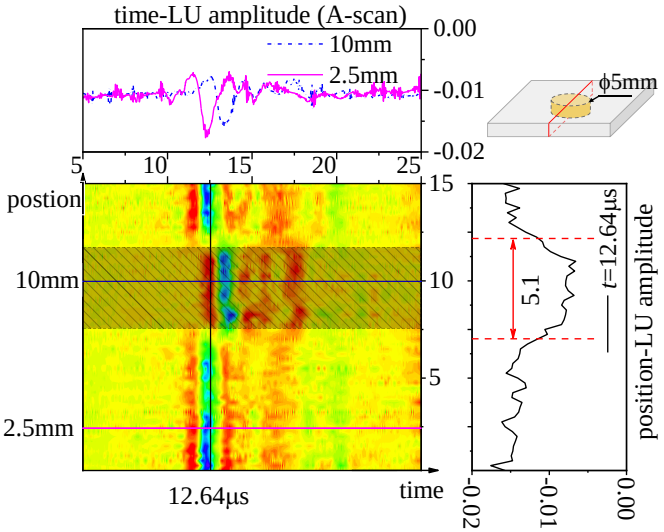

Fig. 1. Time-domain LU results along the diameter scanning and corresponding position profiles as well as A-scan profiles for ϕ5 mm flat-bottom hole in No. 1 specimen.

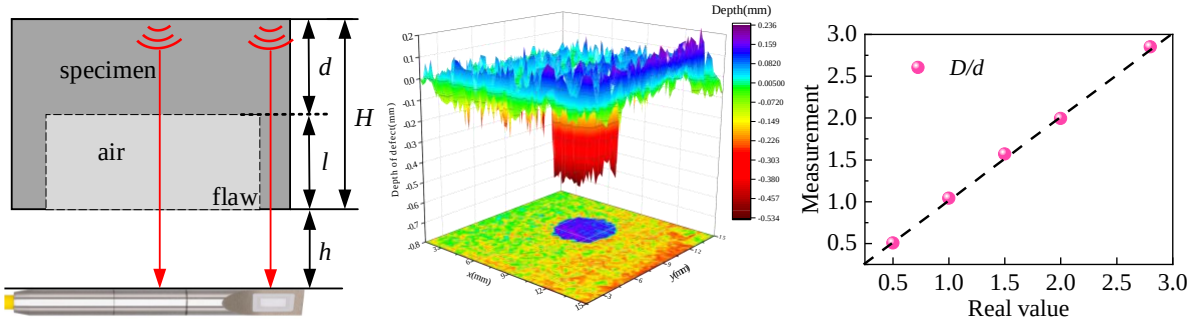

Fig. 2. (a) A diagraph for calculation of the flat-bottom hole using an optical microphone, **(b)** the calculated depth distribution of #3 flat bottom hole (*D*=5 mm, *d*=2.5 mm) in No. 1 specimen, **(c)** comparison of the measurement value with the real value at various diameter to depth ratio of flat-bottom holes

References

[1] B. Fischer, Optical microphone hears ultrasound, Nat Photonics, 10 (2016) 356.

[2] B. Fischer, F. Sarasini, J. Tirillò, F. Touchard, L. Chocinski-Arnault, D. Mellier, and R. Ecault, Impact damage assessment in biocomposites by micro-CT and innovative air-coupled detection of laser-generated ultrasound, Compos Struct, 210 (2019) 922. https://doi.org/10.1016/j.compstruct.2018.12.013.

[3] H. Huan, A. Mandelis, L. Liu, B. Lashkari, and A. Melnikov, Application of linear frequency modulated laser ultrasonic radar in reflective thickness and defect non-destructive testing, NDT & E International, 102 (2019) 84. https://doi.org/10.1016/j.ndteint.2018.11.006.

Lock-in thermography of compressed metal powder metallurgy in pre-sintered state as flaw preventive non-destructive evaluation modality

Sebastian K[(1)], Melnikov A[(1)], Sivagurunathan K[(1)], Guo X[(1)], Mandelis A[(1)*]

(1) Center for Advanced Diffusion-Wave and Photoacoustic Technologies (CADIPT) and Institute for Advanced Non-Destructive and Non-Invasive Diagnostic Technologies (IANDIT). Department of Mechanical & Industrial Engineering, University of Toronto, Toronto, Canada

*Corresponding author's email: mandelis@mie.utoronto.ca

The concept of preventive non-destructive evaluation (P-NDE) is introduced as an important new inspection approach which hinges on the premise of developing adequate analytical and measurement tools to investigate material integrity deficit factors during manufacturing that may lead to catastrophic flaws / cracks before the emergence of such flaws.

Introduction – Automotive industry utilization of powder metallurgy (PM) technology is increasing in popularity due to requirements for intricate and dimensionally accurate neat-shaped components which can be produced at competitive cost. The primary disadvantage of PM technology involves the possibility of seeding both surface and subsurface cracks at high-stress locations due to the powdered materials and non-isotropic pressure issues resulting from multi-ton press equipment adjustment. Therefore, non-destructive evaluation is an important inspection approach.

Methodology – Pre-sintered ("green") compressed metal powder components with known crack locations were studied using lock-in thermography imaging (LITI) which exhibited high crack detection efficiency [1, 2]. Thermal waves were excited by an 808-nm spread and spatially homogenized CW laser modulated beam, and were detected with a high-frame-rate mid-infrared (MIR) camera. 1 Hz modulation frequency was found to be optimal.

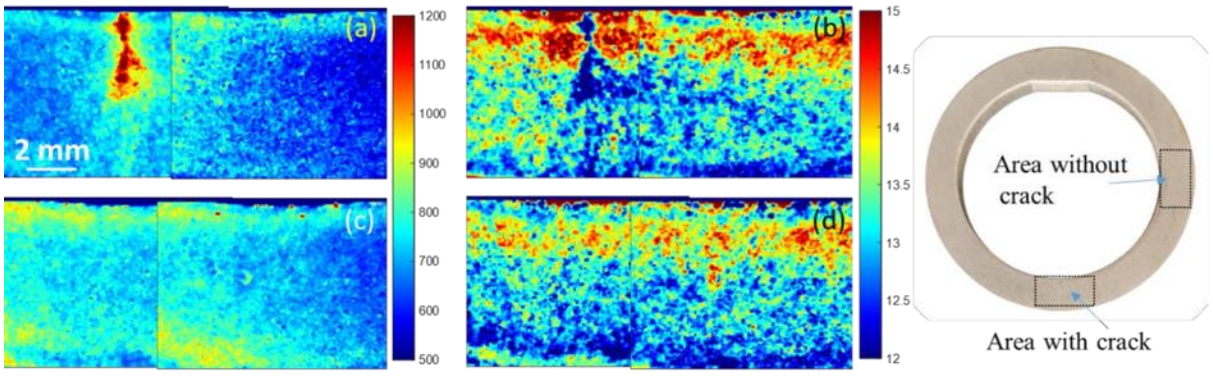

Fig. 1. (a, c) 1-Hz LIT amplitude and **(b, d)** phase of sample area with crack **(a, b)** and without crack **(c, d)**. **(e)** Photograph of a pre-sintered compressed metal powder automotive part. Dashed areas correspond to images (a-d).

Results – Local regions of interest with varying amplitude and phase lags were identified (Fig. 1). The local thermal diffusivity computed from a one-dimensional theoretical model implemented in this study exhibited strong correlation with the local pixel phase outside the immediate crack location. A

proportionality relation was also found between phase lag and independently estimated local sample porosity. Fig. 2 shows the optical image of the polished surface area near the crack that confirms that higher porosity corresponds to larger phase lag.

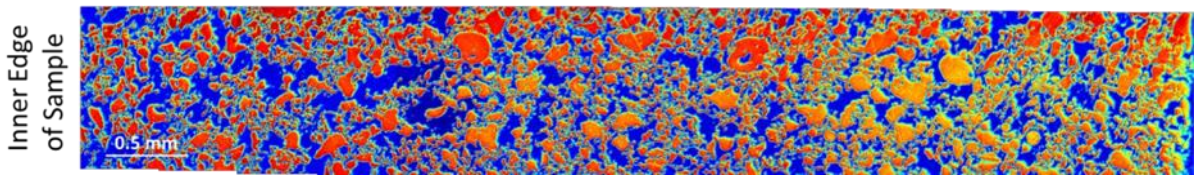

Fig. 2. Optical image of polished surface near the crack shown in Figs. 1a,b.

Discussion – The phase images of the area with the crack clearly confirm that the large lateral amplitude and phase gradients in the vicinity of, and across, the cracks coincided with radial amplitude and phase discontinuities. These produced multi-directional material inhomogeneities at their intersections acting as crack generators. They may be indicators that the metal powder was pressed under non-uniform radial and lateral pressure conditions around the circular sample. The bizonal character of the LIT phases is indicative of radial stresses in the inspected components resulting from density gradients. Under this condition, when radial stress coincides with lateral density gradients, it becomes a multi-directional stress source that is highly likely to generate cracks along the radial direction defined by the lateral density gradient.

Conclusions – This study introduces the concept of preventive non-destructive evaluation (P-NDE) as an early feedback tool for mechanical press corrections during the pre-sintering manufacturing process of metal powder compacts to anticipate and avoid potential cracks in post-sintered manufactured PM components.

References

[1] A. Melnikov, K. Sivagurunathan, X. Guo, J. Tolev, A. Mandelis, K. Ly, R. Lawcock, Non-destructive thermal-wave radar imaging of manufactured green powder metallurgy compact flaws (cracks), NDT&E Int. 86 (2017) 140-152. https://doi.org/10.1016/j.ndteint.2016.12.004.

[2] K. Sebastian, A. Melnikov, K. Sivagurunathan, X. Guo, X. Wang, A. Mandelis, Non-destructive lock-in thermography of green powder metallurgy component inhomogeneities: A predictive imaging method for manufactured component flaw prevention, NDT&E Int. 127 (2022) 102603. https://doi.org/10.1016/j.ndteint.2022.102603.

Three-dimensional reconstruction of subsurface absorbing structures in human skin from photothermal radiometric records

Cvetko T[(1)], Majaron B [(1,2)*]

(1) Faculty of Mathematics and Physics, University of Ljubljana, Slovenia
(2) Department of Complex Matter, Jožef Stefan Institute, Ljubljana, Slovenia

*Corresponding author's email: boris.majaron@ijs.si

Pulsed photothermal radiometry (PPTR) involves analysis of transient changes in mid-infrared (IR) emission from a sample surface after irradiation with a short light pulse. From a radiometric record obtained with a fast IR camera, light-induced temperature field inside the sample can be reconstructed in three dimensions (3D) by solving the inverse problem of heat diffusion and blackbody emission [1]. This could enable visualization of selectively absorbing structures in strongly scattering biological tissues and organs, similarly to photoacoustic microscopy and tomography [1,2]. However, development of a practical, accurate and robust methodology has remained elusive, primarily due to the scale and severe ill-posedness of the iterative image reconstruction process, emphasized by the low signal-to-noise ratios in the available radiometric records.

We present a parametric optimization study of the image reconstruction process using simulated radiometric records based on realistic experimental parameters, such as the mid-IR absorption and thermal properties of human skin (including the convective boundary condition) as well as the spatial resolution, acquisition rates, and noise characteristics of an actual mid-IR camera (FLIR SC7500) equipped with a microscope objective (magnification $M = 1$). The image reconstruction code written in Python performs the multidimensional optimization of the initial, laser-induced temperature field in three dimensions by running non-negatively constrained "ν-method" minimization algorithm [3].

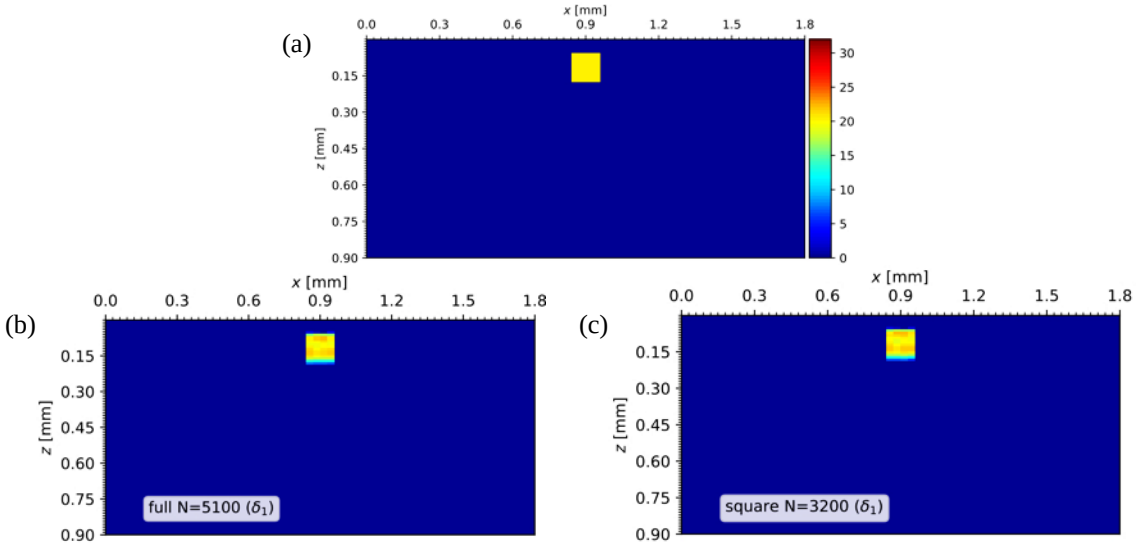

Fig. 5. (a) Postulated initial temperature field, emulating a sub-surface block with a square cross-section (0.12 x 0.12 mm^2) heated to 20 K above the surrounding medium. (b) The cross-sectional image reconstructed from the complete simulated radiometric record, consisting of 1250 IR images at 1000 fps (including noise), and (c) by applying progressive binning of the radiometric frames for significant reduction of the computational time.

The example presented in Fig. 1 involves an extended sub-surface block ("blood vessel") with a square cross-section (0.12 x 0.12 mm^2) and initial temperature 20 K above the surrounding medium. At the spatial discretization of 30 μm in the lateral and 10 μm in the axial direction, the reconstruction of vertical cross section through its center involves optimization of 5400 independent temperature values.

As demonstrated in Fig. 1b, this was accomplished very successfully in 5100 steps of the iterative reconstruction process when using the entire radiometric record, consisting of 1250 images "acquired" at 1000 frames per second (t_{max} = 1.25 s). The obtained image features our object in the correct location and with rather sharp edges, and no artifacts anywhere else in the reconstructed vertical plane.

Moreover, our analyses demonstrate that preconditioning of the input dataset by progressive binning of subsequent radiometric frames can significantly reduce the computational cost of the reconstruction process without adversely affecting the outcome. In the presented example, a nearly identical result was obtained by applying the so-called square temporal binning [4], which reduced the input radiometric record to only 250 images (Fig. 1c). In addition to speeding up the reconstruction process by a factor close to 5, this produced an image of the same quality in only 3200 iteration steps, thus offering an additional 37% reduction of the computation time.

Acknowledgment – This research was supported by the Slovenian Research Agency (grant P1-0192).

References

[1] S.A. Telenkov, D.J. Smithies, D.M. Goodman, B.S. Tanenbaum, J.S. Nelson, T.E. Milner, Infrared imaging of in vivo microvasculature following pulsed laser irradiation, J. Biomed. Opt. 3 (1998) 391-395. https://doi.org/10.1117/1.429848.

[2] B. Choi, B. Majaron, J.S. Nelson, Evaluation of photothermal tomography for imaging the microvasculature in human skin, Proc. SPIE 5318 (2004) 108-112. https://doi.org/10.1117/12.529318.

[3] M. Milanič, I. Serša, B. Majaron, A spectrally composite reconstruction approach for improved resolution of pulsed photothermal temperature profiling in water-based tissues. Phys. Med. Biol. 54 (2009) 2829–2844. https://doi.org/10.1088/0031-9155/54/9/016.

[4] M. Milanič, B. Majaron, Comparison of binning approaches for pulsed photothermal temperature profiling, Proc. SPIE 7371 (2009) 73710O. https://doi.org/10.1117/12.831734.

06
Ultrafast Phenomena & Spectroscopy

PLENARY SESSION

Novel nanophononic structures and devices

Esmann M[(1)], Lamberti FR[(1)] , Ortiz O[(1)] , Rodriguez A[(1)] , Priya P[(1)] , Cardozo de Oliveira E[(1)], Xiang C[(1)], Pastier F[(2)] , Giesz V[(2)], Harouri A[(1)] , Sagnes I[(1)] , Lemaitre A[(1)], Le Gratiet L[(1)] , Lanco L[(1)] , Morassi M[(1)], Lanzillotti Kimura ND [(1)*]

(1) Université Paris-Saclay, CNRS, Centre de Nanosciences et de Nanotechnologies (C2N), 10 Boulevard Thomas Gobert, 91120 Palaiseau, France
(2) Quandela SAS, 10 Boulevard Thomas Gobert, 91120 Palaiseau, France

*Corresponding author's email: daniel.kimura@c2n.upsaclay.fr

Through the engineering of semiconductor nanostructures it is possible to control both the dynamics and the interactions between photons and phonons at ultrahigh frequencies and reduced scales. In this presentation, I will describe devices based on semiconductor multilayers optimized to generate, detect, and confine acoustic phonons and possible applications and devices.

Acoustic-phonons in the GHz-THz range (i.e. acoustic waves with wavelengths in the 1-100 nm range) appear as a suitable platform to study complex wave phenomena, motivating the development of nanophononic devices. The strong interactions with other excitations in solids extend the range of applications to other fields such as nanoelectronics, photonics, communications, NDT, optomechanics, and quantum optics. Contrary to what happens in standard opto-acoustics, at these scales, the wavelength of the photons is comparable or much larger than the wavelength of the acoustic waves.

Coherent phonon generation by optical pump-probe experiments has enabled the study of acoustic properties at the nanoscale in planar heterostructures, plasmonic resonators, cells, micropillars, and nanowires. These experiments rely on the optical mode matching between the incident pump and probe laser fields and the optical modes of the structure under study. The efficient generation of coherent acoustic phonons relies on an efficient coupling of the pump field into the system, while the sensitive detection of phonons requires an efficient coupling of the probe to the optical mode undergoing a phonon-induced modulation. Since the implementation of these experiments usually requires a long mechanical delay line, the main practical challenges for its actual implementation are thus (1) stability of the optical mode overlap, (2) reproducibility of the excitation conditions, and (3) high power densities limiting the range of compatible samples. These shortcomings have so far been a roadblock in establishing the pump-probe as a quantitative spectroscopy tool for nanoacoustics.

In this work, we simultaneously solve the three aforementioned challenges by integrating fibered systems into pump-probe experiments [1], lifting the necessity for any optical alignment during the experiments. We aligned and glued a single mode fiber onto an optophononic micropillar beforehand as shown in Fig. 1. Our approach allows us to observe stable coherent phonon signals over at least a full day even at extremely low excitation powers of 1µW. This excellent stability enabled us to perform detailed power dependence studies revealing complex dynamics of the optical and phononic modes. Taking these dynamics into account, we are able to optimize excitation conditions and observe a mutual coherence between the optical and acoustic mode. The monolithic sample structure is transportable and provides a means to perform reproducible plug-and-play experiments. The integration with fibers might also establish the missing link between high frequency acoustic phonon engineering and stimulated Brillouin scattering in structured optical fibers.

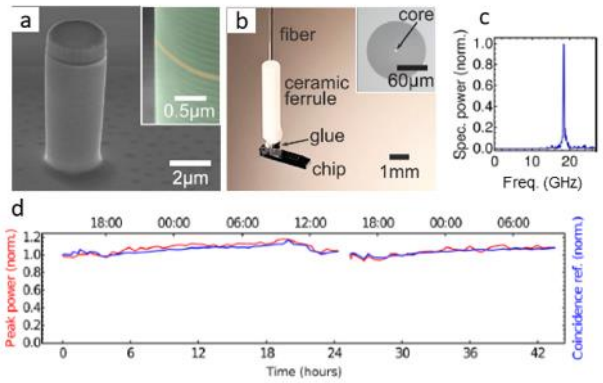

Fig. 6. (a) Optophononic micropillar cavity. **(b)** Device integrated into a single mode fiber. **(c)** Nanophononic response of the device measured by pump-probe spectroscopy. (d) Stability of the response over 42h. Figure adapted from Ref. [1].

In the second part of this presentation, I will describe a series of nanophononic devices based on planar and micropillar resonators, including Fabry-Perot [2], topological [3,4], and adiabatic designs [5]. I will describe how we engineered an optophononic 3D elliptical micropillar resonator based on AlAs/GaAs superlattices to simultaneously confine light and sound with an acoustic mode at 18 GHz. This design results in enhanced optomechanical interactions [2,6]. Due to the pillar ellipticity, the degeneracy of horizontally (H) and vertically (V) polarized cavity mode is lifted, leading to polarization-dependent reflection coefficient r_H and r_V. The splitting between the two optical modes depends on the ellipticity and size of the pillar and enables novel optical filtering strategies.

By bridging the gaps with other research fields such as optomechanics, plasmonics, polaritonics, and quantum technologies, nanophononics has great potential to unlock new paths in the engineering of nanodevices and unveil a plethora of novel and exciting physical phenomena.

References

[1] O. Ortiz, et al. Fiber-integrated microcavities for efficient generation of coherent acoustic phonons, Appl. Phys. Lett. 117 (2020) 183102.

[2] S. Anguiano, A.E. Bruchhausen, B. Jusserand, I. Favero, F.R. Lamberti, L. Lanco, I. Sagnes, A. Lemaître, N.D. Lanzillotti-Kimura, P. Senellart, A. Fainstein, Micropillar Resonators for Optomechanics in the Extremely High 19-95-GHz Frequency Range, Phys. Rev. Lett. 118 (2017) 263901.

[3] G Arregui, et. al. Coherent generation and detection of acoustic phonons in topological nanocavities, APL Photonics 4:3 (2019) 030805.

[4] O. Ortiz, et al. Topological optical and phononic interface mode by simultaneous band inversion, Optica 8:5 (2021) 598-605

[5] O. Ortiz, et al. Phonon engineering with superlattices: Generalized nanomechanical potentials, Physical Review B 100:8 (2019), 085430.

[6] F.R. Lamberti, Q. Yao, L. Lanco, D.T. Nguyen, M. Esmann, A. Fainstein, P. Sesin, S. Anguiano, V. Villafañe, A. Bruchhausen, P. Senellart, I. Favero, N.D. Lanzillotti-Kimura, Optomechanical Properties of GaAs/AlAs Micropillar Resonators Operating in the 18 GHz Range, Opt. Express 25 (2017) 24437.

KEYNOTE SPEAKER

Time-domain Brillouin scattering in paraxial sound and light beams: Contra-intuitive features

Raetz S[(1)], Gusev VE[(1)*]

(1) Laboratoire d'Acoustique de l'Université du Mans (LAUM), UMR 6613, Institut d'Acoustique – Graduate School (IA-GS), CNRS, Le Mans Université, France

*Corresponding author's email: vitali.goussev@univ-lemans.fr

Background – Time-domain Brillouin scattering (TDBS) is an opto-acousto-optical technique for the evaluation of transparent materials. Via optoacoustic conversion, ultrashort pump laser pulses launch coherent acoustic pulses (CAPs) in the sample. Time-delayed ultrashort probe laser pulses monitor the propagation of the CAPs via the photo-elastic effect, which induces light scattering (Fig.1).

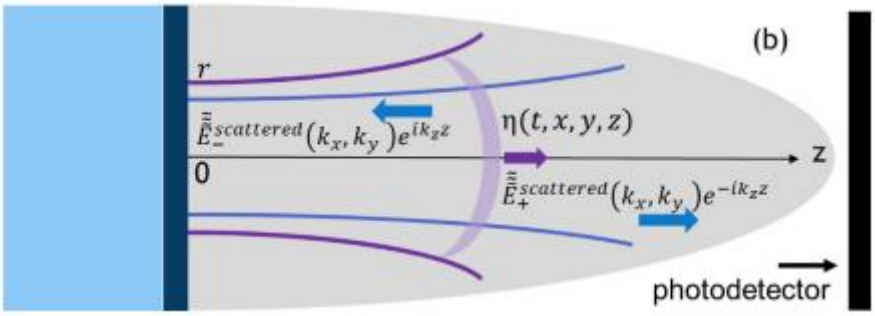

Fig. 1. Schematic presentation of co-focused probe light (in blue) and coherent sound (in violet) fields contributing to TDBS signal detection. Probe light field is due to laser pulses incident from a light transparent medium z > 0 on the sample surface z=0 and the laser pulses reflected from this surface. A CAP $\eta(t, x, y, z)$ is launched in the medium z>0 due the absorption in the sample z < 0 of the pump laser pulses (not presented) co-focused on the surface z = 0 with the probe laser pulses. When the pump laser pulses are incident on the sample before the probe laser pulses, then the acousto-optic interaction between the CAP and the initial probe light field creates optical polarization sources of scattered light. TDBS signal results from heterodyne detection of the initially reflected and acoustically scattered probe light collected by the photodetector

A photodetector collects both the acoustically scattered light and the probe light reflected by the sample structure for the heterodyning and reveals the signal periodically oscillating in time, the so-called Brillouin oscillation (BO). The scattered probe light carries information on the acoustical, optical and acousto-optical parameters of the material for the current position of the picosecond CAP. Thus, among other applications, time-domain Brillouin scattering is a technique for three-dimensional imaging at nanoscale [1]. One of the fundamental applications of the TDBS is the evaluation of the absorption of phonons in the GHz–THz frequency range. This is achieved by measuring the decay in time of the BO amplitude. The pioneer research paper [2] contains the estimates of the other physical factors that could cause the attenuation of the BO and should be properly taken into account to reveal acoustic absorption. Among them is diffraction of both CAPs and the probe laser pulses. Particularly, the theoretical analysis in [2] confirms, that the characteristic spatial scale for the influence of the diffraction phenomena is the Rayleigh range, also sometimes called the diffraction length. However, the theory in [2] is for equal radii of the acoustic and light beams, while the acoustic wavelength in the considered backward Brillouin scattering is tightly related to the probe light wavelength in the medium, being twice shorter.

These circumstances make it impossible to disentangle the roles of the acoustical and optical diffraction in the decay of the BO amplitude predicted in [2].

Theoretical method and results – Analytical theory of the TDBS for the diffracting collinear light and sound beams with different radii was developed in paraxial approximation [3]. The theory revealed a general phenomenon independent of the transverse distributions of the acoustic and probe laser fields at z=0: for the detection of the CAP motion, the heterodyning creates a complex spectral sensitivity function in wave vector domain. For the backward Brillouin scattering process, the phase of this function contains a part, which is conjugated to the paraxial phase of the CAP and cancels it. Consequently, but contra-intuitively, the BO amplitude variation with time does not depend on the variations of the CAP amplitude in the diffraction process. The key origin of this phenomenon is the phase sensitive process of the acoustically scattered and the reflected probe light interference. Sharp focusing of CAPs and probe laser pulses could increase lateral spatial resolution of TDBS imaging, but could potentially diminish its depth. However, the theoretical analysis contra-intuitively demonstrates that the depth and spectral resolution of the TDBS imaging, with collinearly propagating paraxial sound and light beams, do not depend on the focusing/diffraction of sound and only due to the variations of the probe light amplitude caused by light focusing/diffraction.

Comparison with the experimental observations – The developed theory contra-intuitively predicts, that, although the amplitude of the acoustically scattered light is proportional to the product of the local acoustical and probe light field amplitudes, the temporal dynamics of the TDBS signal amplitude is independent of the CAP amplitude dynamics caused by the diffraction/focusing of the CAP. This prediction correlates with earlier reported experimental observations [4]. In addition, the theory provides explanations to some existing experimental observations [5], which are different from the earlier suggested.

Conclusions – The developed theory predicts that, as far as the CAPs, photo-generated by the pump lase rpulses, and the probe laser beam are paraxial, the lateral resolution of the imaging could be enhanced by sharper focusing of the pump laser beam without diminishing the imaging depth and spectral resolution. The theory reveals earlier unexpected features in the TDBS that could be useful and advantageous in the applications of the TDBS imaging and microscopy technique for the fundamental and applied research.

Acknowledgments – This research is supported by the Agence Nationale de la Recherche [project <ANR-18-CE42-I2T2M>]

References

[1] V.E. Gusev, P. Ruello, Advances in applications of time-domain Brillouin scattering for nanoscale imaging, Appl. Phys. Rev. 5 (2018) 031101. https://doi.org/10.1063/1.5017241.

[2] H.-N. Lin, R.J. Stoner, H.J. Maris, J. Tauc, Phonon attenuation and velocity measurements in transparent materials by picosecond acoustic interferometry, J. Appl. Phys. 69 (1991) 3816. https://doi.org/10.1063/1.348958.

[3] V.E. Gusev, Contra-intuitive features of time-domain Brillouin scattering in collinear paraxial sound and light beams, Photoacoustics 20, 100205 (2020). https://doi.org/10.1016/j.pacs.2020.100205.

[4] T. Dehoux, K. Ishikawa, P.H. Otsuka, M. Tomoda, O. Matsuda, M. Fujiwara, S. Takeuchi, I.A. Veres, V.E. Gusev, O.B. Wright, Optical tracking of picosecond coherent phonon pulse focusing inside a sub-micron object, Light: Sci. Appl. 5 (2016) e16082. https://doi.org/10.1038/lsa.2016.82.

[5] T. Dehoux, N. Tsapis, B. Audoin, Relaxation dynamics in single polymer microcapsules probed with laser-generated GHz acoustic waves, Soft Matter 8 (2012) 2586. https://doi.org/10.1039/C2SM07146K.

Ultrafast photoacoustic assessment of mechanical properties in InAs nanowires

Gandolfi M[1,2,3], Peli S[4], Diego M[5], Danesi S[6,7], Giannetti C[3], Alessandri I[1,2,6], Zannier V[8], Demontis V[8], Rocci M[8], Beltram F[8], Sorba L[8], Roddaro S[9], Rossella F[8], Banfi F[4]*

(1) Department of Information Engineering, University of Brescia, Via Branze 38, 25023 Brescia, Italy
(2) CNR-INO (National Institute of Optics) Via Branze 45, 25023 Brescia, Italy
(3) Interdisciplinary Laboratories for Advanced Materials Physics (I-LAMP) & Dipartimento di Matematica e Fisica, Università Cattolica del Sacro Cuore, Brescia I-25121, Italy
(4) Elettra-Sincrotrone Trieste S.C.p.A., 34149 Basovizza, Italy
(5) Femtonanooptics Group, Université de Lyon, CNRS, Université Claude Bernard Lyon1, Institut Lumière Matière, F-69622 Villeurbanne, France
(6) INSTM-UdR Brescia, via Branze 38, 25123 Brescia, Italy
(7) Dept. of Mechanical and Industrial Engineering, Uni. di Brescia, via Branze 38, 25123 Brescia, Italy
(8) NEST, Scuola Normale Superiore & Istituto Nanoscienze-CNR, Piazza S. Silvestro, I-56127 Pisa, Italy
(9) Dipartimento di Fisica, Università di Pisa, Largo Bruno Pontecorvo 3, I-56127 Pisa, Italy

* Corresponding author's email: francesco.banfi@univ-lyon1.fr

Nanowires (NWs) have been at the forefront of research in nanoscience for over two decades because of the wide range of applications driven by their peculiar properties [1]. Among the latter, mechanical properties play a crucial role in view of any device development, but, despite the effort, a clear understanding is still lacking [2]. We report [3] on the ultrafast photoaoustics investigation of the mechanical properties of vertical Wurtzite InAs NW. The assessment of the NW oscillation period versus NW length allows to properly access the elastic dispersion relation and to shed light on the long-standing problem of InAs NW mechanical properties. Specifically, a benchmarked elastic matrix is provided. A novel mechanism, triggering the mechanical oscillations, is unveiled. The nanowire oscillations originate from an impulsive "hammer-like" excitation triggered in the substrate and propagating in a wave-like motion into the NW. This mechanism constitutes a new paradigm, being at variance with respect to direct excitation mechanisms, as commonly encountered in ultrafast experiments on a plethora of nanosystems. The present rationalization of the genesis of the mechanical oscillations impacts ultrafast opto-mechanical applications at large and will contribute designing them beyond a trial-and-error approach.

References

[1] C. Jia, Z. Lin, Y. Huang, X. Duan, Chemical reviews 119 (2919) 9074–9135.

[2] S.O. Mariager, D. Khakhulin, H.T. Lemke, K.S. Kjær, L. Guerin, L. Nuccio, C.B. Sørensen, M.M. Nielsen, R. Feidenhans'l, Nano Letters, 10 (2010) 2461–2465.

[3] S. Peli, E. Cavaliere, G. Benetti, M. Gandolfi, M. Chiodi, C. Cancellieri, C. Giannetti, G. Ferrini, L. Gavioli, F. Banfi, The Journal of Physical Chemistry C, 120 (2016) 8.

[3] M. Gandolfi, S. Peli, M. Diego, S. Danesi, C. Giannetti, I. Alessandri, V. Zannier, V. Demontis, M. Rocci, F. Beltram, L. Sorba, S. Roddaro, F. Rossella F. Banfi, *submitted*.

Detection of coherent acoustic phonons in thin gold films by surface plasmon resonance

Noll F[(1,2)*], Krauß N[(2)], Gusev V[(3)], Dekorsy T[(2,4)], Hettich M[(1,2)]

(1) Research Center For Non-Destructive Testing GmbH (RECENDT), Altenberger Straße 69, Linz, Austria
(2) Department of Physics, University of Konstanz, 78464 Konstanz, Germany
(3) Laboratoire d'Acoustique de l'Université du Mans (LAUM), UMR 6613, Institut d'Acoustique - Graduate
(4) German Aerospace Center, Institute of Technical Physics, Pfaffenwaldring 38-40, 70569 Stuttgart, Germany

*Corresponding author's email: felix.noll@recendt.at

Background – Elastic properties of thin metal films have been investigated in detail by optical pump-probe methods that detect changes in the reflectivity of the material due to mechanical strain. However, for measurements based on photoelastically induced changes in reflectivity, the small signals often pose a significant challenge. Detection in surface plasmon resonance (SPR), which is highly sensitive to changes in the metal dielectric function, has been used to substantially increase the signal to noise ratio [1]. This method further allows for the separation of the real and imaginary part of the temporal dynamics in the materials permittivity [2]. Here, we use a combination of asynchronous optical sampling and detection in SPR geometry to further investigate the potential applications in picosecond ultrasonics.

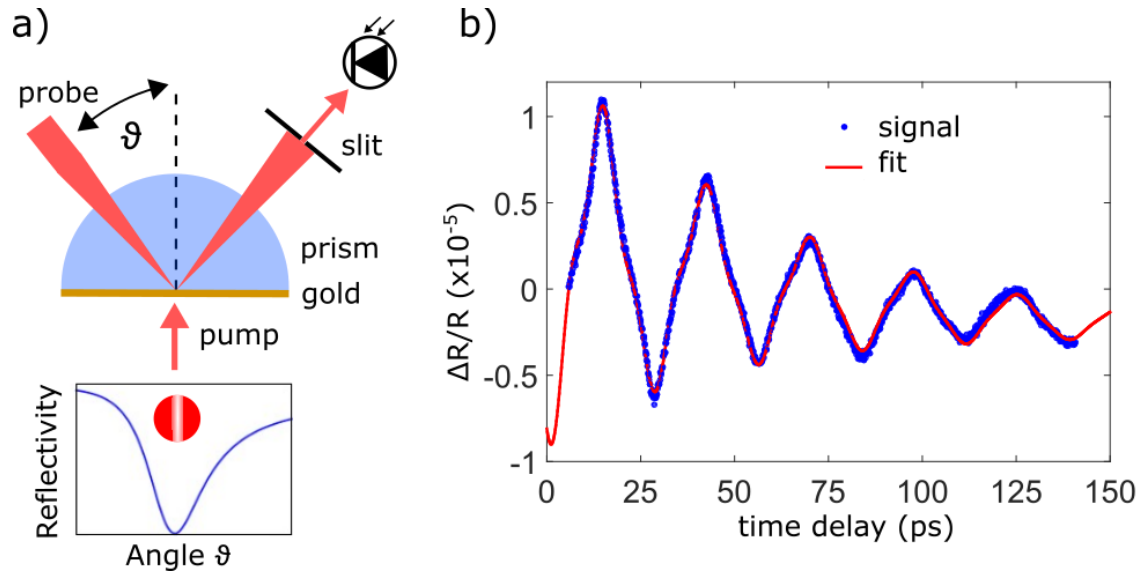

Fig. 1. a) Setup with SPR resonance curve and beam cross section b) Time domain signal of coherent longitudinal phonons

Methods – The principle of the measurements is depicted in Fig. 1. Thin gold films in the range of 30 to 50 nm are evaporated on a glass prism. The coherent acoustic phonon dynamics are optically excited from the air side and detected in Kretschmann configuration, i.e., from the glass side under SPR conditions. A slit is used to select an angle interval for detection. Coherent acoustic phonons in the gold film lead to changes in the plasmon resonance. By measuring at different positions of the SPR curve,

i.e., at different angles, the dependence of the plasmon resonance on the real and imaginary part of the permittivity can be used to separate the respective contributions.

Results – We observe Eigenmodes of the thickness oscillation up to the 7th harmonic. Through comparison of the lifetime of the first and third harmonic we can eliminate the influence of the dominant damping mechanism of transmission to the substrate and access the material intrinsic damping. Further, angle resolved measurements show a high sensitivity of the signal amplitude to changes in the real part of the dielectric function, indicating that the coherent acoustic phonons have only negligible influence on the imaginary part of the dielectric permittivity.

Conclusions – A highly sensitive approach to the detection of acoustic phonons in thin metal films is demonstrated. We find increased damping for higher order thickness modes which indicates the influence of intrinsic damping mechanisms. Further, we find the coherent acoustic phonons to mostly alter the real part of the dielectric permittivity with no detectable influence on the imaginary part. With improvements, this method could yield absolute values of the change in dielectric permittivity through mechanical strain.

References

[1] J. Wang, J. Wu, C. Guo, Resolving dynamics of acoustic phonons by surface plasmons, Opt. Lett. 32 (2007) 719. https://doi.org/10.1364/OL.32.000719.

[2] A. Devizis, V. Gulbinas, Ultrafast dynamics of the real and imaginary permittivity parts of a photoexcited silver layer revealed by surface plasmon resonance, Appl. Opt. 47 (2008) 1632-1637. https://doi.org/10.1364/AO.47.001632 .

Temperature dependent elastic properties and glass transition of nanometric PMMA films by picosecond ultrasonics

Brick D[(1)], Hofstetter M[(1)] , Stritt P[(1)], Rinder J[(1)], Gusev V[(2)], Dekorsy T[(1,3)] , Hettich M[(1,4)*]

(1) Department of Physics, University of Konstanz, 78464 Konstanz, Germany
(2) Laboratoire d'Acoustique de l'Université du Mans (LAUM), UMR 6613, Institut d'Acoustique - Graduate School (IA-GS), CNRS, Le Mans Université, Av. O. Messiaen, 72085 Le Mans, France
(3) Institute of Technical Physics, German Aerospace Center, Pfaffenwaldring 38-40, 70569 Stuttgart, Germany
(4) Research Center For Non-Destructive Testing GmbH (RECENDT), Altenberger Straße 69, Linz, Austria

*Corresponding author's email: mike.hettich@recendt.at

Background – Temperature dependent properties of polymer materials are crucial informations for many applications. A prime example is the glass transition observed between the glassy and rubbery state in polymeric materials. Despite the many developments to measure these quantities in a wide variety of systems from bulk to nanometric films complementary techniques are still of interest in the advent of newly emerging hybrid materials. The idea to use picosecond ultrasonics as a tool for monitoring temperature dependent properties and in particular the glass transition was proposed [1] already early in the beginning of the field. However, only just recently first demonstrations [2-3] emerged. Here, we want to add another approach to the toolset of picosecond ultrasonics that allows to determine the glass transition temperature in soft materials and yields information about temperature dependent film properties.

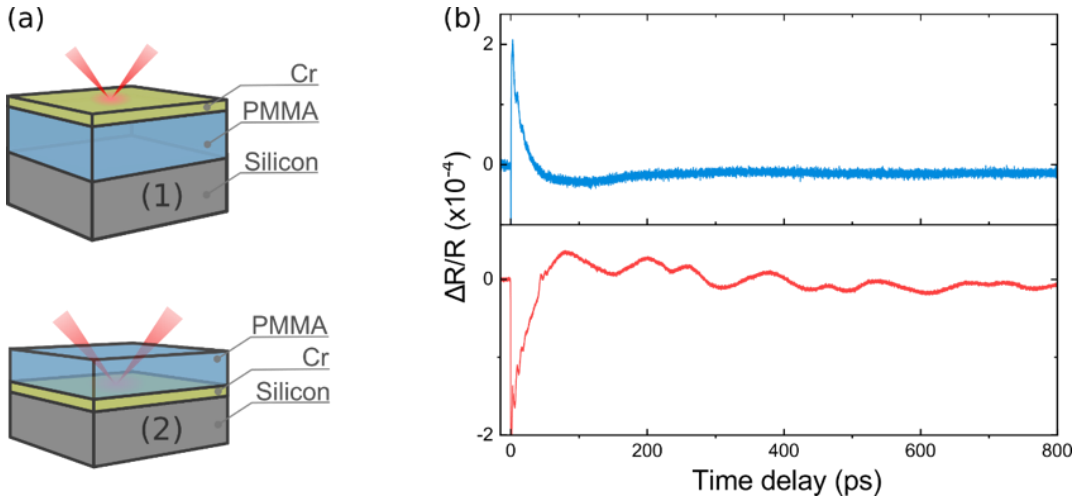

Fig. 1. a) Sketch of sample geometries b) Corresponding time domain signals

Methods – We employ picosecond ultrasonics, based on a femtosecond-resolved pump-probe method, to the investigation of thin PMMA films with thicknesses ranging from 458-32nm. The pump-probe scheme is realized by asynchronous optical sampling. We tested two different sample configurations aiming at different working regimes: pulse-echo and acoustic eigenmode characterization. The

thickness of the spin-coated PMMA films was additionally measured by ellipsometry. Chromium thin films were added to the sample structure by thermal evaporation as opto-acoustic transducers.

Results – As an initial step we compared the signal of the two sample configurations in Fig. 1(a) and (b). We found no clear indication of measurable pulse echoes in configuration I but strong oscillatory components for configuration II. These correspond to the longitudinal acoustic eigenmodes of the PMMA films. In a next step we tracked the individual modes during temperature dependent measurements, i.e. heating of the sample above the expected glass transition temperature. We found a distinct shift of the modes towards lower frequencies and a kink in the temperature-frequency slopes as a direct indicator for the glass transition temperature for all PMMA thicknesses. WE supported these findings by a further analysis based on the assumption of a negligible influence of thickness changes below the glass transition temperature. Additionally the observation of higher order modes provides a convenient way to cross check obtained fitting result of the data.

Conclusions – We observed closed organ pipe modes in thin PMMA layers and tracked their temperature dependent behaviour across the glass transition temperature. The glass transition is observable by a kink in temperature-frequency slopes. We also discuss the current issues in this configuration arising from spurious heating and difficulties arising in the data evaluation due to mode shifts and possible improvements to the presented methodology

References

[1] C.J. Morath, H.J. Maris, Phonon attenuation in amorphous solids studied by picosecond ultrasonics, Phys. Rev. B. 54 (1996) 203. https://doi.org/10.1103//PhysRevB.54.203.

[2] C. Klieber, V.E. Gusev, T. Pezeril, K.A. Nelson, Nonlinear acoustics at GHz frequencies in a viscoelastic fragile glass former, Phys. Rev. Lett. 114 (2015) 1–5. https://doi.org/10.1103/PhysRevLett.114.065701.

[3] H.D. Boggiano, R. Berté, A.F. Scarpettini, A.F. Scarpettini, E. Cortés, S.A. Maier, S.A. Maier, A. V. Bragas, Determination of Nanoscale Mechanical Properties of Polymers via Plasmonic Nanoantennas, ACS Photonics. 7 (2020) 1403–1409. https://doi.org/10.1021/acsphotonics.0c00631.

Development of models for the study of heat transport in ultra-thin layers by transient grating spectroscopy

Aguilar-Jimenez JA[(1)*], Pech-May NW[(2)], Forereo-Sandoval IY[(3)], Alvarado-Gil JJ[(1)]

(1) Deparment of Applied physics, CINVESTAV Mérida, Yucatán, México

(2) Bundesanstalt für Materialforschung und -prüfung (BAM), Berlin, Germany

(3) Institut Pprime, CNRS, Université de Poitiers, Futuroscope Chasseneuil, France

Corresponding author's email: arturo.aguilar@cinvestav.mx

Background – In Transient Grating Spectroscopy (TG), short laser pulses impinging on a sample, create a diffraction pattern on the surface. By analysing, the temporal decay of the temperature in the grating allows to analyse heat transport of the material. Previous studies have shown how thermal decays are sensitive to the grating period size for semi-infinite opaque materials [1,2]. In this work, the development of models to analyse the dynamical heat transport properties (thermal diffusivity and thermal effusivity) in opaque solid materials, using Transient Grating Spectroscopy, is presented. This approach allowed us to determine which thermal properties could be measured, using a specific configuration for thermal contrast, time scale, thermal properties of the layers, as well as grating period for multi-layered systems.

Methods – Heat transport equation for multi-layered systems were solved using appropriate boundary conditions and using the Fourier and Laplace transforms. As a result of complexity of the obtained solutions in Laplace space, the analysis of the temperature in time space was performed applying numerical algorithms to calculate the inverse Laplace transform of the solutions. Using this method, simulations of the thermal profiles in two and three-layer systems, were performed. The special case of glass, molybdenum, stainless steel, polyester-resin were considered.

Results and Conclusions – Figure 1 shows a simulation for two layer system with TG period of 25 μm and a first layer of 50 nm for materials with different themal diffusivities, polyester resin (left), stainless steel (center) and molybdenum (right). The parameter R12 represent the effusivities rate between the first and second layer given by the expression $R_{12} = (e_1 - e_2)/(e_1 + e_2)$. It is possible to observe as the thermal diffusivity of the first layer increases, the technique loses sensitivity in measuring smaller thicknesses, as in the case of molybdenum, where only the substrate is observed figure 1 (right).

Additionally, figure 2 (right) present a thermal decay for three-layer system of gold as a first layer, glass as a second layer and a substrate of stainless steel where it is possible to notice the system's sensitivity of the second layer for thermal diffusivity, where the peak of maximum sensitivity is at 10 ns in figure 2 (left).

Our results how the thickness of the illuminated layer and the kind of substrate affect the thermal decay signal giving us an idea of how the transient grating experiments should be performed to be able to reliably measure the thermal properties for ultrathin layer deposited on different kinds of substrates. It is important to emphasize how the technique is blind for materials with high thermal diffusivity. Therefore, these materials can be used as a coating for non-opaque materials and thus use the models

shown in this work.

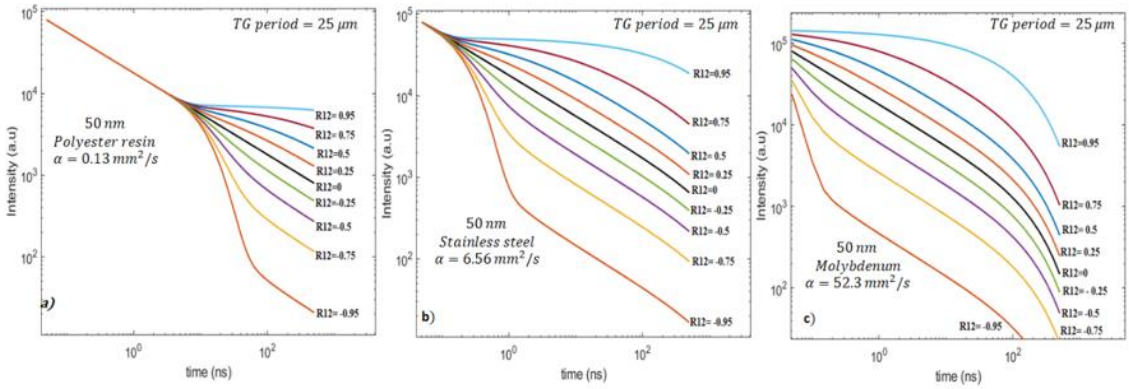

Fig. 7. Thermal decay for 50 nm of Polyester (left), Stainless steel (center) and Molybdenum (right). The parameter R21 goes from -1 to 1 showing the thermal contrast between the thin film and the substrate. Molybdenum is not visible for the technique.

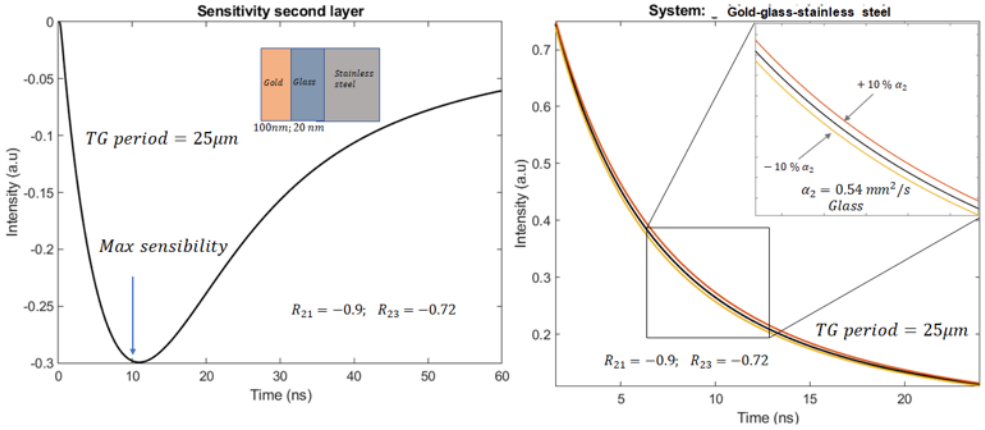

Fig. 8. Thermal decay of three layers system gold(100nm)-resin(20nm)-stainless steel, the first layer has no contribution and allows sensibility for the second layer (thermal diffusivity). (Left) shows the maximum peak of sensibility is between 50 and 100 ns.

References

[1] Vega-Flick et al., Thermal transport in suspended silicon membranes measured by laser-induced transient gratings, AIP Adv. 6:12 (2016) 1–23.

[2] J.A. Johnson et al., Phase-controlled, heterodyne laser-induced transient grating measurements of thermal transport properties in opaque material, J. Appl. Phys. 111:2 (2012).

07
Biomedical imaging and applications

Three-dimensional quantitative optoacoustic tomography

Oraevsky AA(1,2)*

(1) TomoWave Laboratories, Inc. Houston, Texas
(2) Department of Biomedical Engineering, The University of Houston, Houston, Texas

*Corresponding author's email: AO@tomowave.com

Background – The main clinical merit of three-dimensional (3D) optoacoustic tomography (OAT) is its potential capability to provide quantitative volumetric maps of molecular distributions [1]. With blood being pivotal component of human system, quantitative images of the total hemoglobin and blood oxygen saturation can help differentiate abnormal tissues, such as cancer, from normally functioning tissues These functional images have been the subject of extensive research since the first functional photoacoustic microscopy images were demonstrated by X. Wang and L. Wang in 2003 [2]. The goal of the functional imaging is to convert optoacoustic images of the absorbed optical energy, dependent on spatial distribution of the effective optical fluence, into the images of the optical absorption coefficient, independent on heterogeneous distribution of the optical fluence in the laser illuminated volume [1]. The main deficiency of the current methods of qOAT is in the model-based computations applied for the forward problem of the optical fluence distribution through the depth of tissue without *apriori* knowledge of the tissue optical properties. Furthermore, only two-dimensional (2D) *in vivo* functional images were reported using linear spectral unmixing of the optoacoustic signals obtained at multiple wavelengths [3]. While this approach produced an improved accuracy of functional parameters measured from 2D images, it has not yielded acceptable performance in 3D due to (i) the incapability to correct the detected signals for missing low frequencies, and (ii) application of a forward model based on representative (thus potentially inaccurate) values of tissue optical properties from literatures. In contrast, our approach is based on direct measurement of the effective optical attenuation coefficient as a function of the light penetration depth through the entire volume of tissue presented on optoacoustic images [4]. This purely empirical approach resulted in the first three-dimensional quantitatively accurate functional images of live tissue volumes [5].

Methods – We designed and assembled full view 3D optoacoustic tomography systems for preclinical research in small lab animals and clinical research in diagnostic imaging of breast cancer [6,7].

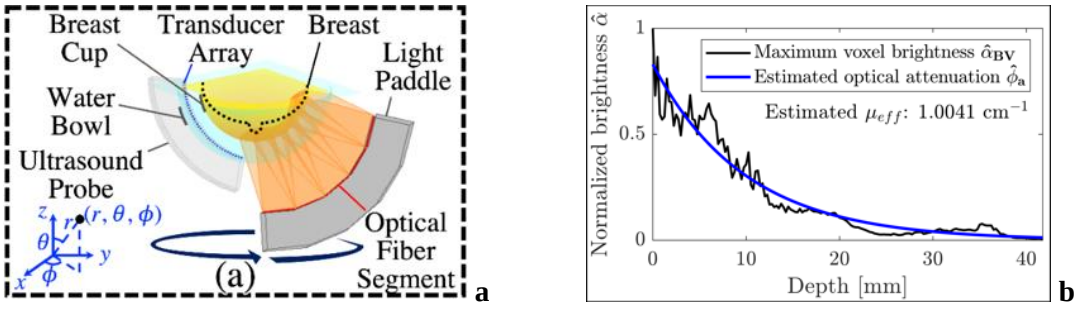

Figure 1. **(a)** Schematic diagram of the laser illumination and acoustic detection implemented in the 3D full view optoacoustic imaging system designed for detection of breast cancer. **(b)** Typical optical attenuation curve measured experimentally from a 3D optoacoustic image acquired using an array of ultrawide-band ultrasonic transducers from breast of a patient at the wavelength of 757 nm. Similar curves have been measured from every point on the skin surface through the depth in the radial direction of light attenuation.

The first mandatory requirement of quantitative OptoAcoustic Tomography (qOAT) is that every point on the entire surface of the volume of interest is illuminated and optoacoustic signals are detected by transducers evenly placed on the spherical surface surrounding the volume of interest (see general schematic diagram in Fig 1a [4]. The major factor in our capability of quantitative optoacoustic tomography was the measurements of the exponential slope of the voxel brightness as a function of depth. This low frequency slope was measured only due to the fact we used ultrawide band ultrasonic transducers sensitive (see typical curve on Fig 1b).

The experimental protocol of functional (qOAT) required innovations and advanced implementation of the system hardware and algorithms of the signal processing and image reconstruction. After many years of research we have been able to achieve the following features of the proposed qOAT method: (1) obtain undistorted optoacoustic signals using ultrawide-band ultrasonic transducers and reversal of signal distortions by deconvolution of acousto-electrical impulse response (EIR) and spatial impulse response (SIR) [8]; (2) acquire coregistered images at two or more wavelengths using a newly designed fast switching the laser wavelengths with every pulse; (3) normalize optical fluence on the illuminated surface and through the volume of interest [4], generate images of the optical absorption coefficient; (4) calibrate images of the optical absorption coefficient using arterial blood as a tissue with well-defined optical properties; and finally (5) generate functional images of [tHb] and [SO2] [5].

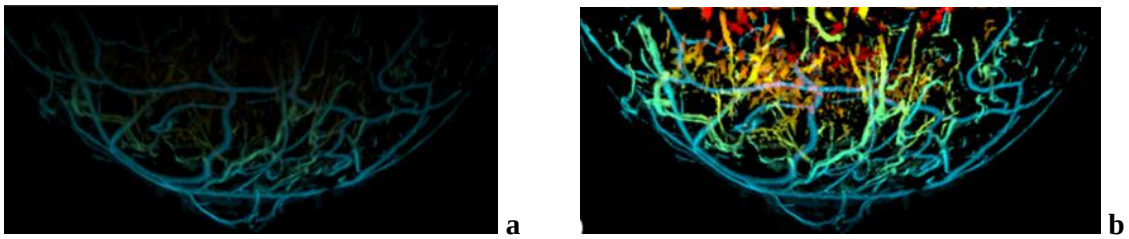

Figure 2. Maximum intensity projections of 3D full view clinical optoacoustic images obtained at the wavelength of 757 nm of a patient breast prior **(a)** and after **(b)** the optical fluence normalization on the surface and through the depth of 45 mm.

In our study, we acquired *in vivo* optoacoustic signals of the mouse at 757 nm (Hb) and 1064 nm (HbO2+H2O) using proprietary ultrawide-band ultrasonic transducers (50 kHz-8 MHz), and the images (i.e., distribution of the absorbed optical energy) were reconstructed incorporating transducer impulse response. The functional images of blood oxygen saturation [sO2] and the total hemoglobin [tHb] were estimated from the coregistered dual-wavelength images via the measurement data-driven normalization of the optical fluence distribution for each wavelength.

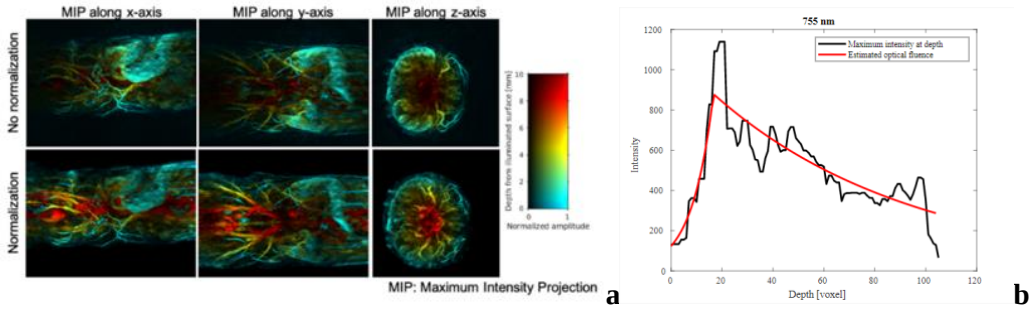

Figure 3. **(a)** Maximum intensity projections of 3D full view optoacoustic images obtained at the wavelength of 757 nm of a mouse body prior and after the optical fluence normalization on the surface and through the depth of the mouse; **(b)** Background absorbed optical energy measured from the experimental optoacoustic image acquired at 757 nm using an array of ultrawide-band ultrasonic transducers.

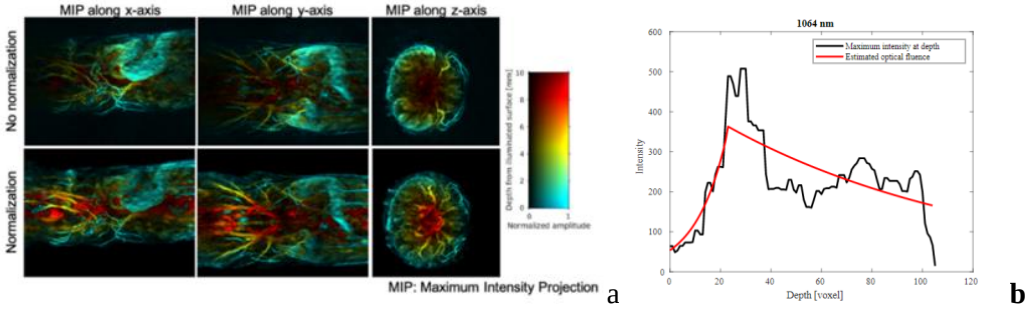

Figure 4. (a) Maximum intensity projections of 3D full view optoacoustic images obtained at the wavelength of 1064 nm of a mouse body prior and after the optical fluence normalization on the surface and through the depth of the mouse; (b) Background absorbed optical energy measured from the experimental optoacoustic image acquired at 1064 nm using an array of ultrawide-band ultrasonic transducers.

The reconstructed functional images reveal high-resolution details of anatomical structures through the entire mouse body. In the computed 3D functional images, arteries, veins and organs were separated based on the oxygen saturation estimates. Using a pair of artery (with assumed [sO2] of 100%) and a vein in a close proximity to each other, we have been able to perform absolute calibration of the venous [sO2], which we measured a value of 71%.

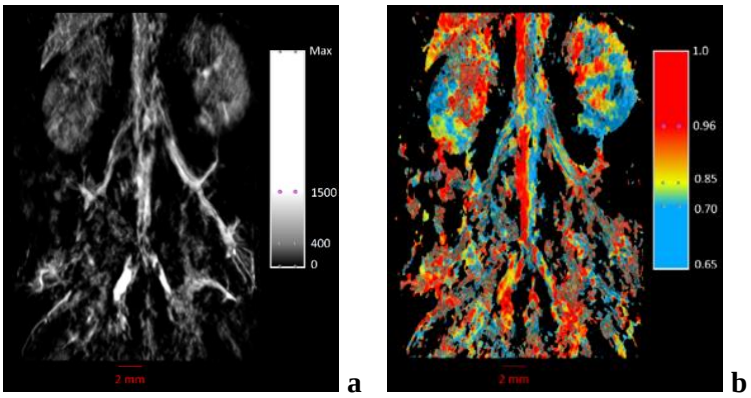

Figure 5. 2 mm thick slice of 3D full view quantitative optoacoustic images around the vena cava. **(a)** Image of the total hemoglobin and **(b)** image of the blood oxygen saturation.

Conclusions – While experimental method of the optical fluence normalization through the entire volume of live tissues requires further refinement through research, the first 3D volumetric functional images of [tHB] and [sO2] show viability of the proposed method for the 3D volumetric deep tissue functional imaging *in vivo*.

Acknowledgements – This lecture is a review of collaborative research performed over the period of 3 years by 3 teams from TomoWave Laboratories (A. Oraevsky, R. Su), University of Illinois (M. Anastasio, S. Park) and Washington University at St. Louis (U. Villa, F. Brooks). Clinical and preclinical three-dimensional optoacoustic tomography systems developed by TomoWave Laboratories with NIH grants R01CA167446, R44 CA110137, have been used in this work.

References

[1] A.A. Oraevsky, Optoacoustic Tomography: From Fundamentals to Diagnostic Imaging of Breast Cancer, in Biomedical Photonics Handbook, Second Edition: Fundamentals, Devices, and Techniques, ed. by T. Vo-Dinh, CRC Press, Boca Raton, Florida, 2014, Vol. PM222, Chapter 21, pp. 715-757.

[2] X. Wang, Y. Pang, G. Ku, X. Xie, G. Stoica, L.V. Wang: Noninvasive Laser-Induced Photoacoustic Tomography for Structural and Functional in Vivo Imaging of the Brain. Nature Biotechnology 21(2003) 803-806.

[3] B. Cox, J.G. Laufer, S.R. Arridge, P.C. Beard: Quantitative spectroscopic photoacoustic imaging: a review, J. Biomed. Opt. 17:6 (2012) 061202.

[4] S. Park, F.J. Brooks, U. Villa, R. Su, M.A. Anastasio, A.A. Oraevsky, Normalization of optical fluence distribution for three-dimensional functional optoacoustic tomography of the breast, J. Biomed. Opt. 27:3 (2022) 210367GR.

[5] R. Su, S. Park, U. Villa, M.A. Anastasio, A.A. Oraevsky, Functional Three-Dimensional Optoacoustic Tomography of Live Tissue, Photoacoustics 26 (2022) (*in review*).

[6] A. Oraevsky, R. Su, H. Nguyen, J. Moore, Y. Lou, S. Bhadra, L. Forte, M. Anastasio, W.T. Yang: Full-view 3D imaging system for functional and anatomical screening of the breast. Proc. SPIE 10494 (2018) 104942Y.

[7] A.V. Liopo, R. Su, A.A. Oraevsky: Melanin nanoparticles for optoacoustic imaging, Photoacoustics 3:1 (2015) 35-43.

[8] K. Wang, S.A. Ermilov, R. Su, H-P. Brecht, M.A. Anastasio, A.A. Oraevsky: An imaging model incorporating ultrasonic transducer properties for three-dimensional optoacoustic tomography. IEEE Trans Med Imaging 30:2 (2011) 203-214.

PLENARY SESSION

A photoacoustic-ultrasound transmission breast tomography system: system overview and first imaging results

Dantuma M[(1)], Lucka F[(2,3)], Kruitwagen SC[(4)], Bulthuis R[(1)], De Santi B[(1)], Javaherian A[(5)], Alink L[(6)], Pompe van Meerdervoort RP[(6)], Nanninga M[(6)], op't Root T[(6)], Budisky J[(7)], Bordovsky G[(7)], Coffy E[(8)], Kasponas T[(9)], Aarnink S[(4)], de Geus-Oei LF[(10,11)], Brochin F[(8)], Martinez T [(8)], Michailovas A[(9)], Muller-Kobold W[(6)], Jaros J[(7)], Veltman J[(1,12)], Cox B[(5)], Manohar S[(1)*]

(1) Multi-Modality Medical Imaging, TechMed Centre, University of Twente, Enschede, The Netherlands
(2) Computational Imaging group, Centrum Wiskunde en Informatica, Amsterdam, The Netherlands
(3) Department of Computer Science, University College London, London, United Kingdom
(4) Medisch Spectrum Twente Hospital, Enschede, The Netherlands
(5) Biomedical Ultrasound group, University College London, London, United Kingdom
(6) P.A. Imaging B.V., Enschede, The Netherlands
(7) Department of Computer Systems, Faculty of Information Technology, Brno University of Technology, Brno, Czech Republic
(8) Imasonic SAS, Besançon, France
(9) Ekspla UAB & FTMC- Center for Physical Sciences and technology, Vilnius, Lithuania
(10) Biomedical Photonic Imaging group, University of Twente, Enschede, The Netherlands
(11) Leiden University Medical Center (LUMC), Leiden, The Netherlands
(12) Ziekenhuisgroep Twente Hospital, Hengelo, The Netherlands

*Corresponding author's email: s.manohar@utwente.nl

We present a hybrid photoacoustic-ultrasound (PA-US) tomographic imaging system, developed within the European consortium PAMMOTH [1]. The system employs a hemispherical geometry with an imaging bowl filled with water into which the breast is positioned. The bowl has 512 ultrasound transducers distributed on its inside surface. Forty optical fibre bundles terminate at the inner surface of the bowl, distributed to illuminate the breast homogenously for photoacoustic excitation. At the proximal end, the fibre bundles are brought together and coupled to a dual laser-OPO system providing 5 nanosecond pulses in the wavelength range 680 - 1060 nm. In addition to functioning in reception mode for photoacoustic imaging, the transducers can be used in emission mode for ultrasound transmission imaging. During a measurement, the imaging bowl and its contents rotate around the breast, which is immobilized in a transparent cup, to acquire multiple projections. Photoacoustic reconstruction is performed using a full-wave inversion model; sound speed images are reconstructed using a bent-ray approach from transmission ultrasound data [2].

To unravel an optimal measurement sequence, in which optimized imaging performances are achieved within as short as possible measurement times, systematic tests were performed on test objects [3], a breast mimicking phantom [4] and healthy volunteers. We present the approach we followed to optimize the optimal measurement sequence of our system. Here, systematic tests on a test objects with sub-resolution PA sources allowed us to investigate the effect of the number of measurement projections and averages on the spatial resolution and signal-to-noise ratio. Multispectral PA measurements on a blood carrying breast phantom (as well as on healthy breasts) helped us to select the optimal excitation

wavelengths for accurate oxygen saturation estimations and large imaging depths. With US transmission measurements on another test object we assessed the accuracy of our system in measuring sound speed distributions. The same measurements in-vivo resulted in sound speeds matching breast tissues, which improves the PA imaging performance in the deep breast when applied in the PA inversion models.

We conclude by demonstrating the functionalities of the imaging system and its imaging capability on healthy volunteers. From the multispectral photoacoustic (PA) mode, we obtain angiographic breast structures in 3D throughout the breast, and provide a measure for the blood oxygen saturation. From the ultrasound (US) mode, the sound speed images serve to improve the accuracy of the PA reconstruction, and also provide morphological information which helps interpretation of the PA images. We touch upon future studies that we aim perform using this system.

References

[1] Photoacoustic Mammoscopy for evaluating screening-detected lesions in the breast (2022) https://www.pammoth-2020.eu/ (retrieved 6 June 2022)

[2] A. Javaherian, F. Lucka, B.T. Cox, Refraction-corrected ray-based inversion for three-dimensional ultrasound tomography of the breast. Inverse Problems 36:12 (2020) 125010.

[3] M. Dantuma, S.C. Kruitwagen, M.J. Weggemans, T.J. Op't Root, S. Manohar, Suite of 3D test objects for performance assessment of hybrid photoacoustic-ultrasound breast imaging systems. Journal of Biomed. Opt. 27:7 (2021) 074709.

[4] M. Dantuma, S.C. Kruitwagen, J. Ortega-Julia, R.P.P. van Meerdervoort, S. Manohar, Tunable blood oxygenation in the vascular anatomy of a semi-anthropomorphic photoacoustic breast phantom. Journal of Biomed. Opt. 26:3 (2021) 036003.

KEYNOTE SPEAKER

Structured illumination photoacoustic imaging using Hadamard encoding

Paltauf G(1)*, Torke PR(1), Mack F(1), Nuster R(1)

(1) Department of Physics, University of Graz, Graz, Austria

*Corresponding author's email: guenther.paltauf@uni-graz.at

Photoacoustic microscopy with optical resolution (OR-PAM) is a method to visualize structures with optical absorption contrast in biological samples [1]. To acquire images, short laser pulses are focused with an objective into the target and are scanned over the imaging plane. The generated acoustic signals are received by an ultrasound sensor. The optical focusing gives a lateral resolution comparable to purely optical microscopy. Due to the small focal area, high fluence values are achieved within the absorbing structures (e.g. blood capillaries), ranging up to 1 J/cm², even if the pulse energy is in the nanojoule range and the radiant exposure on the sample surface is below the ANSI limit for biological tissue. In some biomedical applications, such high fluence values are not desirable or cannot be generated, either due to the potential damage to delicate tissue structures or due to the poor focusing capabilities of the light source.

To enable OR-PAM with much lower fluence values, we propose a technique based on structured illumination of the sample and integrated detection of the resulting acoustic wave. Using methods from computational ghost imaging (GI), the parallel detection of acoustic signals generated over an extended area should give higher signals and better signal-to-noise ratio (SNR) than conventional pixelwise scanning, even if the applied fluence is lower [2]. This is the result of the multiplex advantage, which has been exploited in various imaging scenarios [3,4].

Structured illumination is achieved by projecting patterns obtained from a Hadamard matrix via a digital micromirror device (DMD) onto the object. For an n x n-pixel image, the patterns are obtained from a Hadamard matrix **H** of size n^2 x n^2. After replacing elements equal to -1 by zeros, lines of the matrix are reformatted to the required n x n size for projection. With a depth-dependent fluence (z), the energy density W and initial pressure p_0 generated by heating an object with an absorption coefficient distribution μ_a are given by

$$p_0(x,y,z) = \Gamma W(x,y,z) = \Gamma \Psi(z)\, h_i(x,y)\, \mu_a(x,y,z) \qquad \text{Eqn. 1}$$

where $h_i(x,y)$ is the pattern generated by the i-th row of **H** and is the Grüneisen parameter. Assuming that the recorded pressure signal $s(t)$ is proportional to the initial pressure $p_0(x,y,z = c_s t)$, where c_s is the speed of sound, an image representing the energy density distribution at given depth is reconstructed by

$$I(x,y,z) = \sum_n h_n(x,y)\, s_n\left(t = z/c_s\right) \qquad \text{Eqn. 2}$$

For better performance, the differential ghost imaging method was applied [5], where s_n is the difference between two signals recorded after projecting the original pattern and its inverse, where zeros and ones are swapped. Equation (2) corresponds to a multiplication of the original matrix **H** with a signal representing a multiplication of **H** by the μ_a - distribution weighted with the depth-dependent fluence. Owing to the self-inverse property of **H**, this gives a close representation of the μ_a-distribution.

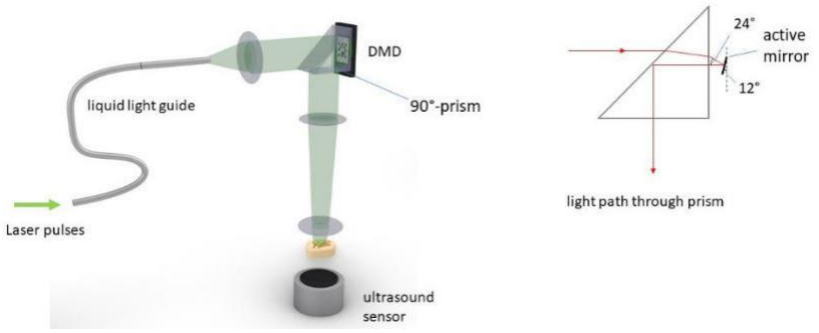

Fig. 1. Experimental setup for ghost imaging. The detail shows how light is reflected by an active mirror on the DMD and redirected via the prism to the sample. An ultrasound sensor with a center frequency of 3.5 MHz records the generated pressure signals.

To test the imaging method, pulses from a 515-nm, nanosecond-pulsed laser were projected via a DMD and an objective lens onto a phantom consisting of black carbon fibers embedded in transparent gel-wax. The setup is shown schematically in Fig.1. Projected patterns had a size of 64 x 64 pixel. A reconstruction for a selected depth is shown in Fig.2a. To demonstrate the performance of the GI approach in comparison with conventional pixelwise scanning, the same phantom was imaged again, activating only a single pixel on the DMD at a time. The result is shown in Fig.2b. In both experiments, the fluence arriving at the absorbing target was about 1.3 mJ/cm². Figure 3c shows the maximum amplitude projection (MAP) image together with a photograph of the phantom.

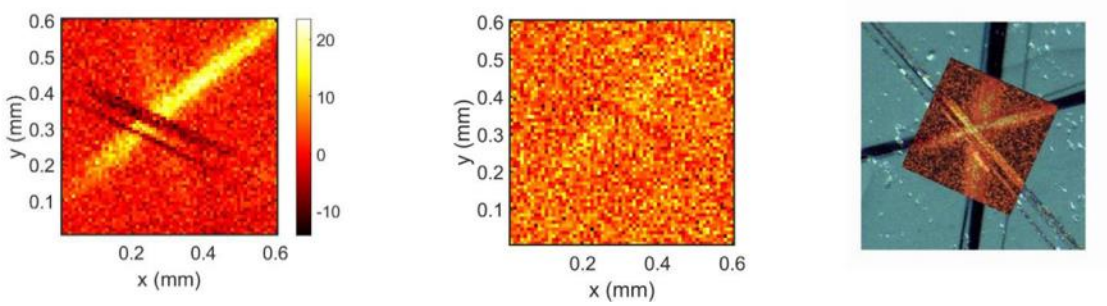

Fig. 2. Images of a carbon fiber phantom with (a) the GI technique, (b) using single-pixel scanning. (c) Shows the phantom, together with a maximum amplitude projection of the GI reconstruction.

These results demonstrate that despite the extremely low incident fluence the GI method still gives satisfactory imaging contrast in comparison to the pixelwise raster scan, where hardly any structures can be perceived. Since the fiber bundles are separated in depth by less than the axial resolution of the ultrasound sensor, the image in Fig. 2a is overlain by an artifact generated by a bundle located a different depth.

The expected depth range of the GI technique in real tissue was investigated in a simulation, where a Monte Carlo method was used to calculate the initial pressure distribution in a phantom containing “blood vessels” at different depths. A detail of the energy density distribution in the phantom is displayed in Fig.3a with logarithmic scaling. In this section, the structured illumination can be observed to a depth of about 400 µm. Nevertheless, as the MAP in Fig.3b demonstrates, even structures at a depth of 760 µm can be recognized in the reconstruction, albeit with very low contrast.

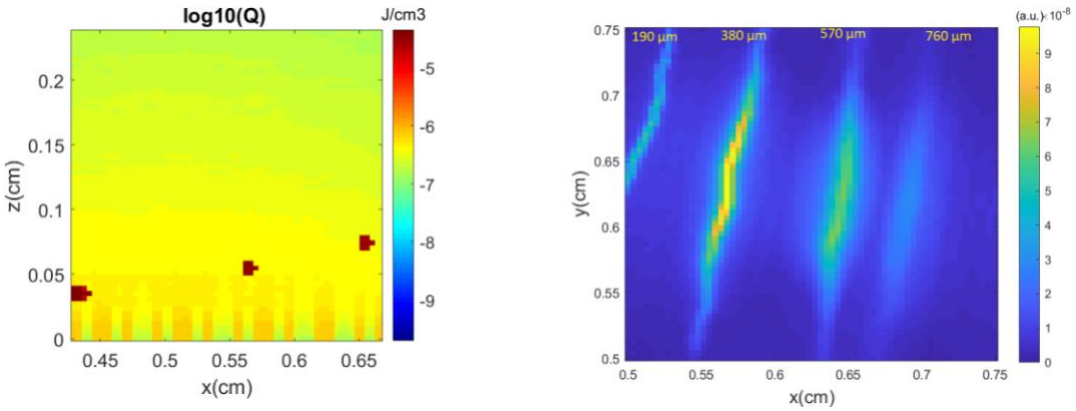

Fig. 3. Simulation results, showing GI of a vessel-phantom. (a) Cross sectional image of the energy density distribution, showing a close-up of the phantom with three "blood vessels" at different depths. (b) Maximum amplitude projection of the reconstructed image, showing some contrast even for the deep vessel located at 760 µm depth.

In conclusion, structured illumination combined with GI reconstruction is able to generate images with much better contrast compared to a raster scan image at the same radiant exposure. This could be of practical use in applications where the exposure is limited, either because of safety precautions or of the properties of the light source. In particular, photoacoustic GI will enable the use of light sources, which cannot be focused to the small spot size required in conventional OR-PAM.

Acknowledgments – This work has been supported by the Austrian Research Promotion Agency (FFG), Project No. 874787.

References

[1] S. Jeon, J. Kim, D. Lee, J. W. Baik, and C. Kim, Review on practical photoacoustic microscopy, Photoacoustics 15 (2019) 10014. https://doi.org/10.1016/j.pacs.2019.100141.

[2] O. Katz, Y. Bromberg, Y. Silberberg, Compressive ghost imaging, Appl. Phys. Lett. 95 (2009) 131110. https://doi.org/10.1063/1.3238296.

[3] J. Liang, L. Gao, C. Li, and L. V. Wang, Spatially Fourier-encoded photoacoustic microscopy using a digital micromirror device, Optics letters 39 (2014) 430–433. https://doi.org/10.1364/OL.39.000430.

[4] T.J. Lane, D. Ratner, What are the advantages of ghost imaging? Multiplexing for x-ray and electron imaging, Opt.Express 28 (2020) 5898–5918. https://doi.org/10.1364/OE.379503.

[5] B. Sun, M.P. Edgar, R. Bowman, L.E. Vittert, S. Welsh, A. Bowman, MJ. Padgett, Differential Computational Ghost Imaging, in Imaging and Applied Optics, OSA Technical Digest (online), CTu1C.4.

KEYNOTE SPEAKER

Triple modality transmission-reflection optoacoustic ultrasound (TROPUS) computed tomography of small animals

Lafci B[(1,2)], Herraiz JL[(3,4)], Deán-Ben XL[(1,2)], Razansky D[(1,2)*]

(1) Institute of Pharmacology and Toxicology and Institute for Biomedical Engineering, Faculty of Medicine, University of Zurich, Switzerland
(2) Institute for Biomedical Engineering, Department of Information Technology and Electrical Engineering, ETH Zurich, Switzerland
(3) Nuclear Physics Group and IPARCOS, Complutense University of Madrid, Madrid, Spain
(4) Health Research Institute of Hospital Clínico San Carlos (IdISSC), Madrid, Spain

*Corresponding author's email: daniel.razansky@uzh.ch

Introduction – Rapid progress in the development of multispectral optoacoustic tomography techniques has enabled unprecedented insights into biological dynamics and molecular processes *in vivo* and noninvasively at penetration and spatiotemporal scales not covered by modern optical microscopy methods [1]. Ultrasound imaging provides highly complementary information on elastic and functional tissue properties and further aids in enhancing optoacoustic image quality [2]. We devised a hybrid transmission-reflection optoacoustic ultrasound (TROPUS) small animal imaging platform that combines optoacoustic tomography with both reflection- and transmission-mode ultrasound computed tomography. The system features full-view cross-sectional tomographic imaging geometry for concomitant noninvasive mapping of the absorbed optical energy, acoustic reflectivity, speed of sound and acoustic attenuation in whole live mice with submillimeter resolution and unrivaled image quality (Fig. 1) [3].

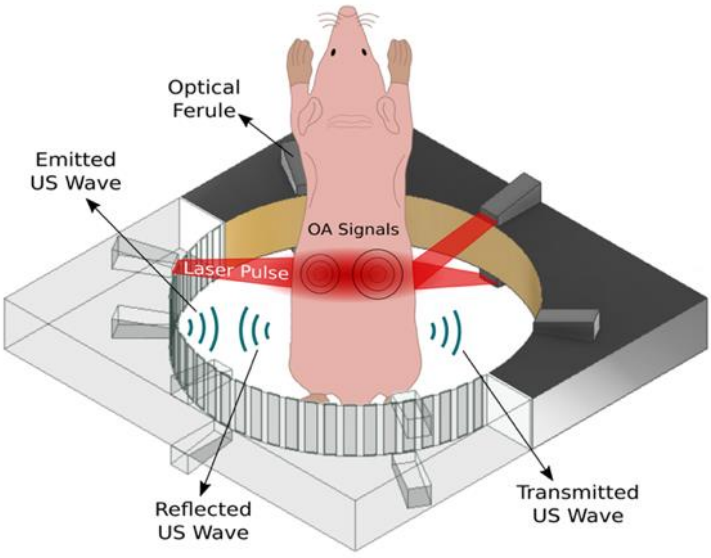

Fig. 1. The tri-modal transmission reflection optoacoustic ultrasound (TROPUS) imaging platform featuring laser excitation and acquisition in the optoacoustic (OA) imaging mode, reflection ultrasound computed tomography (RUCT) mode and transmission ultrasound computed tomography (TUCT) speed of sound (SoS) imaging mode.

Methods – The hybrid TROPUS imaging system consist of four main components, namely, a circular transducer array (512 elements, 40 mm radius, 5 MHz central frequency), a nanosecond pumped laser source, a data acquisition system (DAQ) and a workstation for data saving/processing. The laser wavelength was tuned between 700 and 1000 nm with step size of 20 nm for multispectral OA acquisition. OA images were reconstructed using GPU-accelerated 3D filtered back-projection algorithm [4]. Ultrasound (US) data acquisition was performed using synthetic transmit aperture (STA) technique as elaborated elsewhere [5]. Reflection ultrasound computed tomography (RUCT) images were beamformed by delay and sum algorithm and then compounded to create final high contrast image. Transmission ultrasound computed tomography (TUCT) images representing speed-of-sound (SoS) in tissues were reconstructed from transmitted US waves through the body using full wave inversion method [6].

Results – *In vivo* mouse imaging experiments revealed fine details on the organ parenchyma, vascularization, tissue reflectivity, density and stiffness (Fig. 2). We further used the speed of sound maps retrieved by the transmission ultrasound tomography to improve optoacoustic reconstructions via two-compartment modeling. We further demonstrated the capabilities of TROPUS imaging for detection and assessment of non-alcoholic fatty liver disease (NAFLD), which refers to the early stage of liver fibrosis resulting from accumulation of lipid and scarring in liver tissues. Early detection and treatment of NAFLD is paramount in preventing long-term liver damage. Both *ex vivo* and *in vivo* results show that TROPUS system can be used for detection and assessment of NAFLD development in liver tissues. Specifically, the regions of interest were segmented from RUCT images and the lipid content of liver tissues was quantified by multispectral OA images. In addition, SoS images provided quantitative readings of lipid accumulation ratios in liver tissues.

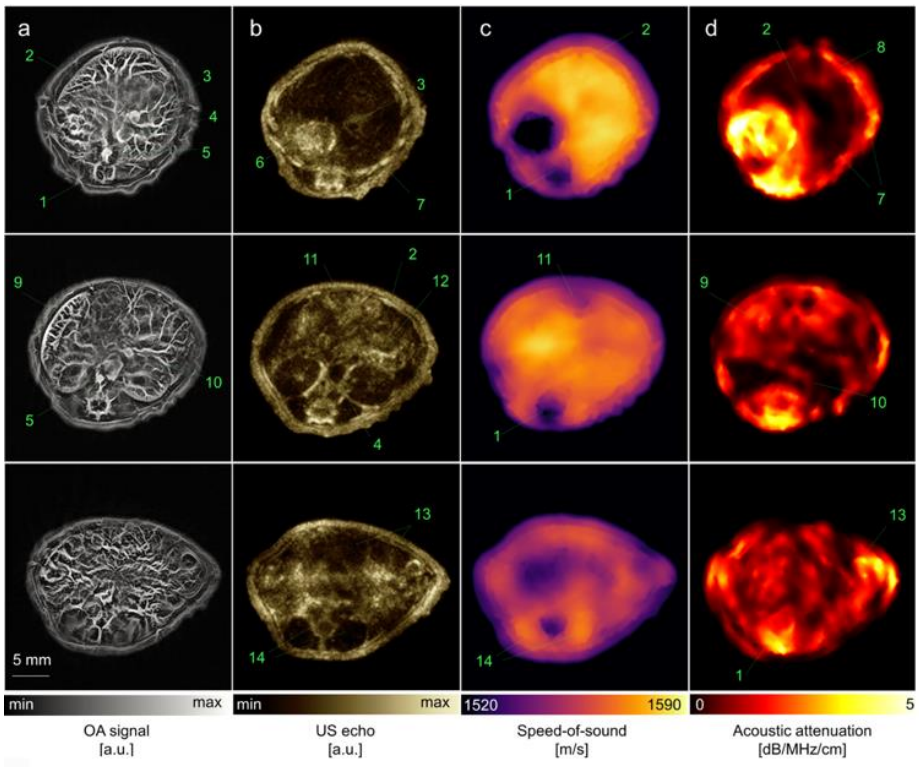

Fig. 2. Hybrid transmission-reflection optoacoustic ultrasound (TROPUS) whole-body mouse imaging. **(a)** Representative cross-sections acquired in the optoacoustic mode. **(b)** The corresponding reflection-mode ultrasound images. **(c), (d)** The corresponding transmission-mode ultrasound images showing the distribution of the speed of sound and acoustic attenuation, respectively. Annotations: 1: spinal cord; 2: liver; 3: vena porta; 4: vena cava; 5: aorta; 6: stomach; 7: ribs; 8: skin/fat layer; 9: spleen; 10: right kidney; 11: cecum; 12: pancreas; 13: intestines; 14: muscle.

Conclusions – The newly developed synergistic multimodal TROPUS combination offers unmatched capabilities for imaging multiple tissue properties and biomarkers with high resolution, penetration and contrast. The results further indicate that the proposed approach is suitable for assessing the NAFLD development in preclinical models.

Acknowledgements – Financial support is acknowledged from the European Research Council under grant ERC-2015-CoG-682379 and the Swiss Data Science Center grant C19-04.

References

[1] X.L. Deán-Ben, S. Gottschalk, B. McLarney, S. Shoham, D. Razansky. Advanced optoacoustic methods for multi-scale imaging of in vivo dynamics. Chem. Soc. Rev. 46 (2017) 2158-2198.

[2] E. Merčep, N.C. Burton, J. Claussen, D. Razansky. Whole-body live mouse imaging by hybrid reflection-mode ultrasound and optoacoustic tomography. Opt. Lett. 40 (2015) 4643-4646.

[3] E. Merčep, J.L. Herraiz, X.L. Deán-Ben, D. Razansky. Transmission-reflection optoacoustic ultrasound (TROPUS) computed tomography of small animals. Light Sci. Appl. 8, 18 (2019).

[4] X.L. Deán-Ben, A. Oezbek, D. Razansky. Volumetric real-time tracking of peripheral human vasculature with GPU-accelerated three-dimensional optoacoustic tomography. IEEE Trans. Med. Imag. 232 (2013) 2050-2055.

[5] B. Lafci, E. Merčep, J.L. Herraiz, X.L. Deán-Ben, D. Razansky. Noninvasive multiparametric characterization of mammary tumors with transmission-reflection optoacoustic ultrasound. Neoplasia 22(12) (2020) 770-777.

[6] M. Pérez-Liva, J.L. Herraiz, J.M. Udías, E. Miller, B.T. Cox, B.E. Treeby. Time domain reconstruction of sound speed and attenuation in ultrasound computed tomography using full wave inversion. J. Acoust. Soc. Am. 141 (2017)1595-1604.

KEYNOTE SPEAKER

Molecular-specific imaging of tissue with photo-thermal optical coherence tomography

Salimi MH[(1)*], Villiger M[(1)], Tabatabaei N[(1)]

(1) Department of Mechanical Engineering, York University, Toronto, ON, Canada

*Corresponding author's email: nima.tabatabaei@lassonde.yorku.ca

Photothermal optical coherence tomography (PT-OCT) is a functional extension of conventional OCT with the potential to generate quantitative maps of molecular absorptions co-registered with the micron-resolution structural tomograms of OCT. Realizing this potential, however, requires refined understanding of the acquired signals and their dependence on system and sample parameters. Such understanding enables implementation of effective strategies for decoupling the various physical effects involved to obtain quantitative measures of molecular concentration/absorption. In this talk, we present an analytical model that considers the opto-thermo-mechanical properties of multi-layered samples in 3-D space, eliminating several assumptions that have been limiting previous models. The model is validated through experimental parametric studies, investigating the effect of sample and system parameters on acquired signals. The proposed model enables better understanding of the effects of system parameters and tissue opto-thermo-mechanical properties on experimental signals. Informed optimization of experimentation strategies is another outcome of proposed model, through which we designed and developed a spectroscopic transient-mode PT-OCT system for detection and differentiation of collagen and lipid at video rate.

Background – OCT is an interferometric optical imaging method capable of providing high-resolution (~10μm) cross-sectional images of tissue structures. The diagnostic value of OCT, however, is frequently limited by lack of chemical specificity. PT-OCT[1] is a pump-probe extension of OCT with the potential to complement the structural images of OCT with co-registered chemical/molecular information. To do so, the wavelength of the intensity-modulated photothermal laser (PT laser; i.e., pump) is selected at the peak absorption band of a molecule of interest (MOI; e.g., 1210nm for lipid). In this arrangement, absorption of the PT light by MOIs generates localized modulated thermoelastic expansions and thermo-optic variations that can be sensed by demodulation of the phase of a time-lapse OCT dataset (probe). Co-registered structural information is simultaneously obtained from the amplitude of the same OCT signal. PT-OCT's ability to produce chemically specific structural images is particularly valuable for applications where the structural signals alone provide insufficient diagnostic information (e.g., identification of rupture-prone atherosclerotic plaques). Quantitative PT-OCT imaging of tissue, however, is complicated by the fact that the PT-OCT signal is influenced not only by the concentration of MOIs but also the optical, thermal, and mechanical properties of tissue. Decoupling the effects of MOI light absorption from other influence parameters requires refined understanding of the complex physics underlying the PT-OCT signal. In this keynote talk, we will discuss our recent 3D opto-thermo-mechanical model for predicting PT-OCT responses in multilayer geometries. This improved model is key to understanding the origins of PT-OCT signals in tissue and the effects of system and sample parameters on experimental signals. We will also present and discuss our latest works focused on spectroscopic imaging of lipid and collagen at video rate with our recently introduced transient-mode PT-OCT (TM-PT-OCT) innovation[2].

Theoretical Model – The source of molecular-specific contrast in PT-OCT is the absorption of PT laser photons by MOIs. Such absorptions lead to formation of local thermal wave fields around the absorbers, and by extension, local modulated thermoelastic expansions. Due to the thermal expansions, the physical length of the sample will change, accompanied also by a variation of the temperature-dependent refractive index. These effects collectively cause a variation in optical path length (OPL) which can be sensed by a phase sensitive OCT system. That is, if the intensity of the PT laser is modulated in a sinusoidal form at a specific modulation frequency, the ensuing temperature field and OPL variations will also modulate at the same sinusoidal frequency. Accordingly, by applying Fourier transformation (FT) to the acquired time-lapse OCT phase signal (aka. M-scan) and evaluating the resulting spectrum at the PT-laser modulation frequency, the modulation amplitude $\Delta\phi$ can be measured at each depth. Based on this sequence of physical phenomena, we proposed a theoretical model to simulate the PT-OCT signals in samples in 3-D space using cylindrical coordinates. The model is comprised of three computing blocks in series: light field, thermal field, and stress/strain field. Each block is fed by the results of the previous block(s), system parameters, and material properties. In the first block, based on the optical properties of the sample and system parameters (e.g., PT laser power and modulation frequency), the PT laser irradiance in the sample is estimated in 3D. The temperature field in the sample is then determined in 3D considering the thermal properties and the light intensity distribution in the sample. The output of this part is the variation of temperature at every point in the sample over time. In the last block, the mechanical stress/strain field in the sample in response to the temperature change and as a function of the material's mechanical properties is obtained. Eventually, the OPL variation and PT-OCT signal are calculated from the mechanical displacements and the temperature changes.

Methodology– The experimental system used in this study[3], Fig. 1(a), is a dual-wavelength spectral-domain PT-OCT system containing a broadband superluminescent diode centered at 1310nm (+/- 75 nm at 10dB), a 2048-pixel line scan camera spectrometer with a maximum acquisition rate of 147 kHz, and two intensity-modulated PT laser at 1040 and 1210nm for detecting collagen and lipid, respectively. The axial and lateral resolutions of the OCT system are both 10µm. Performance test carried out on the system shows a relative displacement error of 3nm at a SNR of 35dB and sensitivity of >100dB which is close to that of a shot-noise-limited system. PT laser modulation pattern was in sinusoidal waveform shape for conventional PT-OCT experiments and in form of a short laser pulse (~400µs) for transient-mode PT-OCT experiments, Fig. 1(b).

For validating the theoretical model, PDMS phantoms containing different concentrations of absorbing dye (IR-806, Sigma Aldrich, USA) were prepared. Mayonnaise and chicken cartilage were used as lipid and collagen samples in spectroscopic TM-PT-OCT experiments.

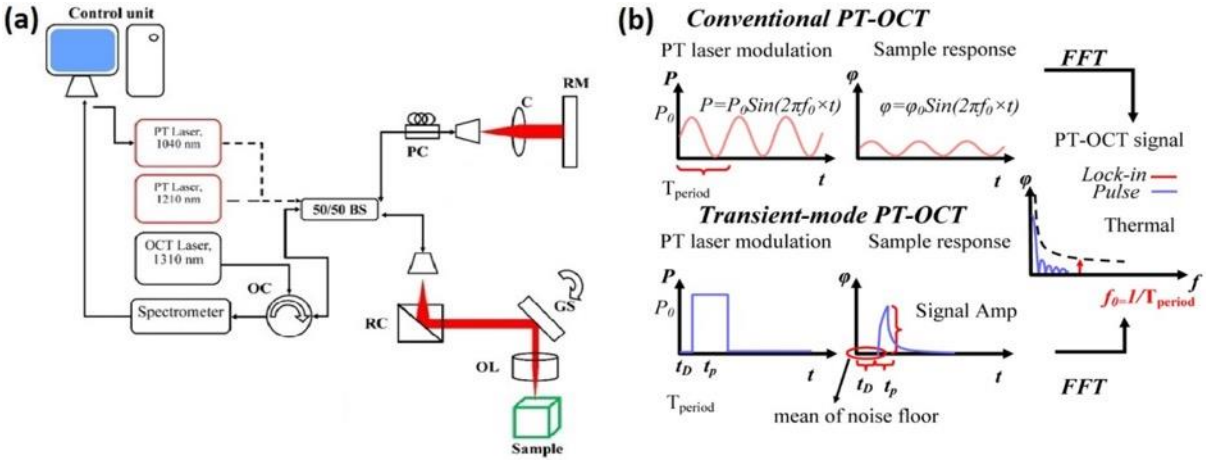

Fig. 1. Schematic of **(a)** experimental PT-OCT system; **(b)** laser modulation and sample responses in conventional PT-OCT and transient-mode PT-OCT.

Results and Discussion – Fig. 2(a) depicts simulated and experimental results of a sample with 2.2mg/ml of absorbing dye concentration (μ_a=10cm^{-1}) at various PT laser powers. Both simulated and experimental signals exhibit monotonic increase with depth. This trend is due to the cumulative nature of PT-OCT signal in a homogenous layer with the signal amplitude at each depth encoding the effect of all preceding layers. It can also be seen that PT-OCT signals exhibit a jump in amplitude at the sample surface (i.e., the Y-intercept) followed by an increase in signal values along depth. The rate of increase in signal values is higher at depths closer to surface because top surfaces of the sample are exposed to higher intensity of PT beam than deeper sample areas which results in larger thermo-elastic expansion of top levels. In Fig. 2(b), the average and standard deviation of experimental PT-OCT signals within a 20μm depth range below the sample surface are plotted in terms of PT laser power at various modulation frequencies. As seen at each modulation frequency, increasing the power on the sample increases the amplitude of the PT-OCT signal. These experimental observations are consistent with the predicted linear increase of the model. Deviations of experimental values from linearity are likely due to noise. Such deviations are larger at lower modulation frequencies due to the pink nature of noise in PT-OCT systems. Fig. 3(c) depicts the simulated and experimental responses of sample as a function of PT laser modulation frequency at 3 different laser powers. The inverse relation of PT-OCT signal strength with increase in laser modulation frequency is characteristic behavior of thermal wave fields. This trend, however, does not necessarily mean that lower modulation frequencies have priority to higher ones because in practice PT-OCT systems suffer from pink noise.

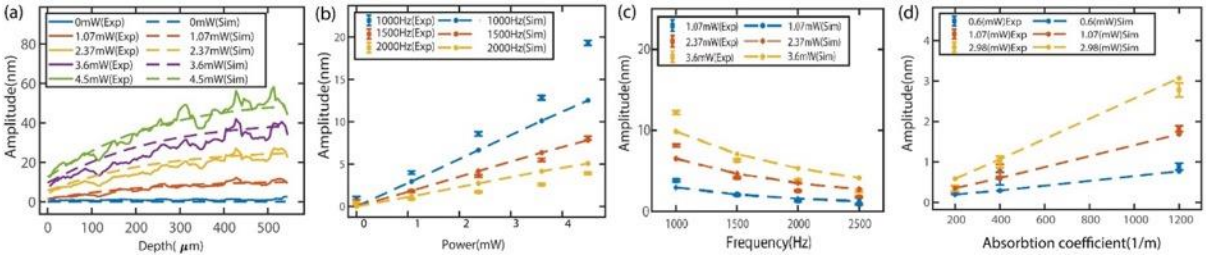

Fig. 2. (a) Effect of sample position with respect to system focal plane on PT-OCT signals. Simulated and experimental PT-OCT signals at **(b)** various PT laser power, **(c)** various PT laser frequencies, and **(d)** various absorption coefficients (MOI concentrations).

To understand the effect of the absorber concentration on PT-OCT signals, single layer samples with three different concentrations of absorber (0.22, 0.43, and 1.3mg/ml) with absorption coefficients (μ_a) of 100, 200, and 600 m^{-1} were imaged under PT illumination at various powers (0.6, 1.07, 2.98mW),

Fig. 3(d). As expected, there is a proportional relation between PT-OCT signal and dye concentration. The slopes of these lines are also directly correlated to the power of the PT laser. At higher concentrations, PT light is absorbed more efficiently, leading to the generation of more heat and eventually larger temperature variations. The greater temperature leads to a greater variation in OPL and subsequently greater PT-OCT signals. Therefore, the effects of the dye concentration and the PT laser power on the PT-OCT signals are identical and cannot be directly distinguished from each other as both parameters influence the thermal energy delivered to the sample. One possible way of decoupling the effects of MOI concentration from PT laser power is to perform spectroscopic PT-OCT at dual PT wavelengths. However, key downside to this approach is the dramatic decrease in imaging speed. To address this issue, we introduced transient-mode PT-OCT (TM-PT-OCT) which forms images based on transient thermal responses of MOIs to short PT laser excitations, Fig. 1(b). This approach enables PT-OCT imaging at high effective A-line rates of 1.5-7.5 kHz which is sufficient for video rate spectroscopic imaging of tissue.

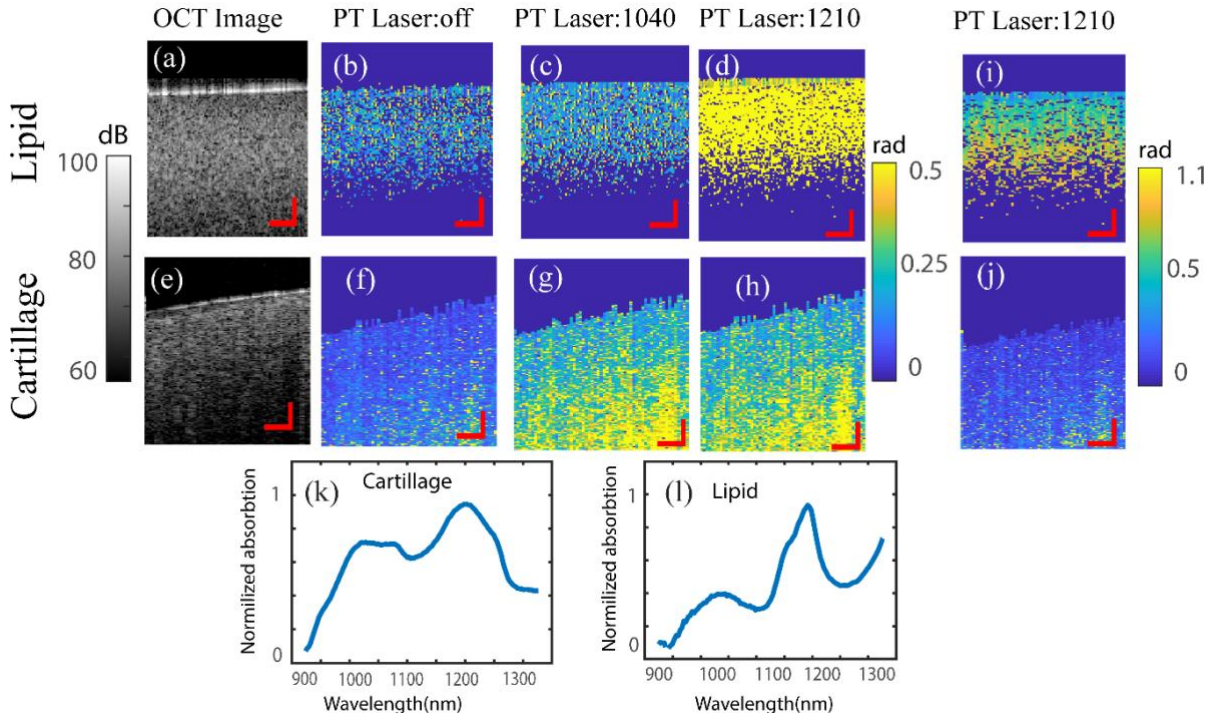

Fig. 3. **(a)** OCT image and **(b-d)** PT-OCT images of lipid, **and (e)** OCT image and **(f-h)** PT-OCT images of collagen samples, absorption spectrum of **(k)** lipid **(l)** collagen, and PT-OCT images of **(i)** lipid and **(j)** collagen with wider color bar.

Fig. 3 shows results of spectroscopic transient-mode PT-OCT for detection and differentiation of collagen and lipid. Panels (a) and (e) depict structural OCT images of lipid and cartilage, respectively, while panels (b) and (f) depict the baseline PT-OCT images of the samples when PT laser was off during imaging. Comparison of lipid 1040nm TM-PT-OCT image (Fig. 3c) with the baseline image (i.e., PT laser off; Fig. 3b), confirms absence of PT-OCT signals from lipid at 1040nm (as expected). At 1210nm (Fig 3d), on the other hand, strong TM-PT-OCT signals are registered from lipid. In the case of collagen, moderate TM-PT-OCT signals are observed for both 1040nm and 1210nm compared to the base-line image (Figs. 3g-h vs Fig. 3f). Results of Fig. 3 demonstrate the ability of TM-PT-OCT in registering the characteristic absorption spectral responses of lipid and collagen. Also, the spectrum obtained from a handheld spectrometer from the lipid and collagen samples (Fig 3.k and l) confirm this spectral response of the samples. TM-PT-OCT images at 1210nm are replotted with a wider colormap in Figs 3.i and 3.j to provide better appreciation of the difference between absorbance of lipid and collagen at

1210nm. As seen in Figs 3.i and 3.j, the signal from lipid is much stronger than those of collagen at 1210nm because of the greater absorbance of lipid at 1210nm.

References

[1] D.C Adler, S.-W. Huang, R. Huber, J.G. Fujimoto, Photothermal detection of gold nanoparticles using phase-sensitive optical coherence tomography. Opt. Express. 6:7 (2008)4376-4393.

[2] M.H. Salimi, M. Villiger, N. Tabatabaei, Transient-mode photothermal optical coherence tomography. Opt. Lett. 46:22 (2001) 5703-5706.

[3] M.H. Salimi, M. Villiger, N. Tabatabaei, Effects of lipid composition on photothermal optical coherence tomography signals. J. Biomed. Opt. 25:12 (2020) 120501.

Camera based photoacoustic imaging: sensitivity and resolution improvement

Nuster R(1)*, Niederwieser M(1), Paltauf G(1)

(1) Department of Physics, University of Graz, Graz, Austria

*Corresponding author's email: ro.nuster@uni-graz.at

Background – Recently, we have shown that an optical camera in combination with a phase contrast Schlieren detection method can be used for biomedical photoacoustic imaging [1,2]. This approach allows projection images of the initial pressure source to be recorded in the shortest possible time, typically in the microsecond range, only limited by the required sound propagation time from inside the sample to the surrounding volume. The reconstruction of the images is performed by backpropagating the recorded wave pattern images that are located within the field of view (FOV) of the camera in Fourier- or Time-Domain. The generation of a 3D image requires the recording of several projection images from different directions, ideally distributed over a semicircle, of the sample with subsequent application of the inverse Radon transform. In view of the achievable resolution and the flexibility for different lighting schemes for the excitation process, due to the optical transparency of the detector, the proposed approach should be preferable compared to conventional methods. However, for many applications these are not the main issues. Rather, sensitivity, compactness and ease of use are decisive, which is why piezo-arrays are still mostly used. In this work it is shown how the sensitivity can be significantly improved without degrading the resolution and maintaining a compact arrangement.

Methods – The basic principle of camera based photoacoustic projection imaging is shown in Fig. 1a. An expanded probe laser pulse projects the 3D pressure field *p(x,y,z,t)* at a defined time instant onto an optical camera. Since a phase contrast detection approach is used, the achievable contrast is directly proportional to the pressure field induced phase variation Δφ [3]:

$$\Delta\varphi(x,z,t) = \frac{2\pi}{\lambda_P} \cdot \frac{\partial n}{\partial p} \cdot \int_0^L p(x,y,z,t)\partial y \qquad \text{Eqn. 1}$$

Beside the amplitude of the pressure field, determined by the photoacoustic source, the strength of Δφ is dependent on the wavelength λ_P of the probe laser pulse, the elasto-optic coupling coefficient *dn/dp* of the material in which the waves propagate, and the interaction length *L* as stated by Eqn.1. These three parameters can be tweaked to improve the sensitivity, but the most effective way is to replace the interaction material with one with a better *dn/dp* value. So far, deionized water has mostly been used as the coupling liquid in order to fulfill the approximation of a homogeneous sound velocity distribution for a fast single-step reconstruction. Replacing water with Fluorinert Liquid (FL), which has an almost four times larger elasto-optic coupling coefficient ($\partial n/dp = 5.13 \cdot 10^{-10} Pa^{-1}$), would boost the sensitivity by the same factor, neglecting any transmission losses due to acoustic impedance mismatches. However, due to the small speed of sound (SoS) value of FL (660m/s), refraction effects at the interface must be considered in the reconstruction process to avoid degradation of the image quality. Adding reflecting walls also helps to improve the overall image quality while keeping at the same time the setup compact [4]. To show the effect of these measures, simulations were performed using modified functions from the k-wave toolbox adapted for the spatial data [5]. In a first step, the forward problem was simulated for the two cases with and without reflecting walls, a defined source

distribution (Fig. 1b), different acoustic properties for the upper and lower half space and a wave propagation time of 45 µs. The upper half space of the simulation domain was considered as water with

properties similar to biological tissue (1500 m/s, 1000 kg/m3) and the lower half space is FL (660 m/s, 1793 kg/m3). The properties of the reflecting steel walls were assumed with a SoS value of 5100 m/s and a density of 7850 m/s. In a second step, the adapted time reversal (TR) algorithm from the k-wave toolbox was applied considering the acoustic inhomogeneities for the cases with and without reflecting walls. Only the region of the wave pattern that can be recorded by the camera (FOV) in a typical experimental setting was used as input dataset.

Results – Figure 1 shows the assumed initial source distribution, the simulated wave pattern structure for both cases, with and without reflecting walls, and the reconstruction results. Applying a standard backpropagating algorithm in frequency domain to the wave pattern, with an assumed average sound speed (1080 m/s), the reconstruction completely fails resulting in an extremely blurred image, depicted in Fig. 1e. The TR reconstruction results (Fig. 1c and 1d), on the other hand, show a qualitative good agreement with the ground truth (Fig.1b). Negative pixel values and horizontal distortions of the structures stem from the limited detection aperture. The result obtained with the reflecting wall (Fig.1d) is slightly better. This is explained by the back-reflection of the wave into the camera's FOV, increasing the detection aperture, which results in an improved image quality.

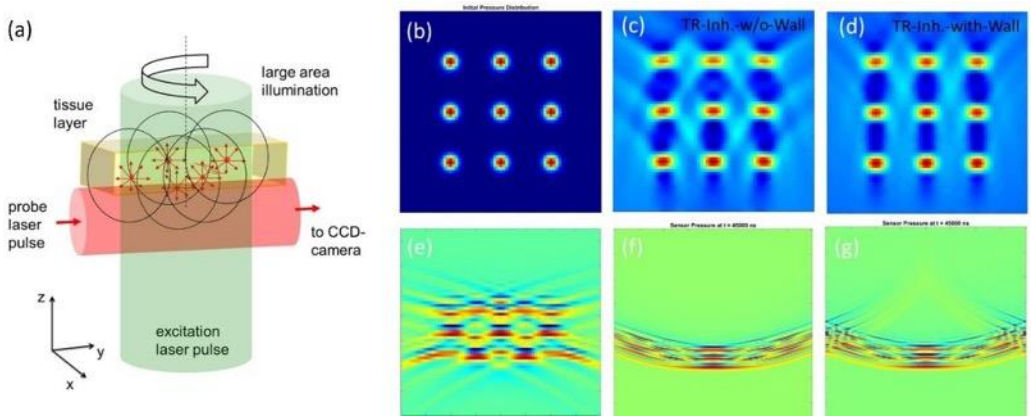

Fig. 1. Schematic of the camera based photoacoustic imaging system **(a)**, the assumed initial pressure source **(b)**, the reconstruction results with TR considering the SoS inhomogeneities without **(c)** and with **(d)** reflecting walls, corresponding simulated wave pattern structures **(f)** and **(g)** and the reconstruction result without considering the SoS inhomogeneities **(e)**.

Conclusions – In summary, the results indicate that water can be replaced with any liquid material that has a better elasto-optic coupling coefficient for a sensitivity improvement as long as it is transparent for the probe laser pulse and the introduced SoS inhomogeneity is considered in the reconstruction process. The disadvantage is that reconstruction methods such as TR, in which the SoS inhomogeneities can be taken into account, are usually not as fast as the standard frequency domain methods, limiting the real-time imaging capability. However, a four times improvement of the detection sensitivity will push forward the application field of the camera based photoacoustic imaging system.

References

[1] R. Nuster, P. Slezak, G. Paltauf, High resolution three-dimensional photoacoustic tomography with CCD-camera based ultrasound detection, Biomed. Opt. Exp.. 5 (2014) 2635–2647. doi.org/10.1364/BOE.5.002635.

[2] R. Nuster, G. Paltauf, Comparison of Piezoelectric and Optical Projection Imaging for Three-Dimensional In Vivo Photoacoustic Tomography, J. Imaging. 5 (2019) 15. https://doi.org/10.3390/jimaging5010015.

[3] T.A. Pitts, A. Sagers, J.F. Greenleaf, Optical phase contrast measurement of ultrasonic fields, IEEE Trans. Ultrasonics, Ferroelectrics, and Frequency Control. 48 (2001) 1686-1694. https://doi.org/10.1109/58.971722.

[4] R. Nuster, G. Paltauf, Optimization of image quality in photoacoustic tomography using spatial projection data, Proc. SPIE 10878. 108784N (2019). doi.org/10.1117/12.2507506.

[5] B.E. Treeby, B.T. Cox, k-Wave: MATLAB toolbox for the simulation and reconstruction of photoacoustic wave fields, J. Biomed. Opt., 15 (2010) 021314. http://dx.doi.org/10.1117/1.3360308.

Nanodroplets loaded with tetrapyrrolic dyes for photoacoustic tomography

Mendes MIP[(1)], Schaberle FA[(1)], Calvete MJF[(1)], Pereira MM[(1)], Arnaut LG[(1)*]

(1) Department of Chemistry, University of Coimbra, Rua Larga, 3004-535 Coimbra, Portugal

*Corresponding author's email: lgarnaut@ci.uc.pt

Photoacoustic tomography (PAT) is an emerging imaging technique. The contrast agents used in PAT transform, through non-radiative decay, absorbed pulsed laser light into an ultrasound wave, called photoacoustic wave (PAW). Hemoglobin can be used as a PAT endogenous contrast agent, but the translation to clinical settings requires the development of better contrast agents that allow a higher resolution and enhanced contrast [1].

Tetrapyrrolic macrocycles have an intense absorption in the phototherapeutic window and can be used in PAT. The complexation of porphyrins derivatives or phthalocyanines with a paramagnetic metal increases the non-radiative decay yield. This allows a rapid transformation of the absorbed light into heat and the subsequent release of a pressure wave that can be detected outside the body.

Nanodroplets are metastable particles composed of a shell (lipid, protein or polymer) and a perfluorocarbon core. The perfluorocarbons used usually have low boiling points facilitating a phase transition and the formation of microbubbles upon small temperature or pressure changes [2]. Nanodroplets have been investigated in ultrasound and PAT, and in this work they were used to carry a tetrapyrrolic contrast agent and increase the photoacoustic contrast upon its activation.

The nanodroplets produced for this study have a perfluoropentane core and an albumin (bovine serum albumin, BSA) shell. New porphyrins and phthalocyanines were synthetized with fluorinated chains to try to increase the solubility in the perfluoropentane. Different paramagnetic metals were used for the complexation reactions to increase the non-radiative decay and photoacoustic signal production (Fig. 1).

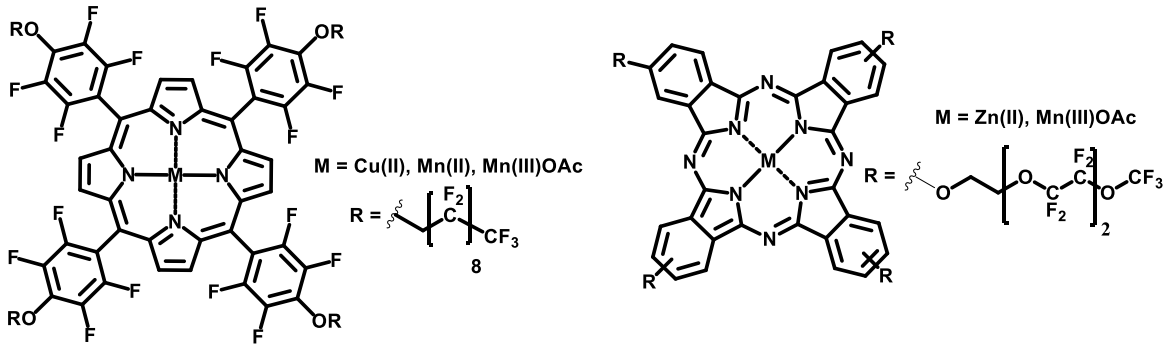

Fig. 1. Schematic representation of the porphyrins (left) and phthalocyanines (right) synthesized.

A diethyl ether stock of each dye is prepared and added to an aqueous BSA solution (2 mg/ml). Perfluoropentane is added to this BSA solution and the final mixture is sonicated to produce dye loaded nanodroplets. To evaluate the vaporization of these structures after pulsed laser light absorption a photoacoustic calorimetry apparatus was used [3].

The photoacoustic signal produced by the nanodroplets was always compared to the respective BSA solution, to evaluate if we were in the presence of a vaporization process. The photoacoustic signal detected after the excitation of the contrast agents is higher in the nanodroplets compared to the BSA solutions, suggesting that the contrast in PAT can be enhanced by using these structures.

The best candidates after the photochemical and photoacoustic characterization are being analyzed with the Vevo LAZR-X Multi-modal Imaging Platform from Fujifilm VisualSonics in animal models. We believe the vaporization of the nanodroplets produced from these dyes will increase the contrast and allow a higher contrast in PAT.

Acknowledgements - This work was financially supported by the Portuguese Science Foundation (PTDC/QUI-OUT/0303/2021). Maria Inês P. Mendes was financially supported by the Portuguese Science Foundation (PD/BD/143129/2019).

References

[1] L. Wang, S. Hu, Photoacoustic Tomography: In Vivo Imaging from Organelles to Organs, Science. 335 (2012) 1458–1462. DOI: 10.1126/science.1216210.

[2] A. Hannah, G. Luke, K. Wilson, K. Homan, S. Emelianov, Indocyanine Green-Loaded Photoacoustic Nanodroplets – Dual Contrast Nanoconstructs for Enhanced Photoacoustic and Ultrasound Imaging, S. ACS Nano, 8 (2014) 250-259. DOI: 10.1021/nn403527r.

[3] L.G. Arnaut, R.A. Caldwell, J.E. Elbert, L.A. Melton, Recent advances in photoacoustic calorimetry: theoretical basis and improvements in experimental design, Rev. Sci. Instrum., 63 (1992) 5381–5389. https://doi.org/10.1063/1.1143407.

Photoacoustic delivery of photosensitizers for photodynamic therapy

Pereira DA[(1)*], Lobo CS[(2)], Mendes MIP[(1)], Arnaut LG[(1)]

(1) CQC, Department of Chemistry, University of Coimbra, 3004-535 Coimbra, Portugal
(2) LaserLeap Technologies, Rua Coronel Júlio Veiga Simão, Edifício B, CTCV, S/N, 3025-307 Coimbra, Portugal

*Corresponding author's email: diogoapereira1@gmail.com

Photoacoustic Waves (PWs) have shown a remarkable versatility for numerous applications. PWs are generated after a fast and efficient conversion of energy from a pulsed laser into pressure. One of the applications of PWs is to transiently permeabilize the outer layers of skin or cell membranes [1].

PWs are a non-invasive physical method that can increase the delivery of a drug to its target. So, it can be used as a way to improve the efficacy of photodynamic therapy (PDT) by increasing the photosensitizer in the diseased tissues. PDT combines a photosensitizer (PS) that can absorb light and molecular oxygen that will form reactive oxygen species, triggering cell death in the illuminated tissues [2]. PDT is widely studied in cancer research as an alternative to conventional chemotherapy. However, the photosensitizer often has excessive molecular weight which can limit the treatment outcome. To overcome this problem, PWs can be locally employed before the irradiation to permeabilize the biological barrier and enhance the local drug delivery [3].

PDT can be performed in two different modalities, vascular (PS is mainly in the vasculature) or cellular (PS is inside the cells). If the drug accumulation in the tumor is poor only the cells close to blood vessels will be exposed to therapeutic concentrations of the PS [4]. Redaporfin is a photosensitizer that is in clinical trials for advanced head and neck cancer [5] and has been studied for vascular-PDT in several animal models. Another characteristic of this PS is the possibility of being used for photoacoustic tomography (PAT). Hence, it is possible to see the concentration of redaporfin in the tumor before the irradiation.

PDT with redaporfin was shown to increase the cures in mice with a variety of subcutaneous tumors. However, orthotopic 4T1 (mammary) tumors, proved to be very difficult to treat. 4T1 orthotopic tumors are particularly challenging because a much lower concentration of drug is expected to reach the tumor microenvironment.

Figure 1 shows the photoacoustic spectra in the tumor collected with Vevo LAZR-X multimodal imaging system from Fujifilm-VisualSonics before and after intravenous administration of redaporfin. Animals who were exposed to photoacoustic waves for 5 min have an increased signal at 750 nm.

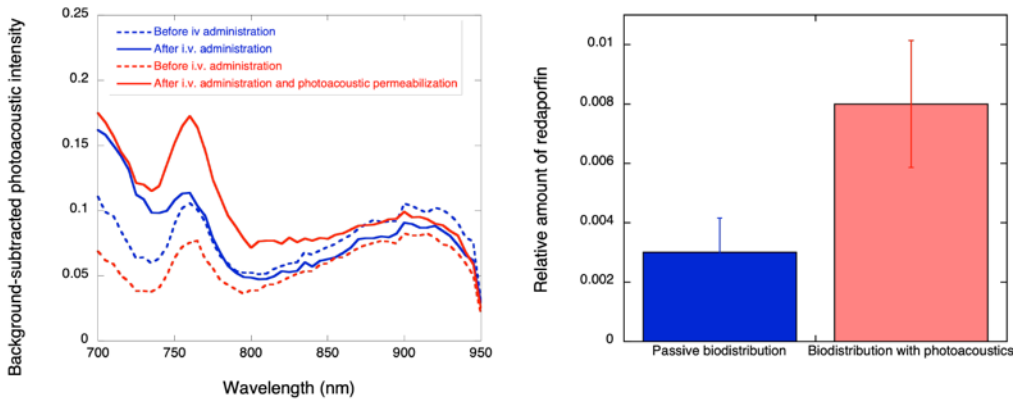

Fig. 1. (a) Background-subtracted photoacoustic spectra in region of the tumor. **(b)** Background-subtracted ratio of photoacoustic spectra at 750nm.

After this permeabilization with PWs, the tumors were irradiated following the standard redaporfin-PDT protocol [6].

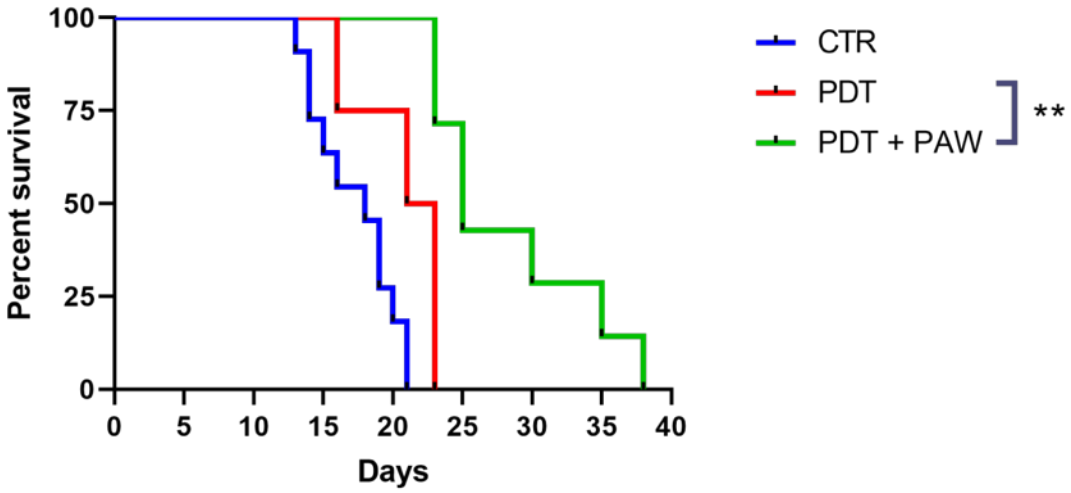

Fig. 2. Survival curve mice orthotopic 4T1 tumours treat with redaporfint-PDT (red) and with photacoustic waves + redaporfin-PDT (green)

As shown in figure 2, exposure of the 4T1 orthotopic tumor to photoacoustic waves before the photodynamic therapy protocol leads to a higher survival rate.

This work is a contribution to overcome a poor drug penetration into solid tumors, that is recognized as one of the major reasons for many treatments' failure. Pulsed high-frequency and high-pressure photoacoustic waves can permeabilize tumor biological barriers leading to an increase of the drug in the tumor and a better treatment outcome.

Acknowledgments – This work was supported by the Portuguese Science Foundation (PTDC/QUI-OUT/0303/2021)

References

[1] G.F.F. Sa, C. Serpa, L.G. Arnaut, Stratum corneum permeabilization with photoacoustic waves generated by piezophotonic materials, J. Control. Release, 167 (2013) 290.

[2] L.G. Arnaut, et al. Photodynamic therapy efficacy enhanced by dynamics: the role of charge transfer and photostability in the selection of photosensitizers, Chem. Eur. J. 20:18 (2014) 5346-5357.

[3] D.A Pereira et al. Imaging of photoacoustic-mediated permeabilization of giant unilamellar vesicles (GUVs), Sci. Rep. 11 (2021) 2775.

[4] A.I. Minchinton, I.F. Tannock, Drug penetration in solid tumours, Nat. Rev. Cancer 6 (2006) 583-592.

[5] L.L. Santos et al. Treatment of Head and Neck Cancer with Photodynamic Therapy with Redaporfin: A Clinical Case Report, Case Rep. Oncol. 11 (2018) 769-776.

[6] A.C.S. Lobo et al. Immune Responses after Vascular Photodynamic Therapy with Redaporfin, J. Clin. Med. 9:1 (2020) 104.

Multispectral pulse truncated-correlation photothermal coherence tomography with applications to dental imaging

Shokouhi EB[1,2], Mandelis A[1,2]*

(1) Center for Advanced Diffusion-Wave and Photoacoustic Technologies, Department of Mechanical and Industrial Engineering, University of Toronto, Toronto, ON, M5S 3G8, Canada
(2) Institute for Advanced Non-Destructive and Non-Invasive Diagnostic Technologies (IANDIT), University of Toronto, Toronto, ON, M5S 3G8, Canada

*Corresponding author's email: mandelis@mie.utoronto.ca

Background – Enhanced Truncated-Correlation Photothermal Coherence Tomography (eTC-PCT) is a dynamic frequency-domain imaging modality which is a promising technique for non-invasive biomedical imaging and for non-destructive testing of industrial materials. Various implementations of eTC-PCT method are possible. For example, an original embodiment of eTC-PCT [1] uses an 808-nm diode laser as excitation source. To obtain molecular specificity in biological samples we introduced multispectral (MS) TC-PCT that employs a Nd:YAG pulsed laser which pumps an optical parametric oscillator (OPO) for wavelength tunability. This work investigates the detection of early stage caries in photothermal images of teeth using MS TC-PCT. Our results have shown that near-surface and deep subsurface features can be imaged, thereby making MS TC-PCT a promising modality for further applications to hard tissue imaging.

Thermophotonic imaging takes advantage of the optical-to-thermal IR photon energy conversion and detection from samples, captured by a mid-infrared (MIR) camera. Detection of depth-integrated distributions of energy is a characteristic of the parabolic nature of diffusion-wave fields which results in poor axial resolution [2]. The eTC-PCT technique [1] overcomes the depth-integrated nature of thermophotonic technologies by using chirped or single pulse excitation with an 808-nm CW diode laser and cross-correlating the photothermal transient signals captured by the MIR camera with the in-phase and quadrature reference signals. The resulting cross-correlation is then truncated based on a time gating filter. eTC-PCT analysis provides two main output channels: amplitude and phase. MS TC-PCT is an extension of eTC-PCT whereby choosing the wavelength of the incident optical pulses, spectroscopic amplitude and phase images can be obtained at different wavelengths, generating molecularly specific thermophotonic diagnostics.

Methods – MS TC-PCT uses a Q-switched Nd:YAG laser (Surelite OPO Plus SLIII-10, Continuum, San Jose, United States) which generates 5-ns laser pulses at 10 Hz repetition rate which is the frequency of its flashlamp discharge. The laser output is frequency doubled to 532 nm, which then pumps an OPO tunable from 675 to 1000 nm. A MIR camera (A6700sc, FLIR, USA, 3–5 μm spectral response) records the thermal evolution of the sample following the laser irradiation. A function generator (Agilent 33220A, USA) captures the electrical pulse from the laser and records it using a high-speed data acquisition module (NI PCI-6281) for synthesizing the reference signal. The details of image reconstruction technique can be found elsewhere [1]. Briefly, the resulting eTC-PCT cross-correlation is truncated using a time gating filter which is calculated based on a user defined slice width and

millisecond delay incrementation. eTC-PCT software reconstructs the depth distribution of photothermal parameters from its main output channels.

Results – Figure 1(a) shows a human tooth with early caries. Figs. 1(b)-(c) show the MS TC-PCT amplitude and phase reconstructions of the tooth at single repetition frequency of 0.5 Hz, and at OPO wavelengths 532 nm, 675 nm, 700 nm, 750 nm, 808 nm, 850 nm, and 900 nm. In the amplitude images, the shorter wavelengths such as 675 nm and 700 nm show the demineralized area with finer details as compared to longer wavelengths (e.g. 808-900 nm) as they capture shallow features such as caries due to the shorter thermal diffusion lengths. Regarding the 532-nm images, the caries appears noisier and this can be due to the highly scattered incident photons at that wavelength which tend to also highlight other built-in near-surface natural tooth inhomogeneities. In the phase images, it can be seen that features such as the borders of the of the tooth are much less pronounced which is due to the phase channel containing almost purely thermal information subject to lateral diffusion. The phase images at 675 nm, and 700 nm show a highly detailed reconstruction of the anatomy of the caries.

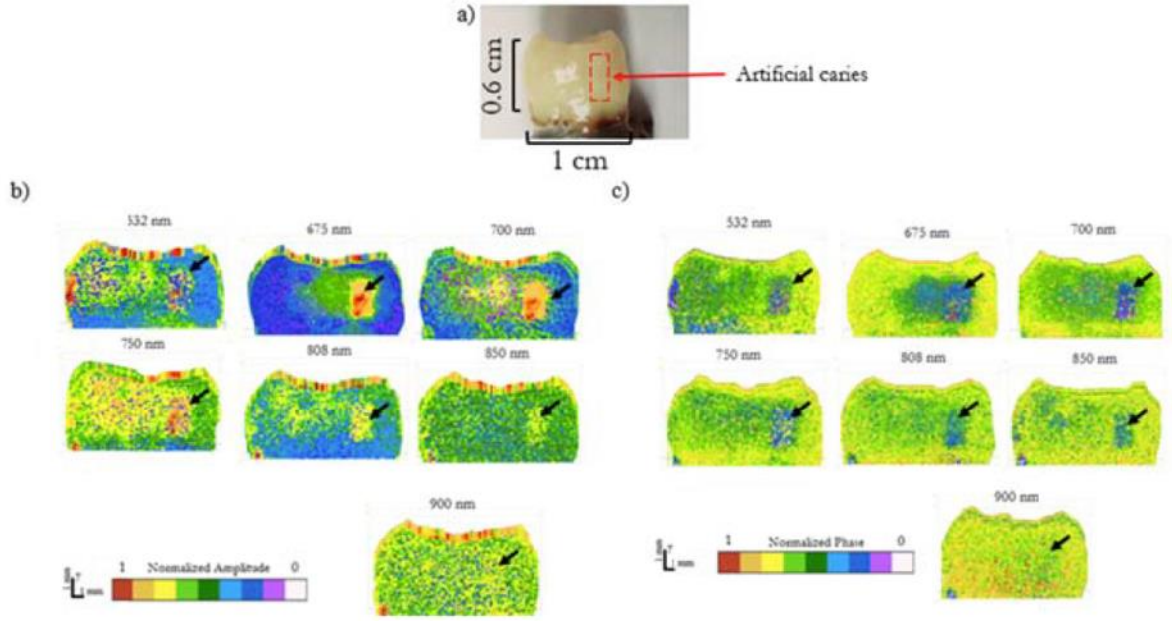

Fig. 1. (a) Tooth sample with caries, **(b)** 3D eTC-PCT amplitude and **(c)** phase reconstruction of a carious lesion in a tooth sample taken at 0.2 Hz at pulsed Nd:YAG laser OPO wavelengths 532 nm, 675 nm, 700 nm, 750 nm, 808 nm, 850 nm, and 900nm. The carious lesion is shown by a black arrow in each reconstruction.

Conclusions – This research reported on the implementation of a MS TC-PCT imaging modality and explored its application to dental caries diagnosis. MS TC-PCT allows one to choose the excitation and detection wavelengths with optimal contrast and resolution based on the tissue-light scattering phenomena in biological samples.

References

[1] P. Tavakolian, K. Sivagurunathan, and A. Mandelis, Enhanced truncated-correlation photothermal coherence tomography with application to deep subsurface defect imaging and 3-dimensional reconstructions, J. Appl. Phys. 122 (2017) 23103. doi: 10.1063/1.4992807.

[2] A. Mandelis, L. Nicolaides and Y. Chen, Structure and the Reflectionless / Refractionless Nature of Parabolic Diffusion Wave Fields, Phys. Rev. Lett. 87 (2) 020801-1 - 020801-4.

Probing cell mechanics with photoacoustic and photothermal methods

Liu L[(1)*], Wei Q[(1)], Beyen A[(1)], Bao J[(2)], Deschaume O[(1)], Bartic C[(1)], Glorieux[(1)*]

(1) Laboratory for Soft Matter and Biophysics, KU Leuven, BE-3001 Heverlee, Belgium
(2) Div. ESAT-TELEMI, KU Leuven, BE-3001, Heverlee, Belgium

*Corresponding authors'email: Liwang.Liu@kuleuven.be; Christ.Glorieux@kuleuven.be

Background – Biological cells are soft and micron-sized objects. The past decade has shown an acceleration in technological possibilities to characterize their mechanics [1], thanks to advances in nanotechnology and quantitative micromanipulation. Existing techniques, among which atomic force microscopy (AFM), micropipette aspiration, and magnetic twisting cytometry, require contact/invasive interrogation [2] with the cells, which can not only cause unintended cell damage but also lead to significant over/under-estimation of the measured values because of the complicated linkages between probes (size, shape, stiffness) and cells. Furthermore, these techniques are often limited to the surface of the cells and they hardly provide information about the internal cell structure, e.g., the cytoskeleton and the nucleus. Therefore, non-contact, non-invasive, and non-destructive techniques for assessing cell mechanics need to be developed in the field of cell mechanics and cell mechanobiology.

Methods – Combining light, heat, and sound, photoacoustic (PA) and photothermal (PT) approaches [3] have reached a mature state for non-contact and non-destructive thermal, mechanical, and interfacial bonding characterization of a variety of materials and layered structures in solid-state physics. This work aims at exploring PA and PT measurement approaches on a microscale on biological cells, thereby addressing the above-mentioned challenges in experimental cell mechanics, including the assessment of contact mechanics at the cell-substrate [4] (e.g., cell adhesion) and intracellular mechanics [5] (e.g., viscoelasticity and compressibility). The quality of contact between a cell and its surroundings can be probed directly by applying and measuring forces and displacements statically or by looking at the transmission and reflection of acoustic waves. An alternative way is by looking at thermal diffusion through the interface by a contactless photothermal approach.

Results – In this work, we demonstrate the application of the photothermal transient thermo-reflectance technique to probe the quality of the contact at the cell/substrate adhesion interface. We study nanoscale thermal transfer across the interface, thus assessing the boundary thermal resistance related to the presence of the adhesion sites. Fig. 1 illustrates the concept and workflow of PT imaging of cell-substrate adhesion with the developed TTR microscope (**A**), in which a pulsed laser (blue) is used to launch transient thermal waves, and their diffusion across the cell adhesion interface is monitored by a continuous wave (CW) probe laser (green). The built-in bright-field microscope and the scanning stage allow to allocate the pump-probe beams onto the interface beneath the cell under study (B). The TTR signals are different at different locations (C). By performing a 2D raster scan, we can image an entire cell with 1-micron lateral resolution (D). Theoretical simulation by a 1D three-layer thermal diffusion model suggests the TTR signals are sensitive to the interfacial thermal resistance, R_{th}. Our results illustrate that the photothermal TTR technique is a feasible tool for non-contact, non-invasive, and quantitative assessment of cell-substrate adhesion with sub-micron resolution.

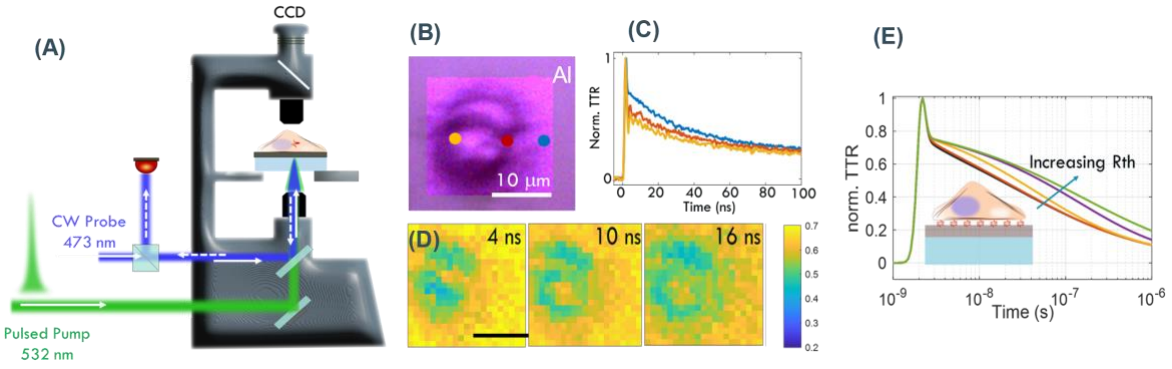

Fig. 1. Schematic illustration of the PT imaging of a single cell on a substrate: (**A**) experimental setup, (**B**) an optical bright-field image of a neuron cell under study, (**C**) Three representative TTR waveforms recorded at the three positions indicated in (B). (**D**) Three snapshots of the thermal wave images with ns time-resolution. On such short time scales, thermal waves ***penetrate cells <100 nm***, estimated by $(\alpha t)^{1/2}$ with α the thermal diffusivity, about 10^{-7} m^2/s for cells. (**E**) the effect of R_{th} on TTR signals simulated by using a 1D three-layer thermal diffusion model. R_{th} values are 10^{-8}, 10^{-7} , 10^{-6} , 10^{-5} Km^2/W, from bottom to top, respectively.

References

[1] E. Moeendarbary, A.R. Harris, Cell Mechanics: Principles, Practices, and Prospects, Wiley Interdiscip. Rev. Syst. Biol. Med. 6 (2014) 371.

[2] P.-H. Wu, D.R.-B. Aroush, A. Asnacios, W.-C. Chen, M.E. Dokukin, B.L. Doss, P. Durand-Smet, A. Ekpenyong, J. Guck, N.V. Guz, P. A. Janmey, J.S.H. Lee, N.M. Moore, A. Ott, Y.-C. Poh, R. Ros, M. Sander, I. Sokolov, J. R. Staunton, N. Wang, G. Whyte, D. Wirtz, A Comparison of Methods to Assess Cell Mechanical Properties, Nat. Methods 15 (2018) 491.

[3] H. Vargas, L. C. M. Miranda, Photoacoustic and Related Photothermal Techniques, Phys. Rep. 161 (1988) 43.

[4] A. Ahmad Khalili and M.R. Ahmad, A Review of Cell Adhesion Studies for Biomedical and Biological Applications, Int. J. Mol. Sci. 16 (2015) 18149.

[5] M.L. Rodriguez, P.J. McGarry, N.J. Sniadecki, Review on Cell Mechanics: Experimental and Modeling Approaches, Appl. Mech. Rev. 65 (2013) 060801.

Subsurface temperature monitoring during hyperthermic laser treatment

Košir J[(1,2)*], Vella D[(2)], Lukač M[(1,3)], Jezeršek M[(2)]

(1) Fotona d.o.o., Ljubljana, Slovenia
(2) Faculty of Mechanical Engineering, University of Ljubljana, Ljubljana, Slovenia
(3) Department of Complex Matter, Jozef Stefan Institute, Ljubljana, Slovenia

*Corresponding author's email: jure.kosir@fotona.com

Background – Advancements in medical laser technology have paved the way for its widespread acceptance in a variety of procedures. Selectively targeting tissue structures with minimally invasive procedures limits the damage to surrounding tissue and shortens post-procedural downtime. Effectiveness of such therapies strongly relies on the ability to closely monitor the temperature of the targeted tissues. These are usually located in the subsurface regions, thus high-energy visible and infrared lasers in combination with surface cooling systems are employed [1–3]. Temperature peak is thus located well below the tissue surface and can be significantly higher than skin temperature (10– 20 °C) [1, 2]. Current approaches for monitoring subdermal temperature are either invasive, complex or offer inadequate spatial resolution [4]. Furthermore, numerical studies are often therapy–tailored and source tissue parameters from the literature, lacking versatility and a tissue–specific approach. In our previous study a time–dependent algorithm was conceptually showcased [1]. We further modified the algorithm for heterogeneous tissues and performed ex–vivo validation study [2]. Here, we present its extended applicability to in–vivo tissues and its implementation with hand–held laser scanner head. Additionally, algorithm recognizes tissue–specific thermal characteristics yielded by a fast calibration process. The algorithm was showcased in–vivo during a Hyperthermic Laser Treatment (HTLT).

Methods – The estimation of thermal parameters (ETP) setup included a 2,940 nm Er:YAG laser source (Dynamis SP, Fotona, Slovenia). The laser beam illuminated the surface through a diverging lens, effectively producing a laser spot approx. 6 cm in diameter. The heating cycle was performed for 30 s with an average intensity I=0.1 W/cm^2 and VLP mode ("Very Long Pulse", pulse duration t_p=1,000 µs, repetition rate f_r=12 Hz). Tissue thermal parameters (thermal diffusivity D, thermal conductivity k and blood perfusion ω) of an individual (28-year-old male with BMI of 32) were yielded by fitting numerically simulated $T_s(t)$ with a measurement recorded during the calibration protocol. After ETP, HTLT was performed in–vivo on 28-year-old individual. Laser system included a hand–held scanner head, which homogeneously irradiated surface area of 5.4 x 5.7 cm^2 for 80 seconds (with Nd:YAG source, 1,064 nm, AvalancheLase LXP, Fotona, Slovenia). In addition, tissue surface was cooled with integrated cooling system. We performed multiple HTLT cycles, each with prolonged active cycle duration (form t_1=40 to t_4=120 s). Cooling settings and average intensity of irradiation I=1.2 W/cm^2 remained constant. During each measurement the temporal evolution of $T_s(t)$ was recorded with newly introduced supervision module that features multiple thermal sensors and RGB camera. The module was integrated within a hand–held scanner head. The $T_s(t)$, recorded during HTLT, were used in STD algorithm to estimate $T(z)$ for each performed HTLT cycle.

Results: During ETP a calibration measurement was performed. The surface temperature response to laser irradiation and the following thermal relaxation reflected the behaviour already reported in other

studies. Recorded T_s was well reproduced by numerical model [2] as depicted in Fig. 1, left panel. Estimated thermal parameters were D_s=1.05·10^{-7}, D_f=1.23·10^{-7} m^2/s, k_s=0.42 and k_f=0.31 W/m^{2}K.

Additionally, blood perfusion rates were estimated as ω_s=0.84 and ω_f=0.28 kgm^3/s for skin and fat respectively. Obtained tissue parameters were used in STD algorithm [2] for estimations of $T(z)$ during in–vivo performed HTLT. Estimated $T(z)$ are depicted in right panel of Fig. 1 for each active cycle duration.

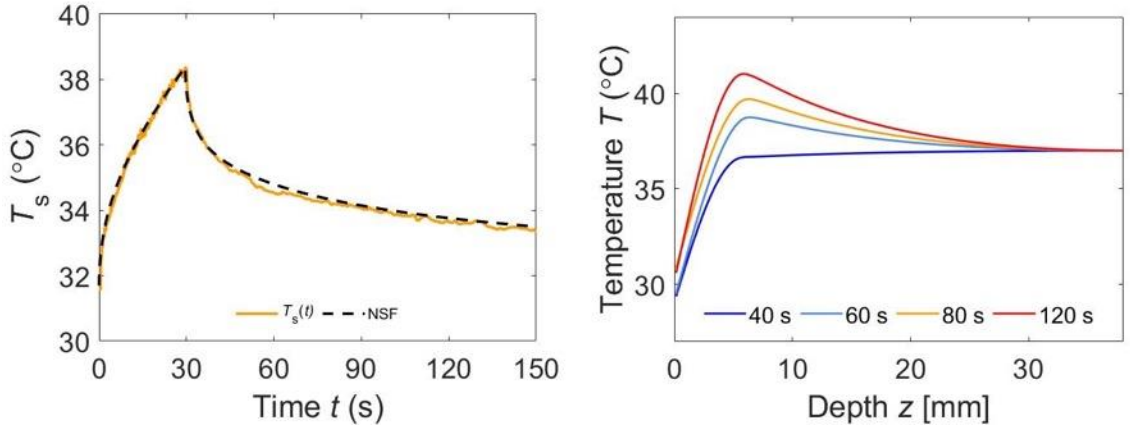

Fig. 1. In–vivo performed HTLT. Left panel depicts recording of $T_s(t)$ during ETP protocol (in yellow) along with numerical simulation fit (NSF). Right panel depicts $T(z)$ estimated during HTLT as irradiation time was prolonged from 40 to 120 s.

The peak's locations z_{max} were estimated to range 5–6 mm from the irradiated surface. This particular range is consistent to the one obtained in the skin–fat sample [2]. The peak temperature T_{max} was trending higher with prolonged irradiation times as depicted in Fig. 1, right panel. In addition, results of in–vivo study presented by Milanič et al. [3] correlate well with our $T(z)$ estimations in regard to temperature distributions, temperature peak values and locations. At t_3=80 s we performed a set of measurements to asses repeatability of treatment's outcome. Within the set of estimated $T(z)$ an average error was ±0,4 mm and ±0,6 °C for z_{max} and T_{max} respectively.

Conclusion: We presented an in–vivo application of a novel approach for estimation of the tissue's thermal parameters ETP and subsurface temperature distribution within tissue after laser irradiation. The estimated $T(z)$ during in–vivo HTLT showed a trend that is comparable to reports of other in– vivo studies. Furthermore, peak temperatures and positions were within range of reported values. The presented method for subsurface temperature monitoring was implemented in a newly developed supervision module that is integrated within a hand–held laser scanner head.

References

[1] M.A. Lewis, R.M. Staruch, R. Chopra, Thermometry and ablation monitoring with ultrasound, Int J Hyperthermia 31:2 (2015) 163–181. doi:10.3109/02656736.2015.1009180.

[2] J. Košir, D. Vella, M. Jezeršek, Non-contact monitoring of the depth temperature profile for medical laser scanning technologies, Sci. Rep. 10, 20242 (2020). https://doi.org/10.1038/s41598-020-77283-9.

[3] J. Košir, D. Vella, M. Lukač, M. Jezeršek, Towards personalized and versatile monitoring of temperature fields within heterogeneous tissues during laser therapies, Biomed. Opt. Express 12:7 (2021) 4530–4543. https://doi.org/10.1364/BOE.428028.

[4] M. Milanič, B.T. Muc, N. Lukač, M. Lukač, Numerical study of hyper–thermic laser lipolysis with 1,064 nm Nd:YAG laser in human subjects, Lasers Surg. Med. 51:10 (2019) 897–909. https://doi.org/10.1002/lsm.23124.

Hemodynamics in self-healing human bruises assessed by combined optical spectroscopy and pulsed photothermal radiometry

Marin A[(1)], Majaron B[(1,2)*]

(1) Faculty of Mathematics and Physics, University of Ljubljana, Slovenia
(2) Department of Complex Matter, Jožef Stefan Institute, Ljubljana, Slovenia

*Corresponding author's email: boris.majaron@ijs.si

Assessment of bruise age in forensic investigations is based on characteristic skin discoloration, due to dynamical processes involving mass diffusion and biochemical transformation of the extravasated hemoglobin into various by-products. However, the current protocol relies exclusively on visual inspection and assessment of discoloration by a medical expert. Aiming toward development of an objective approach for aging of bruises, we have augmented our recently introduced methodology for noninvasive analysis of skin structure and composition, which combines diffuse reflectance spectroscopy (DRS) in visible spectral range and pulsed photothermal radiometry (PPTR). The latter involves irradiation of the test site with a milisecond light pulse at $\lambda = 532$ nm, emitted from a medical-grade laser (DualisVP, Fotona, Slovenia). The subsequent transient change of Planck's emission from the skin surface is acquired with a fast MWIR camera (FLIR SC7500, $\lambda = 3.5–5.1$ μm) at 1000 fps [1].

Data from both techniques are analyzed simultaneously using a numerical model of light and heat transport in human skin, represented by four characteristic layers [1]. In contrast with the previous report, the model used here includes two additional chromophores, β-carotene and bilirubin, and adjustable thickness of the papillary dermal layer. In addition, the analyses of bruises rely on baseline values of skin properties, assessed from measurements of a nearby intact site [2,3,4].

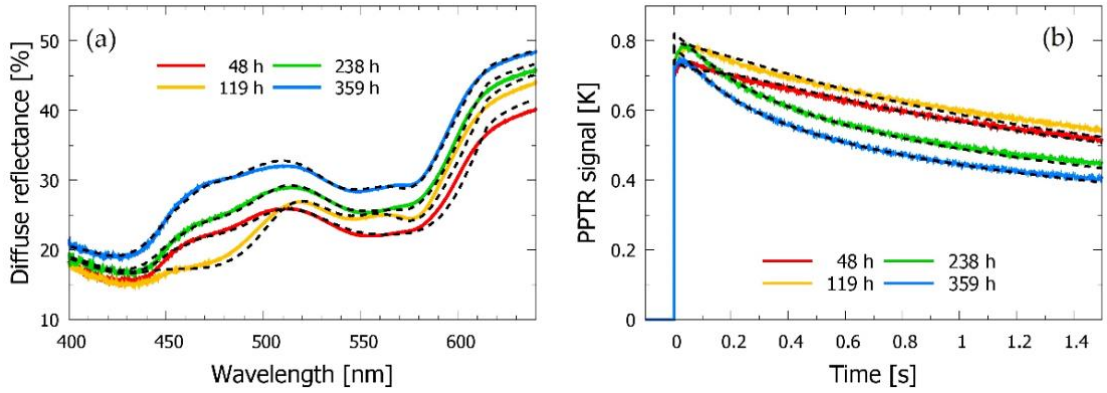

Fig. 9. DRS spectra (a) and PPTR signals (b) obtained from a bruised skin site at different times after the injury (see the legends). Dashed lines represent the best fitting model predictions.

The results obtained from measurements performed in three volunteers over a period of 16 days indicate a dramatic increase of the blood content in the reticular dermis and reduction of its oxygenation level in first days after injury. This is followed by gradual emergence of bilirubin, a long-lived by-product of the hemoglobin decomposition. Eventually, all model parameters relax towards the values characteristic

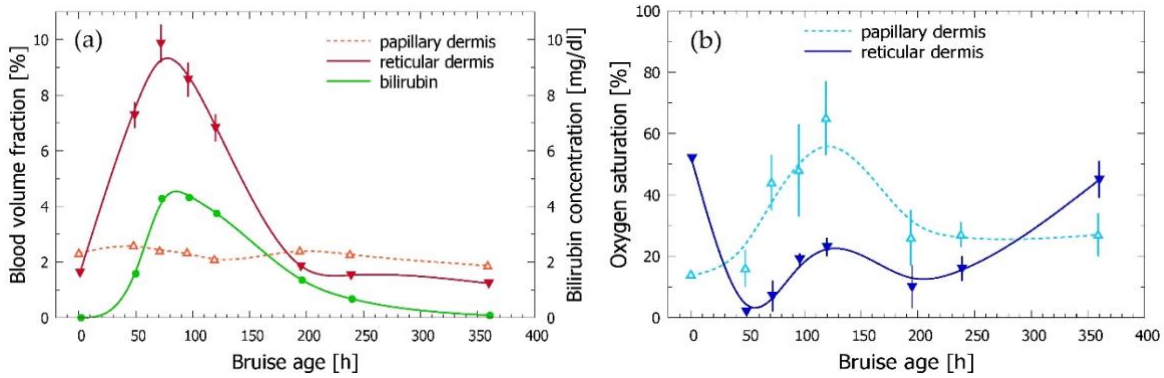

Fig. 2. The assessed dynamics of blood and bilirubin contents (a), and oxygenation level of blood (b) in the papillary and reticular dermis over 15 days after the injury.

for intact skin [3,4]. Moreover, all assessed values and characteristic time intervals are consistent with available literature data.

We will also present and discuss our attempts to match the assessed hemodynamics with a modified version of an earlier proposed analytical model of bruise dynamics with a small number of free parameters, such as the hemoglobin mass diffusivity and characteristic time for its decomposition, depth and duration of blood spillage, etc. [5,6].

We are hopeful that the presented methodology and acquired information may provide a basis for development of a future methodology for objective and robust assessment of the time of injury in forensic investigations.

Acknowledgments – This research was supported by the Slovenian Research Agency (grants P1-0192 and P1-0389). The laser used for PPTR measurements was loaned to us by Fotona, d.o.o. (Ljubljana, Slovenia).

References

[1] N. Verdel A. Marin, M. Milanič, B. Majaron, Physiological and structural characterization of human skin in vivo using combined photothermal radiometry and diffuse reflectance spectroscopy, Biomed. Opt. Express 10 (2019) 944–960. https://doi.org/10.1364/BOE.10.000944.

[2] A. Marin, N. Verdel, M. Milanič, B. Majaron, Influence of healthy skin baseline on bruise dynamics parameters as assessed by optical methods, Proc. SPIE 11075 (2019) 110751O. https://doi.org/10.1117/12.2527083.

[3] A. Marin, N. Verdel, B. Majaron, Hemodynamics in traumatic bruises assessed by diffuse reflectance spectroscopy and photothermal radiometry, Proc. SPIE 11211 (2020) 112110Z. doi.org/10.1117/12.2545876.

[4] A. Marin, N. Verdel, M. Milanič, B. Majaron, Noninvasive monitoring of dynamical processes in bruised human skin using diffuse reflectance spectroscopy and pulsed photothermal radiometry, Sensors 21 (2021) 302. https://doi.org/10.3390/s21010302

[5] L.L. Randeberg, O.A. Haugen, R. Haaverstad, L.O. Svaasand, A novel approach to age determination of traumatic injuries by reflectance spectroscopy, Lasers Surg. Med. 38 (2006) 277–289. doi.org/10.1002/lsm.20301.

[6] L. Vidovič, M. Milanič, B. Majaron, Objective characterization of bruise evolution using photothermal depth profiling and Monte Carlo modeling, J. Biomed. Opt. 20 (2015) 017001. doi.org/10.1117/1.jbo.20.1.017001.

Breast cancer and biomineralization: New insights by means of infrared nanospectroscopy

Petay M(1)*, Deniset-Besseau A(1), Dazzi A(1), Cherfan M(2), Bazin D(1)

(1) Institut de Chimie Physique (ICP), CNRS UMR 8000, Université Paris-Saclay, 91405 Orsay, France
(2) Service Anatomie et Cytologie Pathologiques, Centre Hospitalier René Dubos / GHT NOVO, 95300 Pontoise, France

*Corresponding author's email: margaux.petay@universite-paris-saclay.fr

Introduction – Breast microcalcifications (BMC) are calcium-based mineral deposits within the breast tissue that can be either benign or malign. Their presence on mammograms helps the clinician, as they are considered early signs of breast cancer. However, the correlation between the chemical composition of BMC and breast cancer has been poorly investigated and is still not fully understood. BMC size can range from tens of nanometres to a few hundreds of micrometres. Hence, conventional IR spectroscopy can be used for characterizing the larger BMC but is not suitable for properly describing BMC at the early stage of biomineralization. However, this issue can be addressed by using photothermal infrared spectroscopy such as atomic force microscopy-infrared (AFM-IR) and optical photothermal infrared (OPT-IR) micro-spectroscopy systems.

AFM-IR and OPT-IR are infrared (IR) characterization techniques, based on photothermal phenomena, meaning they probe the thermal expansion of the sample when it absorbs the IR light. OPT-IR uses a visible laser as a probe and has a spatial resolution between 500 nm and 1 µm [1], while AFM-IR senses the thermal expansion of the sample through the tip of an atomic force microscope and has a spatial resolution up to 20 nm [2]. These two technics are non-destructive and do not require specific sample preparation. Therefore, they open new perspectives for the description of complex biological samples at the sub-micrometric scale. For example, AFM-IR was already used to describe, directly in kidney biopsies, vancomycin casts, and more recently crystals involved in cystinosis [3,4]. In that regard, we aim to emphasize that OPT-IR and AFM-IR can contribute to a better understanding of biomineralization in the breast and BMC etiology. Indeed, to this day, two chemical phases - calcium oxalate dihydrate and calcium phosphate apatite - are considered in the breast microcalcification classification. Yet, using IR nanospectroscopy, we will demonstrate the presence of other chemical phases, as well as BMC chemical heterogeneity at the nanoscale.

Materials and Methods – BMC were investigated in patients diagnosed with either in-situ or invasive carcinoma, as well as mastopathies (benign microcalcifications used as control). 4 to 8 µm thick slices of the paraffin- embedded biopsies were placed on low-e microscope slides (substrate compatible with both SEM analysis and IR measurements; MirrIR, Kevley Technologies, Tienta Sciences, Indianapolis). Paraffin was removed using xylene, and microcalcifications chemical analyses were conducted by OPT-IR and AFMIR. OPT-IR measurements were performed using mIRage^{TM} IR microscope from Photothermal Spectroscopy Corp., while AFM-IR measurements were done, in both contact and tapping mode, using NanoIR2 from Bruker nano.

Results – First, we show that AFM-IR and OPT-IR systems are suitable for the description of heterogenous samples and enable the characterization of microcalcifications within their native environment. Thereafter, we demonstrate that a sub-micrometric description of BMC is critical to understand the relationship between biomineralization and breast cancer. We have detected the presence of chemical phases (Figure 1B - dark blue and purple spectra) that aren't considered in the BMC chemical classification (Figure 1B - black and grey spectra) and that have not been described yet by conventional IR spectroscopy. In addition, we highlight BMC local chemical heterogeneity showing that both techniques have a great potential for characterizing BMC and investigating the pathological mineralization processes in breast tissue.

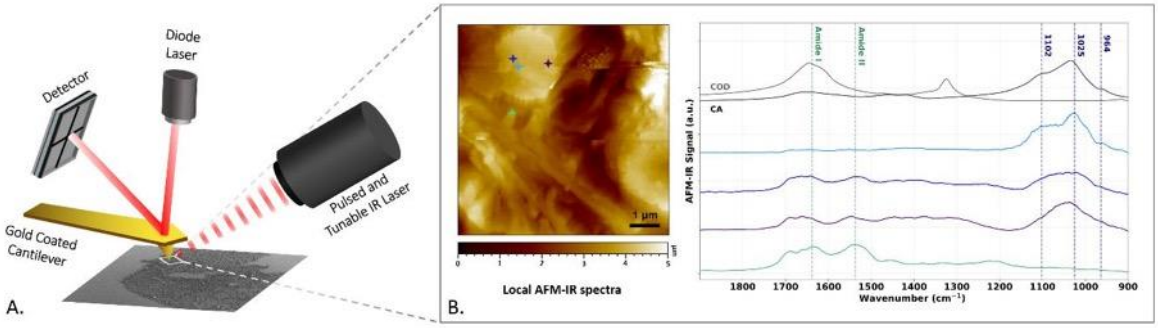

Figure 1 – (A) Representation of the top-down illumination AFM-IR system used to investigated BMC in breast biopsies. **(B)** AFM topography and AFM-IR local spectra in a breast biopsy diagnosed with invasive ductal carcinoma. The coloured stars on the topography indicate the location of the AFM-IR spectra. Grey and black spectra are FTIR reference spectra and correspond, respectively, to Calcium Oxalate Dihydrate (COD) and Calcium Phosphate Apatite (CA): the two chemical phases on which is based the current BMC classification.

Conclusion – Photothermal IR spectroscopy techniques are essential to characterize complex biological samples at the sub-micrometric scale and provide information that isn't accessible through conventional IR micro-spectroscopy. Our results emphasize that BMC implications are still not well understood nor described and prove that AFM-IR and OPT-IR are valuable tools to investigate organic crystals in the breast and evaluate their part in the pathology.

References

[1] M. Kansiz, C. Prater, E. Dillon, M. Lo, J. Anderson, C. Marcott, et al. Optical Photothermal Infrared Microscpectroscopy with Simultaneous Raman - A New Non-Contact Failure Analysis technique for identification of <10 µm Organic Contamination in the Hard Drive and other Electronics Industries, Micros. Today. (2020) DOI: 10.1017/S1551929520000917.

[2] J. Mathurin, A. Deniset-Besseau, D. Bazin, A. Dazzi. Photothermal AFM-IR spectroscopy and imaging: Status, challenges, and trends, J. Appl. Phys. (2022) DOI: 10.1063/5.0063902.

[3] E. Esteve, Y. Luque, J. Waeytens, D. Bazin, L. Mesnard, C. Jouanneau, et al. Nanometric Chemical Speciation of Abnormal Deposits in Kidney Biopsy: Infrared-Nanospectroscopy Reveals Heterogeneities within Vancomycin Casts, Anal. Chem. (2020) DOI: 10.1021/acs.analchem.0c00290.

[4] D. Bazin, M Rabant, J. Mathurin, M. Petay, A. Deniset-Besseau, A. Dazzi, et al. Cystinuria and cystinosis are usually related to L-cystine: is this really the case for cystinosis? A physicochemical investigation at micrometre and nanometre scale, Comptes Rendus Chim. (2021) DOI: 10.5802/crchim.135.

08
Novel Methodologies, Instrumentation, and Applications

PLENARY SESSION

Quartz tuning fork based photoacoustic spectroscopy and sensing

Spagnolo V[(1,2)*], Patimisco P[(1)], Sampaolo A[(1)], Giglio M[(1)], Wu H[(2)], Dong L[(2)]

(1) PolySense Lab - Dipartimento Interateneo di Fisica, University and Politecnico of Bari, Via Amendola 173, Bari, Italy

(2) State Key Laboratory of Quantum Optics and Quantum Optics Devices, Institute of Laser Spectroscopy, Shanxi University, Taiyuan, PR China

*Corresponding author's email: v.spagnolo@poliba.it

Environmental monitoring, as well as safety and security, oil&gas and biomedical applications demand for real time and in-situ solutions together with unambiguous identification and quantification of the chemical analytes composing the investigated samples. Gas spectroscopy exploiting laser sources is a reliable tool providing highly selective and sensitive detection with robust and compact sensor architectures.

Quartz crystal tuning forks (QTFs) resonators are central components for timing and frequency measurements, due to their high stability, high-quality factors and low power consumptions. Thanks to their piezoelectric properties, QTFs are employed as sensitive element in many fields and systems such as atomic Force Microscopy (AFM), near-field, microwave microscopy and mass/viscosity sensor. Since 2002, QTFs are also widely used as a sharply resonant acoustic transducer to detect weak photoacoustic excitation for Quartz-Enhanced Photoacoustic Spectroscopy (QEPAS) [1, 4]

Among most sensitive optical techniques, QEPAS has been demonstrated as the leading-edge technology for addressing these application requirements, providing also modularity, ruggedness, portability and allowing the use of extremely small volumes [1-4]. QEPAS technique does not require an optical detector, it is wavelength independent, it is immune to environmental noise and can operate in a wide range of temperature and pressure. These factors, together with and its proven reliability and ruggedness, represent the main distinct advantages with respect to other laser-based techniques for environmental monitoring and in situ detection. In on-beam QEPAS the laser beam is focused on the gap between the two prongs of QTF and excites the gas molecules (see Figure 1).

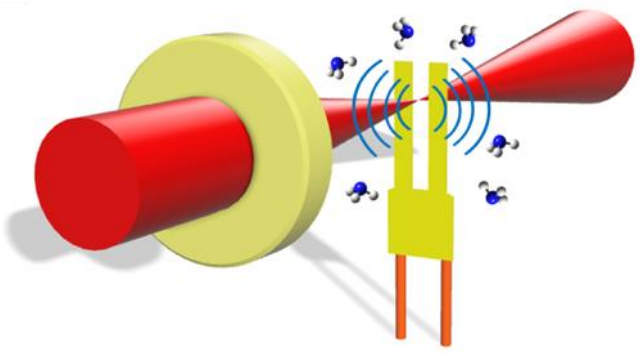

Fig. 1. Schematic diagram of a QTF, a laser and an acoustic wave in on-beam QEPAS.

QTFs have also recently demonstrated their capability to operate as sensitive and broadband infrared photodetectors for absorption spectroscopy. The photodetection process is based on light impacting on

the tuning fork and creating a local temperature increase that generates a strain field. A modulation of the optical power causes periodic heating/cooling, which in turn generates a modulation of accumulated charges on the QTF surface due to quartz piezoelectricity [5-7]. To maximize the photoinduced signal, the laser beam has to focused on the quartz surface where the maximum strain field occurs, typically nearby the QTF prong based (see Fig. 2) and under these conditions the LITES signal-to-noise ratio is proportional to the product of the strain and the QTF accumulation time [6-7].

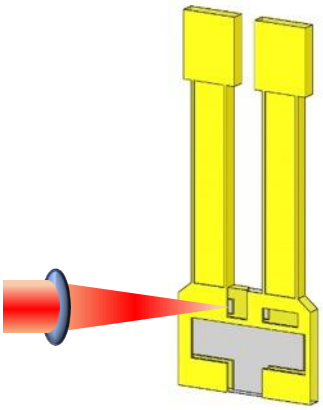

Fig. 2. Schematic of the QTF photodetection process, based on light impacting on the tuning fork.

This technique combined with the tunable diode laser absorption spectroscopy (TDLAS) approach, known as light-induced thermoelastic spectroscopy (LITES), has been explored in the last two years [3]. The typical schematic of LITES is shown in Fig. 3. The QTF can be placed far from the target gas and be sealed in a gas chamber with an inert gas or under vacuum. Therefore, LITES is a non-contact measurement method and can be used for remote and standoff gas detection.

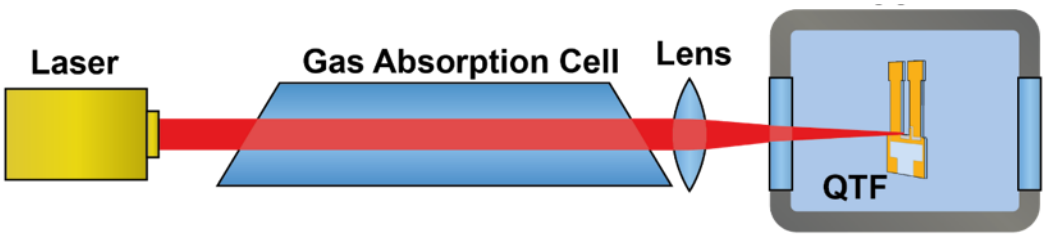

Fig. 3. LITES schematic

Starting from the basic physical principles governing the QTF physics, I will review the main results achieved by exploiting custom QTFs for QEPAS sensing and as photodetector in LITES setup, with a main focus on real-world applications. Finally, a detailed description of an innovative QEPAS shoebox sized sensor system for in-situ operations [8-10] will be provided.

References

[1] P. Patimisco, G. Scamarcio, F.K. Tittel and V. Spagnolo, Quartz-Enhanced Photoacoustic Spectroscopy: A Review, Sensors 14 (2014) 6165-6206.

[2] P. Patimisco, A. Sampaolo, H. Zheng, L. Dong, F.K. Tittel, V. Spagnolo, Quartz-enhanced photoacoustic spectrophones exploiting custom tuning forks: a review, Advances in Physics X 2 (2016) 169-187.

[3] P. Patimisco, A. Sampaolo, L. Dong, F.K. Tittel, V. Spagnolo, Recent advances in quartz enhanced photoacoustic sensing, Appl. Phys. Rev. 5 (2018) 011106.

[4] A. Sampaolo, P. Patimisco, M. Giglio, A. Zifarelli, H. Wu, L. Dong, V. Spagnolo, Quartz-enhanced photoacoustic spectroscopy for multi-gas detection: A review, Anal. Chim. Acta, (2021) 338894. https://doi.org/10.1016/j.aca.2021.338894.

[5] Y. Ma, Y. He, Y. Tong, X. Yu, F.K. Tittel, Quartz-tuning-fork enhanced photothermal spectroscopy for ultra-high sensitive trace gas detection, Opt. Express 26 (2018) 32103–32110.

[6] S. Dello Russo, A. Zifarelli, P. Patimisco, A. Sampaolo, T. Wei, H. Wu, L. Dong, V. Spagnolo, Light-induced thermo-elastic effect in quartz tuning forks exploited as a photodetector in gas absorption spectroscopy, Optics Express 28 (2020) 19074-19084.

[7] T. Wei, A. Zifarelli, S. Dello Russo, H. Wu, G. Menduni, P. Patimisco, A. Sampaolo, V. Spagnolo, L. Dong, High and flat spectral responsivity of quartz tuning fork used as infrared photodetector in tunable diode laser spectroscopy, Appl. Phys. Rev. 8 (2021) 041409.

[8] A. Sampaolo, S. Csutak, P. Patimisco, M. Giglio, G. Menduni, V. Passaro, F.K. Tittel, M. Deffenbaugh, V. Spagnolo, Methane, ethane and propane detection using a compact quartz enhanced photoacoustic sensors and a single interband cascade laser, Sens. Act. B Chem. 282 (2019) 952-960.

[9] A. Sampaolo, et al., Quartz-enhanced photoacoustic spectroscopy for hydrocarbon trace gas detection and petroleum exploration, Fuel 227, 112112 (2020).

[10] F. Sgobba, A. Sampaolo, P. Patimisco, M. Giglio, G. Menduni, A.C. Ranieri, C. Hoelzl, H. Rossmadl, C. Brehm, V. Mackowiak, D. Assante, E. Ranieri, Vincenzo Spagnolo, Compact and portable quartz-enhanced photoacoustic spectroscopy sensor for carbon monoxide environmental monitoring in urban areas, Photoacoustics 25 (2022) 100318.

PLENARY SESSION

Mid-IR laser based photothermal sensing of gases, liquids and imaging

Lendl B[(1)*], Ricchiuti G[(1)], Pinto D[(1)], Waclawek JP[(2)], V. D. dos Santos AC[(1)], Ramer G[(1)]

(1) TU Wien, Institute of Chemical Technologies and Analytics, Vienna, Austria
(2) Competence Center CHASE GmbH, Vienna, Austria

*Corresponding author's email: bernhard.lendl@tuwien.ac.at

Advances in Instrumental Analytical Chemistry are often linked to technological developments in neighbouring disciplines. This is the case with respect to recent advances in Mid-IR quantum cascade lasers (QCLs) which are increasingly used as a new light source in mid-IR spectroscopy. QCLs offer high spectral power densities, fast amplitude and frequency modulation possibilities, polarized and coherent radiation. Based on these properties a range of new sensing schemes, often clearly outperforming established FTIR based analysers, have been developed recently. This presentation will centre on photothermal sensing schemes for trace analysis of gases, liquids as well as label free mid-IR imaging with nanometre spatial resolution. As opposed to established mid-IR absorption spectroscopy based on Beer´s law, mid-IR photothermal spectroscopy is an indirect method where the generated analytical signal scales directly proportional to the laser power. In one way or another it detects temperature induced changes (refractive index changes, sample expansion) in the sample matrix which are caused by absorption of the mid-IR photons by the analyte present in the sample under investigation.

After introducing the general concept of QCL based photothermal spectroscopy in comparison to absorption spectroscopy, applications will be shown covering different fields. For trace gas sensing interferometric cavity assisted photothermal spectroscopy (ICAPS) will be introduced [1]. This technique uses a Fabry-Perot interferometer to read out temperature induced refractive index changes in gaseous samples and achieves single digit ppb sensitivities (1 sigma, 1 second) for SO2, CO and similar IR active gases. ICAPS employs CW operated frequency tuneable distributed feedback QCLs as an excitation source to target isolated ro-vibrational transitions of the target gas molecule and an NIR probe laser to monitor the induced refractive index changes. Recent developments include a fibre coupled readout system and locking of the diode probe laser to the inflection point of transmission function. Because the thermal wave is heavily damped it is possible to develop effective balanced detection schemes in a small sensor architecture. A typical sensing configuration is shown in the Fig. 1 below.

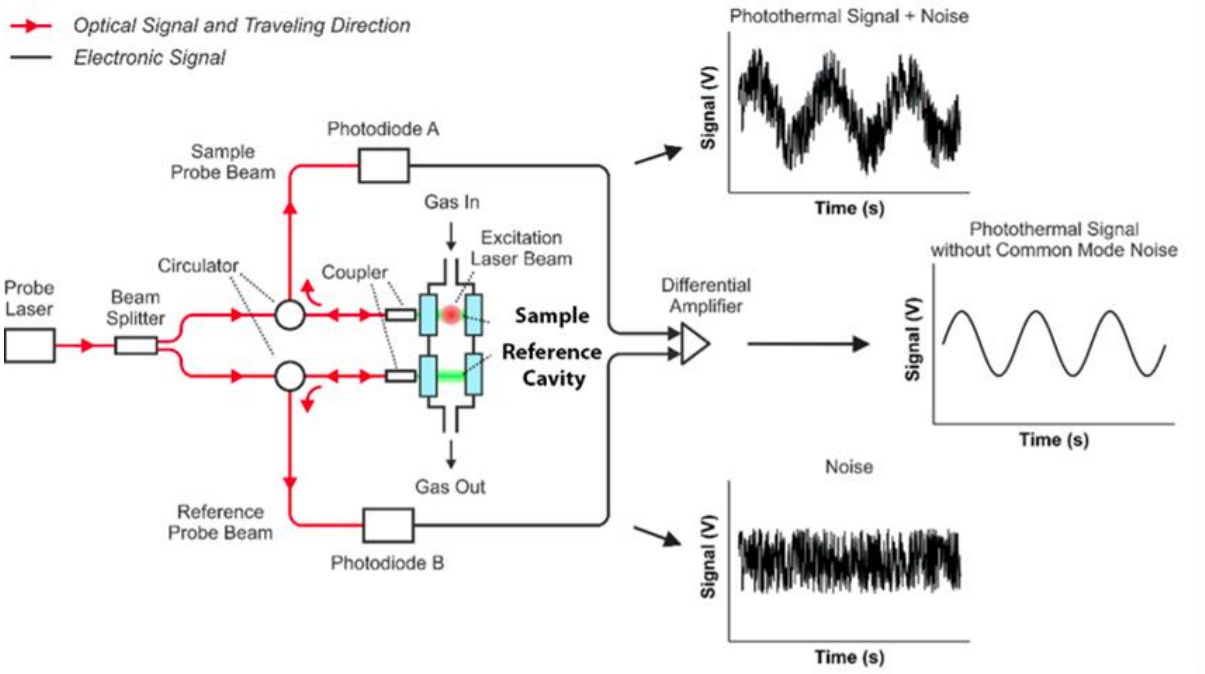

Fig. 1. Principle of balanced-detection ICAPS monitoring the reflectance of the interferometers in an all fibre-coupled probe laser configuration; the probe beam is split into two equal parts – a sample probe beam and a reference probe beam – and coupled by a collimator into two separate but identical interferometers. The sample beam probes the photothermal signal, which is superimposed by noise, whereas the reference beam probes only noise. The reflected light is again collected by the coupler and separated from the forward propagating light coming from the probe laser by a circulator, routing the beam to a photodiode. By subtraction of the two photodiode signals, the photothermal signal is received along with high rejection of common mode noise.

With respect to the analysis of liquids trace analysis of water in organic solvents will be shown and introduced as an alternative to Karl Fischer titration. This technique uses a broadly tuneable pulsed external cavity QCL for measuring the characteristic bending vibration of condensed water. The sample is illuminated by a pulsed mid-IR excitation source causing a periodical heating and cooling of the sample. The resulting photo-induced thermal gradient ΔT can be probed as a consequent refractive index change (Δn) by means of a second laser source, a so called “probe laser”. The challenge lies in detecting the smallest Δn. To do that, we use an interferometric approach. In particular, our liquid PTS IR sensor consists of a Mach-Zehnder Interferometer (MZI) able to sense sub-nm phase shifts $\Delta\varphi$ between its two arms. For that we use a HeNe probe laser and an external cavity (EC)-QCL pump laser tuneable from 1730 to 1565 cm^{-1}. The stability and linearity of our system are ensured by temperature stabilization and holding the MZI in its quadrature point using a PID controlled piezo electric transducer (PZT) glued directly on a mirror in one arm of the MZI. Some of the relevant obtained results are reported in Fig. 2. Achieved limits of detection are in the low ppm region [2].

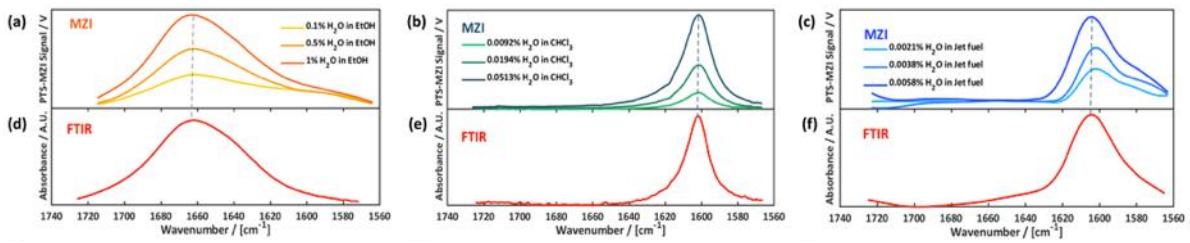

Fig. 2. PTS spectra of the water bending vibration as recorded using the Mach Zehnder Interferometer (MZI) and compared to the those recorded on a standard FTIR spectrometer. **(a),(d):** water in ethanol, **(b),(e)** water in chloroform and **(c),(f)** water in jet-fuel. The differences in the spectral shape result from different H-bonding of the water molecule in the studies solvents and solvent system (jet-fuel).

Nanometre spatial resolution in mid-IR imaging is achieved by coupling an atomic force microscope to a broadly tuneable pulsed EC-QCL source (AFM-IR). After a short introduction to this technique data obtained using tapping mode AFM-IR for the analysis of a PE/PP recyclate blend will be shown. The analysed sample derives from a post-consumer waste stream containing PE, PP, and a rubber component. Using tapping mode AFM-IR for recording spectra and images, and chemometric models for data analysis, we are able to locate the rubber component at the interface of the PE and PP and to detect the presence of other polymer contaminants. The AFM-IR data obtained through spectra and chemical images are in agreement with each other as well as with data obtained from conventional methods (SEM and soluble fraction analysis). The results obtained thus demonstrate that AFM-IR is a valuable tool for the nanoscale analysis of recycled polymer blends. A representative AFM-IR image of a region of only 1,5 µm x 1,5 µm is shown in Fig 3. Plotting the ratio of the characteristic C-H bending vibrations of PP and PE allows detection of small PP inclusion in PE in a direct and label-free way.

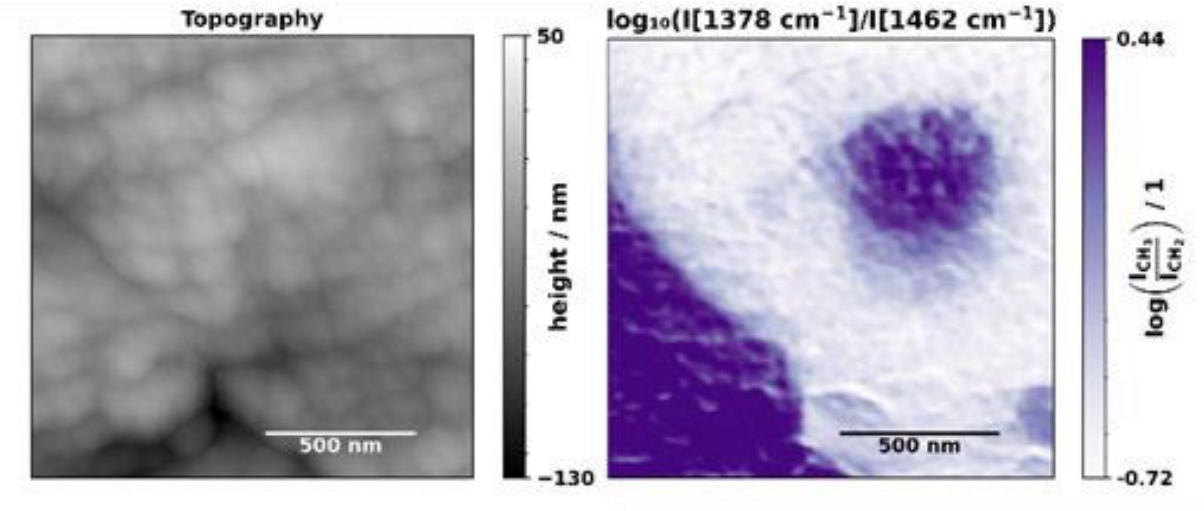

Fig. 3. Topography and band ratio of the bands corresponding to deformation vibrations of CH_2 and symmetric deformation of CH_3 groups (1.5 µm x 1.5 µm).

References

[1] J. P. Waclawek, H. Moser, B. Lendl, Balanced-detection interferometric cavity-assisted photothermal spectroscopy employing an all-fiber-coupled probe laser configuration, Opt. Exp. 29:5 (2021) 7794-7808.

[2] G. Ricchiuti, A. Dabrowska, D. Pinto, G. Ramer, B. Lendl (2022) *submitted.*

[3] A. C. V. D. dos Santos, D. Tranchida, B. Lendl, G. Ramer (2022) *submitted.*

KEYNOTE SPEAKER

Probing micron-sized objects with photoacoustic sensing: Theory and applications

Kolios MC[(1,2,3)*], Strohm EM[(1,2,3)], Bok T[(1,2,3)], Sathiyamoorthy K[(1,2,3)]

(1) Department of Physics, Toronto Metropolitan University (formerly Ryerson University), Toronto, Canada
(2) Institute for Biomedical Engineering, Science and Technology (iBEST), Toronto, Canada
(3) Keenan Research Centre for Biomedical Science, Toronto, Canada

*Corresponding author's email: mkolios@ryerson.ca

The covid-19 respiratory illness resulting from the severe acute respiratory syndrome coronavirus 2 (SARS-CoV-2) has caused a worldwide pandemic over the past two years. Despite various screening methods, vaccinations, and mitigation methods, including masking and social distancing, covid-19 remains a global issue in part due to airborne viral transmission via aerosolization. Current screening methods have a slow response or lack sensitivity. In this study, we explore air-based photoacoustic spectroscopy as a rapid method to screen for the presence of covid-19 via viral RNA within aerosolized droplets.

Background – Transmission of covid-19 primarily occurs via airborne transmission through expelled aerosolized droplets from infected people [1]. Current methods to detect covid viral infections include reverse transcription-polymerase chain reaction (RT-PCR) and rapid antigen lateral flow tests (RAT) [2]. While these methods can confirm an infection, PCR is time-consuming to process, and RAT suffers from low sensitivity in addition to a 15-minute wait period. This study aims to develop a rapid screening system for the detection of viral RNA in aerosolized droplets using air-coupled photoacoustic spectroscopy [3] that can be used to screen people with immediate feedback (like a Breathalyzer), and monitor indoor air space.

We asked whether biological samples in the nanometre range could be sensed using photoacoustic sensing. This work explores whether aerosolized particles (micron size) containing viral particles (nanometre-sized) could be detected with photoacoustic sensing, using kHz ultrasound detection (to enable ultrasound propagation through air). We previously published on how micron-sized objects could be sized using photoacoustics (PA) and ultrasound (US) [4]. We derived simple analytical solutions to rapidly determine the US and PA signal power spectra minima and maxima, that could be used to identify the sample. We showed that using ultrasound frequencies above 100 MHz, the size of cells and cell nuclei could be determined.

Method – A syringe pump was used to push liquid from a 10 mL syringe through a nasal sprayer (Teleflex, USA) to create droplets in the 0.3-10 µm diameter range (figure 1). The liquid used in the syringe pump was water containing black dye (532 nm), acridine orange dye (Sigma, USA), or 50 nm gold nanoparticles (260 nm). The pump was turned on for 8 s while a laser (Radiant HD, Opotek, USA) collimated to a 1 mm beam diameter was aimed through the spray of droplets. Laser energies of 5 mJ (at 532 nm) and 3 mJ (at 260 nm) were used. The photoacoustic signals were detected by a 350 kHz planar ultrasound transducer (Ultran, USA), amplified by a 30 dB amplifier (RF Bay, USA), then

digitized by a Cobramax digitizer at 50 MS/s (Gage Applied, USA). The digitizer was triggered via the laser sync output.

Results – Initial tests using water droplets containing black dye with the 532 nm laser showed that photoacoustic signals were detected from droplets containing black dye, but no photoacoustic signals were detected from plain water droplets. This result demonstrates that air-coupled photoacoustic detection of particulates is possible despite the extremely high sound attenuation in air. The system was switched to a 260 nm laser wavelength and droplets containing acridine orange dye, which has an absorption peak at 270 nm, similar to DNA. Representative photoacoustic signals of plain water droplets and droplets containing acridine orange dye are shown in figure 2A. Generally, the photoacoustic signal amplitude of the orange dye was lower than that of plain water, despite a higher absorption coefficient. The photoacoustic signal amplitudes during the 8 s spray time are shown in figure 2B. As the orange dye concentration decreased, the average photoacoustic signal amplitude increased. The same procedure was then performed using droplets containing 50 nm gold nanoparticles and the 260 nm wavelength laser. The photoacoustic signal amplitude of droplets with plain water and nanoparticles at low, medium, and high concentrations over the 8 s acquisition duration are shown in figure 2C. The photoacoustic amplitude decreased with increasing nanoparticle concentration, the same trend observed with the orange dye.

To understand why the photoacoustic signal amplitude decreased with increasing absorber concentration, Monte Carlo simulations that calculated the photoacoustic signal amplitude from droplets containing varying levels of nanoparticle absorbers were performed. We found that the absorbers block light transmission near the droplet's surface, preventing photons from propagating deeper into the droplet. As the absorber concentration increased, fewer photons could reach the absorbers, resulting in a decreased photoacoustic signal.

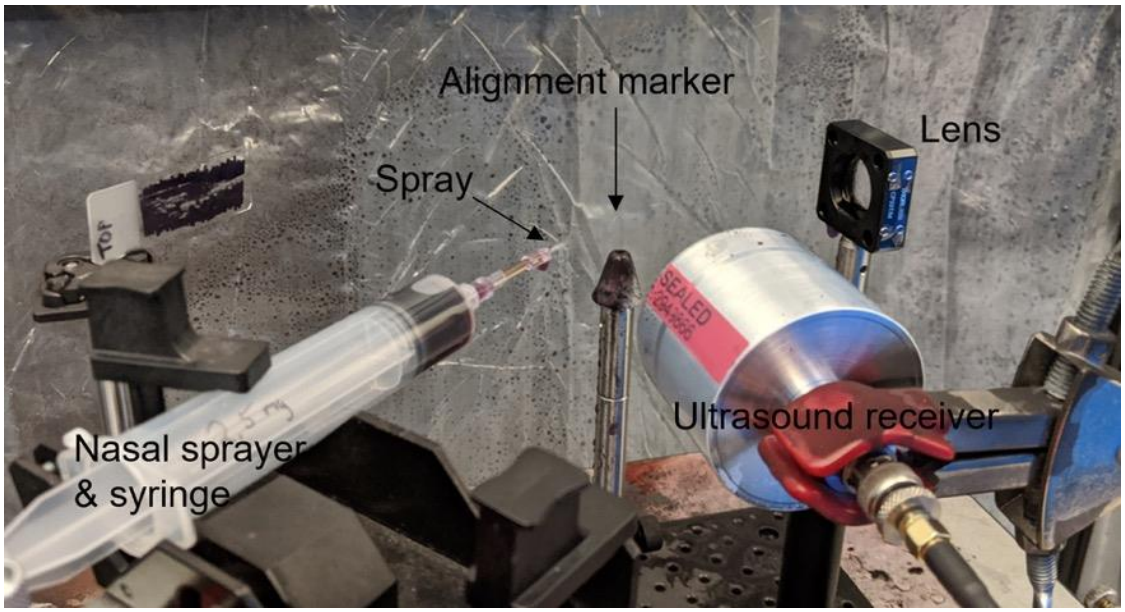

Fig. 1. The system setup to record photoacoustic signals from a droplet cloud.

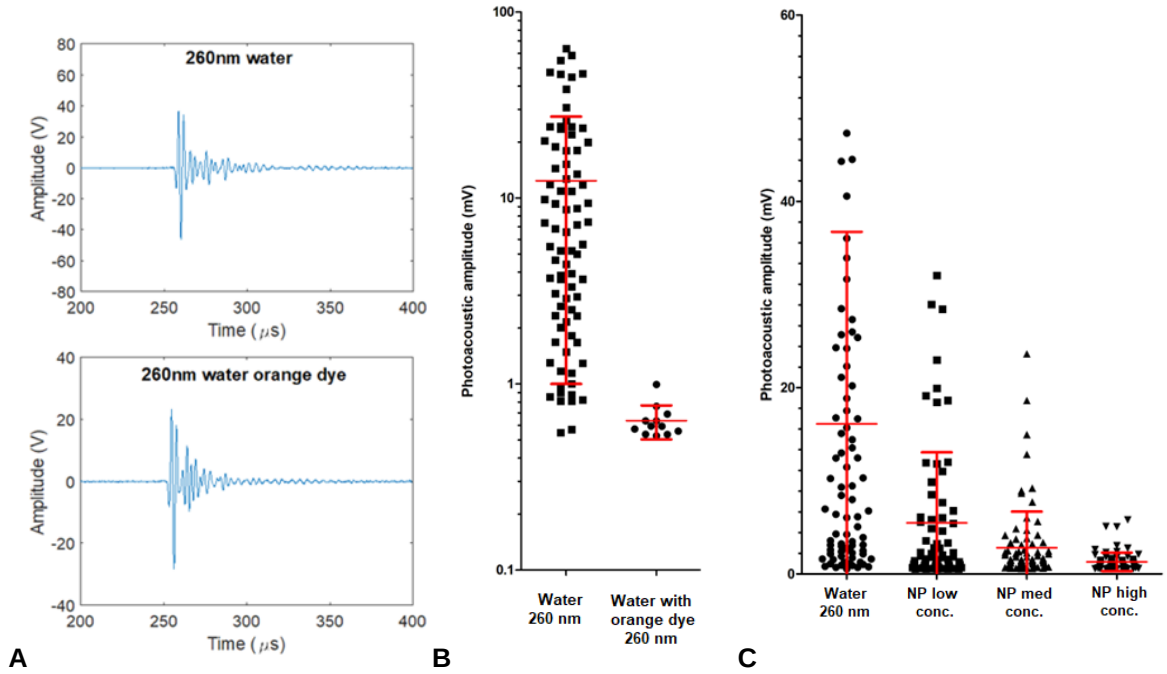

Fig. 2. (A) Representative photoacoustic signals from a droplet of plain water (top) and a droplet with acridine orange dye (bottom), **(B)** Photoacoustic signal amplitudes of droplets of water and water with orange dye recorded over 8 s acquisition, **(C)** Photoacoustic signals of droplets from water and water with nanoparticles at low, medium, and high concentrations.

Conclusion – This preliminary study suggests that air-coupled photoacoustics can be used to detect particulates in aerosolized droplets. The photoacoustic amplitude depends on the absorption and scattering properties of the particulates, where a decrease in signal amplitude with increasing absorber concentration was observed. Future work will use photoacoustic spectroscopy, where multiple wavelengths will be used to identify the particulates within droplets. Tests will be conducted using inactivated viruses to test the ability to detect viral RNA within aerosolized droplets.

References

[1] R. Zhang, Y. Li, A.L. Zhang, Y. Wang, M. J. Molina, Identifying airborne transmission as the dominant route for the spread of COVID-19, Proceedings of the National Academy of Sciences, 117 (2020) 14857–14863.

[2] T. Ji et al., Detection of COVID-19: A review of the current literature and future perspectives, Biosensors and Bioelectronics, 166 (2020) 112455.

[3] A. Rosencwaig, Photoacoustic Spectroscopy, Annual Review of Biophysics and Bioengineering, 9 (1980) 31–54.

[4] M.J. Moore, E.M.Strohm, M.C. Kolios, Assessment of the Nucleus-to-Cytoplasmic Ratio in MCF-7 Cells Using Ultra-high Frequency Ultrasound and Photoacoustics. Int. J. Thermophys. 37 (2016) 118.

KEYNOTE SPEAKER

Nanoscale structural dynamics by extreme ultraviolet transient gratings

Bencivenga F(1)*, Foglia L(1), Masciovecchio C(1), Mincigrucci R(1)

(1) Elettra-Sincrotrone Trieste, Basovizza (TS), Italy

*Corresponding author's email: Filippo.bencivenga@elettra.eu

The coherent pulses of the FERMI seeded free electron laser (FEL) have permitted the development of the transient grating (TG) approach in the extreme ultraviolet (EUV) spectral range [1-3]. The implementation of FEL-pump/FEL-probe capabilities in EUV TG experiments allows to generate TG with spatial periodicities as short as 20 nm and probe the response on the investigated sample on ultrafast timescales [4].

The capability to generate spatial patterns of light on such a fine length-scale has relevant applications in probing dynamical processes on mesoscopic (10's of nm) scales, hardly accessible by other means. In this lecture we will provide examples of applications of this new experimental tool, in particular for nanoscale thermal transport in thin membranes of crystalline silicon and amorphous silicon nitride [4], where the thermal decay time of the nanoscale TG shows a marked deviation, with respect to the diffusive regime, in the crystalline sample. Conversely, in the amorphous sample the wavelength dependence of the thermal transport timescale is consistent with a diffusive behaviour. We will also highlight the possibility to use EUV TG to generate and detect the dynamics of bulk and surface phonons on previously inaccessible wavelength range [4-5].

We finally discuss on the potential of EUV TG in other contexts, such as, e.g., ultrafast magnetic dynamics at the nanoscale [6], as well as the ongoing development, which include the capability to use hard x-rays for TG excitations [7].

References

[1] F. Bencivenga et al., Four-wave mixing experiments with extreme ultraviolet transient gratings, Nature 520 (2015) 205.

[2] L. Foglia et al., First Evidence of Purely Extreme-Ultraviolet Four-Wave Mixing, Phys. Rev. Lett. 120 (2018) 263901.

[3] A.A. Maznev et al., Generation of coherent phonons by coherent extreme ultraviolet radiation in a transient grating experiment, Appl. Phys. Lett. 113 (2018) 221905.

[4] F. Bencivenga et al., Nanoscale transient gratings excited and probed by extreme ultraviolet femtosecond pulses, Science Advances 5 (2019) eaaw5805.

[5] A.A. Maznev et al., Generation and detection of 50 GHz surface acoustic waves by extreme ultraviolet pulses, Appl. Phys. Lett. 119 (2021) 044102.

[6] D. Ksenzov et al., Nanoscale Transient Magnetization Gratings Created and Probed by Femtosecond Extreme Ultraviolet Pulses, Nano Lett. 21 (2021) 2905.

[7] J.R. Rouxel et al. Hard X-ray Transient Grating Spectroscopy on Bismuth Germanate, Nature Photonics 15 (2021) 499.

KEYNOTE SPEAKER

Scanning Thermal Microscopy – current applications and perspectives

Bodzenta J[(1)*], Kaźmierczak-Bałata A[(1)]

(1) Institute of Physics, Silesian University of Technology, Gliwice, Poland

*Corresponding author's email: jerzy.bodzenta@polsl.pl

Background – In the last few decades nanotechnology is of growing importance in many areas of science and technology. A production of structures with the length scale of several nanometres is a standard in electronic industry. Nowadays technology allows fabrication of low-dimensional structures, e.g., quantum dots, nanowires, and 2D materials like graphene, silicene, etc. Transport phenomena in such structures cannot be described by classical laws, new approaches are necessary. In a case of thermal measurements, the scanning thermal microscopy (SThM) is a method with a great potential.

SThM – principle, instrumentation, operation modes – The SThM was developed by Williams and Wickramasinghe in 1986 [1, 2]. Currently used microscopes utilize working principle described by Majumdar *et al.* in 1993 [3]. The idea was to combine topographical imaging by atomic force microscope (AFM) with thermal imaging. For this purpose, special thermal probes (TPs), with the temperature sensor placed near the probe apex, are used. The SThM operates in two basic modes: the temperature contrast mode (TCM) and the conductance contrast mode (CCM). The TCM is a passive mode in which the TP measures the local temperature of sample surface. The CCM is an active mode. The TP is heated, and its temperature rise θ depends on dissipated power P, and the thermal conductance G_{th} for the heat flow J from the TP to the surroundings

$$\theta = \frac{P}{G_{\mathrm{th}}} \qquad \text{Eqn. 1}$$

In a steady-state P is equal to J. A certain part of J flows to the sample and depends on the sample thermal conductivity k. Therefore, the sensor temperature also depends on k. As a result, the SThM can be used for determination of local thermal conductivity of sample.

For quantitative measurement the TP must be calibrated. A calibration in TCM mode is relatively simple. The main problem is that the temperature sensor is not in thermal equilibrium with the sample. Therefore, the probe temperature differs from the one of sample. A few measuring techniques were proposed to solve this problem [4-6]. In the case of CCM mode the situation is more complex. The thermal transport from the TP to the sample is influenced by many factors. The heat flows through the TP-sample contact but also through its surroundings (the air, the water meniscus). Moreover, the energy is also transferred by thermal radiation. Some mechanisms are excluded in the vacuum SThM. The heat transport through the contact depends on: the sample surface roughness, the constriction resistance, and the boundary resistance. Detailed analysis of the problem can be found in review papers [7, 8].

Thermal probes – The probe is a key element of each scanning microscope. It defines the physical quantity, which can be measured, and spatial resolution of measurements. As it was mentioned above, probes used for SThM must provide temperature measurement. Temperature sensors utilize dependence of any physical quantity on temperature. In practice, TPs must meet a few conditions. They should be

compatible with a standard scanning microscope. The probe signal should be easily detected and processed. Probes should have repeatable parameters.

The most popular are resistive TPs, which utilize a dependence of electrical resistance on the temperature. Comprehensive description of commercially available resistive TPs can be found in Ref. [9]. Thermoelectric TPs, with a thermocouple junction on the tip, are also used quite often.

Theory and modelling – The correct interpretation of the SThM measurement results requires an understanding of the thermal transport phenomena occurring in the measuring system. Because of complex geometry of the TP-sample system, exact analytical description of the thermal transport in the system is not possible. Simplified analytical models based on the thermal fin equation with a Joule dissipation term were used [10]. The main advantages of the model are that it allows determination of the temperature distribution along the TP, and its frequency characteristics. However, the thermal fin model corresponds only to the geometry of Wollaston probe. Application of fin model to describe other probes is difficult to justify.

A well-known tool for the heat transfer modelling is the quadrupole method. The method is based on electro-thermal analogies. It was successfully used for analysis of frequency characteristics and sensitivity to G_{th} in SThM measurements with the resistive TP driven by a sum of dc and ac electric currents [11]. The electro-thermal analogies are also used for modelling the TP-sample heat exchange [7, 8].

The SThM measurements are also modelled numerically. The most popular method is the finite element method. This approach allowed analysis of complex geometries and can be use from macroscale to nanoscale. In the case of SThM numerical models, the method allowed either the investigation of radiative thermal transport in nanoscale [12] or processes in the whole TP-sample system [9].

Examples of SThM measurements – Since its development, the SThM found many applications in research. It was used for *k* measurements of thin films [13] and nanowires [14]. It allowed investigation of nanoscale hot spots [6], thermoelectric effects in graphene nanoconstrictions [15], and temperature mapping of operating nanoscale devices [16]. These are just a few examples.

Conclusions – The scanning thermal microscopy is the only method allowing thermal measurements with spatial resolution in the nanometre range. However, it has number of limitations. The thermal conductance for the heat flux to the sample depends on sample roughness; and is also influenced by sample topography. Therefore, samples must be smooth and flat for quantitative measurements. Moreover, the SThM signal is influenced by ambient conditions, e.g., humidity. To exclude environmental influences measurements are often carried out in a vacuum. Quite complex theoretical model of measurement causes that the measurement methodology is not well established. Moreover, the sensitivity of SThM signal to *k* is low. All these difficulties cause that at present the use of the SThM is limited to scientific research. Possible development can be probably achieved by using new TPs, whose construction will be like those used in classical AFM.

Despite all these limitations, it should be underlined that SThM opens a window to observe thermal transport in the nanoscale, where new phenomena can be observed.

References

[1] C.C. Williams, H.K. Wickramasinghe, Scanning thermal profiler, Appl. Phys. Lett. 49 (1986) 1587-1589. https://doi.org/10.1063/1.97288.

[2] C.C. Williams, H.K. Wickramasinghe, High resolution thermal microscopy, 1986 IEEE Ultrasonics Symposium Proceedings (IEEE, New York, 1986), pp. 393-397. https://doi.org/10.1109/ultsym.1986.198771.

[3] A. Majumdar, J.P. Carrejo, J. Lai, Thermal imaging using the atomic force microscope, Appl. Phys. Lett. 62 (1993) 2501-2503, https://doi.org/10.1063/1.109335.

[4] K. Kim, J. Chung, J. Won, O. Kwon, J.S. Lee, S.H. Park, Y.K. Choi, Quantitative scanning thermal microscopy using double scan technique, Appl. Phys. Lett. 93 (2008) 203115. https://doi.org/10.1063/1.3033545.

[5] J. Chung, K. Kim, G. Hwang, O. Kwon, S. Jung, J. Lee, J.W. Lee, G.T. Kim, Quantitative temperature measurement of an electrically heated carbon nanotube using the null-point method, Rev. Sci. Instrum. 81 (2010) 114901. https://doi.org/10.1063/1.3499504.

[6] F. Menges, H. Riel, A. Stemmer, B. Gotsmann, Quantitative thermometry of nanoscale hot spots, Nano Lett. 12 (2012) 596-601. https://doi.org/10.1021/nl203169t.

[7] S. Gomès, A. Assy, P.-O. Chapuis, Scanning thermal microscopy: A review, Phys. Status Solidi A 212 (2015) 477-494. https://doi.org/10.1002/pssa.201400360.

[8] Y. Zhang, W. Zhu, F. Hui, M. Lanza, T. Borca-Tasciuc, M. Muñoz Rojo, A review on principles and applications of scanning thermal microscopy (SThM), Adv. Func. Mater. 29 (2019) 1900892. https://doi.org/10.1002/adfm.201900892.

[9] Y. Zhang, W. Zhu, T. Borca-Tasciuc, Sensitivity and spatial resolution for thermal conductivity measurements using noncontact scanning thermal microscopy with thermoresistive probes under ambient conditions, Oxford Open Mater. Sci. 1 (2021) itab011. https://doi.org/10.1093/oxfmat/itab011.

[10] S. Lefèvre, S. Volz, 3ω-scanning thermal microscope, Rev. Sci. Instrum. 76 (2005) 033701. https://doi.org/10.1063/1.1857151.

[11] J. Bodzenta, M. Chirtoc, J. Juszczyk, Reduced thermal quadrupole heat transport modeling in harmonic and transient regime scanning thermal microscopy using nanofabricated thermal probes, J. Appl. Phys. 116 (2014) 054501. https://doi.org/10.1063/1.4891872.

[12] K.L. Nguyen, O. Merchiers, P.-O. Chapuis, Near-field radiative heat transfer in scanning thermal microscopy computed with the boundary element method, J. Quant. Spectrosc. Radiat. Transf. 202 (2017) 154-167 https://doi.org/10.1016/j.jqsrt.2017.07.021.

[13] J. Juszczyk, A. Kaźmierczak-Bałata, P. Firek, J. Bodzenta, Measuring thermal conductivity of thin films by Scanning Thermal Microscopy combined with thermal spreading resistance analysis, Ultramicroscopy 175 (2017) 81-86. https://doi.org/10.1016/j.ultramic.2017.01.012.

[14] A. El Sachat, J.S. Reparaz, J. Spiece, M.I. Alonso A.R. Goñi, M Garriga, P.O. Vaccaro, M.R. Wagner, O.V. Kolosov, C.M. Sotomayor Torres, F. Alzina, Thermal transport in epitaxial $Si_{1-x}Ge_x$ alloy nanowires with varying composition and morphology, Nanotechnology 28 (2017) 505704. https://doi.org/10.1088/1361-6528/aa9497.

[15] A. Harzheim, J. Spiece, C. Evangeli, E. McCann, V. Falko, Y. Sheng, J.H. Warner, G.A.D. Briggs, J.A. Mol, P. Gehring, O. V. Kolosov, Geometrically Enhanced Thermoelectric Effects in Graphene Nanoconstrictions, Nano Lett. 18 (2018) 7719-7725. https://doi.org/10.1021/acs.nanolett.8b03406.

[16] F. Menges, P. Mensch, H. Schmid, H. Riel, A. Stemmer, B. Gotsmann, Temperature mapping of operating nanoscale devices by scanning probe thermometry, Nat. Commun. 7 (2016) 1-6. https://doi.org/10.1038/ncomms10874.

Pulse gas-microphone photoacoustic signal measured by minimum volume cell set-up including thermal relaxations: Theoretical consideration

Galović SP[(1)*], Todorović D[(2)], Djordjevic KLj[(1)], Popović MN[(3)], Markushev DD[(3)]

(1) University of Belgrade, „VINČA" Institute of Nuclear Sciences - National Institute of the Republic of Serbia, P.O. Box 522, 11000 Belgrade, Serbia
(2) University of Belgrade, Institute for Multidisciplinary Research, P.O. Box 33, Belgrade, 11030, Serbia
(3) University of Belgrade, Institute of Physics Belgrade, National Institute of the Republic of Serbia Pregrevica 118, 11080 Belgrade (Zemun), Serbia

*Corresponding author's email: bobagal@vin.bg.ac.rs

The Photoacoustic (PA) effect is suitable for the development of experimental non-contact and non-destructive methods and allows examining the optical, thermal, elastic, and carrier transport characteristics of various materials: semiconductors, metals, polymers, biological tissues, etc. [1-8]. Additionally, time-domain PA measurements enable in-situ and in-vivo characterization and imaging that are required in many industrial and medical applications [6-8].

In this paper, the theoretical model of the time-domain minimum volume PA measurement is derived. The assumptions of the model are: 1) monochromatic light source uniformly illuminates the surface of the sample, providing a basis for a one-dimensional model; 2) acoustic transducer is at the backside of the medium and the laser pulse is incident on the front side (transmission experimental configuration); 3) non-radiative relaxation processes occur instantaneously on the time scale of the measurement; 4) the temperature variations at the backside of the sample are relevant to the creation of the acoustic wave in the minimum volume cell; 5) the thermal relaxations in the sample is considered in modeling of heat transfer across the optically induced system.

The analysis is restricted to systems illuminated by rectangular pulses. The influence of optical, thermal, and elastic properties of the sample, as well as pulse width, on PA amplitude is discussed. It is shown that the thermal relaxation time of the sample significantly changes the shape and magnitude of the PA response (Fig.1).

The derived model can be used for the analysis of PA responses excited by any time-dependent modulation of the optical beam. Besides, the introduction of thermal relaxation time enables applications of the model for PA characterization of samples with an inhomogeneous inner structure such as porous materials, polymers, soft matter, tissues, etc.

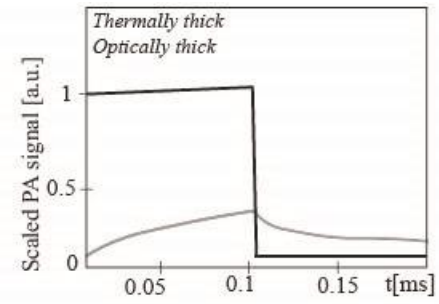

Fig.1. Scaled PA response calculated for optically and thermally thick sample if the thermal relaxation time is neglected, $\tau = 0$, (grey) and if $0 < \tau < T$ where T signifies pulse width (black).

Reference

[1] A. Rosencwaig, A. Gersho, Theory of the photoacoustic effect with solids, J. Appl. Phys., 47 (1976) 64. https://doi.org/10.1063/1.322296.

[2] A. Mandelis, B.S.H. Royce. Time-domain photoacoustic spectroscopy of solids, J. Appl. Phys., 50 (1878) 4330-4338. https://doi.org/10.1063/1.326471.

[3] A. Mandelis, B.S.H. Royce, Relaxation time measurements in frequency and time-domain photoacoustic spectroscopy of condensed phases. J. Opt. Soc. Am. 70:5 (1980) 474-480. doi:10.1364/josa.70.000474

[4] D.M. Todorović, M.D. Rabasović, D.D. Markushev, V. Jović, K.T. Radulović, Investigation of Micromechanical Structures by Photoacoustic Elastic Bending Method, Int. J. Thermophys. 33:10-11 (2012) 2222-2229. doi:10.1007/s10765-012-1242-9.

[5] S. Galović, Z. Šoškić, M. Popović, D. Čevizović, Z. Stojanović, Theory of photoacoustic effect in media with thermal memory, J. Appl. Phys., 116(2) (2014) 024901. doi: 10.1063/1.4885458

[6] S. Liang, B. Lashkari, S.S.S. Choi, V. Ntziachristos, A. Mandelis, The application of frequency-domain photoacoustics to temperature-dependent measurements of the Grüneisen parameter in lipids, Photoacoustics 11(2018) 56-64. doi: 10.1016/j.pacs.2018.07.005.

[7] F. Gao, X. Feng, R. Zhang, S. Liu, R. Ding, R. Kishor, Y. Zheng, Single laser pulse generates dual photoacoustic signals for differential contrast photoacoustic imaging, Scientific Reports, 7 (2017) 626. DOI: 10.1038/s441598-017-00725-4.

[8] B. Choi, E.D. Jansen, A.J. Welch, Acoustic-based measurements of material absorption coefficients: Relationship between laser pulse duration and stress confinement time. Journal of Applied Physics, 94:12 (2003) 7826-7831. doi:10.1063/1.1627464.

Development of a differential photoacoustic system for the determination of the effective permeability coefficient

Martinez-Munoz PE[(1)], Martinez-Hernandez HD[(1)], Rojas-Beltran CF[(2)], Perez-Ospina JL[(2)], Rodriguez-Garcia ME[(3)*]

(1) Posgrado en Ciencia e Ingeniería de Materiales, Centro de Física Aplicada y Tecnología Avanzada, Universidad Nacional Autónoma de México, Campus Juriquilla, Querétaro, Qro., México
(2) Maestría en Ciencias, Instrumentación y Control, Universidad Autónoma de Querétaro, Querétaro, Qro., México
(3) Departamento de Nanotecnología, Centro de Física Aplicada y Tecnología Avanzada, Universidad Nacional Autónoma de México, Campus Juriquilla, Querétaro, Qro., México

*Corresponding author's email: marioga@fata.unam.mx

Background – Photoacoustic (PA) is a technique that has been applied to different fields in materials science to study their electronic and thermal properties, [1] the determination of thermal diffusivity of metals, process monitoring, food science, and water vapor permeability. Changes in PA signal (PAS) can be produced by different physical or chemical processes such as water vapor permeability and the in-situ monitoring of electrochemical reactions, among others. In PA developments, the influence of electronic components for transducing the signal and the effect of the geometry cell was not considered. Water permeability in ceramics,[2] water-diffusion in hydrogels,[3] and a model of the relaxation process depending on water-vapor applied have been studied using a single PAC cell. Non-instrumental function considerations in these works included the instrumental noise when the signal is processed, so that their calculations lack the physical sense since the noise is too high compared with the real sample measurement. As an alternative to avoid the noise in the real measurements, progress in the implementation of new PA systems has been made. Differential PA (DPC) systems are the arrangement most used for removing the noise of the real response.

The aimed work was to develop a Differential Photoacoustic Cell to determine the effective permeability coefficient in office paper film and polystyrene thin film, studying the signal changes within the PAC in relation to the amount of vapor that passes through the thin films and the pressure changes in the cell. The use of a differential cell is to do accuracy the results of the permeability coefficient. The implementation of the second cell has the function of measuring the instrumental contribution and calibrating the instrumental components and comparing the DPC and the reported permeability coefficient in the literature.

Methods – Electronic instrumentation filters out the signal to avoid noise produced by stray frequencies; nevertheless, the total signal measured is composed of the instrumental response and the sample one. To eliminate the instrumental function of the measured signal to obtain the real signal sample is enough to divide the measured signal (given by cell 1) by the instrumental function signal (provided by cell 2). Eqs. (1) and (2) deliver the way to correct amplitude and phase of the real signal sample.

$$S_{sample} = S_m(t) \cdot F_i(t) \qquad \text{Eqn. 1}$$

$$\varphi_{sample} = \varphi_m(t) - \varphi_i(t) \qquad \text{Eqn. 2}$$

S_{sample} is the real sample PA signal, $S_m(t)$ corresponds to the PA signal measured, and $F_i(t)$ represents the instrumental function. φ_{sample} corresponds to sample PA signal phase, $\varphi_m(t)$ represents the PA signal measured phase, and $\varphi_i(t)$ is the instrumental PA signal phase.

Results – Figure 1(a) and 1(b) shows the measure PA amplitude and phase signals, respectively, as a function of the time for a paper foil to determine the effective water permeability coefficient. The PAS increase by the vapor diffusion through the sample changing the absorption coefficient. The PAS tends to stabilize for a long time because the vapor diffused in the confined gas saturates the sample. Phase signal of the sample decreases, indicating changes in the film owing to moisture content and radiation/matter interaction. Figure 1(c) and 1(d) corresponds to the measured PA amplitude and phase for cell 2 (aluminium foil) used as an instrumental function, because there is not water diffusion through it. Figure 1(e) and 1(f) shows the real sample amplitude and phase signals corrected using Eqs. (1) and (2).

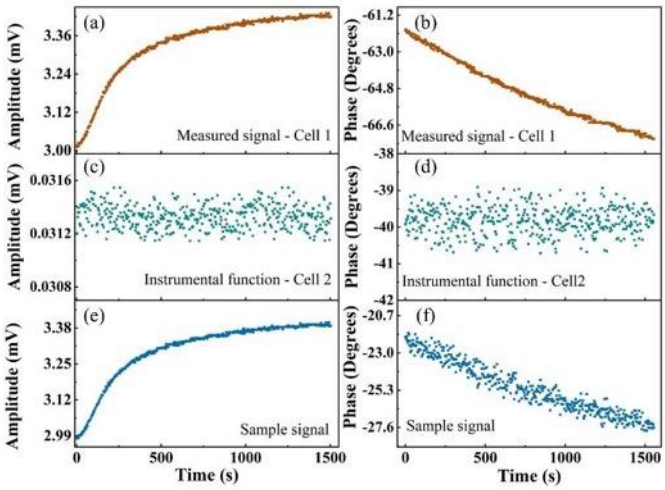

Fig. 1. (a) PA amplitude signal as a function of time. **(b)** PA phase signal as a function of the time. For aluminium as instrumental function: **(c)** PA amplitude signal as a function of the time. **(d)** PA phase signal as a function of time. **(e)** PA corrected amplitude signal as a function of time. **(f)** PA corrected phase signal as a function of time.

Figure 2(a) and (b) shows the office paper PAS. The water vapor diffusion time (τ_D) was determined. The red line corresponds to the best fitting for the PAS, and the black squares represent experimental data. τ_D value in paper was 332 s, and τ_D vapor diffusion time in polystyrene was 142 s. The permeability coefficient (Π) value using Eq. 8, for paper was 458×10^{-13} cm^{-2} s^{-1} Pa^{-1} and for polystyrene, Π value was 334×10^{-13} cm^{-2} s^{-1} Pa^{-1}.

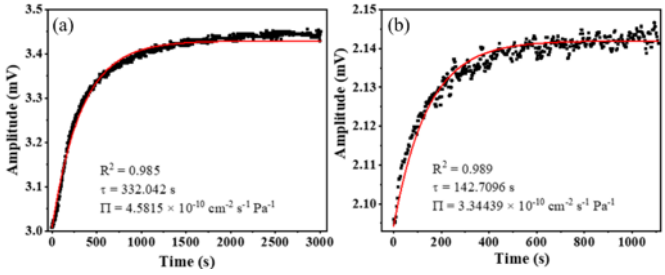

Fig. 2. (a) Office paper PAS

Conclusions – The methodology and metrology proposed in this work allowed to determine the effective water vapor permeability by the correction of the signal using a differential photoacoustic system. As perspectives stay to change the permeant atmosphere environment in the chamber with different gasses modifying the pressure. Electronic noise was reduced by effect of the instrumental function, geometry, and design of the PAC giving more accuracy values. Measured signal for the sample is composed by the instrumental function and the sample contribution, by correction measures have physical sense and it is important to consider the region work where RH is stabilized.

References

[1] J. Liu, M. Han, R. Wang, S. Xu, and X. Wang, J. Appl. Phys. 131, 065107 (2022). https://doi.org/10.1063/5.0082014.

[2] S.A. Tomás, R. E. Sammiguel, A. Cruz-Orea, M.G. Da Silve, M.S. Sthel, H. Vargas, L.C.M. Miranda, Meas. Sci. Technol. 9, 803 (1998). 10.1088/0957-0233/9/5/010.

[3] A.I. Raymundo-Ortiz, E. G. Ramos-Ramirez, A. Cruz-Orea, J.A. Salazar-Montoya, Int. J. Thermophys. 34, 1591 (2013). https://doi.org/10.1007/s10765-013-1391-5.

Open photoacoustic cell for concentration measurements at high flow rates

Fekete J[(1)*], Balogh M[(2)], Spalek D[(1)], Molnár B[(1)], Juhász V[(1)], Ducsay N[(1)], Gulyás G[(1)], Szabó A[(1)], Bozóki Z[(1)], Szabó G[(1)]

(1) Department of Optics and Quantum Electronics, University of Szeged, Szeged, Hungary
(2) Department of Fluid Mechanics, Budapest University of Technology and Economics

*Corresponding author's email: jfekete@titan.physx.u-szeged.hu

Emission monitoring is one of the most important fields of environmental measurements. The pollutants and gases generated by burning of fuels, wood and the illegal burning are harmful to the human body and can lead to severe consequences. Therefore, lots of regulations were made in the last decades in connection with harmful emissions. To fulfil these emission regulations reliable and precise methods and instruments are needed for the authorities as well as for the manufacturers. Photoacoustic spectroscopy is one alternative for this purpose, because of the selectivity of the method, short response time and high sensitivity.

Proper sampling is crucial in the measurement of emission of particulate pollutants and gases mainly in terms of vehicles' emission, but in in other fields as well. Our open PA cell is aiming at the elimination sapling problems, because the complete sample volume flows through the cell. The compact size allows the drastic reduction of response time. However, the realization of this kind of cell is challenging.

In connection with this construction there are more challenges. The gas volume flow can cover wide scale, and noises propagating with the medium and generated by the flow may overload the microphone. The sample flow can easily make the cell dirty, and it can be also really hot which can damage the microphone the optical parts and other instrumentation connected directly to the cell, mainly the parts contacting with the gas. The resonance frequency can be easily alternating with the temperature and the gas composition (in fact with the speed of sound in the medium), so it must be tracked. It is done by chirp measurements and with an ultrasonic sensor. The greatest problem is the noise and the overload of the microphone. The noise can be attenuated with mufflers placed before and after the cell. Besides our developments aiming the reduction of the microphone sensitivity below 7 kHz.

Applications – One of the most important and the most challenging application is in-situ vehicle emission measurement. Exhaust gas is hot, its flowrate fluctuates rapidly, its composition changes drastically. The open cell is a so-called pipe in pipe construction (Figure 1). The inner pipe is the acoustic resonator, the dimensions of the resonator are determined by the desired acoustic mode, the frequency of this mode is around 12500 Hz in room air. The inner pipe is in the centre of the outer pipe connecting with two spokes to it. There are two holes in each spokes, one for the microphone and one for the laser light. The spokes and the resonator are aerodynamically optimised. The cell is water-cooled to avoid overheat.

Another application is connecting to environmental measurements, we are working on the deployment of the open cell to a drone, which could monitor several air components' concentration near the surface without sampling system and with high time resolution. In this case the airflow and the noises are less

disturbing. The measurement seems easier than in the case of vehicle emission, because the conditions are much more stable.

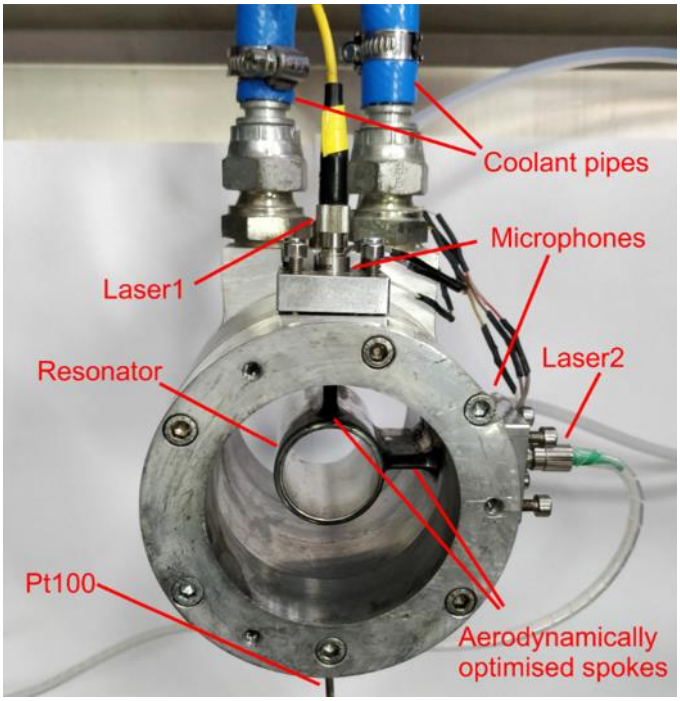

Fig. 1. Open cell optimised for exhaust gas measurement

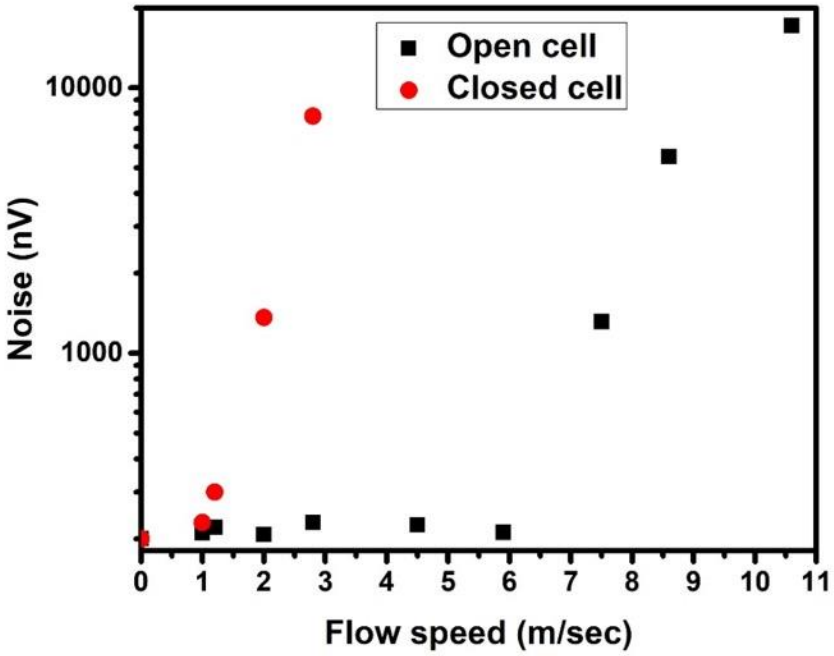

Fig. 2. Flow generated noise in the open cell compared to a conventional closed cell.

Reference

[1] Z. Bozóki, Z., Szabó, A., Mohácsi, Á., Szabó, G. (2010) A fully opened photoacoustic resonator based system for fast response gas concentration measurements. Sensors and Actuators B. 147 (2010) 206-212.

Verification of the basic equation of gas phase photoacoustics

Végh P(1)*, Gulyás G(1), Huszár H(1), Szabó G(1), Bozóki Z(1)

(1) Department of Optics and Quantum Electronics, University of Szeged, Hungary

*Corresponding author's email: pannavegh97@gmail.com

The analytical performance of a photoacoustic gas detection system can be characterized by a sensitivity factor that can be defined in the following form:

$$S = \frac{PAS - A_0}{c} = \left(\frac{c_p}{c_V} - 1\right) \cdot P_{in} \cdot C_{cell}(f) \cdot \alpha_{spec} \qquad \text{Eqn. 1}$$

The sensitivity parameter of a gas phase photoacoustic system depends on two factors: on the frequency dependent acoustical properties of the measuring system and on the heat capacity ratio of the measured gas sample. As far as the earlier works on the measurement of the frequency dependence of the PA system sensitivity is concerned, they are recognized to be incomplete in a sense that the acoustic and the thermal properties are varied simultaneously [1] [2]. Based on the calibration of the PA system with an analyte buffered in various gas mixtures, a method is developed that unravels and quantifies both of these dependencies.

The measurement method starts by a two-phase calibration procedure that eliminates the effect of C_{cell} on the measured S factors. During its first phase a set of calibrations are executed by admixing a mixture of a heavy and a light noble gas (i.e., argon and helium, respectively) to methane in a way that the individual concentrations of the noble gases are varied while their total concentration is kept constant. In this way it is possible to vary the value of the sound speed while (c_p/c_V-1) remains constant, and so the frequency dependence of C_{cell} can be determined unaffectedly from the variation of (c_p/c_V-1). The second part of the proposed method is based on the calibration of the PA system with various gas mixtures that changes both the acoustic frequency of the measuring system and the heat capacity ratio of the gas sample as well. From the results of this second set of calibration the previously determined acoustic frequency dependence can be separated yielding the heat capacity dependence of the sensitivity parameter.

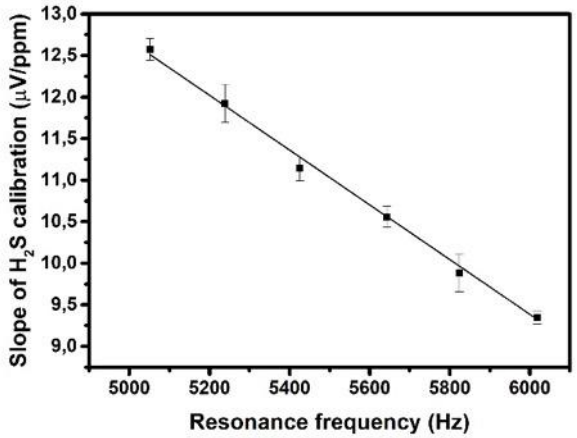

Fig. 1. Slope of the calibration lines as a function of resonance frequency determined during the first phase of the calibration

The reported measurements were executed by using one of the strongest absorption line (λ_1) of H_2S at 1574 nm and a second line (λ_2) that is accessible by the same light source and has an approximately four times smaller line-strength. Frequency dependence of the instrument was determined in the range from 5050 to 6000 Hz, using the λ_1 absorption line of H_2S. In this range a linear relationship was found between the slope of the H_2S calibration line and the resonance frequency for each gas composition. The (c_p/c_V-1) dependence was determined in the range from 0.32 to 0.5 by using both of the λ_1 and λ_2 absorption lines. After the frequency dependence was separated, a linear correlation was found.

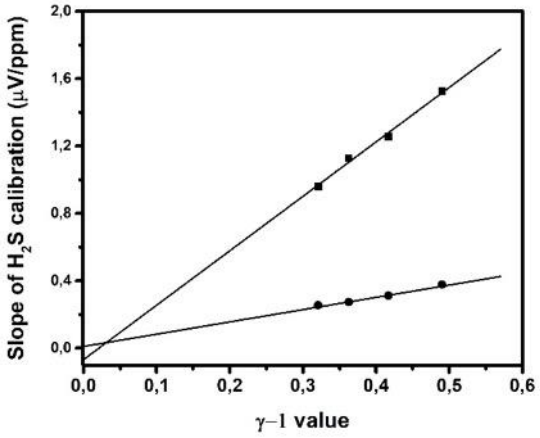

Fig. 2. Variation of calibration slope as a function of the γ-1 value. Squares represent points of the calibration using the λ_1, the circles indicate points using the λ_2 absorption line.

In conclusion, a novel method was developed for the determination of the effect of the two major sources of sensitivity parameter variation, i.e. the frequency dependence of the acoustical properties of the PA system and the variation of the heat capacity ratio of the measured gas with the gas composition, separately. Using this method, the sensitivity parameter of a H_2S measuring PA system containing a longitudinal differential PA cell and a near-infrared diode laser under wavelength modulation was determined and the results prove that - in accordance with the basic theory of photoacoustics - the sensitivity parameter separated from the frequency dependent acoustical properties is directly proportional to the (c_p/c_V-1) factor.

References

[1] V. Hanyecz, Á. Mohácsi, A. Pogány, A. Varga, Z. Bozóki, I. Kovács, G. Szabó, Vibrational Spectroscopy 52 (2010) 63–68

[2] A. Szabó, Á. Mohácsi, G. Gulyás, Z. Bozóki, G. Szabó, Meas. Sci. Technol. 24 (2013) 065501

Determination of cell constant via combined photoacoustic and direct absorption measurement

Fekete J[(1)*], Szakáll M[(1)], Bozóki Z[(1)], Szabó G[(1)]

(1) Department of Optics and Quantum Electronics, Institute of Physics, University of Szeged, Szeged, Hungary

*Corresponding author's email: jfekete@titan.physx.u-szeged.hu

Photoacoustic spectroscopy is one of the most reliable methods for measuring gas or aerosol concentration. Whenever a photoacoustic instrument is operated under field conditions it needs regular calibration, which is typically performed by using a calibration gas cylinder or cylinders. Unfortunately, calibration not only limits the reliability of the instrument (via the uncertainty of the concentration of the calibration gas), but it also increases operational cost significantly, and takes off valuable measurement time, as a typical field calibration lasts about 30 minutes or even more.

Here we suggest an alternative calibration method aiming at elimination of these problems. The proposed method is applicable whenever there is a component in the measured gas sample in a sufficiently high concentration to perform both photoacoustic and optical absorption measurement on its chosen absorption line. Our goal was to reduce the calibration time down to a few minutes.

The photoacoustic signal is the first Fourier-component of the product of the modulated power and absorption, the concentration, the cell constant and the concentration of the sample. All of these parameters are time independent (also the concentration is constant in a period of the signal generation) except the output power and output wavelength of the laser. Based on the measured power-current curve of the laser the photoacoustic signal can be simulated. The cell constant gives the sensitivity of the cell and mainly depends on the gas composition the geometry of the resonator in the cell and the microphone sensitivity [1].

In case of atmospheric aerosol measurement, water vapor is an evident choice as e.g. at the wavelength of 1371 nm it has a relatively strong absorption line which is accessible by a fibre coupled single mode DFB diode laser. This example will be shown in the following.

The proposed calibration procedure starts by recording the power of the diode laser as a function of the driving current of the laser under no modulation with a power meter placed right behind the photoacoustic cell. The temperature of the diode laser is set in a way to ensure that the recorded power-current (P-I) curve includes a well measurable absorption line (see Figure 1). The software, which is developed for this calibration procedure identifies the absorption line, fits a Lorentzian line profile on it, and calculates the absorption at each points. The simulated photoacoustic signal (PA) is based on this fitting. Next the laser current is set to be modulated while the laser temperature is unchanged and the photoacoustic signal PAS is measured by changing the constant component of the driving current. Finally, the following quotient gives the cell constant:

$$C_{cell} = \frac{PAS}{PA} \qquad \text{Eqn. 1}$$

The execution of the proposed method on a longitudinal differential cell yielded a calibration constant of C_{cell}= *20 mV/(mW·cm^{-1})*. By taking into account that the applied microphone has the sensitivity of *10 mV/Pa*, our result is in good agreement with the literature value [1, 2]. Furthermore the cell constant determination takes a couple of minutes, which is a very significant time reduction when compared to the typical length of on-filed calibration of minimum 30 min.

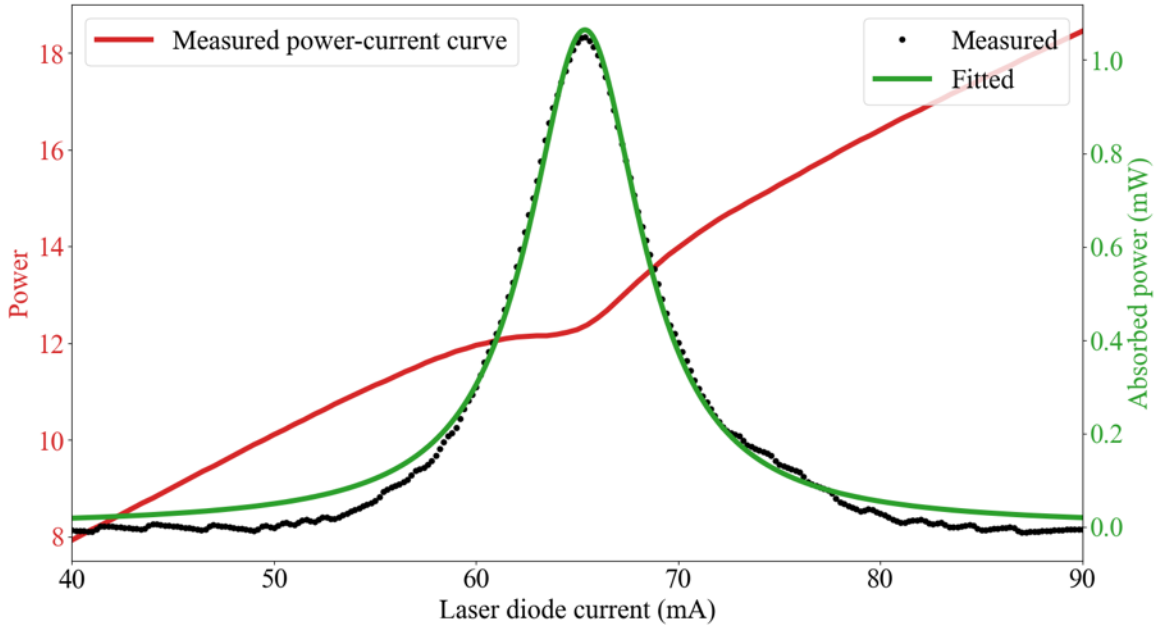

Fig. 1. The red curve shows the light-power as a function of the diode laser current measured by a power meter placed right after the PA cell. The black points are the absorption calculated from the measured data. The green curve is the fitted Lorentzian curve on the light power attenuation due to light absorption within the PA cell.

The method can be used to calibrate photoacoustic aerosol measurement instruments, and for sensitivity check in photoacoustic gas sensors, besides cell constant determination.

References

[1] A. Miklós, P. Hess, Z. Bozóki, Review of Scientific Instruments, 72:4 (2001) 1937-1955.

[2] Z. Bozóki, Á. Mohácsi, G. Szabó, Z. Bor, M. Erdélyi, W. Chen, F. K. Tittel, Applied spectroscopy, Volume 56, Number 6 (2002) 715-719.

Clinical validation of handheld thermo-photonic device for rapid detection and quantification of anti-SARS-CoV-2 antibodies

Thapa D(1), Samadi D(1), Tabatabaei N(1)*

(1) Department of Mechanical Engineering, York University, Toronto, ON, Canada

*Corresponding author's email: nima.tabatabaei@lassonde.yorku.ca

Rapid, on-site, and sensitive detection and quantification of anti-SARS-CoV-2 antibodies is an effective and scalable approach for minimizing the burdens of COVID-19 pandemic. Such capability not only opens the door for better and more effective vaccination, but also enables population-wide serological studies focused on answering pressing questions about COVID-19 infection (e.g., correlation of antibody titers with degree of immunity). Here we report on design, development, and clinical validation of a low-cost and portable thermo-photonic innovation that enables sensitive detection and quantification of COVID-19 antibodies. At the core, this patented technology relies on thermo-photonic lock-in imaging of COVID-19 rapid tests. Our clinical results from $COVID^+$ and $COVID^-$ patients suggest ability of developed technology in quantifying antibody titres within the clinically relevant range and with a limit of detection of 90 ng/ml.

Background – Immunological tests play an important role in the management of COVID-19 pandemic and monitoring the effectiveness of vaccines over time at a population level. Existing immunological solution, such as neutralization assay, chemiluminescent assay (CLIA), and enzyme-linked immunosorbent assay (ELISA) are expensive, time-consuming and requires laboratory facilities and trained personnel, therefore they are not deemed suitable for large-scale serodiagnosis and vaccine evaluation. Lateral flow immunoassays (aka Rapid Tests) are fast, low-cost, and point-of-care approaches to antibody testing; however, these convenient and scalable solutions provide essentially binary information about the presence of antibodies and cannot quantify the antibody level of infected and/or vaccinated individuals.

Method – We have developed a low-cost and portable thermo-photonic lock-in imaging device using a cell phone attachment infrared camera, low-cost control electronics, and a 808nm low-cost laser diode (Fig. 1)[1]. Device is essentially a reader of COVID-19 antibody rapid tests. Sensing mechanism is based on measurement of amplitude of photothermal responses from gold nanoparticles immobilized on rapid test control and test lines. Through calibration, device maps the amplitude of thermal-wave responses (aka amplitude metric) to COVID-19 antibody concentrations. Performance of device was tested on n=28 longitudinal human serum samples from $COVID^+$ and $COVID^-$ patients and compared to results obtained from standard quantitative enzyme-linked immunoassay (qELISA).

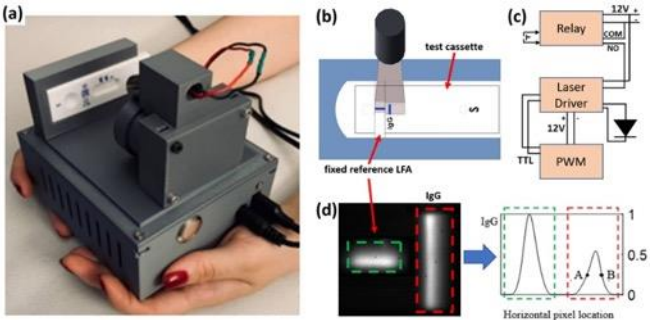

Fig. 3. (a) Schematic of handheld device. Rapid test is illuminated with laser **(b)** controlled by low-cost electronics (c). Themo-photonic lock-in amplitude images are used for prediction of antibody concentrations.

Results and Discussion – Figure 2(a) shows the variation of IgG antibodies with respect to the days of ICU admission for representative COVID− patients (patient IDs 85 and 92) and COVID+ patients (patient IDs 94 and 99). The y1 axis represents the standard ELISA test and the y2 axis represents the thermo-photonic amplitude metric. These plots demonstrate that IgG measurements from ELISA and thermo-photonic device are highly correlated. The bar diagrams in Fig. 2(b) show the mean amplitude metrics between COVID+ and COVID− patients and ELISA+ and ELISA− patients. Statistical analysis (t-test) shows that the mean values are significantly different between the groups (t-test, $p>0.001$). The left panel in Fig. 2(c) shows a best-fit line (regression line) to scattered data points; the high value of R-squared ($R^2=0.92$) suggest produced calibration line can be used to predict the concentration of IgG in serum using a thermo-photonic device, albeit at much lower cost and much faster than laboratory-based quantitative ELISA. To determine the sensitivity of the thermo-photonic system to differentiate IgG+ and IgG− samples, a receiver operating characteristic (ROC) curve was drawn, right panel in Fig. 3c. Ture positive and true negative samples were determined based on the IgG+ and IgG− by ELISA. A high value of area under the ROC curve (AUC=0.99) indicates the high predictive ability of the thermo-photonic device in distinguishing IgG+ from IgG− sera.

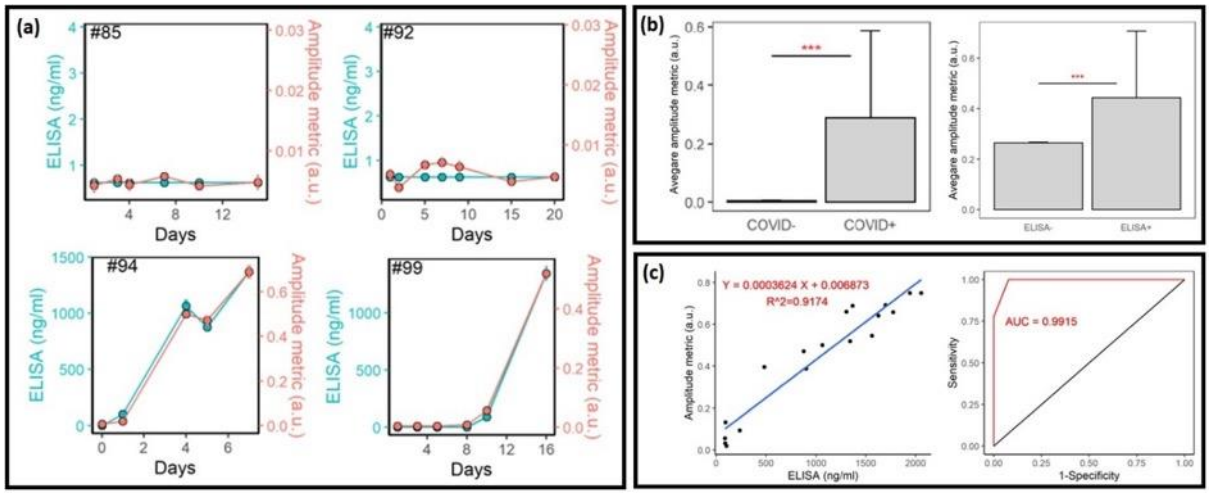

Fig. 2. (a) Representative quantification results of longitudinal human samples using thermo-photonic device and qELISA. **(b)** Bar diagrams showing average amplitude metrics between the COVID− and COVID+ participants and ELISA− and ELISA+ samples. **(c)** Linear regression plot between thermo-photonic device readings and ELISA quantifications as well as the ROC curve that shows the performance of our device for detecting ELISA− and ELISA+ samples.

Conclusions – In this study, we designed, developed, and clinically validated a portable thermo-photonic device for rapid detection and quantification of COVID-19 antibodies. Sensing mechanism of device is based on interrogation of thermo-photonic lock-in responses for gold nanoparticles immobilized on test and control lines of rapid tests. Human serum experiments suggest the developed innovation can detect and quantify COVID-19 antibodies with a performance comparable to that of quantitative ELISA, albeit at much lower cost and significantly faster.

References

[1] D. Thapa, N. Samadi, N. Tabatabaei, Handheld Thermo-Photonic Device for Rapid, Low-Cost, and On-Site Detection and Quantification of Anti-SARS-CoV-2 Antibody. IEEE Sensors Journal. 21:17 (2021) 18504-18511.

Optical photothermal infrared spectroscopy

Prater CB(1)*, Kansiz M(1), Kjoller K(1)

(1) Photothermal Spectroscopy Corp, Santa Barbara CA USA

*Corresponding author's email: craig@photothermal.com

Background – Optical Photothermal Infrared (O-PTIR) spectroscopy[1-6][7] is an emerging yet rapidly growing technique for performing infrared chemical analysis with >10X better spatial resolution than conventional infrared spectroscopy. Infrared spectroscopy is arguably one of the most widely used techniques for performing chemical characterization of samples, but fundamental limits due to optical diffraction constrains the spatial resolution of conventional Fourier Transform Infrared (FT-IR) spectroscopy to the range of 3-30 μm, significantly limiting its applicability for many microscopic applications. The O-PTIR technique leverages a photothermal detection technique using a tightly focused visible probe beam to achieve spatial resolution an order of magnitude better than the limits set by optical diffraction at infrared wavelengths.

Methods – Fig. 1 shows an illustration of the O-PTIR technique. A sample is first illuminated by a beam of radiation from a tuneable infrared laser source. When the IR laser is tuned to a wavelength corresponding to a molecular bond vibration in the sample, the sample will absorb IR light and heat up locally, creating a photothermal modulation in the sample for each IR light pulse. This photothermal modulation is detected with a visible probe beam that is focused to a much smaller spot than the IR beam, thus achieving higher spatial resolution. Infrared absorption spectra can be obtained by measuring the photothermal modulation amplitude as a function of IR wavelength and infrared chemical images can be obtained by measuring the photothermal modulation for one or more IR absorption bands overarangeofdifferentpositionsonthesample. ThevisibleprobebeamusedtomeasureIRabsorption can also be used to perform simultaneous co-located Raman spectroscopy, thus enabling multimodal chemical analysis using two complementary vibrational spectroscopy techniques.

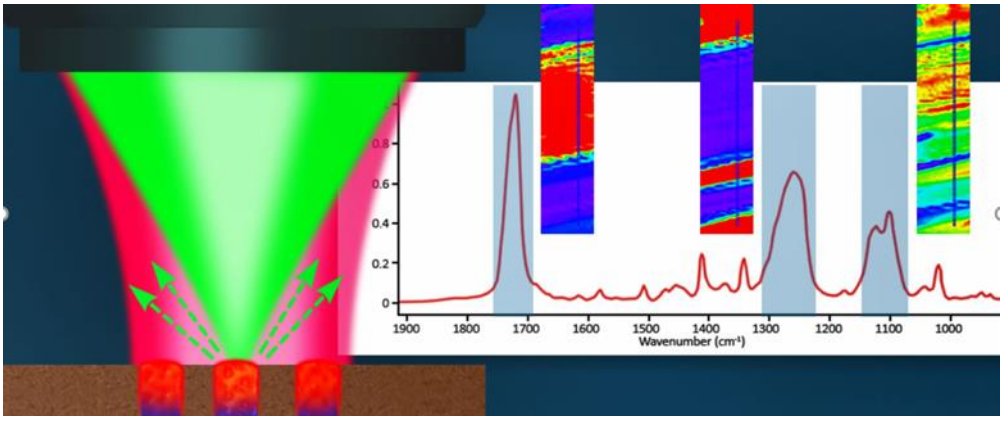

Fig. 1. Optical photothermal infrared (O-PTIR) is an optical microscope based chemical analysis technique where a tightly focused visible probe beam (green) is used to measure photothermal modulation in a sample due to absorption of infrared (IR) radiation. Infrared spectra and chemical images can be obtained with sub-500 nm spatial resolution.

This contribution will review the underlying technology of the O-PTIR approach and discuss various applications including spectroscopic analysis and chemical imaging of in application areas including

life sciences, microplastics/microparticulates, polymer sciences, defect identification, and cultural heritage.

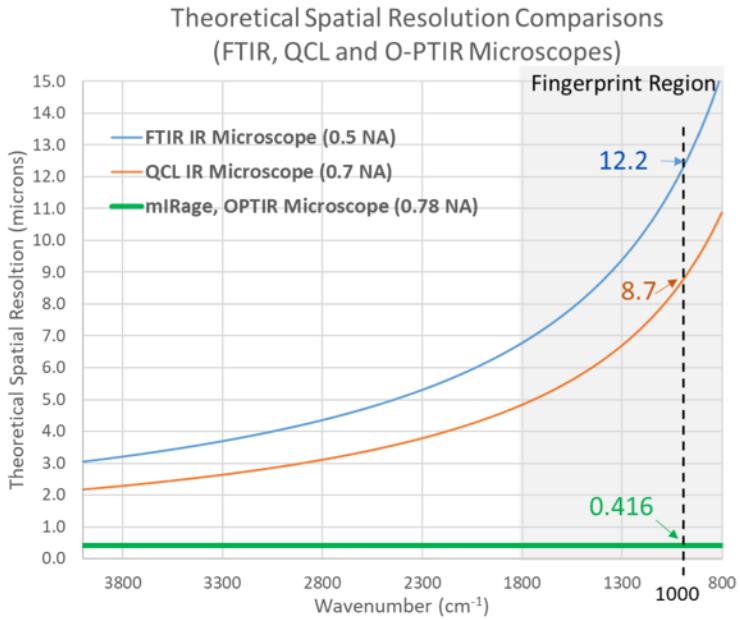

Fig. 2. Comparison of spatial resolution of O-PTIR technique versus conventional IR microscopes based on Fourier Transform Infrared (FT-IR) and quantum cascade laser (QCL) microscopes. The O-PTIR technique achieves up to 30X better spatial resolution than competing techniques and with constant spatial resolution versus wavelength.

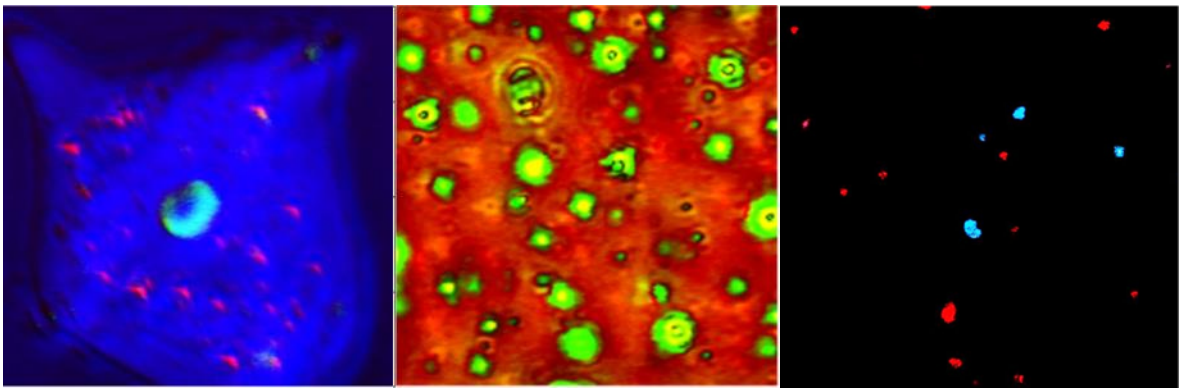

Fig. 3. Example O-PTIR chemical images of human cell (left), polymer blend (center), and microparticles (right).

References

[1] D. Zhang et al., Depth-resolved mid-infrared photothermal imaging of living cells and organisms with submicrometer spatial resolution. Science Advances 2:9 (2016) p. e1600521.

[2] R. Furstenberg et al. U.S. Patent No. US9091594 B2 (2015).

[3] Z. Li, M. Kuno, G. Hartland, Super-resolution Mid-infrared Imaging using Photothermal Microscopy. in Conference on Lasers and Electro-Optics (2016) San Jose, California: Optical Society of America.

[4] M. Kansiz et al., Optical Photothermal Infrared Microspectroscopy with Simultaneous Raman – A New Non-Contact Failure Analysis Technique for Identification of <10 µm Organic Contamination in the Hard Drive and other Electronics Industries. Microscopy Today 28:3 (2020) 26-36.

[5] M. Kansiz et al., Optical Photothermal Infrared Microspectroscopy Discriminates for the First Time Different Types of Lung Cells on Histopathology Glass Slides. Analytical Chemistry, 93:32 (2021) 11081-11088.

[6] Y. Bai, J. Yin, J.-X. Cheng, Bond-selective imaging by optically sensing the mid-infrared photothermal effect. Science Advances, 7:20 (2021) p. eabg1559.

[7] For an extensive list of O-PTIR references go to www.photothermal.com/publications.

Photon-phonon interaction in submicron particles systems – new method of Q-switching

Bi D[1,2], Wu M[2], Karpov MA[1], Kudryavtseva AD[1]*, Mironova TV[1], Savicheva TA[2], Shevchenko MA[1], Tareeva MV[1], Tcherniega NV[1], Umanskaya SF[1]

(1) Lebedev Physical Institute of the RAS, Moscow, Russia

(2) Department of Physics, Bauman Moscow State Technical University, Moscow, Russia

*Corresponding author's email: akudr@sci.lebedev.ru

Background – Intracavity excitation of different kinds of stimulated scattering is very useful method for spectroscopy investigations and for numerous applications. In this method both exciting and scattered radiation propagate in the same cavity, which gives possibility to decrease scattering threshold and to increase its efficiency. Different kinds of stimulated scattering were registered and studied in the intracavity configuration: stimulated Rayleigh scattering, stimulated Brillouin scattering, stimulated Raman scattering [1,2]. We studied experimentally intracavity stimulated low-frequency Raman scattering [3].

Low-frequency Raman scattering (LFRS) is a result of light interaction with acoustic vibrations of nanosized or submicron particles systems. Its frequency shifts are defined by eigenfrequencies of particles vibrations lying in giga- or terahertz range and depend on the particles size and morphology. Stimulated low-frequency Raman scattering (SLFRS) is stimulated analogy of LFRS. It is very useful tool for nanoparticles study, identification and for impact on them. We studied SLFRS in many nanoparticles systems, including biological nanoobjects.

Samples and methods – In this work we show that with the help of intracavity SLFRS it is possible to obtain Q-switching and mode-locking. Suspensions of monodisperse polystyrene particles with similar particle sizes (0.05–1.0 μm) in water were used as samples. The concentration of suspensions was in the range 10^{10}–10^{12} cm^{-3}. We also studied suspensions of diamond, quartz and gold nanoparticles. Size distribution of nanoparticles was obtained with the help of dynamic light scattering.

Intracavity SLFRS was excited by single pulses of ruby laser (λ = 694.3 nm, τ = 20 ns, E_{max} = 0.3 J, $\Delta\nu$ = 0.015 cm^{-1}, divergence $3.5 \cdot 10^{-4}$ rad). Cell with particles suspension was placed inside laser cavity between back (100 %) mirror and ruby rod. SLFRS spectra were registered with the help of Fabry-Perot interferometer with changeable base. Temporal characteristics were obtained with the help of high-speed photodiode connected with oscilloscope.

Results – In the intracavity SLFRS spectra we registered lines corresponding to the radial and quadrupole spheroidal modes. Frequency shift dependence on the reciprocal diameter was shown to be almost linear and different for different modes.

With concentration of nanoparticles in suspension a little larger than that necessary for excitation of SLFRS we could obtain Q-switching. Fig. 1 demonstrates free laser oscillation and Q-switched pulse.

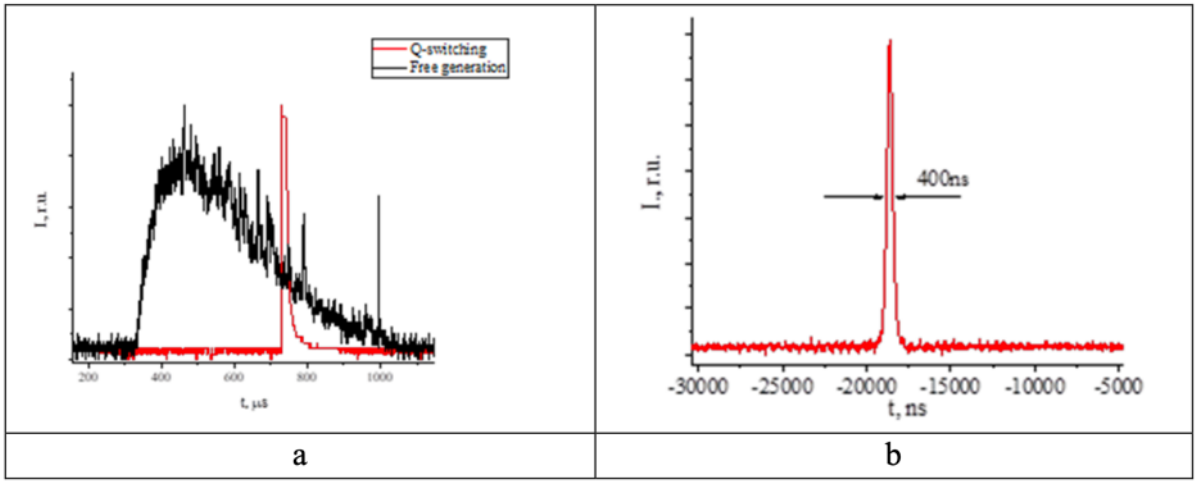

Fig. 1. a - free oscillation of a ruby laser, b - temporal profile of pulse in Q-switching regime.

We also could obtain mode locking in the same experimental setup. The resulting pulse is presented in Fig. 2.

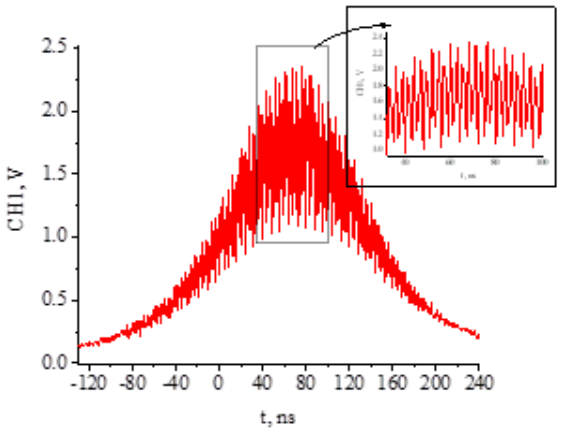

Fig. 2. Mode locking in intracavity SRLFS in a suspension of polystyrene nanoparticles with a size of 300 nm in water.

Conclusions – We for the first time obtained Q-switching and mode locking with the help of stimulated low-frequency Raman scattering, which is caused by photon-phonon interaction in nanosized or submicron particles systems. Conditions (particles size, suspension concentration, threshold) were defined for achieving these effects. Results can be used in nonlinear spectroscopy and for numerous applications, for instance, in remote sensing, laser processing, and optical communications.

Acknowledgements – This work was supported by China Scholarship Council

References

[1] D. Pohl, A New Laser Q-Switch-Technique Using Stimulated Brillouin Scattering, Phys. Lett. 24A (1967) 239-240.

[2] A.Z. Grasyuk, V.V. Rogul'skii, F.S. Faizulov, Formation of Powerful Nanosecond Pulses with the Aid of Mandel'shtam-Brillouin Scattering and Stimulated Raman Scattering, JETP Lett. 9 (1969) 6-9.

[3] M.A. Shevchenko, V.I. Grebenkin, M.V. Tareeva, et al, Intracavity Stimulated Low-Frequency Raman Scattering, Bull. of the Lebedev Phys. Inst. 45 (2018) 397-398.

10
Low-Dimensional Systems, Nanoscale Phenomena and Nanostructures

PLENARY SESSION

Surface phonon-polaritons conduction and radiation

Volz S[(1,2)]

(1) Institute of Industrial Science, The University of Tokyo, Tokyo 153-8505, Japan
(2) Laboratory for Integrated Micro Mechatronic Systems, CNRS-IIS, The University of Tokyo, Tokyo 153-8505, Japan

*Corresponding author's email: volz@iis.u-tokyo.ac.jp

Recent studies indicated that surface phonon-polaritons (SPhPs), which are the evanescent electromagnetic waves generated by the hybridation of the optical phonons and the photons and propagating at the surface of a polar dielectric material surface [1] [2], may potentially serve as novel heat carriers to enhance the thermal performance in micro- and nanoscale devices. We measured thermal conductivities (TCs) of SiN films to study the contribution of SPhPs to heat transfer [3].

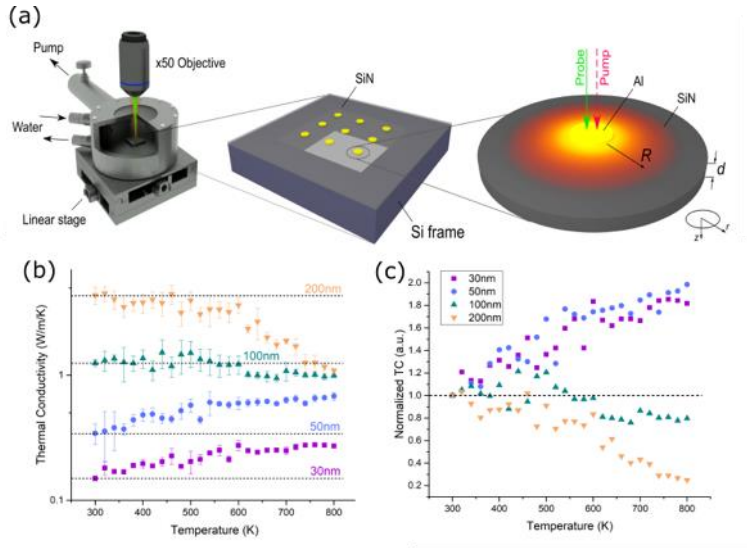

Fig. 10: (a) Schematic of a heating stage and a sample, (b) thermal conductivity as a function of temperature with different thicknesses, (c) thermal conductivities normalized by the one at room temperature, revealing the SPhPs contribution in thinner samples

Figure 1 shows the TCs of SiN films with different thicknesses measured between 300 and 800K. Strong TC enhancement exists at high temperatures by decreasing the film thickness, as expected from the contribution of the SPhPs. Meanwhile for thicker films, TC decreases above 600K and is inversely proportional to temperature, presumably due to the Umklapp scattering and smaller SPhPs contribution.

Acknowledgments – This work is supported by CREST JST, Grant JPMJCR19Q3 and JPMJCR19I1.

References

[1] D.-Z Chen, A. Narayanaswamy, G. Chen, Phys. Rev. B 72 (2005) 155435.

[2] J. Ordonez-Miranda, L. Tranchant, T. Tokunaga, B. Kim, B Palpant, Y. Chalopin, T. Antoni, and S. Volz, J. Appl. Phys. 113 (2013) 084311.

[3] Y. Wu, J. Ordonez-Miranda, S. Gluchko, R. Anufriev, D. De Sousa Meneses, L. Del Campo, S. Volz, M. Nomura, Science Advances 6(40):eabb4461, (2020).

KEYNOTE SPEAKER

Photothermal characterization at a nanoscopic scale

Li Voti R[(1,2)*]

(1) Dipartimento di Scienze di Base ed Applicate per l'Ingegneria, Sapienza Università Roma, Via A. Scarpa 16, 00161 Rome, Italy
(2) FemtoNanoOptics group, Universitè de Lyon, Institut Lumière Matière (iLM), Université Lyon 1 and CNRS 10 rue Ada Byron, 69622 Villeurbanne cedex, France

*Corresponding author's email: roberto.livoti@uniroma1.it

One of the most challenging problems in nanomaterials research is their accurate characterization, which is fundamental for the efficient use of these technologically promising materials. Absolute absorption, quantum efficiency, thermal diffusivity, and the elastic constants are important parameters for photonic applications. Although the conventional absorption or emission techniques can provide the absorption coefficient, the determination of the absolute absorption is not a trivial measurement due to the presence of scattered light. On the contrary Photoacoustic (PAS) and Photothermal Spectroscopy are very sensitive techniques, immune to scattered or reflected light, and easy to be used to measure the absolute absorption in many different wavelength ranges.

In this summary we review recent advances in the methodology of PAS and its novel applications. In particular we highlight some works done to detect circular dichroism of intrinsic chiral materials [1] as well as extrinsic pseudo-chiral metasurfaces [2], showing how PAS can be applied to measure the selective absorption of circularly polarized light depending on the orientation of the metasurface. PAS has been also applied to measure the resonant absorption peaks related to the guided modes of GaAs-based NW on Si in the VIS/IR range [3, 4].

In disordered media PAS is confirmed to be the most appropriate technique to determine separately the absorption and the scattering coefficients allowing to determine the size of both metallic (AgNP) [5], or semiconductor nanospheres (ZnO) [6, 7], or clusters of nanospheres bridged by the ligands [8], in contrast to nanolayered samples [9, 10].On the other hand photothermal deflection spectroscopy (PDS) may be used as a complementary technique to measure the absorbance spectrum in nanostructures so to detect absorption lines, or photonic band gap in photonic crystals [11], or to evaluate the entity of the scattering phenomena in carbon nanotubes. PDS has been used in the UV/VIS/IR range from 250 to 1200 nm and by using a low modulation frequency from 1Hz to 100Hz which limits the spatial resolution so that the optical and thermal measurements are averaged in the volume. We also underline some applications of photothermal radiometry (PTR) used to localize the internal heat sources where the pump light is absorbed, and to measure the effective thermal diffusivity. The modulation frequency obtained by an acousto-optical modulator ranges from 1 Hz up to 100 kHz, allowing the improvement of the thermal resolution till submicron range. We have applied PTR to PCM: VO_2 nanolayered samples and SiO_2/VO_2 synthetic opals [12, 13]. This technique has been applied also to carbon nanotube film deposited onto a silicon substrate: in this case PTR allows to detect the thermal wave interference in the film and to measure the effective thermal diffusivity of the CNT, and the thermal resistance with the substrate [14]. Photothermal radiometry and thermography can be also used to measure the emissivity of nanostructured materials, nanoantennas and metasurfaces designed so to have specific directional emittance properties [15, 16].

In order to investigate the thermal properties at a nanoscopic scale one should necessarily work at higher frequencies in the MHz range, One way is definitively offered by laser picosecond acoustics, by using for example the optical heterodyne force microscopy (OHFM) [17]. This detects photothermally induced surface vibrations in an AFM, and can image subsurface nanoscale features through their effect on the surface displacement produced by a megahertz thermal field that is optically excited directly below the scanning AFM tip. Alternatively the thermoelastic properties of nanomaterials can be probed through imaging MHz variations in thermoreflectance in combination with picosecond ultrasonics [18].

Acknowledgments – The talk summarizes several research topics and works done in collaboration with the Italian National Research Council, the University of Bath, the University of Dayton, the Tampere University of Technology, ICMM – CSIC in Madrid, the IOFFE Institute in S.Petersburg, the Hokkaido University in Sapporo, and the Université Lyon 1.

References

[1] A. Benedetti, et al., Precise detection of circular dichroism in a cluster of nano-helices by photoacoustic measurements, Nat. Sci. Rep. 7 (2017) 5257.

[2] A. Belardini, et al., Chiral light intrinsically couples to extrinsic/pseudo-chiral metasurfaces made of tilted gold nanowires, Nat. Sci. Rep. 6 (2016) 31796.

[3] Leahu, G. et al., Photo-acoustic spectroscopy revealing resonant absorption of self-assembled GaAs-based nanowires Nat. Sci. Rep. 7 (2017) 2833.

[4] E. Petronijevic, et al., Resonant Absorption in GaAs-Based Nanowires by Means of Photo-Acoustic Spectroscopy. Int. J. Thermophys. 39 (2018) 45.

[5] R. Li Voti, et al., Photoacoustic Characterization of Randomly Oriented Silver Nanowire Films Int. J. Thermophys. 36 (2015) 342.

[6] F.R. Lamastra, Diatom frustules decorated with zinc oxide nanoparticles for enhanced optical properties, Nanotechnology 28 (2017) 375704.

[7] F.R. Lamastra, et al., Photoacoustic Spectroscopy Investigation of Zinc Oxide/Diatom Frustules Hybrid Powders, Int. J. Thermophys. 39 (2018) 110.

[8] I. Fratoddi, at al., Electronic Properties of a Functionalized Noble Metal Nanoparticles Covalent Network, J. Phys. Chem. C 121 (2017) 18110.

[9] G. Cesarini, G. Leahu, M.L. Grilli, A. Sytchkova, C. Sibilia, R. Li Voti, Optical and photoacoustic investigation of AZO/Ag/AZO transparent conductive coating for solar cells, Physica Status Solidi (C) 13, (2016) 998.

[10] P. Osewski, et al. New Self-Organization Route to Tunable Narrowband Optical Filters and Polarizers Demonstrated with ZnO–ZnWO4 Eutectic CompositeAdv. Optical Mater. (2020) 1901617.

[11] G. Leahu, R. Li Voti, C. Sibilia, M. Bertolotti, V. Golubev, D.A. Kurdyukov, Study of thermal and optical properties of SiO2/GaN opals by photothermal deflection technique, Opt. Quant. Electron. 39 (2007) 305.

[12] T. Cesca, et al., Correlation between in situ structural and optical characterization of the semiconductor-to-metal phase transition of VO2 thin films on sapphire, Nanoscale 12, 851 (2020).

[13] R. Li Voti, G. L. Leahu, M.C. Larciprete, C. Sibilia, M. Bertolotti, Photothermal Characterization of Thermochromic Materials for Tunable Thermal Devices, Int. J. Thermophys. 36 (2015) 1004.

[14] G. Leahu, R. Li Voti, M.C. Larciprete, C. Sibilia, M. Bertolotti, I. Nefedov, I.V. Anoshkin, Thermal Characterization of Carbon Nanotubes by Photothermal Techniques, Int. J. Thermophys. 36, 1349 (2015).

[15] M. Centini, M.C. Larciprete, R. Li Voti, M. Bertolotti, C. Sibilia, M. Antezza, Hybrid thermal Yagi-Uda nanoantennas for directional and narrow band long-wavelength IR radiation sources, Opt. Express 28 (2020) 19334.

[16] M. Centini, A. Benedetti, M. C. Larciprete, A. Belardini, R. Li Voti, M. Bertolotti, C. Sibilia, Midinfrared thermal emission properties of finite arrays of gold dipole nanoantennas, Phys. Rev. B, 92 (2015) 205411.

[17] O. Matsuda, M.C. Larciprete, R. Li Voti, O. Wright, Fundamentals of picosecond laser ultrasonics, Ultrasonics, 56 (2015) 3.

[18] M. Tomoda, R. Li Voti, O. Matsuda, O.B. Wright, Tomographic reconstruction of picosecond acoustic strain propagation, Appl. Phys. Lett. 90 (2007) 041114.

KEYNOTE SPEAKER

Optomechanical strong coupling in lattices of light fluids and sound

Chafatinos DL(1), Kuznetsov AS(2), Sesin P(1), Papuccio I(1), Mangussi F(1), Bruchhausen AE(1), Reynoso AA(1), Usaj G(1), Biermann K(2), Santos PV(2), Fainstein A(1)*

(1) Centro Atómico Bariloche and Instituto Balseiro, Comisión Nacional de Energía Atómica (CNEA) - Universidad Nacional de Cuyo (UNCUYO), 8400 Bariloche, Argentina
(2) Paul-Drude-Institut für Festkörperelektronik, Leibniz-Institut im Forschungsverbund Berlin e.V., Hausvogteiplatz 5-7, 10117 Berlin, Germany

*Corresponding author's email: afains@cab.cnea.gov.ar

We introduce polaromechanical crystals, two-dimensional arrays of zero-dimensional traps confining fluids of exciton-polariton condensates (simply polaritons) and 20 GHz phonons within a semiconductor microcavity [1]. The traps with dimensions down to 1x1 μm2 exhibit large coherence times for polariton fluids (ns-long) as for confined phonons (100's ns) with no observable reduction with decreasing trap size. These crystals combine strongly interacting hybrid phonon-polariton oscillators at the lattice sites with inter-site coupling mediated by strong optomechanical interactions. They are, thus, conceptually closer to metamaterials with resonant unit cells rather than to conventional optomechanical crystals based on Bragg co-localisation of light and vibrations in planar structures. The optomechanical character of the inter-site coupling has remarkable consequences. It is observed, for instance, that when a lattice site is locally perturbed through non-resonant continuous wave optical excitation, mechanical self-oscillation develops corresponding to very efficient polariton-driven phonon lasing [2]. In addition, the crystal responds by locking the energy detuning with neighbour sites to integer multiples of the phonon quantum, thus evidencing synchronization blockade and collective behaviour of the polariton and phonon fields. The exciton-mediated strong polariton-phonon interactions make accessible the so-called ultra-strong optomechanical coupling regime. The coherent control of quantum light fluids with hyper-sound and, conversely, the coherent control of extremely-high frequency sound with light, are envisaged based on the proposed scalable semiconductor platform.

[1] D.L. Chafatinos, A.S. Kuznetsov, P. Sesin, I. Papuccio, A.A. Reynoso, A.E. Bruchhausen, G. Usaj, K. Biermann, P.V. Santos, and A. Fainstein, Metamaterials of Fluids of Light and Sound, arXiv:2112.00458 [physics.optics]. https://doi.org/10.48550/arXiv.2112.00458.

[2] D.L. Chafatinos, A.S. Kuznetsov, S. Anguiano, A. E. Bruchhausen, A.A. Reynoso, K. Biermann, P.V. Santos, A. Fainstein, Polariton-driven phonon laser, Nature Communications 11, 4552 (2020). https://doi.org/10.1038/s41467-020-18358-z.

KEYNOTE SPEAKER

Thermal-wave diode

Ordonez-Miranda J[(1,2)*], Guo Y[(2)], Alvarado-Gil JJ[(3)], Volz S[(1,2)], Nomura M[(1,2)]

(1) LIMMS, CNRS-IIS UMI 2820, The University of Tokyo, Tokyo 153-8505, Japan
(2) Institute of Industrial Science, The University of Tokyo, Tokyo 153-8505, Japan
(3) Applied Physics Department, CINVESTAV-IPN, Merida, Yucatan 97310, Mexico

*Corresponding author's email: jose.ordonez@cnrs.fr

Based on the spatiotemporal modulation of thermal conductivity and volumetric heat capacity (Eqns. (1a) and (1b)), we propose a thermal-wave diode (Fig. 1) characterized by the rectification of the heat currents carried by thermal waves [1]. By transforming Fourier's law for the heat flux and the diffusion equation for the temperature into equations with constant coefficients (Eqns. (2a) and (2b)), it is shown that: (i) the rectification effect is generated by the simultaneous wavelike modulation of both thermal properties, such that it disappears in the absence of either of them, and (ii) the rectification factor can be optimized and tuned by means of the speed and phase difference of the variations of the heat capacity and thermal conductivity. High rectification factors, greater than 86%, are obtained for lower frequencies driving the propagation of thermal waves (Figs. 2(a) and 2(b)). The proposed thermal-wave diode is thus analogous to its electronic counterpart operating with modulated electrical currents and can open a vista for developing different types of thermal-wave logic components [2].

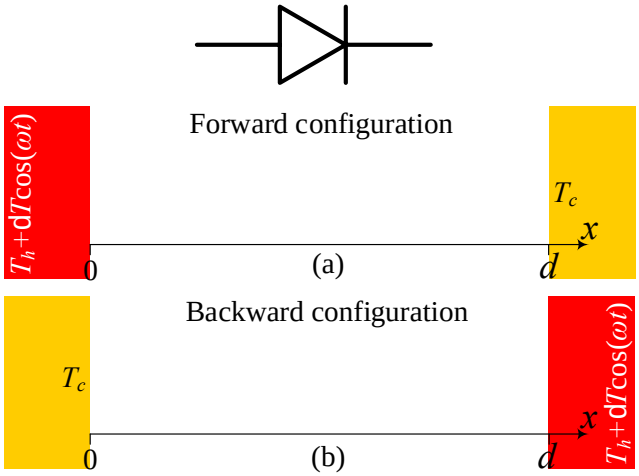

Fig. 1. Scheme of a thermal-wave diode operating in the (a) forward and (b) backward configurations. Arrows along with their amplitudes indicate the propagation direction and intensity of the thermal waves generated by the excitation $\delta T\cos(\omega t)$.

$$k = k_0\{1 + \Delta_k \cos[\sigma(x - vt)]\}, \quad \text{Eqn 1a}$$

$$C = C_0\{1 + \Delta_c \cos[\sigma(x - vt + \varphi)]\}. \quad \text{Eqn 1b}$$

$$\frac{\partial^2\bar{T}}{\partial x^2} = \frac{1}{\alpha}\frac{\partial\bar{T}}{\partial t} + \frac{1}{L}\frac{\partial\bar{T}}{\partial x} + \frac{1}{V}\frac{\partial^2\bar{T}}{\partial x\partial t}, \quad \text{Eqn 2a}$$

$$\bar{q} = -k^*\left(\frac{\partial\bar{T}}{\partial x} + \frac{1}{2V}\frac{\partial\bar{T}}{\partial t}\right). \quad \text{Eqn 2b}$$

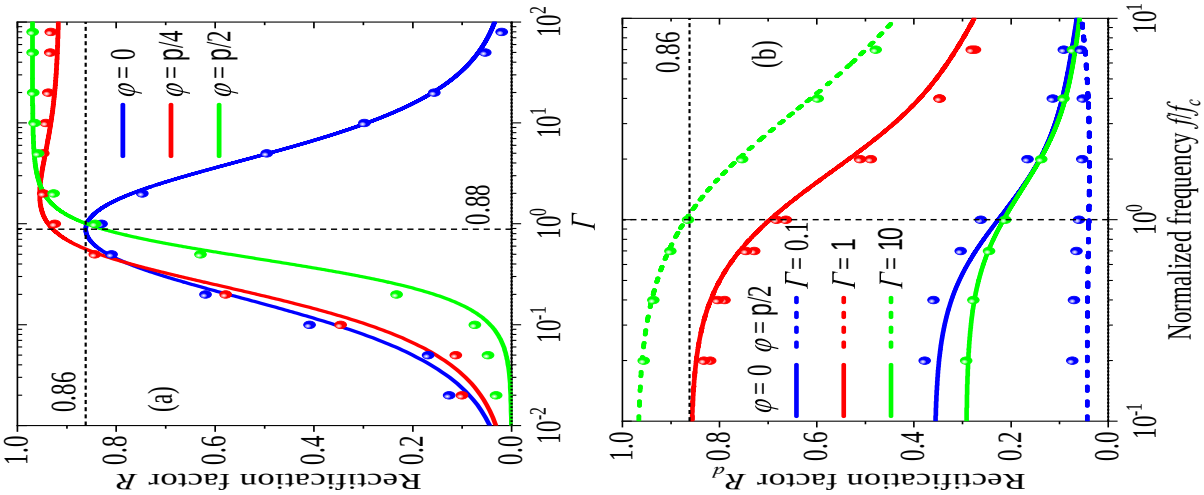

Fig. 2. Rectification factors for the heat fluxes carried by thermal waves at the (a) arrival and (b) departure positions, as functions of the normalized speed $\Gamma = v/\sigma\alpha_0$ and frequency, respectively. Points represent the numerical solution of the diffusion equation for the non-constant thermal properties in Eqns. (1a) and (1b).

References

[1] J. Ordonez-Miranda, Y. Guo, J.J. Alvarado-Gil, S. Volz, M. Nomura, Thermal-Wave Diode, Phys. Rev. Applied 16 (2021) L041002. https://doi.org/10.1103/PhysRevApplied.16.L041002.

[2] I. Forero-Sandoval, J. Chan-Espinoza, J. Ordonez-Miranda, J. Alvarado-Gil, F. Dumas-Bouchiat, C. Champeaux, K. Joulain, Y. Ezzahri, J. Drevillon, C. Gomez-Heredia, J. Ramirez-Rincon, VO2 Substrate Effect on the Thermal Rectification of a Far-Field Radiative Diode, Phys. Rev. Appl. 14 (2020) 034023. https://doi.org/10.1103/PhysRevApplied.14.034023.

Ultrafast excitation of water-immersed Carbon Nanotubes: thermophone vs mechanophone effect

Diego M[(1)*], Gandolfi M[(2)], Rouxel R[(1)], Vialla F[(1)], Crut A[(1)], Casto A[(3)], Bellussi F[(3)], Fasano M[(3)], Maioli P[(1)], Vallee F[(1)], Del Fatti N[(1)], Banfi F[(1)]

(1) Femtonanooptics Group, Université de Lyon, CNRS, Université Claude Bernard Lyon1, Institut Lumière Matière, F-69622 Villeurbanne, France
(2) CNR-INO (National Institute of Optics), Via Branze 45, 25123 Brescia, Italy
Department of Information Engineering, University of Brescia, Via Branze 38, 25023 Brescia, Italy
(3) Department of Energy, Politecnico di Torino, Corso Duca degli Abruzzi 24, 10129 Torino, Italy

*Corresponding author's email: michele.diego@univ-lyon1.fr

The photoacoustic effect in carbon nanotubes (CNTs) provides a new technique for biomedical diagnostics and treatment in living systems [1, 2] and, in general, a mean for acoustic frequency generation ranging in the THz. However, a thorough understanding of the thermoacoustics properties of a matrix embedded CNT is still lacking. In this context, we theoretically and computationally investigate here the transient photothermal acoustic response of CNTs immersed in water, triggered by an ultrafast laser pulse. Given the time and length scales involved, the system requires a multi-physics, multi-scale approach [3]. First, the laser pulse triggers an impulsive temperature increase of the CNT (sub-ps time scale). Heat is then dissipated to the proximal water portion surrounding the CNT (ns time-scale). The thermal exchange at the CNR/water interface is governed by the thermal boundary resistance [4], which we retrieve from dedicated molecular dynamics (MD) simulations [5]. The CNT and water temperature increase leads to their thermal expansion, finally launching a pressure wave in water.

For similar cases, with water-dispersed metallic nanoparticles excited by nanosecond pulses, only the water's expansion plays an effective role in launching the acoustic wave (thermophone effect) [4, 6]. Here, the contributions of the CNT's and water's expansion are discussed in detail, showing the emergence of a new competitive mechanism, which involves the generation of periodic vibrations or impulsive dilation in the CNT upon pulsed excitation, and the direct mechanical launching of a pressure wave in water (mechanophone effect).

Our simulations follow step-by-step the photothermal-acoustic steps involved, thus combining the optical, heat transfer and thermo-acoustic phenomena. The problem is tackled solving, via Finite Element Methods, the macro-physics equations upon insertion of the microscopic thermal parameters calculated from MD.

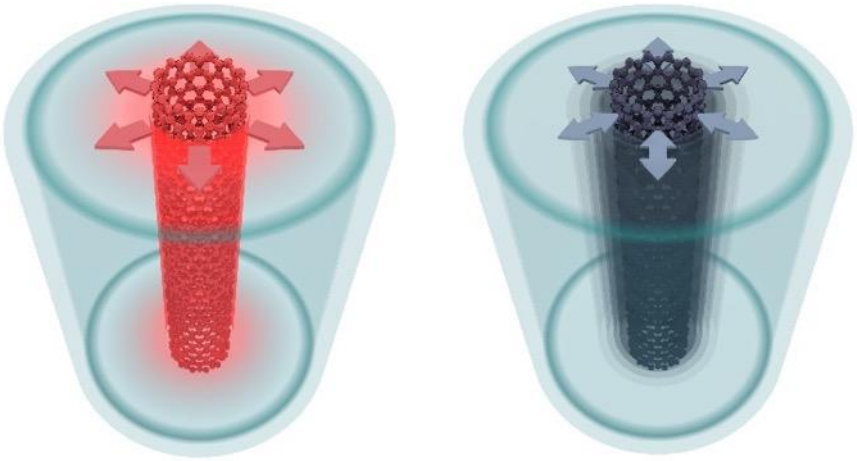

Fig. 1. Schematic representation of the mechanisms for pressure wave generation in water upon nanotube pulsed light excitation. (**Left**) Wave triggered by photothermal dilation of surrounding water, referred to as thermophone. (**Right**) Wave triggered by mechanical expansion of the nanotube, referred to as mecanophone.

References

[1] A. De La Zerda, C. Zavaleta, S. Keren, S. Vaithilingam, S. Bodapati, Z. Liu, J. Levi, B.R. Smith, T. Ma, O. Oralkan, Z. Cheng, X. Chen, H. Dai, B.T. Khuri-Yakub, S.S. Gambhir, Nat. Nanotechnol. 3 (2008) 557.

[2] B. Kang, D. Yu, Y. Dai, S. Chang, D. Chen, Y. Ding, Small 5 (2009) 1292.

[3] C. Caddeo, C. Melis, A. Ronchi, C. Giannetti, G. Ferrini, R. Rurali, L. Colombo, F. Banfi; Phys. Rev. B 95 (2017) 085306.

[4] M. Gandolfi, F. Banfi, C. Glorieuxc; Photoacoustics 20 (2020) 100199.

[5] S.M. Nejad, R. Srivastava, F.M. Bellussi, H.C. Thielemann, P. Asinari, M. Fasano, Int. J. Therm. Sci. 159 (2021) 106588.

[6] Y.S. Chen, W. Frey, S. Aglyamov, S. Emelianov, Small 8:1 (2012) 47-52.

Laser-induced coherent GHz surface acoustic waves in cleaved superlattices

Li C[(1)*], Chigarev N[(1)], Thréard T[(1)], Zhang K[(2)], Delorme N[(3)], Tournat V[(1)], Raetz S[(1)], Lu H[(2)], Gusev VE[(1)*]

(1) Laboratoire d'Acoustique de l'Université du Mans (LAUM), UMR 6613, Institut d'Acoustique – Graduate School (IA-GS), CNRS, Le Mans Université, Le Mans, France
(2) College of Engineering and Applied Sciences, Nanjing University, Nanjing, China
(3) Institut des Molécules et Matériaux du Mans (IMMM), UMR 6283 CNRS, Le Mans Université, Le Mans, France

*Corresponding author's email: changxiu.li@univ-lemans.fr, vitali.goussev@univ-lemans.fr

Background, Motivation and Objective – Coherent GHz surface acoustic waves (SAWs) hold potential usefulness in various fields including nanometrology, nanoimaging, sensoring and filters. The hypersonic frequency enables the fundamental investigations and applications with the nanometer spatial resolution and the picosecond temporal resolution. Experimentally, up to 100 GHz SAWs can be manipulated by using ultrafast lasers on the metallic gratings deposited on a substrate [1]. The nanometer period of the light-absorbing grating determines the spatial period of SAWs. Reaching higher frequency is limited by nanopatterning techniques. In theory we have earlier proposed to engineer unconventional cleaved bulk superlattices (SLs) for SAW transducers [2]. In this way, SLs epitaxially-grown with atomic precision and cleaved along the growth direction provide access to SAWs above 100 GHz. Here, we report the experimental realization of this methodology.

Methods – Ultrafast pump-probe laser experiments with a wide range of excitation/detection wavelength combinations are conducted to monitor SAWs. Semiconductor SLs composed of $Al_xGa_{1-x}As/Al_yGa_{1-y}As$, with different x/y compositions and individual widths, serve as the opto-acoustic (generation) and acousto-optic (detection) transducers. The laser beams are at normal incidence to the cleaved surface with the periodic nanostructure (Fig. 1(a)). For monitoring and identifying the $k \cong 0$ SAW modes, the configuration of the coincident pump and probe lights on SL is employed and the dispersion relation of the SLs with reduced wavevector along the periodicity axis is calculated by finite element methods. By moving the coincident laser beams to approach the SL edge, we search for the evidence of SAW emission from excitation region to outside the SL in the diminishing lifetime of SAWs. Separating the pump and the probe lights spatially enables us to track the propagation of the SAW packet (Fig. 1(b)). The SAW packet is extracted numerically by a band-pass filter from the time-domain reflectivity signal and its envelope is subsequently fitted based on its theoretical diffusive/ballistic propagation modelling.

Results/Discussions – We have optically monitored the folded SAWs and skimming longitudinal and transverse modes at $k \cong 0$. In the SLs with a period of ~70 nm and ~20 nm, first-order Rayleigh modes with the frequencies of ~40 GHz (Figs. 1(c)-(e)) and ~130 GHz are monitored, respectively. Theoretically, the ratio of the imaginary and the real parts of the Rayleigh mode frequency is proportional to the squared weak acoustical contrast (impedance ratio), indicating that the attenuation of the Rayleigh mode is small, which was confirmed by the numerical modelling. We estimated that the width (Δq) of monitored SAW k-spectrum (controlled by laser focusing) is comparable with the width (Δk) of the parabolic part of SAW dispersion relation in GaAs/AlAs SL (Fig. 1(f)), which means

that the diffusive evolution of the SAW packet is dominant. Our experimental observations in these SLs are well fitted by the analytical theory of SAWs diffusion (Fig. 1(g)). By tailoring the composition of Al in the individual layers it was possible to reach in the $Al_{0.4}Ga_{0.6}As/Al_{0.2}Ga_{0.8}As$ SL such reduced acoustic contrast that the width (Δk) of the parabolic part of the dispersion relation is negligible compared to that (Δq) of the photo-excited k-spectrum of SAWs (Fig. 1(h)). Our analytical fittings for the detected SAW packets propagating between two such SLs separated by the GaAs substrate confirm their ballistic propagation (Fig. 1(i)).

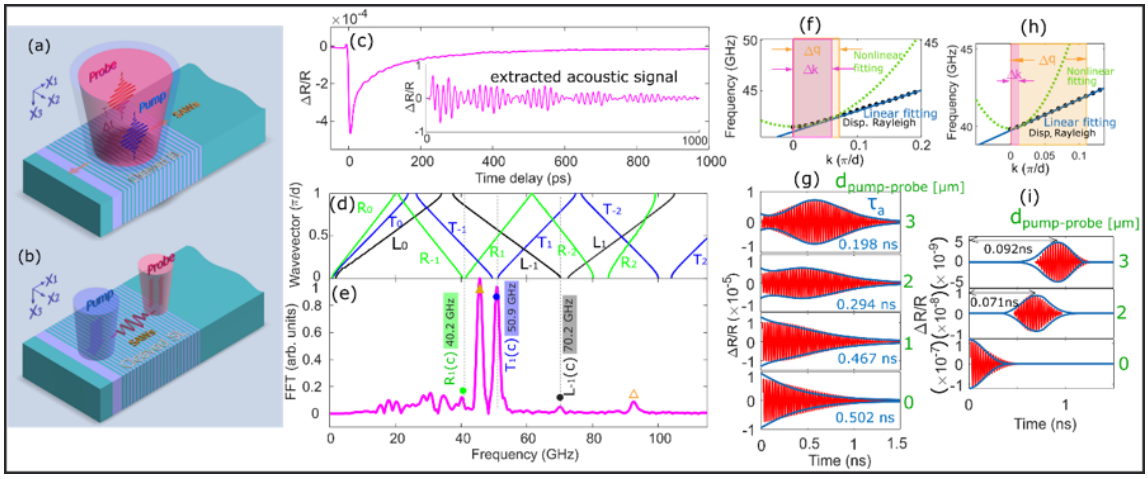

Fig. 1. (a)-(b): Illustration of pump-probe experiments in cleaved SLs. In the 71 nm-period GaAs/AlAs SL: **(c)** measured time-domain signal, **(d)** SAWs dispersion curves, **(e)** acoustic spectrum, **(f)** width of the parabolic part of SAW dispersion (Δk) vs. width of the photo-excited k-spectrum of SAWs (Δq), **(g)** filtered first-order zone-center Rayleigh SAW packets with their diffusive propagation fitting. In the $Al_{0.4}Ga_{0.6}As/Al_{0.2}Ga_{0.8}As$ SL: **(h)** width of the parabolic part of SAW dispersion (Δk) vs. width of the photo-excited k-spectrum of SAWs (Δq), **(i)** filtered first-order zone-center Rayleigh SAW packets with their ballistic propagation fitting.

Conclusions – We have experimentally proved that monitoring SAWs on the cleaved SLs by femtosecond lasers can extend their frequency range to above 100 GHz and decrease their localization depth close to single-digit nanometers. Our progress on SAWs monitoring will pave the way to their advanced applications in fundamental research, materials characterization, sensing, and information and communication technologies.

Acknowledgements – This research is supported by the postdoctoral fellowships of the Institut d'Acoustique – Graduate School (IA-GS) of Le Mans Université and of European Commission's Horizon 2020 research and innovation programme under the Marie Skłodowska-Curie grant agreement No. 101025424 for C. Li.

References

[1] M. Schubert, M. Grossmann, O. Ristow, M. Hettich, A. Bruchhausen, E. C. S. Barretto, E. Scheer, V. Gusev, T. Dekorsy, Spatial-temporally resolved high-frequency surface acoustic waves on silicon investigated by femtosecond spectroscopy, Appl. Phys. Lett. 101 (2012) 013108. https://doi.org/10.1063/1.4729891.

[2] V.E. Gusev, In: D. Bićanić (eds) Photoacoustic and photothermal phenomena III. Springer Series in Optical Sciences, 69, 323 (Springer, Berlin, Heidelberg, 1992).

Photoacoustic monitoring of the process of alignment in liquid dispersions of magnetized carbon nanotubes

Franco-Bacca AP[(1)], Cervantes-Alvarez F[(1)], Ortiz-Salazar M[(1)], Martínez-Torres P[(2)], Alvarado-Gil JJ[(1)*]

[1]Departamento de Física Aplicada, Cinvestav-Unidad Mérida, Carretera Antigua a Progreso Km. 6, Mérida, Yucatán, México, 97310, México
[2]Instituto de Física y Matemáticas, Universidad Michoacana de San Nicolás de Hidalgo, Edificio C-3, Ciudad Universitaria, CP. 58040 Morelia, Michoacán, México

*Corresponding author's email: juan.alvarado@cinvestav.mx

Liquid composites of carbon nanostructures are very promising due to their outstanding electrical, optical, and thermal properties. The physical properties of these materials can be reversibly manipulated inducing an order of the CNTs inside the matrix. This manipulation can be done by applying an external electric field, but it is induced heating ~~hating~~ due to the Joule effect. The magnetic field could be a good option; however, the intrinsic magnetic moment is not high enough to allow low-intensity magnetic fields to manipulate the nanotubes. One of the best options~~,~~ is to magnetize the nanotubes. In this paper, dispersions of magnetized multiwall carbon nanotubes at different concentrations in ethylene glycol and glycerol liquid matrices are presented. The response of the dispersions to the magnetic field was monitored as a function of time using the photoacoustic technique. To analyze the photoacoustic results, a theoretical model was developed based on the magnetic-field induced alignment of the carbon nanotubes in the matrix. Our results provide the evolution of the optical absorption coefficient as a function of time, concentration, and magnetic field.

Keywords Magnetic fluids, external magnetic field, decorated multiwalled carbon nanotubes, photoacoustic, optical absorption coefficient.

References

[1] J. Wang, Y. Chen, W.J. Blau, Carbon nanotubes and nanotube composites for nonlinear optical devices, J. Mater. Chem. 19 (2009) 7425.

[2] J.L Bahr, E.T. Mickelson, M.J. Bronikowski, R.E. Smalley, J.M. Tour, Dissolution of small diameter single-wall carbon nanotubes in organic solvents? Chem. Commun. (2001) 193–4

[3] X. Benedict, S.G. Louie, M.L Cohen, Static Polarizabilities of single-walled carbon nanotubes Phys. Rev. B 52 (1995) 8541–9.

[4] M. Freitag, Y. Martin, J. Misewich, R. Martel, P. Avouris, Photoconductivity of single carbon nanotubes, Nano Lett. 3 (2003) 1067–71.

[5] R. Stanway, Smart fluids: current and future developments, Mater. Sci. Technol. 20 (2004) 931–9.

[6] L. Vivien, P. Lançon, D. Riehl, F. Hache, E. Anglaret, Carbon nanotubes for optical limiting, Carbon N. Y. 40 (2002) 1789–97.

[7] R. Vepa, Biomimetic Robotics, Elsevier Inc. (2013).

[8] C.W. Huang, C.H. Hsu, P.L Kuo, C.T. Hsieh, H. Teng, Mesoporous carbon spheres grafted with carbon nanofibers for high-rate electric double layer capacitors, Carbon N. Y. 49 (2011) 895–903.

[9] T. Prasse, J.Y. Cavaillé, W. Bauhofer, Electric anisotropy of carbon nanofibre/epoxy resin composites due to electric field induced alignment, Compos. Sci. Technol. 63 (2003) 1835–41.

[10] J. Xiang, J. Li, X. Zhang, Q. Ye, J. Xu, X. Shen, Magnetic carbon nanofibers containing uniformly dispersed Fe/Co/Ni nanoparticles as stable and high-performance electromagnetic wave absorbers, J. Mater. Chem. A 2 (2014) 16905–14.

[11] C. Vales-Pinzón, J.J. Alvarado-Gil, R. Medina-Esquivel, P. Martínez-Torres, Polarized light transmission in ferrofluids loaded with carbon nanotubes in the presence of a uniform magnetic field, J. Magn. Magn. Mater. 369 (2014) 114–21.

[12] M.S. Brown, J.W. Shan, C. Lin, F.M. Zimmermann, Electrical polarizability of carbon nanotubes in liquid suspension, Appl. Phys. Lett. 90 (2007).

Unwrapping the soot assisted intra-pigment energy transfer in leaves through the thermal lens technique: Time series analysis in nanobiophotonics

Swapna MS[(1,2)*], Sankararaman S[(1)]

(1) Department of Optoelectronics, University of Kerala Trivandrum, Kerala, 695581, India
(2) Laboratory for Environmental and Life Sciences, University of Nova Gorica, Slovenia

*Corresponding author's email: swapnams.opto@gmail.com

Background – The non-destructiveness of an analysing method is most important in the case of biological samples. Intriguing the energy-harvesting mysteries in plants, (photosynthesis) is important as it is the primary biological process that decides the life on earth. In one of our previous studies, the carbon nanoparticle assisted intra-pigment energy transport in leaves has been detailed through the single beam thermal lens (TL) technique [1]. The study revealed the thermal diffusivity variations of the chlorophyll system with varying concentrations of carbon nanoparticles. The present study is the first attempt of employing the mathematical and statistical tool – Time series analysis (TSA) to the novel interdisciplinary branch Nanobiophotonics. Here, the influence of soot nanoparticles in the energy transport mechanism of the leaf pigments is explored using the sensitive and non-destructive TL technique. The TL signal being a treasure of information regarding the medium of lens formation [2,3], it is found to have applications in studying the thermal diffusivity of materials, trace element and adulterant detection, quantum yield studies, biomedical analysis, pharmacology, and in thermal engineering [2,4,5].

Methods – The diesel soot containing carbon nanoparticles (CNPs) are prepared in different concentrations (0.10, 0.20, 0.60, 1.25, 2.50, 4.00, and 5.00 g/l) and are sprayed over the leaves of *Lablab purpureus (L.) sweet.* The chlorophyll pigments are extracted [6] from the leaves after ten days the UV-Vis absorption spectrum is recorded. The leaf extracts are subjected to laser-assited TL study, and the TL signals recorded are analysed by nonlinear time series and fractal techniques.

Results: The UV-Vis absorption spectrum of the samples shows a decrease in the intensity of the signature peaks (430 nm and 660 nm) of chlorophyll for the soot concentrations up to 0.60 g/l, increases up to 1.25 g/l and saturates after that. For the TSA of the TL signals of each sample, phase portraits are constructed after finding the optimal time delay and embedding dimension. A representative phase portrait for the soot concentration 5 g/l is shown in Fig. 1(a). The phase portrait, sample entropy (S), fractal dimension (FD), and Hurst exponent (H) show a variation in the randomness, disorder, complexity and antipersistence nature with the increase of soot concentration. The analysis becomes more easier when the graphs are divided into 3 regions based on the soot concentration (Fig. 1(b)). The range of soot concentrations 0 to 0.60 g/l, 0.60 to 2.5 g/l, and 2.5 to 5 g/l are considered as region 1, 2, and 3 respectively. Region 1 shows an increase of S and FD, in agreement with the phase portrait, due to the increased rate of out-flow of energy created due to thermal inequilibrium between the leaf system and the surroundings. In region 2, the values of S and FD decreases, indicating the energy trap by the

soot nanoparticles in the chloroplast. The observed lowering of the spread of phase points agrees well with the reduced particle dynamics as revealed through S and FD. Here, the energy absorbed by the CNPs in soot is transferred to the leaf pigments, thereby facilitating intra-pigment energy transport among leaves. We have already reported the CNP assisted intra-pigment energy transport enhancing the photosynthesis rate [1]. In region 3, the UV-Vis absorption spectrum shows a near saturation, which gets reflected in the time series parameters and fractal dimension computed from the TL signal. The saturation of S and FD values for the concentrations in region 3 indicate the non-usefulness of such a CNP concentration in the intra-pigment energy transport. The rising and saturation of S and FD throw light into the intriguing particle/molecular dynamics resulting from increased energy dissipation.

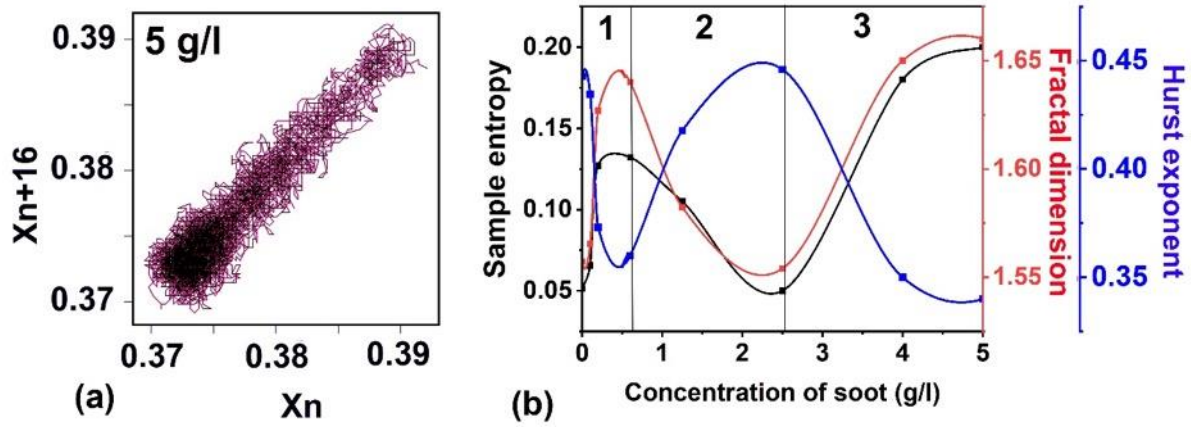

Fig. 1. (a) A representative phase portrait for the soot concentration 5 g/l and **(b)** variation of S, FD, and H with soot concentration.

Conclusions – Thus, the study proposes an optimum concentration of CNPs beneficial to leaves in the intra-pigment energy transport and suggests a possible yield enhancement method from crops. The entropy minimization and its analytical techniques open up its potential application in artificial photosynthesis and dye sensitized solar cells.

References

[1] M.S. Swapna, V. Raj, H. V. Saritha Devi, P.M. Radhamany, S. Sankararaman, Carbon nanoparticles assisted energy transport mechanism in leaves: A thermal lens study, Eur. Phys. J. Plus. 134 (2019) 416. https://doi.org/10.1140/epjp/i2019-12780-1.

[2] M.S. Swapna, R. Vimal, K. Satheesh Kumar, S. Sankararaman, Soot effected sample entropy minimization in nanofluid for thermal system design: A thermal lens study, J. Mol. Liq. 318 (2020) 114038. https://doi.org/10.1016/j.molliq.2020.114038.

[3] B.-X. Wang, L.-P. Zhou, X.-F. Peng, A fractal model for predicting the effective thermal conductivity of liquid with suspension of nanoparticles, Int. J. Heat Mass Transf. 46 (2003) 2665–2672.

[4] M. Franko, Recent applications of thermal lens spectrometry in food analysis and environmental research, Talanta. 54 (2001) 1–13. https://doi.org/10.1016/s0039-9140(00)00608-1.

[5] V. Raj, M.S. Swapna, H.V.S. Devi, S. Sankararaman, Nonradiative analysis of adulteration in coconut oil by thermal lens technique, Appl. Phys. B. 125 (2019) 113. https://doi.org/10.1007/s00340-019-7228-6.

[6] S. Yoshida, D.A. Forno, J.H. Cock, Laboratory manual for physiological studies of rice., Lab. Man. Physiol. Stud. Rice. (1971).

Elastic properties effect of nanoparticles-functionalized alpaca fibers by the photoacoustic method

Quispe-Siccha RM[(1,3)*], Mejía-Uriarte EV[(2,3)], Jauregui-Rosas SR[(3)], Felix-Quintero HA[(3)], Navarrete-Montesinos M[(4)], Aldama-Reyna CW[(5)], Figueroa-Avalos HM[(6)], Siche-Jara RB[(6)],

(1) Unidad de Investigación y Desarrollo Tecnológico, Hospital General de Mexico EL, Mexico City, Mexico
(2) Fotónica de Microondas, Instituto de Ciencias Aplicadas y Tecnología, UNAM, Mexico City**,** Mexico
(3) Departamento Académico de Física, Facultad de Ciencias Físicas y Matemáticas, UNT, Trujillo, Peru
(4) Instituto de Ingenieria, UNAM, Mexico City**,** Mexico
(5) Laboratorio de Óptica y Láseres, UNT, Trujillo, Peru
(6) Ingenieria Agroindustrial, UNT, Trujillo, Peru

*Corresponding author's email: rosa.quispe@gmail.com

The textile industry is one of the essential branches of the economy of many countries globally, and the importance of wool is still immense. Peru is the largest exporter of alpaca and vicuña fiber, considered "natural super-fibers" due to their extraordinary properties. Such as resistance, elasticity, moisture insulation, more efficiency than others in heat exchange, hypoallergenic (without lanolin), and soft contact with the skin, as described by D. Jankowska et al. [1]. By functionalizing the natural fibers with metallic nanoparticles to make them antibacterial and metal oxides to make them superhydrophobic, the capacity of their natural properties will be increased, obtaining a hybrid fabric, as described by H. Memon et al. [2]. However, there is that corroborated if their properties physical- mechanicals no change. For that reason, in this work, we are in charge of evaluating the elastics properties of the alpaca fibers before and after being functionalized using the pulsed photoacoustic technique. These results are corroborated with the traction tests. This research will help some communities in Peru and worldwide that suffer from cold weather and lack water and electricity to clean their clothes. Furthermore, with the knowledge acquired during this research, it is possible to venture into the cotton textile area to translate the same study into sterile whites for hospital environments and sterile and disposable healing material.

Methods – In this work, eight colors of alpaca fibers were studied: white, light beige, medium beige, dark beige, dark brown, shiny dark brown, dark brown-black and black, and one vicuña: light brown, natural and functionalized with nanoparticles: Ag, Au, TiO_2, ZnO. First, the elastic constants of the fibers above were evaluated, following the respective procedure: 1) A cleaning protocol was used to preserve the fibers' natural properties. 2) An optical microscope with a 5Mp camera (Nikon Eclipse, 40x/0.65) was used to measure the diameter of the fibers because it is a necessary variable to calculate the modulus of elasticity. 3) An experimental photoacoustic (PA) arrangement was used for two geometries, that is, in the longitudinal (L) and transverse (T) directions of the fibers, as shown in Figure 1.

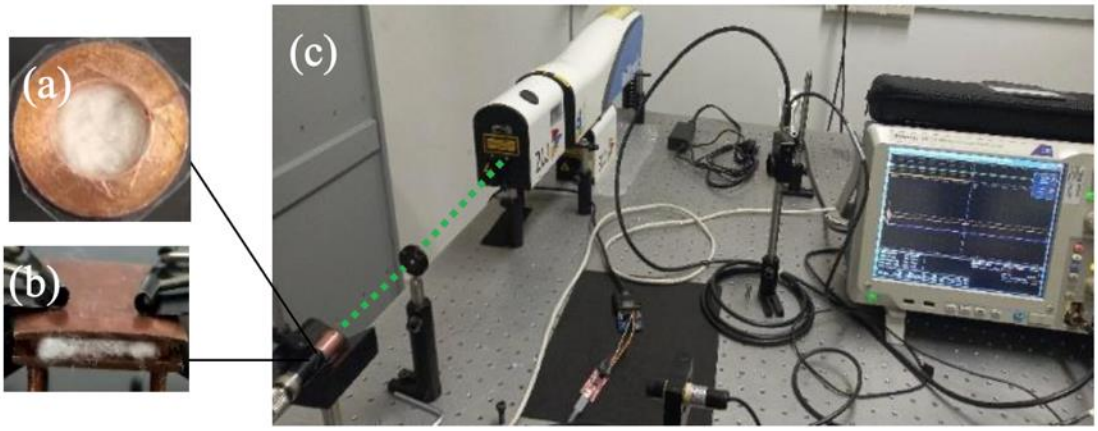

Fig. 1. (a, b) The sample-holders with white fibers in the longitudinal and transverse geometry, **(c)** Photoacoustic experimental setup used for all samples. Consisting of a Nd: YAG laser (λ = 532 nm, F = 10Hz, τ = 5ns, Fluence = 1.25 J/m), a sensor 3.5 MHz (Olympus Panametrics), a digital phosphor oscilloscope 2 GHz (Tektronix), and optical arrays.

4) To corroborate the elastic constants obtained by the two geometries of the PA method, they were compared with the tensile tests using a tensor grip A/TG (Stable Micro System).

Results – The arrival times of all the photoacoustic signals belonging to each color were obtained (eight colors of alpaca fibers and one color of vicuña fiber) using the two configurations(L and T). Measurements were made in triplicate for each color. Figure 2 shows the offset of the PA signal output for each interface that is added in the signal path, given the geometric arrangement shown in Figure 1a. The Young's Modulus or elasticity modulus was also obtained by analyzing the tensile tests for all the samples. Figure 2b shows the average value of Young's modulus of the white alpaca fiber.

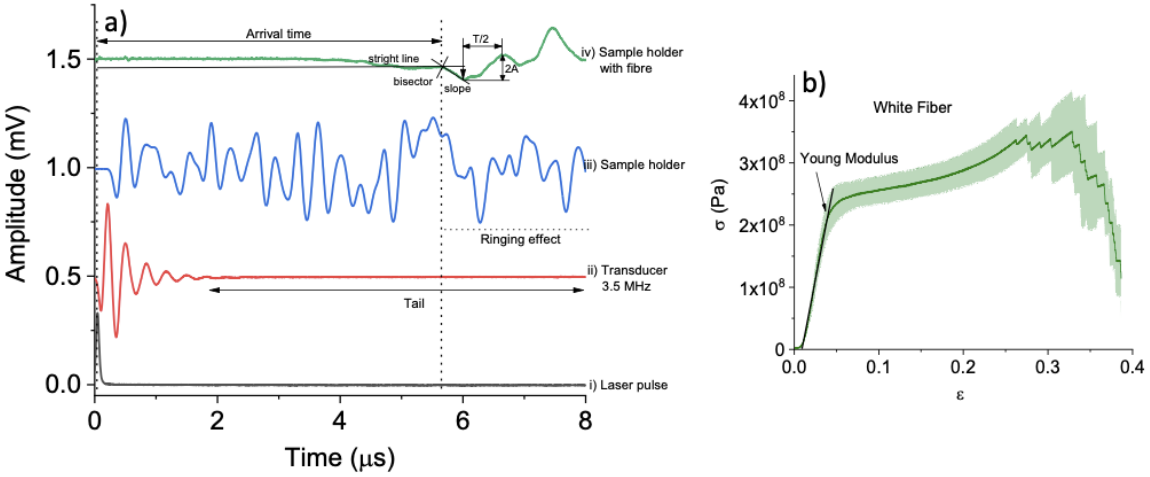

Fig. 2. (a) Arrival times of the PA signals in the L direction for each interface that is added in the signal's trajectory. The corresponding geometric arrangement is shown in Fig. 1a. (i) Laser pulse waveform; (ii) piezoelectric transducer output signal generated by the excitation of the laser pulse; (iii) PA signal generated by the sample holder, without sample, showing the ringing effect; and (iv) PA signal output with the sample fixed inside of the sample holder. **(b)** Average value of Young's modulus of white alpaca fiber obtained by analysis of tensile tests

Conclusions – The determination of the elastic constants in two directions using different geometric arrangements has been demonstrated, considering that the fibers behave as transversely isotropic materials. The properties and performance of nanoparticle fibers depend on the geometric attributes of the fibers, such as volume fraction, density, and size distribution. When another phase, such as metallic nanoparticles or semiconductor metal oxides, is included in the mixing solution, these particles are not

evenly distributed within the long fiber, which changes its mechanical behavior. We find that depending on the concentration of the particles, they behave as defects or reinforcements.

References

[1] D. Jankowska, A. Wyrostek, B. Patkowska–Sokoła, K. Czyż, Comparison of Physico-mechanical Properties of Fibre and Yarn Made of Alpaca, Sheep, and Goat Wool, J. Nat. Fibers 18 (2021) 1512-1517. DOI: 10.1080/15440478.2019.1691126.

[2] H. Memon, H. Wang, S. Yasin, A. Halepoto, Influence of Incorporating Silver Nanoparticles in Protease Treatment on Fiber Friction, Antistatic, and Antibacterial Properties of Wool Fibers, J. Chem. (2018) 1-8. DOI: 10.1155/2018/4845687.

Design, fabrication and characterization of Bragg reflectors based on porous silicon monitored by photoacoustics

Rodriguez-Garcia ME[(1)*], Ramirez-Gutierrez CF[(2)], Martinez-Hernandez HD[(3)], Lujan-Cabrera IA[(2)]

(1) Departamento de Nanotecnología, Centro de Física Aplicada y Tecnología Avanzada, Universidad Nacional Autónoma de México, Campus Juriquilla, Querétaro, Qro., 76230, México
(2) Universidad Politécnica de Querétaro, El Marqués, Qro., México
(3) Posgrado en Ciencia e Ingeniería de Materiales, Centro de Física Aplicada y Tecnología Avanzada,

Universidad Nacional Autónoma de México, Campus Juriquilla, Querétaro, Qro., 76230, México

*Corresponding author's email: marioga@fata.unam.mx

Porous silicon (PSi) is a nanostructured material with diverse porous morphology, varied surface chemistry, and enormous surface area. PSi has been obtained commonly through electrochemical etching in hydrofluoric aqueous media. The optical response of PSi has been studied by photoluminescence, UV-VIS reflectance, ellipsometry, FTIR, among other characterization techniques, finding that the optical properties are tuneable as a function of the porosity percentage. But, the origin of their optical response is still in controversy. In that sense, it has been reported that the mechanism responsible for the total optical response is a complex mixture of surface chemistry and quantum confinement. The self-limited character of the porous silicon electrochemical reaction allows fabricating homogeneous films and heterostructures. Also, it is possible to custom porous silicon properties changing the growing parameters. This makes porous silicon in a candidate to develop optical devices such as porous distributed Bragg reflector and Fabry-Perot cavities. However, the physicochemical properties of porous silicon are critically dependent on the etching parameters and there are not theoretical models to predict PSi properties such as refractive index, absorption coefficient, thickness, porosity, and interfaces roughness [1]. Therefore, this work is focused on establishing a methodology based on photoacoustic (PA) to monitor the Bragg reflectors fabrication and a procedure to design and customize optical devices based on porous silicon. In this direction, it was determined and correlated some of the key points to be able to fabricate high-quality Bragg reflectors such as etching rate, porosity determination, a model to determine the refractive index of porous media by using photoacoustic and effective medium approximation. Also, simulation and design analyses of the optical multilayer system are discussed.

In this work we proposed to fabricate PSi heterostructures with applications in DBR's by controlling the porosity percentage during the formation of PSi films by photoacoustics (FA), with the aim of designing a monitoring and control method to predict and manipulate the refractive indices and the thickness of the layers to obtain PSi-based DBR's with specific spectral positions and bandwidths.

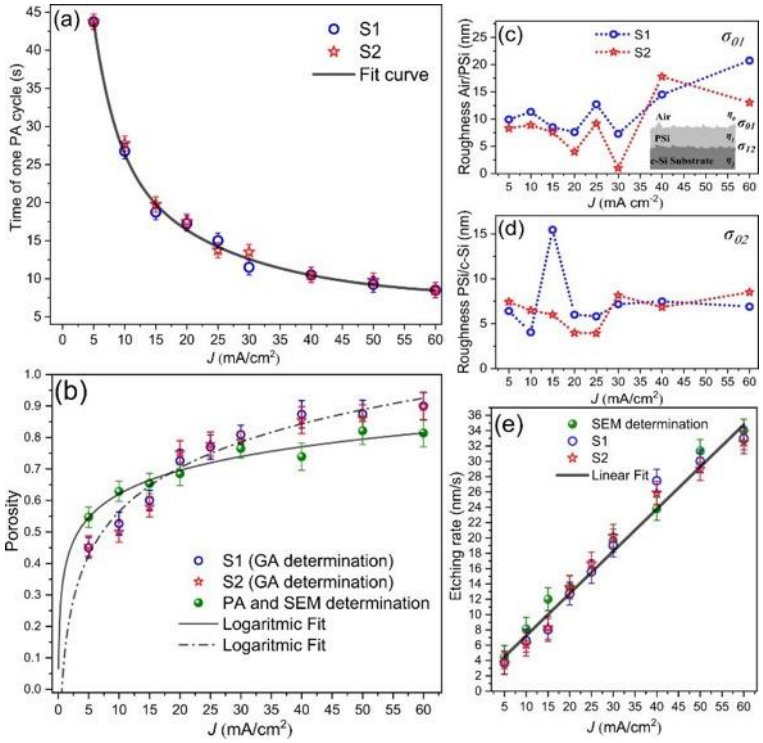

Fig. 1. Calibration series parameters. (a) PA time as a function of current density that exhibits an exponential decay behaviour. (b) Average porosity determined by genetic algorithms (GA) and PA-SEM, (c) and (d) interface roughness as a function of current density determined by GA fitting of UV-Vis spectrum. (e) Etching rate that exhibits linear behaviour.

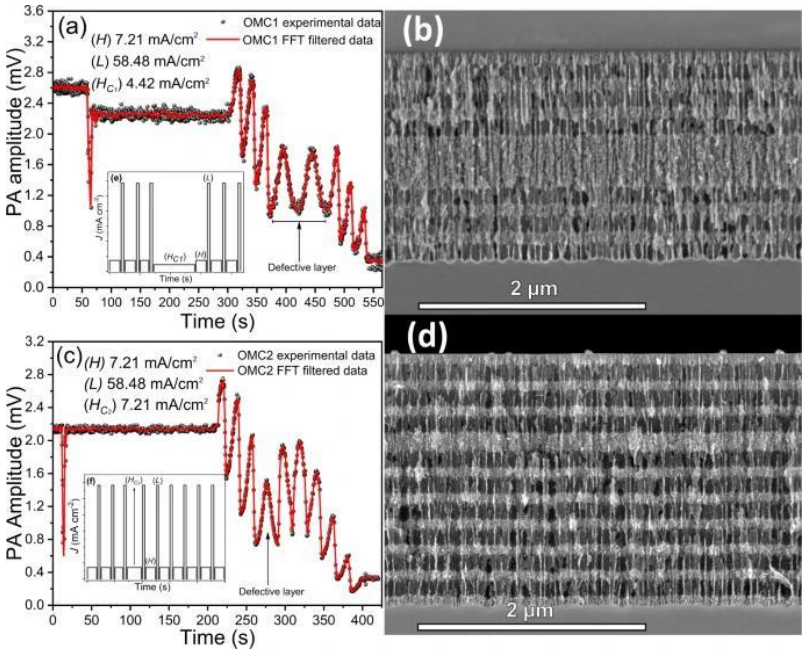

Fig. 2. PA amplitude during optical microcavity (OMC) fabrication. (a) OMC1, (c) OMC2, and its respective SEM cross-sectional images (b,d). Insets (e,f) correspond to the current profiles used for OMC1 and OMC2 fabrication respectively.

References

[1] C.F. Ramirez-Gutierrez, J.D. Castaño-Yepes, M.E. Rodriguez-Garcia, Modeling the photoacoustic signal during the porous silicon formation, Int. J. Appl. Phys., 121 (2017). https://doi.org/10.1063/1.4973940.

Multiple Stokes and anti-Stokes components generation by biharmonic pumping via stimulated low-frequency Raman scattering

Tareeva MV[(1)*], Kudryavtseva AD[(1)], Shevchenko MA[(1)], Umanskaya SF[(1)], Tcherniega NV[(1)]

(1) Optics Department, Lebedev Physical Institute, Russian Academy of Sciences, Moscow, Russia

*Corresponding author's email: tareevamv@lebedev.ru

The process of high efficiency coherent acoustic excitation of the submicron particles system by biharmonic pumping is investigated. This excitation leads to effective multiple Stokes and anti-Stokes high-order components generation. This process can be used for effective generation of the coherent electromagnetic radiation with tunable spectral distribution consisting of several spectral lines separated by a constant frequency spacing of several GHz.

Any spatially limited object, including submicron and nanoscale ones, constantly undergoes thermal vibrations. The set of acoustic eigen frequencies of any object with which it oscillates is determined by its morphology, as well as by the elastic characteristics of its environment. Some of these acoustic excitations are Raman active and can manifest themselves in low-frequency Raman scattering [1] (LFRS) or in stimulated low frequency Raman scattering [2] (SLFRS). Biharmonic pumping is electromagnetic radiation whose spectrum consists of two spectral lines can be used for effective for effective impact on the system of particles in the case of the matching the particles acoustic eigenfrequencies with the frequency shift of biharmonic radiation by analogy with coherently driven molecular vibrations [3]. This process can lead to multiple Stokes and anti-Stokes high-order components generation.

The effect of multiple Stokes and anti-Stokes components generation by biharmonic pumping in nanosecond temporal range was demonstrated in a number of dielectric, semiconductor and metallic submicron particles systems. The effective generation of six equally shifted spectral components was realized. The possible application of the observed phenomenon for spectroscopy of the nanoscale and submicron systems is discussed.

[1] E. Duval, A. Boukenter, B. Champagnon, Vibration Eigenmodes and Size of Microcrystallites in Glass: Observation by Very-Low-Frequency Raman Scattering, Phys. Rev. Lett. 56 (1986) 2052-2055.

[2] N.V. Tcherniega, et al, Experimental observation of stimulated low-frequency Raman scattering in water suspensions of silver and gold nanoparticles, Opt. Lett. 38 (2013) 824-826.

[3] E. Garmire, F. Pandarese and C.H. Towns, Coherently driven molecular vibrations and light modulation, Phys. Rev. Lett. 11 (1963) 110-163.

11

Environmental, Agricultural, and Food Applications

KEYNOTE SPEAKER

FTIR photoacoustic spectroscopy of soils: comparison of FTIR modalities for soil fractions of various agrogenesis

Volkov DS[1, 2],Rogova OB[2], Proskurnin MA[1]

(1) Department of Analytical Chemistry, Chemistry Department, Lomonosov Moscow State University, Moscow, Russia
(2) Dokuchaev Soil Science Institute, Moscow, Russian Federation

*Corresponding author's email: proskurnin@gmail.com

Granulometric fractionation as a source of additional information on organic-matter and inorganic matrix components of soils using FTIR photoacoustic spectroscopy (FTIR PAS) supported by attenuated-total reflection FTIR spectroscopy (ATR–FTIR) and diffuse reflectance FTIR (DRIFT) for a wide range of aggregate fractions (10–5000 μm) was used to compare the sensitivity, reproducibility, information contents, and representativity of fractionated samples. FTIR PAS modality shows a much higher sensitivity in the middle-wave range (SiO_2 overtone range) of the mid-IR range than attenuated total reflection modalities and excels diffuse-reflectance modality as it does not require sample dilution. In addition, FTIR PAS measurements are possible for soil aggregates up to 5 mm without sample decomposition or milling

The studies of the influence of agrogenesis and anthropogenesis on the physical and physicochemical properties of soils experience a notable shift. Apart from traditional approaches to assessing bulk soil properties, the new information level requires determining soil fractions and aggregate structures, including the changes at meso- and microaggregate levels.

FTIR Photoacoustic spectroscopy is a sensitive modality of absorption spectroscopy. It is based on the measurements of the heat caused by the absorption of radiation by the sample. The pressure waves resulting from heating the sample by IR or visible light are detected by a microphone or a piezo-transducer, providing high sensitivity of light-absorption measurements. FTIR PAS features depth profiling, simple and almost non-destructive sample preparation, and small amounts of the test sample.

This study aims to work out the approaches for the identification and assessment of inorganic and organic-matter components of bulk samples and size fractions (by dry sieving) of chernozems and sod-podzolic soils as SiO_2-based soils with a different type of land use by FTIR PAS. Mid-IR PA spectra of size fractions 1–5000 mm were studied. The conditions of FTIR PAS measurements were compared with attenuated-total-reflection (ATR) and diffuse-reflection (DRIFT) measurements. Apart from depth analysis, FTIR-PAS provides relatively reproducible conditions for various size fractions, and these fractions hold more differences than entire soils.

FTIR PAS modality shows a much higher sensitivity in the middle-wave range (SiO_2 overtone range) of the mid-IR range than attenuated total reflection modalities and excels diffuse-reflectance modality as it does not require sample dilution. In addition, FTIR PAS measurements are possible for soil aggregates up to 5 mm without sample decomposition or milling, which is a unique property of this modality [1].

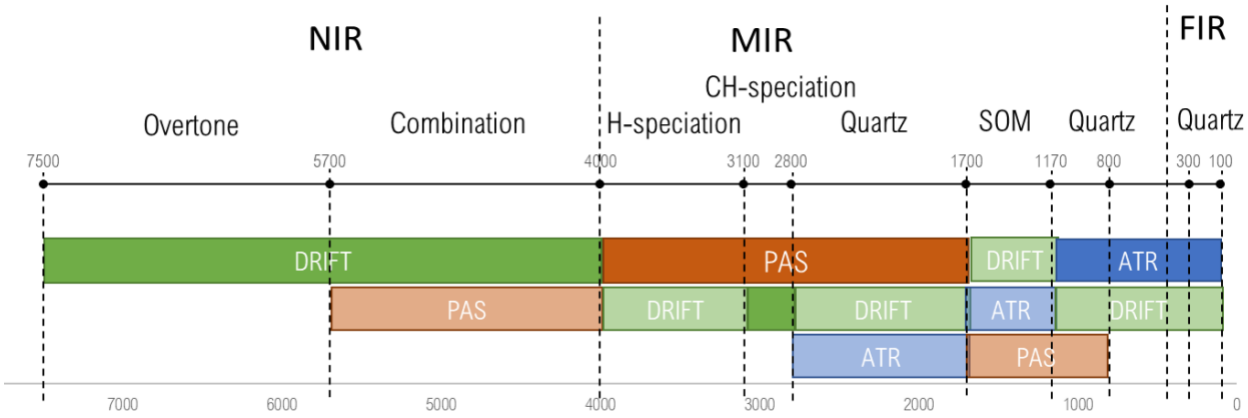

Fig. 1. Applicability of DRIFT, ATR–FTIR, and FTIR–PAS for qualitative analysis for silicate soils. Applicable techniques are shown in full colors, ambiguous, in watercolors, the most informative technique in each subrange is shown at a higher position [2].

For studied silicate-based soils, matrix minerals are dominant in the whole spectrum despite a high concentration of soil organic matter. Therefore, the organic-matter analysis is impossible without destructive sample preparation, organic-matter extraction, or some not-so-obvious assumptions. On the contrary, the inorganic-component analysis appears to be more promising for non-destructive FTIR PAS as it can be based on large mineral databases and approaches to quantitative assessment based on mineral bands of different origins. An essential feature of FTIR PAS of studied soils is that quartz overtone peaks at 2000–1700 cm^{-1} can be used as internal standards of soil samples of the same type for more balanced spectra comparison.

A drawback of FTIR PAS is rather sophisticated data processing, which is a considerable asset in basic research of soils but is rather inappropriate for serial or rapid analysis of multiple samples in large-scale experiments. Therefore, some strict but simple data handling algorithms are required for more reliable and reproducible data in FTIR PAS. Still, the developed methodological approaches and previous findings seem reliable enough for use in soil analysis, including meso- and microaggregate levels.

Acknowledgments – The authors acknowledge the financial support of The Russian Science Foundation, grant no. 19-13-00117.

This research was performed according to the Development program of the Interdisciplinary Scientific and Educational School of Lomonosov Moscow State University, “The future of the planet and global environmental change”.

References

[1] P.K. Krivoshein, D.S. Volkov, O.B. Rogova, M.A. Proskurnin, FTIR Photoacoustic and ATR Spectroscopies of Soils with Aggregate Size Fractionation by Dry Sieving, ACS Omega 7:2 (2022) 2177-2197. doi: 10.1021/acsomega.1c05702.

[2] D.S. Volkov, O.B. Rogova, M.A. Proskurnin, Organic Matter and Mineral Composition of Silicate Soils: FTIR Comparison Study by Photoacoustic, Diffuse Reflectance, and Attenuated Total Reflection Modalities, Agronomy 11:9 (2021) 1879. doi:10.3390/agronomy11091879.

AFM-IR study of carbonaceous chondrites and Ryugu samples returned by the Hayabusa 2 space mission

Mathurin J[(1)*], Dartois E[(2)], Dazzi A[(1)], Deniset-Besseau A[(1)], Bejach L[(3)], Engrand C[(3)], Duprat J[(4)], Kebukawa Y[(5)], Yabuta H[(6)], Yurimoto H[(7)], Nakamura T[(8)], Morita T[(9)], Kikuiri M[(9)], Amano K[(9)], Kagawa E[(9)], Noguchi T[(9)], Okazaki R[(10)], Naraoka H[(10)], Sakamoto K[(11)], Tachibana S[(11,12)], Watanabe S[(13)], Tsuda Y[(11)] and the Hayabusa2-initial-analysis IOM and STONE teams

(1) Institut Chimie Physique (ICP), Univ. Paris-Saclay/CNRS, 91405 Orsay, France
(2) ISMO, Univ. Paris-Saclay/CNRS, 91405 Orsay, France
(3) IJCLab, Univ. Paris-Saclay/CNRS, 91405 Orsay, France
(4) IMPMC/MNHN, SU, Paris, France
(5) Faculty of Engineering, Yokohama National University, Japan
(6) Hiroshima University, Higashi-Hiroshima 739-8526, Japan
(7) Hokkaido University, Sapporo 060-0810, Japan
(8) Tohoku University, Sendai 980-8578, Japan
(9) Kyoto University, Kyoto 606-8502, Japan
(10) Kyushu University, Fukuoka 812-8581, Japan
(11) ISAS/JAXA, Sagamihara 252-5210, Japan
(12) The University of Tokyo, Tokyo 113-0033, Japan
(13) Nagoya University, Nagoya 464-8601, Japan

*Corresponding author's email: jeremie.mathurin@universite-paris-saclay.fr

Background – The distribution of chemical bonds in organic matter (OM) of interplanetary samples (meteorites and micrometeorites) can be efficiently and non-destructively characterized using infrared (IR) vibrational spectroscopy. Conventional IR microscopy provides a global view of the dust grain physico-chemical composition but remains spatially limited by diffraction [1]. In state-of-the-art synchrotron-based µ-FTIR microscopy, spot sizes of a few microns at best can be achieved in the mid-IR range. Such diffraction limited sampling can be circumvented by using AFM-IR microscopy [2], allowing, for the first time, to compare the distribution of chemical bonds at the sub-micron scale.

Methods – AFM-IR is now a well-established microscopy technique in the vibrational field, combining an atomic force microscope (AFM) and a tunable IR laser source to record the photo-thermal effect and access chemical information at the sub-micrometric scale [3]. This technique is applied in a wide diversity of scientific fields, and was recently used to analyze OM-rich extraterrestrial samples [2], [4]. As AFM-IR reaches a high resolution (tens of nanometers) compared to the size of the studied objects (few tens to hundreds of microns), regions of interest were first localized and selected using conventional and synchrotron FTIR microscopy.

Results – Firstly results were obtained on carbonaceous chondrites which were prepared without chemical pre-treatment. The extended analyses give a complete insight on the different chemical components involved in these meteoritic samples. The study has then been extended to more precious samples from the Japanese space mission Hayabusa2, that returned samples from the primitive asteroid

Ryugu. Ryugu samples were received from the "IOM" and "Stone" initial analysis teams led by Dr. H. Yabuta and Dr. T. Nakamura, respectively. Several samples from two different sample chambers (A and C, corresponding to two different collecting sites) were prepared by crushing small fragments on diamond windows. The analyzed areas were chosen based on previous µ-FTIR synchrotron analyses. It was then possible to localize OM inclusions in samples from chamber A (not shown here) and chamber C (Fig. 1). Figure 1 presents the signal from the Si-O stretching mode of the silicates (1020 cm^{-1} - in green) and that from the OM contributions of the C=C absorption (1600 cm^{-1} - in blue) and C=O absorption (1720 cm^{-1} - in red). It shows that the OM inclusions recorded by AFM-IR range from 50 nm to 500 nm in size, and that chemical heterogeneities are observed at small scales: parts of the inclusions seem to exhibit local enrichment in C=O (redder) while other a local enrichment in C=C (bluer). This is confirmed by the local IR spectra which show locally different C=C and C=O contributions.

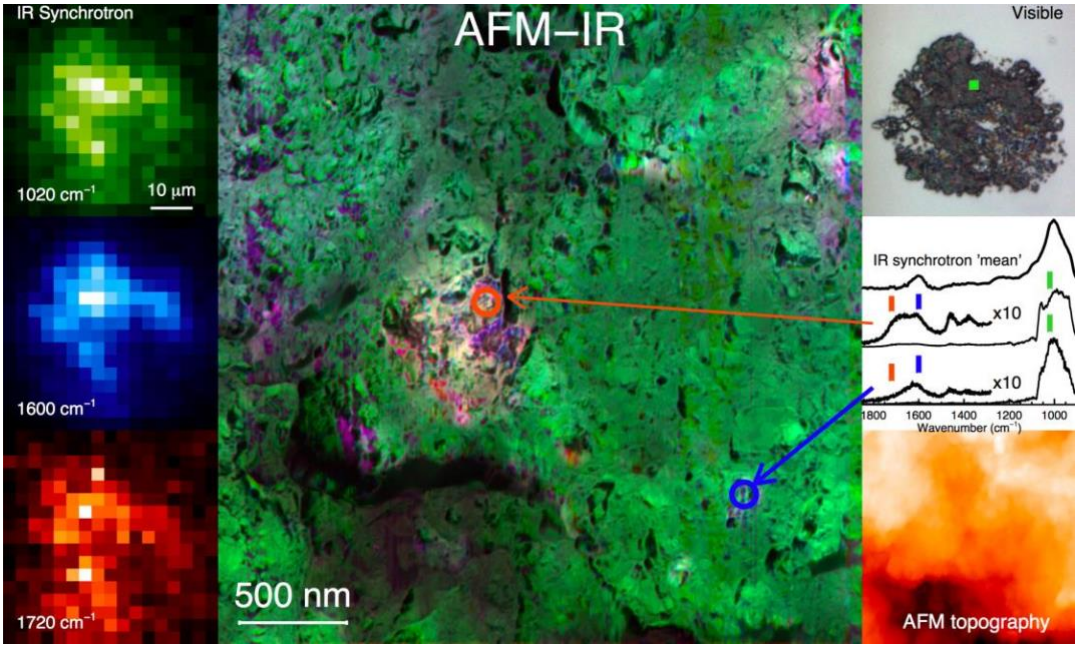

Fig. 1. AFM-IR study of chamber C sample C109-04, in the context of µFTIR maps. Left panels: maps obtained by transmission synchrotron µFTIR and corresponding to the absorption of Si-O (silicates at 1020 cm^{-1}, green), C=C (1600 cm^{-1}, blue) and C=O (1720 cm^{-1}, red) – Middle panel: 3 x 3 µm RGB composite image combining the AFM-IR absorption mapping obtained at same wavenumber (and corresponding colors) as the µFTIR synchrotron maps. The size of the image corresponds to that of one pixel in the synchrotron µFTIR maps – Right panels: Top: optical image of the crushed sample; Middle (from top to bottom spectra): average µFTIR synchrotron spectra obtained on the whole sample, local spectra obtained by AFM-IR highlighting the presence of OM with and without a C=O signature at 1720 cm^{-1}). The red, blue and green dashes indicate the wavenumber positions of the IR mapping with the same color; Bottom: AFM topography of the 3 x 3 µm area studied in AFM-IR

Conclusions – The AFM-IR technique appears as an optimal method to study the physico-chemical characteristics of meteoritic samples below submicrometric scale. Both on chondritic meteorites and Ryugu samples, measurements demonstrate the presence of organic inclusions intimately mixed with minerals at the sub-micron scale. Focusing on the OM-rich zones of Ryugu samples it is possible to unveil, without any chemical treatment, heterogeneities in the IR signature of the chemical bondings in the OM, such as local C=O enrichment with spots of a few tens of nm.

References

[1] E. Dartois et al., Dome C ultracarbonaceous Antarctic micrometeorites, Astron. Astrophys. 609 (2018) A65.

[2] J. Mathurin et al., Nanometre-scale infrared chemical imaging of organic matter in ultra-carbonaceous Antarctic micrometeorites (UCAMMs), Astron. Astrophys. 622 (2019).

[3] A. Dazzi, R. Prazeres, F. Glotin, J.M. Ortega, Local infrared microspectroscopy with subwavelength spatial resolution with an atomic force microscope tip used as a photothermal sensor, Opt. Lett., vol. 30:18 (2005) pp. 2388

[4] Y. Kebukawa et al., Nanoscale infrared imaging analysis of carbonaceous chondrites to understand organic-mineral interactions during aqueous alteration, Proc. Natl. Acad. Sci. U. S. A. 116:3 (2019) 753–758.

Soot selective size distribution measurement. A demonstrative study

Hodovány S(1), Ajtai T(1), Kurilla B(1), Szabó G(1), Bozóki Z(1)

(1) Department of Optics and Quantum Electronics, University of Szeged, H-6720 Szeged, Dóm tér 9, Hungary

*Corresponding author's email: hszabolcs@titan.physx.u-szeged.hu

In this work we propose a novel methodology for soot selective size distribution measurement using instrument combination of multi wavelength photoacoustic spectrometer (4λ-PAS) and differential mobility particle sizer (SMPS). We experimentally demonstrated that the phase of the photoacoustic signal depends on the characteristic size of the soot aerosol. The experimental result is agreed well with the theoretical calculation using the excitation parameter of the laser and microphysical properties of the aerosol. The inherent phase shift of the instrument was considered in fitting procedure. The particle related phase shift not, but the inherent instrument phase shift shows definite wavelength dependency. The inherent instrument phase shift shows decreased tendency towards the longer wavelength.

Background – the size distribution and the number-concentration of the carbonaceous particulate matter (CPM) dispersed in the atmosphere is critical issue in many perspectives i.e., climate and health effect of CPM. Despites of its importance there are no existing methodology for soot selective size distribution and number-concentration measurements of atmospheric soot aerosol. The photoacoustic spectroscopy is the only method which can measure the soot aerosol spectral responses selectively. Moreover, Moosmüller et al [1] has theoretically verified that the phase of the photoacoustic signal depends on the characteristic size of the soot aerosol. Therefore, take advantage of the synergy of selectivity and size dependency of the PA signal makes possible to investigate the size of the soot aerosol in a selective way. In this work we propose a demonstrative study for soot selective investigation of the size of soot aerosol assembly.

Methods – The investigation of the size dependency of the phase of the photoacoustic signal was made in the set up described in Fig.1. The soot assembly was generated by laser ablation. For the selection of the given size and the counting of the size selected aerosol assembly differential mobility analyzer (DMA - GRIMM, model 5403 with Kr85 neutraliser model) was used in a closed loop configuration. For the measurement of the photoacoustic signal phase at four different wavelength multi-wavelength photoacoustic spectrometer (4λ-PAS) was used. The operational principle and the characteristic parameters of 4λ-PAS is described in an earlier study [2].

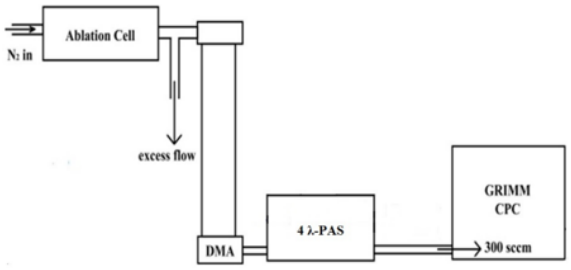

Fig. 1. Experimental set up for the measurement of PA phase in the function of particle size

Results – The PA phase measured at four different sizes (200 nm, 400 nm, 600 nm, 800nm) at the operational wavelength of 4λ-PAS and the theoretically calculated phase in the 10nm to 850nm size domain are showed in Fig.2. since the theoretical calculation does not take into account the inherent phase shift of the instrument simple translation of the calculated function was made to fit the theoretically calculate values to the measured data. the translation value was arbitrary determined by the differences of the measured at calculated values at 200nm size at all wavelengths. One can see form the figure that the measured and the calculated values agreed well in the whole size domain. However, the inherent instrument phase shift shows wavelength dependency resulted in decreasing values in phase towards the longer wavelength. However, it is worth to note that the inherent phase shift of the instrument is not correlated anyhow to the phase shift associated to the particle cooling period in the photoacoustic signal generation.

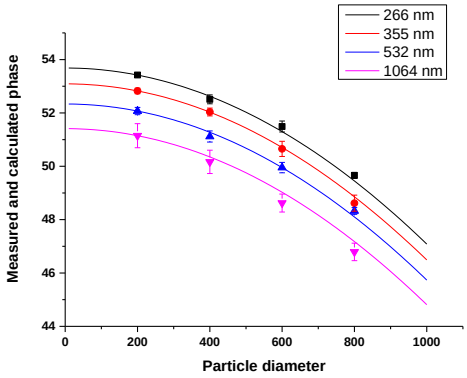

Fig.2. Measured and calculated phase of the generated soot assembly at a given size and the whole size domain using the operational wavelength of the 4λ-PAS.

Conclusions – In this study we experimentally confirmed first that the phase of the photoacoustic signal is depends on the size of the particles. We also verified that considering the inherent instrument phase shift (which is depends on the wavelength) the theoretically calculated and the experimentally measured phase are goes together in the investigated size domain. Finally, we experimentally demonstrated that the instrument combination of 4λ-PAS and SMPS makes possible to chemically selective size distribution measurement of atmospheric soot.

References

[1] H. Moosmüller, R.K. Chakrabarty, W.P. Arnott, Aerosol light absorption and its measurement: A review. J. Quant. Spec. and Rad. Trans., 110:11 (2009) 844-878.

[2] T. Ajtai, Á. Filep, M. Schnaiter, C. Linke, M. Vragel, Z. Bozóki, G. Szabó, T. Leisner, A novel multi–wavelength photoacoustic spectrometer for the measurement of the UV–vis-NIR spectral absorption coefficient of atmospheric aerosols. J. aerosol sci. 41:11 (2010) 1020-1029.

Air pollutants detection with QEPAS sensors

Giglio M(1)*, Zifarelli A(1), Menduni G(1), De Palo R(1), Di Gioia M(1), Sampaolo A(1,2), Patimisco P(1,2), Spagnolo V(2)

(1) PolySense Lab, Dipartimento Interateneo di Fisica, University and Politecnico of Bari, Via Amendola 173, Bari,70126 Italy
(2) PolySense Innovations Srl, Via Amendola 173, Bari, Italy

*Corresponding author's email: marilena.giglio@poliba.it

In this work we report on two multi-gas sensors based on QEPAS technique for environmental monitoring purposes. Both sensors have been validated and calibrated using certified concentrations of gas sample, in controlled pressure, flow and humidity conditions. Then, the sensors have been demonstrated by analysing laboratory air samples.

Background – Gas detection has a great impact in a wide range of applications. For example, the use of high sensitivity gas detectors is widespread in atmospheric science to measure different gas species, including greenhouse gases, and detect harmful gases leaks. Laser absorption-based gas sensors can provide highly sensitive and selective detection, with fast response time. In particular, quartz-enhanced photoacoustic spectroscopy (QEPAS) has been demonstrated as a powerful tool for trace gas detection [1,2].

Methods – QEPAS technique consists in: i) exciting the target gas molecules with a modulated laser light matching an absorption feature of the selected molecules and; ii) detecting the sound waves generated by the non-radiative molecules' energy relaxation using a quartz tuning fork (QTF), usually coupled to a pair of micro-resonator tubes to further amplify the sound waves [3]. Pressure waves hitting the QTF deflect its prongs and put them in vibration. These vibrations are mainly damped by air- and support-related losses [4]. The prongs mechanical stress causes piezoelectric charges accumulate on the QTF surface that can be collected by gold electrodes. QEPAS signal depends on the target molecules absorption coefficient, the laser optical power, the QTF quality factor, and the generated the vibrational-to-vibrational and vibrational-to-translational energy relaxation paths.

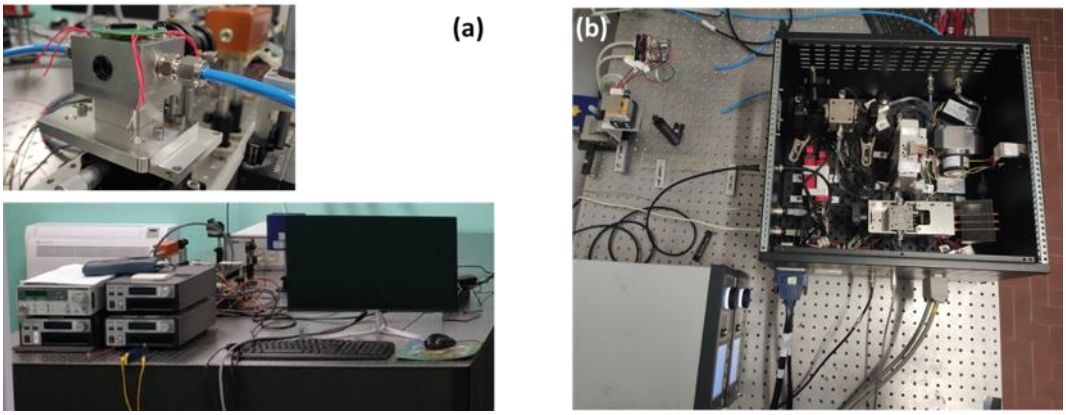

Fig. 1. Picture of the QEPAS sensor for carbon monoxide, nitrous oxide, carbon dioxide, and water vapor **(a)** and for methane, nitric oxide, and water vapour detection **(b).**

The first QEPAS sensor exploits a Vernier-effect quantum cascade laser to detect carbon monoxide, nitrous oxide, carbon dioxide, and water vapor. This innovative laser behaves as a switchable, multi-

colour, electrically tunable light source with an extended tuning range, ranging from 2100 cm^{-1} to 2220 cm^{-1} [5]. A picture of the developed setup is shown in Fig. 1(a).

The second QEPAS sensor exploits two distributed-feedback quantum cascade lasers to detect methane, nitric oxide, and water vapor. Here, the realization of the QEPAS sensor required the design of an innovative box sensor architecture and a dedicated LabVIEW-based software driving the devices and processing the QTFs signal. The sensor architecture is shown in Fig. 1(b).

Results – Both sensors were validated and calibrated using gas cylinders with certified concentration of the target gas in nitrogen. The detection limits achieved with the two allowed multi-gas detection test on laboratory air samples. The retrieved concentrations matched the typical values of the amount of these gas species in air.

Conclusions

In this work we presented two recent QEPAS sensors developed for atmospheric detection of air pollutants. The sensors operation was demonstrated by measuring the concentration of carbon monoxide, nitrous oxide, carbon dioxide, and water vapor or methane, nitric oxide, and water vapor in the air of our laboratory.

References

[1] A. Sampaolo, P. Patimisco, M. Giglio, A. Zifarelli, H. Wu, L. Dong, V. Spagnolo, Quartz-enhanced photoacoustic spectroscopy for multi-gas detection: A review, Anal. Chim. Acta. (2021) 338894. https://doi.org/10.1016/j.aca.2021.338894.

[2] M. Giglio, P. Patimisco, A. Sampaolo, A. Zifarelli, R. Blanchard, C. Pfluegl, M.F. Witinski, D. Vakhshoori, F.K. Tittel, V. Spagnolo, Nitrous oxide quartz-enhanced photoacoustic detection employing a broadband distributed-feedback quantum cascade laser array, Appl. Phys. Lett. 113 (2018) 1–5. https://doi.org/10.1063/1.5049872.

[3] M. Giglio, A. Elefante, P. Patimisco, A. Sampaolo, F. Sgobba, H. Rossmadl, V. Mackowiak, H. Wu, F.K. Tittel, L. Dong, V. Spagnolo, Quartz-enhanced photoacoustic sensor for ethylene detection implementing optimized custom tuning fork-based spectrophone, Opt. Express. 27 (2019) 4271. https://doi.org/10.1364/oe.27.004271.

[4] M. Giglio, G. Menduni, P. Patimisco, A. Sampaolo, A. Elefante, V.M.N. Passaro, V. Spagnolo, Damping Mechanisms of Piezoelectric Quartz Tuning Forks Employed in Photoacoustic Spectroscopy for Trace Gas Sensing, Phys. Status Solidi Appl. Mater. Sci. 216 (2019) 1–7. https://doi.org/10.1002/pssa.201800552.

[5] A. Zifarelli, R. De Palo, P. Patimisco, M. Giglio, A. Sampaolo, S. Blaser, T. Gresch, O. Landry, A. Müller, V. Spagnolo, Multi-gas quartz-enhanced photoacoustic sensor for environmental monitoring exploiting a Vernier-effect based quantum cascade laser, ACS Sensors. (2022).

Optimization of PTD system for characterization of transparent and semi transparent samples

Budasheva H(1), Korte D(1)*, Franko M(1)

(1) Laboratory of Environmental and Life Sciences, University of Nova Gorica, Nova Gorica, Slovenia

*Corresponding author's email: dorota.korte@ung.si

Photothermal beam deflection (PTD) spectroscopy belongs to a group of high sensitivity methods that are used to measure the optical absorption and determine the thermal characteristics of samples. [1] The basic principle behind the PTD technique is that the excitation and associated nonradiative de-excitation of the molecules of the material due to photon absorption result in the temperature oscillations (TOs) of the sample and the surrounding medium that further changes its refractive index, which is probed by a laser beam passing through it. [2, 3]

In this study, the PTD system setup is upgraded by the introduction of a resonant cavity (RC) for both the excitation (EB) and pump beam (PB) (Fig. 1) to provide better spatial resolution and higher sensitivity of the analysis. In case of EB, it enables to use low power lasers. The aim of applying RC for PB is to enhance its intensity change by increasing the length of its interaction with TOs, thus, further increasing the sensitivity of the technique.

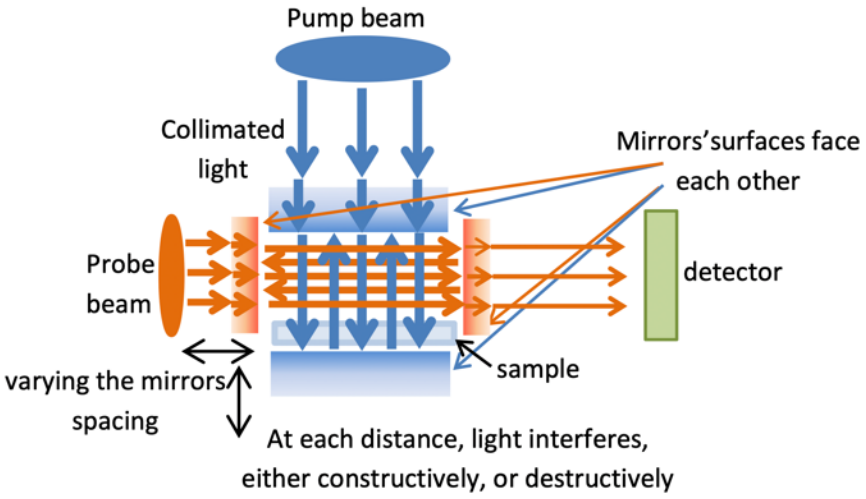

Fig. 1. Geometry of the upgraded PTD system with a resonant cavity

The effect of the PTD system optimisation on the value of its signal was examined by the use of transparent polyacrylamide gel (APA) and semi-transparent Chelex-100 resin. The gels are used in a passive sampling method of transition metals from the aquatic environments [4] and therefore are of great interest for research. The coloured complex of iron (Ferroin) with the maximum absorption at 510 nm was chosen to be uploaded into the gels. Firstly, the gels were immersed in a solution containing different concentrations of Fe^{2+} (0 – 1000 nM) for 5 days. Then they were transferred into the o-

phenanthroline solution (c = 3000 nM) for 1 day in order to produce the Ferroin complex inside the gels. After that, the samples were dried on the glass slides and finally, the PTD measurements were performed.

In order to enhance the PTD signal, the number of EB passes through the sample was increased using the additional mirror under the sample. As an excitation beam, a solid-state laser of 532 nm output wavelength and 30 mW output power (BWI-532-10-E/66966) was used, which corresponds to the absorption of the chosen sample. The measurements with two additional mirrors directing the PB passages twice through the TOs were performed as well. He-Ne laser (Uniphase, Model 1103P) was used as a probe beam source of 633 nm output wavelength and 3 mW output power.

The calculated values of the experiment are presented in Table 1.

Table 1. Results of the gels analysis

Type of the gel	**Linear regression equation and correlation coefficient**			**Limit of detection** / [nM]		
	Standard setup	**Multiplied EB**	**Multiplied PB**	**Standard setup**	**Multiplied EB**	**Multiplied PB**
APA	y = 0.001x - 0.026 r^2 = 0.998	y = 0.002x + 0.011 r^2 = 0.995	y = 0.004x + 0.093 r^2 = 0.994	110	70	50
Chelex-100	y = 0.003x - 0.050 r^2 = 0.996	y = 0.003x - 0.042 r^2 = 0.997	y = 0.008x + 0.049 r^2 = 0.996	60	50	20

Limits of detection (LODs) for APA gel are higher in case of multiplied EB compared to measurements on the standard setup of the system. This is due to the fact that the EB is reflected by the mirror and passes through the sample more than once, thereby increasing the value of PTD signal. In the case of Chelex-100 gel, LODs are hardly changed. This is due to the fact that the Chelex-100 resin is semi-transparent and strongly scatters EB, thus, the signal is not enhanced. Opposite to that the increasing PB passes through TOs has an effect on the LODs values for both gels.

It was found that the optimization of the PTD technique by the addition of a reflecting mirror under the sample in order to increase the number of passages of the EB through the sample is useable only when working with a transparent sample. The optimization of the PTD technique by adding mirrors increasing the PB passers through the TOs is useful in case of both, transparent and semi-transparent samples.

References

[1] S. Soumya, R. A. Kumar, V. Raj, M. S. Swapna, S. Sankararaman, Thermal diffusivity of molybdenum oxide nanowire film: A photothermal beam deflection study, Opt. Laser. Technol. 139 (2021) 106993. https://doi.org/10.1016/j.optlastec.2021.106993.

[2] A. Mathew, J. Ravi, K.N. Madhusoodanan, K.P.R. Nair, T.M.A. Rasheed, Thermal diffusivity measurements of semiconducting amorphous Ge_xSe_{100-x} thin films by photothermal deflection technique, Appl. Surf. Sci. 227 (2004) 410–415. https://doi.org/10.1016/j.apsusc.2003.12.020.

[3] M. A. Proskurnin, D. Korte, O. B. Rogova, D. S. Volkov, M. Franko, Photothermal beam deflection spectroscopy for the determination of thermal diffusivity of soils and soil aggregates, Int. J. Thermophys. 39 (2018) 1–13. https://doi.org/10.1007/s10765-018-2401-4.

[4] H. Budasheva, A. Kravos, D. Korte, A. Bratkič, Y. Gao, M. Franko, Determination of Dissolved Iron Redox Species in Freshwater Sediment using DGT Technique Coupled to BDS, Acta. Chim. Slov. 66 (2019) 239–246. http://doi.org/10.17344/acsi.2018.4848.

12
Analytical Chemistry and Photochemistry

PLENARY SESSION

Time-resolved detection of photoinduced heating and volume changes during protein reactions

Terazima M[(1)*]

(1) Department of Chemistry, Graduate School of Science, Kyoto University, Kyoto, 606-8502, Japan

*Corresponding author's email: mterazima@kuchem.kyoto-u.ac.jp

Background – The photothermal methods detect heating of various materials after illumination. The heating is caused by the nonradiative transition from the excited states, and it is general phenomena particularly in condensed phase. We have been using the photothermal techniques, in particular, the transient grating (TG) and transient lens (TrL) methods, to understand chemical reactions of biomolecules in solution. Since these methods detect the refractive index change upon photoexcitation, a variety of properties, e.g., thermodynamical properties and diffusion, can be detected. There are many advantages in these methods. One of the merits is very high time-resolution. Changes in the thermodynamics properties can be monitored in time domain. For example, although the thermodynamics have been playing very important roles in revealing the nature of molecules, the thermodynamic properties are not easily accessible for transient species. The TG and TrL methods remove this limitation. Here we will report on the thermodynamical studies of short-lived intermediate species of a biological protein, phototropins.

Phototropins (phots) are blue-light sensors, and the photoreactions have been widely investigated. In particular, the reaction of the LOV2 domain with the linker region from phot of *Arabidopsis thaliana* have been extensively studied by a variety of methods, and all results indicated that the linker helix is eventually unfolded upon the photoexcitation of the LOV2 domain. Using the TG method, we have determined the reaction scheme and the kinetics of this protein (Fig.1) [1]. Although this is a very prominent reaction, the driving force of the unfolding of the linker has not been well elucidated. On this aspect, we proposed that structural fluctuations might be essential for this reaction. For proving the importance of the structural fluctuation during the reaction, we tried to measure the compressibility of the intermediate species by using the TG and TrL methods with a special designed high pressure optical cell. From the pressure dependence data, the compressibility changes for the short lived intermediate and the final product formation were determined. The compressibility change will be discussed in terms of the cavities inside the protein.

Methods – The protein Arabidopsis phot1-LOV2-linker was dissolved in buffer solution. The purified protein was concentrated by ultrafiltration and then used for the measurements.

The pressure resistance of a high pressure cell we used was up to 500 MPa. High pressure was generated by pumping water with a compact hand pump. The sample temperature was controlled by circulating temperature-controlled water through a hole drilled within the cell. The sample solution was encapsulated in an inner cell and incorporated into the high-pressure apparatus. The pressure was reset to 0.1 MPa after every compression (high pressure experiment) to check the recovery of the signal. The signals were confirmed to be completely reversible.

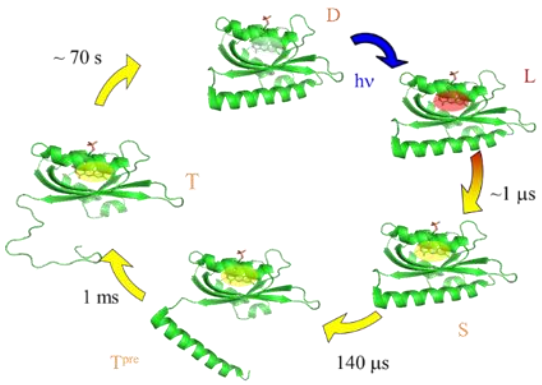

Fig. 1. Reaction scheme of a blue light sensor protein, phot1LOV2-linker determined by the TG method. D: dark state, L: excited triplet state, S: initial intermediate, T^{pre}: precursor state of the T state, T: final photoproduct state.

For the TG and TrL measurements, a XeCl excimer laser-pumped dye laser beam (λ = 462 nm) was used for the excitation laser. The signal was detected by a photomultiplier tube. The repetition rate of excitation was usually 0.015 Hz and the laser power for excitation was usually set to be weak enough to not excite the photoexcited protein twice by the laser pulse. A CW diode laser (835 nm) was used as a probe light source. The grating wavenumber, q value, at each experimental setup was determined from the decay rate of the thermal grating signal of the calorimetric reference.

Results and discussion – The compressibility change can be determined simply by measuring the volume changes after photoexcitation at various pressures, if the reaction yield does not depend on pressure. However, since proteins are generally flexible, the protein reaction yield could be pressure dependent. If this is a case, the measurement of the compressibility change is difficult. Hence, we first investigated a pressure dependent reaction yield using the pressure dependence of the transient absorption method of the phot1LOV2-linker. The pressure effects on the UV-Vis absorption spectra in the dark state were found to be negligible after the correction of the increase in the density of the solution. This fact ensures that the conformation, at least around the chromophore, does not change with pressure over the range of 0.1 - 400 MPa. Next, the pressure dependence of the reaction yield of the S state formation was measured. The time profiles of the absorption changes after the photoexcitation of the phot1LOV2-linker at various pressures was slightly dependent on the pressure. However, the change was minor, so that the pressure effect can be corrected.

The time-evolution of the TG signal after photoexcitation of the phot1LOV2-linker at 0.1 MPa consists of five components: the adduct formation process (occurs over a few μs), the thermal grating component (decay rate constant $D_{th}q^2$ (D_{th}: thermal diffusivity)), a volume contraction process associated with the transition from the S state to the T state with a time constant of ~1 ms, and a peak of the molecular diffusion signal, which represents the diffusion of the T and D species. By taking the sum of these contributions, the signal was expressed well by an equation of;

$$I_{TG}(t) = \alpha\{\delta n_{th} \exp(-D_{th}q^2t) + \delta n_P \exp(-D_Pq^2t) - \delta n_R \exp(-D_Rq^2t)\}^2 \qquad \text{Eqn. 1}$$

where α is a constant, subscripts of th, P, and R represent the thermal component, product, and reactant, respectively, δn_i is the peak-to-null refractive index difference in sinusoidal modulation at t = 0, and q is the grating wavenumber. For measuring the volume change associated with the unfolding process of the linker (S → T process), we used the TrL methods.

The isothermal compressibility (κ_T) reflects the volume fluctuation. We succeeded in detecting a transient enhancement of the isothermal compressibility (i.e., fluctuation) in the S state, and also in the T state compared with the D state at ambient pressure. The observed enhancement of the compressibility relative to the dark state are shown in Fig.2. Using this value, the observed enhancement of the structural fluctuation in the S state is an increase of ~9.3% from the D state. This increase of 9.3% in the

compressibility does not come from the whole protein, but is likely to be localized probably around an important region involved in the subsequent reaction. Hence, we consider that this is a relatively large enhancement and that this enhancement of the fluctuation can trigger the unfolding of the linker-helix. The extent of the enhancement of the compressibility in this LOV domain sample is surprisingly similar to that of the BLUF domain protein [2]. The similar extent of the increase of the fluctuation suggests that the dissociation of the LOV domain and the linker domain is also controlled by the fluctuation of the LOV domain.

An important contribution to the compressibility could be cavities inside the protein. A detailed description that explains the enhanced compressibility is obtained from the crystal structure of the phot1LOV2-linker for dark and light states. Using the PDB data, which correspond to the dark and light structures, we calculated their cavities by the 3D program with a water probe radius of 1.5 Å. We found that the cavity volume of the light state was larger than that of the dark state. This change may be sufficient to explain the observed compressibility change.

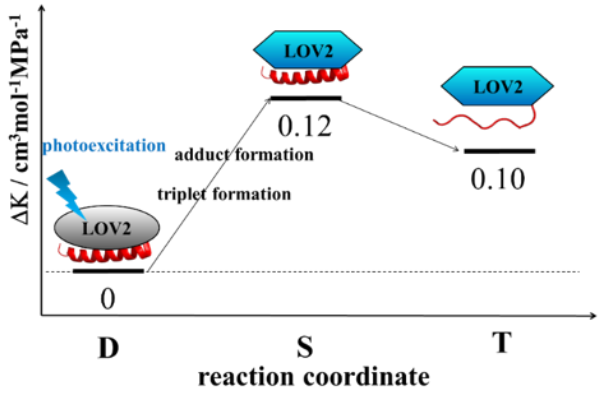

Fig. 2. Compressibility changes along the reaction coordinate of phot1LOV2-linker.

References

[1] K. Takeda, Y. Nakasone, K. Zikihara, S. Tokutomi, M. Terazima, J. Phys. Chem. B, 117 (2013) 15606–15613.

[2] K. Kuroi, K. Okajima, M. Ikeuchi, S. Tokutomi, T. Kamiyama, M. Terazima, J. Phys. Chem. B, 119 (2015) 2897-2907.

KEYNOTE SPEAKER

Photothermal spectroscopy for nanoscale chemical imaging

Ramer G(1)*, Santos C(1), Yilmaz U(1), Holub E(1), Zhang Y(1), Lendl B(1)

(1) TU Wien, Institute of Chemical Technologies and Analytics, Getreidemarkt 9, A-1060 Vienna, Austria

*Corresponding author's email: georg.ramer@tuwien.ac.at

Diffraction limits in mid-IR microscopy – Technological progress over the last decade has in large part been contingent of understanding, designing and controlling materials and devices at ever smaller length scales. As theses length scales keeping going down established analytical chemistry tools end up not being able to resolve them anymore. For example, while mid-IR spectroscopy coupled to an optical microscope is a great tool for rapid chemical imaging at the millimetre and micrometre scale, it relies on the interaction of micron range (2 µm to 20 µm) electromagnetic radiation with the specimen. Hence, the diffraction limit prevents us from building mid-IR optical microscopes that can resolve structures on the nanoscale.

Chemical imaging below the diffraction limit – We can circumvent the diffraction limit by building a nearfield imaging system, i.e., by moving the detector and/or the light source as close to our specimen as possible. One approach to move the "detector" closer that has found wide acceptance for mid-IR spectroscopy is to use photothermal expansion induced by a tuneable pulsed laser for detection of local absorption. This PTIR (photothermal induced resonance) or AFM-IR (atomic force microscopy induced resonance) technique reads the local thermal expansion using an AFM tip to enable nanometre scale spatial resolution chemical imaging. AFM-IR can be used to collect mid-IR absorption spectra from nanoscale samples that resemble conventional bulk spectra and it can be used to image the chemical makeup of the sample at nanoscale lateral resolution without the need for labelling or staining [1].

Within the last decade AFM-IR has found applications across fields and disciplines, from microbiology [2] and medicine [3] to polymer science [4] and material science [5]. AFM-IR has been used to study the secondary structure of peptides in water [6] and to detect a chemotherapeutic at the zeptomole level inside a nanoscale drug carrier [7]. AFM-IR can also be used to determine thermal conductivity and interfacial thermal resistance at the nanoscale [8].

Nanoscale chemical imaging – One of the most exciting aspects of AFM-IR is that it can be used to apply multivariate chemical imaging techniques that are well established for IR microscopy at the nanoscale. These enable to combine information from multiple spectra or multiple single wavelength images into actual maps of chemical composition (see fig. 1) – if we are doing it right. "Doing it right" requires an understanding of the signal transduction chain in AFM-IR and the peculiarities of scanning probe microscopy. It also requires to understand optical effects that limit the linear range of AFM-IR [9].

This presentation will discuss the AFM-IR signal transduction chain and which of its parameters can (need to be) controlled to achieve reproducible AFM-IR measurements and what the particular challenges are in applying chemometric algorithms to AFM-IR datasets.

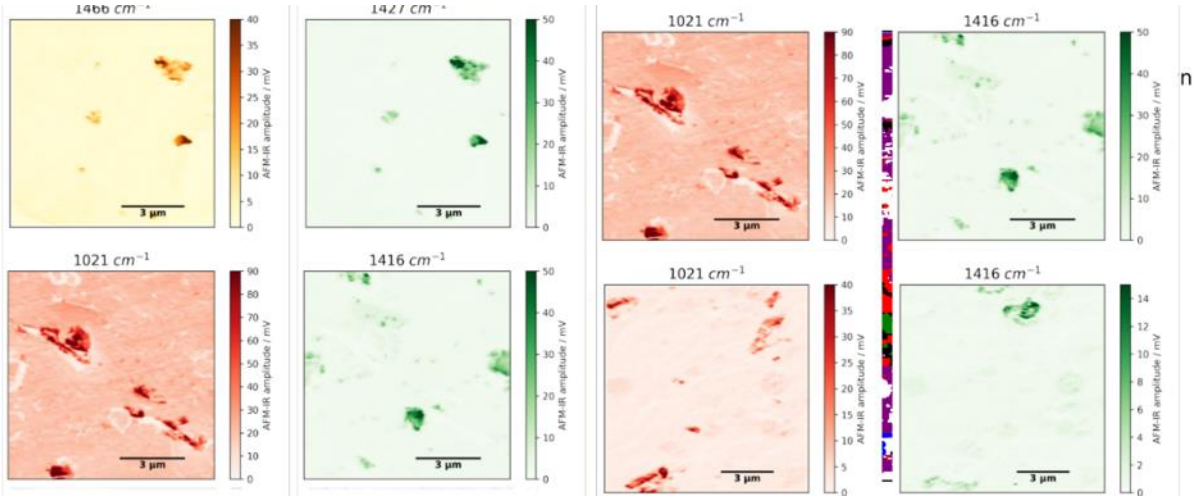

Fig. 1. Left: Topography and single wavelength images of a polymer material. Right: Chemical image calculated via Gaussian unmixing (reproduced from [10]).

References

[1] A. Dazzi, C. B. Prater, Q. Hu, D.B. Chase, J.F. Rabolt, C. Marcott, AFM–IR: Combining Atomic Force Microscopy and Infrared Spectroscopy for Nanoscale Chemical Characterization, Appl. Spectrosc., 66, 12 (2012) 1366–1384 doi: 10.1366/12-06804.

[2] C. Mayet, a Dazzi, R. Prazeres, F. Allot, F. Glotin, J.M. Ortega, Sub-100 nm IR spectromicroscopy of living cells., Opt. Lett. 33, 14 (2008) 1611–3.

[3] F. Ruggeri et al., Identification of Oxidative Stress in Red Blood Cells with Nanoscale Chemical Resolution by Infrared Nanospectroscopy, Int. J. Mol. Sci. 19, 9, (2018) p. 2582. doi:10.3390/ijms19092582.

[4] S. Morsch, Y. Liu, S.B. Lyon, S.R. Gibbon, Insights into Epoxy Network Nanostructural Heterogeneity Using AFM-IR," ACS Appl. Mater. Interfaces, 8, 1 (2016) 959–966. doi:10.1021/acsami.5b10767.

[5] G. Ramer et al., High-Q dark hyperbolic phonon-polaritons in hexagonal boron nitride nanostructures, Nanophotonics, 9, 6 (2020) doi: 10.1515/nanoph-2020-0048.

[6] G. Ramer, F.S. Ruggeri, A. Levin, T.P.J. Knowles, A. Centrone, Determination of Polypeptide Conformation with Nanoscale Resolution in Water, ACS Nano, 12, 7, (2018) 6612–6619. doi: 10.1021/acsnano.8b01425.

[7] K. Wieland, G. Ramer, V.U. Weiss, G. Allmaier, B. Lendl, A. Centrone, Nanoscale chemical imaging of individual chemotherapeutic cytarabine-loaded liposomal nanocarriers, Nano Res. (2018). doi: 10.1007/s12274-018-2202-x.

[8] J. Chae et al., Nanophotonic Atomic Force Microscope Transducers Enable Chemical Composition and Thermal Conductivity Measurements at the Nanoscale, Nano Lett. 17, 9, (2017) 5587–5594 doi: 10.1021/acs.nanolett.7b02404.

[9] G. Ramer, V.A. Aksyuk, A. Centrone, Quantitative chemical analysis at the nanoscale using the PTIR technique, Anal. Chem., 89, 24, (2017) 13524–13531. doi:10.1021/acs.analchem.7b03878.

[10] A.C.V.D. dos Santos, B. Lendl, G. Ramer, Systematic analysis and nanoscale chemical imaging of polymers using photothermal-induced resonance (AFM-IR) infrared spectroscopy, Polym. Test. 106 (2022) p. 107443. doi: 10.1016/j.polymertesting. 2021.107443.

Calibrating filter photometers with direct measurements of aerosol absorption using a dual-wavelength photo-thermal interferometer

Drinovec L[1,2,3], Jagodič U[1,2], Pirker L[2,4], Škarabot M[2], Kurtjak M[5], Vidović K[6], Ferrero L[7], Visser B[8], Röhrbein J[8], Weingartner E[8], Kalbermatter DM[9], Vasilatou K[9], Bühlmann T[9], Pascale C[9], Müller T[10], Wiedensohler A[10], Močnik G[1,2,3]*

(1) Haze Instruments d.o.o., Ljubljana, Slovenia
(2) Department of Condensed Matter Physics, Jožef Stefan Institute, Ljubljana, Slovenia
(3) Center for Atmospheric Research, University of Nova Gorica, Nova Gorica, Slovenia
(4) Faculty for mathematics and physics, University of Ljubljana, Ljubljana, Slovenia
(5) Advanced Materials Department, Jozef Stefan Institute, Ljubljana, Slovenia
(6) Department for Analytical Chemistry, National Institute of Chemistry, Ljubljana, Slovenia
(7) GEMMA center, University of Milano-Bicocca, Milano, Italy
(8) Institute for Sensors and Electronics, University of Applied Sciences Northwestern Switzerland, Windisch, Switzerland
(9) Federal Institute of Metrology METAS, Bern, Switzerland
(10) Leibniz Institute for Tropospheric Research, Leipzig, Germany

*Corresponding author's email: grisa.mocnik@ung.si

The direct measurement of aerosol light absorption coefficient is preferrable over indirect methods. Using filter photometers is challenging due to systematic artifacts and the lack of standardized calibration procedures [1]. A photothermal interferometer probes the change of the refractive index caused by light absorption in (and the subsequent heating of) the sample – the detection is linear and can be traced to first principles. Measurement at two wavelengths determines the absorption wavelength dependence and the Ångström exponent (AAE).

The photothermal aerosol absorption monitor (PTAAM) uses a folded Mach-Zender interferometer (similar to that described in [2] and [3]). Pump lasers at 532 and 1064 nm are modulated at different frequencies and focused in the sample using an axicon for simultaneous measurement. The signal is detected by two photodiodes and resolved by dual-channel lock-in amplifiers measuring at the two frequencies.

The photo-thermal aerosol absorption monitor PTAAM-2λ (Haze Instruments) was used to directly measure the absorption coefficient at 532 nm. The green channel is calibrated traceably to primary standards using ~1 µmol/mol NO_2 and calibration is transferred to the IR using aerosolized nigrosin [4].

Aerosol optical properties can be calculated if the particle shape and the complex refractive index (RI) are known. Soot particles form complex agglomerates that make the calculation of mass concentration and optical properties difficult. On the other hand, particles generated by nebulisation of water-soluble pigments are spherical, which enables Mie calculations using the measured size distribution.

We have used water-soluble nigrosin pigment (CAS 8005-03-6) for the calibration of photo-acoustic instruments [5,6]. Nigrosin has a wide absorption spectrum and allows for calibration also in the infra-red. Unfortunately, the RI of nigrosin has been reported for the visible part of the spectrum only.

We have prepared thin film samples of nigrosin and measured their absorbance (400-1200 nm) using an integrating sphere photometer (Shimadzu UV-3600). We used nigrosin film thickness, measured using atomic force microscopy, and the absorbance, to determine the imaginary part of the RI. The real part of the RI at 1064 nm was determined by a Brewster angle measurement.

Nigrosin solution was aerosolized using a Topas ATM 226 nebuliser. The size distribution of the aerosol particles was measured using a scanning mobility particle sizer (TSI model 3080). These data were used in a Mie calculation of the aerosol absorption coefficient for wavelengths between 400 and 1200 nm.

PTAAM was characterized and its uncertainties quantified (Table 1). We calibrated filter photometers (CLAP, AE33) in green and near IR with soot, and determined their cross-sensitivity to scattering for ammonium sulfate particles, resulting in wavelength and size dependent calibration parameters.

Table 1. Uncertainties of the measured parameters.

$b_{abs,532nm}$	4%
$b_{abs,1064nm}$	6%
AAE	9%

Similar multiple scattering parameter values were found for ambient aerosols and laboratory experiments. We determined the absorption enhancement using laboratory measurements with uncoated and soot and soot coated with secondary organic matter - Fig. 1 [7].

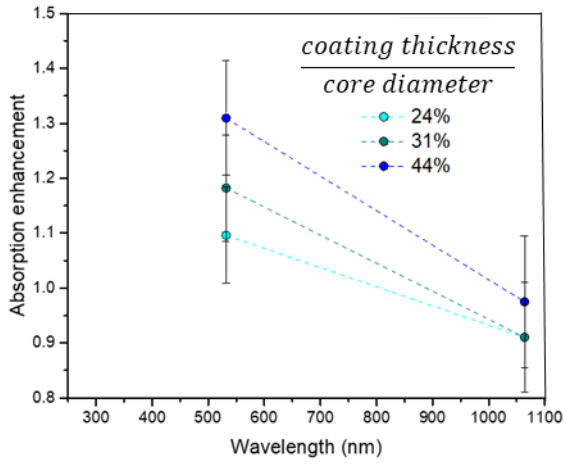

Fig. 1. Absorption enhancement due to coating of BC cores with secondary organic matter as a function of the wavelength.

Acknowledgements – We thank European Space Agency, SNSF, EUROSTARS, ARRS, and EMPIR (Black Carbon, AeroTox).

References

[1] E. Weingartner et al., Absorption of light by soot particles: Determination of the absorption coefficient by means of aethalometers, J. Aerosol Sci. 34 (2003) 1445-1463.

[2] H. Moosmüller, W.P. Arnott, Folded Jamin interferometer: a stable instrument for refractive-index measurements, Opt. Lett. 21 (1996) 438-440.

[3] A.j. Sedlacek, Real-time detection of ambient aerosols using photothermal interferometry: Folded Jamin interferometer, Rev. Sci. Instrum., 77:064903 (2006) 1-8.

[4] L. Drinovec et al., A dual-wavelength photothermal aerosol absorption monitor: design, calibration and performance, Atmo. Meas. Tech. Discuss. (2022) *accepted for publication.* 10.5194/amt-2022-21.

[5] D. Lack et al., Aerosol Absorption Measurement using Photoacoustic Spectroscopy: Sensitivity, Calibration, and Uncertainty Developments, Aerosol Sci. Technol. 40:9 (2006) 697-708.

[6] N. Bluvshtein et al., Calibration of a multi-pass photoacoustic spectrometer cell using light-absorbing aerosols, Atmos. Meas. Tech. 10 (2017) 1203–1213, https://doi.org/10.5194/amt-10-1203-2017.

[7] D.M. Kalbermatter et al., Comparing black-carbon- and aerosol-absorption-measuring instruments – a new system using lab-generated soot coated with controlled amounts of secondary organic matter (2022). Atmos. Meas. Tech., 15 (2022) 561–572.

Selective measurement of ammonia isotopes by using photoacoustic spectroscopy

Awuor E[(1)*], Huszár H[(1)], Ajtai T[(1)], Szabó G[(1)], Janáky C[(2)], Bozóki Z[(1)]

(1) Department of Optics and Quantum Electronics, University of Szeged, Szeged, Hungary
(2) Department of Physical Chemistry and Materials Science, University of Szeged, Szeged, Hungary

*Corresponding Author's email: mlawuor252@gmail.com.

Introduction – Different application areas, whether industrial or environmental requires a fast and automatic NH_3 detection system, which can reliably measure its concentration at sub ppm levels be it as a gas or isotopes without interference of common contaminants. One notable area is the electrochemical synthesis of NH_3, a field that is still largely in the research and development stage and shows great promise of substituting the Haber-Bosch process which has been reported to be energy intensive and a significant contributor to climate change due to its high greenhouse gas emissions. A major concern of the electrochemical synthesis process, is the low (< 1ppm) NH_3 generated whose detection and measurement is a challenge. Recent studies have highlighted the need to detect $^{15}NH_3$, in the presence of $^{14}NH_3$ and N_2 gas to guard against false-positive results, while providing information on the presence of contaminants [1].

Currently, several field and analytical methods have been employed for NH_3 isotopic measurements largely depending on their availability, cost and purpose (e.g., monitoring, process control etc.) [2]. Greatest disadvantage of these methods is the inability to suppress water signal in order to quantify the $^{15}NH_3$ signal owing to the small mass difference between H_2O and $^{15}NH_3$, which causes uncertainties in the detection of $^{15}NH_3$ at low ammonia concentrations. This work therefore seeks to design and construct a near infra-red diode laser-based photoacoustic (NIR-PA) system capable of selectively measuring and differentiating between ammonia gas isotopes ($^{14}NH_3$ & $^{15}NH_3$) which will be useful in the detection and quantification of the discharged ammonia gas during the electro-reduction process of nitrogen gas and water or steam.

Methods – A multi-wavelength measurement was incorporated, first to suppress the spectral interference, secondly, to improve the sensitivity of the ammonia isotope measuring NIR-PA system and lastly to be able to measure different components simultaneously. This was achieved by using a longitudinal differential PA cell operating in the first longitudinal resonance (0,0,1 mode) with a cell constant of C≈20 mV/cm^{-1}/Mw as a detection unit. A laser beam was projected through a window on one side of the chamber, made of quartz glass and coated with an anti-reflection layer, parallel to the longitudinal axis and exited on the other side where a back reflecting mirror was mounted on the window. The purpose of the mirror was to increase the signal to noise ratio by doubling the path through which light was absorbed within the PA cell. Next, a widely tuneable external cavity diode laser (ECDL) was used to identify possible wavelength ranges which were optimal for NH_3 isotope sensitive detection, while avoiding interference with water vapor. A coupled Distributed Feedback laser operated in a wavelength modulated mode was then employed to tune the laser wavelength on the sub-second timescale by varying its driving current rather than using the much slower temperature tuning. This enabled the system to achieve maximum sensitivity. The experimental setup used for the $^{14}NH_3$ and $^{15}NH_3$ spectra measurements and calibration consisted of two main parts; the mass-flow controller mixing mode and the chemical reaction-based mode which offered the possibility of generating various

mixtures of the $^{14}NH_3$ and $^{15}NH_3$ to the NIR-PA system, operated either by an ECDL or by a DFB diode laser.

Results – The developed NIR-PA system was able to identify four wavelengths within the range of 1531.3 nm -1531.8 nm using both the ECDL and DFB diode laser as shown in Figure 1.

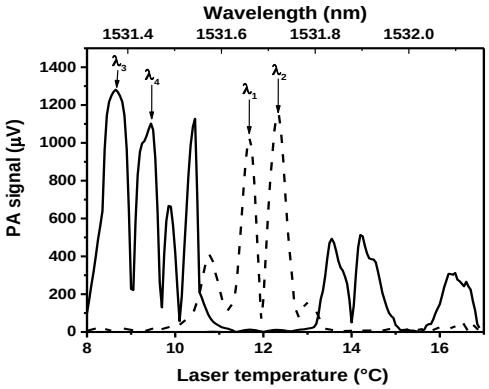

Fig. 11: PA spectra of the ammonia isotopes as recorded by DFB diode laser temperature tuning. Solid and dashed lines are the recorded spectrum of $^{15}NH_3$, and $^{14}NH_3$, respectively. The two wavelength pairs used for selective determination of the $^{14}NH_3$ and $^{15}NH_3$ isotope concentrations are indicated as λ_1, λ_2 and λ_3, λ_4 respectively.

Upon current tuning this wavelength range and optimising the modulation parameters using the DFB laser, the system achieved a detection limit and sensitivity of 0.15 ppm and 6.3 µV/ppm for $^{14}NH_3$ and 0.73 ppm and 1.3 µV/ppm for $^{15}NH_3$ (with an inaccuracy below 0.1%), response. The response of the system to sudden concentration variation was 3.5 sec.

Conclusions – The NIR-PA system presented has proven to be capable of sensitively and selectively measuring $^{15}NH_3$ from a mixture of isotopically labelled NH_3 gas. The system is also robust, highly responsive and has very low cross-sensitivity to water vapour. This makes it ideal for the targeted application i.e. electrochemical synthesis of NH_3.

References

[1] S.Z. Andersen, V. Čolić, S. Yang, J.A. Schwalbe, A.C. Nielander, J.M. McEnaney, K. Enemark-Rasmussen, J.G. Baker, A.R. Singh, B.A. Rohr, M.J. Statt, S.J. Blair, S. Mezzavilla, J. Kibsgaard, P.C.K. Vesborg, M. Cargnello, S.F. Bent, T.F. Jaramillo, I.E.L. Stephens, J.K. Nørskov, I. Chorkendorff, A rigorous electrochemical ammonia synthesis protocol with quantitative isotope measurements, Nature. 570 (2019) 504–508. https://doi.org/10.1038/s41586-019-1260-x.

[2] G. Qing, R. Ghazfar, S.T. Jackowski, F. Habibzadeh, M.M. Ashtiani, C.P. Chen, M.R. Smith, T.W. Hamann, Recent Advances and Challenges of Electrocatalytic N_2 Reduction to Ammonia, Chem. Rev. 120 (2020) 5437–5516. https://doi.org/10.1021/acs.chemrev.9b00659.

H_2S detection in complex gas matrices

Sampaolo A[(1,2)*], Olivieri M[(1)] , Menduni G[(1)], Zifarelli A [(1)], Giglio M [(1)], Patimisco P[(1,2)], Spagnolo V[(1,2)]

(1) PolySense Lab, Dipartimento Interateneo di Fisica, University and Politecnico of Bari, CNR-IFN, Via Amendola 173, Bari,70126 Italy
(2) PolySense Innovations srl, Via Amendola 173, Bari,70126 Italy

*Corresponding author's email: angelo.sampaolo@poliba.it

In this work we report on two quartz-enhanced photoacoustic sensors for H_2S trace detection in natural gas leaks dispersed in air. The challenge for these two spectroscopic approaches consists in avoiding methane interference and detect hydrogen sulfide at the sub-ppm level.

Background – Hydrogen sulfide is a toxic gas and is a threat to human health, since it is rapidly absorbed by the lungs. Exposure to H_2S at high concentration levels will cause unconsciou

sness and death, because of respiratory paralysis and asphyxiation. Thus, due to its toxicity, flammability, and corrosivity, it is extremely important to detect and monitor its presence in situ and real time [1].

Optical detectors are a field-proven detection solution in many industrial applications because of the high selectivity provided by the use of lasers as gas target excitation source, and high sensitivity achieved through the implementation of several diverse spectroscopic approaches [2].

Standard photoacoustic and QEPAS sensors for in situ and real-time detection of multiple hydrocarbons in near- and mid-IR were already demonstrated [3], as well as H_2S sensors employing diode lasers in the near- IR [4] and quantum cascade lasers (QCLs) in the mid-IR [5].

The main issue related with H_2S detection consists in the fact that most of the hydrogen sulfide leaks in atmosphere are associated with natural gas leaks. This means that H_2S needs to be detected over a strong background of methane absorption, whose bands are partially or totally overlapping with H_2S bands all over the infrared region.

Methods – The first QEPAS configuration we implemented for H_2S detection within a methane-based gas matrix consists in on-beam sensor employing a custom 12 kHz quartz tuning fork, equipped with resonator tubes. The laser employed is an interband cascade laser emitting at 2636 nm. The main criteria adopted for identifying the optimum spectral conditions in this wavelength range were i) selecting a H_2S absorption line well separated from the surrounding features related to atmospheric absorbers, such water vapor, and from methane, which is the main component in a natural gas leak dispersed in air: the most suitable H_2S feature was found at 3793 cm^{-1}; ii) investigating the trade-off working pressure minimizing the spectral overlap between H_2S absorption line and the absorption background without losing too much in the photoacoustic signal: this value was found at 100 torr.

The sensing system was tested for different gas mixtures containing traces of H_2S in a matrix of i) N_2, ii) N_2 with methane up to percent scale, iii) standard air with methane up to percent scale.

As an alternative to the near-IR QEPAS sensor, we designed and developed a THz sensor based on a pulsed laser emitting at 2.87 THz and exciting a H_2S absorption line falling at 95.63 cm^{-1} [6].

In fact, the smartest approach to detect real-time traces of H_2S in natural gas is to exploit its intense absorption bands in the THz range, where hydrocarbons absorption cross-sections are several orders of magnitude smaller. In the THz region, the absorption lines of H_2S are the strongest of the whole infrared spectrum. These optical transitions are divided into three groups, corresponding to energy levels related to the molecule rotation around the three axes and are perfectly spaced of 0.62 THz, 0.54 THz, and 0.28 THz, respectively. This situation avoids interference effects from hydrocarbons, enables a fast and easy H_2S detection scheme and creates an ideal spectral environment, where H_2S isotopes can be also discriminated and high precision measurements on isotopic ratios can be performed.

The two sensor architectures are shown in Fig. 1.

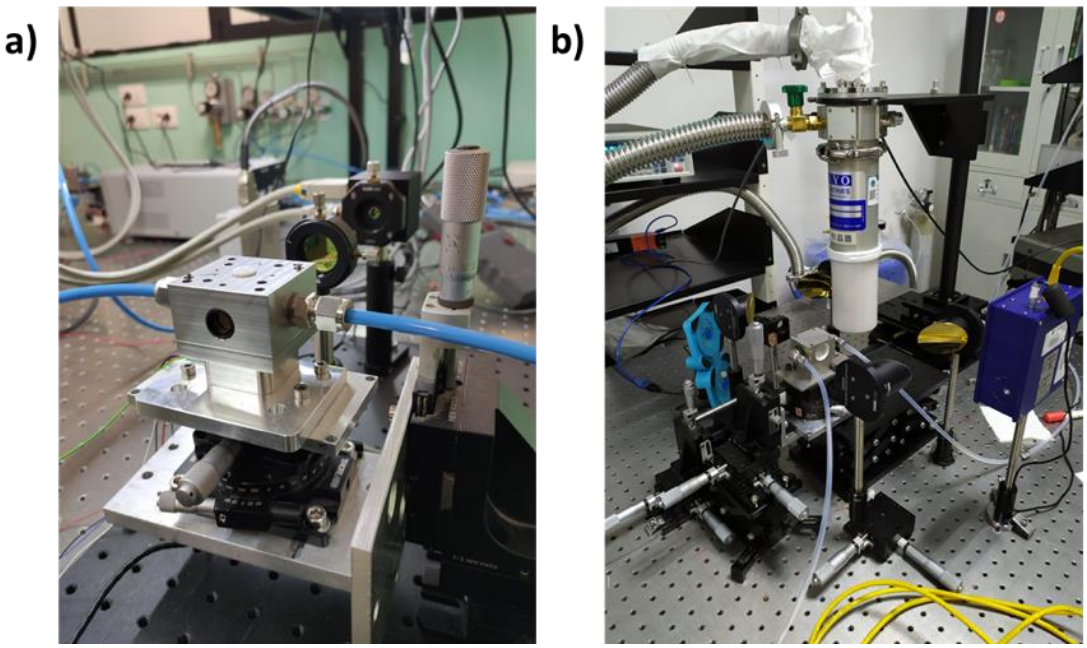

Fig. 1. Picture of the near-IR H_2S QEPAS sensor (a) and of the THz H_2S QEPAS sensor (b).

Results – The near-IR sensor proved to detect hydrogen sulfide at sub ppm level, in mixtures of standard air and methane at the percent concentration, at a working pressure of 100 Torr and an integration time of 10 s. The THz sensor has also demonstrated a sub-ppm sensitivity level in detection of H_2S at an integration time of 10 s and a working pressure of 60 Torr.

Conclusions – In this work we demonstrated two approaches for pursuing hydrogen sulfide detection in a natural gas leak dispersed in air. The sensor implementing the laser diode is a ready-to-use solution for discriminating H_2S presence in a matrix where CH_4 concentration does not exceed the 10%. This is due to a minimal CH_4 absorption background affecting the H_2S detection sensitivity. In the case of H_2S THz detection, there are no restrictions for CH_4 concentration in the matrix, since its absorption cross-sections are ~7 orders of magnitude lower with respect to H_2S. The drawback is that THz sources are still far for commercialization and thus the related gas sensing technology.

References

[1] Toxicological Review of Hydrogen Sulfide, US Environmental Protection Agency, 2003 in Support of Summary Information on the Integrated Risk Information System (IRIS).

[2] J. Hodgkinson, R.P. Tatam, Meas. Sci. Technol. 24:1 (2013) 012004.

[3] A. Sampaolo, P. Patimisco, M. Giglio, A. Zifarelli, H. Wu, L. Dong, and V. Spagnolo, Anal. Chim. Acta (2021) 338894.

[4] H. Wu, A. Sampaolo, L. Dong, P. Patimisco, X. Liu, H. Zheng, X. Yin, W. Ma, L. Zhang, W. Yin, V. Spagnolo, S. Jia, F.K. Tittel, Appl. Phys. Lett. 107 (2015) 111104.

[5] M. Siciliani de Cumis, S. Viciani, S. Borri, P. Patimisco, A. Sampaolo, G. Scamarcio, P. De Natale, F. D'Amato, V. Spagnolo, Opt. Expr. 22:23 (2014) 28222.

[6] A. Sampaolo, C. Yu, T. Wei, A. Zifarelli, M. Giglio, P. Patimisco, H. Zhu, H. Zhu, L. he, H. Wu, L. Dong, G. Xu, and V. Spagnolo, Photoacoustics 21 (2021) 100219.

POSTER CONTRIBUTIONS

CONTENTS – Poster Contributions

01 Thermophysical Properties

A modified mode-mismatched thermal lens spectrometry Z-scan model: An exact general approach

Rahman A *et al.* (presented by Abdul Rahman) ..... - 280 -

Optical and thermal characterization of Fe_3O_4 nanoparticles covered with turmeric extract

Alvarado-Noguez ML *et al.* (presented by Margarita Lizeth Alvarado Noguez) ..... - 282 -

Thermal study of porous and compact SiO_2 nanoparticle nanoliquids by TWRC technique

García-Vidal UO *et al.* (presented by Usiel Omar Garcia Vidal) ..... - 284 -

Thermal characterization of hydrocarbon- water interfaces

Vargas-Vargas A *et al.* (presented by Aldrin David Vargas-Vargas) ..... - 287 -

Characterization of TiO_2 thin film deposited on Silicon membrane using neural networks

Djordjević KLj *et al.* (presented by Mioljub Nešić) ..... - 289 -

Estimation of heat propagation speed in the thin graphene-oxide foil by photoacoustic spectroscopy

Misovic A *et al.* (presented by Mioljub Nešić) ..... - 291 -

Towards a point spread function for nanoscale chemical imaging

Zhang Y *et al.* (presented by Yide Zhang) ..... - 293 -

Study of thermal and optical properties of composites made of silver iodomercurate (Ag_2HgI_4) in a polymeric matrix

Chan-Espinoza JA *et al.* (presented by Fernando Cervantes Alvarez) ..... - 295 -

Thermal lens spectroscopy: an analytical model for a pulsed-laser

Isidro-Ojeda MA *et al.* (presented by Juan Jose Alvarado-Gil) ..... - 297 -

Influence of the VO_2 metal-insulator transition on the thermoelectric properties of composites based on a $Bi_{0.5}Sb_{1.5}Te_3$ matrix

Alvarez-Guerrero S *et al.* (presented by Juan Jose Alvarado-Gil) ..... - 298 -

Effect of mesoporous cerium oxide nanofluids on the thermal conductivity

Montes de Oca LM *et al* .(presented by Jose Luis M. Montes de Oca) ..... - 301 -

Thermal characterization of natural clay using photothermal radiometry technique for thermal insulation applications

Venegas-Montaño HM *et al.* (presented by Fernando Cervantes Alvarez) ..... - 303 -

Thermal characterization of emulsions stabilized by Sodium Dodecyl Sulfate

Ceja-Morales M *et al.* (presented by Juan Jose Alvarado-Gil) ..... - 305 -

UV light-induced thermal and optical properties of functionalized polymers with strong push-pull azo chromophores in side chain

Trefon-Radziejewska D *et al* .(presented by Ameneh Mikaeeli) ..... - 307 -

Simultaneous reconstruction of density and thermal conductivity depth profiles in sintered metal powder compacts using a novel inverse thermal-wave method

Kooshki S *et al.* (presented by Alexander Melnikov) ..... - 308 -

02 Materials Research and Characterization

Photothermal techniques for 3D printing polymer characterization

Luna-Sánchez, JL *et al.* (presented by Usiel Omar Garcia Vidal) ..... - 312 -

Photothermal characterization of polyester composites loaded with parallelly arranged graphite rods

Aguilar-Jimenez JA *et al.* (presented by Jose Arturo Aguilar Jimenez) ..... - 314 -

Evaluation of optical and acoustical properties of $Ba_{1-x}Sr_xTiO_3$ material library by a multi-technique approach including picosecond laser ultrasonics

Sathyan S *et al.* (presented by Sandeep Sathyan) ..... - 316 -

Thermal, mechanical and optical characterization of calcium caseinate biopolymers with borax as crosslinking agent

Franco-Bacca AP *et al.* (presented by Fernando Cervantes Alvarez) ..... - 318 -

Double and multiple pump pulse time-domain thermoreflectance measurements

Chatterjee A *et al.* (presented by Ankur Chaterjee) ..... - 320 -

Infrared emissivity of vanadium dioxide thin films coated on cotton fabrics

Misano M *et al.* (presented by Roberto Li Voti) ..... - 322 -

Characterization of multilayered drug delivery systems for orthopedic implants by beam deflection spectrometry
Budasheva H *et al.* (presented by Dorota Korte) ..... - 324 -
Analysis of SiO_2 and $BaSO_4$ leachates from dental composites by thermal lens spectrometry
Korte D *et al.* (presented by Dorota Korte) ..... - 326 -
Infrared emissivity of microcapsules of organic phase change materials dispersed into smart wearable textiles
Agharahimli K *et al* .(presented by Khayala Agharahimli) ..... - 329 -

03 Laser Ultrasonics

Detection of defects in multilayer solids with laser-induced surface acoustic waves
Saurer M *et al.* (presented by Markus Saurer) ..... - 331 -
Laser-induced shockwaves and cavitation bubbles in different water matrices
Dular M *et al.* (presented by Jaka Mur) ..... - 334 -
Adaptive polarized photoacoustic computed tomography
Zhang Y *et al.* (presented by Yang Zhang) ..... - 336 -

05 Infrared Thermography

Thermographic super resolution reconstruction using 2D pseudo-random pattern illumination
Lecompagnon J *et al.* (presented by Julien Lecompagnon) ..... - 338 -
3D Browsing of historical books by means of Active Infrared Thermography
Orazi N *et al.* (presented by Noemi Orazi) ..... - 340 -
Infrared thermography study of historical bronze composition effects on the transport properties
Paoloni S *et al* (presented by Ugo Zammit) ..... - 342 -
Thermal anisotropy of polyethersulfone woven textiles by infrared thermography
Larciprete M *et al.* (presented by Roberto Li Voti) ..... - 344 -

06 Ultrafast Phenomena and Spectroscopy

Thermal characterization of polymeric thin films by photoacoustic spectroscopy
Fernández-Olaya MG *et al.* (presented by Juan Jose Alvarado-Gil) ..... - 348 -
Efficient picosecond ultrasonics with a common-cavity dual-comb laser
Pupeikis J *et al.* (presented by Justinas Pupeikis) ..... - 350 -

07 Biomedical Imaging and Applications

Measurement of glycated haemoglobin through photoacoustic spectroscopy, a non-destructive assessment
Olvera LI *et al.* (presented by Lilia Ivonne Olvera Cano) ..... - 354 -
In vivo monitoring of laser tattoo removal using pulsed photothermal radiometry and diffuse reflectance spectroscopy
Golmajer Zima N *et al.* (presented by Neža Golmajer Zima) ..... - 357 -
Long-wave and mid-wave photothermal coherence tomography imaging of human teeth
Thapa D *et al.* (presented by Andreas Mandelis) ..... - 359 -
Optothermal and photoacoustic characterization of protein corona and blood using plasmonic nanoparticles: pharmaceutical aspects
Khosroshahi ME *et al.* (presented by Andreas Mandelis) ..... - 361 -

08 Novel Methodologies, Instrumentation, and Applications

Machine learning based determination of photoacoustic signal parameters for different gas mixtures
Lukić M *et al.* (presented by Mladena Lukic) ..... - 365 -
The reduction of neural network input vector for efficient optimization of photoacoustic calibration
Jordovic-Pavlovic MI *et al.* (presented by Mirolsava Jordovic Pavlovic) ..... - 367 -
Finding the optimal TDLS wavelength
Bahr M-S et *al.* (presented by Marcus Wolff) ..... - 369 -
New voltage control technique for Mach-Zehnder modulators
Vervoort S *et al.* (presented by Marcus Wolff) ..... - 371 -
Mid-infrared photothermal spectroscopy in aqueous media
Holub E *et al.* (presented by Elisabeth Holub) ..... - 373 -

Novel approach for bottom-illuminated photothermal nanoscale chemical imaging with a flat silicon sample carrier
Yilmaz U *et al.* (presented by Ufuk Yilmak) ..... - 375 -
Dual-resonant mode T-type cell-based photoacoustic spectroscopy for simultaneous trace gas detection
Zhang L *et al.* (presented by Le Zhang) ..... - 377 -
Ppb-level methane sensor using a multi-pass mode photoacoustic spectroscopy technology
Zhang X *et al.* (presented by Xueshi Zhang) ..... - 379 -
Analytical method for estimating chemical composition of bio-samples under photothermal investigation
Memeu DM *et al.* (presented by Daniel Maitethia Memeu) ..... - 382 -
Windowless photoacoustic cell for trace gas detection
Liu L *et al.* (presented by Lixian Liu) ..... - 384 -
Photoacoustic SO_2 gas sensor in SF_6 buffer gas employing a 266 nm LED
Yin X *et al.* (presented by Xukun Yin) ..... - 386 -
Doppler effect for thermal waves: theory and applications
Li Voti R *et al.* (presented by Gianpaolo Bei) ..... - 388 -
Twin-focus thermal lens microscopy: A theoretical description
Liu M (presented by Minqiang Liu) ..... - 391 -
Three-dimensional truncated correlation photothermal coherence tomography image optimization using linear iso phase imaging
Welch R *et al.* (presented by Andreas Mandelis) ..... - 393 -
Photoacoustics in the study of micromechanical structures
Todorovic DM (presented by Dragan Todorovic) ..... - 396 -

09 Non-destructive Evaluation

Measuring the depth and width of delaminations by photothermal radiometry
Salazar A *et al.* (presented by Augustin Salazar) ..... - 398 -
The feature detection of GFRP subsurface defects using fast randomized sparse principal component thermography
Shen P *et al.* (presented by Hui Zhang) ..... - 400 -
Non-contact measurement of sub-micron-level ultrasonic vibration by near-field microwave
Peng C *et al.* (presented by Cuiling Peng) ..... - 401 -
Intelligent identification for delamination defects of aviation honeycomb sandwich composites (HSCs) using convolution neural network fusion lock-in thermography
Wang F *et al.* (presented by Fei Wang) ..... - 403 -
Research on multi-dimensional feature recognition for PCBs typical defects using laser ultrasonic imaging
Yue Z *et al.* (presented by Zhouyan Yue) ..... - 404 -

10 Low-Dimensional Systems, Nanoscale Phenomena and Nanostructure

Tareeva MV *et al.* (presented by Maria Tareeva) ..... - 406 -
Study of the thermal properties of resin/graphene nanocomposite for 3D print applications
García-Vidal UO *et al.* (presented by Usiel Omar Garcia Vidal) ..... - 407 -
Thermal study of ferromagnetic nanoparticles coated with mesoporous silicon oxide
García-Vidal UO *et al.* (presented by Usiel Omar Garcia Vidal) ..... - 410 -

11 Environmental, Agricultural, and Food Applications

Characterization of natural hepatoprotectors and added foods by photoacoustic spectroscopy and colorimetry
Saucedo-Alfonzo DA *et al.* (presented by David A. Saucedo Alfonzo) ..... - 413 -
Thermal properties measurement of chitosan-based films for agricultural applications
Correa-Pacheco ZN *et al.* (presented by Usiel Omar Garcia Vidal) ..... - 415 -
Characterization of plasma-treated gooseberry (Physalis Peruviana L.) seeds using photoacoustic techniques
Romero-Galindo R *et al.* (presented by Raul Romero-Galindo) ..... - 417 -
Optical and thermal properties of Mexican native maize and tortilla
Contreras-Gallegos E *et al.* (presented by Eder Contreras-Gallegos) ..... - 419 -
Photopyroelectric technique applied to sodium alginate hydrogel characterization
Pessoa PAC *et al.* (presented by Andre Oliveira Guimaraes) ..... - 421 -

12 Analytical Chemistry and Photochemistry

Absolute fluorescence quantum yield spectra of light scattering samples determined using thermal lens spectroscopy aided by optical absorbance and fluorescence measurements

Vargas E *et al.* (presented by Fidel Roberto Castellanos Duran) ..... - 424 -

Photoacoustic calorimetry study of the conformational variation of the chignolin peptide induced by a pH jump

Amado D *et al.* (presented by Daniela Amado Santos) ..... - 425 -

Miniaturized gel electrophoresis-thermal lens technique as a highly sensitive photothermal detection method

Abbasgholi-NA B *et al.* (presented by Behnaz Abbasgholi Nejad Asbaghi) ..... - 427 -

01
Thermophysical Properties

A modified mode-mismatched thermal lens spectrometry Z-scan model: An exact general approach

Rahman A[(1,2)], Rahim K[(3)], Ashraf I[(2)], Cabrera H[(1)*]

(1) Optics Lab, STI Unit, The Abdus Salam International Centre for Theoretical Physics, Trieste 34151, Italy
(2) Department of Physics, Quaid-i-Azam University, Islamabad
(3) Department of Basic Sciences, University of Engineering and Technology, Taxila

*Corresponding author's email: hcabrera@ictp.it

In this work we introduce a modified pump-probe mode-mismatched thermal lens Z-scan theoretical model for measurement of absorption coefficient and thermal diffusivity of semi -transparent liquids. We present an exact solution for the thermal lens signal which consider validity of the experimental parameters in any experimental configuration. In the proposed approach, the pinhole size ρ_0 was considered and optimized, with different distances from sample to detector (L). We illustrate its validity by calculating the thermal lens signal in situations of small and large L values and measuring the absorption coefficient and thermal diffusivity of water performing Z-scan experiment.

Theoretical Model – Previously developed theoretical models, to study TL signals, were based on Fresnel- diffraction approximations, for situations in which the sample is located at a fixed position [1]. Later on, Marcano et al. [2] developed a model for Z-scan experiment based on same approximation, which also included the aberration nature of the TL. This model successfully describes TL signal generated by using a focused excitation beam by measuring transmission of probe light through a small aperture. They claimed an excellent agreement by performing Z-scan experiments between theory and experiment for specific case when the radius of aperture ρ_0 was ignored. However, in more general cases it is necessary to consider the ρ_0 influence on the TL signal. We present the exact analytical theory for Z-scan in far field approximation and discuss theoretical results in mode mis-matched configuration with the exact solution which includes ρ_0 dependence. We perform Z-scan measurement on water and compare results of water absorption coefficient and thermal diffusivity obtained by different TL models. The TL signal including aperture size and L effect is

$$S(z,t) = \Phi_0 \int_{t'}^{1} \frac{2M_1(z,0)M_0(z,\tau)}{(1-exp\{-2\rho_0^2 M_1(z,0)y^2\})M_0(z,0)M_4(z,\tau)} \frac{d\tau}{\tau} [sin\{arctan[\frac{M_2(z,0)-M_2(z,\tau)}{M_1(z,0)+M_1(z,\tau)}] + M_3(z,0) - M_3(z,\tau)\} - exp\{-2\rho_0^2(M_1(z,0)+M_1(z,\tau)y^2)\} \times sin\{arctan[\frac{M_2(z,0)-M_2(z,\tau)}{M_1(z,0)+M_1(z,\tau)}] + \rho_0^2 y^2 (M_2(z,0) - M_2(z,\tau)) + M_3(z,0) - M_3(z,\tau)\}] \quad \text{Eqn. 1}$$

With

$$M_0(z,\tau) = \frac{1}{\sqrt{(1+2m(z)\tau)^2+v(z)^2}}, \quad \text{Eqn. 2}$$

$$M_1(z,\tau) = \frac{(1+2m(z)\tau)}{4((1+2m(z)\tau)^2+v(z)^2)}, \quad \text{Eqn. 3}$$

$$M_2(z,\tau) = \frac{v}{4((1+2m(z)\tau)^2+v(z)^2)}, \quad \text{Eqn. 4}$$

$$M_3(z,\tau) = arctan\{-\frac{v(z)}{1+2m(z)\tau}\}, \quad \text{Eqn. 5}$$

$$M_4(z,\tau) = \sqrt{(M_1(z,0)+M_1(z,\tau))^2 + (M_2(z,0)-M_2(z,\tau))^2} \quad \text{Eqn. 6}$$

m is the degree of the mode mismatching with

$$v(z) = (z - a_p)/z_p + (z_p/L)[1 + (z - a_p)^2/z_p^2] \quad \text{Eqn. 7}$$

here a_p and z_p are waist and Rayleigh parameters of probe beam respectively. The results show there is strong dependence of signal on ρ_0 and L contrary to [2].

Experimental verification – In order to validate the presented modified model we calculate the absorption coefficient and thermal diffusivity of water using the experimental setup shown. A probe beam of 2 mW He-Ne laser at 632 nm and a 532 nm diode-pumped solid state laser (DPSS) with power 480 mW has been used. The presented theory allows to perform fitting on the experimental data using the values of Φ0 and diffusivity as fitting parameters without considering *L* as a critical unknown parameter. To test the validity of our model, we performed mode-mismatched Z-scan experiment using double distilled and deionized water as a sample. The obtained values for the absorption coefficient and thermal diffusivity match pretty well with literature values.

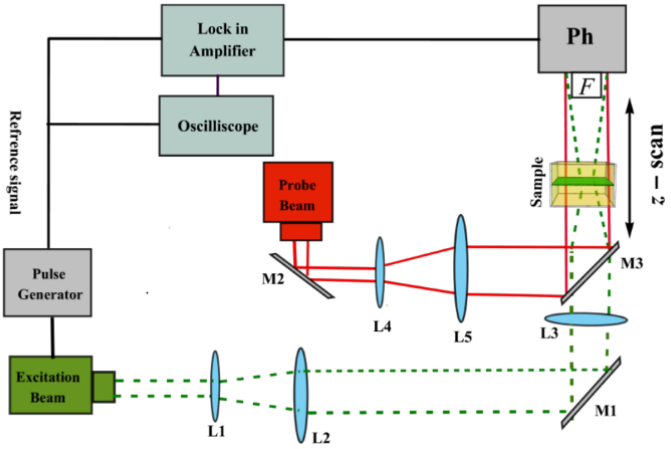

Fig. 1. Experimental configuration of the pump-probe TL setup. Ph: photodetector; L1-L5: lenses; M1-M2: turning mirror, M3: dichroic mirror, F: filter.

References

[1] J. Shen, R.D. Lowe, R.D. Snook, A model for cw laser induced mode-mismatched dual-beam thermal lens spectrometry, Chem. Phys. 165 (1992) 385–396.

[2] A. Marcano, C. Loper, N. Melikechi, Pump–probe mode-mismatched thermal-lens z scan, JOSA B 19 (2002) 119–124.

Optical and thermal characterization of Fe_3O_4 nanoparticles covered with turmeric extract

Alvarado-Noguez ML[(1,2)*], Matías-Reyes AE[(1)], Domínguez-Pacheco A[(2)], Cruz-Orea A[(1)], Santoyo-Salazar J[(1)], Hernandez-Aguilar C[(2)]

(1) Departamento de Física, Centro de Investigación y de Estudios Avanzados-IPN, Av. IPN No. 2508, Col. San Pedro Zacatenco, 07360 Ciudad de México, México
(2) Posgrado en Ingeniería de Sistemas, SEPI – ESIME - Zac., Instituto Politécnico Nacional, Ciudad de México, México

*Corresponding author's email: malvaradon0900@alumno.ipn.mx

Superparamagnetic iron oxide nanoparticles (SPION's) have been used to develop biological applications such as hyperthermia therapy, diagnostic agent, and/or drug delivery [1]. Magnetite (Fe_3O_4) nanoparticles (MNP´s) are considered as addressable magnetic target, which can be stimulated by an external AC magnetic field [2]. Moreover, for biomedical applications, the green synthesis route is highly recommended because it decreases the toxicity of nanoparticles and reduces toxic waste from synthesis [3]. In this work, magnetite nanoparticles covered with Curcuma extract were obtained by green synthesis. Also, these MNPs were optical and thermally characterized by using photothermal techniques, obtaining their optical absorption spectrum, thermal diffusivity, effusivity, conductivity, and heat capacity per volume unit.

Figure 1 shows the optical absorption spectrum of the synthetized MNP´s, where it is possible to observe an absorption region from 300nm to 550nm.

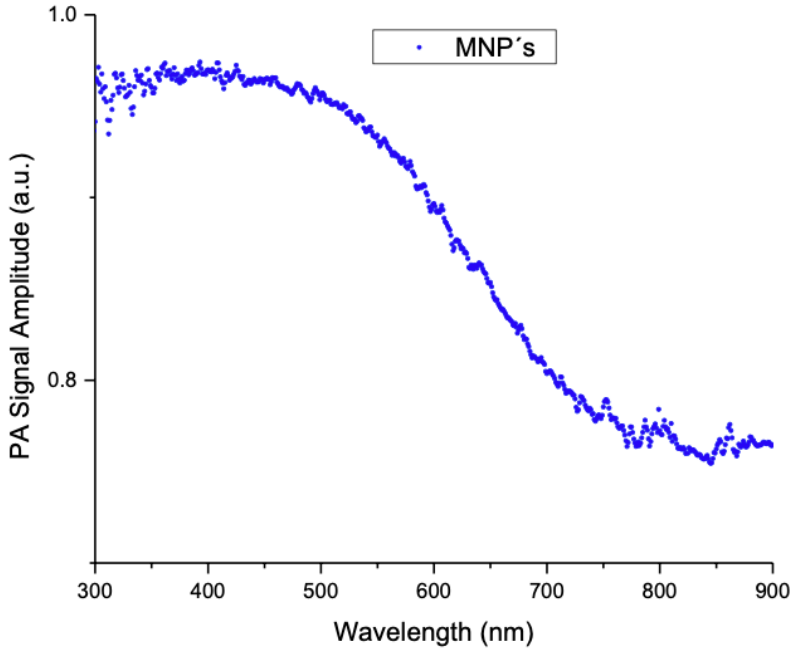

Fig. 1. Optical absorption spectrum of MNP´s.

The thermal diffusivity and effusivity values of MNP´s, were obtained by Thermal wave resonator cavity (TWRC) and inverse photopyroelectric (IPPE) photothermal techniques, respectively. The

obtained thermal parameters are similar to the water thermal values due to the fact that MNP´s were measured in water solutions [4].

References

[1] A. Khosravi, A. Hasani, K. Rahimi, A. Aliaghaei, M. Pirani, N. Azad, F. Hejazi, Ameliorating effects of curcumin-loaded superparamagnetic iron oxide nanoparticles (SPIONs) on the mouse testis exposed to the transient hyperthermia: A molecular and stereological study. Acta Histochemica. 122:8 (2020) 151632. https://doi.org/10.1016/j.acthis.2020.151632.

[2] M. Ramazanov, A. Karimova, H. Shirinova, Magnetism for drug delivery, MRI and hyperthermia applications: A review. Biointerface Res. Appl. Chem. 11 (2020) 8654-8668. https://doi.org/10.33263/BRIAC112.86548668.

[3] A.L. Ramirez-Nuñez, L.F. Jimenez-Garcia,G.F. Goya, B. Sanz, J. Santoyo-Salazar, In vitro magnetic hyperthermia using polyphenol-coated Fe3O4@ γFe2O3 nanoparticles from Cinnamomun verum and Vanilla planifolia: the concert of green synthesis and therapeutic possibilities. Nanotechnology. 29:7 (2018) 074001. https://doi.org/10.1088/1361-6528/aaa2c1.

[4] A. Bejan, A.D. Kraus (Eds.) Heat transfer handbook, Vol. 1 (2003) John Wiley & Sons.

Thermal study of porous and compact SiO_2 nanoparticle nanoliquids by TWRC technique

García-Vidal UO[(1)*], Jiménez-Pérez JL[(1)], Sánchez-Ramírez JF[(2)], Correa-Pacheco ZN[(3)], López-Gamboa G[(4)], Gutiérrez-Fuentes R[(5)], Cruz-Orea A[(6)]

(1) Unidad Profesional Interdisciplinaria en Ingeniería y Tecnologías Avanzadas-Instituto Politécnico Nacional, Av. IPN, No. 2580, Col. Barrio La Laguna Ticomán, Gustavo A. Madero, C.P. 07340 Mexico City, Mexico

(2) Centro de Investigación en Biotecnología Aplicada-Instituto Politécnico Nacional, Ex-Hacienda San Juan Molino Carretera Estatal Tecuexcomac-Tepetitla, Km 1.5, C.P. 90700 Tlaxcala, Mexico

(3) Centro de Desarrollo de Productos Bióticos, Instituto Politécnico Nacional, Carretera Yautepec-Jojutla km 6, San Isidro, Yautepec, Morelos 62731, Mexico.

(4) Tecnológico Nacional de México Campus Toluca, dirección Avenida Tecnológico s/n. Colonia Agrícola Bellavista, Metepec, C.P. 52149, Mexico State, Mexico

(5) Tecnológico de Estudios Superiores de Villa Guerrero. Dirección: Carretera Federal Toluca - Ixtapan de la sal Km 64.5, Col. La Finca, Villa Guerrero, Mexico State, Mexico

(6) Departamento de Física, CINVESTAV-IPN, Av. Instituto Politécnico Nacional, No. 2508, Col. San Pedro Zacatenco, Ciudad de México C.P. 07360, Mexico.

*Corresponding author's email: ugarciav0700@alumno.ipn.mx

Background – Photothermal studies were carried out to evaluate the thermal characteristics of silicon nanoparticles (NPs). Compact and mesoporous silicon NPs were synthesized using the modified Stöber method. Thermal wave resonance cavity (TWRC) technique was used to determine the thermal diffusivity and effusivity of compact and porous SiO_2 water based-nanoliquids by scanning the cavity length by moving a cylindrical probe relative to a photopyroelectric (PPE) detector in a liquid medium in a thermally thick region. This technique has potential in the measurements of the thermal diffusivity and effusivity of small volumes of nanoliquids and thick non-transparent samples. The complementary technique dynamic light scattering (DLS) was used to determine the particle size.

Methods – For the synthesis of compact SiO_2 NPs, 60 mL of ethanol containing 25 mL of distilled water, 1 mL of TEOS and 4.2 mL of ammonia hydroxide were employed. The reaction solution was stirred (300 rpm) for 3.5 h at room temperature to carry out the TEOS hydrolysis and condensation process. The resulting colloidal suspension was centrifuged (4000 rpm, for 15 min). The particles were recovered in a methanol/water wash in a 1:1 volume ratio, repeating the process at least 5 times. Finally, they were left to dry in a muffle at 70ºC [1].

On the other hand, for the synthesis of porous SiO_2 NPs, 0.2 g of CTAB surfactant were added to 100 mL of distilled water with 1 mL of NaOH at 2 Molar at a temperature of 80º C. At this point, 1 mL of TEOS was injected and maintained at 500 rpm. Synthesis was left for 2 h. The solution was separated by centrifugation at 4000 rpm for 10 min and the white precipitate was placed in a flask and stirred at 200 rpm for 10 min with distilled water. This procedure was followed at least 3 times to wash the NPs. When the particles were washed, to remove the surfactant, they were subjected to a thermal treatment in a muffle. The white precipitate was placed in a high temperature crucible and ramp heating at 10ºC/min was used until it reached 550ºC, at which point it was left for 4 h at this temperature and allowed to cool to room temperature. A white powder was obtained for the mesoporous NPs. It was pulverized in a mortar for further use [2].

Results – For the diffusivity analysis, the theoretical model of the TWRC was used, for thermally thick samples, where qLs>>1, so the sensor output voltage of the magnitude of the complex expression, Eqn. 1 can be deduced as:

$$V(Ls) = V_0 e^{-qLs} \qquad \text{Eqn. 1}$$

For the analysis of the effusivity, the theoretical model was used:

$$\theta(\omega) = \frac{[(1-e^{\sigma_p l_p})(1+b)+(e^{-\sigma_p l_p}-1)(1-b)]}{[(g-1)(1-b)e^{-\sigma_p l_p}+(1+g)(1+b)e^{\sigma_p l_p}]} \qquad \text{Eqn. 2}$$

where $\theta(\omega)$ is the output signal of the pyroelectric detector, $\omega = 2\pi f$, $\sigma_p = \frac{1+i}{\mu_p}$, $\mu_p = \sqrt{\frac{\alpha_p}{\pi f}}$, α_p, l_p are the pyroelectric thermal diffusivity and its thickness respectively, $b = \frac{e_s}{e_p}$ y $g = \frac{e_g}{e_p}$, con e_s, e_g, y e_p the thermal effusivities of sample, gas (air), and pyroelectric, respectively. Taking the PPE signal as a function of the frequency sweep, it is possible to obtain the thermal effusivity of the sample from the best fit of Eqn. 2 to the experimental data, taking b as the adjustment parameter [3,4].

Table 1. Thermal properties values for the graphene NPs /resin

Type	Diameter	$\alpha_{Amplitude}$ $\times 10^{-7}$(cm^2/s)	Effusivity (Ws$^{1/2}$/mk)	Thermal conductivity (W/mK)	Enhancement %	Literature value
Distilled water	--	1.4	1580	0.5606	-	
Compact SiO_2	211 ± 12nm	1.49 ± 0.02	1672 ± 36	0.6914	15.1%	0.95x10^{-7} [2]

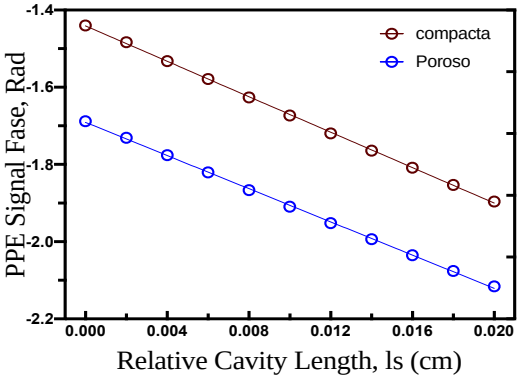

Fig. 1. (a) Thermal diffusivity of SiO_2 nanoparticles porous and compact. (b) Thermal effusivity of SiO2 nanoparticles porous and compact

The compact and porous silica NPs were analyzed using the TWRC technique to determine the diffusivity, effusivity and thermal conductivity, where an increase in the thermal diffusivity of the porous SiO_2 NPs of 23.33% was obtained compared with the diffusivity of water and a 15.1% enrichment of compact SiO_2 compared to the diffusivity of water.

Conclusions – Compact and porous SiO_2 NPs were synthesized with monodisperse Stöber and modified Stöber method. The analyzes showed that having a larger surface area in the porous SiO_2 nanoparticles increases the thermal diffusivity compared to the diffusivity of the compact SiO_2. The TWRC technique is a promising technique for analyzing transparent, opaque, and thermally thick nanofluids.

References

[1] A. Netzahual-Lopantzi, J.F. Sánchez-Ramírez, J.L. Jiménez-Pérez, D. Cornejo-Monroy, G. López-Gamboa, Z.N. Correa-Pacheco, Study of the thermal diffusivity of nanofluids containing SiO_2 decorated with Au nanoparticles by thermal lens spectroscopy, Appl. Phys. A, 125 (2019) 588:1-9. https://doi.org/10.1007/s00339-019-2891-3.

[2] V.L. Zholobenko, S.M. Holmes, C.S. Cundy, J. Dwyer, Synthesis of MCM-41 materials: an in situ FTIR study, Microporous Mater., 11 (1-2) (1997) 83-86. https://doi.org/10.1016/S0927-6513(97)00033-3.

[3] G. Lara-Hernández, E. Suaste-Gómez, A. Cruz-Orea, J.G. Mendoza-Alvarez, F. Sánchez-Sinéncio, J. P. Valcárcel, A: García-Quiroz, Thermal Characterization of Edible Oils by Using Photopyroelectric Technique, Int. J. Thermophys., 34 (2013) 962-971. https://doi.org/10.1007/s10765-013-1419-x.

[4] J.A. Balderas-López, A. Mandelis, and J.A. Garcia, Thermal-wave resonator cavity design and measurements of the thermal diffusivity of liquids, Rev. Sci. Instrum., 71 (2000) 2933-2937. https://doi.org/10.1063/1.1150713.

Thermal characterization of hydrocarbon-water interfaces

Vargas-Vargas A(1)*, Isidro-Ojeda MA(1, 2), Marín E(1)

(1) Instituto Politécnico Nacional, Centro de Investigación en Ciencia Aplicada y Tecnología Avanzada (CICATA) Unidad Legaria, Legaria 694, Colonia Irrigación, Delegación Miguel Hidalgo, Ciudad de México 11500, Mexico

(2) Facultad de Ingeniería, Universidad Autónoma de Yucatán, A.P. 150, Cordemex, Mérida, Yucatán, Mexico

*Corresponding author's email: aldrindavid.vargas2@gmail.com

The interest in systems containing mixtures of non-miscible liquids makes them important, among others, the study of heat transport at their interfaces. Although there are many studies on interfaces solid-solid and liquid-liquid, very few studies have been focused on liquid-liquid interfaces [1]. The knowledge of the behavior of thermal properties in these soft interfaces is important to understand heat transfer mechanisms in systems such as cellular environments, oil fields, some solvents, etc. In this work, the thermo-optical technique of transient thermal lens [2] was used to monitor the behavior of characteristic parameters along the direction normal to the interface between water and some n-alkanes described by the formula $C_N H_{2N+2}$, with $N = 5 - 8$, including isooctane. In that technique, a laser beam (pump or excitation) is focused on a point of the sample. The radiation energy is partially absorbed and transformed into heat, generating a local gradient in the refractive index that acts as a thermal lens modifying the intensity of another laser beam (test or probe) that travels the excitation region. The temporal evolution of this intensity during excitation is measured in the far field with a photodetector in front of which a small hole is placed to only let pass a portion of the test beam. Ensuring that the initial and boundary conditions of a model developed for very low optical absorption samples are experimentally met [2] a data fit is made with that model to determine the thermal diffusivity and the parameter

$$\theta = -\frac{P_{in}\beta\ell_0}{k\lambda_p}\frac{dn}{dT} \qquad \text{Eqn. 1}$$

which depends on its thermal conductivity (k), the optical absorption coefficient (β), the thickness of the sample (l_0), the temperature coefficient of the refractive index (dn/dT), the pump beam power (P_{in}), and the wavelength of the probe beam (λ). Preliminary measurements suggest a behavior of some characteristic parameters, such as thermal diffusivity, around the interface, which qualitatively matches previously literature reports for the thermal lens signal in solid-solid interfaces [3], as shown in Fig. 1.

Using the estimated interfacial thermal diffusivity, the interface thickness and typical value of the heat capacity per unit volume reported for condensed matter [4], it was possible to calculate the interfacial thermal resistance value.

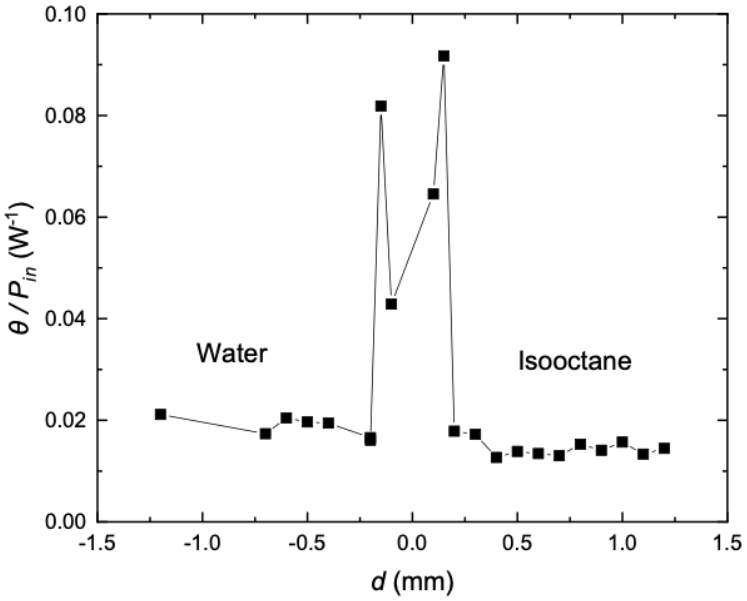

Fig. 1. Parameter θ normalized to the pump beam power used for each measurement, as a function of the distance (d) perpendicular to the interface, which is located at d = 0.0 mm.

References

[1] H.A. Patel, S. Garde, P. Keblinski, Thermal Resistance of Nanoscopic Liquid-Liquid Interfaces: Dependence on Chemistry and Molecular Architecture, Nano Lett. 5:11 (2005) 2225–2231. https://doi.org/10.1021/nl051526q

[2] J. Shen, R.D. Lowe, R.D. Snook. A model for cw laser induced mode-mismatched dual-beam thermal lens spectrometry. Chem. Phys. 165 (1992) 385-396. https://doi.org/10.1016/0301-0104(92)87053-C

[3] T.T.J. Rossteuscher, A. Hibara, K. Mawatari, T. Kitamori. Lateral spatial resolution of thermal lens microscopy during continuous scanning for nonstaining biofilm imaging. J. Appl. Phys. 105:102030 (2009) 1-6. https://doi.org/10.1088/0143-0815/10/1/002.

[4] A. Salazar. On thermal diffusivity. Eur. J. Phys. 24 (2003) 351–358. https://doi.org/10.1088/0143-0807/24/4/353

Characterization of TiO_2 thin film deposited on Silicon membrane using neural networks

Djordjević KLj[(1)*], Markushev DK[(2)], Popovic MN[(2)], Nesic MV[(1)], Galović SP[(1)], Lukić DV[(2)], Markushev DD[(2)]

(1) University of Belgrade, "VINČA" Institute of Nuclear Sciences - National Institute of the Republic of Serbia, University of Belgrade, PO box 522, 11000 Belgrade, Serbia
(2) University of Belgrade, Institute of Physics Belgrade, National Institute of the Republic of Serbia, Pregrevica 118, 11080 Belgrade (Zemun), Serbia

*Corresponding author's email: katarina.djordjevic@vin.bg.ac.rs

Background – This paper presents a theoretical analysis of the possibility of thermal characterization of a thin TiO_2 film deposited on a 30 μm thick Si membrane as a wafer in the frequency domain of photoacoustics from 20 Hz to 20 kHz. For this purpose, photoacoustic signals generated by such a sample were used (Figure 1) in which the membrane parameters were known and constant, while the film parameters were changed in the ranges of thickness $l_f = (475-525)\,\mathrm{nm}$, thermal expansion coefficient $\alpha_f = (1.045-1.155)\cdot 10^{-5}\,\mathrm{K}^{-1}$, and thermal diffusivity $D_f = (3.515-3.885)\cdot 10^{-6}\,\mathrm{m^2 s^{-1}}$. It can be seen from the Figure 1 that changes in the signal amplitude for the given changes in the film parameters cannot be noticed, while in the phase such changes are clearly noticeable. Within the classical approach of photoacoustic signal processing, non-distinguishing of amplitudes requires the introduction of an additional process of their normalization. In this paper, we will show that well-trained neural networks have no problem distinguishing signal amplitudes and that networks recognize precisely the parameters of thin films on such signals, knowing that the thickness of the films can be two orders of magnitude thinner than their wafers.

Results – The neural networks used in this paper were trained with the basis of photoacoustic signals from Figure 1. The supervised learning algorithm was used by connecting the data of the frequency amplitude-phase characteristics of the input layer signals with the values of the given parameters of the output layer change. The network architecture is very simple and consists of one input (144 neurons), one hidden (10 neurons), and an output layer (3 neurons). The number of input layer neurons corresponds to 144 points that define the photoacoustic signal (72 amplitudes + 72 phases). The three neurons of the output layer are connected to the thin-film parameters: l_f, α_f and D_f. In the case of the thin film thickness, the obtained network performances are 4.3106 x 10^{-6} for 4 epochs, in the case of coefficient of thermal expansion 3.567 x 10^{-5} for 7 epochs, and in the case of thermal diffusivity 0.0044842 for 4 epochs. The prediction of neural networks on test signals with errors of less than 1% shows that the networks are sensitive to small changes in TiO_2 parameters.

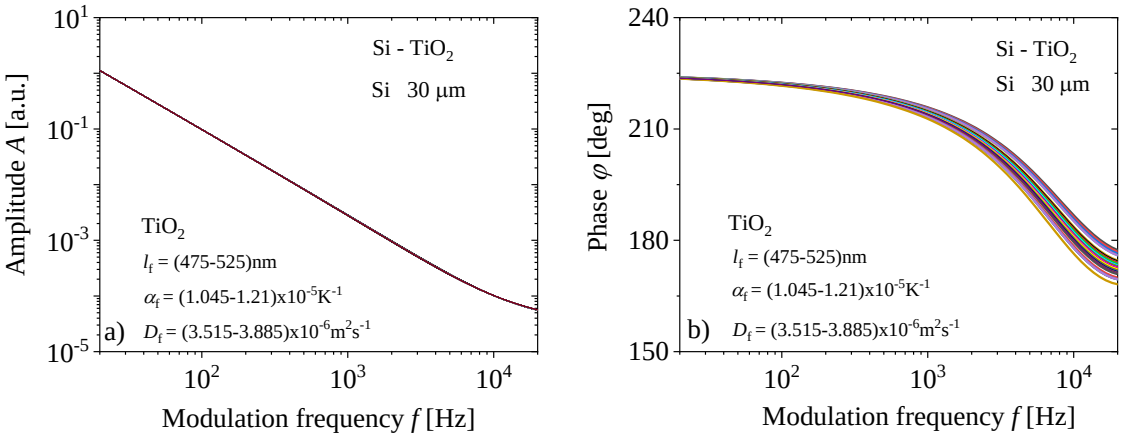

Fig. 1. Photoacoustic signals: a) amplitudes and b) phases of the two-layer model of the TiO2 layer on the Silicon sample obtained by changing the parameters of thickness l_f, expansion α_f and diffusivity D_f of the TiO_2 layer.

Conclusions – Our analysis shows that neural networks have a significant sensitivity to changes in the characteristics of thin layers of TiO_2 deposited on silicon membranes. This fact points to the possibility that neural networks, in combination with photoacoustics, can be a powerful tool in characterizing thin single-layer or multilayer coatings, important for the production of MEMS and NEMS sensors, as well as for the electronics and automotive industries in general.

References

[1] D.M. Todorović, M.D. Rabasović, D.D. Markushev, Photoacoustic elastic bending in thin film—Substrate system, J. Appl. Phys. 114, 213510 (2013); doi: 10.1063/1.4839835.

[2] N. Jovančić, D. K. Markushev, D.D. Markushev, S.M. Aleksić, D.S. Pantić, D. Korte, M. Franko, Thermal and Elastic Characterization of Nanostructured Fe2O3 Polymorphs and TiO2-Coated Fe2O3 Using Open Photoacoustic Cell, Int. J. Thermophys. 41, 90 (2020), https://doi.org/10.1007/s10765-020-02669-w.

[3] K. Lj. Djordjevic, D.D. Markushev, Ž.M. Ćojbašić, et al. Photoacoustic Measurements of the Thermal and Elastic Properties of n-Type Silicon Using Neural Networks. Silicon (2019) doi:10.1007/s12633-019-00213-6.

[4] K. Lj. Djordjevic, D.D. Markushev, Ž.M. Ćojbašić, S.P. Galović, Inverse problem solving in semiconductor photoacoustics by neural networks, Inv. Prob. Scie. En. 29 (2020) 248 - 262. https://doi.org/10.1080/17415977.2020.1787405.

[5] S.M. Aleksić, D.K. Markushev, D.D. Markushev, D.S. Pantić, D.V. Lukić, M.N. Popović, S.P. Galović, Photoacoustic Analysis of Illuminated Si-TiO_2 Sample Bending Along the Heat-Flow Axes. Silicon (2022). https://doi.org/10.1007/s12633-022-01723-6.

Estimation of heat propagation speed in the thin graphene-oxide foil by photoacoustic spectroscopy

Misovic A[(1)], Nesic MV[(1)], Djordjevic KL[(1)*], Markushev DK[(2)], Popovic MN[(2)], Markushev DD[(2)], Galovic SP[(1)]

(1) University of Belgrade, "VINČA" Institute of Nuclear Sciences - National Institute of the Republic of Serbia, PO box 522, 11000 Belgrade, Serbia
(2) University of Belgrade, Institute of Physics Belgrade, National Institute of the Republic of Serbia

Pregrevica 118, 11080 Belgrade (Zemun), Serbia

*Corresponding author's email: katarina.djordjevic@vin.bg.ac.rs

The amplitudes and phases of photoacoustic signal measured for the thin foil of graphene oxide (about 20 micrometers) in dependence of modulation frequencies of excitation laser beam are presented. Measurements were performed in a gas-microphone photoacoustic transmission configuration with an open cell of minimum volume [1]. Periodic changes in amplitude and phase at frequencies higher than 4 kHz (Fig.1) were interpreted as a possible consequence of thermal resonances in the sample, which occur due to the thermal memory of graphene oxide [2]. Based on both, the generalized model of photoacoustic response for media with thermal memory [2,3] and the presented measurements, the velocity and diffusion lengths of heat propagation in graphene oxide were determined. The estimated value of the heat propagation speed indicates the presence of relaxation phenomena in graphene oxide whose rate is of the same order of magnitude as in polymeric materials [4] and which are much slower than those in crystalline solids. It is in agreement with existing knowledge about structure properties of graphene oxide [5,6].

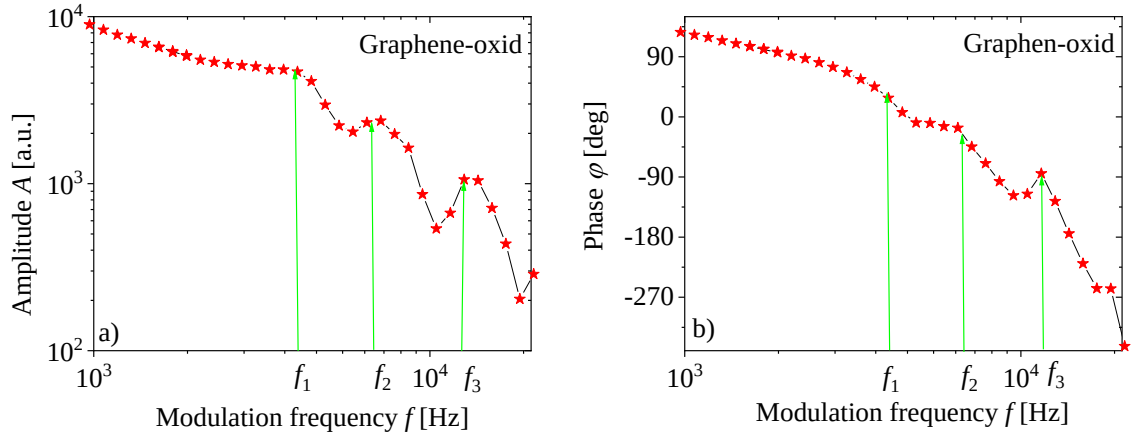

Fig. 1. Experimental measurements of **(a)** amplitudes and **(b)** phases of photoacoustic response of graphene-oxide foils which thickness is 20 micrometers. Measurements were performed in a gas-microphone photoacoustic transmission configuration with an open cell of minimum volume

References

[1] M.D. Rabasović, M.G. Nikolić, M.D. Dramićanin, M. Franko, D.D. Markushev, Low-cost, portable photoacoustic setup for solid state, Meas. Sci. Technol, 20 (2009) 9. doi:10.1088/0957-0233/20/9/095902.

[2] S. Galović, D. Kostoski, Photothermal wave propagation in media with thermal memory. Journal of Applied Physics, 93:5 (2003) 3063-3070. doi:10.1063/1.1540741.

[3] S. Galović, Z. Šoškić, M. Popović, D. Čevizović, Z. Stojanović, Theory of photoacoustic effect in media with thermal memory, J. Appl. Phys., 116:2 (2014) 024901. https://doi.org/10.1063/1.4885458.

[4] A. Saiter, H. Couderc, J. Grenet, Characterisation of structural relaxation phenomena in polymeric materials from thermal analysis investigations, J. Therm. Anal. Calorim. 88:2 (2007) 483-488. https://doi.org/10.1007/s10973-006-8117-x.

[5] D.Y. Kornilov, S.P. Gubin, Graphene Oxide: Structure, Properties, Synthesis, and Reduction (A Review), Russ. J. Inorg. Chem., 65 (2020) 1965–1976. https://doi.org/10.1134/S0036023620130021.

[6] A.T. Dideikin, A.Y. Vul, Graphene Oxide and Derivatives: The Place in Graphene Family, Front. Phys. 28 (2019) https://doi.org/10.3389/fphy.2018.00149.

Towards a point spread function for nanoscale chemical imaging

Zhang Y(1)*, Yilmaz U(1), Lendl B(1), Ramer G(1)

(1) Institute of Chemical Technologies and Analytics, TU Wien, 1060, Vienna, Austria

*Corresponding author's email: yide.zhang@tuwien.ac.at

Background – Atomic force microscopy-infrared (AFM-IR) is an AFM based technique that measures mid-IR absorption spectra at nanometre spatial resolution. One of the most attractive advantages of AFM-IR for chemical spectroscopist is that it provides spectra which compare well to conventional FTIR absorption spectra [1]. The technique of AFM-IR relies on the detection of the pulsed wavelength tuneable IR laser induced thermal expansion of the sample area underneath the AFM tip. While this mode of signal generation sounds simple enough it is still not fully understood.

In this work, we present a theoretical investigation of the laser heating induced thermal expansion process and model it as a point spread function (PSF). This approach draws parallels to super resolution microscopy where the PSF is used to determine spatial resolution and to resolve features below the diffraction limit. The biggest challenge in determining the PSF of AFM-IR is the fact that it relies on the thermal diffusion process and depends on material and sample properties in addition to laser repetition rates and pulse lengths. Nevertheless, we theorize, that the AFM-IR signal in many real-world samples can be approximated using Green's functions for semi-infinite, homogenous media.

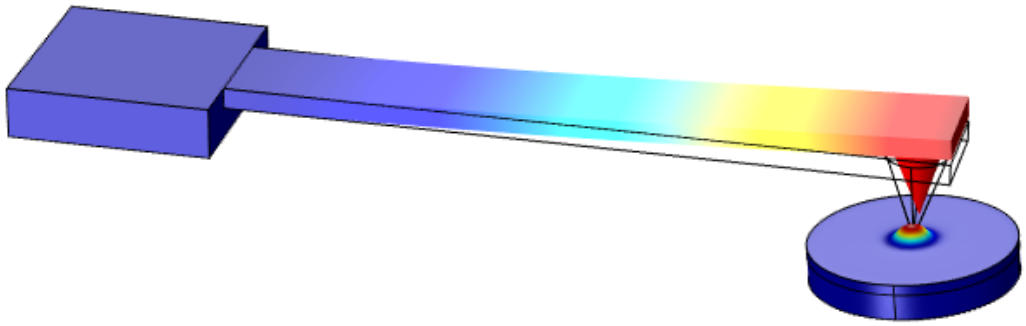

Fig. 1. Finite element simulation of thermal expansion of a spherical absorber by IR laser irradiation and detection by AFM cantilever in COMSOL.

Methods – In a homogeneous sample the resolution in an AFM-IR experiment is determined by how the temperature increases and distributes inside the sample following each laser pulse, hence it is governed by the Fourier's law [2]

$$\frac{1}{\alpha}\frac{\partial T}{\partial t} = \frac{Q}{V\kappa} + \Delta T \qquad \text{Eqn. 1}$$

Where α is the thermal diffusivity, κ is the heat conductivity and V the volume size of the sample. $Q(t)$ is a volumetric heat source which linked to the laser heating. If the sample geometry is simplified enough (substrate replaced by heat sink, air layer replaced by insulating boundary, homogeneous and semi-infinite slab sample), Green's functions can be used to calculate the evolution of the sample after each laser pulse. These same Green's functions, evaluated at specific laser pulse repetition rates then serve as AFM-IR's PSF. To verify that these simplifications do not result in

a significantly changed behaviour a finite element model of heat conduction in solids and fluids (implemented in COMSOL Multiphysics 5.6) of more realistic sample geometries is used. In this case we consider a cylindrically shaped sample with a single spherical element thermally heated by a laser pulse. The sample is placed on a thick substrate and covered by an air layer (see fig. 2).

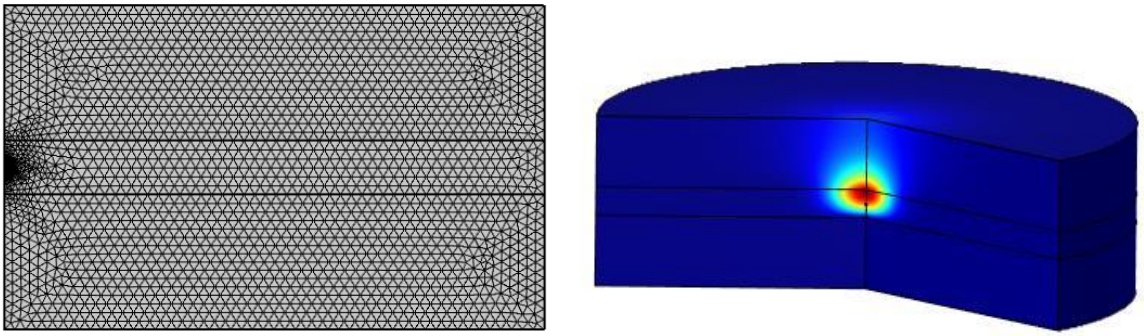

(a) Mesh sample structure (b) Simulated temperature distribution inside the sample

Fig. 2. Designed sample structure and heat transfer in solid and fluid model with COMSOL Multiphysics. The top layer is air, bottom layer is substrate and middle layer is sample matrix with buried single molecule in the middle.

Finally, the theoretical considerations yielding the PSF are compared to experimental data. Test samples are prepared by embedding fluorescent labelled spherical absorbers in a polymer matrix. Confocal fluorescence microscopy is used to determine the lateral and vertical information of the berried molecules and localize the positions where molecules might be among the centimetre scaled sample absorbers. Then the same sample area is measured in AFM-IR.

Results and Conclusion – First results how that there is a frequency (pulse repetition rate), pulse length and sample geometry dependence of the PSF in AFM-IR. The achievable spatial resolution is improved for short pulses, high frequencies and when the absorbers are closer to the substrate. These results provide guidance for experimental parameters which can be considered as trade-off between spatial resolution and signal intensity.

References

[1] A. Dazzi, F. Glotin, R. Carminati, Theory of infrared nanospectroscopy by photothermal induced resonance, J. Appl. Phys. 107 (2010) 124519. https://doi.org/10.1063/1.3429214.

[2] D.W. Hahn, M.N. Özişik, Heat conduction, John Wiley & Sons, 3rd ed. (2012).

Study of thermal and optical properties of composites made of silver iodomercurate (Ag_2HgI_4) in a polymeric matrix

Chan-Espinoza JA[(1)], Franco-Bacca AP[(1)], Forero-Sandoval IY[(1)], Chocolatl-Torres M[(2)], Salazar-Kuri U[(2)], Cervantes-Alvarez F[(1)*], Alvarado-Gil JJ[(1)*]

(1) Departamento de Física Aplicada, Cinvestav-Unidad Mérida, Carretera Antigua a Progreso Km. 6, Mérida, Yucatán, México, 97310, México

(2) Instituto de Física, Benemérita Universidad Autónoma de Puebla, Apdo. Postal J-48, 72570 Puebla, México

*Corresponding Authors' email: fernando.cervantes@cinvestav.mx, juan.alvarado@cinvestav.mx

During the last years, the study of thermochromic materials has increased notably due to their numerous applications as temperature sensors, smart windows, logic gates, among many others [1-4]. Thermochromic materials are characterized by a reversible color change produced by an increase in temperature [5]. Another important characteristic observed in these materials is the variation in their structural, optical, thermal and electrical properties [4,6-9]. This variation occurs in a continuously or discontinuously way, depending on the material [10-11]. Silver iodomercurate (Ag_2HgI_4) is a thermochromic material that exhibits a discontinuous change in their properties [6]. At room temperature, this material is in the stable β phase with a tetragonal crystal lattice structure and the samples exhibit a yellow color [12]; above 323 K the material changes to the disordered α phase with a cubic crystal lattice structure and the samples exhibit an orange color [13]. Ag_2HgI_4 is a superionic conductor because its electrical conductivity is similar to the one of molten salts at the high temperature α phase [13]. In this work, a composite made of Ag_2HgI_4 powder, synthesized by the co-precipitation method, embedded in a polyester resin matrix, is reported

The concentration of Ag_2HgI_4 was varied from 1 to 5 wt%. The hysteresis loop of the thermal diffusivity was measured, in a temperature range from 20 to 70 °C, using the modified Angstrom method. During the heating and cooling processes it can be observed how the reversible phase transition occurs gradually. Thermal diffusivity decreases by 50% on average during the phase transition, whose minimum values are found at 56 and 57.6 °C when heating and cooling respectively. In order to complement our studies, the emissivity of the samples as a function of temperature, was measured using photothermal radiometry. Additionally, the shift of the band gap, due to the phase transition, was determined by UV-Vis spectroscopy.

References

[1] D. Cao, C. Xu, W. Lu, C. Qin, S. Cheng, Sunlight-Driven Photo-Thermochromic Smart Windows, Solar RRL, 2:4 (2018) 1700219.

[2] I. Forero-Sandoval, J. Chan-Espinoza, J. Ordonez-Miranda, J. Alvarado-Gil, F. Dumas-Bouchiat, C. Champeaux, K. Joulain, Y. Ezzahri, J. Drevillon, C. Gomez-Heredia, J. Ramirez-Rincon, VO_2 Substrate Effect on the Thermal Rectification of a Far-Field Radiative Diode, Physical Review Applied, 14:3 (2020) 034023.

[3] C.R. Smith, D.R. Sabatino, T.J. Praisner, Temperature sensing with thermochromic liquid crystals, Experiments in Fluids, 30:2 (2001)190-201.

[4] C. L. Gomez-Heredia, J. A. Ramirez-Rincon, J. Ordonez-Miranda, O. Ares, J. J. Alvarado-Gil, C. Champeaux, F. Dumas-Bouchiat, Y. Ezzahri, K. Joulain, Thermal hysteresis measurement of the VO_2 emissivity and its application in thermal rectification, Scientific Reports, 8:1 (2018) 26687-9.

[5] M. A. White, M. LeBlanc, Thermochromism in Commercial Products, Journal of Chemical Education, 76:9 (1999) 1201.

[6] M. Chocolatl-Torres, A. P. Franco-Bacca, J. A. Ramírez-Rincón, C. L. Gómez-Heredia, F. Cervantes-Alvarez, J. J. Alvarado-Gil, R. Silva-Gonzalez, M. Toledo, U. Salazar-Kuri, Study of structural and optical properties of the thermochromic silver and copper tetraiodomercurates (Ag2, Cu2) HgI4 ceramics, Applied Physics A, 126:7 (2020) 525.

[7] M. Yang, Y. Yang, Bin Hong, L. Wang, K. Hu, Y. Dong, H. Xu, H. Huang, J. Zhao, H. Chen, L. Song, H. Ju, J. Zhu, J. Bao, X. Li, Y. Gu, T. Yang, X. Gao, Z. Luo, C. Gao, Suppression of Structural Phase Transition in VO2 by Epitaxial Strain in Vicinity of Metal-insulator Transition, Scientific Reports, 6:1 (2016) 23119.

[8] G. Hamaoui, N. Horny, C. L. Gomez-Heredia, J. A.Ramirez-Rincon, J.Ordonez-Miranda, C.Champeaux, F. Dumas-Bouchiat, J. J. Alvarado-Gil, Y. Ezzahri, K. Joulain, M. Chirtoc, Thermophysical characterisation of VO2 thin films hysteresis and its application in thermal rectification, Scientific Reports, 9:1 (2019) 45436.

[9] Y. Zhao, J. Hwan Lee, Y. Zhu, M. Nazari, C. Chen, H. Wang, A. Bernussi, M. Holtz, Z. Fan, Structural, electrical, and terahertz transmission properties of VO2 thin films grown on c-, r-, and m-plane sapphire substrates, Journal of Applied Physics, 111:5 (2012) 053533.

[10] P. K. Coughlin, S. J. Lippard, Copper (II) chemistry in hexaaza binucleating macrocycles: hydroxide and acetate derivatives, Journal of the American Chemical Society, 106:8 (1984) 2328–2336.

[11] D. E. Fenton, U. Casellato, P. Vigato, M. Vidali, The evolution of binucleating ligands, Inorganica Chimica Acta, 62, (1982) 57–66.

[12] S. Hull, D. A. Keen, Structural characterization of thebetatoalphasuperionic transition in Ag2HgI4and Cu2HgI4, Journal of Physics: Condensed Matter, 12:16 (2000) 3751–3765.

[13] J. Boyce, B. Huberman, Superionic conductors: Transitions, structures, dynamics, Physics Reports, 51:4 (1979) 189–265.

Thermal lens spectroscopy: an analytical model for a pulsed-laser

Isidro-Ojeda MA[(1)*], Alvarado-Gil JJ[(2)], Zambrano-Arjona MA[(1)]

(1) Facultad de ingeniería, Universidad Autónoma de Yucatán, A. P. 150, Cordemex, Mérida, Yucatán, Mexico
(2) Departamento de Física Aplicada, Centro de Investigación y de Estudios Avanzados del IPN-Unidad Mérida, Carretera Antigua a Progreso km. 6, A. P. 73 Cordemex, Mérida, Yucatán, Mexico

*Corresponding author's email: michel.isidro15@gmail.com

Maybe, principal advantages of the pulsed over the continuous laser beam are the tenability and sensitivity. Then, it is an excellent alternative to improve the detection limit of the thermal lens technique. Also, the time response of the pulsed is faster than continuous method [1]. Pulsed thermal lens spectroscopy has been used to characterize organic liquids by using a sample reference [2].

Because of the lack of an analytical model for pulsed thermal lens spectroscopy in mode-mismatched configuration, the analytical model for continuous beam has been used as an alternative to fit the data obtained by using a pulsed beam in experiments [3]. Then, a simple analytical model based on the Fresnel diffraction [4] approximation and considering only the center of the laser is developed, some limits of application are shown too.

References

[1] K. Mori, T. Imasaka, and N. Ishibashi, Thermal lens spectrophotometry based on pulsed laser excitation. 54 (1982) 2034–2038. https://doi.org/10.1021/ac00249a029.

[2] V. Bindhu, S. S. Harilal, V.P.N. Nampoori, C.P.G. Vallabhan, Thermal diffusivity measurements in organic liquids using transient ther-mal lens calorimetry, 37 (1998) 2791 – 2794. https://doi.org/10.1117/1.601825.

[3] M. Mohebbifar, Experimental comparison of methods based on falling andrising signal regions for thermal diffusivity measurement by pulsed dual-beam thermal lens spectroscopy. 156 (2020) 107611. https://doi.org/10.1016/j.measurement.2020.107611.

[4] J.W. Goodman, Introduction to Fourier Optics.

Influence of the VO_2 metal-insulator transition on the thermoelectric properties of composites based on a $Bi_{0.5}Sb_{1.5}Te_3$ matrix

Alvarez-Guerrero S[(1)*], Ordonez-Miranda J[(2, 3)], De Coss R[(1)], Alvarado-Gil JJ[(1)]

(1) Departamento de Física Aplicada, Centro de Investigación y de Estudios Avanzados del I.P.N-Unidad Mérida, Carretera Antigua a Progreso km. 6, A.P. 73 Cordemex, Mérida, Yucatán 97310, México
(2) LIMMS, CNRS-IIS UMI 2820, The University of Tokyo, Tokyo 153-8505, Japan
(3) Institute of Industrial Science, The University of Tokyo, Tokyo 153-8505, Japan

*Corresponding author's email: santiago.alvarez@cinvestav.mx

Thermoelectric (TE) materials enable direct and reversible heat-into-electricity conversion, for constituting the basis for green and environment-friendly energy technology. Considerable effort has been devoted to improving the efficiency of BiTe-based materials. Currently, methods for improving the performance of TE materials are related to the use of low dimensionality for decreasing the phonon thermal conductivity and increasing the product S^2n, where S is the Seebeck coefficient and n is the charge carrier concentration. It is well known that thermoelectric properties of strongly correlated electron systems could contribute to the semiconductor to metal transition (SMT) [1]. Vanadium dioxide (VO_2) is a strongly correlated oxide [2], which shows a SMT close to room temperature, which induces remarkable changes in its structural, optical, and electrical properties. These characteristics have made vanadium dioxide the basis in the development of a great diversity of technological applications, such as temperature sensors [3], energy storage media [4], thermally-driven radiative diodes [5], among others. However, VO_2 has received little attention in the field of thermoelectricity [2] and scarce applications for VO_2 in thermoelectricity has recently emerged [6,7].

Inspired by the fact that vanadium dioxide shows a fully reversible first-order metal-to-insulator transition accompanied by a relatively little change in its thermal conductivity and an abrupt jump by nearly two orders of magnitude in its electrical conductivity on heating [8], we have investigated the influence of VO_2 on the electrical conductivity, thermal conductivity and Seebeck effect for $VO_2/Bi_{0.5}Sb_{1.5}Te_3$ composites. We combine the Bruggeman scheme [9], considered as one of the most accurate for high filler volume fractions and the accuracy of the finite element methods [10] to evaluate the thermal conductivity, electrical conductivity, and Seebeck coefficient for composites of three different vanadium dioxide concentrations.

The ETC values as a function of temperature are plotted in Fig. 1(a), the inset in the figure shows a good agreement with the experimental results reported by Back et al. [7] within the temperature range for T < 350 K. from these results we estimate the interface thermal resistance between $Bi_{0.5}Sb_{1.5}Te_3$ and VO_2 as R = 1.91 m^2KGW^{-1}. Figure 1(b) shows the dimensionless thermoelectric figure of merit (ZT) for pure $Bi_{0.5}Sb_{1.5}Te_3$ and for the composites as function of temperature. It can be observed that ZT values of all composites increase with increasing temperature to reach a maximum value and then to decrease with further increase in temperature. Moreover, the ZT values significantly increased with the incorporation of VO_2 nanoparticles and it is notable that there is a good agreement between the experimentally determined ZT values and our calculations of $VO_2/Bi_{0.5}Sb_{1.5}Te_3$ composites for f = 29.4% VO_2. The low ZT values of composites at low temperatures is a consequence of changes that

VO_2 undergoes for both thermal and electrical properties. Nevertheless, the composite with f = 34.0% exhibited a maximum ZT value of ~0.7 at 375 K, which is around 10% higher than that of BST matrix. For higher temperatures, the figure of merit values showed a significant improvement of around 20% compared with pure $Bi_{0.5}Sb_{1.5}Te_3$. Thus, this improvement is primarily due to the enhancement of the electrical conductivity and reduction in thermal conductivity.

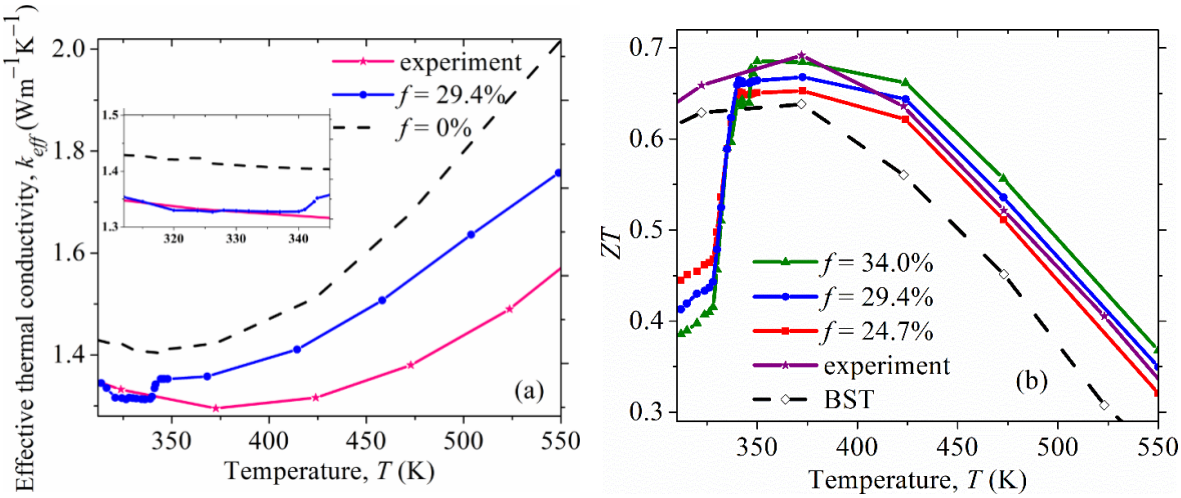

Fig. 1. (a) Comparison between the temperature dependence of the thermal conductivity of the experimental results and our simulations. **(b)** Comparison between the ZT calculated values and the experiment [7]

Conclusions – The thermoelectric properties of $VO_2/Bi_{0.5}Sb_{1.5}Te_3$ composites with volume fractions of 0, 24.7%, 29.4% and 34.0% have been investigated across the metal-insulator transition of VO_2 and for temperatures up to 550 K, by means of simulations based on Finite Element Methods. We have shown that VO_2 nanoparticles with a concentration of 34.0% enhance the electrical conductivity by approximately 16% for temperatures higher than 350 K. The resulting maximum value of ZT = 0.7 shows up at 375 K, which represents an increase of 10% in comparison with the corresponding one of the matrix.

References

[1] M. Gatti, F. Bruneval, V. Olevano, L. Reining, Understanding Correlations in Vanadium Dioxide from First Principles, Phys. Rev. Lett., 99 (2007) 266402.

[2] G.R. Khan, B. Ahmad, Effect of quantum confinement on thermoelectric properties of vanadium dioxide nanofilms, Appl. Phys. A, 123 (2017) 1.

[3] K.S. Karimov, M. Mahroof-Tahir, M. Saleem, M.T.S. Chani, A.K. Niaz, Temperature sensor based on composite film of vanadium complex (VO2(3-fl)) and CNT, J. Semicond., 36 (2015) 73004.

[4] A. Paone, M. Joly, R. Sanjines, A. Romanyuk, J.-L. Scartezzini, A. Schüler, Thermochromic films of VO2:W for smart solar energy applications, in Opt. Model. Meas. Sol. Energy Syst. III (International Society for Optics and Photonics, (2009) 74100F.

[5] I.Y. Forero-Sandoval, J.A. Chan-Espinoza, J. Ordonez-Miranda, J.J. Alvarado-Gil, F. Dumas-Bouchiat, C. Champeaux, K. Joulain, Y. Ezzahri, J. Drevillon, C.L. Gomez-Heredia, VO2 Substrate Effect on the Thermal Rectification of a Far-Field Radiative Diode, Phys. Rev. Appl., 14 (2020) 34023.

[6] I. Kosta, C. Navone, A. Bianchin, E. García-Lecina, H. Grande, H.I. Mouko, J. Azpeitia, I. García, Influence of vanadium oxides nanoparticles on thermoelectric properties of an N-type $Mg_2Si_{0.888}Sn_{0.1}Sb_{0.012}$ alloy, J. Alloys

Compd., 856 (2021) 158069.

[7] S.Y. Back, J.H. Yun, H. Cho, G. Kim, J.-S. Rhyee, Materials (Basel), Phonon Scattering and Suppression of Bipolar Effect in MgO/VO2 Nanoparticle Dispersed p-Type $Bi_{0.5}Sb_{1.5}Te_3$ Composites, 14 (2021) 2506.

[8] F.J. Morin, Oxides Which Show a Metal-to-Insulator Transition at the Neel Temperature, Phys. Rev. Lett., 3, (1959) 34.

[9] J. Ordonez-Miranda, Y. Ezzahri, K. Joulain, J. Drevillon, J.J. Alvarado-Gil, Modeling of the electrical conductivity, thermal conductivity, and specific heat capacity of VO2, Phys. Rev. B, 98 (2018) 1.

[10] L. Wang, L. Zhao, Z. Jiang, G. Luo, P. Yang, X. Han, X. Li, R. Maeda, Effect of the Metal–Insulator Transition on the Thermoelectric Properties of Composites Based on $Bi_{0.5}Sb_{1.5}Te_3$ with VO_2 Nanoparticles, AIP Adv., 9 (2019) 95067.

[11] S. Alvarez-Guerrero, J. Ordonez-Miranda, R. de Coss, and J.J. Alvarado-Gil, Effect of the Metal–Insulator Transition on the Thermoelectric Properties of Composites Based on $Bi_{0.5}Sb_{1.5}Te_3$ with VO_2 Nanoparticles, Int. J. Therm. Sci., 172 (2022) 107278.

Effect of mesoporous cerium oxide nanofluids on the thermal conductivity

Montes de Oca LM[(1)*], Borjas-García SE[(1)], Vargas Correa AJ[(2)], Alvarado-Gil JJ[(3)], Martínez-Torres P[(1)]

(1) Institute of Physics and Mathematics, Universidad Michoacana de San Nicolás de Hidalgo, Edificio C-3, Ciudad Universitaria, 58040 Morelia, Michoacán, Mexico
(2) Facultad de Ciencias Físico-Matemáticas, Universidad Michoacana de San Nicolás de Hidalgo, Edificio xxx, Ciudad Universitaria
(3) Department of Applied Physics, Cinvestav-Unidad Mérida, Carretera Antigua a Progreso, Km. 6, 97310 Mérida, Yucatán, Mexico

*Corresponding author's email: luismontesdeocafis@gmail.com

Nanofluids are suspensions formed by a liquid matrix, containing nanoparticles as a dispersed phase. There is a high interest in the study of the thermal properties of nanofluids due to their applications in the thermal energy storage or heat dissipation of electronic devices. To enhance and control the thermal properties of the nanofluids, nanoparticles like alumina, diamond, silver, gold, among others have been used [1]. It is known that the thermal conductivity of nanofluids depends upon the concentration and the collective aggregation of nanoparticles, even though, several factors remain misunderstood, such as the effect of size and porosity of nanoparticles. In this work, we used the thermal wave resonator cavity (TWRC) technique to obtain the thermal diffusivity of nanofluids loaded with cerium oxide mesoporous nanoparticles [2,3]. We also used mathematical effective thermal models to study the effect of these parameters.

Mesoporous cerium oxide nanoparticles were synthesized by the sol-gel method with a soft hydrothermal treatment. In a typical sample preparation, two solutions were prepared, the first one was obtained by dissolving 0.05 mol cerium chloride heptahydrated and 0.02 milimol of Pluronic F127 in 5 grs of distilled water (S1). The second solution was obtained by dissolving 0.04 mol sodium hydroxide in 4 grs of distilled water (S2). Later the two solutions were mixed, S2 was added slowly to S1, which was kept under constant stirring at 350 rpm at room temperature while S2 was added. Once S2 was added to S1, the xerogel obtained was stirred around 60 rpm for 24 h inside closed flask with cap at room temperature. The molar ratio was precursor: surfactant: NaOH: H2O = 1: 0.004: 8: 100. Subsequently, the xerogel was hydrothermally treated in static condition at 80 °C, for 24 h. After hydrothermal treatment, the sample was washed with distilled water and centrifuged. Finally, the resulting material was dried at 80 °C for 24 h. The powders were calcinated at 560 °C for 1 h to eliminate organic waste. Critical synthesis parameters such us amount of alkaline material, surfactant, temperatures of synthesis and hydrothermal treatment were changed in order to get better surface area and mesoporosity in samples.

The TWRC technique was used to determine the thermal diffusivity of the nanoparticle suspensions as is described in reference [4]. In this technique, the liquid sample is heated at a fixed frequency by a modulated laser diode. The signal of the modulated laser is driven by a Lock-in amplifier. The temperature changes are detected by a pyroelectric sensor that is connected to a lock-in amplifier, used to read the amplitude and phase of the signal as the length of the cavity varies. Under the thermally thick regime, it is possible to estimate the complex voltage of the pyroelectric sensor, as was measured

by the Lock-in amplifier, using the following equation [5]:

$$V(L,\alpha,f) = F(f)e^{-L(i+1)/\sqrt{\pi f\alpha}} \qquad \text{Eqn. 1}$$

where *F(f)* is a transfer function that depends on the modulation frequency of the thermal wave.

Plots of ln(voltage) and phase versus length can be obtained. From Eqn. 1, the amplitude is $ln|V| = C_V - \sqrt{\pi f\alpha}$L and the phase is $\varphi = C_\varphi - \sqrt{\pi f\alpha}L$, both equations follow a linear behaviour. Therefore, from the slopes m_V and m_φ of the experimental data, the thermal diffusivity of the samples is determined by

$$\alpha = \frac{\pi f}{m_V^2} \text{ and } \alpha = \frac{\pi f}{m_\varphi^2} \qquad \text{Eqn. 2}$$

References

[1] B. Bakthavatchalam, K. Habib, R. Saidur, B.B. Saha, K. Irshad, Comprehensive study on nanofluid and ionanofluid for heat transfer enhancement: A review on current and future perspective, J. Mol. Liq, 305 (2020) 112787. https://doi.org/10.1016/j.molliq.2020.112787.

[2] A. Taghizadeh, M. Taghizadeh, M. Azimi, A.S. Alsagri, A.A. Alrobaian, M. Afrand, Influence of cerium oxide nanoparticles on thermal conductivity of antifreeze: Preparation and stability of nanofluid using surfactant, J. Therm. Anal. Calorim, 139:1 (2020) 225–236. https://doi.org/10.1007/s10973-019-08422-2.

[3] Y. Yan, M. Li, S. King, T. Galy, M. Marszewski, J.S. Kang, L. Pilon, Y. Hu, S.H. Tolbert. Controlling Thermal Conductivity in Mesoporous Silica Films Using Pore Size and Nanoscale Architecture, J. Phys. Chem. Lett, 11:9 (2020) 3731–3737. https://doi.org/10.1021/acs.jpclett.0c00464.

[4] J. Shen, A. Mandelis, Thermal-wave resonator cavity, Rev. Sci. Instrum, 66:10 (1995) 4999–5005.

[5] C. Vales-Pinzon, D. Gonzalez-Medina, J. Tapia, M.A. Zambrano-Arjona, J.A. Mendez-Gamboa, R.A. Medina-Esquivel, Thermal diffusivity of compounds loaded with carbon nanofibers, Int J Thermophys. 39:7 (2018) 1–10.

Thermal characterization of natural clay using photothermal radiometry technique for thermal insulation applications

Venegas-Montaño HM(1), Montes-de-oca LM(2), Cervantes-Alvarez F(3), Alvarado-Gil JJ(3), Domínguez-Almaraz GM(1), Martínez-Torres P(2)

(1) Faculty of Mechanical engineering, Universidad Michoacana de San Nicolás de Hidalgo, W building, Ciudad Universitaria, 58040, Morelia, Michoacán, México

(2) Institute of Physics and Mathematics, Universidad Michoacana de San Nicolás de Hidalgo, C-3 building, Ciudad Universitaria, 58040 Morelia, Michoacán, México

(3) Department of Applied Physics, Cinvestav-Unidad Mérida, Carretera Antigua a Progreso, km. 6, 97310 Mérida, Yucatán, México

*Corresponding author's email: 0468633k@umich.mx

Clay is a natural powder material that is constituted by granular mineral capable of becoming ceramic once it receives a heating treatment. It has been used as a building material in different communities in Mexico. Properties of clay mostly depend on the composition and minerals of the ground in the area where is recollected [1]. In this work, we study the thermal properties of natural clay ceramics to be used as thermal insulator material [2]. The clay from the Mexican village of Tlalpujahua, Michocán, México was chosen because in that area there is an abundant amount of clay, as well as their rich historical tradition making handcrafts and artistic figures. Under this motivation, determining the thermal properties of clay is of paramount importance [3]. These properties depend on the mineral composition and porosity caused during the thermal treatment [4]. In this study, clay was thermally treated at different temperatures (500, 750, 1000 °C) to obtain the thermal diffusivity using infrared photothermal radiometry.

The Photothermal Radiometry technique was used to determine the thermal properties of the samples in the forward emission configuration (see Fig. 1). A modulated laser at frequency was sent directly to the aluminum foil-clay. As a result of the laser heating, thermal waves were generated in the clay, which emits periodic radiation. The radiation emitted by the clay was collected by two parabolic mirrors and focused on an infrared detector (PVI-4 TE-6 VIGO System S.A.) The signal captured by the infrared sensor was sent to a lock-in amplifier (Stanford Research System SR830) and the amplitude and phase are recorded in function of frequency by the computer. The thermal-wave field at the back surface of the clay is given by [5]:

$$T(l_{AL}+l_C)=\frac{2\eta(1-R)I_0}{\sigma_{AL}k_{AL}+\sigma_C k_C}\left[\frac{e^{-\sigma_{AL}l_{AL}}e^{-\sigma_C l_C}}{1+g\left(e^{-2\sigma_C l_C}-e^{-2\sigma_{AL}l_{AL}}\right)-e^{-2\sigma_C l_C}e^{-2\sigma_{AL}l_{AL}}}\right], \quad \text{Eqn. 1}$$

where the clay´s thickness is l_C, thermal diffusivity is α_C, thermal conductivity is k_C and thermal effusivity is e_C. The aluminium foil thickness is l_{AL} with thermal diffusivity α_{AL}, thermal conductivity k_{AL} and effusivity e_{AL}. I_0 is the intensity of the incident light, η is the efficiency of the conversion from optical to thermal energy, R is the optical reflection coefficient at the wavelegth of the ligth source, and $g=\frac{e_{AL}-e_C}{e_{AL}+e_C}$. The thermal diffusion length of the clay is given by $\sigma_C=(1+i)/\mu_C$ with $\mu_C=\sqrt{\alpha_C/\pi f}$,

in the same way $\sigma_{AL} = (1+i)/\mu_{AL}$ with $\mu_{AL} = \sqrt{\alpha_{AL}/\pi f}$ the thermal diffusion length of the aluminium.

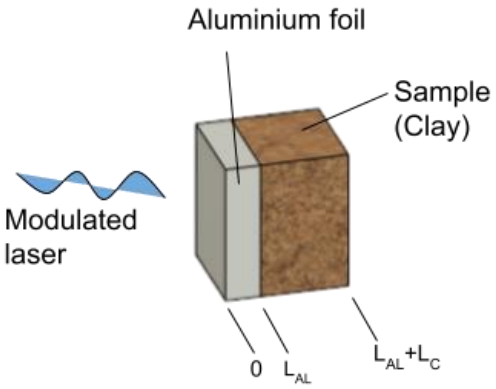

Fig. 1. Schematic of sample to be measured in the transmission configuration.

References

[1] T. Buchner et al. A multitechnique, quantitative characterization of the pore space of fired bricks made of five clayey raw materials used in European brick industry" Applied Clay Science 200 (2021) 105884. https://doi.org/10.1016/j.clay.2020.105884.

[2] D.V. Voronin et al. Clay composites for thermal energy storage: A review. Molecules 25.7 (2020) 1504. https://doi.org/10.3390/molecules25071504.

[3] P.-M. Nigay, et al. Structure and properties of clay ceramics for thermal energy storage.Journal of the American Ceramic Society 100.10 (2017) 4748-4759. https://doi.org/10.1111/jace.15014.

[4] M. Kubiś, et al. "On the anisotropy of thermal conductivity in ceramic bricks. Journal of Building Engineering 31 (2020): 101418. https://doi.org/10.1016/j.jobe.2020.101418.

[5] P. Martínez-Torres, A. Mandelis, J.J. Alvarado-Gil. Photothermal determination of thermal diffusivity and polymerization depth profiles of polymerized dental resins. Journal of Applied Physics 106.11 (2009) 114906. https://doi.org/10.1063/1.3266007.

Thermal characterization of emulsions stabilized by Sodium Dodecyl Sulfate

Ceja-Morales M[(1)*], Montes-de-Oca LM[(1)], Martínez-Torres P [(1)], Alvarado-Gil JJ[(2)]

(1) Institute of Physics and Mathematics, Universidad Michoacana de San Nicolás de Hidalgo, C-3 building, Ciudad Universitaria, 58040 Morelia, Michoacán, México
(2) Department of Applied Physics, Cinvestav-Unidad Mérida, Carretera Antigua a Progreso, km. 6, 97310 Mérida, Yucatán, México

*Corresponding author's email: miguel.ceja@umich.mx

Emulsions are systems formed by drops of one liquid phase, suspended in another continuum phase immiscible to the dispersed phase. Emulsions are of great interest in food, cosmetics, and drug delivery, due to their ability to encapsulate and store molecules of biological interest inside the suspended drops. As emulsions are metastable systems, their lifetime depends upon factors as the bulk viscosity, interfacial tension and elasticity between phases and interfacial viscosity; size of drops and densities are also important [1]. Despite the numerous applications which emulsions have, the mechanisms of destabilization are still poorly understood. Therefore, development of new ways of characterization is required.

Photothermal techniques have been used successfully for the study of nanofluids, conformed by solid nanoparticles suspended in a liquid matrix [2]. In particular, the thermal wave resonant cavity (TWRC) technique together with the use of mathematical effective media thermal models has proven to be a good approach for the study of thermal transport across these colloidal systems. In this work, we propose the use of the (TWRC) technique for characterization of emulsions with different drop sizes and volume fractions of the dispersed phase.

The emulsions were prepared using olive oil as the organic phase and a solution of deionized water containing 200 mM of sodium dodecyl sulfate (SDS) anionic surfactant as the aqueous phase. The emulsification was reached, first by stirring at 200 rpm with a drip between 3 s to 5 s, then it is mixed at 300 rpm during 30 min at room temperature to do the drop size homogeneous [3]. Fresh emulsions were observed after the emulsion formation under bright field optical microscopy. The mean diameter of the emulsion drops was obtained using the image processing software ImageJ.

The thermal wave resonator cavity (TWRC) is a technique to determine thermal properties of fluid samples. This technique is based on the study of the thermal wave behavior, which is generated by a modulated laser beam, and is propagated through the material and monitored with a sensor [4]. Using the heat diffusion equation, it is possible determine the thermal properties of the fluids based in the thickness of the samples.

Fig. 1 shows the water/oil emulsions obtained by stirring. On left side it shows the emulsions of two volume fractions of oil and on the right side are observed the emulsion drops using an optical microscope.

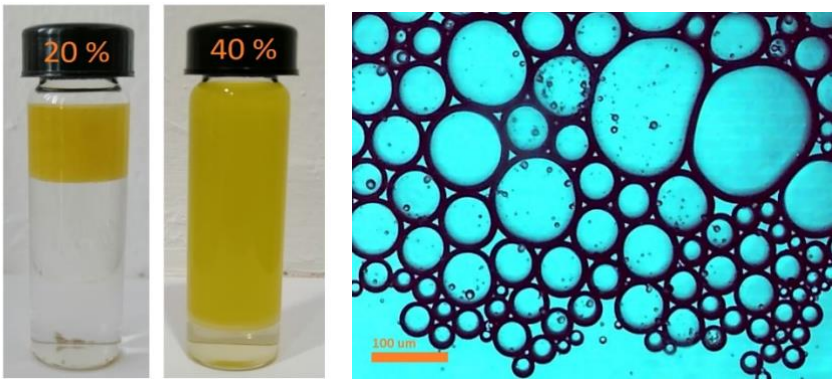

Fig. 1. Left: emulsion of water in oil at different oil volume fractions. Right: emulsion under bright field microscopy. Scale bar is 100 µm

Results for thermal diffusivity are shown in table 1. It shows thermal diffusivity of continuum phase fluid of SDS and olive oil. Effective thermal conductivity models are used to analyse the behaviour of the emulsion as the concentration is change.

Table 1. Thermal diffusivity of the phase fluid SDS and oil.

Fluid	**Thermal diffusivity [m^2 s^{-1}]**
SDS	1.350
Olive Oil	0.884

References

[1] J. Sjöblom, P. Stenius, S. Simon, B.A. Grimes. Emulsion Stabilization. In: Tadros T. (eds) Encyclopedia of Colloid and Interface Sci. Springer, Berlin, Heidelberg (2013). https://doi.org/10.1007/978-3-642-20665-8_83.

[2] R.A. Medina-Esquivel, C. Vales-Pinzon, G. Quiñones-Weiss, M.A. Zambrano-Arjona, J.A. Mendez-Gamboa, C. Cab, J. J. Alvarado-Gil, Thermal conductivity of a diamond magnetite composite fluid under the effect of a uniform magnetic field, Diamond and Related Materials, 53 (2015) 45–51. https://doi.org/10.1016/j.diamond.2015.01.008.

[3] M.C. Vlachou, K.A. Zacharias, M. Kostoglou, T.D. Karapantsios, Droplet size distributions derived from evolution of oil fraction during phase separation of oil-in-water emulsions tracked by electrical impedance spectroscopy, Colloids and Surfaces A: Physicochemical and Engineering Aspects, 586 (2020) 124292, https://doi.org/10.1016/j.colsurfa.2019.124292.

[4] J.A. Balderas-Lopez, A. Mandelis, J.A. Garcia, Thermal-wave resonator cavity design and measurements of the thermal diffusivity of liquids, Review of Scientific Instruments, 71:7 (2000) 2933-2937. https://doi.org/10.1063/1.1150713.

UV light-induced thermal and optical properties of functionalized polymers with strong push-pull azo chromophores in side chain

Trefon-Radziejewska D[(1)*], Juszczyk J[(1)], Pawlak M[(2)], Mikaeeli A[(2,3)], Chatterjee A[(2,3)], Opilski Z[(4)], Hamaoui G[(5)], Smokal V[(6)], Krupka O[(6)], Jukam N [(3)], Wieck A[(3)], Derkowska-Zielińska B[(2)]

(1) Institute of Physics Center for Science and Education, Silesian University of Technology, Konarskiego 22B, 44-100 Gliwice, Poland
(2) Institute of Physics, Faculty of Physics, Astronomy and Informatics, Nicolaus Copernicus University in Torun, Grudziadzka 5, 87-100 Torun, Poland
(3) Chair of Applied Solid-State Physics, Experimental Physics VI, Ruhr-University Bochum, Universitaetsstrasse 150, D-44780 Bochum, Germany
(4) Department of Optoelectronics, Silesian University of Technology, Konarskiego 22B, 44-100 Gliwice, Poland
(5) ESYCOM UMR 9007, Université Gustave Eiffel, CNRS, CNAM, F-77454 Marne-la-Vallée, France
(6) Taras Shevchenko National University of Kyiv, 64/13 Volodymyrska St., 01601, Kyiv, Ukraine

*Corresponding author's email: Dominika.Trefon@polsl.pl

Aminoazobenze (B2) and pseudostilbene-type (B1, B3-B5) azobenzene polymer thin films were deposited on glass substrates by spin coating. The azo polymers were thermally and optically investigated in their two isomeric forms: trans and cis. First, scanning thermal microscopy (SThM) and photothermal radiometry (PTR) were used for thermal conductivity (κ) examination of azo polymers in trans state. Spectroscopic ellipsometry (SE) was used to obtain transmittance spectra (T). Azo polymers were then illuminated with UV light of 405 nm and 300 mW/cm2 for 100 min while successive T were recorded. Hereby, different optical dynamics of trans-cis isomerization for investigated azo polymers were observed. The B1-B3, and B5 samples are characterized by a long return time to the trans state (weeks). In contrast the B4 sample has a return time of approximately 1 hour. Once more κ was determined using SThM in cis phase. Additionally, for B4 azo polymer, thermal conductivity dynamics along the trans-cis-trans transition were followed. We observed a decrease of the κ value (by 44%, 39%, 28%, 21%, 25% for B1-B5, respectively) between the cis and trans state for all investigated azo polymers. The differences in optical and thermal properties changes, induced by UV illumination, between particular azo polymers can be attributed to the different substituents in their polymeric system, as well as the type of charge transport according to the type of azobenzene (amino or pseudostilbene). Additionally, atomic force microscopy (AFM) was used to examine and compare the surface topography of azo polymers in the trans and cis state.

Simultaneous reconstruction of density and thermal conductivity depth profiles in sintered metal powder compacts using a novel inverse thermal-wave method

Kooshki S[(1)], Melnikov A[(1)], Mandelis A[(1)*]

(1) Center for Advanced Diffusion-Wave and Photoacoustic Technologies (CADIPT), Department of Mechanical and Industrial Engineering, University of Toronto, Toronto, Ontario M5S 3G8, Canada
(2) Institute for Advanced Non-Destructive and Non-Invasive Diagnostic Technologies (IANDIT), University of Toronto, Ontario M5S 3G8, Canada

*Corresponding author's email: mandelis@mie.utoronto.ca

An inverse method is proposed to determine simultaneous density and thermal conductivity depth profiles in a general inhomogeneous solid. A novel integral-equation based solution for thermal-wave boundary value problems is introduced combined with a 2-stage iterative inverse algorithm to reconstruct both thermal conductivity and density depth profiles as expansions of judiciously selected continuous depth functions with several unknown parameters.

Introduction – Historically, many research reports have been presented for the reconstruction of thermophysical properties of inhomogeneous materials using inverse algorithms and numerical methods [1-4]. Unlike the foregoing single property reconstructions to-date, the novelty of the current work is in the simultaneous reconstruction of *both* density and thermal conductivity from the measurement of amplitude and phase of the modulated surface temperature vs. frequency.

Methodology – The proposed inverse method which is based on photothermal frequency scans of depth inhomogeneous metal powder compacts used in automotive manufacturing, was coupled with the depth-variable thermal-wave field model and applied in two stages. In the first stage, an initial guess for the thermal conductivity depth profile was assumed and the density depth profile was expanded in a bounded series of depth-continuous basis functions with several unknown parameters using a simple inverse analysis based on the global Competitive Imperialist Algorithm (CIA) [5]**.** In the second stage, the unknown thermal conductivity distribution was considered as an independent expansion in a series of depth-continuous functions, also with several unknown parameters. Reconstruction of these unknown parameters was done using the results obtained in the first stage and by another inverse analysis based on CIA. This 2-stage inverse algorithm was repeated while the reconstructed parameters at each stage were used as known parameters for the next stage. The iteration of the 2-stage inverse algorithm continued until the absolute value of differences between the reconstructed parameters from two iterations of the 2-stage inverse algorithm was smaller than the desired tolerance to which unknowns were calculated.

Results and Discussion – Reconstruction of density and thermal conductivity depth profiles was performed using a sintered metal powder compact sample with known near-surface density inhomogeneity and measuring the amplitude and phase of the surface thermal-wave field detected with the MCT detector of a conventional photothermal radiometry system [1]. The measured amplitude and phase of the thermal-wave signal vs. frequency are plotted in Fig. 1. The amplitude response in Fig. 1 was normalized to the independently measured amplitude response of the homogeneous solid bulk using

homogeneous semi-infinite thermal-wave theory [6]. Fig 2(a) indicates that the reconstructed density curve decays to a constant – bulk – value as expected from the analysis. Fig. 2(b) shows the near-surface reconstructed density depth profile along with the actual independently measured density depth profile. Fig. 2(c) shows the simultaneously reconstructed thermal conductivity depth profile, an essentially constant value equal to the bulk thermal conductivity. The inverse algorithm in Fig. 2(b) very closely reconstructed the measured density depth profile. All Fig. 2 profiles were obtained after 6 iterations of the 2-stage inverse algorithm.

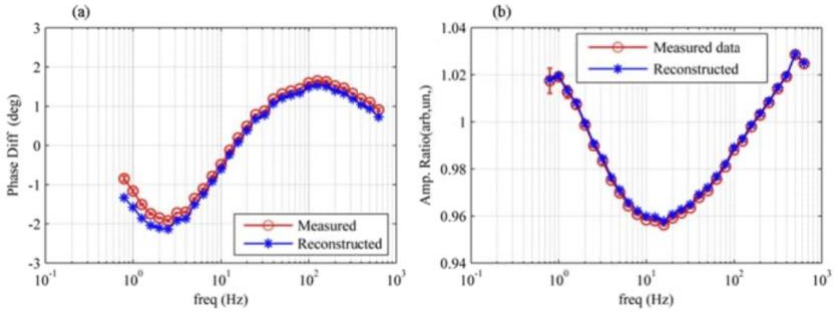

Fig. 1. Experimental frequency data, **(a)** reconstructed phase difference and **(b)** amplitude ratio, both normalized to the bulk substrate frequency response.

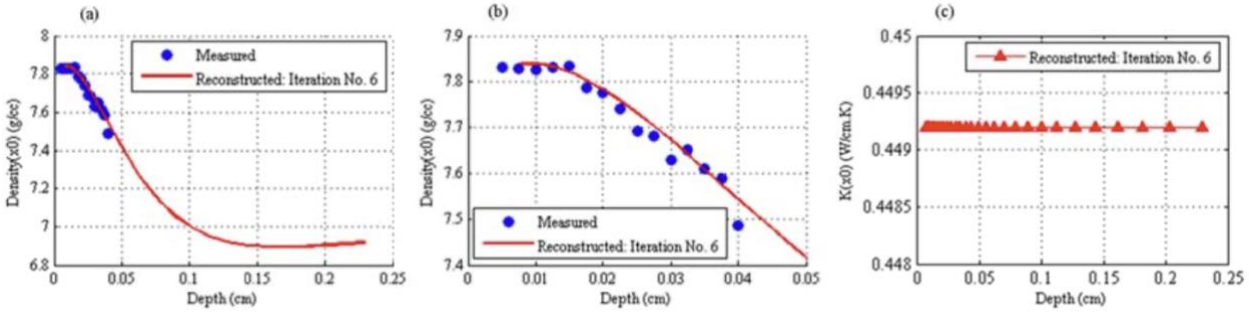

Fig. 2. Reconstructed density profile and the actual measured density data and the reconstructed thermal conductivity profile: **(a)** the much deeper profile; **(b)** the shallow depth profile; **(c)**: the reconstructed thermal conductivity profile

Conclusions – An inverse method was developed based on an integral equation representation of the inhomogeneous thermal-wave boundary-value problem which was subsequently used with a 2-stage inverse algorithm. This methodology connects the frequency scan data (amplitude and phase) with the unknown density and thermal conductivity depth profiles. Simultaneous reconstruction is an advantage of this methodology in comparison with other inverse thermal-wave problems developed to-date. This method was applied to non-destructive, non-contacting reconstruction of density and thermal conductivity depth profiles of a sintered automotive manufacturing part.

References

[1] M. Munidasa, F. Funak, A. Mandelis, Perspective on non-invasive and non-destructive photoacoustic and photothermal applications, J. Appl. Phys. 83:7 (1998) 3495-3498.

[2] S. Kooshki, A. Mandelis, A. Khodadad et al., Determination of thermophysical properties and density volume fractions of Al2O3/Y-ZrO2 layered composite materials using transient thermography and two-stage inverse nonlinear heat conduction analysis, J. Appl. Phys. 127:4 (2020) 045110.

[3] T.T.N. Lan, U. Seidel, H.G. Walther, Theory of microstructure depth profiling by photothermal measurements, J. Appl. Phys. 77(9) (1995) 4739-4745.

[4] T.T.N. Lan, U. Seidel, H.G. Walther, G. Goch, B Schmitz, Experimental Results of Photothermal Microstructural Depth Profiling, J. Appl. Phys.78:6 (1995) 4108-4111.

[5] E. Atashpaz-Gargari, C. Lucas, Imperialist competitive algorithm: An algorithm for optimization inspired by imperialistic competition, in 2007 IEEE Congress on Evolutionary Computation, IEEE (2007) 4661-4667.

[6] A. Mandelis, Chap. 2: Thermal-Wave Fields in One Dimension, Diffusion-Wave Fields, Springer, New York (2001).

02
Materials Research and Characterization

Photothermal techniques for 3D printing polymer characterization

Luna-Sánchez, JL[(1)], Jiménez-Pérez J[(1)*], García-Vidal UO [(1)], Cruz-Orea A[(2)], Macías-Mier M[(2)], López-Gamboa G[(3)], Pérez-González M[(4)]

(1) Unidad Profesional Interdisciplinaria en Ingeniería y Tecnologías Avanzadas. Instituto Politécnico Nacional. 07340 México City, México
(2) Physics Departament, CINVESTAV-IPN, AP 14-740, 07360 Mexico City, Mexico
(3) Universidad Politécnica del Valle de Toluca, 50904, Estado de México, Mexico.
(4) Área Académica de Matemáticas y Física, Instituto de Ciencias Básicas y de Ingeniería, Universidad Autónoma del Estado de Hidalgo, 42184, Hidalgo, México.

*Corresponding author's email: jimenezp@fis.cinvestav.mx

Background – Additive Manufacture (AM), also called 3D printing (3DP), includes several technologies that have raised great expectation because it could reduce costs and time to produce prototypes and single pieces. Despite such expectations few organizations have used it and still less have incorporated it into its chain of production [1]. The wide variety in materials, printer models and technologies make standardization a slow process that most investors would desire to be better defined before they could incorporate 3DP to their processes. A concern common to every AM process is to use standardized polymer and assure its quality to minimize the variation due to raw materials in the printing process. Photothermal techniques offer great analytical advantages as high sensibility and accurateness, at a low cost to characterize the polymers used in 3D printing; due to its easy implementation, non-destructive techniques, low cost instruments and easy interpretation they can be incorporated to an economic plan. As an example, in that research, we explored the application of Photoacoustic Spectroscopy (PA) and Thermal Lens Spectroscopy (TL) to thermally characterize nanocompounded acrylic resins.

Methods – Round Silver nanoparticles (AgNPs) with 15.7 nm average diameter synthesized by a green method [2], and Silver nanowires (AgNWs) with 150 x 50 nm average length x transversal diameter synthesized by the Polyol Method [3], were dispersed into a liquid Acrylic resin at 4 x 10^{-6} to 20 x 10^{-6} vol % to conform two different nanocomposites series. Essential characterization techniques as TEM, SEM, FTIR, and UV-vis were used to characterize separately AgNPs, AgNWs and resin's morphology, physical and chemical aspects. A TL experimental setup in a mismatched configuration [4] was used to determine the liquid sample's Thermal Diffusivity (D), and, PA in an Open Cell (OPC) configuration [2] was used to determine the nanocomposite's Characteristic Curing Time (τ).

Results – Thermal Diffusivity (D) tested by TL resulted in similar trends between the two nanocomposites series, with AgNPs and with AgNWs as showed in Fig. 1 (A). Slight differences were found in the variation range from0 to 50 x 10^{-4} (cm/s). In contrast, the Characteristic Curing Time (τ) tested by PA-OPC resulted in two different trends that unambiguously indicates us if the tested sample belongs to AgNWs or AgNPs series; the samples containing AgNPs ranged from 20 to 60 s while the samples containing AgNWs ranged from 480 to 1650 s; such difference is theoretically assigned to the difference in filler´s shape.

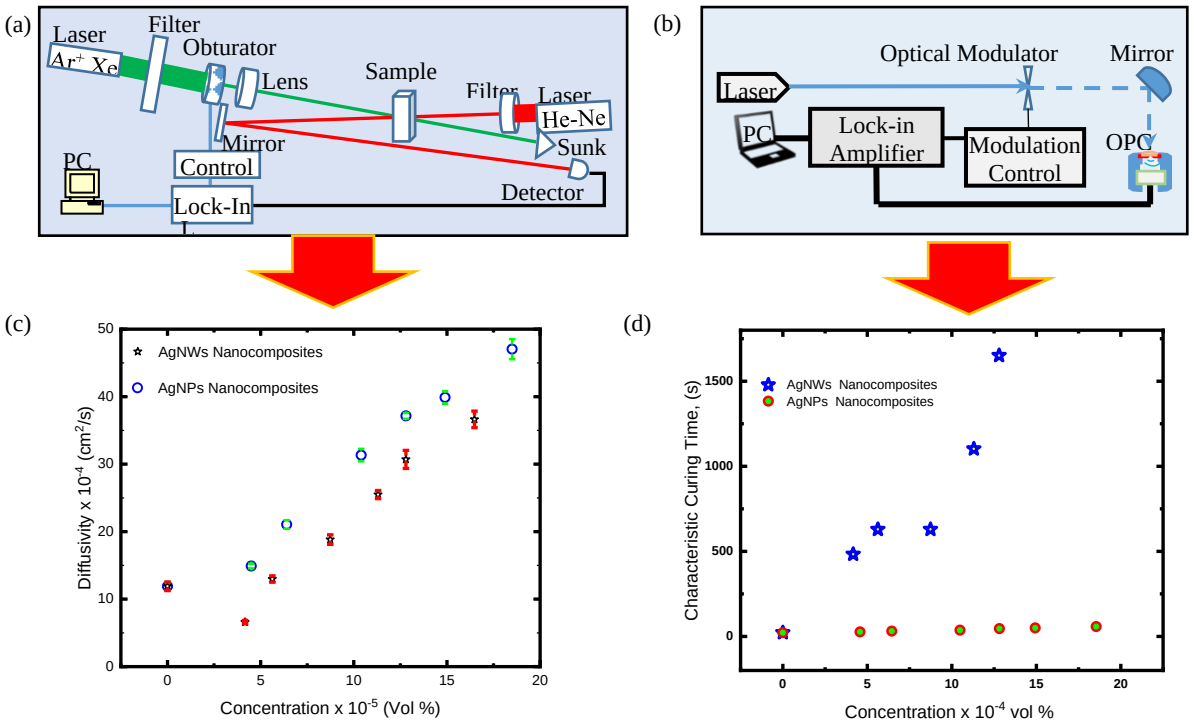

Fig. 1. (a) Thermal Lens experimental set up. (b) Photoacoustic Spectroscopy Open Cell experimental set up. (c) Thermal Diffusivity of nanocomposites by TL technique. (d) Characteristic Curing Time of nanocomposites by PA-OPC technique. Concentration ranged from 4 x 10^{-6} to 25 x 10^{-6} vol % of AgNPs and AgNWs.

Conclusions – PA-OPC and TL are reliable techniques whose accuracy can differentiate among samples having small differences in their components' concentration. The performed tests showed sensitivity to nanometrical differences in the filler's structure. The optical elements used to set up the experimental array can be found as ordinary elements in a physics laboratory and they don't require special environments or supplies. Photothermal techniques can help minimize variation in 3DP process revealing subtle differences in polymers that could be originated by the manufacture process, storage environmental conditions or aging.

References

[1] J. Ding et al., The economics of additive manufacturing: Towards a general cost model including process failure, Int. J. Production Economics, 237 (2021) 108087. https://doi.org/10.1016/j.ijpe.2021.108087.

[2] J.L. Luna-Sánchez et al., Green synthesis of silver nanoparticles using Jalapeño Chili extract and thermal lens study of acrylic resin nanocomposites, Thermochimica Acta, 678 (2019) 178314. https://doi.org/10.1016/j.tca.2019.178314.

[3] R. Carvajal-Valdes, Experimental investigation on thermal properties of Ag nanowires nanofluids at low concentrations, Thermochimica Acta, 671 (2019) 83-88. https://doi.org/10.1016/j.tca.2018.11.015.

[4] B. Stephen E. Bialkowski, Photothermal Spectroscopy Methods for Chemical Analysis, Wiley-Interscience (1995).

[5] S. Manohar, D. Razansky, Photoacoustics: a historical review, Advances in Optics and Photonics, 8(4) (2016). http://dx.doi.org/10.1364/AOP.8.000586.

Photothermal characterization of polyester composites loaded with parallelly arranged graphite rods

Aguilar-Jimenez JA[(1)*], Pech-May NW[(2)], Forereo-Sandoval IY[(3)], Alonzo-Zapata IA[(4)], Ordonez-Miranda J[(3)], Alvarado-Gil JJ[(1)]

(1) Deparment of Applied physics, CINVESTAV Mérida, Yucatán, México
(2) Bundesanstalt für Materialforschung und -prüfung (BAM), Berlin, Germany
(3) Institut Pprime, CNRS, Université de Poitiers, ISAE-ENSMA Futuroscope Chasseneuil, France
(4) Université de Limoges, CNRS, IRCER, UMR 7315, F-87000, Limoges, France

Corresponding author's email: arturo.aguilar@cinvestav.mx

Background – One of the most important techniques to measure thermal diffusivity is front flash developed by Parker et al. [1]. But in order to perform a complete thermal caracterization of a material it is necessary to find two important thermal properties, thermal diffusivity (D) and thermal effusivity (e). It is possible to find the thermal conductivity of the material using a simple relation $e = K/\sqrt{D}$ [2]. Composite materials are always of great interest as they provide improvements in the thermal and mechanical properties of simple materials. Composites with fillers in a resin matrix have been studied by several authors, showing how oriented fillers can improve thermal diffusivity of the composite [3,4].

In this work we present results of how graphite rods can help to improve the thermal properties of a polymeric resin and whether the the arrangement of the rods within the resin has any influence.

Methods – The polyester matrix used was an unsaturated polyester resin elaborated by Plastic Polyforms S.A. The graphite rods were loaded in the matrix resin orientated in the thickness direction with concentrations of 4.31% (m30), 5.75% (m40), 7.81% (m50) and 8.62% (m60) v/v. Additionally, the rods inside the matrix were placed in three different configurations for each graphite concentration, polygonal, rectangular, radial (figure 1). Those composites were compared with a composite with the same v/v concentration, but the graphite inside the resin was powdered and randomly arranged.

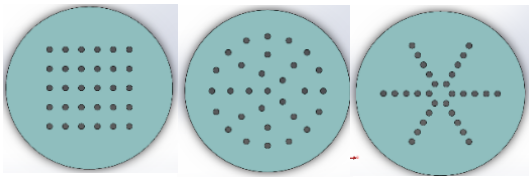

Fig. 1. Composites schematic for 4.31% v/v (m30) with the graphite rods in three different configurations. Rectangular (left), radial (center) and polygonal (right).

A two-layer system was used to create a thermal contrast to find thermal effusivity and thermal diffusivity of the samples. Composites of 1 mm thickness were used as a first layer and water as a semi-infinite fluid backing. Using the approach of Pech et al [5] in Laplace space, the thermal properties were determined using the front flash thermography.

$$T(0) = \frac{P_0 \chi}{e_1 \sqrt{s}} \frac{cosh(x\sqrt{s}) + b_{21} sinh(x\sqrt{s})}{\left(b_{21} + \frac{h_p}{\sqrt{s}}\right) cosh(x\sqrt{s}) + \left(1 + \frac{h_p b_{21}}{\sqrt{s}}\right) sinh(x\sqrt{s})}; \qquad b_{21} = \frac{e_2}{e_1}; \quad x = \frac{L}{\alpha} \qquad \text{Eqn. 1}$$

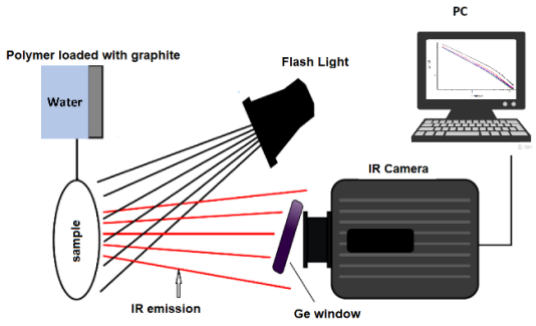

Fig. 2. Experimental setup

Results and Conclusions – Our results indicate that samples loaded with the same graphite concentration as we can see in figure 3 (left) present different thermal decays for samples with graphite with powder in random arrangement compared with composites with graphite rods, which present similar behaviour and the configuration has significative effects in thermal decays. On the other hand, figure 3 (right) present thermal decays for several graphite concentrations for polygonal configuration where it is possible to notice that there is a region where the increase of thermal properties stops due to a possible graphite saturation.

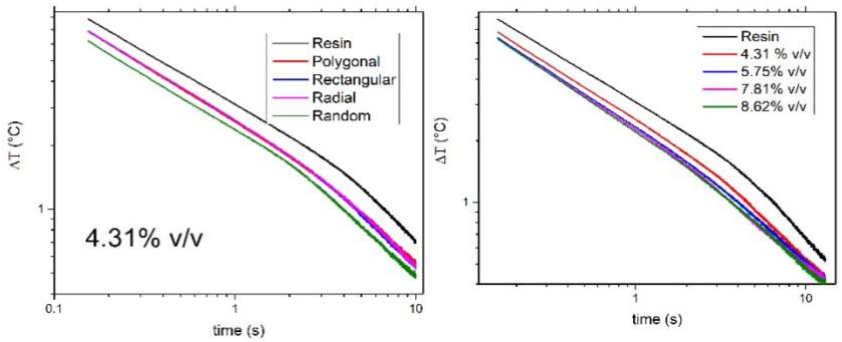

Fig. 3. Thermal decay for composites with 4.31 % v/v graphite concentration with different configurations (left) and composites with polygonal configuration changing the graphite concentration from 4.31 to 8.62 % v/v (right).

References

[1] W.J Parker, R. J. Jenkins, C.P. Butler, G.L. Abbott. Flash method of determining thermal diffusivity, heat capacity, and thermal conductivity, J. appl. Phys. 32 (1961) 1679.

[2] A. Salazar, On thermal diffusivity, Eur. J. Phys. 24:2 (2003) 351–358.

[3] R.A. Medina-Esquivel, M.A. Zambrano-Arjona, J.A. Mendez-Gamboa, J.M. Yanez-Limon, J. Ordonez-Miranda, J.J. Alvarado-Gil, Thermal characterization of composites made up of magnetically aligned carbonyl iron particles in a polyester resin matrix. J. Appl. Phys. 111, 054906 (2012).

[4] N.W. Pech-May, C. Vales-Pinzon, A. Vega-Flick, A. Cifuentes, A. Oleaga, A. Salazar, J.J. Alvarado-Gil, Study of the thermal properties of polyester composites loaded with oriented carbon nanofibers using the front-face flash method. Polymer Testing 50 (2016) 255-261.

[5] N.W. Pech-May, A. Cifuentes, A. Mendloroz, A. Oleaga, A. Salazar, Simultaneous measurement of thermal diffusivity and effusivity of solids using the flash technique in the front-face configuration. Measurement Science and Technology 26 (2015).

Evaluation of optical and acoustical properties of $Ba_{1-x}Sr_xTiO_3$ material library by a multi-technique approach including picosecond laser ultrasonics

Sathyan S[(1)*], Raetz S[(1)*], Wolfman J [(2)], Negulescu B[(2)], Liu G[(2),†], Longuet J-L [(3)], Thréard T[(1)], Gusev VE[(1)*]

(1) Laboratoire d'Acoustique de l'Université du Mans (LAUM), UMR 6613, Institut d'Acoustique – Graduate School (IA-GS), CNRS, Le Mans Université, Le Mans 72085, France
(2) Laboratoire GREMAN, UMR CNRS 7347, Université de Tours, INSA CVL, Parc de Grandmont, 37200, Tours, France
(3) CEA, DAM, Le Ripault, 37260 Monts, France
† Current address: School of Physical Science and Technology, Suzhou University of Science and Technology, Suzhou 215009, China

* Corresponding authors' email: sandeep.sathyan@univ-lemans.fr, samuel.raetz@univ-lemans.fr, vitali.goussev@univ-lemans.fr

Background – Materials with graded chemical composition have diverse applications, such as laterally graded aperiodic crystals based on $Si_{1-x}Ge_x$ used for radiation path control in high-resolution X-ray monochromators and the out-of-plane graded bandgap semiconductors to improve solar energy harvesting. When films with continuously varying chemical composition are prepared for particular applications via epitaxial growth, their local physical parameters are generally different from bulk materials of the same chemical composition. So, the continuous spatial variation of the materials composition requires developing a high throughput measurement technique to locally and non-destructively characterize the library with high spatial resolution. The typical experimental methods used to examine such material systems are the energy or wavelength dispersive X-ray spectroscopy, high-resolution X-ray diffraction, and Raman spectroscopy/microscopy. However, optical, acoustical, and acousto-optical parameters have never been evaluated in vertical or lateral compositionally graded films. In this work, we report on the first application of the picosecond laser ultrasonics (PLU) technique for the evaluation of acoustical and optical parameters of lateral compositionally graded film, the $Ba_{1-x}Sr_xTiO_3$ ($0 \leq x \leq 1$) material library [1], denominated BST-x for short in the following.

Methods – An epitaxial 250 nm-thick BST-x ($0 \leq x \leq 1$) continuous composition spread film library was prepared by combinatorial pulsed laser deposition onto a (001) $SrTiO_3$ 1 cm^2 substrate buffered by a 120 nm-thick $La_{0.9}Sr_{1.1}NiO_4$ electrode. The lateral composition of the BST-x film was characterized by EDS and WDS. Opaque $La_{0.9}Sr_{1.1}NiO_4$ film served as an optoacoustic transducer for launching CAPs in BST-x coating, which was transparent at optical wavelengths of 354, 517, and 535 nm of our laser pulses. We implemented PLU with a fast data acquisition technique based on asynchronous optical sampling.

Results and Conclusions – We demonstrated an application of PLU in combination with XRD, EDS, EPMA, SEM and AFM for the measurements of the dependencies on x of the optical refractive index n and of the sound velocity v in an epitaxially grown thin film BST-x library (Fig. 1). We applied new

protocol for modeling and fitting the PLU signals, which accounts for the significant roughness of the film surface revealed by AFM measurements. The film was not dedicatedly prepared for its opto-acousto-optic evaluation by PLU, exhibiting significant lateral variations in thickness and surface roughness. Therefore, the achieved measurements of the sound velocity and of the optical refractive index, and characterization of the surface roughness confirm the robustness of the PLU technique for thin film evaluation. Our results on the acoustical and optical properties of epitaxial grown BST-*x* library layer by PLU technique accomplished here could provide the parameters required for more extended predictive design of the phononic, photonic and phoxonic mirrors and cavities with superior properties/functionalities for novel multifunctional nanodevices.

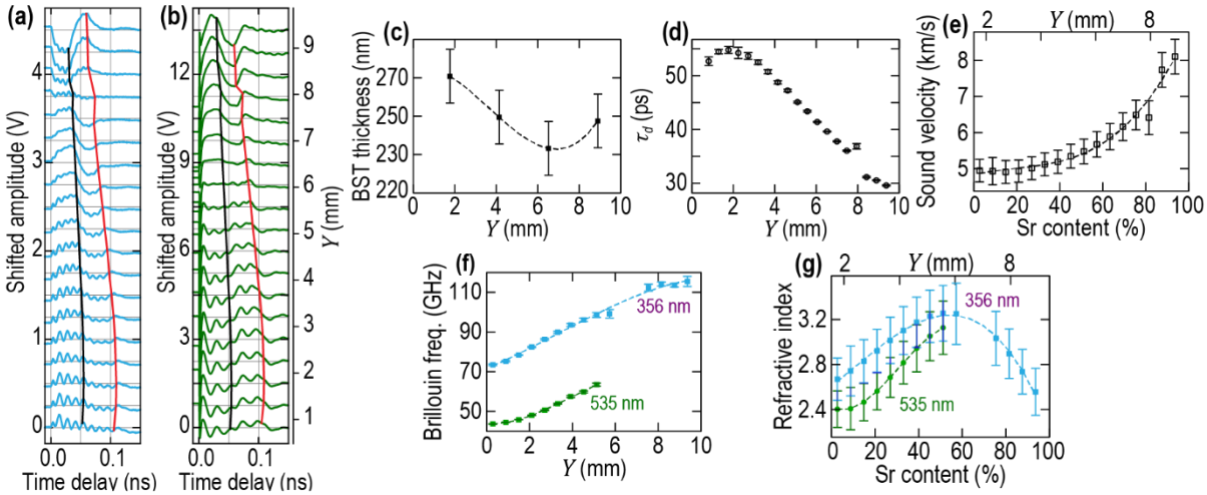

Fig. 1. **(a,b)** Raw transient reflectivity signals detected at different lateral positions of the BST-*x* library using 517 nm pump and either (a) 354 nm or (b) 535 nm probe. The black (red) solid lines connecting the raw signals vertically stand for the CAP arrival times at the free surface of the BST-*x* library layer (at the surface between the BST-*x* library layer and the OAT). **(c)** BST-*x* library thickness as a function of the position along the graded direction. **(d)** Time-of-flight of the acoustic wave propagating from the generator surface through the BST-*x* layer to its free surface estimated using the fitting procedure. **(e)** Sound velocity in the BST-*x* library as a function of the Sr content (bottom horizontal axis) and the position along the graded direction (top horizontal axis) estimated from the data in (c, d). **(f)** Brillouin frequencies as a function of the position along the graded direction. (g) Refractive index in the BST-*x* library as a function of the Sr content (bottom horizontal axis) and the position along the graded direction (top horizontal axis) estimated from the data in (e, f)

Acknowledgments – This research is supported by the Agence Nationale de la Recherche (project ANR-18-CE42-I2T2M).

References

[1] S. Sandeep, S. Raetz, J. Wolfman, B. Negulescu, G. Liu, J.-L. Longuet, T. Thréard, V.E. Gusev, Evaluation of Optical and Acoustical Properties of $Ba_{1-x}Sr_xTiO_3$ Thin Film Material Library via Conjugation of Picosecond Laser Ultrasonics with X-ray Diffraction, Energy Dispersive Spectroscopy, Electron Probe Micro Analysis, Scanning Electron and Atomic Force Microscopies, Nanomaterials, 11 (2021) 3131. https://doi.org/10.3390/nano11113131.

Thermal, mechanical and optical characterization of calcium caseinate biopolymers with borax as crosslinking agent

Franco-Bacca AP[(1)], Cervantes-Alvarez F[(1)*], Becerra ME[(2)], Ávila AC[(2)], Giraldo Osorio O[(3)], Arias NP[(4)], Rodríguez-Gattorno G[(1)*], J. J. Alvarado-Gil G[(1)*]

(1) Departamento de Física Aplicada, Cinvestav-Unidad Mérida, Carretera Antigua a Progreso Km. 6, Mérida, Yucatán, México, 97310, México
(2) Departamento de Ingeniería Química, Facultad de Ingeniería y Arquitectura, Universidad Nacional de Colombia-Sede Manizales, Kilómetro 9 vía al aeropuerto, La Nubia, Manizales 170003, Colombia
(3) Departamento de Física y Química, Facultad de Ciencias Exactas y Naturales, Universidad Nacional de Colombia-Sede Manizales, Kilómetro 9 vía al aeropuerto, La Nubia, Manizales 170003, Colombia
(4) Facultad de Ingeniería, Universidad de Sucre, Carrera 28 No. 5–267, Sincelejo 70003, Sucre, Colombia

*Corresponding authors' emails: fernando.cervantes@cinvestav.mx, geonelr@cinvestav.mx, juan.alvarado@cinvestav.mx

Calcium caseinate is a low-cost and biocompatible protein. Calcium caseinate biofilms show suitable mechanical properties, and they are helpful as a barrier to protect food from oxygen, slowing down its degradation. This study is aimed to characterize calcium caseinate biodegradable films by adding borax at different concentrations to improve their physical properties. The results of the thermal diffusivity, measured with photothermal radiometry, showed that the increase in borax concentration favors thermal transport until reaching a saturation point at 1.40% volume fraction concentration. The mechanical properties, tested with a mechanic stress machine, do not show a significant increase for borax concentrations greater than 1.00% volume fraction. Additionally, UV-Vis spectroscopy showed that the addition of borax increases the percentage of transmitted light. These results open the possibility of using biodegradable films of calcium caseinate with borax added as material packaging to extend shelf life and quality of perishables, maintaining their quality, in specially those which must be kept in refrigeration and protected them from microbial contamination, delaying their deterioration.

References

[1] M.P. Arrieta, M.A. Peltzer, M.D.C Garrigós, A. Jiménez, Structure and mechanical properties of sodium and calcium caseinate edible active films with carvacrol. J. Food Eng. 114 (2013) 486–494. doi:10.1016/j.jfoodeng.2012.09.002.

[2] L. Vermeiren, F. Devlieghere, M. Van Beest, N. De Kruijf, J. Debevere, Developments in the active packaging of foods. Trends Food Sci. Technol. 10 (1999) 77–86. doi:10.1016/S0924-2244(99)00032-1.

[3] M.A. Zambrano-Arjona, R. Medina-Esquivel, J:J Alvarado-Gil, Photothermal radiometry monitoring of light curing in resins. J. Phys. D. Appl. Phys. 40 (2007) 6098–6104. doi:10.1088/0022-3727/40/19/050.

[4] M. Rodríguez, J. Osés, K. Ziani, J:I Maté, Combined effect of plasticizers and surfactants on the physical properties of starch based edible films. Food Res. Int. 39 (2006) 840–846. doi:10.1016/j.foodres.2006.04.002.

[5] A. Jiménez, M:J: Fabra, P. Talens, A. Chiralt, Effect of sodium caseinate on properties and ageing behaviour of corn starch based films. Food Hydrocoll. 29 (2012) 265–271. doi:10.1016/j.foodhyd.2012.03.014.

[6] P.L.M Barreto, A:T:N Pires, V. Soldi, Thermal degradation of edible films based on milk proteins and gelatin

in inert atmosphere. Polym. Degrad. Stab. 79 (2003) 147–152. doi:10.1016/S0141-3910(02)00267-7.

[7] P- Mariana, P.; M.I. Aranguren, N.E. Marcovich, Characterization of Chitosan/Caseinate Films. J. Appl. Polym. Sci. 116 (2007) 2658–2667. doi:10.1002/app.27052.

[8] I.Y. Elbeyli, Production of crystalline boric acid and sodium citrate from borax decahydrate. Hydrometallurgy 158 (2015) 19–26, doi:10.1016/j.hydromet.2015.09.022.

[9] D.W. Zhuang, H. Dai, Bin, P. Wang, Hydrogen generation from solvolysis of sodium borohydride in ethylene glycol-water mixtures over a wide range of temperature. RSC Adv. 3 (2013) 23810–23815. doi:10.1039/c3ra43136c.

[10] S. Geng, F:U: Shah, P. Liu, O.N. Antzutkin, K. Oksman, Plasticizing and crosslinking effects of borate additives on the structure and properties of poly(vinyl acetate). RSC Adv. 7 (2017) 7483–7491. doi:10.1039/c6ra28574k.

[11] M. Schou, A. Longares, C. Montesinos-Herrero, F.J. Monahan, D. O'Riordan, M. O'Sullivan, Properties of edible sodium caseinate films and their application as food wrapping. LWT - Food Sci. Technol. 38 (2005) 605–610, doi:10.1016/j.lwt.2004.08.009.

[12] N.W. Pech-May, C. Vales-Pinzón, A. Vega-Flick, Á. Cifuentes, A. Oleaga, A. Salazar, J.J Alvarado-Gil, Study of the thermal properties of polyester composites loaded with oriented carbon nanofibers using the front-face flash method. Polym. Test. 50 (2016) 255–261. doi:10.1016/j.polymertesting.2015.12.011.

[13] C. Huang, X. Qian, R. Yang, Thermal conductivity of polymers and polymer nanocomposites. Mater. Sci. Eng. R Reports, 132 (2018) 1–22. doi:10.1016/j.mser.2018.06.002.

[14] U. Manna, S. Patil, Borax mediated layer-by-layer self-assembly of neutral poly(vinyl alcohol) and chitosan. J. Phys. Chem. B 113 (2009) 9137–9142. doi:10.1021/jp9025333.

Double and multiple pump pulse time-domain thermoreflectance measurements

Chatterjee A[(1,2)*], Mikaeeli A[(1,2)], Jukam N[(2)], Wieck AD[(2)] , Pawlak M[(1)]

(1) Institute of Physics, Faculty of Physics, Astronomy and Informatics, Nicolaus Copernicus University inTorun, Grudziądzka 5, 78-100 Torun, Poland

(2) Chair of Applied Solid State Physics, Experimental Physics VI, Ruhr-University Bochum, Universitätsstrasse 150, 44780 Bochum, Germany

*Corresponding author's email: connecttoankur94@doktorant.umk.pl

Measurements of the thermal conductivity of thin layers can be performed using techniques such as photothermal radiometry [1], the 3-omega method [2], frequency domain thermoreflectance (FDTR) measurements [3] and time-domain thermoreflectance (TDTR) measurements [4]. TDTR measurements are performed with femtosecond lasers and thus have the potential to measure heat transport across the thinnest layers which take place on fast times scales. In the frequency-domain short times scales correspond to high frequencies. The diffusion length (or penetration) depth of the thermal waves in FDTR is proportional to the square root of the inverse modulation frequency. For maximum sensitivity the diffusion length should be on the order of the length of the layer. FDTR thus has an advantage since the modulation frequency can be adjusted to maximise sensitivity. However for TDTR measurements, a wide frequency bandwidth is present.

In this contribution we numerically investigate double and multiple pump TDTR measurements. Double pump femtosecond pulses can be produced with a single beam splitter while multiple femtosecond pulses can be produced using femtosecond pulse shaping techniques [5]. If the time delay between two consecutive femtosecond pulses is varied, the composite spectrum of any system response will also be varied [6]. For thin layers the sensitivity of thermal conductivity measured with double and multiple femtosecond laser pulses is compared with traditional single pump-pulse TDTR measurements.

References

[1] M. Pawlak et al., Measurement of thermal transport properties of selected superlattice and thin films using frequency-domain photothermal infrared radiometry, Measurement 166 (2020) 108226. https://doi.org/10.1016/j.measurement.2020.108226.

[2] D.G. Cahill, Thermal conductivity measurement from 30 to 750 K: the 3ω method, Rev. of Sc. Instr. 61 (1990) 802. https://doi.org/10.1063/1.1141498.

[3] A.J. Schmidt, R. Cheaito, M. Chiesa, A frequency-domain thermoreflectance method for the characterization of thermal properties, Rev. Sci. Instr. 80 (2009) 094901. https://doi.org/10.1063/1.3212673.

[4] P. Jiang, X. Qian, R. Yanga, Tutorial: Time-domain thermoreflectance (TDTR) for thermal property characterization of bulk and thin film materials, J. Appl. Phys. Lett. 124 (2018) 161103. https://doi.org/10.1063/1.5046944

[5] A.M. Weiner, Femtosecond pulse shaping using spatial light modulators, Rev. Sci. Instr. 71 (2000) 1929. https://doi.org/10.1063/1.1150614.

[6] S. Markmann et al., Spectral modification of the laser emission of a terahertz quantum cascade laser induced by broad-band double pulse injection seeding Appl. Phys. Lett. 107 (2015) 111103. https://doi.org/10.1063/1.4930993.

Infrared emissivity of vanadium dioxide thin films coated on cotton fabrics

Misano M(1), Agharahimli K(1), Larciprete M(1), Cesarini G(1), Sibilia C(1), Ballesio G(2), Li Voti R(1)*

(1) Department of Science Based Applications for Engineering, Sapienza Università di Roma, Via Antonio Scarpa 16, 00161 Rome, Italy
(2) Ballesio Fratelli srl - Via Domodossola n.19, 10145 Torino, Italy

*Corresponding author's email: roberto.livoti@uniroma1.it

In the last years there has been an increasing interest in the realization and characterization of innovative smart textiles for several applications such as thermal radiation control as well as infrared (IR) radiation manipulation. Their promising properties, such as flexibility, light weight and cost effectiveness, enable the realization of smart, adaptive clothes. However, component materials, fiber-woven characteristics and structure are important factors affecting the thermal physical properties of the resulting textile [1-4].

Vanadium dioxide of monoclinic structure VO_2 is regarded as the most important and promising material, since it exhibits phase transition at the temperature T_C=68 °C, with dramatic changes of optical properties in the IR range. Below the transition temperature, monoclinic VO_2 is a semiconductor, while above T_c, it switches to metallic state with a rutile structure [5]. Such a phase transition is fully reversible and associated with dramatic changes in electrical, magnetic and optical properties [6-8]. Therefore, with such properties, VO_2 can be considered as a promising candidate for a variety of potential applications such as energy efficient window coatings [9], thermal sensors [10], cathode materials for reversible lithium batteries [11], electrical and infrared light switching device [12-14]. However, there were few reports about the infrared stealth property of VO_2 in the literatures. Among them, Guinneton pointed out there was a fall of 60% in normal integrated emissivity of VO_2 thin film between 8 and 12 μm, which made it possible to be a kind of potential material for infrared stealth [6,7,15-17]. The adaptive infrared camouflage property of VO_2 coated fabric was reported in several recent scientific papers [18]. Results showed that infrared emissivity in the range 8–12 μm of 300 □m VO_2 coated fabric decreases by only about 0.1 during the phase transition. In this paper we wish to study, optimize and experimentally measure the infrared emissivity dynamic range of vanadium dioxide thinner films on cotton fabrics.

Different solutions of VO_2 powder with polyurethane (PU) have been prepared with several concentrations. The solution has been deposited with a blade and spread homogeneously on the fabric. Subsequently, by applying hot air on the sample, the cotton fabric is brought to the maximum temperature of 90/100 °C for a few seconds and then kept at the constant temperature of 60 °C for 5 minutes, so to allow the PU polymerization and drying. Optical images show the homogeneity of a thin coating of about 40□m over a large area at macroscopic range.

The infrared stealth performance was investigated by Infrared Thermography in the infrared range 8 - 14 μm, and in the temperature range from 40 °C to 80 °C. The thickness of the dry vanadium dioxide coating is around 40 μm, that is enough to produce a measurable change of the emissivity properties of the cotton fabric.

The infrared emissivity of the pure cotton (without vanadium dioxide) is ε=0.86, and temperature independent. On the contrary the coated sample exhibits a lower emissivity ε=0.82 already at room temperature (20 – 40 °C), with a drastic decrease to ε=0.72 at 80 °C, after the vanadium dioxide phase transition to metallic state.

The infrared properties of the coated fabric samples at a macroscopic scale have been tested again by infrared thermography in the range 8-14 □m. The samples have been placed in thermal contact with a suitable heater with a Peltier temperature control system so to produce continuous heating/cooling cycles from 40 °C to 80 °C with a quasi-static temperature scan of 1°C /min.

Thermal infrared images of coated fabric after undergoing several cycles of heating and cooling process has been used to test the excellent durability of vanadium dioxide phase transformation. The apparent temperature taken by the thermal infrared images together with the real temperature measured by the thermocouples, are processed so to obtain the emissivity map of the coated textiles.

These preliminary results opens a new strategy to design, optimize smart textiles using the natural infrared stealth property of VO_2 so to manipulate the infrared emission and the infrared signature of large size objects.

References

[1] M.C. Larciprete, S. Paoloni, R. Li Voti, Y.S. Gloy, C. Sibilia, Int. J. Therm.Sci. 132 (2018) 168.

[2] M.C. Larciprete, Y.S. Gloy, R. Li Voti, G. Cesarini, G. Leahu, M. Bertolotti, C. Sibilia, C. International Journal of Thermal Sciences 113 (2017) 130.

[3] M.C. Larciprete, M. Centini, R. Voti, C. Sibilia, C. J. Opt. Soc. Am. B: 34 (2017) 1459.

[4] M.C. Larciprete, M. Centini, R. Voti, M. Bertolotti, C. Sibilia, Appl. Phys. A: Mat. Sci. Proc. 122 (2016) 343.

[5] F.J. Morin, Phys. Rev. Lett. 3 (1959) 34.

[6] F. Guinneton, L. Sauques, J.C. Valmalette, F. Cros, J.R. Gavarri, J. Phys. Chem. Solids 66 (2005) 63.

[7] F. Guinneton, L. Sauques, J.C. Valmalette, F. Cros, J.R. Gavarri, J. Phys. Chem. Solids 62 (2001) 1229.

[8] J. Livage, Coord. Chem. Rev. 391 (1999) 190.

[9] G. Xu, C.M. Huang, P. Jin, M. Tazawa, D.M. Chen, J. Appl. Phys. 104 (2008) 053101.

[10] C. Sella, M. Maaza, O. Nemraoui, J. Lafait, N. Renard, Y. Sampeur, Surf. Coat. Technol. 98 (1998) 1477.

[11] J. Ni, W.T. Jiang, K. Yu, Y.F. Gao, Z.Q. Zhu, Electrochim. Acta 56 (2011) 2122.

[12] Cesca, T., Scian, C., Petronijevic, E., Leahu, G., Li Voti, R., Cesarini, G., Macaluso, R., Mosca, M., Sibilia, C., Mattei, G., Nanoscale 12 (2020) 851.

[13] R. Li Voti, M.C. Larciprete, G.L. Leahu, C. Sibilia, M. Bertolotti, J. Appl. Phys. 112 (2012) 034305.

[14] R. Li Voti, M.C. Larciprete, G. Leahu, C. Sibilia, M. Bertolotti, Journal of Nanophotonics 6 (2012) 061601.

[15] G. Cesarini et al International Journal of Thermal Sciences 146 (2019) 106061.

[16] G. Cesarini et al, Infrared Physics and Technology 93 (2018) 112.

[17] R. Li Voti, G. L. Leahu, M. C. Larciprete, C. Sibilia, M. Bertolotti, Int J Thermophys, 36 (2015) 1004.

[18] Z. Mao, W. Wang, Y. Liu, L. Zhang, H. Xu, Y. Zhong, Thin Solid Films 558 (2014) 208.

Characterization of multilayered drug delivery systems for orthopedic implants by beam deflection spectrometry

Budasheva H(1), Korte D(1), Bračič M(2), Finšgar M(2), Franko F(1)*

(1) University of Nova Gorica, Laboratory for environmental and life sciences, 5000 Nova Gorica, Slovenia

(2) University of Maribor, Faculty of chemistry and chemical engineering, 2000 Maribor, Slovenia

*Mladen.Franko@ung.si

Advances in transplantation surgery lead to a significant increase in the use of implantable medical components to replace the hips, knees, some spinal joints etc. The most commonly used materials for orthopedic purposes are titanium alloys, different ceramics, and stainless steel. Such materials must be biocompatible with body tissues and fluids, be able to withstand wear and corrosion, exhibit similar mechanical properties as bone, etc. To fulfil all these requirements, they need a deposition of a coating loaded with special combination of drugs. Among the coatings of interest, the polysaccharide-based systems were found to be the most promising regarding the enhancement of implant compatibility and functionality [1, 2]. They are used to construct a sophisticated drug delivery system (DDS) that delivers drug to the target tissue in a controlled way [3]. This leads to enhancement of patient compliance, drug efficiency and reduces the side effects of drugs.

In this study the smart drug delivery device was constructed by the use of the layer-by-layer (LbL) technology that forms multilayered systems of tailored architecture and with a high level of control of drug usage [4]. The multilayered structures (Fig. 1) consist of hyaluronic acid (HA), amoxicillin (AX) and fucoidan (FU) layers that are deposited on a medical grade stainless AISI 316LVM type support (MSS).

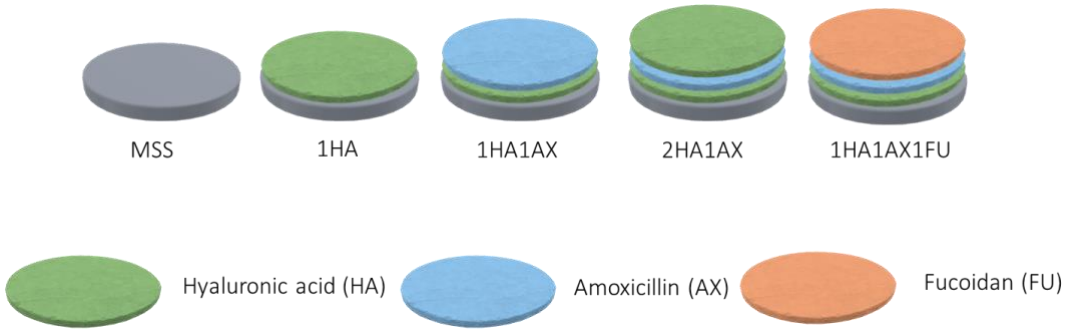

Fig. 1. Structure of examined multilayered drug delivery system.

Such systems require the development of new techniques for their characterization that provide high quality control, precision, sensitivity and reproducibility, as well as proper chemical and structural characterization of the examined materials, which includes the determination of their physical properties. The characterization of such polysaccharide multilayered structures was performed by the use of photothermal beam deflection spectrometry (BDS). It was based on monitoring the changes in

thermal parameters of different layers of the system to obtain information about the structure of sub-surface microlayers, as well as changes in concentration of pharmaceutical compounds in the layers.

In the BDS an intensity modulated excitation beam (EB) of light illuminates the surface of an absorbing sample [5]. As a result of nonradiative deexcitation processes the absorbed light is converted into heat that diffuses into the sample and into the adjacent medium generating periodic temperature disturbance, i.e., the thermal waves (thermal oscillations – TOs). TOs further cause changes in the refractive index of the medium in which they are induced. The resulting refractive index gradients in turn affect the propagation of the probe beam (PB) passing through the adjacent medium while grazing the sample surface. The BDS signal contains information about the thermal parameters (thermal diffusivity and conductivity) of the examined sample, which are governed by the chemical composition and structural characteristics (thickness, porosity, surface roughness) of the sample.

The results of this work show that substantial diffusion of AX into HA as well as FU occurs. It is demonstrated as the decrease of the thermal properties within the diffusion layer. This observation is possible because of the large difference in the thermal properties of AX ($D = 0.036\ mm^2s^{-1}$) as compared to HA ($D = 0.078\ mm^2s^{-1}$) and FU ($D = 0.106\ mm^2s^{-1}$), which are the consequence of larger relative proportion of carboxylic groups in HA as compared to AX, while FU contains sulfonic acid groups. All these functional groups contribute to higher polarity of chemical compounds present in the coatings. Higher polarity is in turn related to higher values of thermal parameters, as it was also confirmed experimentally [6].

It can be concluded from the changes in thermal parameters that after doping AX diffuses into the HA, while a similar process occurs also after deposition of the second HA layer or the FU layer on top of the AX layer. Diffusion of AX extends 18-19 μm into the initial HA layer, while the diffusion into the second HA or FU layer is slightly shorter (16 μm). At the same time, as could be expected, the thickness of the layer dominated by the thermal properties of AX in 2HA1AX and 1HA1AX1FU samples is reduced as compared to 1HA1AX sample. The change in concentration of AX with distance is however not linear, but a gradient of AX concentration within HA and FU layers can be predicted, since the distance required for the same change in D values becomes longer and longer in direction of layers which contain no AX.

References

[1] L.S. Liu, M.L. Fishman, K.B. Hicks, Pectin in controlled drug delivery - A review. Cellulose (2007) https://doi.org/10.1007/s10570-006-9095-7.

[2] G. Horvat, K. Xhanari, M. Finšgar, L. Gradišnik, U. Maver, Z. Knez., Z. Novak, Novel ethanol-induced pectin–xanthan aerogel coatings for orthopedic applications. Carbohydr. Polym. (2017) https://doi.org/10.1016/j.carbpol.2017.03.008.

[3] J. Rojo, A. Sousa-Herves, A. Mascaraque, Perspectives of Carbohydrates in Drug Discovery. Compr. Med. Chem. III, 1 (2017) 1-8.

[4] C. Vilela, A.R.P. Figueiredo, A.J.D. Silvestre, C.S.R Freire. Multilayered materials based on biopolymers as drug delivery systems. Expert Opin. Drug. Deliv. (2017) https://doi.org/10.1080/17425247.2016.1214568.

[5] D. Korte, M. Franko. Application of complex geometrical optics to determination of thermal, transport, and optical parameters of thin films by the photothermal beam deflection technique. J. Opt. Soc. Am. A (2015) https://doi.org/10.1364/josaa.32.000061.

[6] M. Franko, C.D. Tran. Thermal lens effect in electrolyte and surfactant media. J. Phys. Chem. 95 (1991) 6688-6696.

Analysis of SiO_2 and $BaSO_4$ leachates from dental composites by thermal lens spectrometry

Korte D[(1)*], Jereb V[(2)*], Franko M[(1)]

(1) University of Nova Gorica, Laboratory for environmental and life sciences, 5000 Nova Gorica, Slovenia
(2) Polident d.o.o., 5293 Volčja Draga, Slovenia

* Corresponding authors' email: Dorota.Korte@ung.si, Vesna.Jereb@polident.si

Nowadays ceramics and resin-based dental composites containing micro (MPs) and nanoparticles (NPs) are used for restoring dental caries or other defects instead of conventional alloys due to the improved mechanical properties (strength, toughness, surface hardness, durability) of the whole matrix. This is of high importance especially in the case of large area restorations [1, 2]. Furthermore, resin-based dental composites are the most popular restorative materials and are mainly composed of a resin polymeric matrix, inorganic filler particles and silane coupling agents [3]. In the present study, the inorganic filler in the resin-based composite is microsized SiO_2 with traces of nanosized SiO_2. Additionally, the resin-based material contains small amounts (a few tenths of a percent) of nanosized $BaSO_4$ used as a functional additive during production. Incorporation of these two components in dental materials introduces the oral route of exposure for these NMs. Their absorption in the gastrointestinal tract may be high due to their small particle size causing histopathological changes in liver and kidneys or alterations in blood parameters [4]. Furthermore, oral uptake of SiO_2 and $BaSO_4$ NPs from dental materials is likely to occur at low doses over long periods of time leading to their accumulation in body tissues [5]. Thus, monitoring of their leachates requires highly sensitive detection techniques.

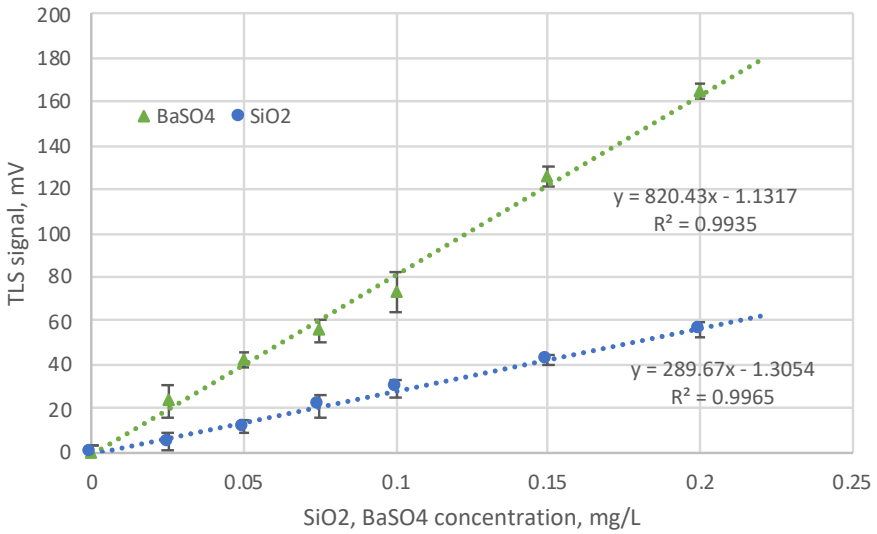

Fig. 1. Calibration curves used in the study for SiO_2 and $BaSO_4$ determination.

In the present study, thermal lens spectrometry (TLS) is applied for the determination of the amount of SiO_2 and $BaSO_4$ NPs released from artificial teeth under chewing simulation. TLS is based on probing the temperature rise in illuminated samples that induce related changes in their properties (refractive

index, density etc.), which are a result of non-radiative relaxation of the energy absorbed from an excitation laser beam [6]. SiO_2 and $BaSO_4$ determination was performed by the use of the calibration curve presented in Fig. 1.

The obtained LOD for SiO_2 and $BaSO_4$ determination was 30 and 10 ppb, respectively, whereas RSDs were between 1-5% indicating the high sensitivity and good reproducibility of the method.

Table 1. Values of SiO_2 and $BaSO_4$ leachates from resin-based dental composite obtained in the study.

Sample no.	SiO_2/ppb	$BaSO_4$/ppb
D1	31	ND*
L1	28	ND
D2	36	9
L2	33	7

*not detected

It was found that the release of SiO_2 from the designed resin-based composites is at the level of LOD of the detection method, whereas $BaSO_4$ under LOD. It can be also stated that the designed resin-based composites that contain SiO_2 MPs and NPs are promising dental materials with improved mechanical properties such as enhanced hardness and scratch resistance, since they do not release SiO_2 or $BaSO_4$ NPs from artificial teeth under long term chewing simulation. Thus, such materials seem to be an excellent choice as dental resins especially in cases of large area restoration where the mechanical stresses under use are of large value.

References

[1] Y. Liu, Y. Sun, F. Zeng, X. Weili, Y. Liu, L. Geng, Effect of nano SiO_2 particles on the morphology and mechanical properties of POSS nanocomposite dental resins, J. Nanopart. Res. 16 (2014) 2736-2744. https://doi.org/10.1007/s11051-014-2736-0.

[2] L.H. Prentice, M.J. Tyas, M.F. Burrow, The effect of ytterbium fluoride and barium sulphate nanoparticles on the reactivity and strength of a glass-ionomer cement. Dent. Mater. 232(8) (2006) 746-751. https://doi.org/10.1016/j.dental.2005.11.001.

[3] Advanced dental biomaterials, Elsevier (2019) edited by Z. Khurshid, S. Najeeb, M. Sohail, Zafar, F. Sefat

[4] A.T. Florence, Nanoparticle uptake by the oral route: fulfilling its potential? Drug Discov. Today: Technol. 2 (2005) 75–81. https://doi.org/10.1016/j.ddtec.2005.05.019.

[5] S. Dekkers, H. Bouwmeester, P.M.J. Bos, R.J.B. Peters, A. Rietveld, A. Oomen, Knowledge gaps in risk assessment of nano- silica in food: evaluation of the dissolution and toxicity of different forms of silica. Nanotoxicol. 7(4) (2013) 367–377. https://doi.org/10.3109/17435390.2012.662250.

[6] D. Korte, A. Grahovac, A. Jerkič, O. Vajdle, J. Anojčić, V. Guzsvány, B. Budič, M. Franko, Speciation and determination of ionic and trace-level colloidal silver in selected personal care products by thermal lens spectrometry. Pharm. Anal. acta. 9 (2018) 1-10. http://doi.org/10.4172/2153-2435.1000573.

Infrared emissivity of microcapsules of organic phase change materials dispersed into smart wearable textiles

Agharahimli K(1)*, Larciprete M(1), Cesarini G(1), Sibilia C(1), Li Voti R(1), Ballesio G(2), Thida W(3)

(1) Department of Science Based Applications for Engineering, Sapienza Università di Roma, Via Antonio Scarpa 16, 00161 Rome, Italy
(2) Ballesio Fratelli srl - Via Domodossola n.19, 10145 Torino, Italy
(3) Physics, School of Science, Walailak University Nakhon Si Thammarat, Thailand, 80161

*Corresponding author's email: khayala.agharahimli@uniroma1.it

Smart textiles are becoming more integrated with service ecosystems that go beyond the current horizontal textile value chain. These novel products that have been developed by many researchers with specific functionalities and features and they are gaining much importance in the advent of wearable and e-textiles. Phase change materials (PCMs) can make great example of smart wearable textiles which can bring the change at the functionality of traditional textiles such as, thermoregulation effect. The textiles used in this paper can modify their infrared radiation emission, thus they can be envisioned to exploit thermal shielding applications. During the heating and cooling processes, dispersed microencapsulated PCMs exhibit different emissivity due to their capacity to absorb, store and release heat energy. In this study infrared thermographic technique is used to measure the thermal properties such as, infrared emissivity. The obtained experimental results show a dynamic tuning of IR emissivity during two different heating and cooling process.

References

[1] Martijn ten Bhömer, Oscar Tomico, Stephan Wensveen, Advances in Smart Medical Textiles: Treatments and Health Monitoring, Cambridge, UK: Woodhead Publishing Series in Textiles, (2016) 155-175 https://doi.org/10.1016/B978-1-78242-379-9.00007-4.

[2] Subhankar Maity, Kunal Singha, Pintu Pandit, Applications of Advanced Green Materials, Woodhead Publishing in Materials, (2021) 239-263. https://doi.org/10.1016/B978-0-12-820484-9.00010-6.

[3] M.C. Larciprete, S. Paoloni, G. Cesarini, et al., Thermo-regulating properties of textiles with incorporated microencapsulated Phase Change Materials, MRS Advances, 5 (2020) 1023–1028. https://doi.org/10.1557/adv.2020.106.

03
Laser Ultrasonics

Detection of defects in multilayer solids with laser-induced surface acoustic waves

Saurer M(1), Bauer P(1), Moser F(2), Kleb U(2), Paltauf G(1), Nuster R(1)*

(1) Department of Physics, University of Graz, Graz, Austria
(2) Policies, JOANNEUM RESEARCH, Graz, Austria

*corresponding author's email: ro.nuster@uni-graz.at

Ultrasonic waves are a common tool in industrial quality assurance to detect defects in components. Laser ultrasound (LUS) techniques use short laser pulses absorbed at the sample surface to excite a variety of acoustic modes and a continuous laser to measure the propagation of ultrasound waves, by measuring the surface displacements at defined positions. Since non-contact and non-destructive measurements are possible with a LUS setup, it is frequently used for in-line structural health monitoring (SHM). In addition, the LUS method is used to determine elastic parameters of materials. The advantages of the LUS technique are its speed, good spatial resolution, and the easy control of the bandwidth of the ultrasonic waves. [1] To detect defects such as cracks, delaminations and foremost inclusions in multilayer devices, a LUS setup (see Fig. 1), optimized for detecting surface acoustic waves (SAWs), was installed.

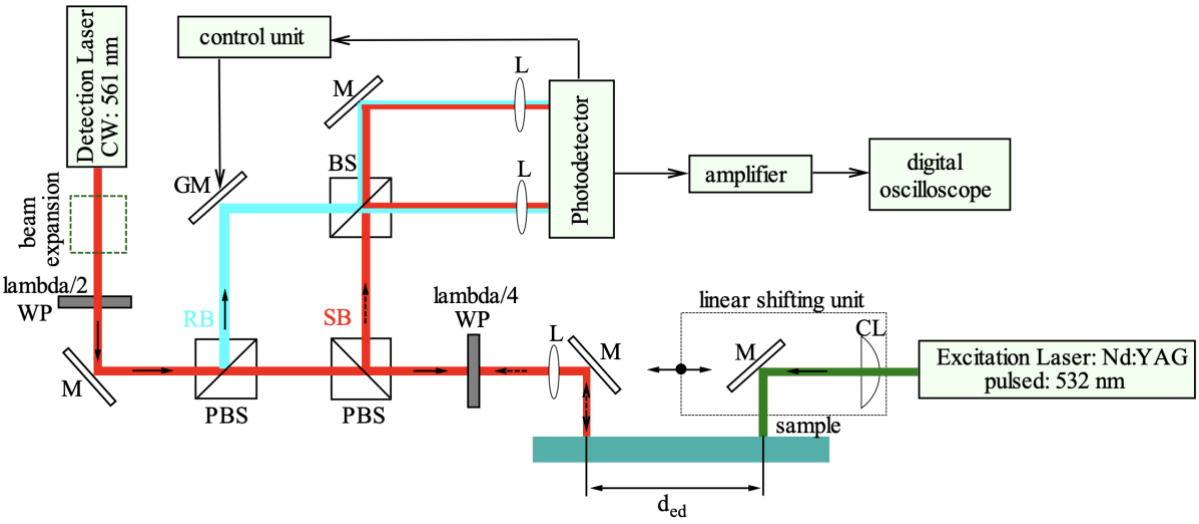

Fig. 1. LUS setup optimized in the detection of surface acoustic waves

In this LUS setup the ultrasonic waves were generated by focusing a pulsed laser beam via a cylindrical lens on a line on the sample surface. The optical and thermal properties of the sample surface determined how the irradiated energy was absorbed and converted into elastic stresses. These initial elastic stresses served as the source of the ultrasonic waves. How the ultrasonic waves propagate in the material depends on the elastic properties of the sample and is affected by any defects. [1] To detect SAWs, a stabilized Mach-Zehnder interferometer was used to record the displacement of the sample surface at specific points. With this LUS measurement system SAWs with frequencies ranging from 100 kHz up to 350 MHz could be detected.

To investigate the effect of inclusions in a multilayer structure on the propagation of SAWs, self-made samples consisting of 800 nm silver on a 725 µm thick silicon wafer substrate were prepared by physical vapor deposition. Twelve copper inclusions with different thicknesses d_{Cu} ranging from 50 nm to

400 nm and different widths, ranging from 1 mm to 3 mm were introduced between the silicon and the silver layer. For non-destructive testing of these samples, the pulse energy of the excitation laser can be up to 300 µJ at a repetition rate of 10 Hz. The dispersion behaviour of the SAWs in the samples with the different inclusions was extracted from the measured raw data by a time-frequency analysis and compared with each other and with theoretical dispersion curves calculated with the Global Matrix Method (see Fig 2 left hand side). A good agreement between theory and experiment could be achieved in this first comparison.

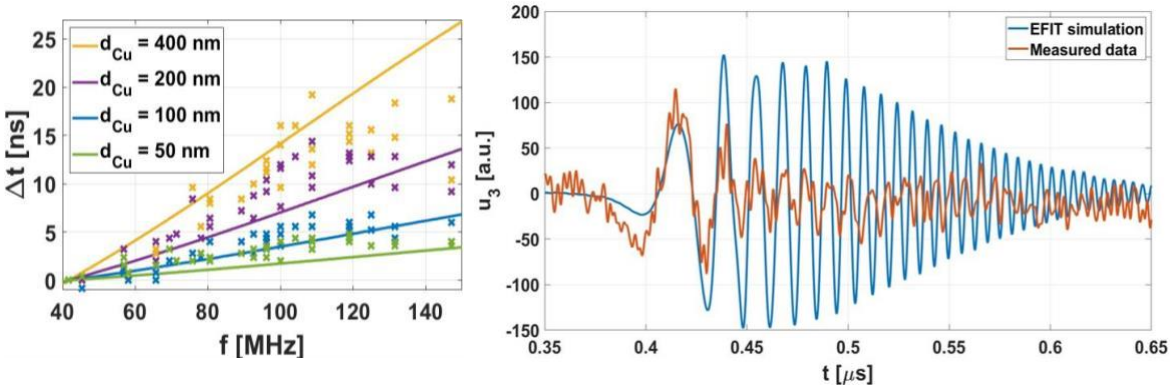

Fig. 2. Left: Comparison between extracted (crosses) and calculated (solid lines) dispersion behaviour of SAWs in multilayer samples with different inclusions.
Right: Comparison of the simulated (blue) and measured (red) propagation of a SAW in a multilayer sample.

Furthermore, the relationship between measured LUS signals and inclusion characteristics (width and thickness) of the self-made samples was investigated by a data-driven Functional Regression approach. For this purpose, Function-on-Scalar as well as Scalar-on-Function models [2] were estimated based on filtered signal data.

Because generally the ultrasonic wave propagation in materials cannot be solved analytically, a program was written that numerically solves the equations of ultrasonic wave propagation in elastic, homogeneous materials. This program is based on the Elastodynamic Finite Integration Technique (EFIT) and solves the elastodynamic equations of motion in their integral form on a discrete staggered grid. A leapfrog algorithm was used for the discrete time steps of the temporal evolution. The advantages of the EFIT method are that different geometries and boundary conditions can be implemented rather easily. [3] Time signals simulated with EFIT on a sample without inclusions were compared and found in good agreement with the measured signals (see Fig 2 right hand side). There are some discrepancies at high frequencies, which are probably due to the different material parameters for silver in simulations and experiment. Since the material parameters of silicon have already been determined, the next step would be to determine the material parameters of silver based on LUS measurements. In conclusion, the detection of SAWs with the LUS setup has proven to be a reliable tool for detecting inclusions in multilayer structures.

Acknowledgements – This study was part of the LUSI-Q project (number 877421) funded by the Austrian Research Promotion Agency (FFG).

References

[1] C. Scruby, L. Drain. Laser Ultrasonics: Techniques and Applications (2019). doi:10.1201/9780203749098.

[2] S. Brockhaus, D. Rügamer, S. Greven, Boosting Functional Regression Models with FDboost. Journal of Statistical Software, 94:10 (2020), 1–50. https://doi.org/10.18637/jss.v094.i10.

[3] K. Nakahata et al. A Large Scale Simulation of Ultrasonic Wave Propagation in Concrete Using Parallelized EFIT. Journal of Solid Mechanics and Materials Engineering 2 (2008) 1462–1469. doi: 10.1299/jmmp.2.1462.

Laser-induced shockwaves and cavitation bubbles in different water matrices

Dular M(1), Kozmus G(1), Mur J(1), Petkovšek R(1)*

(1) Faculty of Mechanical Engineering, University of Ljubljana, Aškerčeva cesta 6, SI-1000 Ljubljana, Slovenia

*Corresponding author's email: rok.petkovsek@fs.uni-lj.si

Cavitation, nowadays a renowned topic among scientists, is a physical phenomenon accompanied by chemical processes that can occur in liquids. The phenomenon encompasses the growth and collapse of vaporous or gaseous cavities in a liquid, accompanied by shockwave emission. Even though cavitation has been in the centre of numerous investigations through the years there are many aspects of the phenomenon which still need to be elucidated. A big gap, for example, exists between observing and understanding the effects that addition of different compounds has on cavitation behaviour. Specifically, how it influences the governing mechanisms of cavitation, such as bubble growth and collapse, and how it influences the shockwave generation, propagation and pressure. To get a better understanding of this aspect, basic experiments should thus be conducted in a simple matrix – tap water (TW) and then compared to behaviour in more complex matrices.

Figure 1 shows the experimental setup.

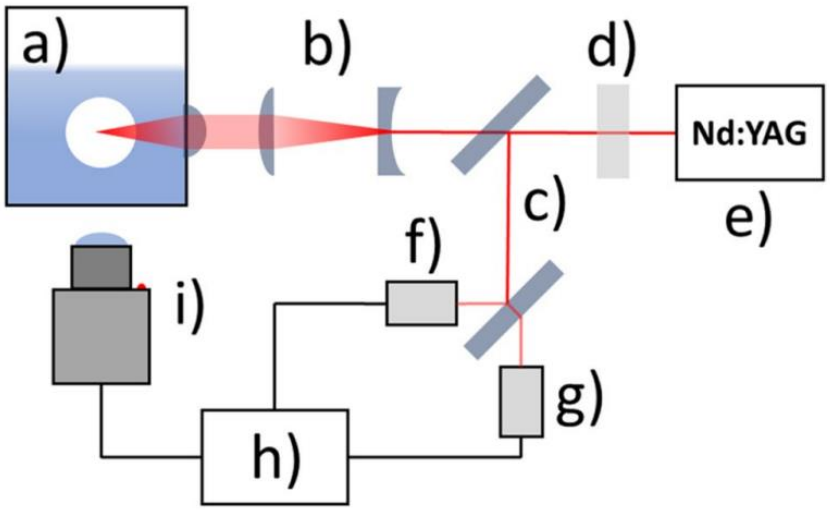

Fig. 1. Experimental setup

A similar setup was used as in [1] and was used to create a buble. A liquid container (a) with the wall integrated focusing lens (b) with the numerical aperture value of 0.23 was used, which helps minimize losses in the optical system. The beam expander (b), splitter (c) and attenuator condition the laser beam from the 1064 nm Q-switched Nd:YAG pulsed laser source (e), which has a pulse duration in ns range and up to 15 mJ with minimum attenuation. Laser pulses energy is measured at (f), assuring the variance is kept below 1.5%. A trigger photodiode (g) is used to synchronize the laser pulse and the high-speed camera (i).

The evolution of the cavitation bubble was recorded by a high-speed camera Photron Fastcam SA-Z with a frame rate of 210,000 fps (Fig. 2). The whole region of interest was 10×4 mm big and resolved by 384×160 pixels, leading to the pixel size of approximately 25 μm. LED light source Ryobi One+(50,000 lm) served as a backlight illumination source.

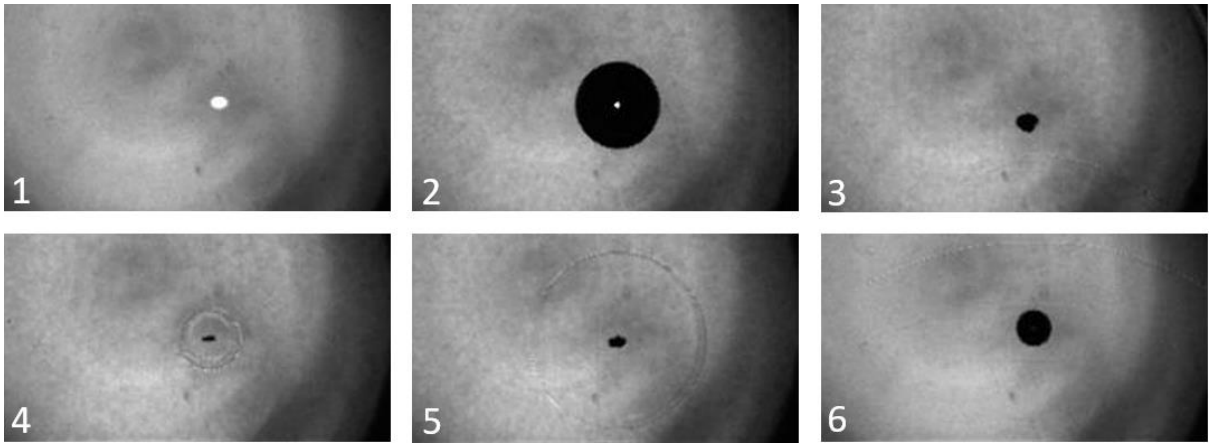

Fig. 2. Typical evolution of the bubble. Plasma initialization (1), max size (2), collapse (3) and the shock wave emission (4,5, and 6). The sequence is 230 μs long

Bubble was initiated in different water solutions containing different quantities of salt, ethanol, furfuryl alcohol, salicylic acid, histidine, methanol and hydrogen peroxide. All the solutions are commonly used in investigations of chemical effects of cavitation, hence it is essential to know their influence on the bubble dynamics and the characteristics of the emitted shock wave.

We show that even extremely low concentrations of additives significantly affect the extent and dynamics of cavitation and shock wave characteristics. This is mainly due to minute changes in surface tension which influences the last stages of bubble collapse.

Understanding the effects of water matrix on bubble dynamics and shock wave characteristics will enable the estimation of the usefulness of each additive in the process of wastewater treatment by cavitation and help to select the optimal concentration of the additive for the analysis of the chemical effects of cavitation. Further research, using higher optical magnification imaging combined with single-nanosecond illumination pulses, will be used for further investigation of detailed shockwave properties as possibly influenced by the different water matrices.

References

[1] D. Horvat, U. Orthaber, J. Schille et al,. Laser-induced bubble dynamics inside and near a gap between a rigid boundary and an elastic membrane, International Journal of Multiphase Flow, 100 (2018) 119–126. https://doi.org/10.1016/j.ijmultiphasefow.2017.12.010.

Adaptive polarized photoacoustic computed tomography

Zhang Y(1), Xia Z,(1) Hou R,(1) Liu X(1)*, Xiong J(1)*

(1) School of Electronic and Optical Engineering, Nanjing University of Science and Technology, Nanjing 210094, China

*Corresponding author's email: liuxf_1956@sina.com, jichuan.xiong@njust.edu.cn

Background – Photoacoustic computed tomography (PAT) is widely studied in biomedical fields due to its advantages of high optical contrast and high spatial resolution imaging [1,2]. However, conventional PACT commonly treats the absorption coefficient as a scalar variable. In practice, the molecular arrangement in many biological tissues exhibit ordered, which means that their light absorption coefficients are dichromatic [3,4].

Methods – In this work, we proposed a novel imaging method called adaptive polarized photoacoustic computed tomography (APPAT), which can improve the quality of conventional PAT and measure the dichroic amplitude of tissue. By the linearly polarized laser beams in different directions as excitation source, and then the adaptive algorithm collects the photoacoustic signal according to the dichroic amplitude reflected by the tissue to reconstruct the image.

Results – We demonstrated the performance of APPAT by imaging the plastic polarizing film and the isolated bovine tendon.

Conclusions – The APPAT method can not only improve the imaging ability of PACT, but also provides an effective strategy for tissue polarimetry, prefiguring great potential for biological imaging and material inspection.

References

[1] L.V. Wang, S. Hu, Photoacoustic tomography: in vivo imaging from organelles to organs, Science, 335 (6075), (2012) 1458-1462.

[2] S. Zackrisson, S.M.W.Y. van de Ven, S. S. Gambhir, Light in and sound out: emerging translational strategies for photoacoustic imaging, Cancer Res., 74(4) (2014) 979–1004.

[3] V. Sergey Plotnikov, C. Andrew Millard, J. Paul Campagnola, A. William Mohler, Characterization of the Myosin-Based Source for Second-Harmonic Generation from Muscle Sarcomeres, Biophysical Journal, 90(2) (2006) 693-703.

[4] Jeroen Mollink, Michiel Kleinnijenhuis, Anne-Marie van Cappellen van Walsum, N. Stamatios Sotiropoulos, Michiel Cottaar, Christopher Mirfin, P. Mattias Heinrich, Mark Jenkinson, Menuka Pallebage-Gamarallage, Olaf Ansorge, Saad Jbabdi, L. Karla Miller, Evaluating fibre orientation dispersion in white matter: Comparison of diffusion MRI, histology and polarized light imaging, NeuroImage, 157 (2017) 561-574.

05
Infrared Thermography

Thermographic super resolution reconstruction using 2D pseudo-random pattern illumination

Lecompagnon J[(1)*], Hirsch PD[(1)], Rupprecht C[(2)], Ziegler M[(1)]

(1) Bundesanstalt für Materialforschung und -prüfung (BAM), 12200 Berlin, Germany (2) Technische Universität Berlin (TUB), 10623 Berlin, Germany

*Corresponding author's email: julien.lecompagnon@bam.de

Thermographic non-destructive testing is based on the interaction of thermal waves with inhomogeneities. The propagation of thermal waves from the heat source to the inhomogeneity and to the detection surface according to the thermal diffusion equation leads to the fact that two closely spaced defects can be incorrectly detected as one defect in the measured thermogram. In order to break this spatial resolution limit (super resolution), the combination of spatially structured heating and numerical methods of compressed sensing can be used.

The improvement of the spatial resolution for defect detection then depends in the classical sense directly on the number of measurements. Current practical implementations of this super resolution detection still suffer from long measurement times, since not only the achievable resolution depends on performing multiple measurements, but due to the use of single spot laser sources or laser arrays with low pixel count, also the scanning process itself is quite slow. With the application of most recent high-power digital micromirror device (DMD) based laser projector technology this issue can now be overcome.

In this work we share our progress on improving the defect/inhomogeneity characterization using fully 2D spatially structured illumination patterns instead of scanning with a single laser spot. The experimental approach is based on the repeated blind pseudo-random illumination using modern projector technology and a high-power laser (see Fig. 1).

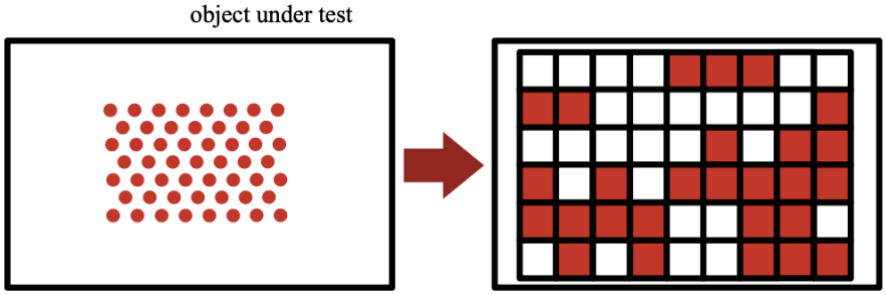

Fig. 1. Point-wise heating pattern with single laser spots; each spot is illuminated one after another to guarantee independent measurements (Left); pixelated pseudo-random pattern illuminated as a whole; multiple of those patterns are used for the subsequent defect reconstruction (Right).

In the subsequent super resolution based defect reconstruction several measurements are combined by taking advantage of the joint sparsity of the defects within the sample. Here, enhanced nonlinear convex optimization techniques are utilized for solving the underlying ill-determined inverse problem

for typical simple defect geometries. As a result, a higher resolution defect/inhomogeneity map can be obtained at a fraction of the measurement time previously needed.

3D Browsing of historical books by means of Active Infrared Thermography

Orazi N[(1)*], Mercuri F[(1)], Paoloni S[(1)], Zammit U[(1)], Caruso G[(2)], D'Annibale E[(2)], Ronchi D[(2)], Ferdani D[(2)], Florise Amadei C[(2)], Pietroni E[(2)]

(1) Department of Industrial Engineering, University of Rome Tor Vergata, via del Politecnico, 00133, Rome, Italy

(2) ISPC- CNR, Via Salaria km 29,300, 00010 Montelibretti, Italy

*Corresponding author's email: noemi.orazi@uniroma2.it

Digitization activity in in the field of archives and library materials is usually focused on their content and, to this aim, standard 2D scanning and photography techniques are employed [1]. However, not only the content but also the structural features of an ancient book like the bookbinding, the book block and the decorative elements are important from both a historical and a codicological point of view. In addition, some of the most valuable information often lie below the binding of a book. Sub-surface elements can reveal for instance hidden texts on waste material used in the binding manufacturing process, binding components and damage, often, not accessible through the simple visual inspection. These elements are of the highest importance for scholars and conservators and highly fascinating to the general public. Nevertheless, many of such elements are not visible because faded or buried inside the book structure and it would be important to display their position in a 3D digital representation of the book. This can be obtained by integrating the 3D image-based techniques with other imaging diagnostics able to reveal and also characterize sub-surface features [2-3].

In this study the depth-resolved analysis capability provided by active infrared thermography (IRT) is applied in combination with 3D image-based techniques in order to obtain a representation of the subsurface features buried into historical books. The procedure utilized for the generation of thermal texturing [4] makes use of a texture mapping algorithm. Active thermography has been employed to record thermograms of the investigated manuscripts from different viewpoints and beside the manuscript. Moreover, in order to perform a robust orientation among thermal and RGB images, homologous image, obtained by shooting the same checkboard, coordinates were used (Fig. 1). As it will be shown, the image coordinates of such markers play a crucial role in the model thermal texturing.

Fig. 1. Photograph of the markers used to align thermal and RGB cameras

The final result consists of a 3D thermographic texturing showing features lying at different depths (Fig. 2) allowing to display the book from different angles. Finally, the 3D representations should go beyond current levels of visual depictions, support information integration, shape-related analysis and provide the necessary semantic information for in-depth studies.

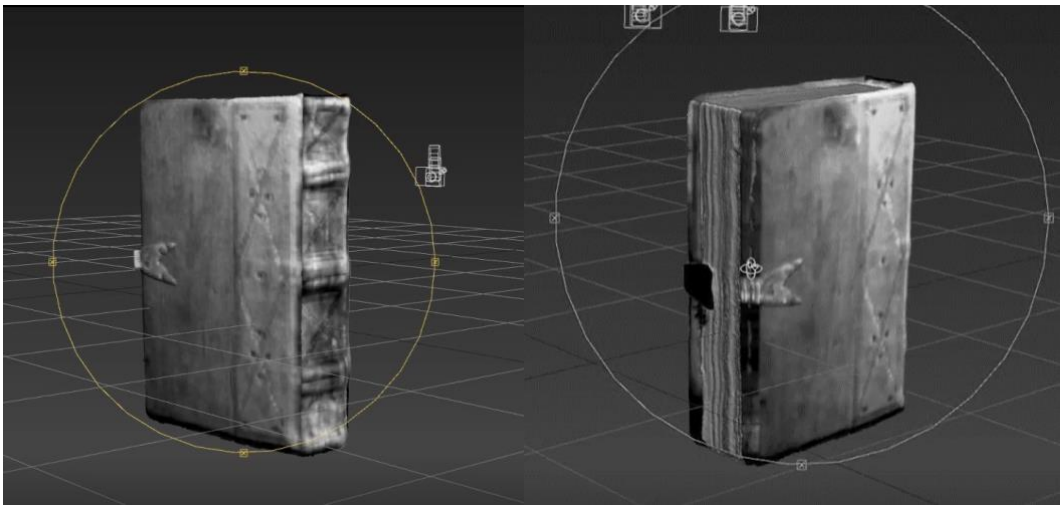

Fig. 2. Book's thermographic texturing

Acknowledgements – The authors wish to thank Ilaria Vercillo and Lucia Marchi, Biblioteca Casanatense of Rome.

Funded project: “Codex 4D | Viaggio in 4D nel manoscritto.” CUP: B79J21002850002.

References

[1] S. Carrico, Book Review: Handbook for Digital Projects: A Management Tool for Preservation and Access, Library Resources & Technical Services, 45(2) (2011) 111-112.

[2] N. Orazi, Mid-wave Infrared Reflectography and Thermography for the Study of Ancient Books: A Review, Stud. Conserve., 65 (2020) 8. https://doi.org/10.1080/00393630.2020.1734383.

[3] F. Mercuri, N. Orazi, S. Paoloni, C. Cicero, U. Zammit, Pulsed Thermography Applied to the Study of Cultural Heritage, Applied Science,7 (2017) 1010. https://doi.org/10.3390/app7101010.

[4] Y. Yongkai, C. Hailong, M. Xiang, Y. Xiulun, P. Xiang, Texture mapping based on photogrammetric reconstruction of the coded markers, Applied Optics, 58 (2019) 5. https://doi.org/10.1364/AO.58.000A48.

Infrared thermography study of historical bronze composition effects on the transport properties

Paoloni S[(1)], Mercuri F[(1)], Zammit U[(1)*], Orazi N[(1)], Caruso G[(2)], Ferretti M[(2)], Porcinai S[(2)]

[(1)] Department of Industrial Engineering, University of Rome Tor Vergata, Rome, Italy
[(2)] DISPC CNR, Rome, Italy

*Corresponding author's email: zammit@uniroma2.it

Bronze has always been one of the most popular materials for the manufacture of statues mainly because of its suitable metallurgical properties. In fact, bronze is durable and ductile, thus allowing the artist to more conveniently apply fine details to the statue after its main casting. In this respect, it is worth reminding that since ancient times it was used to appropriately introduce slight modifications in the alloy compositions to obtain low melting point, resistance to corrosion, color change for the insertions, etc. Therefore, the characterization of the bronze alloy composition of the different parts composing a given statue may allow one too gather valuable information about the process followed by the artist in the manufacture of the artefact, thus providing useful information for both scholars and restorers.

Presently, a large variety of experimental techniques is used for such a purpose among which Energy Dispersive X-ray Spectrometry, X-Ray Fluorescence, neutron-diffraction, involving complicated or expensive apparatus, or being not practical when applied to real artifacts. Among the non-destructive techniques applied to the investigation of cultural heritage items and, more specifically, of ancient bronze statuary, over the recent years active infrared thermography (IRT) has been proven to be a very effective tool. In particular, by means of such a technique it has been possible to both detect and characterize the workings undertaken after the main casting such the ones carried out to mend the openings occurred because of casting faults and the insertions. Finally, IRT has also been used for the evaluation of the local thermal diffusivity in ancient bronze statues. The thermal diffusivity, D, is known to be very sensitive to the bronze composition. Therefore, if the dependence of D on the concentration of particular elements in the alloy were known, its evaluation could lead to the determination of the concentration of such elements in the alloy. The knowledge of such a parameter is crucial for the quantitative characterizations of the geometrical characteristics of defects or insertions in ancient bronzes [1, 2].

In this study IRT has been applied to the measurement of the thermal diffusivity of specifically prepared bronze alloys containing different amounts of Sn and Pb, which are the major constituents in alloys used for the manufacture of ancient statues. Electrical conductivity measurements, linearly related to the thermal conductivity in metals, have been also carried out on the same set of samples to probe whether they followed a composition dependence similar to that of the thermal diffusivity.

Fig. 1 reports the values of D measured on the test samples, as well as some values reported in the literature as a function of C_{eff}, the total effective "weighed" concentration of Sn and Pb atoms. Here, the concentration of Pb was divided by a factor n to account for the known considerable smaller effects of

the Pb than the Sn atoms to affect the transport properties in bronze, as observed for the electrical conductivity [3]. When such a procedure is adopted, with *n*=5.3, all the values follow a common trend characterized by a steep profile for the lower concentration range tending to saturate asymptotically for values exceeding approximately 10%. Such a trend could be fitted with the empirical expression:

$$D(C_{eff}) = D_{Cu} e^{-\alpha C_{eff}} + B \qquad \text{Eqn. 1}$$

where D_{Cu} =1.15 cm^2/s is the thermal diffusivity value for pure Cu, obtained and α= 0.23 and B=0.08 cm^2/s. Such a curve can constitute a useful tool to determine the D value once the concentration in the alloy of tin and lead are known, and, perhaps, vice versa.

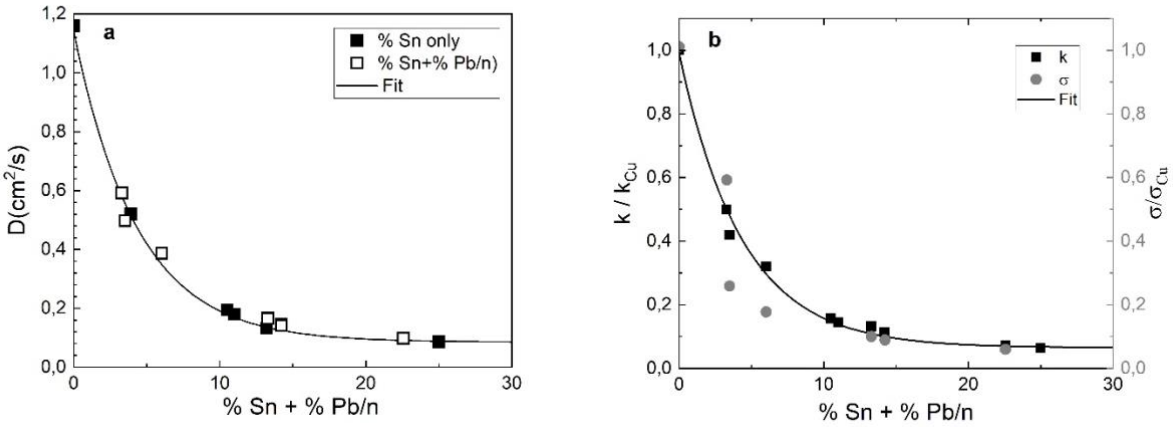

Fig. 1. (a) Thermal diffusivity as a function of the effective Sn+Pb/n weighed concentration with n=5.3 ; (b) normalized thermal conductivity, *k*, and electrical conductivity, σ, as a function of the effective Sn+Pb/n weighed concentration.

In Fig. 1(b), the values of both *k*, derived from *D*, and σ are reported, normalized to the respective values for pure Cu, as a function of the previously mentioned C_{eff}. It can be observed that the profile of both such quantities can also be reasonably well characterized by the same common trend previously reported for the thermal diffusivity. In fact, the reported continuous line.is obtained by the same expression as Eqn. 1, with the same value of α but with a different offset value.

References

[1] F. Mercuri, S. Paoloni, N. Orazi, C. Cicero, U. Zammit, Pulsed infrared thermography applied to quantitative characterization of the structure and the casting faults of the Capitoline She Wolf, Appl. Phys. A, 123 (2017) 327.

[2] F. Mercuri, G. Caruso, N. Orazi, U. Zammit C. Cicero, O. Colacicchi Alessandri, M. Ferretti, S. Paoloni, Interface thermal conductance characterization by infrared thermography: A tool for the study of insertions in bronze ancient Statuary, Infrared Physics and Technology, 90 (2018) 31.

[3] https://www.911metallurgist.com/copper-electrical-conductivity/

Thermal anisotropy of polyethersulfone woven textiles by infrared thermography

Larciprete M(1), Orazi N(2), Gloy YG(3), Paoloni S(2), Sibilia C(1) , Li Voti R(1)*

(1) Dipartimento di Scienze di Base ed Applicate per l'Ingegneria, Sapienza Università di Roma, Via Scarpa 16, 00161 Rome, Italy
(2) Dipartimento di Ingegneria Industriale, Università degli Studi di Roma Tor Vergata, Via del Politecnico 1, 00133 Rome, Italy
(3) Sächsisches Textilforschungsinstitut e.V. (STFI), 09125 Chemnitz, Germany

*Corresponding author's email: roberto.livoti@uniroma1.it

Over the recent period, there has been growing interest in knitted fabrics for the realization of electrically driven functional fabrics, so-called smart textiles. Such an interest is due to several technological advances such as the emergence of conductive and elastic yarns for stretchable electronics, the development of conductive inks as well as advances in miniaturization and printing techniques. In this respect, special attention has been de-voted to the development of flexible patch antennas and electronics for wearable telemedicine and defence applications [1–3], as well as power-assisted garments for personal thermal management. Thanks to their peculiar properties including flexibility and light weight, such devices can be easily integrated into textiles, thus allowing the manufacturing of smart clothes. As regards the production of textile antennas, different fabric materials such as cotton, polyester and nylon are typically employed for the realization of the substrate, while copper adhesive tape, silver conductive ink or conductive paper are usually adopted as radiating materials, to name some [4,5].

Among different material textiles, polyethersulfone (PES) is the most widely employed due to its relevant physical properties. In particular, PES allows the realization of textiles where the fibers are interlaced according to different geometries as those, for in-stance, required for the realization of integrated antennas. However, several problems re-main unsolved and, among others, the dissipation of the heat produced by the integrated electronic devices through the substrate textile is among the most important issue, which still deserves further studies in order to optimize the effective thermal diffusivity and infrared emissivity of these structures [6–8].

Fabrics can be viewed as consisting of repeated units of porous yarns and air spaces. Therefore, the heat flow through textiles depends on several factors such as the thermal conductivity of the fibrous material, air volume content and weave pattern, i.e., the way the warp and weft yarns interlace with each other. It is thus evident that one of the fundamental issues to be addressed in the design of smart textiles is to understand how the microscale thermophysical properties of the single bundle of fibers may affect the effective properties of textiles on the macroscopic scale.

Given the considerations reported above, the characterization of the thermal proper-ties of PES textiles is of crucial importance. In this respect, it is worth mentioning that both mechanical, electrical [9] and thermal [10] properties of fabrics have been shown to be extremely anisotropic and, consequently, woven textiles are also expected to exhibit anisotropic thermal transport properties which are significantly affected by fiber structure. In particular, the heat produced by the current flowing into the electrically conductive yarns has been shown to be mainly spread in the plane of the fibers rather than

in the perpendicular direction [11,12]. In this regard, it has been recently reported that the presence of anisotropy in the fiber-woven structure [13,14], such as those due to different density of warp and weft yarns [15] or yarn count differences in warp and weft directions [16], may lead to a significant anisotropic behavior of the thermal transport properties.

The main idea of this study is to get some further insights about the dependence be-tween the textiles features and the macroscopic heat conduction properties. To this aim, thermal diffusivity measurements have been carried out in PES textiles characterized by different fiber density and weaving pattern. Among different textile thermal properties, thermal diffusivity D plays a crucial role in the determination of the transient thermal response of textile material resulting from time-varying heat flow within the material.

In this study, the thermal diffusivity measurements have been carried out by means of an active infrared thermography (IRT) technique, which nowadays can be considered one of the most well-established techniques for the remote and nondestructive evaluation of materials thermal properties. In particular, in these investigations the lock-in IRT con-figuration (LI-IRT) [17] has been employed since it allows the straightforward evaluation of the in-plane thermal diffusivity. As mentioned before, such an information can be extremely useful when taking into account that heat dissipation in smart textiles is expected to take place mainly along the sample surface rather than in the orthogonal direction. In addition, the LI-IRT technique enables the prompt evaluation of the thermal diffusivity along different directions on the sample surface [18,19,20] and hence, the detection of a possible anisotropic features of the thermal diffusivity, which may result from the textile physical properties and geometrical structure, which can be optimized and exploited for smart design processes.

References

[1] Roshni, S.B.; Jayakrishnan, M.P.; Mohanan, P.; Surendran, K.P.. Smart Mater. Struct. 26 (2017) 105011.

[2] Karimi, R.; Mohtaram, F.; Mottaghitalab, V.; Mehrizi, M.K. J. Ind. Text. 47 (2018) 765–780.

[3] Ha, S.; Jung, Y.; Kim, D.; Jung, C.W. Microwave Opt. Technol. Lett. 54 (2012) 2697–2702.

[4] SCharjan, C.; Sreemathy, R.; Terdalkar, S. Int. J. Wirel. Mob. Comput. 13 (2017) 232–244.

[5] Mohtaram, F.; Mottaghitalab, V.; Baghersalimi, G. J. Text. Inst. 108 (2017) 1888–1898.

[6] Larciprete, M.C.; Paoloni, S.; Orazi, N.; Mercuri, F.; Orth, M.; Gloy, Y.S.; Centini, M.; Voti, R.L.; Sibilia, C. Int. J. Therm. Sci. 146 (2019) 106109.

[7] Larciprete, M.C.; Paoloni, S.; Voti, R.L.; Gloy, Y.S.; Sibilia, C, Int. J. Therm. Sci. 132 (2018) 168–173.

[8] Larciprete, M.C.; Gloy, Y.S.; Voti, R.L.; Cesarini, G.; Leahu, G.; Bertolotti, M.; Sibilia, C. Int. J. Therm. Sci. 113 (2017) 130–135.

[9] Peng, L.; Fan, W.; Li, D.; Wang, S.; Liu, Z.; Yu, A.J. Adv. Mater. Technol. 5 (2020) 1900599.

[10] Felczak, M.; de Mey, G.; Więcek, B.; Michalak, M. Fibres Text. East. Eur. 4 (2015) 61–65.

[11] Yoshihiro, Y.; Hiroaki, Y.; Hajime, M. Effective thermal conductivity of plain weave fabric and its composite material made from high strength fibers. J. Text. Eng. 54 (2008) 111–119.

[12] Bhattacharjee, D.; Kothari, V.K. Int. J. Heat Mass Transf. 52 (2009) 2155–2160.

[13] Peng, L.; Fan, W.; Di, L.; Wang, S.; Liu, Z.; Yu, A.; Jiang, X. Smart Adv. Mater. Technol. 5 (2020) 1900599.

[14] Wu, E.; Gao, Q.; Li, M.; Shi, Y.; Mandelis, A. NDT E Int. 94 (2018) 56–61.

[15] Dolatabadi, M.K. J. Text. Inst. 2017, (2017) 1537–1544.

[16] Siddiqui, M.O.R.; Sun, D. J. Ind. Text. 48 (2017) 685–712.

[17] Maldague, X. Theory and Practice of Infrared Technology for Nondestructive Testing; Wiley-Interscience: New York, NY, UAS, 2001.

[18] Paoloni, S.; Scudieri, M.E.T.F.; Mercuri, F.; Marinelli, M.; Zammit, U. Appl. Phys. A Mater. Sci. Processing 98 (2010) 461.

[19] Ishizaki, T.; Nagano, H.. Infrared Phys. Technol. 99 (2019) 248.

[20] M. Larciprete, N. Orazi, Y. S. Gloy, S. Paoloni, C. Sibilia and R. Li Voti, Sensors, 22 (2022) 940.

06
Ultrafast Phenomena and Spectroscopy

Thermal characterization of polymeric thin films by photoacoustic spectroscopy

Fernández-Olaya MG[(1)], Franco-Bacca AP[(1)], Ruiz-Gómez MA[(2)], Martínez-Torres P[(3)], Alvarado-Gil JJ[(1)] *

(1) Applied Physic Department, CINVESTAV, Mérida, México
(2) Applied Physic Department, CONACYT-CINVESTAV, Mérida, México
(3) Physics Institute, Universidad Michoacana de San Nicolás de Hidalgo, Hidalgo, México

*Corresponding author's email: juan.alvarado@cinvestav.mx

The determination of the thermal properties is an important and well stablished application of Photoacoustic techniques. These methodologies are non-destructive methods based on the generation of thermal waves using a modulated light source [1,2]. However, the study of thin films is limited due to the restrictions established by the thermal diffusion length. In this work, we show a methodology which allows to perform a complete thermal characterization of thin films as a two-step characterization process in the same photoacoustic cell.

The heat diffusion equation for a modulated flux, was solved considering a flat two-layer system, surrounded by air. Two configurations were considered, the first one with a perfect match between the layers and the second with a thermal interface resistance between both the layers (e.g., Fig. 1).

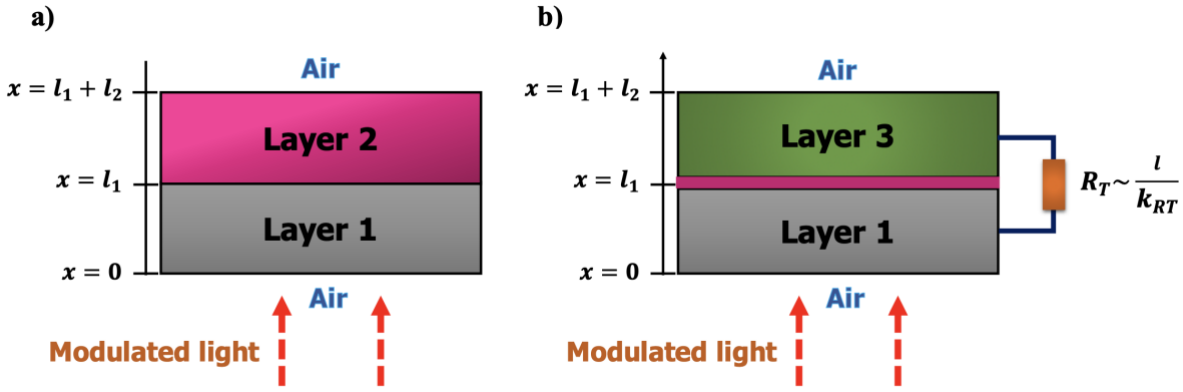

Fig. 1. Two-layer system diagram **a)** with temperature continuity between layers, and **b)** with thermal interface resistance

The first step of the experiment consists in depositing a layer of variable thickness (layer 2) on a substrate (layer 1). If the thickness of layer 1 is made very thin, the normalized temperature at the front face can be expressed as

$$\Delta T = 4\frac{1}{e_1} * \frac{e^{-2\sigma_1 l_1}}{1-e^{-4\sigma_1 l_1}} (\rho C)_2 \left[\sqrt{2\pi f}\, l_2 - \frac{2\pi f}{\sqrt{\alpha_2}} {l_2}^2\right] \quad \text{Eqn. 1}$$

$$\text{with} \quad \sigma_1 = (1+i)\sqrt{\frac{\pi f}{\alpha_1}}$$

Where ΔT is the gap between the beginning and the final of the signal, f is the frequency, e_1 and α_1 are the thermal effusivity and diffusivity of layer 1, respectively. Indicating a simple dependence on the volumetric heat capacity $(\rho C)_2$, the thermal diffusivity α_2, final thickness l_2 of layer 2.

For the second step system a third layer is deposited on top of layer 2. Considering a temperature discontinuity between both layer as a thermal resistance, R_T, which is related to the thermal conductivity [3], the temperature at the front face is given by

$$T(x=0) = \frac{Q}{\sigma_1 k_1}\left(\frac{1+R'_{31}e^{-2\sigma_1 l_1}}{1-R'_{31}e^{-2\sigma_1 l_1}}\right) + QR_T\left[\frac{(1-R'_{31})}{1-R'_{31}e^{-2\sigma_1 l_1}}\right]^2 e^{-2\sigma_1 l_1} \qquad \text{Eqn. 2}$$

$$\text{with } R'_{31} = \frac{R_{31}+e^{-2\sigma_3 l_3}}{1+R_{31}e^{-2\sigma_3 l_3}}, \quad R_{31} = \frac{1-e_3/e_1}{1+e_3/e_1}, \quad \sigma_j = (1+i)\sqrt{\frac{\pi f}{\alpha_j}}$$

Where Q is the power of the laser, k , l , e and α are de thermal conductivity, thickness, thermal *jjjj*

effusivity and diffusivity of each layer (j = 1, 3), respectively. The subscripts 1 and 3, refer to the layers 1 and 3 (e.g., Fig. 1b).

This expression allows to determine the thermal conductivity of the inner layer. Both equations 1 and 2 allow to perform the complete thermal characterization of the film.

The experiments were performed using a closed photoacoustic cell and 304- stainless steel as a substrate. Polymeric solution of starch biopolymers and PEDOT: PSS were dropped on the substrate and the amplitude signal was recorded on time. At the end of the evaporation process a film is formed and the amplitude of the photoacoustic signal becomes stable. Applying Eqn. 1, the volumetric heat capacity and thermal diffusivity of the sample were obtained, in agreement with reported parameters [1,4].

On the top of the film formed a thick drop of colloidal graphite is deposited, and the phase signal is recorded as a function of the frequency. The data are fitted using Eqn. 2, and changes in the signals are related to the thermal conductivity and thickness of the polymeric film enclosed.

The conditions under our methodology can provide reliable results for films of a few micros are presented and discussed.

References

[1] P. Martínez-Torres, J.J Alvarado-Gil, Applied. Physics A, 105:4 (2011) 975-986. https://doi.org/10.1007/s00339-011-6524-8.

[2] F.A. McDonald, G.C. Wetsel, Journal of Applied Physics, 49:4 (1978) 2313-2322. https://doi.org/10.1063/1.325116.

[3] J.L Pichardo, J.J Alvarado-Gil, Journal of Applied Physics, 89:7 (2001) 4070-4075. https://doi.org/10.1063/1.1342021

[4] A.P Franco-Bacca, F. Cervantes-Alvarez, J.D Macías, J.A Castro-Betancur, R.J Pérez-Blanco, O.H Giraldo Osorio, J.J Alvarado-Gil et al. Heat Transfer in Cassava Starch Biopolymers: Effect of the Addition of Borax. Polymers, 13:23 (2021), 4106. https://doi.org/10.3390/polym13234106.

Efficient picosecond ultrasonics with a common-cavity dual-comb laser

Pupeikis J[(1)*], Hu W[(1)], Willenberg B[(1)], Nussbaum-Lapping A[(1)], van den Hooven T[(2)], Planken P[(2)], Phillips CR[(1)], Keller U[(1)]

(1) Department of Physics, ETH Zurich, Zurich, Switzerland
(2) ARCNL, Amsterdam, the Netherlands

*Corresponding author's email: pupeikis@phys.ethz.ch

We show how to predict the equivalent time sampling (also known as asynchronous optical sampling (ASOPS)) pump-probe measurement noise floor based on the laser parameters. We use this knowledge to obtain a high-sensitivity measurement configuration reaching $<5x10^{-5}$ sensitivity for the relative reflectivity change ΔR/R in a single 12-ns-long trace with 250-fs delay resolution and an acquisition time of only 2 ms. We demonstrate the usefulness of this highly sensitive measurement configuration by studying ultrasonic signals in ruthenium thin films.

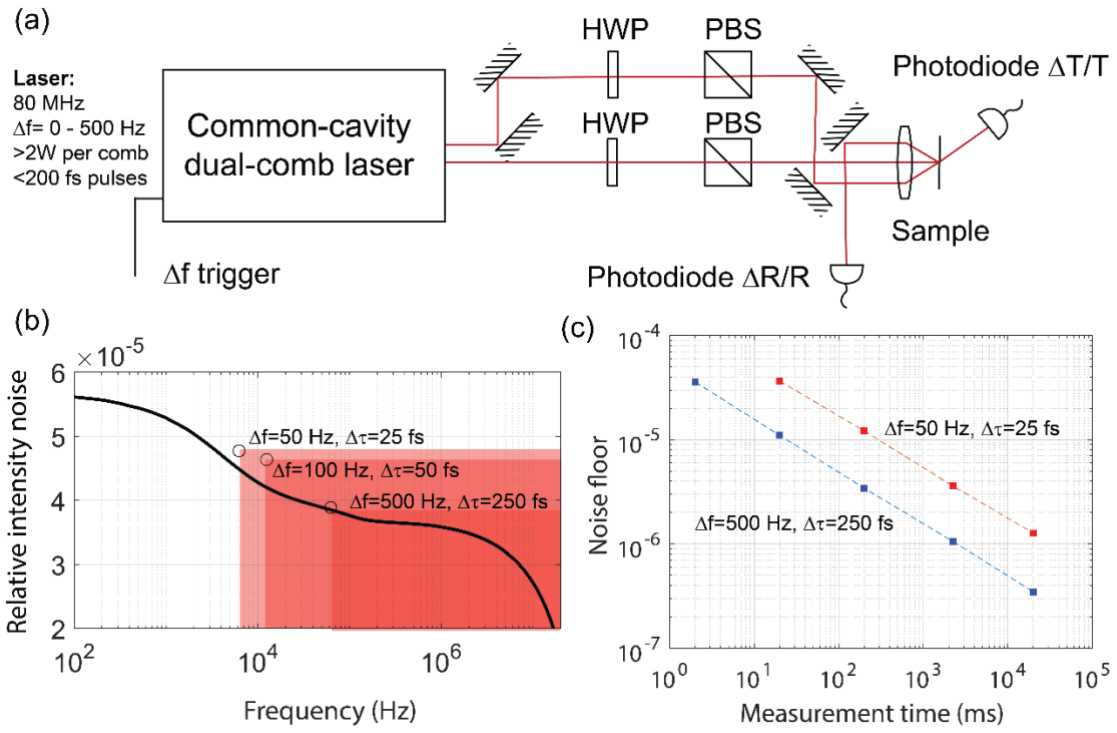

Fig. 1. (a) Experimental setup. HWP – half-waveplate, PBS – polarizing beam splitter. **(b)** Probe beam relative intensity noise (RIN) measured with a signal source analyser and integrated from 25 MHz (black curve). Black circles indicate the noise floor (standard deviation of the background) of a 100 ps long pump-probe time window. Δf indicates the repetition rate offset of the two combs and Δτ indicates the measurement time resolution based on the signal detection bandwidth (here set to 25-MHz acquisition bandwidth). The lower frequency bound is determined from the 100 ps acquisition window and the comb scale factor Δf/f. **(c)** Measurement noise floor versus acquisition time (averaging) for two different acquisition cases.

Picosecond ultrasonics is a widely adopted ultrafast measurement technique which allows for the characterization of thin-film structures. One advantageous approach to picosecond

ultrasonics is the use of the ASOPS method. However, the classical ASOPS implementations are complex since two lasers and locking electronics are required. Lately, common-cavity dual-comb lasers have emerged as a cost- effective alternative and have proven to be well-suited for picosecond ultrasonics [1]. In this submission we apply a new common-cavity dual-comb laser [2] to picosecond ultrasonics and study signal to noise properties using the setup shown in Fig. 1(a).

Firstly, we show that the laser relative intensity noise (RIN) measurement can be used to predict the noise floor in the picosecond ultrasonics measurement (Fig. 1(b)) if the probe power arriving on the photodiode is known. Secondly, we show that an ultra-low noise floor can be obtained by averaging the traces (Fig. 1(c)) reaching 3.5×10^{-7} in 20-second-long acquisition.

We apply this high-sensitivity pump-probe setup to study ruthenium thin-films at different thicknesses. Ruthenium it is a promising replacement for copper interconnects in computer chips [3]. The pump-probe response of ruthenium films of different thicknesses is shown in Fig. 2(a). We observe clear localized strain waves in the 100 nm thick sample. As the sample thickness is reduced, instead of a localized strain wave, we observe a standing wave motion, showing an oscillatory signal. Furthermore, we look at relative transmission and reflection channels as shown in Fig 2(b). We find that a measurement of the change in relative transmission $\Delta T/T$ gives the same but sign-inverted response as the corresponding $\Delta R/R$ measurement.

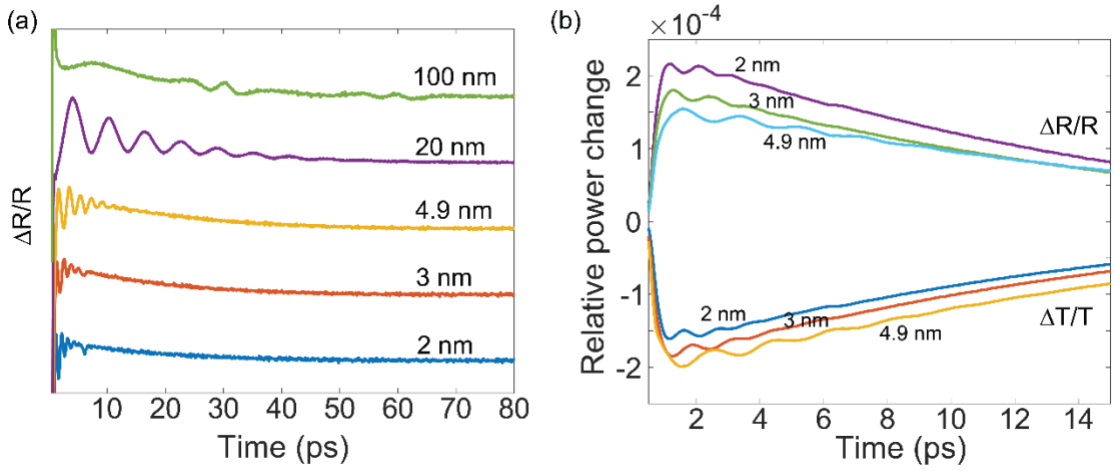

Fig. 2. (a) Relative reflectivity change $\Delta R/R$ for five different ruthenium thin films. The shown signal traces are offset vertically for better visibility. The background was removed with a slowly moving average to enhance the visibility of the fast signals. **(b)** Corresponding measurements of relative transmission and reflectivity of ruthenium samples of different thicknesses.

To conclude, we have demonstrated that a common-cavity dual-comb laser presents an efficient approach to pump-probe measurements. Firstly, the ultra-low RIN of the solid-state laser architecture enables excellent measurement sensitivity. Secondly, by using a sufficiently high repetition rate difference, we can position the signal frequencies to be close to the shot-noise limit. This is a cost-effective approach to high-performance measurements.

References

[1] J. Pupeikis, B. Willenberg, F. Bruno, M. Hettich, A. Nussbaum-Lapping, M. Golling, C.P. Bauer, S.L. Camenzind, A. Benayad, P. Camy, B. Audoin, C.R. Phillips, U. Keller, Picosecond ultrasonics with a free- running dual-comb laser, Opt. Express 29 (2021) 35735–35754. https://doi.org/10.1364/OE.440856.

[2] J. Pupeikis, B. Willenberg, S.L. Camenzind, A. Benayad, P. Camy, C.R. Phillips, U. Keller, Spatially multiplexed single-cavity dual-comb laser for equivalent time sampling applications, arXiv:2203.08536.

[3] S. Dutta, S. Kundu, A. Gupta, G. Jamieson, J.F.G. Granados, J. Bömmels, Z. Tökei, C. Adelmann, Highly Scaled Ruthenium Interconnects, 38 (2017), 949-951 https://doi.org/10.1109/LED.2017.2709248.

07
Biomedical Imaging and Applications

Measurement of glycated haemoglobin through photoacoustic spectroscopy, a non-destructive assessment

Olvera LI[(1)], Villanueva C[(2)], Cruz A[(3)*]

(1) Instituto Politecnico Nacional, Escuela Superior Física y Matemáticas, Ciudad de México, México.

(2) Instituto Politécnico Nacional, Escuela Superior de Medicina, Ciudad de México, México.
(3) Departamento de Física, CINVESTAV-IPN. Ciudad de México, México.

*Corresponding author's email: alfredo.cruzorea@cinvestav.mx

Global diabetes prevalence has reached epidemic proportions. It was estimated that diabetes prevalence in adults was 10.1% in 2021 (536.6 million people), with a projected rise to 12.2% in 2045 (783.2 million people) [1]. Chronic complications are the main cause of morbidity and mortality in diabetes. According to the American Diabetes Association diabetes diagnosis criteria include fasting plasma glucose (PG, 100-125 mg/dL), 2 h PG during a 75 g oral glucose-tolerance test (140-199 mg/dL), random PG (200 mg/dL) and 5.7-6.4% glycated haemoglobin (HbA1c) [2]. HbA1c is the most accurate variable for metabolic monitoring of diabetes. Variability of HbA1c is associated with chronic complications and predicts outcome of cardiovascular events [3]. There are several techniques to measure Hb1Ac [2]. However, samples >200 μL, are required, they are manipulated, destroyed, and only used for the measurement of HbA1c. In previous work we used photoacoustic spectroscopy (PAS) to correlate glycemia with haemoglobin and p450 cytochrome [4,5]. PAS, a non-destructive technology used to measure different substances in body fluids [6], is based on the following phenomena: A sample is confined into a close chamber where it is illuminated with a modulated light beam. The sample absorbs the incident light and heat is produced. [7] The release of heat to the environment is periodic, generating a pressure wave or an acoustic wave (signal) that is detected by a microphone. [7].

The goal of the present study was to measure HbA1c through PAS. Photoacoustic (PA) absorption spectra were obtained according to previous work [4,5]. In short, 60 μL of six Bio-Rad Lyphochek HbA1c standards were used instead of blood. Concentrations of HbA1c were from 3.1 to 19.8 %. Five measurements were performed for each standard. Absorption spectra were detected from 250 to750 nm. Spearman correlation was calculated. Significance level was $p<0.05$. Data are shown as mean ± standard error of the mean (SEM). Figure 1 shows concentration dependent spectra. Figure 2 shows a significant correlation of the area under the curve (AUC, 250-750 nm) and the percentage of HbA1c. As far as we know, it is the first time that PAS is used to measure and standardize HbA1c concentrations. The advantages of PAS over the other techniques used to measure HbA1c include using small volume (less than 100 μL) and a non-destructive technique that allow the measurement of HbA1c and other substances at the same time, *ie* albumin, creatinine, p450 cytochrome, which are important for the evaluation of patients with diabetes. It is concluded that PAS a non-destructive technique that could be used to measure HbAlc, which opens a new horizon in the evaluation of patients with diabetes.

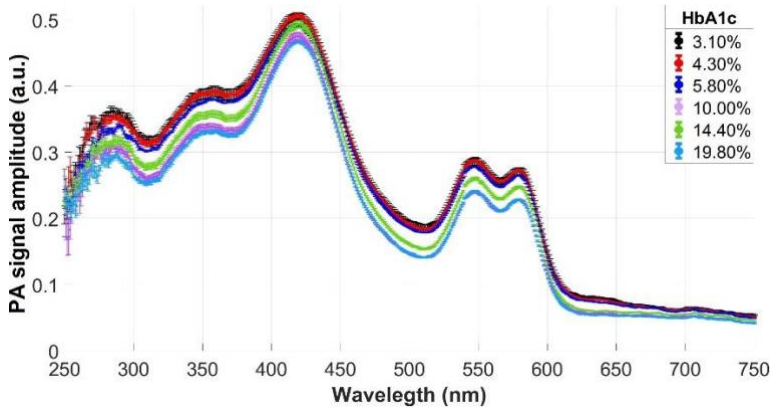

Fig. 1. Photoacoustic absorption spectra from 250 to 750 nm of HbA1c standards. The figures shows the mean ± standard error of the mean (SEM) of five measurements. Concentrations of the standards are from 3.1 to 19.8%.

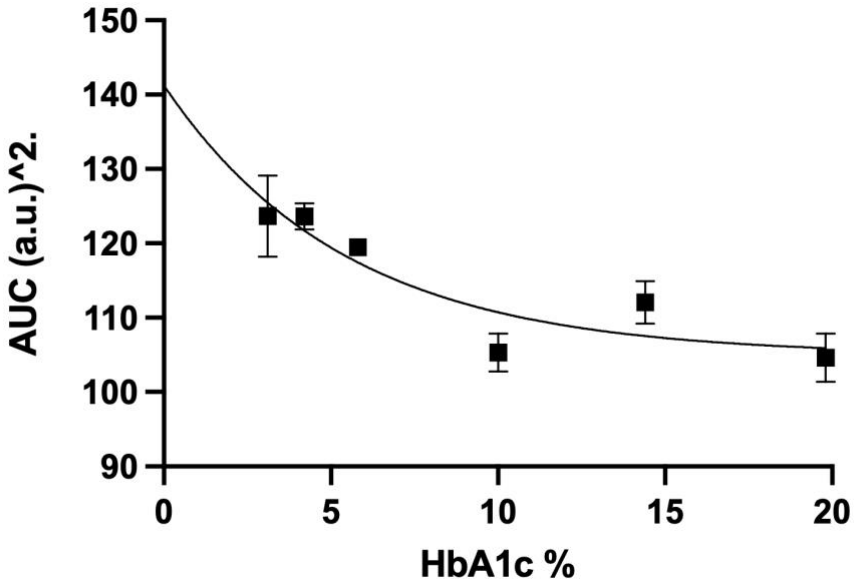

Fig. 2. Area under the curve (AUC) obtained from photoacoustic spectra (figure 1). It is shown the mean ± SEM. R= - 0.94, p = 0.01. Spearman correlation. a.u. = arbitrary units.

Acknowledgements – The authors thank E. Ayala, R. Fragoso, M. Guerrero, A. B. Soto for their technical support at the Physics Department, CINVESTAV-IPN. The study was supported by grants SECTEI No. 282-2019 and SIP20212108. In addition, the study was supported by Technological Development Projects or Innovation for IPN students.

References

[1] H. Sun et al., IDF Diabetes Atlas: Global, regional and country-level diabetes prevalence estimates for 2021 and projections for 2045, Diabetes Res Clin Practice. 183 (2022) 109119. https://doi.org/10.1016/j.diabres.2021.109119.

[2] American Diabetes Association. 2. Classification and diagnosis of diabetes: Standards of Medical Care, Diabetes Care 44 (2021):S15-S33. https://doi.org/10.2337dc21-S002.

[3] A. Ceriello, et al., HbA1c variability predicts cardiovascular complications in type 2 diabetes regardless of being at glycemic target. Cardiovasc Diabetology 21 (2022):13. https://doi.org/10.1186/s12933-022- 01445-4.

[4] L.I. Olvera Cano, et al, Photoacoustic Spectroscopy and Hyperglycemia in Experimental Type 1 Diabetes, Appl. Spectrosc. 75 (2021) 1465–1474. https://doi.org/10.1177/00037028211047257.

[5] L.I. Olvera Cano,et al, Photoacoustic spectroscopy allows to make correlations between blood p450 cytochrome and glycemia in type 1 experimental diabetes, J Physics: Conf Series, 2090(2021) 0121152. https://doi.org/10.1088/1742-6596/2090/1/012152.

[6] Q. Pan, et al, Application of Photoacoustic Spectroscopy to Human Blood, Photoacoust. Phothermal Phenom. (1988) 542–545. https://doi.org/10.1007/978-3-540-48181-2_146.

[6] A. Rosencwaig, et al, Theory of the photoacoustic effect with solids, J. Appl. Phys. 47 (1976) 64–69.

In vivo monitoring of laser tattoo removal using pulsed photothermal radiometry and diffuse reflectance spectroscopy

Golmajer Zima N(1), Verdel N(1), Lukač M(1,2), Majaron B(1,3)*

(1) Department of Complex Matter, Jožef Stefan Institute, Ljubljana, Slovenia
(2) Fotona, d.o.o., Ljubljana, Slovenia
(3) Faculty of Mathematics and Physics, University of Ljubljana, Slovenia

*Corresponding author's email: neza.golmajer-zima@ijs.si

Background and Methods – We present an innovative attempt to noninvasively characterize black tattoos in a human volunteer and objectively monitor the effectiveness of laser tattoo removal treatment. To that end, we have adapted a recently introduced methodology for assessment of the structure and composition of human skin *in vivo* by combining two optical techniques [1,2]. The approach combines pulsed photothermal radiometry (PPTR), involving time-resolved measurements of mid-infrared emission with a fast infrared camera (FLIR Systems SC7500) after irradiation with a millisecond laser pulse at 532 nm, and diffuse reflectance spectroscopy (DRS) in visible part of the spectrum (λ = 400–650 nm). Both data sets are fitted simultaneously with the respective predictions of a numerical model of light- and heat transport in human skin (with or without the tattoo) [3]. In intact skin, this approach allows assessment of the contents of specific chromophores (e.g., melanin, oxy- and deoxy-hemoglobin) as well as scattering properties and thicknesses of the epidermis and dermis [1,2].

In present study, four test sites in a homogeneous black tattoo of a healthy volunteer were treated using a medical-grade laser instrument (StarWalker® MaQX by Fotona d.o.o., Slovenia; λ = 1064 nm) with radiant exposures of 1.5, 3.0, 4.5, and 6.0 J/cm^2, respectively.

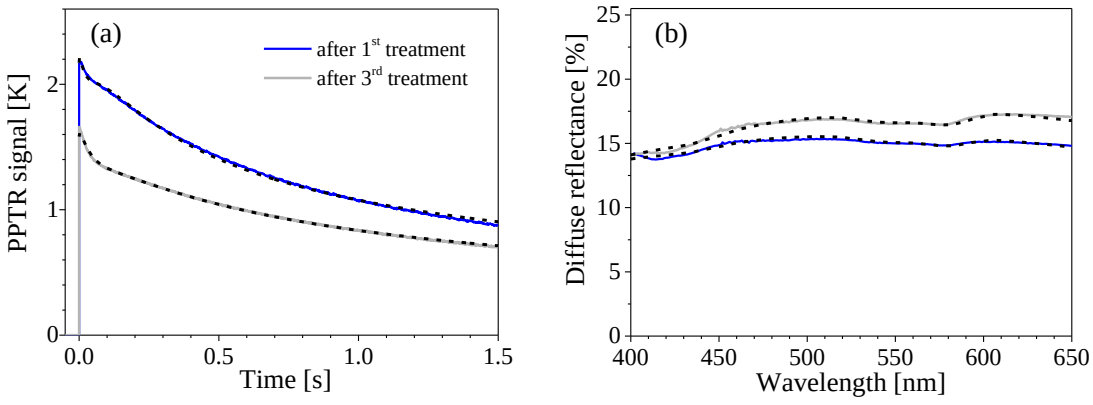

Fig. 3. (a) PPTR signals and **(b)** DRS spectra as measured in a black tattoo in human skin in vivo after the first (blue solid lines) and third laser treatment (grey) at radiant exposure of 6 J/cm^2. The dashed lines are best fitting predictions from our numerical model, based on a 3-layer optical model of the tattooed skin.

Results and Discussion – The results of our analyses (Fig. 2a) reveal a significant reduction of the tattoo ink content after both first and second treatment in the test site irradiated with 6 J/cm^2, but only

after the second one at 4.5 J/cm^2. In contrast, the decrease of the ink content is only marginal in the site treated with 3 J/cm^2, and insignificant at 1.5 J/cm^2. In addition, the results also indicate a gradually increasing depth of the tattoo ink layer with the applied radiant exposure and number of treatments.

Both results match very with the visual inspection of the test sites, which demonstrates a good sensitivity and robustness of our approach. Moreover, the presented technique provides an objective assessment of the treatment success, even in the cases where the effect may be difficult to see with a naked eye.

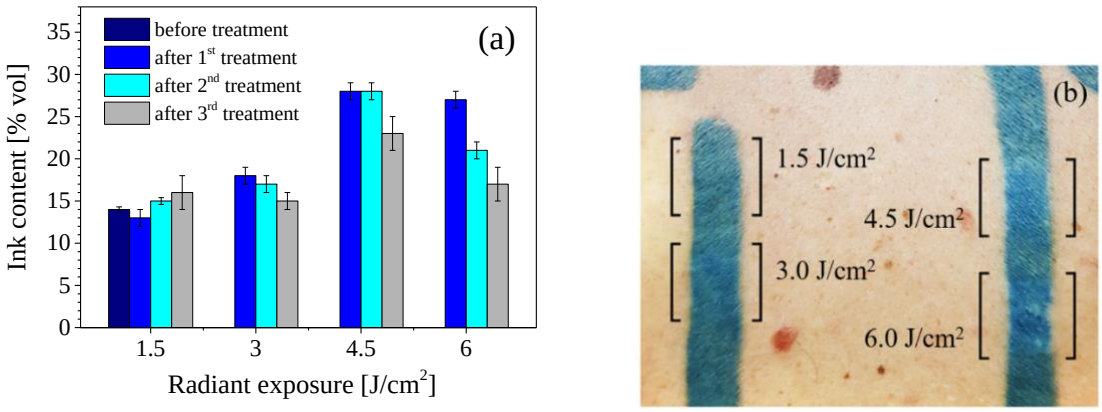

Fig. 4. (a) The assessed contents of the tattoo ink in dermis over the course of three laser treatment sessions. **(b)** Photograph of the four test sites several weeks after the second laser treatment, with the applied radiant exposure values.

Acknowledgments – This research was supported by the Slovenian Research Agency (grants P1-0192 and PR-10471). The authors thank Fotona, d.o.o. (Ljubljana, Slovenia) for the loan of medical-grade laser used for PPTR measurements (DualisVP), and for performing the tattoo removal treatments.

References

[1] N. Verdel, A. Marin, M. Milanič, B. Majaron, Physiological and structural characterization of human skin in vivo using combined photothermal radiometry and diffuse reflectance spectroscopy, Biomed. Opt. Express 10 (2019) 944–960. https://doi.org/10.1364/BOE.10.000944.

[2] N. Verdel, J. Tanevski, S. Džeroski, B. Majaron, Predictive model for the quantitative analysis of human skin using photothermal radiometry and diffuse reflectance spectroscopy, Biomed. Opt. Express 11 (2020) 1679–1696. https://doi.org/10.1364/BOE.384982.

[3] N. Verdel, B. Majaron, Objective noninvasive monitoring of laser tattoo removal in a human volunteer: a proof of principle study, Proc. SPIE 11585 (2020) 115850A. https://doi.org/10.1117/12.2582137.

Long-wave and mid-wave photothermal coherence tomography imaging of human teeth

Thapa D[(1)], Welch R[(1)], Sivagurunathan K[(1,2,3,4)], Tabatabaei N[(5)], Mandelis A[(1,2,3,4)*]

(1) Department of Mechanical and Industrial Engineering, University of Toronto, Toronto, Canada
(2) Center for Advanced Diffusion-Wave and Photoacoustic Technologies (CADIPT), Toronto, Canada
(3) Institute for Advanced Non-Destructive and Non-invasive Diagnostic Technologies, Toronto, Canada
(4) Quantum, Dental Technologies, Toronto, Canada
(5) Department of Mechanical Engineering, York University, Toronto, Canada

*Corresponding author's email: mandelis@mie.utoronto.ca

Enhanced truncated-correlation photothermal coherence tomography (eTC-PCT) using mid-wave infrared (MWIR) cameras (spectral range 3-5 μm) has recently been shown to offer tomographic visualization of early dental caries. However, it has been theorized that long-wave infrared (LWIR) eTC-PCT systems may offer better tomographic performance by taking advantage of the intrinsic attenuation of direct radiative emission by dental enamel in the LWIR spectral range (8- 14 μm), enabling more effective delayed conductive thermal contributions from subsurface caries. In this study, we compare the performance of LWIR and MWIR eTC-PCT systems for detecting natural caries, bacterial caries, and artificially demineralized enamel surfaces. The comparative results show that the LWIR eTC-PCT system provides 3D visualization of early caries and internal micro-cracks similar to those obtained from the MWIR-based eTC-PCT system, albeit with ~1.3 dB lower signal-to-noise ratio.

Background – The infrared transmission spectrum of human enamel shows that the enamel is significantly more opaque in the long-wave infrared band (8-14 μm) compared to the mid-wave infrared band (3-5 μm). Therefore, direct radiative transfer competes with conductive heat transfer in MWIR while the conductive heat transfer is more dominant in LWIR. For tomographic imaging, direct radiative emissions are unwanted as they are instantaneous/in-phase, possibly dominating the delayed and depth-dependent conductive thermal contributions of defects. 3D tomographic visualizations of dental caries using a MWIR camera and an eTC-PCT system have been frequently reported; however, tomographic imaging using a LWIR eTC-PCT system has not yet been explored. Therefore, the purpose of this study is to assess the performance of LWIR eTC-PCT in detecting dental caries and compare this modality to conventional MWIR eTC-PCT.

Methods – We adopted the same experimental setup and eTC-PCT data processing software as thosereported in [1]. LWIR and MWIR eTC-PCT systems featured similar configurations and components but were equipped with a LWIR and a MWIR camera each, as the goal was to study the eTC-PCT image characteristics in the mid-wave and long-wave IR spectral emission regions corresponding to the spectral responses of the two cameras. Three dental samples: one with natural caries and an internal crack, one with bacterial caries, and one with an artificially demineralized enamel surface were tested. 2D slice-by-slice images were extracted from the amplitude and phase channels and compiled to yield 3D images of the samples. Then, the 3D images obtained from both LWIR and MWIR systems were compared.

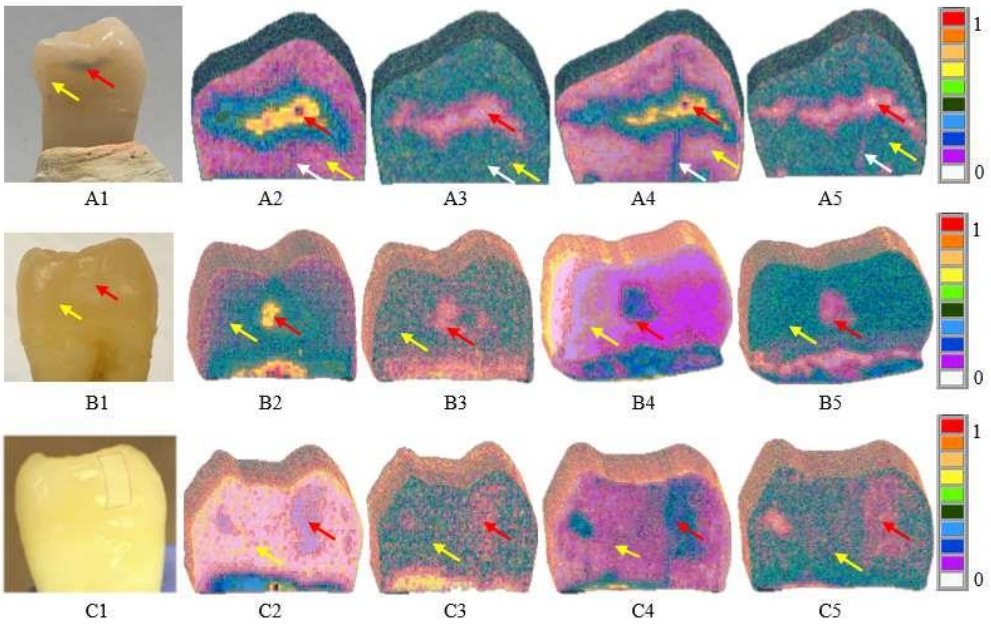

Fig. 1. Panel 1 shows photographs of dental samples with natural caries (A1), bacterial caries (B1), and an artificially demineralized surface (C1). Panels 2 and 3 show the 3D visualization of these samples with the LWIR eTC-PCT imager in the amplitude and phase channels, respectively. Similarly, Panels 4 and 5 correspond to the 3D visualization with the MWIR eTC-PCT imager.

Results – The 3D reconstructed images of the dental samples are shown in Fig. 1. The defective regions, such as natural caries, bacterial caries, and artificially demineralized surface (shown by red arrows in Panel 1), are clearly distinguishable from the corresponding intact areas (yellow arrows in Panel 1) in both 3D reconstructed images, amplitude (Panel 2) and phase channels (Panel 3) of the LWIR eTC-PCT imager; and amplitude (Panel 4) and phase (Panel 5) channels of the MWIR eTC-PCT imager, respectively. The carious regions are visible in both 3D amplitude and phase images. However, the amplitude channel reveals higher contrast compared to the phase channel. The hidden crack (white arrow in natural caries in Panel A) is shown in both the LWIR and MWIR systems; however, the MWIR system exhibits clearly higher contrast and "crisper" features compared to those obtained with the LWIR system.

Conclusions – The LWIR eTC-PCT imager provides 3D visualization of early caries and micro-cracks similar to those obtained from (the more expensive) MWIR eTC-PCT imager at the cost of lower SNR and spatial resolution of small size flaws and lesions. The carious sites are more prominently revealed in the 3D images compared to visual inspection. A hidden crack invisible under visual inspection was made visible in the 3D reconstructed images. While MWIR eTC-PCT imagers provide optimal imaging quality, contrast and resolution of dental lesions with superposed radiative and conductive photothermal image capability, LWIR eTC-PCT imagers can serve as a lower-cost purely conductive imaging alternative for the slice-by-slice detection of dental caries at different depths and 3D visualization of caries.

References

[1] S. Roointan et. al. 3D dental subsurface imaging using enhanced truncated correlation-photothermal coherence, Nature Sci. Rep. 9:16788 (2019) 1-12.

Optothermal and photoacoustic characterization of protein corona and blood using plasmonic nanoparticles: pharmaceutical aspects

Khosroshahi ME[(1,2)*], Woll-Morison V[(1)], Kim K[(1,3)], Lashkari B[(4)], Mandelis A[(2,4)*]

(1) Nanobiophotonics & Biomedical Research Laboratory, M.I.S. Electronics Inc., Richmond Hill, L4B 1B4, Canada
(2) Institute for Advanced Non-Destructive & Diagnostic Technologies (IANDIT), University of Toronto, Toronto M5S 3G8, Canada
(3) University of Waterloo, Department of Biochemistry, Waterloo, Canada
(4) Center for Advanced Diffusion-Wave and Photoacoustic Technologies, Department of Mechanical and Industrial Engineering, University of Toronto, M5S 3G8, Canada

*Corresponding authors' email: m.khosro@miselectronics.com; mandelis@mie.utoronto.ca

Introduction – Plasmonic nanoparticles such as gold nanoparticles (GNP) exhibit unique physical properties compared to bulk counterparts due to their aspect ratio, high surface free energy, and localized surface plasmon resonance (LSPR) [1]. When NPs are administrated into biological fluids, an interaction occurs between the biomolecules and blood plasma resulting in the formation of a layer of adsorbed biomolecules on the surface of NP known as 'protein corona' [2]. Therefore, the adsorption of proteins can modify the physicochemical properties such as size, shape, surface charge, surface composition, biocompatibility, biodistribution, and functionality, which effectively gives a new identity to NP compared to its original condition [3]. This is a critical factor in nanomedicine such as drug delivery in pharmaceutical industry. In this research, citrate-capped gold nanourchins (GNU) were conjugated to the model protein bovine serum albumin (BSA) via passive adsorption. GNU have unique optical properties compared to spherical gold nanoparticles of the same core diameter where the spiky uneven surface causes a redshift in the SPR peak and a larger enhancement of the electromagnetic field at the GNU spike tips in smaller and more localized volume [4]. A non-invasive technique that can used to study the corona is photoacoustic (PA) imaging. However, considering that the drug carriers are normally stabilized by BSA, its interaction will be at tissue or cellular levels. This implies an optimization of laser power interaction with cells to avoid possible damage particularly if it is in blood-containing environment. For this purpose an experiment was performed to assess an *in-vitro* PA effect on GNP-blood combination.

Experimental and results – Fig. 1(a) shows the experimental setup, and the Wavefront Sensor (WFS) results are seen in Fig.1(b). The WFS demonstrated an oscillatory response at given concentrations of GNU with a non-linear intensity distribution, Fig. 2(a). The CdS results showed a gradual transmission decrease followed by an increase after a short time but a faster rate at higher GNU concentrations. Thermal effects on bioplasmonic solution induced by a 800-nm diode laser were investigated using probe beam monitoring and a mid-infrared (MIR) camera, Fig. 2(b). The temperature variation due to protein unfolding and denaturation exhibited a similar non-linear pattern at different GNU volumes.

However, the temperature was lower at higher GNU concentrations indicating a higher rate of protein adsorption,

which effectively mitigates the LSPR heating. An 800-nm diode laser was used for photoacoustic radar imaging (PARI) with linear chirp laser modulation to provide visualization of blood with and without the use of GNPs. The PA signal amplitudes in different samples increased linearly up to 2.5 W in the order of S5>S2>S1 where S1 is blood only, S2 blood+10% (3.8 µg/mL) GNPs, and S5 S5 (de-oxygenated blood); from there onwards the signals decreased sharply. The cellular deformation time of S1 was found to be faster than S2 and S5 but from 2.5 W afterwards S1 and S2 showed the same rate of decrease.

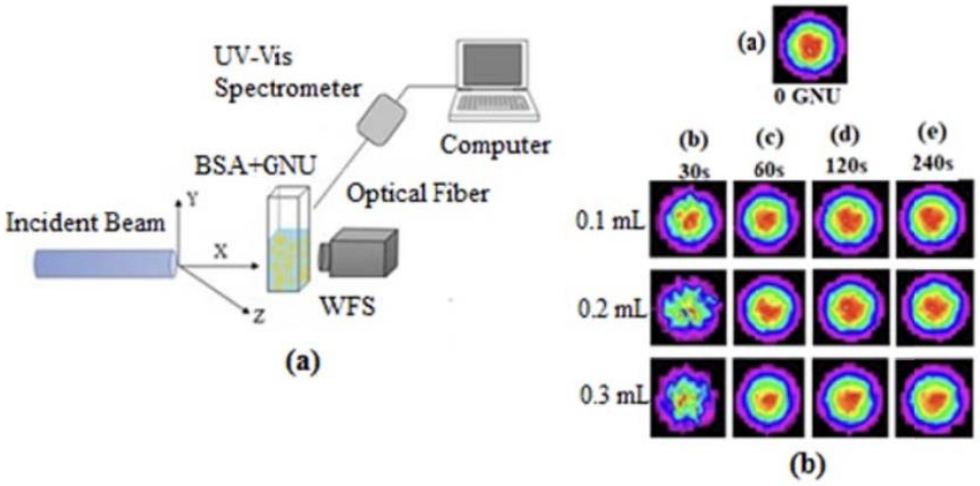

Fig. 1. (a) Experimental setup, **(b)** WFS oscillatory pattern of corona variation

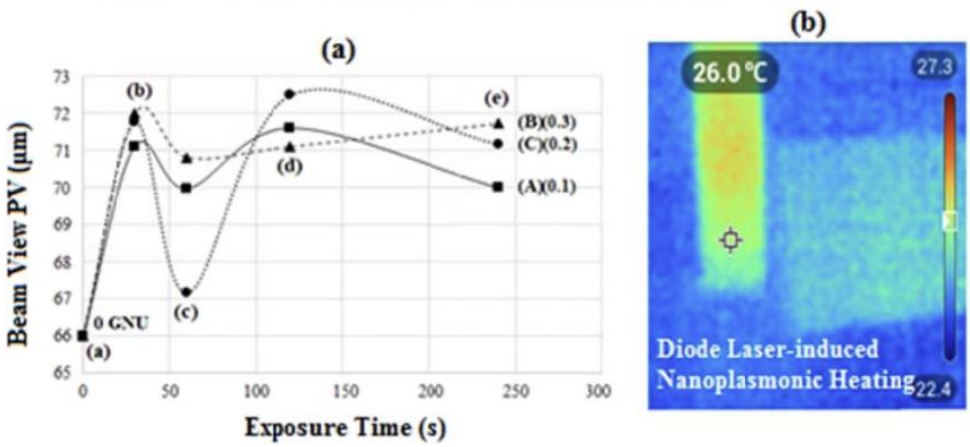

Fig. 2. (a) WFS beam view displacement versus laser exposure time, **b)** An example of nonbioplasmonic solution heated by a 2W diode laser

Conclusions – Optical and thermal characterization of protein and corona behavior is not only important in understanding the underlying principles, but will also assist in development of more smart drug delivery systems where the integrity of drug is preserved during the delivery process. Further research is needed to explore the short- (ms) and long-time (hours) effects of optical and thermal parameters on corona and its interaction with biofluid in regard to drug delivery system.

References

[1] M.E. Khosroshahi, A. Mandelis, B. Lashkari, J. Biomed. Opt. 20 (2015) 076009.

[2] M. Lundqvist, J. Stigler, L. Lynch, Proc. Natl. Acad. Sci. 105 (2008)14265-14270.

[3] P. Roach, D. Farrar, C. Perry, J. Am. Chem. Soc. 127 (2005) 8168-8173.

[4] R. Rodríguez-Oliveros R, J.A. Sánchez-Gill, Opt. Express 20 (2012) 621-626.

08
Novel Methodologies, Instrumentation, and Applications

Machine learning based determination of photoacoustic signal parameters for different gas mixtures

Lukić M(1)*, Ćojbašić Ž(2), Markushev D(3)

(1) Faculty of Occupational Safety, University of Nis, Carnojevica 10a, Nis 18000, Serbia
(2) Mechanical Engineering Faculty, University of Nis, Aleksandra Medvedeva 14, Nis 18000, Serbia
(3) Institute of Physics, University of Belgrade, Pregrevica 118, Belgrade-Zemun 11080, Serbia

* Corresponding author's email: mladenalukic@gmail.com

Detection of different trace gases with the same instrument is one of the important requirements for in situ measurement. Benefits of computational intelligence (CI) implementation in photoacoustic spectroscopy (PAS) such as real-time operation and accuracy are confirmed [1], but whether intelligent PAS method can provide high selectivity in the detection of different trace gases? In this paper pulsed PAS is used to study C_2H_4+Ar gas mixture. Experimental signals are generated in the C_2H_4+Ar gas mixture, at absorber pressures $p_{(C2H4)} = 0.47$ mbar, total mixture pressure $p_{tot} = 100$ mbar, and laser fluence $\Phi = 1\ \mathrm{Jcm^{-2}}$ [2]. Although multilayer perceptron network (MLPN) determines parameters of PA signal (spatial laser beam radius and vibrational-to-translational relaxation time) successful, selection of optimal MLPN architecture through a trial-and-error process, can be computational cost. To overcome problems related to network architecture Generalized Regression Neural Network (GRNN) is used to estimates PA signal parameters [3]. GRNN has some advantages such as fixed structure (there is no requirements for overall network optimization to select parameters of hidden neurons), and fast training (without an iterative procedure). Networks were trained in an off-line regime. Theoretical PA signals (1) as the solution of the nonhomogeneous linearized wave equation, are calculated by the Fourier method [4] for top-hat spatial laser beam profile and different values of parameter ε (relaxation time) ∈ [0.5-4] and parameter r^* (laser beam radius) ∈ (39, 39.5, 40, 40.5).

$$\delta p(r^*, t^*) = \frac{RE_0}{C_v V}\int_0^\infty (l^2+\varepsilon^2)^{-1}[-\varepsilon exp(-\varepsilon t^*) + lsinlt^* + \varepsilon coslt^*]J_0(lr^*)h(l)ldl. \quad \text{Eqn. 1}$$

where ε related with relaxation time τ_{V-T} ($\varepsilon = \tau_p/\tau_{V-T}$) and r^* related to the radius of the laser beam r_L ($r^* = r/r_L$). GRNN was trained with 284 theoretical PA signals (Fig. 1). Several network structures were designed with different numbers of neurons in input layers (21 to 50) to test network prediction under different numbers of neurons in the input layer. To compare the efficiency and effectiveness of MLPN prediction for SF_6+Ar gas mixture and GRNN prediction for C_2H_4+Ar, a regression network was designed with 21 input neurons (as well as the MLPN). GRNN with 50 input neurons (Fig. 2) estimated parameters ε and r^* with errors 0.79%, and 0,02% respectively. GRNN with 21 input neurons provides better prediction in

comparison with MLPN primary for parameters ε. Molecules SF_6 and C_2H_4, are medium-sized polyatomic molecules with common relaxation characteristics, so possible limitations for in situ measurement are discussed.

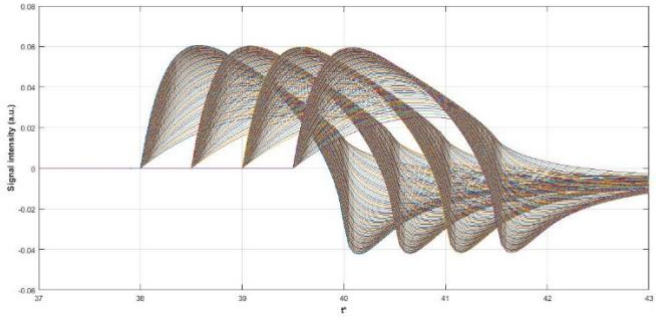

Fig. 1. Training set of 284 PA signals calculated by the Fourier method for top hat spatial laser beam profile and ε ∈ [0.5-4] and r^*∈ (39, 39.5, 40, 40.5).

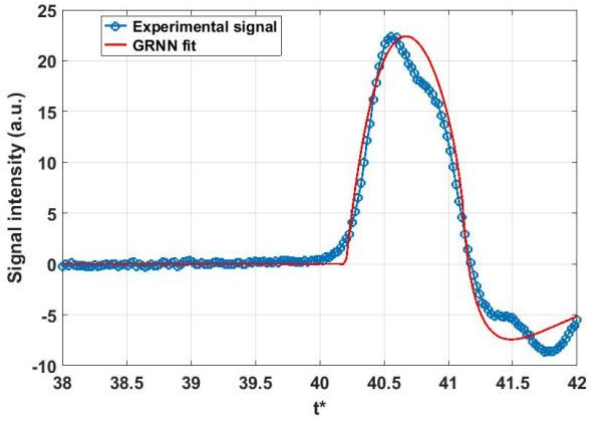

Fig. 2. Comparison between experimental PA signal and PA signal estimated by GRNN with 50 input neurons.

References

[1] M. Lukić, Ž. Ćojbašić, M.D. Rabasović, D.D. Markushev, Computationally intelligent pulsed photoacoustics, Meas. Sci. Technol. 25 (2014) 125203 (9pp). https://doi.org/10.1088/0957-0233/25/12/125203.

[2] Rabasović, M.D., Nikolić, J.D. & Markushev, D.D. (2006b) Pulsed photoacoustic system calibration for highly excited molecules: II. Influence of the laser beam profile and the excitation energy decay. Meas. Sci. Technol. 17 (2006) 1826–1837. https://doi.org/10.1088/0957-0233/17/7/022.

[3] D.F. Specht, A General Regression Neural Network, IEEE Trans. Neural Netw. 2 (1991) 568-576. https://doi.org/10.1109/72.97934.

[4] K.M. Beck, A. Ringwelski, R.J. Gordon, Time-resolved optoacoustic measurements of vibrational relaxation rates, Chem. Phys. Lett. 121 (1985) 529 – 534. https://doi.org/10.1016/0009-2614(85)87134-7.

The reduction of neural network input vector for efficient optimization of photoacoustic calibration

Jordovic-Pavlovic MI(1)*, Popovic MN(2), Galovic SP(3), Djordjevic KLj(3), Nesic MV(3), Markushev DK(2), Markushev DD(2)

(1) Faculty of information technology, Metropolitan University, Belgrade
(2) Institute of Physics, University of Belgrade, Belgrade - Zemun, Serbia
(3) Vinca Institute of Nuclear Sciences- National Institute of the Republic of Serbia, University of Belgrade, Belgrade, Serbia

*Corresponding author's email: miroslava.pavlovic@metropolitan.ac.rs

The research presented in this paper is part of an effort to improve the process of calibration procedure optimization of model - dependent diagnostic techniques (transmission frequency photoacoustics) using a machine learning approach. A regression model for recognizing the characteristics of a microphone as a photoacoustic detector has already been developed and significant results have been obtained, first in reducing the influence of measuring instruments, then in significantly reducing the processing time of measured data, reaching the so-called work in real time, while maintaining the basic requirements - to make measurements reliable and accurate. Testing the model under different conditions (theoretical or experimental signals, with and without noise, different types of microphones, different samples) we found that the accuracy of the model is high and that the processing speed of measured data does not change significantly by reducing the input vector dimension of the machine learning algorithm. The question is how far can the reduction go without losing the quality of measurements? Computational intelligence algorithms - artificial neural networks and principal component analysis of main characteristics (amplitude and phase), supplemented by discussion of their correlations and expert knowledge can indicate a solution: the data set can be reduced to 10 characteristics, which means that the measurement procedure is reduced to 5 measuring points. We confirmed this assumption in this paper with satisfactory accuracy and reliability by a regression model for the characterization of three types of microphones. It has been shown that the procedure of measuring and characterizing a microphone can be performed simply and quickly by measuring at 5 defined points. At the same time, the problem of different number of measuring points is generalized by a new reduced set of characteristics.

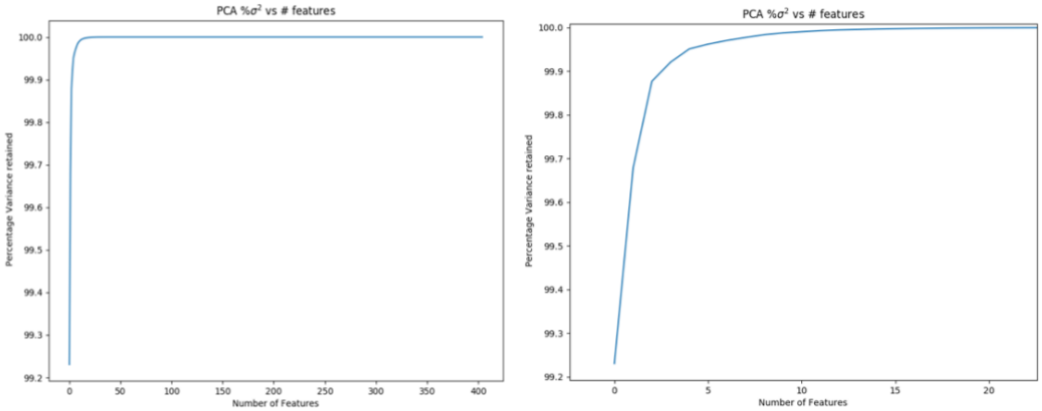

Fig. 1. *a. Reduced dataset variance depending of number of features, analyzed for microphone ECM30B (dataset original dimension: 400 x 67 500), b. zoom of diagram a. to lower number of features*

Table 1. Regression model performance on reduced data set for three types of microphones

Average deviation from the accurate value expressed in percentage of the accurate value on the test set, microphone ECM30B, accuracy of the regression model 97.8 %					
Parameter	f_2	f_3	f_4	ξ_3	ξ_4
Average deviation	0.05664359	0.13738047	0.0719733	1.290471	1.2778711
Average deviation from the accurate value expressed in percentage of the accurate value on the test set, microphone ECM60, accuracy of the regression model 98.32 %					
Parameter	f_2	f_3	f_4	ξ_3	ξ_4
Average deviation	0.06761368	0.08670316	0.05289495	0.85380656	1.0646605
Average deviation from the accurate value expressed in percentage of the accurate value on the test set, microphone WM66, accuracy of the regression model 98.02 %					
Parameter	f_2	f_3	f_4	ξ_3	ξ_4
Average deviation	0.0737425	0.13992077	0.08633012	1.1550651	1.2725114

References

[1] M.I. Jordović-Pavlović, M.M. Stanković, M.N. Popović, Ž.M. Ćojbašić, S.P. Galović, D.D. Markushev, The application of artificial neural networks in solid-state photoacoustics for the recognition of microphone response effects in the frequency domain, J. Comput. Electron., 19:3 (2020) 1268–1280. https://doi.org/10.1007/s10825-020-01507-4.

[2] M.I. Jordovic-Pavlovic et al., Computationally intelligent description of a photoacoustic detector, Opt. Quantum Electron., 52:5 (2020) 1–14. https://doi.org/10.1007/s11082-020-02372-y.

[3] T. I. Jolliffe, J. Cadima, "Principal component analysis: a review and recent developments," Philos. Trans. R. Soc. A Math. Phys. Eng. Sci., vol. 374, no. 2065, (Apr. 2016). doi: 10.1098/rsta.2015.0202

[4] E. Martel et al., Implementation of the Principal Component Analysis onto high-performance computer facilities for hyperspectral dimensionality reduction: Results and comparisons, Remote Sens., 10: 6 (2018). doi: 10.3390/rs10060864.

Finding the optimal TDLS wavelength

Bahr M-S[1,2], Baumann B[1] and Wolff M[1]*

(1) Heinrich Blasius Institute for Physical Technologies, Hamburg University of Applied Sciences, Hamburg, Germany
(2) School of Computing, Engineering and Physical Sciences, University of the West of Scotland, Paisley, UK

*Corresponding author's email: marcus.wolff@haw-hamburg.de

We present a mathematical method which allows determination of the optimal spectral range for gas mixture analysis based on theoretical absorption spectra. The algorithm is particularly suited for tunable diode laser spectroscopy (TDLS) and represents a multi-step mathematical calculation which can easily be implemented in almost any programming language. We applied the method to exemplary mixtures of hydrocarbons and present the according results.

Introduction – Laser spectroscopy is nowadays a well-established method for the analysis of gaseous mixtures [1,2]. When designing a laser spectrometer, the definition of the laser's emission wavelength or, if tunable, its spectral range is crucial for its potential applications. In practice the identification of a suited spectral range for a certain application, i.e. for the analysis of a certain mixture of gases, is often an educated guess based on known spectra [2,3]. We present, to the best of our knowledge, the first quantitative method to determine a well suited spectral range for sensitive and selective gas analysis. The procedure is customized for lasers of a certain tuning range, such as semiconductor lasers, and delivers its optimal center wavelength.

Mathematical procedure – Fig. 1 shows the flowchart of the mathematical procedure. Prerequisite for the application is that absorption spectra of all relevant components in the mixture are known. They can be measured beforehand or extracted from according databases.

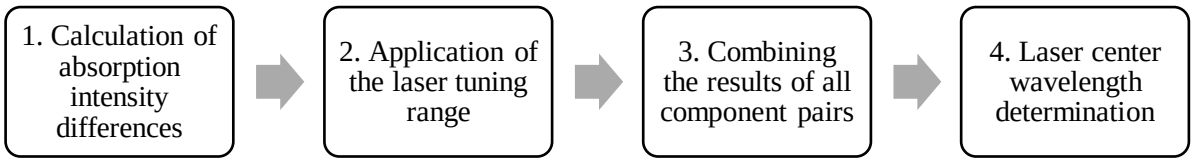

Fig 5. Flowchart of the mathematical procedure.

In order to detect the individual gas components selectively, i.e. with least ambiguity, it is necessary to identify the wavelengths at which the absorption spectra maximally differ from one another [4]. These spectral regions are found in a first step by calculating the intensity differences for each pair of gases. The application of the laser tuning range, approximately 10 nm in case of an interband cascade laser, is implemented in a second step by integrating the single difference spectra over that 10 nm. This integration can be considered a window function that slides over the entire spectral range. In order to combine the contribution of all gas pairs, the "filtered" differences are multiplied. This third step delivers the wavelengths at which the single gas pairs maximally differ and, at the same time, absorption is strong. The wavelength region around the maximum of this function indicates the spectral range in which the center wavelength of the laser should be located. In a fourth step the median of this range is calculated and considered to be the optimum laser center wavelength.

Exemplary results – The mathematical procedure described above was programed in MATLAB and applied to assumptive gas mixtures. Fig. 2 shows the results for a mixture of $^{12}CH_4$ and $^{13}CH_4$. Fig. 3 shows them for a mixture of $^{12}CH_4$, $^{12}C_2H_4$ and $^{12}C_2H_6$. The resulting optimum laser center wavelengths λ_C are 3320.7 nm and 3347.3 nm, respectively. The yellow boxes mark the respective laser tuning ranges.

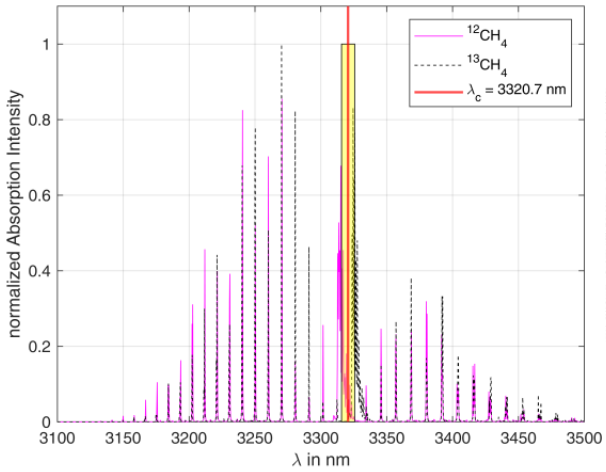

Fig. 2 Mixture of $^{12}CH_4$ and $^{13}CH_4$ [5].

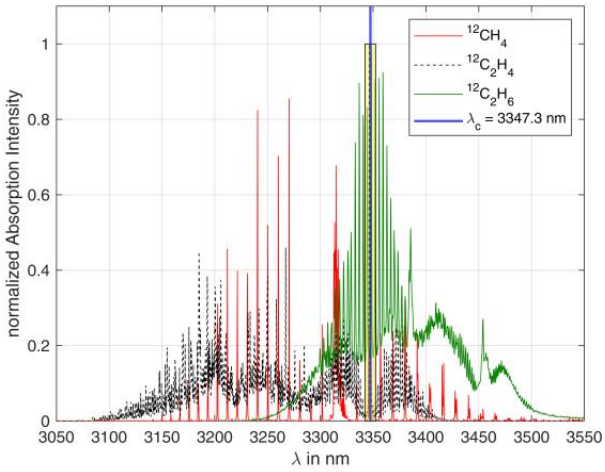

Fig. 3 Mixture of $^{12}CH_4$, $^{12}C_2H_4$ and $^{12}C_2H_6$ [5-7].

References

[1] W. Demtröder, Laserspektroskopie 1: Grundlagen. Germany: Springer Berlin Heidelberg (2011).

[2] W. Demtröder, Laserspektroskopie 2: Experimentelle Techniken. Germany: Springer Berlin Heidelberg (2013).

[3] C. Dyroff, Tunable Diode-Laser Absorption Spectroscopy for Trace-Gas Measurements with high Sensitivity and low Drift. Germany: Universitätsverlag Karlsruhe (2009) pp 40.

[4] T. Tomberg, M. Vainio, T. Hieta, et al. Sub-parts-per-trillion level sensitivity in trace gas detection by cantilever-enhanced photo-acoustic spectroscopy. Sci Rep 8 (2018) 1848. https://doi.org/10.1038/s41598-018-20087-9.

[5] I.W Gordon, L.S. Rothman, R.J Hargreaves, et al. The HITRAN2020 molecular spectroscopic database, JQSRT 277 (2022) 107949

[6] A. Loh, M. Wolff, Absorption cross sections of ^{13}C ethane and propane isotopologues in the 3 µm region. JQSRT 203 (2017) 517-521.

[7]A. Loh, M. Wolff, High Resolution Spectra of ^{13}C Ethane and Propane Isotopologues photoacoustically measured using Interband Cascade Lasers near 3.33 and 3.38 µm, respectively, JQSRT 227 (2019) 111-116.

New voltage control technique for Mach-Zehnder modulators

Vervoort S[(1,2)], Wolff M[(1)*]

(1) Heinrich Blasius Institute for Physical Technologies, Hamburg University of Applied Sciences, Hamburg, Germany

(2) School of Engineering and Computing, University of the West of Scotland, Paisley, UK

*Corresponding author's email: marcus.wolff@haw-hamburg.de

Introduction – For amplitude-modulated Photoacoustic Spectroscopy (PAS) the optical power of the laser must be periodically varied to excite the sample in a way that an acoustic signal develops. The modulation of a radiation source that cannot be directly modulated, such as an Optical Parametric Oscillator (OPO), can be achieved electro-optically by means of a Pockels Cell (PC) and a Mach-Zehnder Interferometer [1,2].

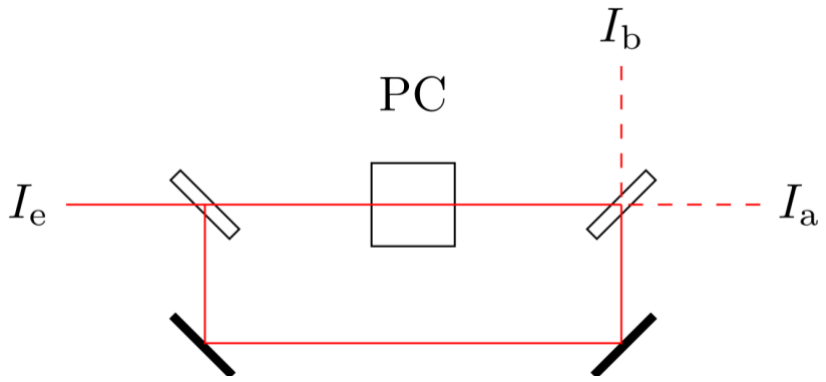

Fig. 1. Mach-Zehnder Intensity Modulator including PC, entrance beam I_e and both outlet beams I_a and I_b.

The basic setup of such a Mach-Zehnder Intensity Modulator (MZM) is shown in Fig. 1. At the first beam splitter (left), the continuous-wave laser is divided equally into two partial waves. Subsequently, one beam is phase-modulated by the PC. When the two beams reunite behind the second beam splitter, the interference leads to intensity-modulated outputs [3].

Method – Since the photoacoustic detection module with its resonator acts as a bandpass filter and cuts off signals outside the bandpass, a high stability of the modulation frequency is required. However, MZMs often suffer from phase drifts that cause operating point fluctuations and signal instabilities. By controlling the bias voltage of the PC it is possible to maintain its quadrature operating point [4]. From the ratio between the average output power and the first-order harmonic signal the required bias correction can be calculated. An approach using a Fast Fourier Transform to control the PC bias voltage achieved stable operation (phase shift: ±0.08°) over three hours [5].

Since the optical wavelength influences the required half-wave voltage of the PC, measurements over a wider spectral range, such as with an OPO, require a control-loop for both, the half-wave and the bias voltage to maintain its optimum operation point. We developed a new concept of a control-loop based on Discrete Fourier Transform (DFT) that allows control of both voltages simultaneously.

Results – A mathematical model of the MZM allows mimicking the influences of the bias voltage and the half-wave voltage on the intensity modulation. Fig. 2 shows two different states in which the MZM does not operate optimally. The upper two diagrams show the case that the bias voltage does not compensate for the phase drift. The lower two diagrams demonstrate what happens if the modulation voltage does not properly match the half-wave voltage of the PC. In both cases harmonics occur. However, the two phenomena can be distinguished from each other: only the half-wave voltage influences the odd harmonics while both voltages excite the even harmonics. The new DFT based control-loop evaluates the DC component, the fundamental and the first two harmonics.

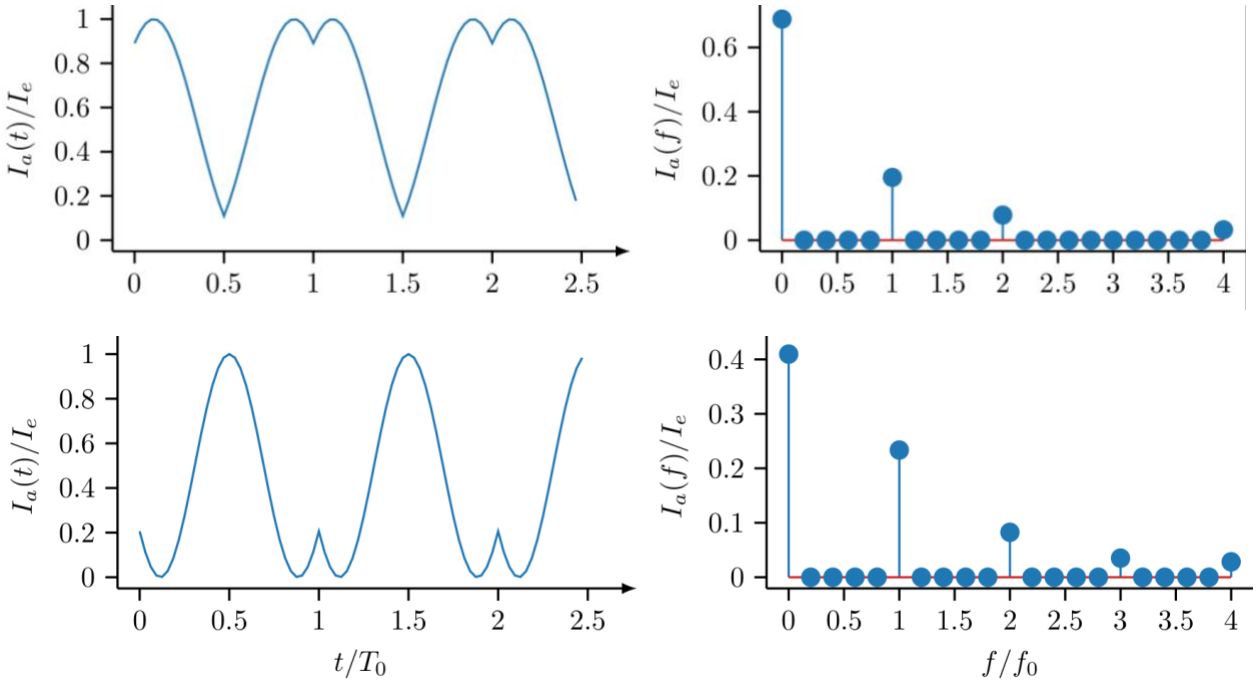

Fig. 2. Intensity ratio between output I_a and entrance I_e in time domain (left) and frequency domain (right). Mismatch of bias voltage (top), mismatch of half-wave voltage (bottom) (modulation frequency; f_0; period: T_0).

References

[1] L. Zehnder, Ein neuer Interferenzrefraktor, Zeitschrift Für Instrumentenkunde 11 (1891) 275–285.

[2] L. Mach, Ueber einen interferenzrefraktor, Zeitschrift Für Instrumentenkunde 12 (1892) 89.

[3] H. Bruhns, Y. Saalberg, M. Wolff, Photoacoustic Hydrocarbon Spectroscopy Using a Mach-Zehnder Modulated cw OPO, Sensors & Transducers 188 (2015) 40.

[4] Y. Li, Y. Zhang, Y. Huang, Any Bias Point Control Technique for Mach–Zehnder Modulator, IEEE Photonics Technology Letters 25 (2013) 2412–2415. https://doi.org/10.1109/LPT.2013.2285184.

[5] J. Svarny, S. Chladek, Model-Based Bias Controller for a Mach-Zehnder Intensity Modulator, Journal of Lightwave Technology 40 (2022) 720–727. https://doi.org/10.1109/JLT.2021.3122460.

Mid-infrared photothermal spectroscopy in aqueous media

Holub E(1)*, Ramer G(1), Lendl B(1)

(1) TU Wien, Institute of Chemical Technologies and Analytics, Getreidemarkt 9, A-1060 Vienna, Austria

*Corresponding author's email: elisabeth.holub@tuwien.ac.at

Background – Photothermal spectroscopy (PTS) leverages site-specific changes in the refractive index upon the absorption of infrared (IR) radiation to analyse the chemical properties of a sample. Given that the refractive index of a material changes with temperature, sample molecules irradiated by a (mid-)IR pump beam will create a refractive index profile, which is detected by a second laser beam. The pump laser wavelengths exploit the strong absorption capacity of biological tissues, while the probe laser wavelength is usually in the visible (VIS) spectrum to achieve sub-micron spatial resolution.

The combination of high-resolution imaging and spectroscopy makes mid-IR PTS a particularly suitable tool for the examination of biological specimens. In addition, Quantum Cascade Lasers (QCLs) can be tuned to very narrow IR wavelength bands to target specific molecular vibrations. This allows for the highly sensitive and label-free detection of different cell constituents and offers a huge potential for identifying different cell and tissue types.

Photothermal experiments on biological specimens are rare, especially in aqueous media. Transmission imaging examples include single preadipocyte cells (cf. [2]) and cancer cells in saline solution (cf. [5]). Measurements in a backscattering configuration were performed on ovarian cancer cells (cf. [1]) as well as bacteria and fungal cells (cf. [4]).

As forward scattering becomes increasingly dominant with increasing size of the scatterer (cf. [3]) and sub-cellular structures are hundreds of nanometres long, a transmission geometry is expected to provide the strongest photothermal signal. Moreover, backscattering setups have made use of highly reflective substrates and are not deemed suitable for imaging of samples in aqueous environments.

Based on the above considerations, a mid-IR PTS instrument was developed and optimised for the broadband-IR measurement of sub-micron structures. The technique will be evaluated with regard to its potential for the analysis of samples in aqueous media or organ-on-a-chip platforms.

Methods – To optimise the mid-IR PT setup for broadband IR laser sources, simulations were carried out in python and FRED (Photon Engineering, https://photonengr.com/fred-software) to test critical components.

A schematic of the mid-IR PTS setup is illustrated in Fig. 1. The visible laser beam (light blue line) is produced by a 633 nm diode laser, while the infrared beam source (red line) is a 4-chip EC-QCL tuneable between 3.4 µm and 11.2 µm (covering marker bands for proteins, lipids, DNA/RNA and carbohydrates). Both beams are combined using a custom beam splitter (BS) and directed towards a reflective objective (Ealing, 36x, focal length: 5.4 mm, NA: 0.5). The sample holder has an IR-transparent window on its bottom and an IR-opaque window on its top to filter out remaining IR pump radiation. The photothermal signal is collected by a visible objective (Nikon CF IC Plan ELWD, focal

length: 5.4 mm, NA: 0.55). After passing a pinhole, the PT signal is read out by a silicon photodiode detector (Thorlabs) and processed by a lock-in amplifier (not shown).

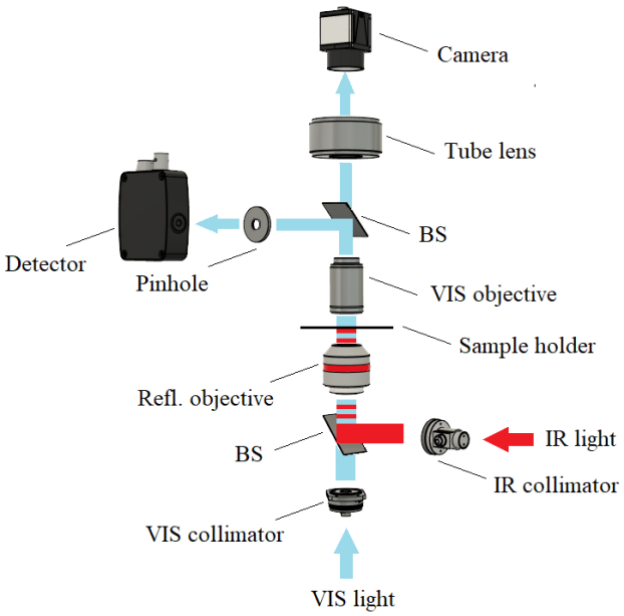

Fig. 1. Experimental PTS setup. The blue line illustrates the visible beam, the red line the IR beam. BS - beam splitter.

To test the sensitivity of the PTS setup and its ability to accurately reproduce absorption features, sub-micron-sized polystyrene beads will be analysed both with the PTS setup and a commercial FTIR microscope (Bruker Hyperion 3000). To test the suitability of mid-IR PTS for probing sub-micron structures in aqueous solutions, the beads will also be measured in saline before being inspected with the PTS setup.

Results and Conclusions – In this work, a PTS mid-IR chemical imaging setup is designed and optimised for the analysis of cells in liquid. In contrast to the conventional spectrometer, the PTS microscope does not only provide better resolution, but is also able to measure test beads when they are immersed in aqueous media (saline). Moreover, the experimental PTS setup covers a large fraction of the mid-IR spectral range.

References

[1] Y. Bai, D. Zhang, L. Lan, Y. Huang, K. Maize, A. Shakouri and J.-X. Cheng, Ultra-fast chemical imaging by widefield photothermal sensing of infrared absorption, Sci. Adv. 5(7) (2019) eaav7127.

[2] E.S. Lee and J.Y. Lee, High resolution cellular imaging with nonlinear optical infrared microscopy, Opt. Express 19(2) (2011) 1378–1384.

[3] M. Selmke, Photothermal Single Particle Detection in Theory and Experiments. Doctoral Thesis, Universität Leipzig (2013).

[4] C. Yurdakul, H. Zong, Y. Bai, J.-X. Cheng, M. Selim Ünlü, Bond-selective interferometric scattering microscopy, Journal of Physics D: Applied Physics 54(36) (2021) 4002-4012.

[5] D. Zhang, C. Li, C. Zhang, M.N. Slipchenko, G. Eakins and J.-X. Cheng, Depth-resolved mid-infrared photothermal imaging of living cells and organisms with sub-micrometer spatial resolution, Sci. Adv. 2(9) (2016), e1600521.

Novel approach for bottom-illuminated photothermal nanoscale chemical imaging with a flat silicon sample carrier

Yilmaz U(1)*, Lendl B(1), Ramer G(1)

(1) Institute of Chemical Technologies and Analytics, TU Wien, Getreidemarkt 9, 1060 Wien, Austria

*Corresponding author's email: ufuk.yilmaz@tuwien.ac.at

Background – Infrared (IR) spectroscopy is the method of choice when it comes to chemical identification within spectroscopic methods, but it has certain drawbacks: First, there is the limited spatial resolution of IR-spectroscopy due to the Abbé limit. Second, many important solvents (especially water) exhibit strong absorption in the mid-IR range. The second issue can be overcome using an attenuated total reflection (ATR) setup, which restricts the interaction between radiation sample to the evanescent field within the first few hundreds of nanometers of the sample. A popular approach to solve the problem of lack of spatial resolution in mid-IR imaging, photothermal scanning probe microscopy is used. This hybrid technique called AFM-IR combines atomic force microscopy with mid-infrared spectroscopy. The working principle is based on a local, short-lived photo-thermal absorption of infrared light induced by a pulsed, tuneable EC-QCL source. This excitation then is measured by the sharp tip of an atomic force cantilever. It has been shown that the oscillation amplitude of the cantilever induced by photothermal expansion is proportional to the optical absorption coefficient [1]. Thus, by tuning the wavelength of the infrared laser an absorption spectrum is generated, by keeping the wavelength fixed and scanning the AFM tip absorption images can be generated. AFM-IR can be combined with ATR type illumination to enable measurements of solid samples in absorbing liquids (e.g., to analyse protein fibrils in aqueous media) [2, 3]. Conventionally, high-refractive index prims (e.g., ZnSe) are used as substrate in these experiments (Fig.1 a.). For AFM-IR experiments these ZnSe prisms unfortunately have several drawbacks: ZnSe is not suitable for every type of sample (e.g., acidic samples or liquids). The handling and sample preparation on those prisms is not easy. Furthermore, ZnSe is a comparatively "exotic" material and there exists comparatively little literature on surface functionalization or micro structuring of ZnSe. Last but not least, the cost of a ZnSe ATR prism for AFM-IR lies in the order of several hundreds of Euros.

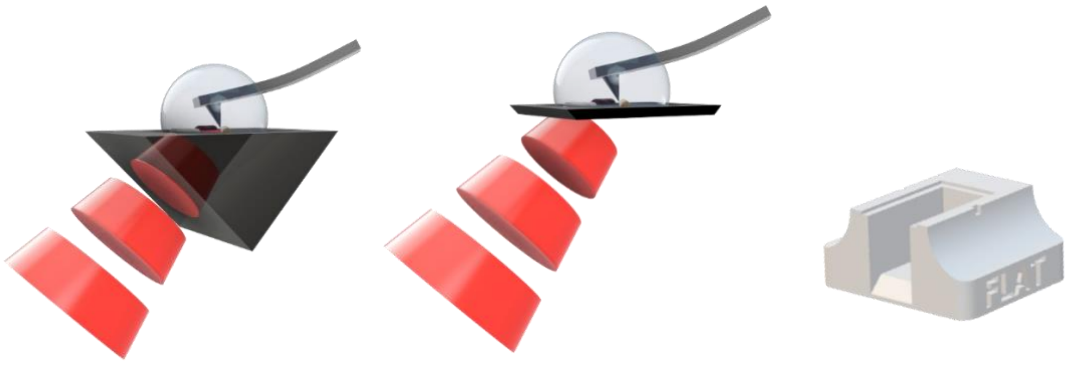

a) **b)** **c)**

Fig. 1. (a) conventional high-refractive-index prism in AFM-IR liquid measurements; **(b)** the novel flat Si-ATR and **(c)** sample holder fitting the new flat sample carrier designed by rapid prototyping.

In this work we introduce a novel sample carrier for liquid AFM that is more chemically resistant, easier to handle and cheaper than the state of the art ZnSe prisms. Our approach uses micro-machined flat silicon-wafer that can be used for AFM-IR experiments. This opens up new ways for measuring AFM-IR in liquids. The flat shape allows easy handling and spin coating of samples on the carrier. Because the carrier is made of silicon, surface functionalization is well understood. Changing a system build around the use of ATR prisms, of course needs some adjustments to the instrumentation. Using rapid prototyping these new, flat Si-carriers can be made compatible with existing commercial AFM-IR instruments. For highest sensitivity, adjustments to the beam path are required to account for this new substrate's geometry, as there is the change from a high-refractive index prism to a flat ATR holder of different material. This was achieved with an additional, removable collimating lens.

Results – We were able to show the feasibility of this new approach. With our sample carrier it is possible to perform cost effective measurements on the nanoscale in air and in liquids. In Fig. 2. a measurement of a PMMA/PS – polymer blend is shown, where IR-spectra is taken and chemical imaging at two distinct wavelengths is shown.

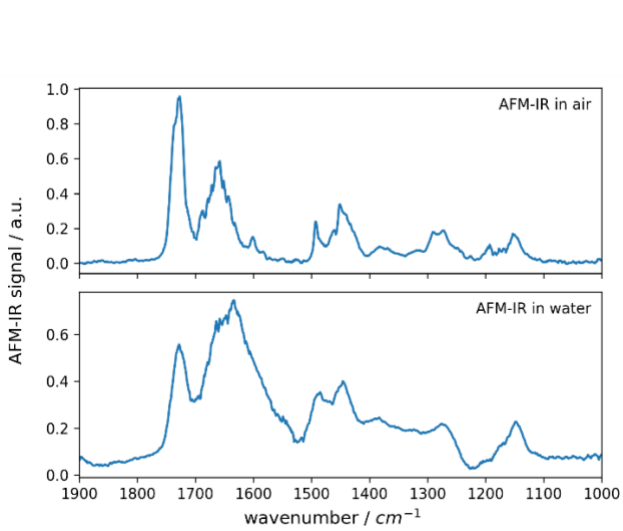

a)

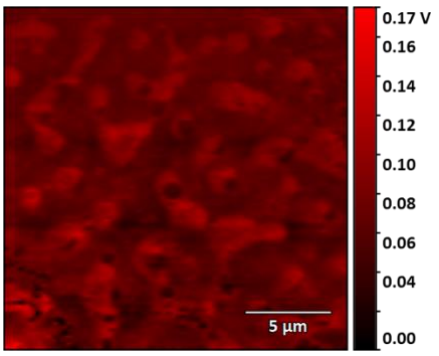

b)

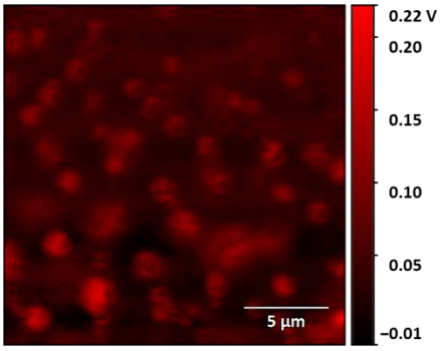

c)

Fig. 2. a) spectra taken on PMMA/PS blend in air & liquid; **b)** IR imaging at 1732 cm^{-1}; **c)** IR imaging at 1660 cm^{-1}.

References

[1] A. Dazzi, F. Glotin, R. Carminati, Theory of infrared nanospectroscopy by photothermal induced resonance, Journal of Applied Physics 107 (2010) 124519. https://doi.org/10.1063/1.3429214.

[2] M. Jin, F. Lu, M.A. Belkin, High-sensitivity infrared vibrational nanospectroscopy in water, Light: Science & Applications 6 (2017) https://doi.org/10.1038/lsa.2017.96.

[3] G. Ramer, F.S. Ruggeri, A. Levin, P. Tuomas, J. Knowles, A. Centrone, Determination of Polypeptide Conformation with Nanoscale Resolution in Water, ACS Nano 12:7 (2018) 6612-6619. https://doi.org/10.1021/acsnano.8b01425.

Dual-resonant mode T-type cell-based photoacoustic spectroscopy for simultaneous trace gas detection

Zhang L(1), Liu L(1,2)*, Zhang X(1), Yin X(1), Huan H(1), Liu H(1), Shao X(1)

(1) School of Physics and Optoelectronic Engineering, Xidian University, Xi'an 710071, China
(2) CAS Key Laboratory of Spectral Imaging Technology, Xi'an 710119

*Corresponding author's email: lixianliu@xidian.edu.cn

Multi-component gas on-line detection is a topic of considerable interest in recent years because of its importance in numerous applications [1]. Miniaturization, multi-wavelength excitation and multi-frequency detection are the recent development trends of photoacoustic spectroscopy (PAS). Therefore, a dual-frequency T-type resonator-based PAS sensor system by using a frequency division multiplexing (FDM) technique was demonstrated for the simultaneous detection of C_2H_2 and CH_4. Instead of multi-resonator PAS scheme [2], utilizing two resonant modes of a single T-type photoacoustic cell (PAC) with multi-wavelength excitation enables dual-gas simultaneous measurement, which can decrease the bulk and energy loss.

In general, conventional cylindrical longitudinal resonant H-type PAC has large amplitude difference operating in the two resonant modes, which is not capable of the simultaneous detection using two frequencies. The novel T-type resonator can compensate the amplitude difference by flexibly adjusting the sizes of the vertically distributed absorption and resonance cylinders. This T-type resonant PAC has advantages of fast response time, periodic pressure amplification, background noise suppression, high PAC constant, low resonance frequency and multicomponent capability [3].

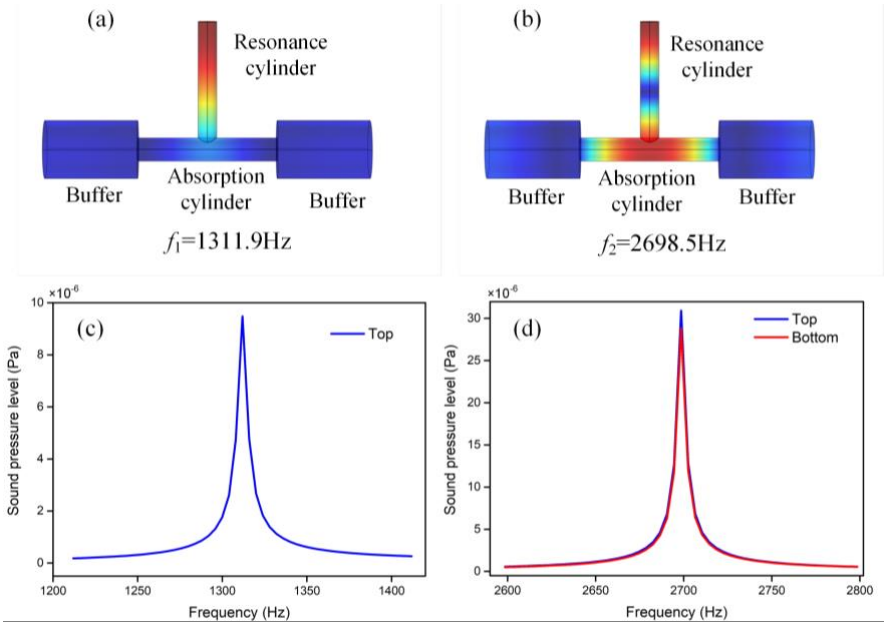

Fig. 1. The resonance modes of T-type photoacoustic cell by finite element simulation. **(a)(b)** The fundamental and overtone modes of T-resonator. **(c)(d)** The pressure levels with frequencies at antinodes.

As shown in Fig. 1, the different modes of identical T-type PAC and pressure levels at antinodes are presented by finite element method simulation (COMSOL Multiphysics ® v5.4). By adding two buffers at both ends of the absorption cavity, the standing wave antinodes of overtone mode will be located at the central bottom of the T-type PAC. The size of two identical cylindrical buffers was 40mm long and 25mm inner diameter, and the absorption cylinder was 60mm long and 10mm inner diameter. The length and inner diameter of the resonance cylinder were 50mm and 8mm, respectively. The fundamental and overtone modes can be exploited to detect gas molecules at two different modulation frequencies. Using microphones located at the top and bottom of the PAC to detect the photoacoustic signals can reduce the transmission loss of acoustic energy, and improve the utilization efficiency of the sound waves. In contrast to the multi-resonator, this T-type PAC is more flexible, miniaturized and effective without the guide tubes.

A schematic of the sensor setup is shown in Fig. 2. Two DFB lasers operating at 1532nm (NEL) and 1653nm (NEL) were used as excitation sources with different frequency current modulation for matching the two resonant modes for C_2H_2 and CH_4 measurement, respectively. Two electret microphones placed at the top and bottom of PAC were used to detect the acoustic waves generated by gas molecules with different frequency mode excitation. The second harmonic photoacoustic signals were demodulated by lock-in amplifiers. Thus, the PA spectra and concentration responses of dual sample gases can be retrieved. The performance of this PA system could be further improved by optimization of its configuration, the parameters of the T-resonator, and higher optical powers.

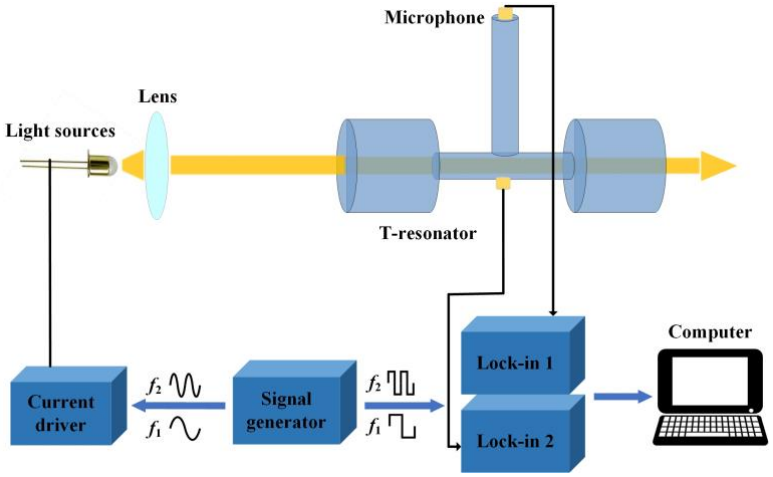

Fig. 2. A schematic of T-resonator-based dual-gas photoacoustic system.

Acknowledgements – The authors are grateful to the National Science Foundation of China (Grant No. 62175194, 62105252, 61805187 and 61801358). This work was also supported by "the Fundamental Research Funds for the Central Universities" (Grant No. JB20190412 and XJS190505).

References

[1] H. Wu, X. Yin, L. Dong, et al. Simultaneous dual-gas QEPAS detection based on a fundamental and overtone combined vibration of quartz tuning fork. Applied Physics Letters 110 (2017) 121104.

[2] K. Liu, J. Mei, W. Zhang, et al. Multi-resonator photoacoustic spectroscopy. Sensors and Actuators B: Chemical 251 (2017) 632–636.

[3] L. Liu, H. Huan, A. Mandelis, et al. Design and structural optimization of T-resonators for highly sensitive photoacoustic trace gas detection. Optics and Laser Technology 148 (2022) 107695.

Ppb-level methane sensor using a multi-pass mode photoacoustic spectroscopy technology

Zhang X(1), Liu L(1), Zhang L(1), Yin X(1), Huan H(1), Shao X(1)*

(1) School of Physics and Optoelectronic Engineering, Xidian University, Xi'an 710071, China

*Corresponding author's email: xpshao@xidian.edu.cn

The demand for trace gas detection is increasing in wide fields, such as electric facility maintenance, industrial production, and combustion research. Photoacoustic spectroscopy (PAS) is superior to other trace gas detection techniques due to its wide dynamic range, fast response, high sensitivity, reliability and chemical selectivity [1-2]. One of the PAS advantages is the sensor performance could be improved by increasing the optical power. For the sake of improving the performance, the photoacoustic cell was placed inside the laser resonator to obtain higher optical power [3-4]. However, additional optical distortion and optical losses is a big strike against this intracavity PAS sensor. In this paper, a multi-pass photoacoustic cell consists of two flat metallic mirrors was designed to reflect the laser to pass through the photoacoustic cell, which quintupled the photoacoustic signal for methane detection. The multi-pass cell based PAS sensor has the advantages of simple design and non-interference in the laser resonator.

A schematic diagram of the multi-pass cell based PAS sensor which consisted of a differential photoacoustic cell, two flat metallic mirrors, two microphones and a transimpedance differential preamplifier was shown in the Fig. 1. The photoacoustic cell was made up of two identical parallel resonators (Φ8×40 mm) and two symmetric cylindrical buffers (Φ20×10 mm). One of the mirrors was a fully coated aluminium flat mirror, and the other was partially coated, which allowed laser beam to enter the photoacoustic cell through a circular hole. The two mirrors were employed as two reflectors of the photoacoustic cell. The laser beam could propagate thoroughly between these mirrors, consequently, the optical length was increased significantly. Such multi-pass mode will lead to the increase of background noise. Therefore, wavelength modulation spectroscopy and 2nd harmonic demodulation techniques were used to reduce the background noise. A distributed feedback laser emitted at the wavelength of the methane absorption (1653.7 nm) was used for generating acoustic signals. The acoustic signals were directed to the transimpedance differential preamplifier and then transfer to the lock-in amplifier to retrieve the methane concentration.

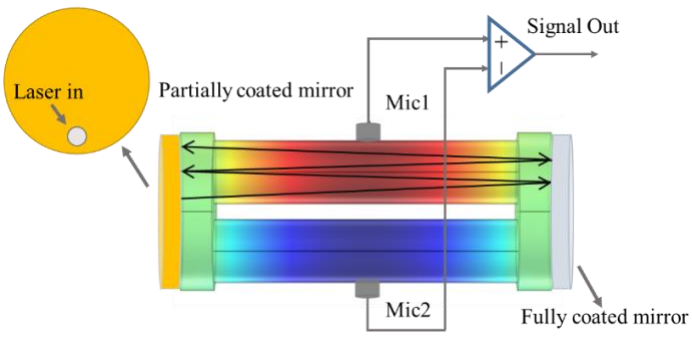

Fig. 1. Schematic diagram of the multi-pass cell based PAS sensor.

In order to verify the performance of the multi-pass cell based PAS sensor, a 2000 ppm methane gas was used as the sample and detected by the multi-pass photoacoustic cell and an original photoacoustic cell in which laser passed through the resonator only once. Fig. 2(a) illustrated that the 2*f* signal of the multi-pass mode was 16.5 mV, a 4 folds higher than the original mode (3.3 mV). As shown in Fig. 2(b), due to the absorption of mirror and wall, the average amplitude of background noise of multi-pass mode (20 μV) was 9 folds higher than the original mode (2 μV). However, the standard deviation of the noise did not increase significantly when using the multi-pass mode (from 1.1 μV to 1.4 μV). By using the multi-pass mode, the signal-to-noise of the 2*f* signal was quadrupled. The noise-equivalent concentration (NEC) for methane detection was calculated as 170 ppb, corresponding to a normalized noise equivalent absorption (NNEA) coefficient of 2.7×10^{-9} $cm^{-1}W/Hz^{-1/2}$.

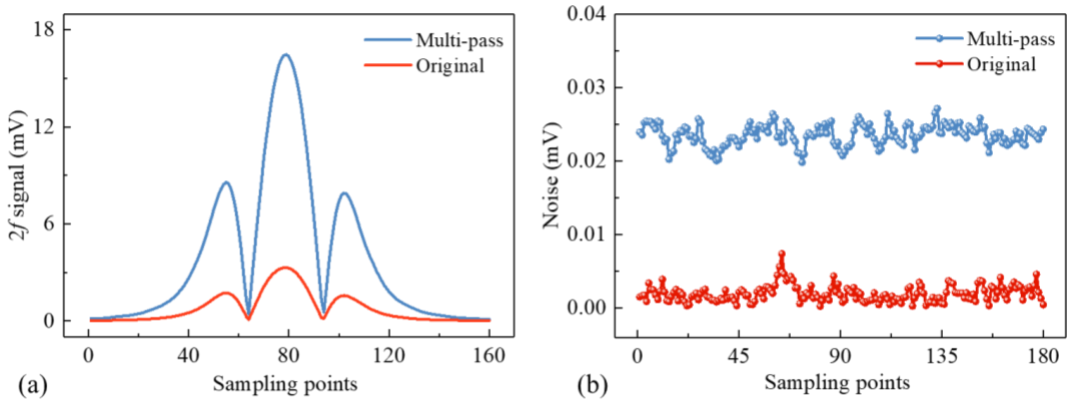

Fig. 2. (a) Original 2*f* signal and multi-pass 2*f* signal of 2000ppm methane; **(b)** Noise determination of original and multi-pass mode.

In conclusion, a multi-pass cell-based PAS sensor was developed for methane sensing. Two flat metallic mirrors were used as the reflectors to increase the optical length of the sensor, resulting in a quintuple photoacoustic signal amplitude. The NEC for methane detection was 170 ppb, corresponding to an NNEA coefficient of 2.7×10^{-9} $cm^{-1}W/Hz^{-1/2}$. The results make the multi-pass mode promising for PAS sensor performance improvement.

Acknowledgement – This work was grateful to the National Natural Science Foundation of China (Grant No. 62175194, 62105252, 61805187 and 61801358). This work was also supported by the Natural Science Foundation of Shaanxi Province with Grant No. 2020JQ-293. This work was also supported by "the Fundamental Research Funds for the Central Universities" (Grant No. JB20190412 and XJS190505) and the Guangdong Basic and Applied Basic Research Foundation with Grant No. 2020A1515111012.

References

[1] Y. Cao, N.P. Sanchez, W. Jiang, et al., Simultaneous atmospheric nitrous oxide, methane and water vapor detection with a single continuous wave quantum cascade laser, Opt. Express. 23(3) (2015) 2121–2132. https://doi.org/10.1364/OE.23.002121.

[2] K. Chen, S. Liu, B. Zhang, et al., Highly sensitive photoacoustic multi-gas analyzer combined with mid-infrared broadband source and near-infrared laser, Opt. Lasers Eng. 124 (2020) 105844. https://doi.org/10.1016/j.optlaseng.2019.105844.

[3] V.S. Starovoitov, J.F. Kischkat, M.P. Semtsiv, et al., Intracavity photoacoustic sensing of water vapor with a continuously tunable external-cavity quantum-cascade laser operating near 5.5 μm, Opt. Lett. 41(21) (2016) 4955–4958. https://doi.org/10.1364/OL.41.004955.

[4] Q. Wang, Z. Wang, J. Chang, et al., Fiber-ring laser-based intracavity photoacoustic spectroscopy for trace gas sensing, Opt. Lett. 42(11) (2017) 2114–2117. https://doi.org/10.1364/OL.42.002114

Analytical method for estimating chemical composition of bio-samples under photothermal investigation

Memeu DM[(1,2)*], Merenga SA[(2)], Ciira WM[(3)], Kinyua DM[(1,4)]

(1) Department Physical Science, Meru University of Science and Technology, Meru, Kenya
(2) Physics Department, Kenyatta University, Nairobi, Kenya
(3) Department of Electrical and Electronics Engineering, Dedan Kimathi Technical University, Nyeri, Kenya
(4) Department of Pure and Applied Sciences, Kirinyaga University, Kirinyaga, Kenya

*Corresponding author's email: dmaitethia@must.ac.ke

Thermal Lens spectroscopy is a photo-thermal technique used for detection and quantification of analytes in liquid samples. The technique boosts from high detection sensitivity and relatively simple instrumentation. However, reproducibility of photo-thermal signals is a challenge and depends on the tightness of alignment of optical elements and use of similar experimental design and reference sample standards for calibration purposes. In this paper we report the development of a simple but universal analytical method that determines the ratio of changes of specific molar extinction coefficients ($\frac{\Delta\varepsilon_{\lambda_1}}{\Delta\varepsilon_{\lambda_2}}$) for a sample being probed with light of wavelength (λ_3) and alternately pumped up to optical saturation using optical beams of wavelengths (λ_1, λ_2). The model takes as its inputs, the acquired photo-thermal signals (I_1 and I_2) obtained upon sample excitation with the two pump beams. The output, ($\frac{\Delta\varepsilon_{\lambda_1}}{\Delta\varepsilon_{\lambda_2}}$) is a parameter that is related to the chemical composition of the sample and therefore can aid in identification of biomarkers of interest present. The model is independent of the design of the photothermal setup. The model was applied in detection of hemozoin present in malaria infected blood probed using a simple photo-thermal setup comprising of a RGB light emitting diode and a 3D printed optical microscope fitted with a Raspberry Pi camera. After incorporating the model in processing the acquired photothermal signals, a machine learning classification was performed and a classification accuracy of 100% between malaria infected and non-infected samples was attained.

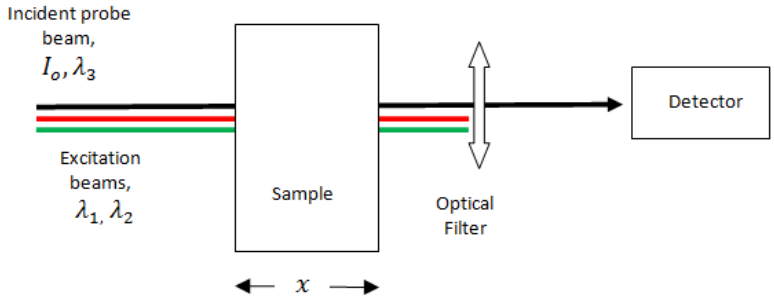

Fig. 1. Schematic diagram showing the required setup for implementation of the photo-thermal model.

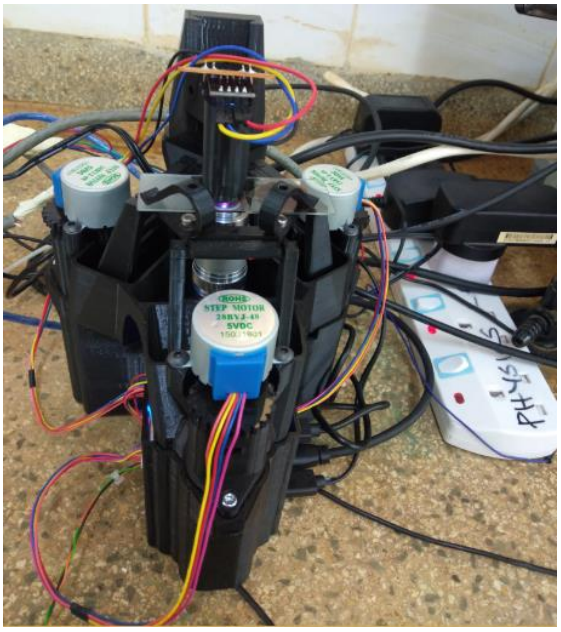

Fig. 2. An Image of the actual instrumentation setup used in the implantation of the model.

Equation (1) shows how the parameter $\frac{\Delta\varepsilon_{\lambda 1}}{\Delta\varepsilon_{\lambda 2}}$, is to be computed using the measured photo-thermal signals

$$\frac{\Delta\varepsilon_{\lambda 1}}{\Delta\varepsilon_{\lambda 2}} = \ln\left(\frac{I_1 - I_2}{I_3}\right) \qquad \text{Eqn. 1}$$

Table 1. Results showing the classification accuracies for photo-thermal signals processed according to equation 1.

	Precision	Recall	F1-Score
Negative	1.00	1.00	1.00
Positive	1.00	1.00	1.00

Windowless photoacoustic cell for trace gas detection

Liu L[(1,2,3)*], Huan H[(1,2)], Zhang L[(1)], Zhang X[(1)], Yin X[(1)], Shao X[(1)], Mandelis A[(2)]

(1) School of Physics and Optoelectronic Engineering, Xidian University, Xi'an 710071, China
(2) Center for Advanced Diffusion-Wave and Photoacoustic Technologies (CADIPT), Department of Mechanical and Industrial Engineering, University of Toronto, Toronto, Ontario M5S 3G8, Canada
(3) CAS Key Laboratory of Spectral Imaging Technology, Xi'an 710119

*Corresponding author's email: Lixianliu@xidian.edu.cn

Photoacoustic Spectroscopy (PAS) technology is a widely recognized method for its excellent performance in trace gas detection and simplicity of the experimental setup [1,2]. The detectivity of the laser PAS configuration achieves down to ppm ~ ppb levels, thanks to high power and narrow band of laser sources and the high sensitivity of resonant cells. However, spurious signal generated by the resonator windows persists a challenge for the improvement of trace gas detection sensitivity. Unless incoherent noise [3], the noise originated by the window absorption is almost impossible to be removed by the classical filtering methods, e.g., amplitude and wavelength modulation. The closed photoacoustic resonators may be limited to particular applications due to the inlet and exhaust of the target gas. A windowless photoacoustic cell based on T-resonator [4] is presented in this paper for trace gas detection.

T-resonator depicted in Fig. 1(a) comprises resonance and absorption cylinders. The reason that T-resonator is appropriate for the windowless cell design lays in its resonant frequency is mainly determined by the resonance cylinder perpendicular to the light absorption path.

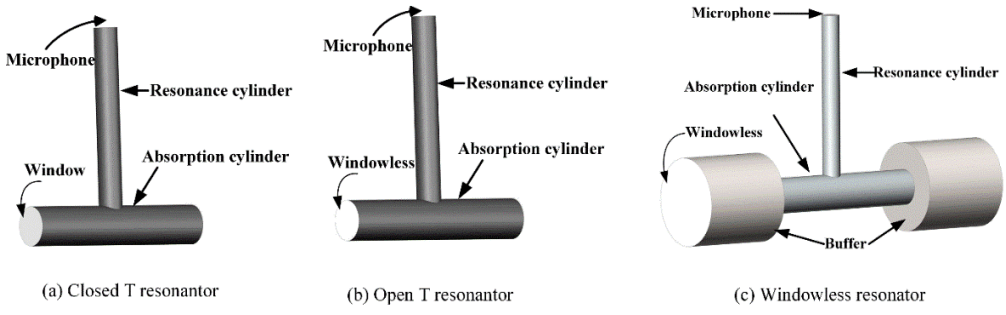

Fig. 1. T typed resonator models.

The proposed windowless cell is presented in Fig.1 (c) which consists of T-typed resonator and buffer cylinders. The penetration of the external acoustic noise is attenuated through the two buffer volumes at both ends of the absorption cylinder. The diameter and length of the buffers are selected in such a way the acoustic impendence of which is relatively high at the resonance frequency.

The three different T-type resonator models shown in Fig.1 were built with COMSOL Multiphysics 5.2. The geometry of absorption and resonance cylinders is identical for the three resonators and the lossy boundary conditions were adapted due to thermal and viscous losses at the resonator boundary. The finite element method (FEM) simulated amplitude response results are presented in Fig.2 which exhibits the good performance of the windowless resonator and the details are shown in Table 1. Although there is a large deviation of the resonance frequency of the three cells, the full width at half

maximum (FWHM) of the windowless resonator is similar to the closed resonator, much better than the behavior of the open resonator. The windowless resonator with two buffers at both ends of the absorption cylinder has the capability for the noise suppression and can be used an open cell in the trace gas detection application.

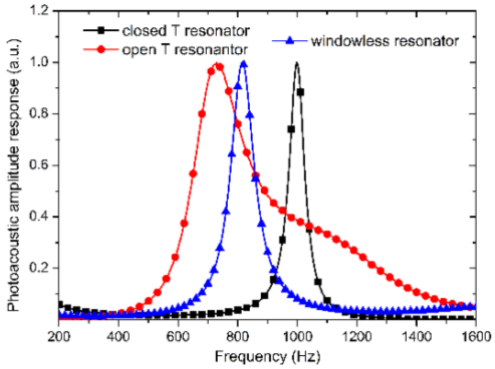

Fig. 2. The photoacoustic amplitude simulated response of three different resonators.

The FEM simulation results demonstrate that the windowless resonator comprising the T cell and buffer volume is an appropriate photoacoustic design for the elimination of the coherent spurious signal generated by the window absorption and the isolation of outside background noise. Thus, the windowless resonator is an effective open cell for trace gas detection.

Table 1. The simulation results of the three T typed resonators

Cell Type	Resonance frequency (Hz)	FWHM (Hz)
Closed resonator	998	28
Open resonator	728	105
Windowless resonator	816	34

Acknowledgements – The authors are grateful to the National Science Foundation of China (Grant No. 62175194, 62105252, 61805187 and 61801358). This work was also supported by "the Fundamental Research Funds for the Central Universities" (Grant No. JB20190412 and XJS190505).

References

[1] Z. Yu, J. Assif, G. Magoon, P. Kebabian, W. Brown, W. Rundgren, J. Peck, R. Miake-Lye, D. Liscinsky, B. True, Aerosol Science and Technology 51:12 (2017) 1438. doi: 10.1080/02786826.2017.1363866.

[2] L. Liu, A. Mandelis, H. Huan, K.H. Michaelian, Optics Letters 42 (7), 1424 (2017). doi: 10.1364/OL.42.001424.

[3] L. Liu, A. Mandelis, H. Huan, A. Melnikov, Applied Physics B 122:268 (2016). doi: 10.1007/s00340-016-6545-2.

[4] L. Liu, A. Mandelis, H. Huan, K.H. Michaelian, A. Melnikov, Vibrational Spectroscopy 87: 94 (2016). doi: 10.1016/j.vibspec.2016.09.013.

Photoacoustic SO_2 gas sensor in SF_6 buffer gas employing a 266 nm LED

Yin X(1), Zhang X(1), Zhang L(1), Liu L(1), Shao X(1)*

(1) School of Physics and Optoelectronic Engineering, Xidian University, Xi'an 710071, China

*Corresponding author's email: xpshao@xidian.edu.cn

A ppb-level SO_2 photoacoustic sensor for SF_6 decomposition analysis by use of a compact light emitting diode (LED) ultraviolet (UV) and a differential photoacoustic cell (PAC). The mW-level UV laser emits at 266 nm due to a strong electronic SO_2 spectrum as well as effectively avoiding interference from SF_6 absorption bands in the infrared spectral region. A symmetrical differential PAC was designed to address the issue of SF_6 flow noise. As a result, the reported SO_2 photoacoustic sensor system can achieve real-time, on-line measurements with a continuous sample gas flow 7 times larger than that with a single resonator PAC. A new optical source, a novel PAC design and a strong target spectrum result in a SO_2 minimum detection limit of ~74 ppb, which meets the requirement for monitoring of electric power systems.

Background – High voltage gas insulated apparatus such as the gas insulated switchgears (GIS) and the gas insulated lines (GIL) have been widely used in power transmission and distribution systems around the world. Due to the high dielectric strength, chemically inactive and environmentally acceptable property, sulfur hexafluoride (SF_6) was widely chosen as the preferred dielectric gas for electrical insulation or interruption purposes in electric power systems. However, GIS/GIL failures occur from time to time from manufacturing defects [1-2]. The monitoring of decomposed by-products can efficiently identify and determine the occurrence of fault types in electrical equipment and thus minimize security risks. When the SO_2 concentration is > 8 ppm, the power equipment must be overhauled [1-3]. Currently the most research of diagnosis is focused on photoacoustic spectroscopy combined with the incoherent excitation source, which limits the detection sensitivity to reach <1 ppm. Health monitoring of gas insulated apparatus is critical to improve the reliability and to reduce the life cycle cost. Among the various methods for the monitoring, optical sensing developed fast in recent years due to their highly sensitive and anti-electromagnetic interference characteristic [3-4].

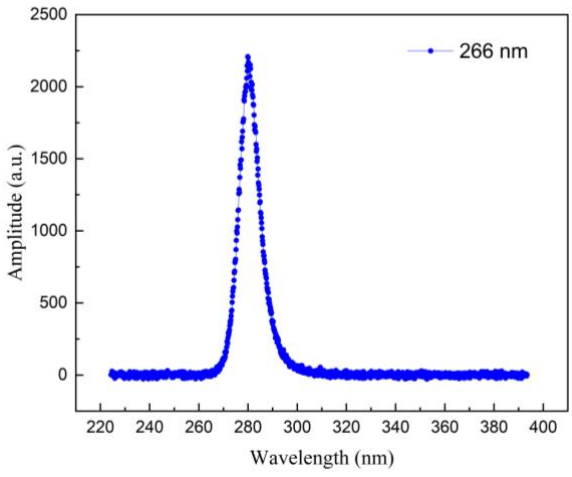

Fig. 1. Spectral emission of the 266 nm LED

Light source – A low-cost LED was employed as the excitation light source, which emitting at 266 nm. The output power was ~ 5mW at the room temperature. An optical spectrum analyzer (Avantes, AVS-DESKTOP-USB2) was used to measure the emission spectrum of the laser. As show in Fig. 1, the laser linewidth is < 8 nm. The corresponding SO_2 absorption cross section is ~ 4.8×10^{-19} $cm^2/molecule^{-1}$.

Experiment – A differential photoacoustic cell was designed for the detection of SO_2 acoustic signal. Two identical cylindrical acoustic resonators (Φ5×90 mm in size) were arranged independently and in parallel. Two buffer volumes (Φ20×10 mm) were added at both ends of the resonators to constitute two identical open-open resonators. At the outsides of the buffer volumes, two quartz windows (Φ25.4×5 mm) and two rubber O-type rings were used to seal the PAC. The measured resonance frequency of the PAC was 683.6 Hz with a FWHM of 8.1 Hz in SF_6. In order to verify the linearity of the sensor performance, the average signal amplitudes of 100 data points were plotted in Fig. 2(a) for different gas concentration levels. The linear fitting *R*-Square value >0.9995 confirms the linearity of the sensor response to concentration. In PAS, the pressure is a critical parameter, since the *Q*-factor of the acoustic cell, the V-T relaxation rate of target gas and the intensity of the absorption spectrum are pressure dependent. The relationship between the signal amplitude of a 100 ppm SO_2/N_2 and the pressure are plotted in Fig. 2 (b). A linear increase of the signal amplitude with the total gas pressure was observed.

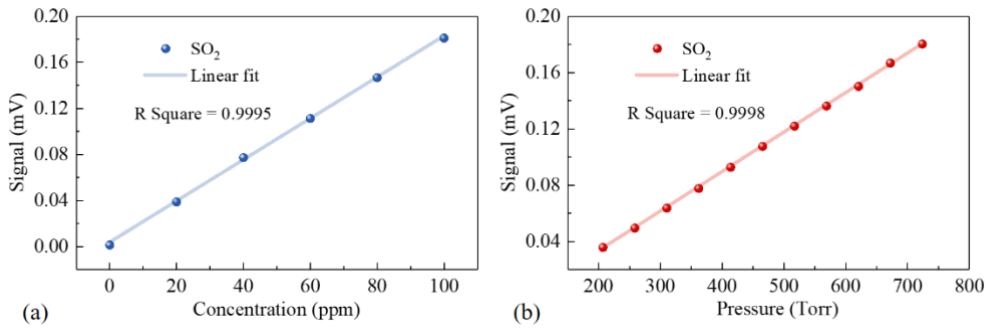

Fig. 2. The linearity of the SO_2 photoacoustic signal under different concentrations (a) and pressures (b).

A 266 nm LED was used for SO_2 detection in SF_6 buffer gas. Based on the data of the 100 ppm SO_2/SF_6 gas sample, the noise equivalent (1σ) concentration is ~1.3 μV, which corresponds to a signal-to-noise ratio (SNR) of 143 and a detection limit of 695 ppb.

References

[1] X.X. Zhang, B. Yang, X.J. Wang, C.C. Luo, Effect of plasma treatment on multi-walled carbon nanotubes for the detection of H_2S and SO_2, Sensors (Basel). 12:7 (2012) 9375–9385.

[2] R. Kurte, C. Beyer, H.M. Heise, D. Klockow, Application of infrared spectroscopy to monitoring gas insulated high-voltage equipment: electrode material-dependent SF_6 decomposition, Analytical & Bioanalytical Chemistry. 373:7 (2002) 639-646.

[3] X.K. Yin, L. Dong, H.P. Wu, W.G. Ma, L. Zhang, W.B. Yin, X.L. Tuan, S. T. Jia, and F. K. Tittel, Ppb-level H_2S detection for SF_6 decomposition based on a fiber-amplified telecommunication diode laser and a background-gas-induced high-*Q* photoacoustic cell, Appl. Phys. Lett. 111:03 (2017) 031109.

[4] H.D. Zheng, L. Dong, X.K. Yin, X.L. Liu, H.P. Wu, L. Zhang, W.G. Ma, W.B. Yin, S.T. Jia,Ppb-level QEPAS NO_2 sensor by use of electrical modulation cancellation method with a high power blue LED, Sensor. Actuat. Biol. Chem. 208 (2015) 173–179.

Doppler effect for thermal waves: theory and applications

Li Voti R(1)*, Bei G(1), Bertolotti M(1)

(1) Dipartimento di Scienze di Base ed Applicate per l'Ingegneria, Sapienza Università Roma, Via A. Scarpa 16, 00161 Rome, Italy

*Corresponding author's email: roberto.livoti@uniroma1.it

The change in frequency of an electromagnetic wave when the source and the receiver are in relative motion one with respect to the other was described by Christian Doppler [1] in 1842. He wrongly applied the effect to explain the different colours of stars. Buys Ballot made experiments with sound waves and later Fizeau in 1848 proposed that lines in optical spectra might show variations in frequency depending upon the relative velocities of the source and the observer. The prediction was confirmed by Sir William Huggins, who showed the change in frequency towards the red of hydrogen lines recorded from Sirius, indicating a recessive motion. The effect has since then become the more and more important in the description of our world. In photoacoustics, the Doppler effect of the emitted acoustic waves from moving amplitude modulated optical sources has been explored several decades ago by Soviet researchers including Bozhkov, Bunkin, and Kolomenskii as well as by researchers in the United States, but a clear analytical approach was missing. More recently the full theory on moving photoacoustic sources in one, two, and three dimensions has been deeply discussed by W. Bai and G.J. Diebold [2] giving application to trace gas detection with dynamic photoacoustic spectroscopy (DPAS). Finally, in photothermal infrared thermography several groups have introduced the "flying spot" technique where a c.w. laser beam is moved at constant velocity for a quick inspection of the material thermal parameters and detection of cracks [3]. Here the authors showed the asymmetric thermal field profile. However, they did not investigate the Doppler effect for the induced thermal field [4]. In the present paper we give the solution for the thermal waves generated by a modulated source moving in solid media, derive the Doppler effect for thermal waves giving the expression of the frequency shift, and eventually showing some possible applications for nondestructive evaluation and testing of materials [5].

Thermal waves are wave-like temperature fields induced by a harmonic heating process. Monitoring thermal diffusion caused by a periodically modulated heat source was already used by Lord Kelvin and A.J. Ångström to investigate the thermal diffusivity of bodies, but only recently, in the early 80's, have been called "thermal waves", arousing a remarkable clamour. Presently the scientific community still debates on their very nature, even if their formalism is widely accepted to describe the temperature field in periodical regime, and most of the fundamental wave phenomena as reflection, refraction [6], interferometry [7], resonance [8] and scattering [9] have been already both theoretically and experimentally demonstrated, and used in many applications.

The differential equation of heat conduction in a moving medium has been treated for the first time in fluids by HA Wilson in 1904 as reported in the well known textbook by Carlslaw and Jaeger where the modified Fourier equation has been extended for any moving medium. The case of a plane heat source (yz plane) modulated at the angular frequency ω, and moving at constant speed $-V_S$ in the opposite direction of the x axis has been widely discussed in Ref. 5, showing that the thermal wave in the moving reference $x'=x-x_S$ can be expressed by the following analytical formula [5]

$$\begin{cases} x' \geq 0; \quad T(x',t) = \mathrm{Re}\left\{ A \exp\left[\left(\gamma_s - \sqrt{\gamma_s^2 + 2j} \right) \frac{x'}{\mu} \right] \exp(j\omega t) \right\} \\ x' < 0; \quad T(x',t) = \mathrm{Re}\left\{ A \exp\left[\left(\gamma_s + \sqrt{\gamma_s^2 + 2j} \right) \frac{x'}{\mu} \right] \exp(j\omega t) \right\} \end{cases} \qquad \text{Eqn.1}$$

where $A = \dfrac{I}{2e\sqrt{\omega}\sqrt{\gamma^2/2 + j}}$ and $\gamma_S = \dfrac{V_S}{\sqrt{2\omega D}}$ is the ratio between the source velocity V_S and the phase velocity of the thermal wave. But the most appealing example to observe the Doppler effect with thermal waves is looking at the distortion of both amplitude and phase wave fronts when the medium is heated by a single point harmonic heat source moving again at constant speed $-V_S$ In the 3D case the solution cannot be expressed in a simple form and should be simulated numerically (see Fig.1). It is worth nothing that in the reference at rest a Doppler shift of the angular frequency $\Delta\omega=\omega'-\omega$ can be observed as follows [5] $\dfrac{\Delta\omega}{\omega} = \pm\gamma_{o,s} \cdot \sqrt{\dfrac{1}{2}\left(\sqrt{\gamma_s^4 + 4} - \gamma_s^2\right)}$ where $\gamma_{o,s} = V_{O,S} / \sqrt{2\omega D}$ and $V_{O,S}$ is the relative speed when both observer and source are moving away from each other, and the plus sign is for the reciprocal approach.

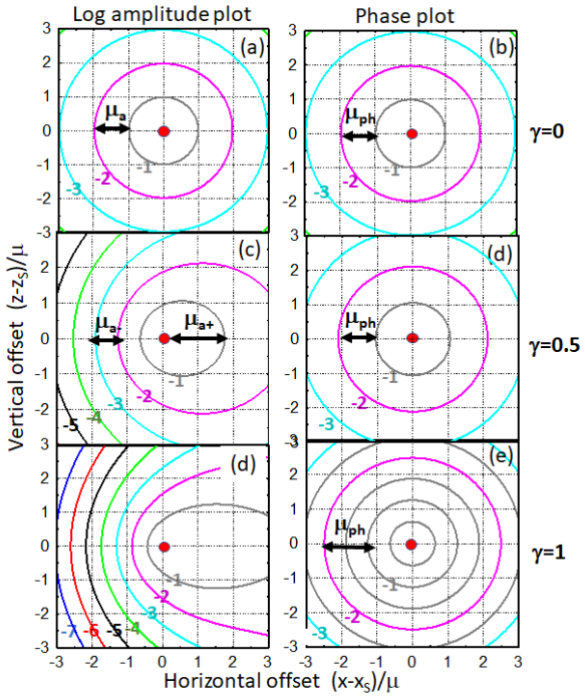

Fig. 1. Contour plot of the induced temperature field in the reference frame of the source. Modulated heat source is in the origin. Both coordinates are dimensionless because normalized to the thermal diffusion length. (a),(c),(d) Logarithmic amplitude contour plot respectively for γ_S=0, 0.5, and 1; (b),(d),(e) phase contour plot respectively for γ_S =0, 0.5, and 1.

References

[1] C Doppler, Uber das farbige Licht der Doppelsterne und einiger anderer Gestirne des Himmels. Abhand!. konig!. bohm. Goesellschaft d. Wiss. 2 (1842) 465.

[2] W. Bai, G.J. Diebold, Photoacoustic effect in a stratified atmosphere, Phys. Rev. E, 98, 032125 (2018).

[3] A. Bedoya, J. González, J. Rodríguez-Aseguinolaza, A. Mendioroz, A. Sommier, J.C. Batsale, C. Pradere, A. Salazar, Measurement of in-plane thermal diffusivity of solids moving at constant velocity using laser spot infrared thermography, Measurement 134 (2019) 519–526.

[4] M. Colom et al., Measuring the in-plane thermal diffusivity of moving samples using laser spot lock-in thermography, Int. J. Therm. Sci. 151, 106277 (2020).

[5] R. Li Voti, M. Bertolotti, Thermal waves emitted by moving sources and the Doppler effect, International Journal of Heat and Mass Transfer, 176, 121098 (2021)

[6] M. Bertolotti, G.L. Liakhou, R. Li Voti, S. Paoloni, C. Sibilia, Thermal wave reflection and refraction: Theoretical and experimental evidence, J.Appl. Phys 85, 3540 (1999).

[7] R. Li Voti, et al., Thermal waves physics, Journal of Optoelectronics and Advanced Materials 3, 779 (2001).

[8] M. Bertolotti, G.L. Liakhou, R.L Voti, S.Paoloni, C. Sibilia, Thermal Wave Resonator: In Situ Investigation by Photothermal Deflection Technique, Int. J. Thermophys. 19, 603 (1998).

[9] R. Li Voti, C. Sibilia, M.Bertolotti, Photothermal Depth Profiling by Thermal Wave Backscattering and Genetic Algorithms, Int. J. Thermophys. 26, 1833 (2005).

Twin-focus thermal lens microscopy: A theoretical description

Liu M[(1)*]

(1) School of Mathematics and Physics, Southwest University of Science and Technology, Mianyang 621010, China

*Corresponding author's email: mqliu3677@163.com

Sensitive and specific detection of trace nonfluorescent targets in microanalytical devices is the foremost task in chemical and biological analyses. Conventional thermal lens microscopy (TLM) can realize sensitive detection of nonfluorescent analytes down to a nanoparticle and is insensitive to scattering background [1]. However, the conventional TLM (usually working in time-domain intensity-modulation mode) suffers low detection performance when there exists a large background absorption, which could come from interferents in light path, such as pollutants on optical elements or absorptive agents (nanoparticles, surface coatings, etc. [2]) within and around the micro space. When the intensity of excitation laser is modulated, the background absorption will introduce an undesired background noise, which can prevail over the real TL signal from the analyte. One direct way to remove these background noises is to keep the excitation laser running continuously without modulation, which will however suppress the conventional TLM signal of analyte as well. To overcome this contradiction, we must employ a new TLM scheme, which can eliminate the background noise while keeping the TL signal from the analyte in target region unaffected.

Here, I introduce a twin-excitation-focus thermal lens microscopy (TF-TLM). Instead of modulating the excitation intensity in time domain in conventional TLM, the excitation focus is modulated back and forth between the positive and negative signal zones of TF-TLM (Fig. 1, left), which can produce a periodic signal from the analyte of target with little contribution from the background interferents. The axial excitation focus modulation can be realized by a beam-parameter-adjustment unit, which consists of an electro-optic modulation, a polarization beam splitter and four reflecting mirrors.

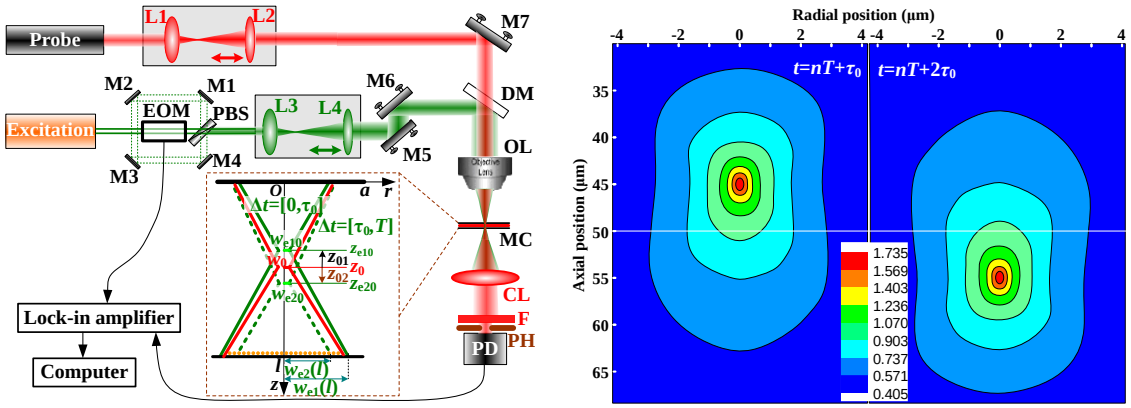

Fig. 1. Schematic of TF-TLM (left). CL: condenser lens; DM: dichroic mirror; EOM: electro-optic modulator; F: interference filter; L0-L4: lenses; M1-M7: mirrors; MC: microfluidic chip; OL: objective lens; PBS: polarization beam splitter; PD: photodiode; PH: pinhole. And temperature profiles in sample at the end of 1st and 2nd excitation half-cycles in one modulation cycle (right), with w_{e0}=0.42 μm and f=10 kHz

The theoretical model of TF-TLM is similar to conventional TLM, except that the temperature distribution should be rededuced under excitation of a quasi-continuous twin-focus excitation. Detailed description of the temperature and photothermal signal model will be given elsewhere. I first simulated the temperature profiles at the end of the 1st and 2nd excitation half-cycles in one modulation cycle (Fig. 1, right). When the excitation focus shifts from the positive to negative signal zone, the temperature around z_{e10}=45 µm shows an increase in the 1st excitation half-cycle and a decrease in the 2nd excitation half-cycle, while the temperature around z_{e20}=55 μ m shows an opposite change during these two excitation durations. This temporally and spatially periodic change of photothermal effect can result in a periodic change of probe beam intensity at the detector.

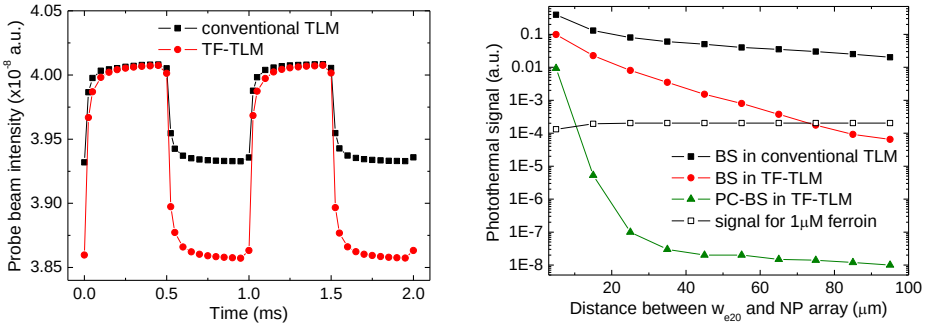

Fig. 2. Temporal change of photothermal signal of an ensemble sample at (z_{e10}=45 μ m and z_{e20}=55 μ m) and at (z_{e10}=48 μ m and z_{e20}=52 μ m) (left). And change of the photothermal signal with the distance (z_{23}) between w_{e20} and gold nanoparticle array at the bottom of the sample cell(right). BS: background signal; PC-BS: power-compensated background signal.

Figure 2 (left) gives the temporal intensity change of probe beam, whose beam waist is at the center of two excitation foci, namely z_{01}=z_{02} (Fig. 1, left). Following the temperature change, the intensity takes on a periodic change. In the 1st excitation half-cycle, the probe beam shows an increase, while a decrease is observed in the 2nd excitation half-cycle when the excitation focus shifts to the negative signal zone. In comparison with the conventional TLM, the intensity change is nearly doubled in TF-TLM, which will induce a two-fold increase in TLM detection sensitivity. Figure 2 (right) shows the impact of background absorption on the TLM. When the gold nanoparticle (NP) array on the sample-cell wall absorbs the excitation light intensity, temperature gradient occurs around the array. While the lateral phase shows a periodic change in conventional TLM, the phase changes slightly between the 1st and 2nd excitations. The small difference comes from the discrepant excitation light intensities (due to the inconsistency in $w_{e1}(l)$ and $w_{e2}(l)$). In comparison with the signal of sample, the background signal in conventional TLM is 1000-fold higher while the background signal in TF-TLM is only 10-fold higher. By adjusting the power of one of the excitation beams (EB1 or EB2), the background signal can be greatly suppressed or even eliminated. For example, when the power of EB2 (dashed line around EOM) is reduced to 9 mW, the background signal will disappear. This is quite promising for weak absorption detection when a background absorption cannot be ignored.

In conclusion, this novel TF-TLM, which shows twice higher sensitivity and moreover a nearly background-free detection in comparison with conventional TLM, provides a robust tool for sensitive detection of trace analytes in complex micro spaces.

References

[1] T. Kitamori, M. Tokeshi, A. Hibara, K. Sato, Thermal lens microscopy and microchip chemistry, Anal. Chem. 76 (2004) 52A-60A.

[2] Y. Du, N. Li, H. Yang, C. Luo, Y. Gong, C. Tong, Y. Gao, S. Lü and M. Long, Mimicking liver sinusoidal structures and functions using a 3D-configured microfluidic chip, Lab on A Chip 17 (2017) 782-794.

Three-dimensional truncated correlation photothermal coherence tomography image optimization using linear iso phase imaging

Welch R[(1,2)], Sivagurunathan K[(1,2)], Tavakolian P[(1,2)], Mandelis A[(1,2)*]

(1) Center for Advanced Diffusion-Wave and Photoacoustic Technologies (CADIPT) Department of Mechanical and Industrial Engineering, University of Toronto, Toronto, Ontario M5S 3G8, Canada
(2) Institute for Advanced Non-Destructive and Non-Invasive Diagnostic Technologies (IANDIT), University of Toronto, Ontario M5S 3G8, Canada

*Corresponding author's email mandelis@mie.utoronto.ca

This is a study of the effect thermal transient truncation in the Truncated Correlation Photothermal Coherence Tomography (TC-PCT) algorithm. A new phase channel is introduced which was coined the name Linear Iso Phase (LIOP). The channel improves the conventional TC-PCT phase by redevising its matched-filter sampling scheme and removing the effect of circular aliasing artifacts introduced in the frequency-domain-transformed cross-correlation (CC) calculations.

Background – Introduction. - A brief overview of the existing TC-PCT [1] and enhanced TC-PCT (eTC-PCT) [2] algorithms will be presented to better understand their signal processing differences, followed by a new phase imaging channel algorithm termed the Linear Iso Phase (TC-PCT LIOP) which uses an alternative sampling procedure and linear-cross correlations for improved volumetric reconstructions as opposed to the circular cross-correlations used by the TC-PCT phase channel. The algorithms are applied to imaging a multi-layered sample and comparisons are made between the volumetric reconstructions produced.

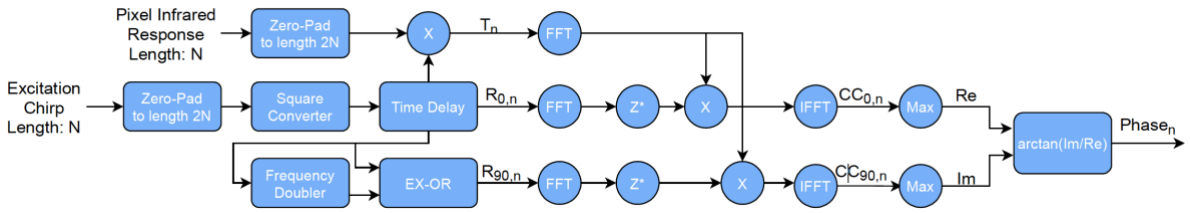

Fig. 1. Linear Iso-TCPCT Phase signal processing diagram.

Image processing – The new LIOP channel was introduced to reduce the sparsity-induced noise present in the TC-PCT phase while maintaining its strong thermal-wave localization character. This image reconstruction in the time-delay domain is that the infrared signal tends to decay in amplitude strength as the delay time increases. This results in three-dimensional reconstructions requiring large dynamic range which are difficult to display as the surface slice amplitude is generally much greater than its deeper (longer delay times) counterparts. This limits the visualization of small local features making it difficult to detect their presence and becomes more of an issue as the deposited pulse energy increases. For visualization purposes, the spatial correlation of features matters more than their signal intensities. Hence, the image intensities can be readjusted to improve feature visibility while preserving spatial coherence on a slice-by-slice method. To do so, it was found that by applying global histogram

equalization [3] to each tomographic slice, the contrast of the reconstructions, particularly for the amplitude channels, can be greatly improved.

Experimental and results. - To implement this algorithm, the Scikit Image [4] Python package was used and applied to the tomographic reconstructions on a slice-by-slice basis. In this method, each equalized slice is rescaled between (0,1), ensuring a lower volumetric dynamic range than the input volume resulting in enhanced slice contrast. The effectiveness of this algorithm in improving subtle feature visibility can be seen in Figs. 2 which are 3D image reconstructions of the marquetry art sample of Fig. 1 using multi-pulse excitation signals. The LIOP reconstruction (Fig. 2) shows clear separation between the sample's surface and hidden hole, with slowly developing wood grains, producing a more faithful reconstruction of deep inhomogeneities.

Fig. 1. (**A)** The irradiated mahogany veneer front layer of the marquetry sample. (**B)** The pine layer of the art sample with a 14-mm diameter drilled through-hole in the pine layer only.

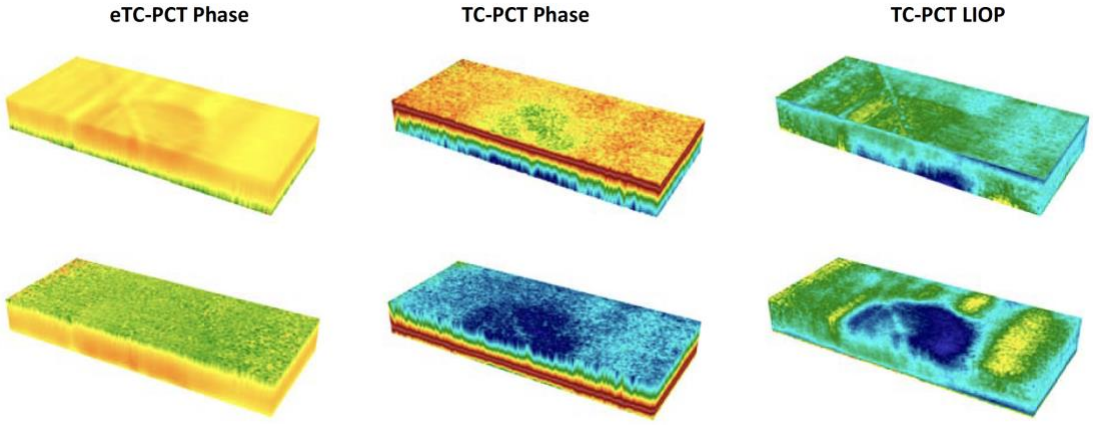

Fig. 2. Tomographic phase reconstructions of Fig. 1 derived from a 0.2-0.4-Hz, 17-s chirp with 5x pulses at 10-ms widths and 100-ms slice widths for all the reconstructions. The top row shows the irradiated surface facing upwards, and the bottom row shows the hidden backside facing upwards for the eTC-PCT Phase (left column), TC-PCT Phase (middle column) and TC-PCT LIOP (right column) algorithms. The blind hole and woodgrains are 0.7 mm below the irradiated surface.

Conclusions. - A new TC-PCT phase channel, termed "Linear Iso Phase" (LIOP) was introduced, which exhibits improved experimental phase reconstruction quality by removing the effects of circular aliasing resulting from frequency-domain-transformed cross-correlation operations, while enhancing subtle feature resolution even at very low thermal-wave modulation frequencies.

References

[1] S. Kaiplavil, A. Mandelis. Nature Photon 8 (2014) 635–642.

[2] P. Tavakolian, K. Sivagurunathan, A. Mandelis, J. Appl. Phys., 122 (2017) 023103.

[3] R. Gonzalez, R. Woods, Digital Image Processing, Second Edition, Chap. 3, Prentice Hall, NJ (2002).

[4] S. Van Der Walt, J. Schönberger, J. Nunez-Iglesias, F. Boulogne, J. Warner, N. Yager, E. Gouillart, T. Yu et al., Scikit-image: Image processing in Python (2014) PeerJ 2:e45.

Photoacoustics in the study of micromechanical structures

Todorovic DM[(1)*]

(1) University of Belgrade, Belgrade, Serbia

*Corresponding author's email: dmtodor@afrodita.rcub.bg.ac.rs

Photoacoustics and Elastics – Micro-Electro-Mechanical-Systems (MEMS) technologies enable the production of compact, lightweight, highly sensitive transducers (sensors, actuators, detectors and converters), whose work is based on elastic deformations and vibrations of micromechanical structures (MMS). A particularly important group consists of the so-called optical MEMS transducers - Micro-Opto-Mechanical- Systems (MOMS), in which elastic deformations and vibrations are generated by the absorption of modulated optical energy. Photoacoustic (PA) and photothermal (PT) effects are important as driven mechanisms for MMS (MOMS). In addition, PA and PT methods are important for measuring and analyzing the elastic displacements (deformations) and elastic characteristics of MMS. The connection between the theory of elasticity and PA and PT science is briefly presented.

Micromechanical Structures – The production of MMS (MEMS) takes place on pre-prepared pieces (Si wafers) of monocrystalline silicon (c-Si), the most commonly used technological process - anisotropic etching. MSs produced by micromachining process have an anisotropic structure (cubic crystal structure), which requires complex analysis in the elastic (mechanical) domain. Depending on the application, MMS is made in very different shapes (3D structures mechanically coupled to the frame; typically frame and MMS form the mechanical part of the microelectronic chip). Analysis of mechanical properties of these microstructures (elastic deformations, displacements, vibrations, ...) is a very complex problem, which requires different methods of modeling and measurements.

Photoacoustic Effect in Micromechanical Structures – A general theoretical analysis of the transport processes in a semiconductor MMS is presented by modeling the complex system of the plasma, thermal and elastic wave phenomena. This theoretical treatment enables quantitative accounting of the amplitude and phase of the carrier density, temperature and elastic displacement and describes their functional dependence on the modulation frequency and thermal, elastic, and carrier transport properties of the MMS.

Photoacoustic (PA) effect in semiconductor MMS is based on the photogeneration of electron-hole pairs, i.e. plasma waves, generated by the absorbed intensity-modulated (time-varying; pulse, periodical) optical excitation. Depth-dependent plasma waves (the carrier-density or plasma field) contribute to the generation of space and time-varying heat (the temperature field) and mechanical vibrations (the elastic displacement field), i.e. thermal and elastic waves. Thermal waves can propagate to the surfaces of the sample, i.e. may cause temperature changes in the gas layer near the sample surface. Changes in gas temperature cause a change in gas pressure, i.e. acoustic response to optical excitation - PA signals. This is the so-called thermodiffusion (TD) mechanism of PA signal

generation (thermal piston). On the other hand, the thermal and plasma waves in the MMS can cause elastic vibrations - the thermoelastic (TE) and plasmaelastic (PE) mechanism of PA signal generation. Vector sum of the TE and PE components forms mechanical PA signal (mechanical piston).

In linear elastic materials it is possible to use the principle of superposition, i.e. consideration of separate components of elastic displacement and their addition in order to find the field of total elastic displacements as a vector sum. For example, given the PA experimental configuration considered a uniformly optically excited square membrane. In mechanical point of view, the membrane is modeled as a thin elastic plate (Kirchhoff-Love plate theory). Two components of the elastic displacement of the thin elastic plate have significant influence on the measured PA signal. These two components are out-of-plane displacements and they defined separately as: a) pure elastic expanding W_E along thickness and b) pure elastic bending W_B of the uniformly optically excited plate.

In the PA solid-gas-microphone detection configuration, using the composite-piston model, the PA signal in Si MMS can be written as a vector sum of five components: one thermal - the thermodiffusion S^{TD}, and four mechanical: S_E^{TE}, S_E^{PE}, S_B^{TE} and S_B^{PE}, where S_B correspond to the elastic bending, and S_E to the elastic expanding.

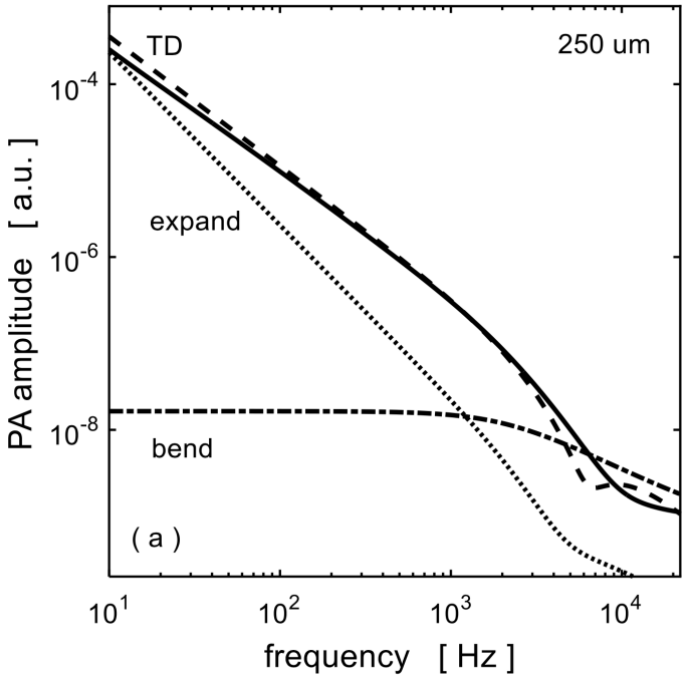

Fig. 1. PA amplitude of a Si micromechanical structure vs. frequency of modulation of the optical excitation. Micromechanical structure is Si chip with frame and square membrane (length L = 3000 and thickness h = 250 μm). In mechanical point of view, in this case the membrane is modeled as a thin elastic plate. PA components: (– –) TD; (···) expanding; (–.–) bending.

The comparison of the experimental and theoretical PA spectra confirms the previously obtained results of the theoretical analysis and shows the possibilities of applying the PA method for testing the elastic characteristics of MMS. This research is important for many practical experimental situations (atomic force microscopy, thermal microscopy, thermoelastic microscopy, etc.) and sensors and actuators.

09
Non-destructive Evaluation

Measuring the depth and width of delaminations by photothermal radiometry

Salazar A(1)*, Mendioroz A(1)

(1) Departamento de Física Aplicada, Escuela de Ingeniería de Bilbao, Universidad del País Vasco UPV/EHU, Plaza Ingeniero Torres Quevedo 1, 48013 Bilbao, Spain.

*Corresponding author's email: agustin.salazar@ehu.es

Photothermal methods have been widely used for sizing the depth of delaminations. However, less attention has been paid to size their width. In this work, we use modulated photothermal radiometry (PTR) to measure the depth and width of narrow delaminations by fitting the theoretical temperature expression to the experimental frequency spectrum of the PTR signal. We have established a general detectability limit that includes the material's properties: in good thermal conductors, submicronic delaminations can be sized down to 10 mm, whereas in thermal insulators it is difficult to go below 0.5 mm. Experiments on calibrated delaminations confirm these predictions.

Theory – Let us consider a semi-infinite an opaque sample containing a delamination of infinite area parallel to the sample surface, buried at a depth d and having a width w. The front surface of the sample is uniformly illuminated by a CW laser modulated at a frequency f (ω=2πf). The surface temperature of the delaminated sample normalized to a sound one is given by

$$T_n = \frac{2K_{air} + \sqrt{i\omega}\varepsilon w\left(1+e^{-2\sqrt{i\omega}d/\sqrt{D}}\right)}{2K_{air} + \sqrt{i\omega}\varepsilon w\left(1-e^{-2\sqrt{i\omega}d/\sqrt{D}}\right)}, \qquad \text{Eqn. 1}$$

where K, D and ε are the thermal conductivity, diffusivity and effusivity of the sample respectively. Note that the delamination depth and width are correlated to the thermal diffusivity and effusivity of the sample respectively.

With the aim of stablishing the sizing limits of ideal delaminations, we show in Fig. 1 the minimum quantifiable width for a given depth. We have selected an arbitrary but reasonable criterion for a delamination to be measurable: when it produces a normalized phase contrast higher than 5º. This corresponds to the green area in Fig. 1. The slope of the diagonal border indicating the transition from non-measurable to measurable regions is 200/3 mKW^{-1}. We have added another practical criterion to avoid using too low frequencies: the delamination is sizable if the normalized phase minimum appears at frequencies higher than 0.2 Hz. This corresponds to the red line in Fig. 1. In this way, the crossing point between the diagonal and the red lines indicates the highest retrievable depth, limited by the modulation frequency. Note that Fig. 1 is general in the sense that it is applicable to any material of known thermal properties.

Experimental results and discussion – In order to obtain calibrated delaminations we have prepared a sample by combining a glassy carbon plate of known thickness (0.52, 0.97 and 2.01 mm) and a thick sample of the same material. These samples are put in contact using some pressure. In order to calibrate the air gap between the plates, metallic tapes 0, 25, 75 and 125 μm thick are sandwiched between the carbon plates, at two opposite edges, producing an air gap between the glassy carbon pieces. For

normalization purposes, we divide the PTR signal of the sandwiched sample by the PTR signal of a thick homogeneous sample of the same material.

Experiments have been performed using a conventional modulated PTR setup. In Fig. 2 we show by dots the experimental PTR frequency spectrum of the normalized phase for one of the delamination depths studied in this work: d = 0.52 mm and several delamination widths. The continuous lines are the best fits to Eq. (1), using two free parameters: d/sqrt(D) and εw. Since the thermal properties of the glassy carbon and air are known, the depth and width of the delamination are obtained simultaneously and are given in the inset of Fig. 2. As can be observed, the data feature low noise and the quality of the fittings is very good.

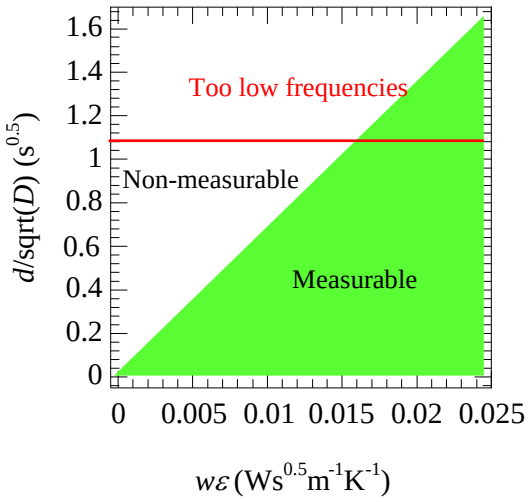

Fig. 1. This graphic indicates, for a given material (known thermal properties D and ε), whether a particular delamination (d,w) is measurable or not.

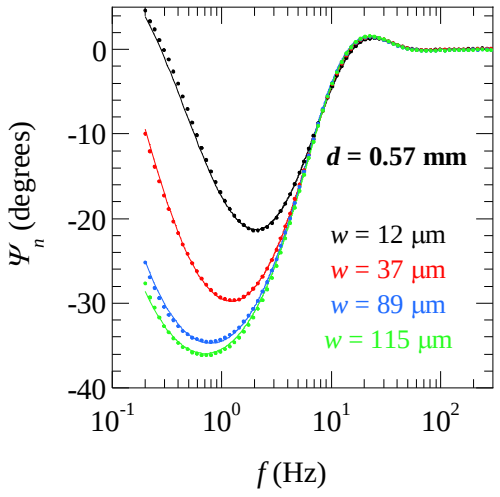

Fig. 2. Experimental frequency dependence of the normalized PTR phase (symbols) for a nominal depth d = 0.52 mm. Four nominal delamination widths are studied: 0, 25, 75 and 125 μm. The continuous lines are the fits to Eq. (1), leading to the d and w values given in the inset.

The depth of the delamination is slightly overestimated (10%), probably due to radiation between the glassy carbon surfaces in contact. Regarding the delamination width, if we look at the case of nominal width w = 0 (black dots and lines in Fig. 2), the retrieved width is not zero but a value of 12 μm, indicating that the contact between the two plates is not perfect. Even though the surfaces in contact are polished and some pressure is applied to the combined pieces in contact, it is difficult to obtain a perfect thermal match between them. Accordingly, when putting the metallic plates the retrieved delamination widths are affected by this offset. Anyway, the results confirm the validity of the model, and show that it is possible to size the width and depth of ideal delaminations within the established detectability limits.

Acknowledgments – This work has been supported by Ministerio de Ciencia e Innovación (Grant PID2019-104347RB-I00 funded by MCIN/AEI/10.13039/501100011033) and by Universidad del País Vasco UPV/EHU (GIU19/058).

The feature detection of GFRP subsurface defects using fast randomized sparse principal component thermography

Shen P[(1)†], Luo Z[(1)†], Wang S[(1)], Mao F[(1)], Su Z[(1)], Zhang H[(1)*]

(1) Jiangsu Key Laboratory for Design and Manufacture of Micro-Nano Biomedical Instruments, School of Mechanical Engineering, Southeast University, Nanjing 211189, China

†Peng Shen and Zhi-Tao Luo contributed equally to this work.

*Corresponding author's email: seuzhanghui@seu.edu.cn

Machine learning methods play an increasingly important role in the nondestructive testing and evaluation of composites. As a popular feature extraction and dimension reduction method of thermographic data, principal component thermography is often used. However, the interpretability of its PCs and its ability to handle large-scale thermographic data affect the applicability of PCT for high-resolution thermographic NDT. In this paper, a fast randomized sparse principal component thermography (FRSPCT) is used to detect the subsurface defects of glass fiber reinforced polymer (GFRP) composites. The effectiveness of the method is demonstrated by the large-scale thermographic data of GFRP with subsurface defects. The comparison results show that the FRSPCT method gives the overall highest signal-to-noise ratio (SNR), detection rate (DR), and satisfactory runtime. In addition, the method can also provide more easily interpretable defect detection results and highlight the hidden details of irregularly-shaped abnormal defects.

Non-contact measurement of sub-micron-level ultrasonic vibration by near-field microwave

Peng C(1), Huan H(1)*, Chen X(1)*, Liu L(1)

(1) School of Mechano-Electronic Engineering, Xidian University, Xi'an 710071, China

*Corresponding authors' email: ckpcl96@163.com; hthuan@xidian.edu.cn, xlchen@mail.xidian.edu.cn

Background – Microwave non-destructive has been widely applied in dielectric properties [1] and internal defects [2] of materials, and moisture content, etc. Sub-micron-level ultrasonic vibration is conventionally detected with piezoelectric transducers which require directly contact. Optical non-contact vibrometry has excellent accuracy but requires sophisticated setup and good surface finish on the measured object. Alternatively, near-field microwave has high sensitivity in perceiving local change of dielectric property and distance, which makes it applicable in testing small ultrasonic vibrations in metal.

Theoretical modelling – Sub-micron ultrasonic vibrations are usually generated by pulse or modulated lasers in photoacoustic techniques [3]. They also occur in piezoelectric transducers operating at a frequency range far away from its resonance states [4]. As depicted in Fig. 1(a), a piezoelectric patch was modeled in an FEM software (COMSOL Multiphysics) and operating at 80 kHz.

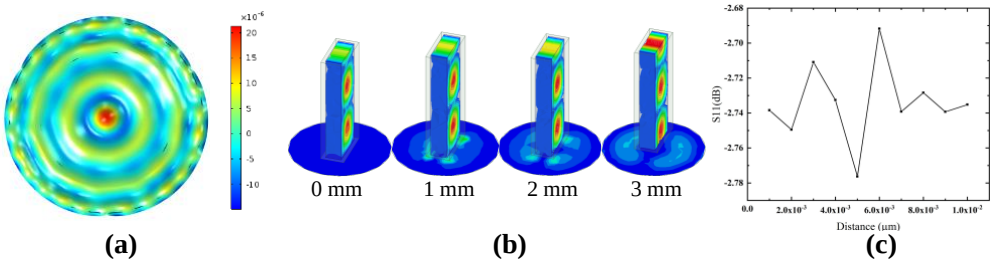

Fig. 1. The finite element simulation of (a) a piezoelectric patch operating at 550 kHz, (b) electromagnetic simulation between open-ended waveguide and sample with distance changes from 0 mm to 3 mm and (c) the received energy simulation.

The carrier signal $T(t)$ is fed into the waveguide and travels towards the sample, and vibration signal $x(t)$ is modulated to the high frequency carrier signal. The modulated signal $M(t)$ received by waveguide can be expressed as

$$T(t) = \cos(2\pi ft) \qquad \text{Eqn. 1}$$

$$M(t) = \alpha(d)\cos(2\pi ft - \frac{4\pi x(t)}{\lambda}) \qquad \text{Eqn. 2}$$

where d indicates the distance between the piezoelectric patch and the open-ended waveguide. The back propagated microwave is sensitively to the distance, which add $\alpha(d)$ on the amplitude of the modulated signal. The frequency was chosen at 18 GHz with 10^{-3} μm distance stepping changes on 1mm, and the results is shown in Fig. 1(c).

Experimental and discussion – As shown in Fig. 2(a). The open-ended waveguide was placed perpendicular to the piezoelectric patch to obtain the vibration signal directly. The microwave was fed into the measuring system which consists a coupler and a circulator to the open-ended waveguide. Vibration signal was modulated by the microwave and received by open-ended waveguide and sent to the demodulating system, the lock-in amplifier demodulated vibration signal and analyzed by the computer.

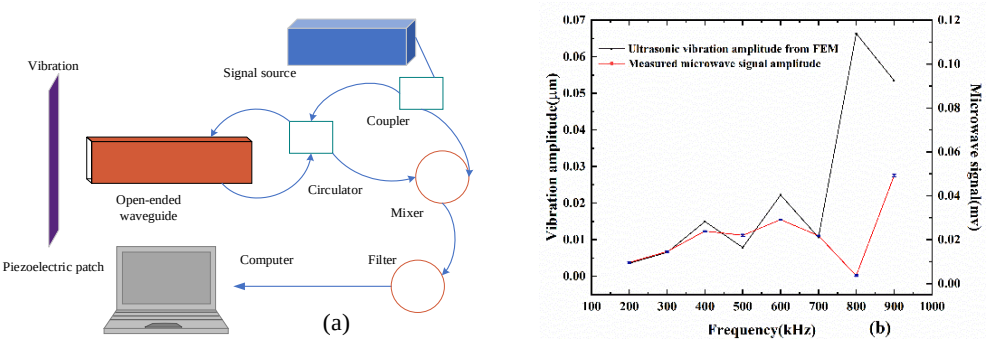

Fig. 2. (a) The measurement of vibration signal by microwave measurement system **(b)** Ultrasonic vibration amplitude from FEM; Measured microwave signal amplitude

Fig. 2(b) shows the experimental frequency-dependent vibration changes and the measured vibration signal in voltages at different frequencies. The result shows the amplitude of demodulated microwave signal has certain qualitative analogy with respect to the sub-micron ultrasonic vibration amplitude. The change trend of voltage signal is basically consistent with the finite element simulation.

Conclusion – A near-field microwave vibrometric configuration was proposed. Ultrasonic sub-micron-level vibration is successfully interpreted by the demodulated microwave voltage signal, which makes it promising for noncontact ultrasonic testing.

References

[1] M.S. Sim, Directric and Magnetic Properties of Epoxy with Dispersed Iron Phosphate Glass Particles by Microwave Measurement, JOM OAEA (2020).

[2] S.M. Ali, N.K. Nikolova, N.T. Sangary, Microwave Nondestructive Defect Identification using Sensitivity Analysis, IEEE Antennas and Propagation Society International Symposium, Albuquerque, NM (2006) 1391-1394.

[3] D.A. Hutchins, Mechanisms of pulsed photoacoustic generation. Can. J. Phys., 64 (1986) 1247-1264.

[4] B. Fu, T. Hemsel, J. Wallaschek, Piezoelectric transducer design via multiobjective optimization, Ultraonics, 22 (2006) 747-752.

Intelligent identification for delamination defects of aviation honeycomb sandwich composites (HSCs) using convolution neural network fusion lock-in thermography

Wang F[(1,2)], Yue Z[(1,2)], Zhao J[(1,2)], Liu J[(1,2)] *, Yang F[(1,2)], Wang Y[(1,2)], Chen M[(1,2)], Yue H[(1,2)]

(1) School of Mechatronics Engineering, Harbin Institute of Technology, Harbin, 150001, P. R. China.
(2) State Key Laboratory of Robotics and System (HIT), Harbin, 150001, P. R. China.

*Corresponding author's email: ljywlj@hit.edu.cn

We demonstrated the convolution neural network fusion lock-in thermography two-dimensional features approach, and this technique can realize the intelligent identification, classification and quantitative characterization for defects of aviation honeycomb sandwich composite (HSCs). Initially, HSCs specimen with delamination defects was detected by halogen lamp-induced lock-in thermography, and the frequency-domain characteristic images were extracted by lock-in algorithm. Furthermore, the image is used as defect feature database after image preprocessing (include contrast enhancement, threshold segmentation, mosaic data enhancement). Convolutional neural network is designed to realize defect identification, classification and size quantization. Finally, based on pixel calibration combining convolutional neural network model with image segmentation and morphological processing, quantitative measurement experiments of defect size and area of HSCs were carried out, and the range and measurement error of quantitative measurement of defect size and area of HSCs were investigated, and the relationship between measurement error and locking frequency was analyzed to realize quantitative measurement of defect size and area of HSCs.

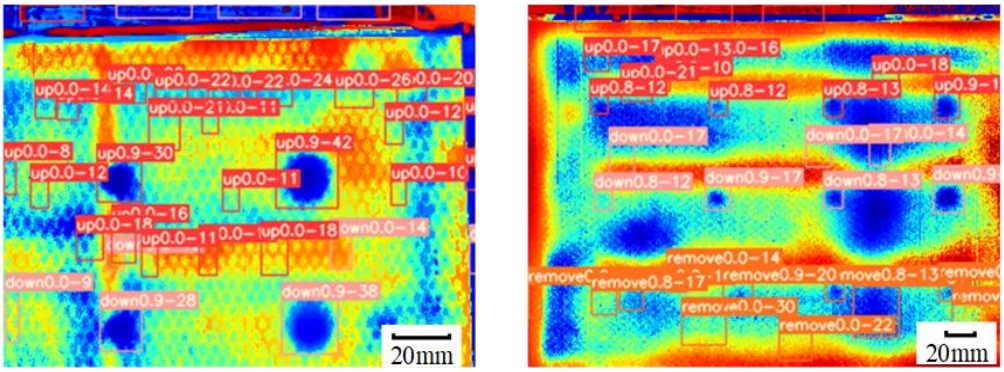

Fig. 1. Defect identification results

References

[1] F. Wang, J. Liu, P. Song et. al., Multimodal optical excitation pulsed thermography: Enhanced recognize debonding defects of the solid propellant rocket motor cladding layer, Mechanical Systems and Signal Processing, 163:108164 (2022).

Research on multi-dimensional feature recognition for PCBs typical defects using laser ultrasonic imaging

Yue Z[(1,2)], Wang F [(1,2)*], Liu J[(1,2)*], Song P[(3)], Wang Y[(1,2)], Chen M[(1,2)], Yue H[(1,2)]

(3) School of Mechatronics Engineering, Harbin Institute of Technology (HIT), Harbin, 150001, P. R. China
(4) State Key Laboratory of Robotics and System (HIT), Harbin, 150001, P. R. China
(5) School of Instrumentation Science and Engineering (HIT), Harbin, 150001, P. R. China

*Corresponding authors' email: wangfeipublic@hit.edu.cn (F. Wang), ljywlj@hit.edu.cn (J. Liu)

In this paper, a new laser ultrasonic nondestructive testing technique scheme is proposed for the typical defect detection of PCBs. Firstly, based on the laser ultrasonic excitation theory, a three-dimensional mathematical model of ultrasonic excitation by pulsed laser on the dielectric surface of PCBs board is established, and sparse principal component analysis (spare PCA), independent component analysis (ICA) and partial least squares regression (PLSR) are briefly described and utilized to extract the characteristic of laser-induced ultrasonic signal. Furthermore, laser ultrasonic imaging detection system was established based on the principle of laser ultrasonic theory, the detection experiment of simulated debonding flat bottom hole defects is carried out, and the transmission approach is used for C-scan experiment. The influence of the eigenvalues extracted by different algorithms on the imaging effect is analyzed from the perspective of quantification of signal-to-noise ratio, and the obtained detection results are compared with the infrared thermal wave imaging detection technology. The experimental results show that laser ultrasonic testing has the characteristics of high resolution and the advantages of imaging in small diameter. Therefore, it is of great significance to study a set of feasible laser ultrasonic technique for PCBs defect detection.

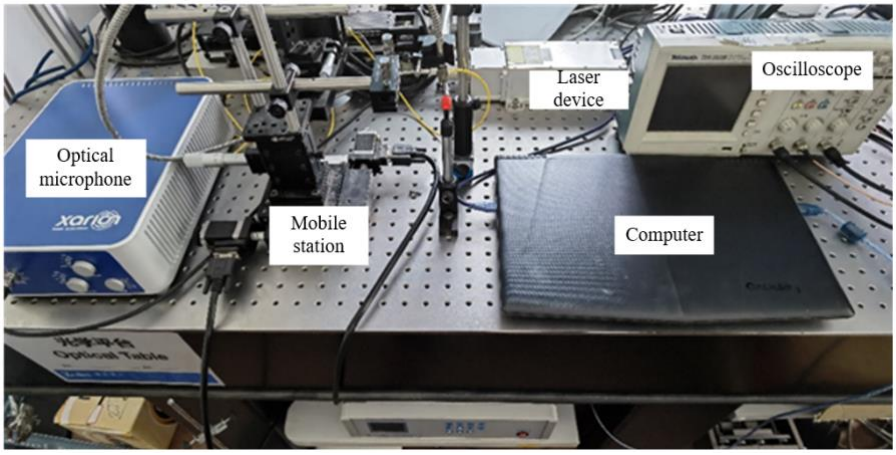

Fig. 1. General schematic diagram of laser ultrasonic imaging detection system

10
Low-Dimensional Systems, Nanoscale Phenomena and Nanostructure

Multiple Stokes and anti-Stokes components generation by biharmonic pumping via stimulated low-frequency Raman scattering

Tareeva MV[(1)*], Kudryavtseva AD[(1)], Shevchenko MA[(1)], Umanskaya SF[(1)], Tcherniega NV[(1)]

(1) Optics Department, Lebedev Physical Institute, Russian Academy of Sciences, Moscow, Russia

*Corresponding author's email: tareevamv@lebedev.ru

The process of high efficiency coherent acoustic excitation of the submicron particles system by biharmonic pumping is investigated. This excitation leads to effective multiple Stokes and anti-Stokes high-order components generation. This process can be used for effective generation of the coherent electromagnetic radiation with tunable spectral distribution consisting of several spectral lines separated by a constant frequency spacing of several GHz.

Any spatially limited object, including submicron and nanoscale ones, constantly undergoes thermal vibrations. The set of acoustic eigen frequencies of any object with which it oscillates is determined by its morphology, as well as by the elastic characteristics of its environment. Some of these acoustic excitations are Raman active and can manifest themselves in low-frequency Raman scattering [1] (LFRS) or in stimulated low frequency Raman scattering [2] (SLFRS). Biharmonic pumping is electromagnetic radiation whose spectrum consists of two spectral lines can be used for effective for effective impact on the system of particles in the case of the matching the particles acoustic eigenfrequencies with the frequency shift of biharmonic radiation by analogy with coherently driven molecular vibrations [3]. This process can lead to multiple Stokes and anti-Stokes high-order components generation.

The effect of multiple Stokes and anti-Stokes components generation by biharmonic pumping in nanosecond temporal range was demonstrated in a number of dielectric, semiconductor and metallic submicron particles systems. The effective generation of six equally shifted spectral components was realized. The possible application of the observed phenomenon for spectroscopy of the nanoscale and submicron systems is discussed.

[1] E. Duval, A. Boukenter, B. Champagnon, Vibration Eigenmodes and Size of Microcrystallites in Glass: Observation by Very-Low-Frequency Raman Scattering, Phys. Rev. Lett. 56 (1986) 2052-2055.

[2] N.V. Tcherniega, et al, Experimental observation of stimulated low-frequency Raman scattering in water suspensions of silver and gold nanoparticles, Opt. Lett. 38 (2013) 824-826.

[3] E. Garmire, F. Pandarese and C.H. Towns, Coherently driven molecular vibrations and light modulation, Phys. Rev. Lett. 11 (1963) 110-163.

Study of the thermal properties of resin/graphene nanocomposite for 3D print applications

García-Vidal UO[(1)], Jiménez-Pérez JL[(1)*], Moreno-Rocha JM[(1)], Luna-Sánchez JL[(1)], Correa-Pacheco ZN[(2)]

(1) Unidad Profesional Interdisciplinaria en Ingeniería y Tecnologías Avanzadas-Instituto Politécnico Nacional, Av. IPN, No. 2580, Col. Barrio La Laguna Ticomán, Gustavo A. Madero, C.P. 07340 Mexico City, Mexico

(2) Centro de Desarrollo de Productos Bióticos, Instituto Politécnico Nacional, Carretera Yautepec-Jojutla km 6, San Isidro, Yautepec, Morelos 62731, Mexico

*Corresponding author's email: jljimenez@ipn.mx

Background – In recent decades, the use of multiple polymers for 3D part printing applications has been intensively exploited. Therefore, the use of new resin-based composite resins, mixed with graphene oxide (GO), is necessary. This composite is of great interest, because this material is produced from the exfoliation of graphite, which has interesting properties of resistance, rigidity and thermal conductivity. Lately, graphene nanotechnology has become a main topic in current research, since this material has a high surface area, which is greater in its exfoliated form. Therefore, it increases overall performance when is used in compounds. Similarly, some authors suggest that GO can be used to increase matrix properties in nanostructures. Hence, it is important to know their thermal properties such as thermal diffusivity when is added to nanocomposites, for small amounts of sample. In this work, the thermal wave resonant cavity (TWRC) technique was used, by means of a pyroelectric detector with a length sweep in the resonant cavity. The accuracy and precision of this technique was established by comparing the thermal diffusivity of distilled water. From the results obtained, an increase in the thermal diffusivity of the nanocomposite with concentration was observed. To obtain a strong resin-nanostructure interface remains a challenge for many researchers.

Methods – For the synthesis of the selected nanocomposites, a set of samples of polymer resins (PMMA) of the same weight were determined, then samples of graphene oxide enriched with COOH were obtained. For the mixture of both compounds, a mechanical mixture was first carried out for approximately 1 hour and then the sample was subjected to a sonification process for approximately 3 hours, once the graphene was fully integrated into the resin. The weight concentrations of 0.02 to 0.12 wt%.

For resin/graphene thermal characterization, the TWRC arrange was used. In this technique, a small amount of the liquid resin was placed in a chamber composed of a metal foil and a PZT temperature sensor. Then, the light of a laser beam modulated by an oscillator is absorbed by the resin acting as thermal wave generator. Then, the temperature variation is measured by a pyroelectric sensor as function of sample thickness. The signal was detected by a lock-in amplifier. Thermal diffusivity was measured using the back-photopyroelectric technique [1].

Results – The results for thermal diffusivity are shown in Table 1. Representative graphs of thermal diffusivity (*D*) for graphene NPs/resin are shown in figure 1 and Theoretical equation 1 [1]. Thermal diffusivity (*D*) in amplitude, phase, enhancement and literature values are also shown in Table 1.

$$Ln(V(L,\alpha,\omega)) = ln(Const(\omega)) + ln(e^{-qL}),\ q = \sqrt{\frac{\pi f}{\alpha_l}} \qquad \text{Eqn.1}$$

Table 1. Thermal properties values for the graphene NPs /resin

Wt%	$\alpha_{Amplitude}$ ×10^{-7}(cm^2/s)	α_{Phase} ×10^{-7}(cm^2/s)	***Enhancement*** %	***Literature* value**
0.12	1.27	1.03x10^{-7}	33.68	
Resin	0.915	0.885x10^{-7}		0.95x10^{-7} [2]
Distilled water	1.47	1.45x10^{-7}		15.9069x10^{-3} [3]

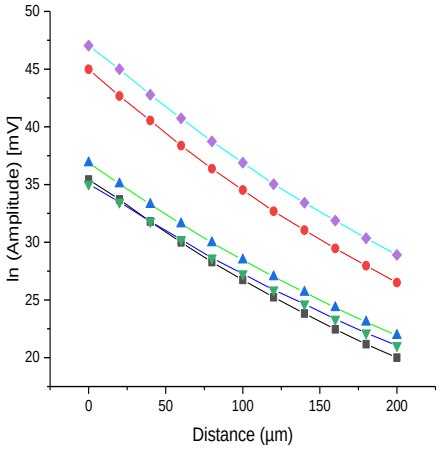

Fig. 1. Thermal diffusivity graphs of amplitude for graphene NPs /resin. The continued line is the best fit for the experimental values.

From the results, thermal diffusivity of graphene NPs/resin was higher than for pure resin. From calculation, the highest thermal diffusivity value was of 1.27×10^{-7} m^2/s for a 0.12 wt% concentration of graphene NPs /resin. The results found in this work are of special interest because the process is associated with the improvement of the interfaces between the NPs and the matrix as well as the morphology of the GO NPs (nanoplatelets), the thermal diffusivity increases by several times [4].

Conclusions – For the pure liquid resin studied, a higher diffusivity was obtained with a concentration of 0.12 wt% graphene NPs, followed by an enrichment of 33.7% and finally the increase in thermal diffusivity is related to the surface area, phononic network, morphology and interfaces between the NPs and the matrix [18]. In addition, the thermal diffusivity was calculated with the TWRC technique. Further research studies are needed to explore the mechanisms of thermal transport through graphene/polymer interfaces.

References

[1] G. Lara-Hernández, J.C. Benavides-Parra, A. Cruz-Orea, E. Contreras-Gallegos, C. Hernández-Aguilar, J.J.A. Flores-Cuautle. Thermal characterization of castor oil as additive in lubricant oil using photothermal techniques. Sup. Vacío 3:1 (2018) 6-9.

[2] A.C. Sparavigna, M. Omini, A. Pasquarelli, A. Strigazzi, Thermal diffusivity of amorphous plastic materials. High Temperatures-High Pressures 24 (1992) 175-175.

[3] J. Balderas-López, A. Mandelis, Simple, accurate, and precise measurements of thermal diffusivity in liquids using a thermal-wave cavity", Review of Scientific Instruments, 72: 6, (2001) 2649-2652. 10.1063/1.1372677.

[4] A. Kumar, K. Sharma, A.R. Dixit, Carbon nanotube- and graphene-reinforced multiphase polymeric composites: review on their properties and applications, J. Mater. Sci. 55 (2020) 2682–2724.

Thermal study of ferromagnetic nanoparticles coated with mesoporous silicon oxide

García-Vidal UO[(1)*], Jiménez-Pérez JL[(1)], Correa-Pacheco ZN[(2)], López-Gamboa G[(3)], Gutiérrez-Fuentes R[(4)]

(1) Unidad Profesional Interdisciplinaria en Ingeniería y Tecnologías Avanzadas-Instituto Politécnico Nacional, Av. IPN, No. 2580, Col. Barrio La Laguna Ticomán, Gustavo A. Madero, C.P. 07340 Mexico City, Mexico

(2) Centro de Desarrollo de Productos Bióticos, Instituto Politécnico Nacional, Carretera Yautepec-Jojutla km 6, San Isidro, Yautepec, Morelos 62731, Mexico.

(3) Tecnológico Nacional de México Campus Toluca, dirección Avenida Tecnológico s/n. Colonia Agrícola Bellavista, Metepec, C.P. 52149, Mexico State, Mexico

(4) Tecnológico de Estudios Superiores de Villa Guerrero. Dirección: Carretera Federal Toluca - Ixtapan de la sal Km 64.5, Col. La Finca, Villa Guerrero, Mexico State, Mexico

*Corresponding author's email: ugarciav0700@alumno.ipn.mx

Background – Magnetite (Fe_3O_4) superparamagnetic nanoparticle (NPs) systems are a promising option for applications in biomedicine such as hyperthermia therapies, drug delivery, imaging. Fe_3O_4 NPs with less than 20 nm in size have unique properties being capable of following a magnetic field and lose magnetization when this field is removed. This reduces the risk of nanoparticle aggregation, avoiding a negative impact. Incorporating an external matrix of mesoporous SiO_2 allows to combine the properties of Fe_3O_4 and silicon, which are important to reduce its toxicity with the advantage of load drugs or markers within the mesoporous SiO_2 matrix. In this work, a simple methodology to synthesize these nanocomposites, using the co-precipitation method for the development of Fe_3O_4 nanoparticles and using the modified Stöber method to incorporate the mesoporous SiO_2 matrix was developed. The thermal characterization of the nanoparticles by thermal lens and thermal wave resonant cavity (TWRC) techniques were used.

Methods – NPs Fe3O4 were elaborated from two different processes, by precipitation and heating. NPs with a particle size of 20 nm were obtained and characterized by EDS to determine their composition. Before SiO_2 shell coating, the Fe_3O_4 NPs were modified with citric acid to obtain better dispersibility. 0.02 g of Fe_3O_4 NPs and citric acid were dissolved in deionized water with mechanical stirring for 1 h in a flask. Another solution mixed with 10 ml of distilled water, 50 ml of absolute alcohol, 5 ml of aqueous ammonia and 0.2 g of CTAB was mechanically stirred at room temperature for 10 min and then injected into the above flask. After that, 1 ml of TEOS, which will serve as silicon precursor was added. The mixture solution was continuously stirred for 2 h, which was named Fe3O4@-SiO2 [1,2]. Thermal analyzes were performed with the TWRC and thermal lens (TL) techniques.

Results – Figure 1 shows the characteristic spectrum of the evolution of the signal by the TWRC technique for a measurement of Fe_3O_4 nanofluid. The straight line is the best fit of the equation Eq. 1 to the experimental values of 6 measurements. The fit constant (q) was found by means of the slope of the line. The value of the thermal diffusivity of distilled water was obtained by this same technique. The thermal diffusivity is 1.3 $x10^{-3}$ cm^2/s for a concentration of 0.1 mg/mL, increases with the size of the NPs, showing a thermal enrichment of 80% for a constant weight concentration. Fig 1 shows the phase signal as a function of the scan distance of the resonator in the liquid sample. This value is

important to determine the thermal diffusivity based on the size of the particle, concentration and coverage of the NPs, for heat transport in medical applications.

$$Ln(V(L,\alpha,\omega)) = ln(Const(\omega)) + ln(e^{-qL}),\ q = \sqrt{\frac{\pi f}{\alpha_l}} \qquad \text{Eqn.1}$$

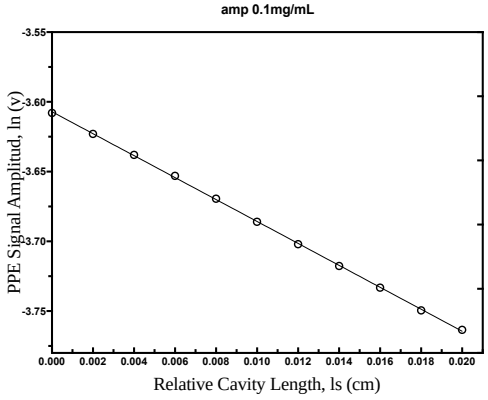

Fig. 1. PPE signal amplitude v.s, relative cavity length for Fe_3O_4 nanofluid. The continuum line is the best fit for the experimental values.

Conclusions – In summary, the thermal diffusivity of magnetic nanofluids was measured for 3 different particle sizes using two photothermal techniques TL and TWRC, obtaining a growth of diffusivity as a function of size. The results of the amplitude of the TWRC signal were similar to the thermal diffusivity of TL, in agreement for the thermally transparent region. Therefore, in the inverse process of the signal phase of the TWRC technique, the thermal diffusivity is higher than the diffusivity of the TL. The obtained values of thermal diffusivity by TWRC were similar to the values reported in the literature. Possibly the increase of the thermal diffusivity is related to the precipitation of the NPs in the resonant cavity, concentration and due to the cover of the NPs with the Fe oxide.

References

[1] J. A. Fuentes-García, A.I. Diaz-Cano, A. Guillen-Cervantes, J. Santoyo-Salazar. Magnetic domain interactions of Fe_3O_4 nanoparticles embedded in a SiO_2 matrix. Sci. Rep. 8 (2018) 5096:1-10. https://doi.org/10.1038/s41598-018-23460-w

[2] L. Yang, P. Zou, J. Cao, Y. Sun, D. Han, S. Yang, G. Chen, X. Kong, J. Yang. Facile synthesis and paramagnetic properties of Fe_3O_4@SiO_2 core–shell nanoparticles. Superlattice Microst. 76 (2014) 205-212. https://doi.org/10.1016/j.spmi.2014.10.011.

11

Environmental, Agricultural, and Food Applications

Characterization of natural hepatoprotectors and added foods by photoacoustic spectroscopy and colorimetry

Saucedo-Alfonzo DA[(1)], Dominguez-Pacheco A[(1)*], Hernandez-Aguilar C[(1)], Orea-cruz A[(1)]

(1) Posgrado en Ingeniería de Sistemas, SEPI – ESIME - Zac., Instituto Politécnico Nacional, Ciudad de México, México
(2) Departamento de Física, CINVESTAV–IPN, A. P. 14-740, 07360, Ciudad de México, México

*Corresponding author's email: fartur@hotmail.com

The pandemic and crisis of metabolic diseases necessitates the development and consumption of foods with a higher nutrient content that have a better impact in the quality health. The improvement of mixtures daily foods by adding nutraceutical materials by bioactive substances has a favorable effect on products and consumers [1-2]. This kind of materials and mixtures is possible to characterize them by photothermal techniques using some of distinct configurations like photoacoustic spectroscopy (PAS) open cell (OC) and closed cell, photoacoustic microscopy (PAM) and photopyroelectric (PPE), etc. Through use of these techniques diversity thermal and optical parameters have been obtained such as the optical absorption coefficient (β), the diffusivity, effusivity and thermal images [3-5]. Also, using the colorimetric techniques in the materials in the variables (CIEL*a*b*) can be used for the analysis of foods. In the present study were characterized optically by PAS and colorimetry the natural hepatoprotective food and with the mixtures of commercial cornmeal were made tortillas adding 2, 4,6 and 8% of black radish powder. The PA spectra of the natural hepatoprotectors and the tortillas were obtained to analyze their differences. In the Figure 1 showed spectra PA of natural hepatoprotectors, it can be observed that the behavior of the FA signal in the range of 250 to 400 nm has the maximum signal amplitude on the study samples. The PAS technique and colometry permit the study of naturals hepatoprotectors and blends of cornmeal added with black radish.

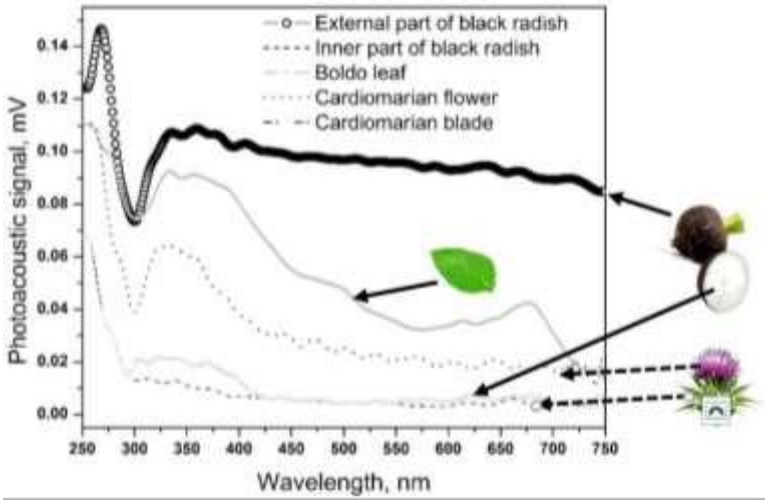

Fig 1. Photoacoustic spectra of black radish, Silybum marianum and boldo (Peumus boldus).

References

[1] C. Hernandez-Aguilar, A. Dominguez-Pacheco, C. Valderrama-Bravo, A. Cruz-Orea, E. Martínez Ortiz, J. Ordonez-Miranda, Photoacoustic spectroscopy in the characterization of bread with turmeric addition. Food Bioproc. Tech. 13 (2020) 2104-2119.

[2] C. Hernandez-Aguilar, A. Dominguez-Pacheco, M. Palma Tenango, C. Valderrama-Bravo, M. Soto Hernández, A. Cruz-Orea, J. Ordonez-Miranda, Lentil sprouts: a nutraceutical alternative for the elaboration of bread. J. Food Sci. Technol., 57 (2020) 1817-1829.

[3] M. Kovács, O. Dóka, D. Bicanic, Z. Ajtony, Application of laser-based photoacoustic spectroscopy and colorimetry for quantification of anthocyanin in hard boiled candy. Microchem. J. 135 (2017) 100-104.

[4] P. Tavakolian, A. Mandelis, Perspective: Principles and specifications of photothermal imaging methodologies and their applications to non-invasive biomedical and non-destructive materials imaging. Int. J. Appl. Phys. 124 (2018) 160903.

[5] O. Delgado-Vasallo, A.C. Valdes, E. Marin, J.A.P. Lima, M.G. Da Silva, M. Sthel, H. Vargas, S.L. Cardoso, Optical and thermal properties of liquids measured by means of an open photoacoustic cell. Meas. Sci. Technol.11 (2000) 412.

[6] E. Cuevas, D. Zaldivar, M. Perez, procesamiento digital de imágenes usando Matlab & Simulink. Alfaomega, 479 (2010).

[7] H. Lawless, H. Heymann, Color and Appearance. In: Sensory Evaluation of Food. Food Science Text Series. Springer, New York, NY. (2010) 295-297.

Thermal properties measurement of chitosan-based films for agricultural applications

Correa-Pacheco ZN[(1)*], Jiménez-Pérez JL[(2)], Cruz-Orea A[(3)], Bautista-Baños S[(1)], García-Vidal UO[(2)]

(1) Centro de Desarrollo de Productos Bióticos, Instituto Politécnico Nacional, Carretera Yautepec-Jojutla km 6, San Isidro, Yautepec, Morelos 62731, Mexico.
(2) Unidad Profesional Interdisciplinaria en Ingeniería y Tecnologías Avanzadas-Instituto Politécnico Nacional, Av. IPN, No. 2580, Col. Barrio La Laguna Ticomán, Gustavo A. Madero, C.P. 07340 Mexico City, Mexico
(3) Departamento de Física, Centro de Investigación y de Estudios Avanzados del Instituto Politécnico Nacional, Gustavo A. Madero, 07360, Mexico City, Mexico.

*Corresponding author's email: zcorreap@ipn.mx

Background – Nowadays, the use of pesticides for preservation of horticultural products represents a big issue concerning environmental contamination. Therefore, new sources based on natural polymers should be sought. Among these polymers, chitosan is of special interest due to its non-toxicity, biodegradability, barrier properties, antimicrobial activity and film forming capacity. Moreover, antimicrobial effectiveness can be improved with bioactive agents such as essential oils and propolis. An additional way to enhance the effect of the coating films is nanotechnology due to the surface area to volume ratio which increases this activity. Although some physiological and quality variables have been evaluated for the coated-fruit or vegetables, there is few information about its thermal properties, which are related to the variables above mentioned before through the fruit ripening process and storage. In the present study the thermal diffusivity and thermal effusivity were measured by using open photoacoustic cell (OPC) and photopyroelectric techniques, respectively. From the results, highest diffusivity and lowest effusivity values were found for chitosan-based NPs film.

Methods – For nanoparticles elaboration, the nanoprecipitation method [1] was followed. Briefly, a chitosan solution (0.05%) was prepared using glacial acetic acid and distilled water. On the other hand, a solution containing methanol (40 mL) and the bioactive agent (thyme essential oil or propolis, 5%) and Tween 20 (1%) was prepared. Then, 2.5 mL of the chitosan solution was dropped into the methanol and active agent solution with a peristaltic pump and finally concentrated to 2 mL by using a rotary evaporator. A formulation, based on the synthesized nanoparticles (33%), glycerol (0.3%), and a chitosan solution at 1% (66.7%), was placed into a homogenizer and cast-films elaborated in a convection oven at 40±1 ^{o}C for 3 h. For films thermal characterization, thermal diffusivity was measured by OPC technique, based on the periodic heating of the sample by absorption of laser light pulses, on the sample front surface, which results in a temperature variation of a thin air layer, in contact with the sample back surface, inside of the photoacoustic cell causing a pressure fluctuation that can be registered by the microphone. The thermal effusivity was measured through the front-photopyroelectric technique using the thermal wave resonance cavity (TWRC), in which a small cut piece of the film was placed in a chamber composed of a metal foil and a piezoelectric temperature sensor. Then, the light of a laser beam modulated by an oscillator was absorbed by the metal foil acting as thermal wave generator. Then, the temperature variation was measured by a pyroelectric sensor as function of sample thickness. The signal was detected by a lock-in amplifier [2].

Results – Thermal diffusivity (*D*), effusivity (*e*) and conductivity (*k*) results are shown in Table 1. Representative graphs of thermal diffusivity of chitosan NPs film and thermal effusivity for propolis-chitosan NPs film are shown in figures 1a) and 1b), respectively.

$$k = e\sqrt{D} \qquad \text{Eqn. 1}$$

Table 1. Thermal properties values for the chitosan-based films

Film	***D*** [x 10^{-3} m^2/s]	***e*** [$Ws^{1/2}/m^2K$]	***k*** [x 10^{-3} $Wm^{-1}K^{-1}$]
Chitosan NPs	0.00010±0.00002	45.618±0.001	0.456±0.046
Thyme essential oil-chitosan NPs	0.00009±0.00031	56.039±0.002	0.532±0.030
Propolis-chitosan NPs	0.00008±0.00001	67.592±0.007	0.605±0.022

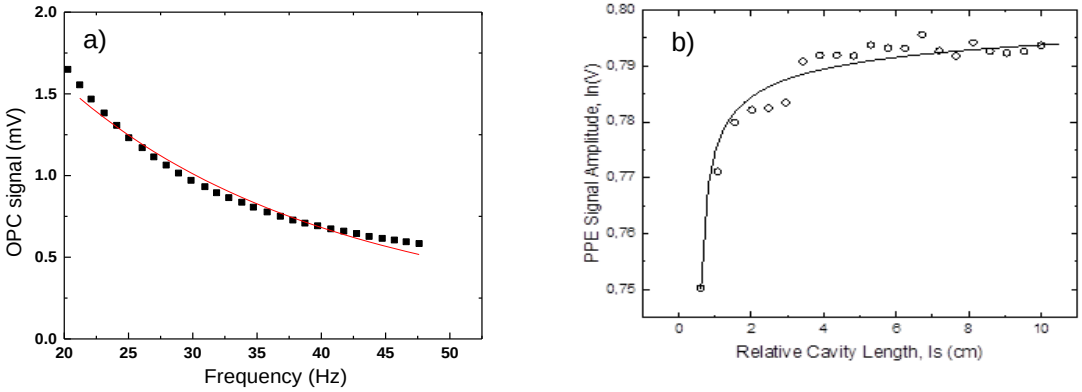

Fig. 1. a) Thermal diffusivity and **b)** thermal effusivity graphs for chitosan NPs film. The line is the best fit for the experimental values (dots).

From the results, the highest value of thermal diffusivity was for the chitosan NPs film and the lowest for the propolis-chitosan NPs. The effusivity behaviour was the opposite as expected. From calculations, the highest thermal conductivity value was for propolis-chitosan NPs. The results found in this work are of special interest because the senescence process of the fruit is usually associated to water loss from the agricultural produce and the barrier property of the coatings for gas and liquid exchange.

Conclusions – For the studied chitosan-based NPs films, lower diffusivity and higher effusivity was obtained for the propolis-chitosan NPs, followed by the thyme essential oil-chitosan NPs, and finally the chitosan NPs. More studies related to water vapor permeability and moisture content are in progress.

References

[1] A.G. Luque-Alcaraz, J. Lizardi, F.M. Goycoolea, M.A. Valdez, A.L. Acosta, S.B. Iloki-Assanga, I. Higuera-Ciapara, W. Arguelles-Monal. Characterization and antiproliferative activity of Nobiletin-loaded chitosan nanoparticles. J. Nanomater. 265161 (2012) 1-7. https://doi:10.1155/2012/265161

[2] G. Lara-Hernández, J.C. Benavides-Parra, A. Cruz-Orea, E. Contreras-Gallegos, C. Hernández-Aguilar, J.J.A. Flores-Cuautle. Thermal characterization of castor oil as additive in lubricant oil using photothermal techniques. Sup. Vacío 3:1 (2018) 6-9.

Characterization of plasma-treated gooseberry (Physalis Peruviana L.) seeds using photoacoustic techniques

Romero-Galindo R(1), Hernández-Aguilar C(1), Domínguez-Pacheco A(1)*, Cruz-Orea A(2)

(1) Posgrado en Ingeniería de Sistemas, SEPI – ESIME - Zac., Instituto Politécnico Nacional, Ciudad de México, México
(2) Departamento de Física, CINVESTAV–IPN, A. P. 14-740, 07360, Ciudad de México, México

*Corresponding author's email: fartur@hotmail.com

Climate change has altered hydrological patterns generating drought problems in agricultural production systems, such as decreased production yields, reduction of arable areas, crop loss, physiological and biochemical changes in plants [1, 2]. On the other hand, seed treatment with plasma has been used to improvement the plant´s antioxidant defense system and counteract the negative effects of Reactive Oxygen Species that are produced in drought stressful situations, as well as to improve its physiological variables [3]. Many techniques have been used to evaluate the changes produced in the seeds due to plasma treatments; however, it is necessary to use non-invasive sustainable techniques to avoid destroying samples, such as photothermal techniques, which consist of generating and detecting thermal waves in the study materials to obtain their thermal properties, absorption spectra, permeability, photosynthesis, among others [4]. In this research, gooseberry seeds were treated under three conditions: control, vacuum, and plasma at different exposure times, then they were characterized by photoacoustic microscopy (PAM), scanning the sample, and obtaining their thermal images. Fig 1 shows the thermal images obtained by means of PAM of the seed without treatment and treated with vacuum and the degradation that it suffers can be observed, this could make the seeds more permeable and reduce the imbibition time to achieve a successful emergence.

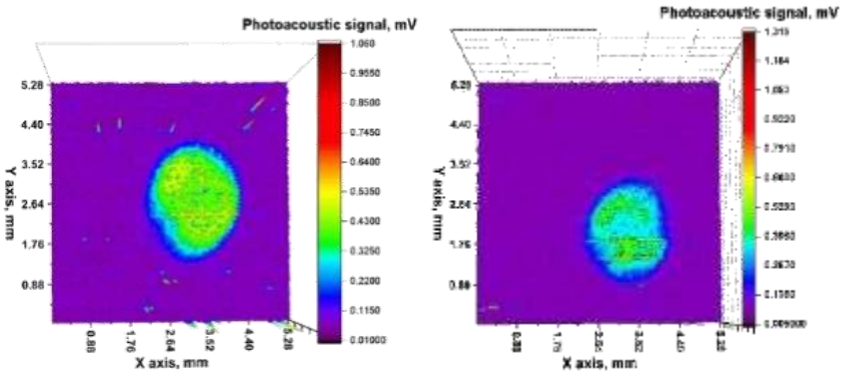

Fig. 1. Thermal images of gooseberry seeds (*Physalis Peruviana L.*) a) without treatments and b) vacuum treated.

References

[1] L. Baghel, S. Kataria, K.N. Guruprasad, Effect of static magnetic field pretreatment on growth, photosynthetic performance, and yield of soybean under water stress, Photosynthetica 56 (2018) 718-730. https://doi.org/10.1007/s11099-017- 0722-3.

[2] Q. Guo, Y. Wang, H. Zhang, G. Qu, T. Wang, Q. Sun, D. Liang, Alleviation of adverse effects of drought stress on wheat seed germination using atmospheric dielectric barrier discharge plasma treatment, Nature Sci. Rep. 7 (2017) 1-14. https://doi.org/10.1038/s41598-017-16944-8.

[3] R. Moluna, C. López-Santos, A. Gómez-Ramírez, A. Vilchez, J.P. Espinos, A.R. González-Elipe, Influence of irrigation conditions in the germination of plasma treated Nasturtium seeds. Nature Sci. Rep. 8 (2018) 1-11. https://doi.org/10.1038/s41598-018-34801-0.

[4] G.P. Pardo, A.D. Pacheco, S.A. Tomás, A.C. Orea, C.H. Aguilar, Characterization of Aged Lettuce and Chard Seeds by Photothermal Techniques, Int. J. Thermophys. 39 (2018) 1-10. https://doi.org/10.1007/s10765-018-2438-4.

Optical and thermal properties of Mexican native maize and tortilla

Contreras-Gallegos E[(1)], Hernández-Aguilar C[(2)], Domínguez-Pacheco A[(2)], Cruz-Orea A[(1)*]

(1) Departamento de Física, Centro de Investigación y de Estudios Avanzados-IPN, Av. IPN No. 2508, Col. San Pedro Zacatenco, 07360 Ciudad de México, México

(2) Posgrado en Ingeniería de Sistemas, SEPI – ESIME - Zac., Instituto Politécnico Nacional, Ciudad de México, México

*Corresponding author's email: alfredo.cruzorea@cinvestav.mx

Maize is one of the most important cereal grains in global production, economy, and consumption. It is a staple food that provides nutrients to the population and is consumed in different forms depending on the region of the world. In Mexico and some regions of Latin America, corn is frequently nixtamalized for making table tortillas and other foods; this process gives good properties, both physically and nutritionally [1,2]. Photoacoustic spectroscopy (PAS) has been considered a potential tool for the optical characterization of the different components found in foods [3]. In this work, PAS is used to analyze the optical absorption spectra to determine the changes in phytochemical compounds in the tortilla production process of six Mexican native maize grains (NMG). The nixtamalized dought of each NMG is blended with different concentration percentages of turmeric (TC) to make tortillas later. The correlation between the optical absorption spectra generated by the phytochemical compounds and TC concentration rates for native maize dough (NMD) and tortillas (NMT) is obtained by PAS. The photoacoustic spectra of pure NMG are shown in Figure 1. In these spectra it is possible to observe an absorption band, from 300 nm to 450 nm, corresponding to the optical absorption of phenolic acids and flavonoids [4]. The absorption band of anthocyanins (525 nm) in NMG varies significantly depending on the maize genotype, obtaining a higher absorption signal for those with orange, blue and red colorations than those with light yellow or white appearance [5].

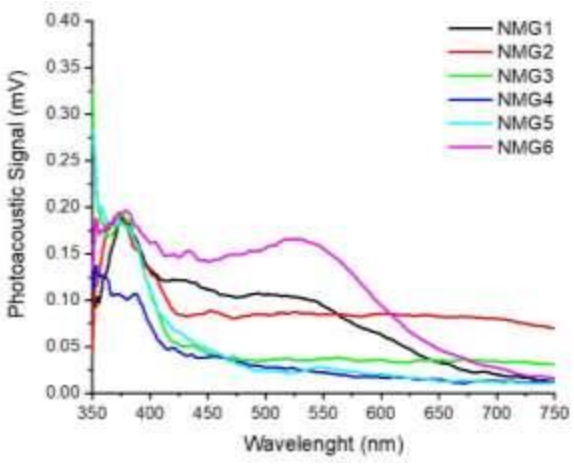

Fig. 1. Optical absorption spectra, obtained by photoacoustic spectroscopy of different Mexican native maize grains (NMG).

To determine the changes in thermal parameters due to nixtamalization and the process to make tortillas, the thermal effusivity (e) and diffusivity (α) of each NMD, NMT, and their corresponded TC blends,

are measured by using the Front Photopyroelectric (FPPE) configuration and the Open Photoacoustic Cell (OPC) techniques, respectively. Then, the thermal conductivity (k) and the heat capacity per volume unit (ρc) are calculated by the relationships $k = e\sqrt{\alpha}$ and $\rho c = k/\sqrt{\alpha}$.

References

[1] S. O. Serna-Saldivar, in Ref. Modul. Food Sci., Elsevier (2016).

[2] J.A. Gwirtz, M.N. Garcia-Casal, Ann. N. Y. Acad. Sci. 1312 (2014) 66.

[3] C. Hernández-Aguilar, A. Domínguez-Pacheco, A. Cruz-Orea, R. Ivanov, J. Spectrosc. 1 (2019).

[4] C. Hernandez-Aguilar, A. Dominguez-Pacheco, C. Valderrama-Bravo, A. Cruz-Orea, E. Martínez Ortiz, J. Ordonez-Miranda, Food Bioprocess Technol. 13 (2020) 2104.

[5] L.X. Lopez-Martinez, R.M. Oliart-Ros, G. Valerio-Alfaro, C.-H. Lee, K.L. Parkin, H.S. Garcia, LWT - Food Sci. Technol. 42 (2009) 1187.

Photopyroelectric technique applied to sodium alginate hydrogel characterization

Pessoa PAC(1), Moll PAAMM(1), Guimarães AO(1)*, Soffner ME(1), da Silva EC(1), Pereira NR(2), Waldman WR(3)

(1) Laboratório de Ciências Físicas, Universidade Estadual do Norte Fluminense (UENF), Campos dos Goytacazes, Brazil
(2) Laboratório de Tecnologia de Alimentos, Universidade Estadual do Norte Fluminense (UENF), Campos dos Goytacazes, Brazil
(3) Departamento de Física, Química e Matemática, Universidade Federal de São Carlos, Sorocaba, Brazil

*Corresponding author's email: aguimaraes@uenf.br

The search for new friendly and biodegradable products on scientific and industrial demand has been increasing in the last years. Hydrogels based on polymeric and biopolymeric materials forming a three-dimensional network, are considered promising options in medical and pharmaceutical fields, as well as in food industry, being used as emulsifiers, stabilizers and encapsulating agent. Among them is sodium alginate (SA), a water-soluble polysaccharide, isolated from brown algae species. The chemical structure, consisted of high molecular weight linear copolymers of β-D-mannuronic and α-L-guluronic acids, presents selective binding capacity for polyvalent cations (e.g., Ca^{2+}). The gel is formed by ionic exchange between Na^{+} and Ca^{2+} ions, crosslinking the polymer chain in egg-box structure, which is achieved in mild conditions.

Among the photothermal techniques, the photopyroelectric (PPE) methodology is the most appropriate for a complete thermal characterization of liquid and pasty samples. The temperature oscillations are measured by a pyroelectric transducer, in contact with the sample, by induced changes in the surface polarization charge over the sensor electrodes, which is detected as ac electric signal by a lock-in analyser. The PPE technique enables the investigation of the dynamic thermal properties such as thermal conductivity, diffusivity and effusivity, in addition to the specific heat [1].

In this work, we used the back (BPPE) and front (FPPE) photopyroelectric configuration, to measure thermal diffusivity and effusivity, respectively, of sodium alginate. Aqueous solutions of Sodium Alginate in different concentrations (1, 2 and 3%) were measured, as well as standard samples used as reference. Besides, for the 3% sample, we measured thermal diffusivity and effusivity during the gelation process, which happens simultaneously with drying.

In the experimental setup, we used a 305 μm thick PZT (lead–titanium–zirconate) sensor, for both BPPE and FPPE. The radiation source was a 60mW diode laser (630 nm) electronically modulated. For the BPPE configuration, the sample thickness is controlled by an attached micrometer. For the FPPE configuration, a frequency scan is performed. In both configurations the sample and sensor were considered thermally thick, and the pyroelectric signal was measured by a SR830 lock-in analyser, using current mode. The hydrogels were produced using sodium alginate (Sigma-Aldrich) and Ca-EDTA (Ethylenediamine tetraacetic acid) (Sigma-Aldrich), with glacial acetic acid (Vetec, P.A) being used to release Ca^{2+} and give rise to the ionic exchange/gelation.

Measurements of thermal diffusivity and effusivity for reference samples, as ethylene glycol, water and ethanol, are in agreement with literature (accuracy of 1-3%). SA samples were characterized in three

concentrations (aqueous solutions of 1%, 2% and 3%) and the values of thermal diffusivity and effusivity do not present significant differences, with values in the ranges (1.45 - 1.46)x10^{-7} m^2/s and (1460 – 1510) $W.s^{1/2}.m^{-2}.K^{-1}$, respectively.

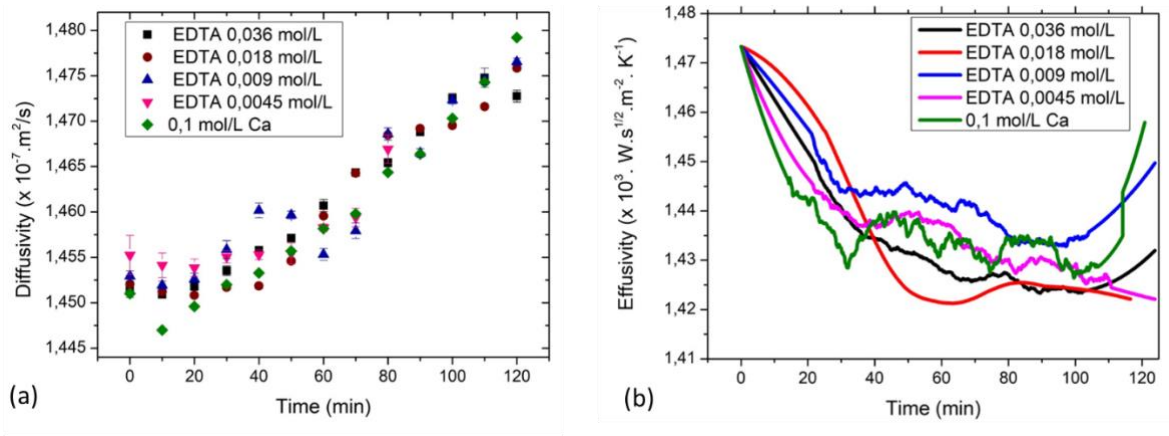

Fig. 1. (a) Thermal diffusivity and **(b)** thermal effusivity of the 3% alginate sample as function of time.

Figure 1(a) shows the thermal diffusivity of the 3% alginate sample, for several EDTA concentrations. The values seem to be constant until 30 minutes and then present a linear increase. The same behaviour is observed for all EDTA concentrations. For the same alginate concentration (3%), figure 1(b) presents the thermal effusivity as function of time, for several EDTA concentrations. We observe a slightly decreasing during the first 30 minutes followed by a noisy constant-like behaviour.

The PPE methodology showed to be suitable for hydrogels thermal characterization and sensitive to changes promoted by the gelation process. It is worth to mention that we also have the drying of the hydrogels, which happens simultaneously to the gelation (data not shown). It is well known that the gelation process occurs mainly during the 20-30 minutes [2], so that thermal effusivity seem to be more sensitive than thermal diffusivity, which probably undergo the changes in Fig. 1(a) more due to drying than the gelation.

References

[1] A.O. Guimarães et al., Investigating thermal properties of biodiesel/diesel mixtures using photopyroelectric technique, Thermochimica Acta. 527 (2012) 125-130. https:// doi:10.1016/j.tca.2011.10.016

[2] P.O. Vargas et al., Shrinkage and deformation during convective drying of calcium alginate, LWT - Food Science and Technology. 97 (2018) 213-222. https://doi.org/10.1016/j.lwt.2018.06.056

12
Analytical Chemistry and Photochemistry

Absolute fluorescence quantum yield spectra of light scattering samples determined using thermal lens spectroscopy aided by optical absorbance and fluorescence measurements

Vargas E(1), Castellanos-Duran F(1)*, Mendicuti E(2), García-Segundo C(2), Rojas-Trigos JB(1), Calderón A(1), Marín(1)

(1) Instituto Politécnico Nacional, Centro de Investigación en Ciencia Aplicada y Tecnología Avanzada (CICATA) Unidad Legaria, Legaria 694, Col. Irrigación, Ciudad de México 11500, Mexico
(2) Instituto de Ciencias Aplicadas y Tecnología (ICAT), Universidad Nacional Autónoma de México, Circuito Exterior S/N, Ciudad Universitaria, AP 70-186, 04510, Ciudad de México, Mexico

*Corresponding author's email: fcastellanosd2100@alumno.ipn.mx

It has been demonstrated that thermal lens spectroscopy can be a useful tool to characterize the quantum yields of scattering [1] and fluorescence [2] in samples that experience separately these phenomena in their interaction with light. However, to the authors knowledge there are not reports about the measurement of this parameter when both phenomena are present simultaneously, as can occur often, for example in biological media. In this work, we implemented a pump-probe thermal lens spectrometer that uses a broadband high pressure Xe-arc lamp and a monochromator to generate the pump light source of variable wavelength between 350 and 700nm. The light is focused onto the sample to generate the thermal lens effect that is sensed by a collimated probe light beam provided by a low-power HeNe laser. The intensity of the pump beam is periodically modulated at a low frequency and the probe beam intensity is measured at the far field using a photodiode whose signal is fed to a Lock-in amplifier synchronized at the light modulation frequency. This home-made system is fully automatized to record a photothermal spectrum of a sample in a few minutes. A commercial UV- Vis Spectrophotometer is coupled to the experimental system to also record the sample´s absorbance and fluorescence excitation spectra. Combining these measurements, the quantum yield efficiency spectrum of fluorophores in a scattering solution can be determined and compared with that obtained without scattering. The test-samples studied were ethanol solutions of the Rhodamine 6G fluorophore, and scattering was produced by colloidally suspended polystyrene microbeads. The effects of luminescence quenching by a KI salt were also studied. We discuss an application of the technique for the characterization whole blood.

References

[1] A. Marcano, S. Alvarado, J. Meng, D. Caballero, E. Marín, R. Edziah, White light photothermal lens spectrophotometer for the determination of absorption in scattering samples, Appl. Spect. 68 (2014) 680-685. https://doi.org/10.1366/13-07385.

[2] J. Hung, A. Marcano, J. Castillo, J. González, V. Piscitelli, A. Reyes, A. Fernández, Thermal lensing and absorbance spectra of fluorescent dye solution, Chem. Phys. Lett. 386 (2004) 206-210. https://doi.org/10.1016/j.cplett.2004.01.058.

Photoacoustic calorimetry study of the conformational variation of the chignolin peptide induced by a pH jump

Amado D(1)*, Serpa C(1)

(1) CQC-IMS, Department of Chemistry, University of Coimbra, 3004-535 Coimbra, Portugal

*Corresponding author's email: samadodaniela2@gmail.com

Background – Most proteins need to fold into a certain tridimensional structure, known as its native structure, to perform its biological functions. Thus, understanding all the mechanisms involved in protein folding is important to the development of models capable of predicting the impact that certain variables might have on the thermodynamics and kinetics of these processes and consequently improve the comprehension of certain diseases. The study of small peptides, such as β-hairpins, may help to understand these questions. These motifs may incorporate important catalytic residues and they can also be nucleation sites in the early stages of protein folding. All these features together make them good models for studying protein folding.

Chignolin is a decapeptide (GYDPETGTWG) designed by Honda et al.[1]. Its stability is mainly due to the number of non-covalent interactions (hydrogen bonds and hydrophobic interactions between Tyr2-Trp9 and Tyr2-Pro4), established during the folding process. CD and RMN studies carried out by Honda and collaborators, have shown that the peptide does not have any intermediate state. With the aim to study the folding mechanism of chignolin in an atomic level, computational studies have been performed. However, there are contradictory trends among them. Whereas some reports have been claiming the hydrophobic collapse model, first presented by Dinner et al.[2], Harada and Kitao, defend the zipper model developed by Muñoz et al.[3] Thus, the folding/unfolding mechanism for chignolin is still not totally unravelled, needing additional experimental assays and further computational calculations to clarify it.

Here, we intend to study the specific role of Tyr2-Trp9 in the short-length β-hairpin peptide Chignolin in aqueous media. Laser induced pH jump coupled with time-resolved photoacoustic calorimetry (TR-PAC) in a controlled temperature setup is unique for the investigation of the conformational protonation effects on this single stabilizing structure. The structural rearrangement is characterized in terms of kinetics and volume changes.

Methods – Experiments of laser-induced pH jump coupled with TR-PAC were accomplished using a homemade time-resolved photoacoustic calorimetry flow cell with temperature control and automatic injection (Figure 1). The photoacoustic pressure waves were detected using both 2.25 and 1 MHz frequency microphones. Analysis of the photoacoustic waves was performed with the CPAC software developed in our laboratory and available online (http://cpac.qui.uc.pt/) [4]. We carried out circular dichroism studies in the near and in the far-UV with the chignolin peptide.

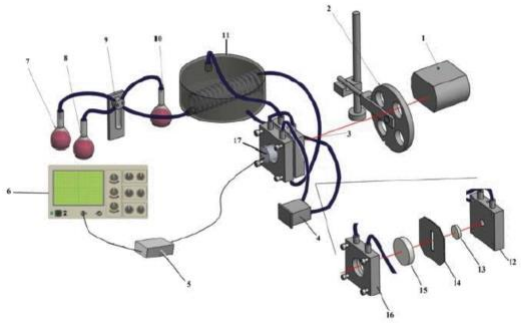

1- Laser
2- Neutral filters
3- Photoacoustic cell
4- Thermal bath
5- Ultrasonic amplifier
6- Oscilloscope
7,8,10-Syringes
9- Pump
11- Chamber
12,16- Blocks
13- Quartz window
14- Copper foil
15- Dielectric mirror

Results and conclusions – We first performed circular dichroism studies which allowed us to conclude that at a pH over 10 there is a loss of the β-sheet structure, possibly due to deprotonation of the Tyr2 side chain, which has a pKa of approximately 10.3. Considering this, we performed two-temperature TR-PAC experiments to characterize the protonation of the amino acid model Ac-Tyr-NH_2, the protonation of the Tyr2 side chain, which is embedded in the peptide chain, and the refolding process resultant from this protonation. This approach allowed us to calculate the lifetime and the volume change of these reactions, using the software CPAC. For the model Ac-Tyr-NH_2 the rate constant associated with the protonation of its side chain was approximately $8.5x10^9$ $M^{-1}s^{-1}$ and the corresponding volume changes was 8.7 mL mol^{-1}. For Tyr2 we obtained a rate constant of $2.8x10^{10}$ $M^{-1}s^{-1}$ and volume change of 4.9 mL mol^{-1}. For the process of refolding associated with the protonation of the side chain of Tyr2, we obtained a volume change of roughly 10.4 mL mol-1, indicating that the folding of chignolin is related to a volume expansion. Regarding the time related to this event, our experiments point out to a refolding time of ~1.15 μs. Based on these results, we presume that the hydrophobic collapse model, developed by Dinner et al. [2], is possibly the most accurate at describing the mechanism of folding of chignolin.

Acknowledgments – This work was supported by the Portuguese Science Foundation FCT (UIDB/00313/2020).

References

[1] S. Honda, K. Yamasaki, Y. Sawada, and H. Morii, 10 Residue folded peptide designed by segment statistics, Structure, 12(8) (2004) 1507–1518. doi: 10.1016/j.str.2004.05.022.

[2] L. T. Karplus M, A.R. Dinner, Understanding β -hairpin formation Proc. Natl. Acad. Sci. USA, 96 (1999) 9068–9073.

[3] V. Muñoz, E. R. Henry, J. Hofrichter, and W. A. Eaton, A statistical mechanical model for β-hairpin kinetics, Proc. Natl. Acad. Sci. U S A., 95(11) (1998) 5872–5879, doi: 10.1073/pnas.95.11.5872.

[4] F. A. Schaberle, F. D. A. M. G. Rego Filho, L. A. Reis, L. G. Arnaut, Assessment of lifetime resolution limits in time-resolved photoacoustic calorimetry vs. transducer frequencies: Setting the stage for picosecond resolution, Photochem. Photobiol. Sci., 15(2) (2016) 204–210. doi: 10.1039/c5pp00397k.

Miniaturized gel electrophoresis-thermal lens technique as a highly sensitive photothermal detection method

Abbasgholi-NA B[(1,2)*], Alsadig A[(1,3)], Casalis L[(1)], Parisse P[(1)], Cabrera H[(2)]

(1) NanoInnovation Laboratory, Elettra-Sincrotrone Trieste S.C.P.A, Trieste, Italy
(2) Optics Lab, STI Unit, The Abdus Salam International Centre for Theoretical Physics, Trieste 34151, Italy
(3) PhD School in Nanotechnology, University of Trieste, Piazzale Europa, 1, 34127 Trieste TS, Italy

*Corresponding author's email: Be.asbaghi@yahoo.com

Miniaturized Gel Electrophoresis Chip-Thermal Lens Microscopy (MGEC-TLM) can represent a powerful detection method based on photothermal phenomena for monitoring the electrophoretic mobility of biofunctionalized nanoparticles [1]. It is crucial to optimize the amount of DNA on the surface of biosensors-based DNA functionalized AuNPs [2-3]. Here, MGEC-TLM was used to detect the coverage density of thiol-functionalized oligonucleotides on the surface of gold nanoparticles (AuNPs).

TLM is a powerful photothermal technique that relies on the measurement of temperature changes, caused by the heat generated as a result of absorbed optical radiation. In other words, it is an indirect absorption spectroscopic detection method, which its sensitivity is at least a hundred-fold higher than that of optical absorbance spectrometry. The reason is that the sensitivity of the technique is proportional to the so-called enhancement factor ($E = [P(\partial n/\partial T)/\lambda k)]$ which depends on the thermo-optical properties of the sample such as the temperature coefficient of the refractive index ($\partial n/\partial T$), the wavelength of the probe beam (λ), the excitation power (P) and the thermal conductivity (k) [4]. Moreover, Thermal Lens Microscopy (TLM) offers high spatial resolution and can measure low volumes of nonfluorescence molecules or nanoparticles subjected to analysis in a microchannel.

In this system a 532 nm diode-pumped solid-state laser of maximum power of 100 mW is used as an excitation source (EL). A signal generator (SG) modulates the EL at a frequency of 118 Hz. A neutral density filter (NF) is placed after the EL to adjust its power to 15 mW. The excitation beam coming from the EL is first collimated by the lens L1 and L2. After that, the beam is focused onto the MGEC channel using a 0.25NA focusing objective. The probe laser (PL), a He-Ne laser, is collimated by a set of lenses and directed to the sample using the mirrors. Then the beam is directed to a Silicon detector (PD) across a 0.5 mm pinhole (P) and an interference filter (F2). The 532 nm filter (F1) was used for removing any residual emission of the fundamental wavelength 1064 nm. The analog signal from the photodiode is filtered and amplified using a lock-in amplifier and further digitalized at 1 k samples/s sampling rate. The data acquisition system mainly consists of a microcontroller based digitization Arduino board and a graphical user interface (GUI) running on a PC. The GUI was build using the LabVIEW graphical programming software to visualize the incoming data, capture the TLS signal (peaks) and online recording of data. A power supply (EPS) is used to supply the desired voltage for electrophoretic nanoanalysis of NPs in the MGEC (Fig.1).

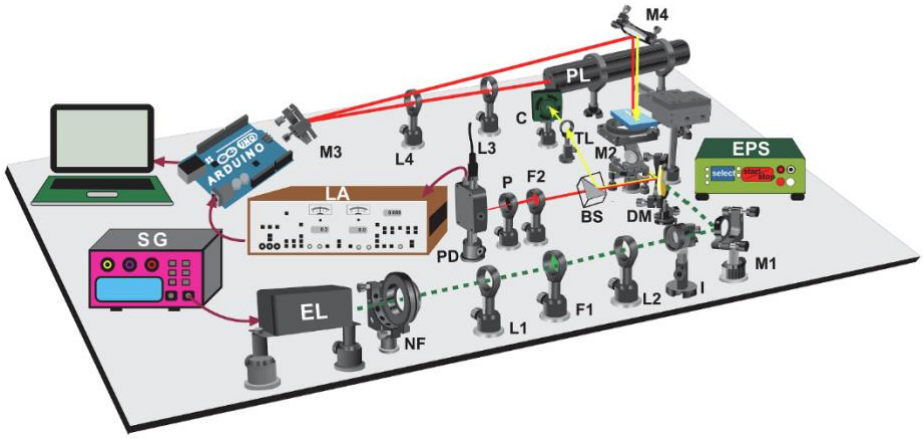

Fig. 1. Schematic illustration of MGEC-TLM, EL: excitation laser, PL: probe laser, C: CMOS camera, PD: photodiode, NF: neutral densityfilter, L1 to L4: lenses, M1 to M4: mirrors, DM: dichroic mirror, OL: focusing objective, P: pinhole, F1: 532 nm filter, F2: 632.8 nm filter, I: iris, BS: beam spliter, TL: tube lens, SG: signal generator, LA: lock-in amplifier, EPS: electrophoresis power supply

We developed a rapid yet sensitive approach for online monitoring the surface coverage of ssDNA loaded on AuNPs using MGEC coupled with TLS. Unlike conventional methods for determining the surface coverage, the design presented here does not require long signal acquisition times or tedious post-treatment steps including chemical modifications. With our implementation, we demonstrated an excellent electrophoretic analysis of DNA strands attached to AuNPs and a rapid nanoparticle separation in the gel. We showed that for 13 nm-AuNPs and short DNA strands (<30 bases), 300 DNA/AuNPs density can fully coat the particles, which represent a conjugate with high stability. The lowest detectable concentration of 10 nm AuNPs was found to be 23 pM. The use of TLS coupled with MC and MGEC holds great promise in biotechnology and nanotechnology fields, given its efficiency, speed, and throughput.

References

[1] B. Abbasgholi-NA, A. Alsadig, Cabrera H. Online electrophoretic nanoanalysis using miniaturized gel electrophoresis and thermal lens microscopy detection. Journal of Chromatography A 1657 (2021) 462596.

[2] L. Olofsson, T. Rindzevicius, I. Pfeiffer, M. Kall, F. Hook, Surface-based gold-nanoparticle sensor for specific and quantitative DNA hybridization detection, Langmuir (2003) 10414-10419.

[3] A. Alsadig, H. Vondracek, P. Pengo, L. Pasquato, P. Posocco, P. Parisse, L. Casalis, Label-Free, Rapid and Facile Gold-Nanoparticles-Based Assay as a Potential Spectroscopic Tool for Trastuzumab Quantification, Nanomaterials 11:12 (2021) 3181.

[4] M. Liu, M. Franko, Progress in thermal lens spectrometry and its applications in microscale analytical devices, Crit. Rev. Anal. Chem. 44:4 (2014) 328–353.

ICPPP21

Bled • Slovenia

https://indico.ung.si/event/5/

University *of Ljubljana*

Jožef Stefan Institute